<div align="center">

STRUCTURE
OF ORGANIC COMPOUNDS

</div>

Crystal Structure of the New Radical Cation Salt
($DOET$)$_4$[Fe(CN)$_5$NO]$_{1.25}$(C$_6$H$_5$Cl)$_{0.75}$

L. V. Zorina*, S. S. Khasanov*, R. P. Shibaeva*, I. Yu. Shevyakova**,
A. I. Kotov**, and É. B. Yagubskiĭ**

* Institute of Solid State Physics, Russian Academy of Sciences, Chernogolovka,
Noginskiĭ raĭon, Moscow oblast, 142432 Russia
e-mail: skhasan@issp.ac.ru
** Institute for Problems of Chemical Physics, Russian Academy of Sciences,
Chernogolovka, Noginskiĭ raĭon, Moscow oblast, 142432 Russia
Received August 1, 2003

Abstract—A new radical cation salt based on 4,5-(1,4-dioxanediyl-2,3-dithio)-4',5'-ethylenedithiotetrathiaful-valene ($DOET$) with the photochromic anion [Fe(CN)$_5$NO]$^{2-}$, namely, ($DOET$)$_4$[Fe(CN)$_5$NO]$_{1.25}$(C$_6$H$_5$Cl)$_{0.75}$, is synthesized. Single crystals of this salt are studied using X-ray diffraction [$a = 10.398(2)$ Å, $b = 11.168(2)$ Å, $c = 18.499(4)$ Å, $\alpha = 103.14(3)°$, $\beta = 92.80(3)°$, $\gamma = 106.02(3)°$, $V = 1996.3(7)$ Å^3, space group $P\bar{1}$, and $Z = 1$]. In the structure, radical cation layers alternate with anion layers along the c axis. The centrosymmetric dimers are formed by $DOET$ radical cations in the donor layer with packing of the β type. Like the vast majority of $DOET$-based salts, the new salt possesses semiconductor properties. © 2004 MAIK "Nauka/Interperiodica".

INTRODUCTION

In recent years, considerable research attention has been focused on the design of new synthetic functional (conducting and magnetic) materials that can serve as an alternative to traditional conductors and magnets. These materials are promising for technical application in new fields of engineering due to their specific features and (or) an unusual combination of properties.

From this point of view, molecular organic conductors are especially interesting objects of investigation. Materials based on organic molecules exhibit a great variety of conducting properties. Among these materials are semiconductors, stable metals, and superconductors with the highest superconducting transition temperature $T_C = 14.2$ K [1–4]. The unique properties manifested by compounds of this class have stimulated a purposeful search for new methods of synthesizing multifunctional molecular materials with controlled properties, in particular, through introducing anions with specific physical properties into a conducting organic matrix.

Following this idea, we synthesized and investigated a number of new radical cation salts with the photochromic nitroprusside anion [Fe(CN)$_5$NO]$^{2-}$ on the basis of different π-electron organic donors, such as bis(ethylenedithio)tetrathiafulvalene ($BEDT$-TTF) [5–8], bis(ethylenedioxo)tetrathiafulvalene ($BEDO$-TTF) [5, 9], ethylenedithiotetrathiafulvalene (EDT-TTF) [5, 10], bis(dithiolanylidene)tetrathiapentalene (BDH-TTP) [11], tetrathiotetracene (TTT), and tetraselenotetracene ($TSeT$) [12]. In the present work, we continued

this series of investigations and studied a new salt based on the donor 4,5-(1,4-dioxanediyl-2,3-dithio)-4',5'-eth-ylenedithiotetrathiafulvalene ($DOET$), C$_{12}$H$_{10}$S$_8$O$_2$.
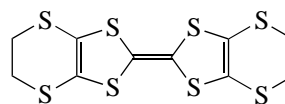
BEDT-TTF
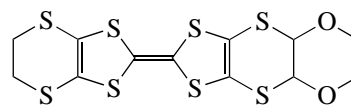
DOET

The modification of parent donor molecules is an efficient method for synthesizing new salts, which allows an understanding of the influence of the donor nature on the structure and properties of organic conductors. The majority of organic conductors and superconductors were prepared on the basis of the organic donor $BEDT$-TTF. The $DOET$ molecule differs from the $BEDT$-TTF molecule by an additional six-membered heterocycle containing two oxygen atoms. Owing to the presence of this heterocycle in the $DOET$ molecule, first, the total number of heteroatoms increases and, hence, the probability of forming side intermolecular contacts of the heteroatom···heteroatom type (in particular, additional contacts S···O and C···O) that provide interaction in the radical cation layer is higher. Second, the presence of oxygen atoms leads to the formation of C–H···O hydrogen bonds between the neighboring radical cations.

A distinguishing feature of the *DOET* molecule is its strongly bent shape: carbon atoms of the oxygen heterocycle form a plane nearly perpendicular to the plane of the central skeleton of the molecule. The formation of such a conformation can easily be explained in terms of the geometry of bonds. In the *BEDT-TTF* molecule, all carbon atoms, except for the carbon atoms involved in the outer ethylene groups, are characterized by a planar C_{sp}^2 configuration. In the oxygen heterocycle of the *DOET* molecule, both the outer and inner C–C bonds are single bonds and the stable C_{sp}^3 electronic state of the corresponding carbon atoms is provided by the attachment of an additional hydrogen atom. Therefore, the inner carbon atoms of the oxygen heterocycle adopt a bulk tetrahedral coordination, which, in turn, determines the bond directionality and the molecular shape.

The influence of the specific features revealed in the molecular structure of the *DOET* radical cation on the structure and properties of the salts synthesized will be demonstrated by using the example of a new radical cation salt, namely, $(DOET)_4[Fe(CN)_5NO]_{1.25}(C_6H_5Cl)_{0.75}$. In this work, we described the synthesis of the aforementioned new radical cation salt, performed an X-ray diffraction analysis of its crystal structure, and investigated the conducting properties of the single crystals.

EXPERIMENTAL

Synthesis of $(DOET)_4[Fe(CN)_5NO]_{1.25}(C_6H_5Cl)_{0.75}$

4,5-(1,4-Dioxanediyl-2,3-dithio)-4',5'-ethylenedithiotetrathiafulvalene (*DOET*) was synthesized according to the procedure described in [13] and purified chromatographically. Potassium nitroprusside $K_2[Fe(CN)_5NO] \cdot 2H_2O$ was prepared using the procedure proposed in [14]. Chlorobenzene (Aldrich) was twice distilled over P_2O_5. 18-Crown-6 (Flucka) was purified by recrystallization in acetonitrile and dried under vacuum at a temperature of 30°C. Ethanol (Aldrich) was allowed to stand for 10 h over freshly calcinated calcium oxide at the boiling temperature (78.3°C) and was then distilled. All the solvents used were stored in an inert atmosphere.

The $(DOET)_4[Fe(CN)_5NO]_{1.25}(C_6H_5Cl)_{0.75}$ radical cation salt was prepared by electrochemical oxidation of *DOET* in the presence of a $K_2[Fe(CN)_5NO] \cdot 2H_2O$ supporting electrolyte [15]. *DOET* (1.14×10^{-3} mol/l) and a mixture of $K_2[Fe(CN)_5NO] \cdot 2H_2O$ (2.4×10^{-3} mol/l) with 18-crown-6 (4.9×10^{-3} mol/l) were placed in different arms of an *H*-shaped electrochemical cell and dissolved in a mixture of chlorobenzene (20 ml) with ethanol (1 ml). The dissolution was carried out at room temperature for 4 h in an argon atmosphere with continuous stirring. Then, the electrochemical cell was sealed, placed in an air thermostat, and connected to a

dc power supply. A platinum wire 1 mm in diameter was used as electrodes.

Electrocrystallization was performed under direct current conditions ($I = 0.5 \mu A$) at a temperature of 25°C for 12 days. Crystals grew on the anode in the form of black plates approximately $0.8 \times 0.9 \times 0.07$ mm^3 in size. The crystals were filtered off, washed thoroughly with acetone, and dried in air.

X-ray Diffraction Analysis

The main crystal data are as follows: $a = 10.398(2)$ Å, $b = 11.168(2)$ Å, $c = 18.499(4)$ Å, $\alpha = 103.14(3)°$, $\beta = 92.80(3)°$, $\gamma = 106.02(3)°$, $V = 1996.3(7)$ Å^3, space group $P\bar{1}$, $Z = 1$ for the formula composition $C_{58.75}H_{43.75}Cl_{0.75}Fe_{1.25}N_{7.5}O_{9.25}S_{32}$, $M = 2125.1$, $F(000) = 1080$, $\rho_{calcd} = 1.768$ g/cm^3, and $\mu(MoK_\alpha) = 11.54$ cm^{-1}. The experimental set of diffraction data involving 7336 reflections (6999 unique reflections, $R_{int} = 0.012$, $R_\sigma = 0.022$) was collected on an Enraf–Nonius CAD4 automated diffractometer (MoK$_\alpha$ radiation, $\lambda = 0.71073$, graphite monochromator, $\theta = 2.5°$–25.0°, ω scan mode) at room temperature. The structure was solved by direct methods with subsequent Fourier syntheses according to the SHELXS97 software package [16] and refined by the full-matrix least-squares procedure with the SHELXL97 software package [17]. All non-hydrogen atoms (except for the disordered atoms in positions with a low occupancy in the *DOET* molecule **I** and the anion) were refined in the anisotropic approximation. The hydrogen atoms were located from geometric considerations with the isotropic thermal parameters $U_H = 1.2U_C$. The final *R* factor is equal to 0.056 and *GOOF* = 1.047 for 5483 unique reflections with $I > 2\sigma(I)$ for 699 parameters refined.

Conductivity Measurements

The conducting properties were investigated on an automated setup in the temperature range 315–4.2 K. The resistance was measured by the standard four-point probe method under direct current along the long crystal edge, which coincides with the *a* axis. The sample was cemented to platinum wires (10 μm in diameter) of the measuring unit with the use of a conducting graphite paste (Dotite paint, XC-12).

RESULTS AND DISCUSSION

The $(DOET)_4[Fe(CN)_5NO]_{1.25}(C_6H_5Cl)_{0.75}$ crystals have a layered structure in which the radical cation layers alternate with the anion layers along the *c* axis. Figure 1 shows the projection of the structure along the [110] direction. In the conducting donor layer, there are two crystallographically independent radical cations *DOET* **I** and **II** (Fig. 2). The terminal ethylene groups and oxygen heterocycles in both radical cations are disordered, and the atomic positions are separated. The
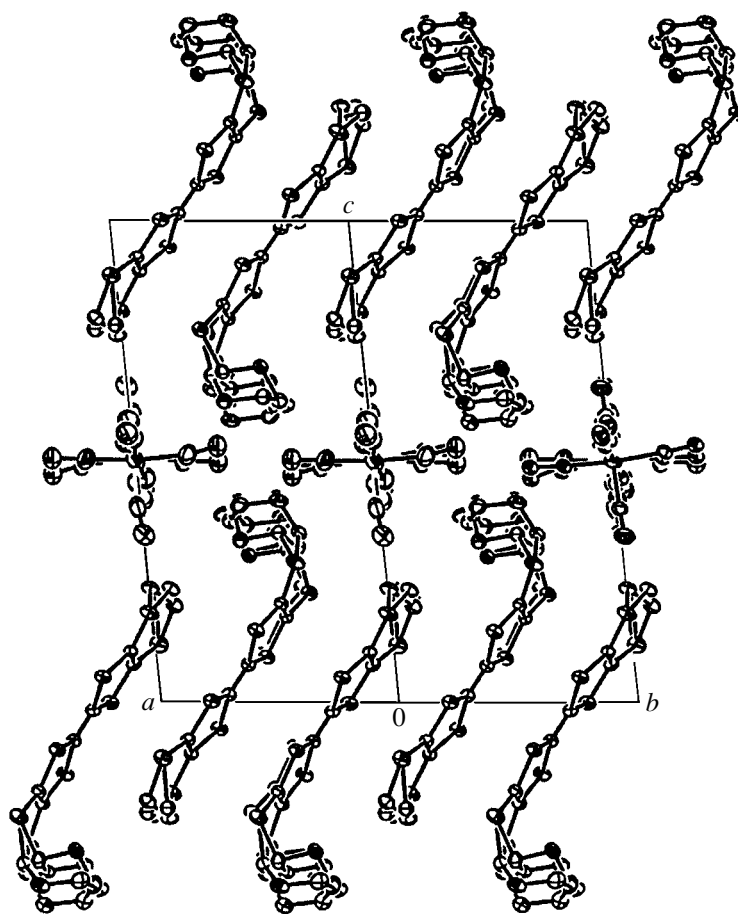
Fig. 1. Projection of the $(DOET)_4[Fe(CN)_5NO]_{1.25}(C_6H_5Cl)_{0.75}$ structure along the [110] direction.

central *DOET* skeleton is more planar than that in the neutral molecule [13, 18]: the dihedral angles between the planes of three S_4C_2 fragments are equal to 1.6° and 5.6° in *DOET* **I** and 3.0° and 5.5° in *DOET* **II**. The bond lengths in the *DOET* radical cations are given in Table 1. The length of the central C=C bond in the *TTF* fragment is equal to 1.363(5) Å in *DOET* **I** and 1.373(5) Å in *DOET* **II**. This corresponds to a formal charge of +2/3 in the *DOET* radical cation. The angles between the plane formed by the carbon atoms of the oxygen heterocycle and the central plane of the *DOET* cation are equal to 99.5° or 93.1° (in **Ia** and **Ib**, respectively) and 99.2° or 98.1° (in **IIa** and **IIb**, respectively). These angles are close to the corresponding angle (97.1°) in a similar molecule considered in [19]. The C_4O_2 heterocycles adopt a chair conformation: the oxygen atoms deviate in different directions from the midplane of the carbon atoms by –0.582(6) and +0.658(6) Å in *DOET* **Ia**, –0.85(4) and +0.72(4) Å in *DOET* **Ib**, +0.607(8) and –0.681(8) Å in *DOET* **IIa**, and –0.074(2) and +0.67(2) Å in *DOET* **IIb**. The hydrogen atoms bonded to the inner carbon atoms of the oxygen heterocycle occupy the *cis* positions with respect to

each other. The angles between the C–H bonds are approximately equal to 50°.

Most likely, the perpendicular position of the oxygen heterocycle favors the formation of a stable β structure of the conducting layer with a considerable mutual longitudinal displacement of radical cations in *DOET* salts. This displacement provides a way of arranging bent molecules in a layer (Figs. 3a, 3b). Earlier, the β-type packing was also found in the $(DOET)_2ReO_4$ [20], $(DOET)_2BF_4$ [21], and $(DOET)_2HSO_4$ [22] salts. In $(DOET)_4Hg_2Cl_6$ and $(DOET)_4Hg_2Br_6$ crystals [22, 23], the packing of radical cations is intermediate between the α- and β-type packings but more similar to the β-type packing: the *DOET* molecules of adjacent stacks are not parallel to each other, and the dihedral angle between their midplanes is equal to 12°–14° [23].

In the conducting layer of the $(DOET)_4[Fe(CN)_5NO]_{1.25}(C_6H_5Cl)_{0.75}$ structure, all the radical cations are parallel to each other and form stacks along the [1$\bar{1}$0] direction. Centrosymmetric dimers are formed by the *DOET* cations in the stacks (Fig. 3b). Radical cations **I–I**$_i$ and **II–II**$_i$ are characterized by direct overlapping (Fig. 4a). In each dimer,
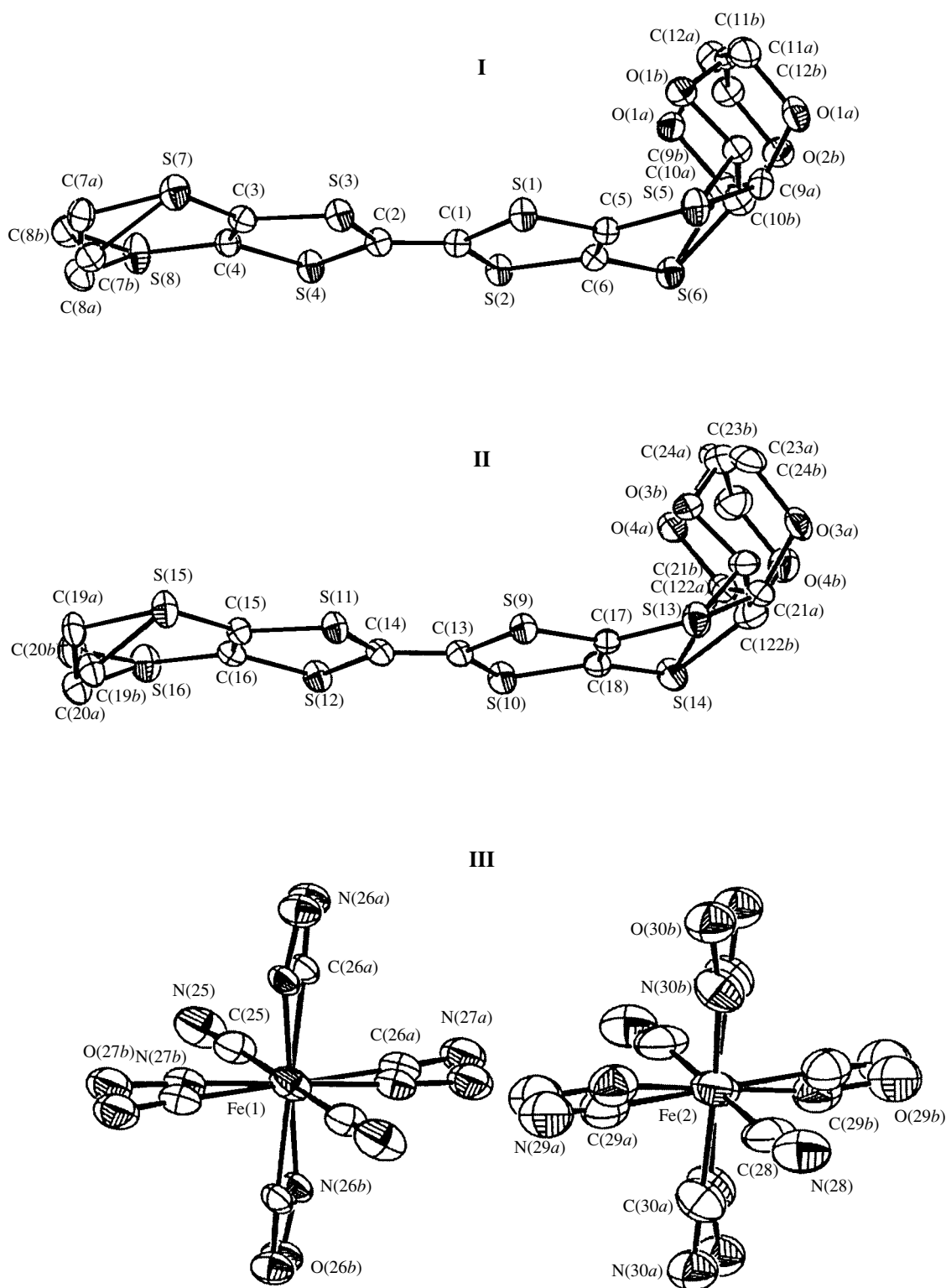
I

II

III

Fig. 2. Atomic numbering in radical cations *DOET* **I** and **II** and nitroprusside anions.

there are four shortened intermolecular contacts S···S ≤ 3.70 Å (Table 2). The distances between the central planes of the *DOET* cations in dimers are very close to each other and equal to 3.62(2) and 3.630(6) Å, respec-tively. The adjacent dimers are almost parallel to each other: the dihedral angle between the midplanes of rad-ical cations **I** and **II** is equal to 2.05(7)°. The oxygen heterocycles of the donors are located between the

Table 1. Bond lengths (*d*, Å) in radical cations *DOET* **I** and **II** in the studied structure

Bond in **I**	*d*	Bond in **II**	*d*
S(1)–C(1)	1.737(4)	S(9)–C(13)	1.734(4)
S(1)–C(5)	1.739(4)	S(9)–C(17)	1.736(4)
S(2)–C(6)	1.730(4)	S(10)–C(13)	1.736(4)
S(2)–C(1)	1.742(4)	S(10)–C(18)	1.738(4)
S(3)–C(3)	1.728(4)	S(11)–C(14)	1.728(4)
S(3)–C(2)	1.733(4)	S(11)–C(15)	1.744(4)
S(4)–C(2)	1.729(4)	S(12)–C(16)	1.730(4)
S(4)–C(4)	1.747(4)	S(12)–C(14)	1.733(4)
S(5)–C(5)	1.732(4)	S(13)–C(17)	1.738(4)
S(5)–C(9*b*)	1.814(10)	S(13)–C(21*b*)	1.792(9)
S(5)–C(9*a*)	1.865(4)	S(13)–C(21*a*)	1.888(6)
S(6)–C(6)	1.744(4)	S(14)–C(18)	1.734(4)
S(6)–C(10*a*)	1.790(4)	S(14)–C(22*a*)	1.785(5)
S(6)–C(10*a*)	1.833(10)	S(14)–C(22*b*)	1.865(9)
S(7)–C(3)	1.734(4)	S(15)–C(15)	1.732(4)
S(7)–C(7*a*)	1.775(5)	S(15)–C(19*a*)	1.782(10)
S(7)–C(7*b*)	1.94(3)	S(15)–C(19*b*)	1.823(12)
S(8)–C(8*b*)	1.67(3)	S(16)–C(20*b*)	1.678(12)
S(8)–C(4)	1.726(4)	S(16)–C(16)	1.736(4)
S(8)–C(8*a*)	1.818(5)	S(16)–C(20*a*)	1.907(11)
C(1)–C(2)	1.363(5)	C(13)–C(14)	1.373(5)
C(3)–C(4)	1.360(5)	C(15)–C(16)	1.356(5)
C(5)–C(6)	1.347(5)	C(17)–C(18)	1.351(5)
C(7*a*)–C(8*a*)	1.501(8)	C(19*a*)–C(20*a*)	1.490(17)
C(7*b*)–C(8*b*)	1.57(4)	C(19*b*)–C(20*b*)	1.541(17)
C(9*a*)–O(1*a*)	1.400(5)	C(21*a*)–O(3*a*)	1.418(6)
C(9*a*)–C(10*a*)	1.522(6)	C(21*a*)–C(22*a*)	1.519(7)
C(10*a*)–O(2*a*)	1.403(6)	C(22*a*)–O(4*a*)	1.394(6)
O(1*a*)–C(11*a*)	1.431(6)	O(3*a*)–C(23*a*)	1.448(7)
O(2*a*)–C(12*a*)	1.439(7)	O(4*a*)–C(24*a*)	1.444(9)
C(11*a*)–C(12*a*)	1.510(9)	C(23*a*)–C(24*a*)	1.498(10)
C(9*b*)–O(1*b*)	1.403(10)	C(21*b*)–O(3*b*)	1.394(9)
C(9*b*)–C(10*b*)	1.524(11)	C(21*b*)–C(22*b*)	1.519(9)
C(10*b*)–O(2*b*)	1.406(10)	C(22*b*)–O(4*b*)	1.409(9)
O(1*b*)–C(11*b*)	1.42(2)	O(3*b*)–C(23*b*)	1.417(17)
O(2*b*)–C(12*b*)	1.441(13)	O(4*b*)–C(24*b*)	1.415(14)
C(11*b*)–C(12*b*)	1.52(2)	C(23*b*)–C(24*b*)	1.520(18)

dimers. Therefore, the distance between *DOET* **I** and *DOET* **II** is rather large [3.85(5) Å] and the relative displacement of radical cations *DOET* **I** and *DOET* **II** is approximately equal to 1/3 of the length of the *DOET* molecule. There arises an overlapping of the "bond-over-ring type": the C_4S_2 outer six-membered ring is located above the central C=C bond of the adjacent molecule (Fig. 4b). All the S···S and S···C distances between *DOET* **I** and *DOET* **II** are larger than the sum of the van der Waals radii. However, the bent shape of the molecules leads to the formation of two C–H···O terminal contacts: C(8*b*)–H(8*b*2)···O(4*a*) = 2.52 Å (angle, 116.4°) and C(19*a*)–H(19*b*)···O(1*b*) = 2.59 Å (angle, 114.7°). A large number of shortened contacts (especially of the S···S type) are formed in the conducting layer between stacks (Table 2).

In the *DOET* structure, the oxygen heterocycles of adjacent layers are virtually parallel to each other and are rather closely spaced. However, unlike the $(DOET)_2ReO_4$ salt, no shortened contacts of the C–H···O type are formed between these heterocycles [20]. The shortest H···O distances between *DOET* molecules **I** located in different layers are equal to 2.72 and 2.82 Å, and the corresponding distances between *DOET* molecules **II** are larger than 3.08 Å. Most likely, this is associated with the difference in the size and shape of the anions: large-sized octahedral nitroprusside anions create a higher barrier to approach of radical cations of adjacent layers as compared to smaller sized ReO_4 tetrahedra.

Apart from the nitroprusside anions, the anion layer contains chlorobenzene solvent molecules. The nitroprusside anions occupy two independent positions in the layer (Fig. 5). One position is completely occupied, and the second position is occupied by the anion and the solvent molecule in the ratio 0.25 : 0.75. Both anions are characterized by a disordered structure: two CN groups approximately aligned along the *c* axis are ordered, the other four positions partially contain NO groups (approximately 25%), and the positions of the CN and NO groups are separated. A large number of shortened intermolecular contacts of the S···N (3.256–3.304 Å), C···N (2.80–3.31 Å), C···O (2.82–3.29 Å), O···N (2.33–2.85 Å), and O···O (2.54 and 2.61 Å) types are formed between the cation and anion layers.

The electrical conductivity of the $(DOET)_4[Fe(CN)_5NO]_{1.25}(C_6H_5Cl)_{0.75}$ crystals at room temperature is equal to 0.9 Ω^{-1} cm^{-1} and exhibits a semiconductor temperature dependence (the activation energy E_a = 0.035 eV).

A large number of radical cation salts were prepared on the basis of the *DOET* donor. These salts contain discrete anions with different geometries (linear, tetrahedral, octahedral, etc.) [13, 21, 22]. Among them, the majority of compounds possess a low conductivity, several salts are metals with temperatures of the transition to the dielectric state from 30 to 170 K, and only one compound, $(DOET)_4Hg_2Cl_6$, retains metallic properties down to 4 K [22, 23]. The low conductivity of the $(DOET)_4[Fe(CN)_5NO]_{1.25}(C_6H_5Cl)_{0.75}$ salt can be associated with the dimerization within stacks in the conducting layer and the localization of charges in dimers.

Kotov *et al.* [22] noted that, among the *DOET*-based salts, the $(DOET)_2ReO_4$ crystals are characterized by
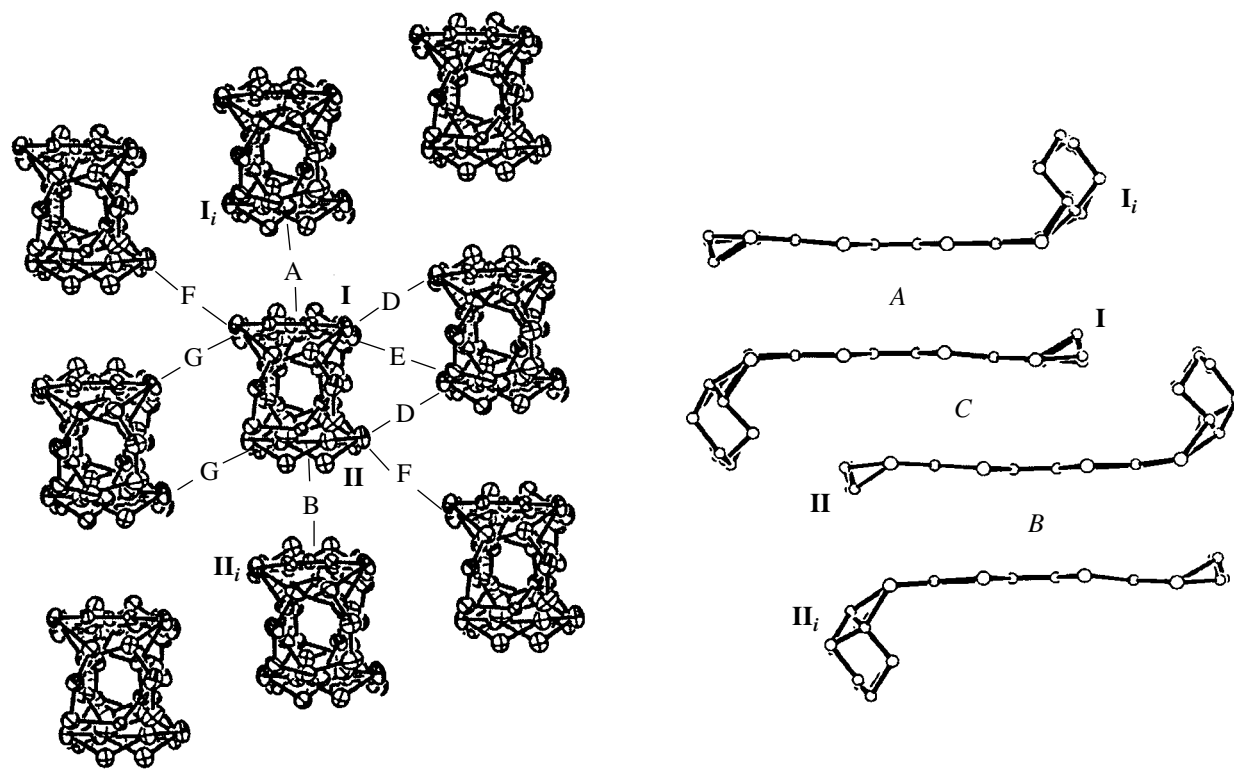
Fig. 3. (a) Projection of the radical cation layer along the central C=C bond of *DOET* and (b) lateral view of the *DOET* stack.
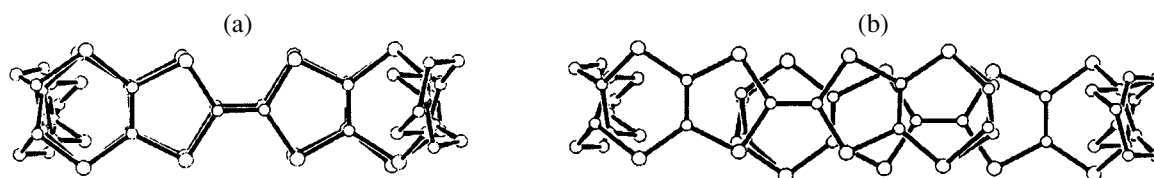

Fig. 4. Overlapping of the radical cations in a stack: (a) **I–I**$_i$ (*A*) and **II–II**$_i$ (*B*) and (b) **I–II** (*C*).

the strongest dimerization in the radical cation layer and possess semiconductor properties, whereas salts with a less pronounced dimerization are metals undergoing metal–dielectric transitions at different temperatures. In the $(DOET)_2ReO_4$ structure, the interplanar distance between dimers is equal to 3.69 Å and exceeds the intradimer distance by 0.1 Å [20]. In the salt studied in the present work, the distance between the *DOET* planes in the dimer (3.62 Å) is virtually identical to that observed in the $(DOET)_2ReO_4$ compound; however, the dimers are located at a larger distance (3.85 Å). This means that the degree of dimerization is higher. The differences in the structure of the conducting layer are in complete agreement with the salt properties: the $(DOET)_4[Fe(CN)_5NO]_{1.25}(C_6H_5Cl)_{0.75}$ compound is also a semiconductor, but its conductivity at room temperature is lower than that of the $(DOET)_2ReO_4$ compound. Therefore, for *DOET*-based salts, there is a pro-

nounced effect of anions of different configurations and sizes on the structure of the conducting layer with the same packing. As a consequence, these compounds possess different conducting properties.

A comparative analysis of the structures and properties of the salts based on different organic donors with the $[Fe(CN)_5NO]^{2-}$ anion [5–11] demonstrates that the asymmetric radical cations *EDT-TTF* and *DOET* form semiconductor crystals with a similar β-type packing of the conducting layer in which the radical cations are dimerized. The crystals based on the symmetric radical cations *BEDT-TTF*, *BEDO-TTF*, and *BDH-TTP* have a structure of the radical cation layer (β" or κ) which is favorable for conduction; these crystals are metals stable to liquid-helium temperatures.

As was noted above, the bent conformation of the *DOET* radical cation is most likely responsible for the formation of the stable β structure of the conducting
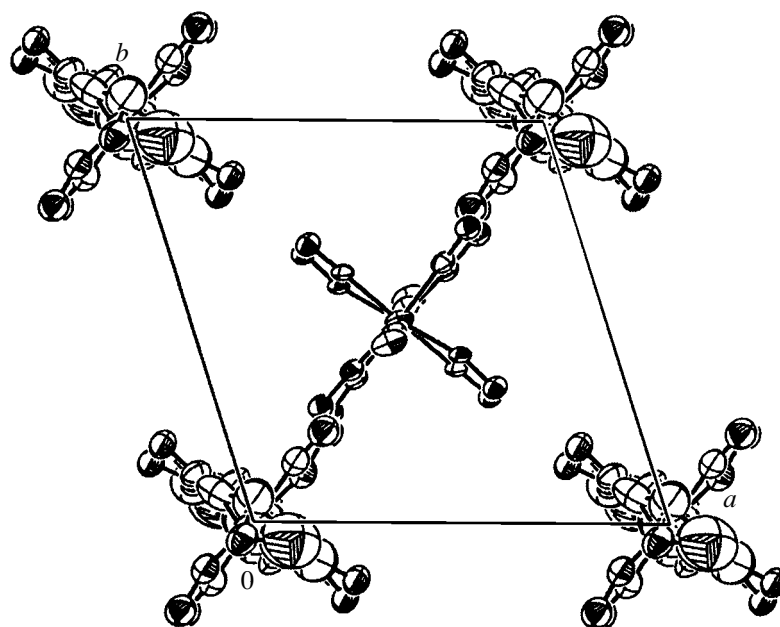
Fig. 5. Projection of the anion layer in the $(DOET)_4[Fe(CN)_5NO]_{1.25}(C_6H_5Cl)_{0.75}$ structure along the c direction.

layer. The other radical cations containing oxygen atoms in the outer heterocycle have a similar conformation [19, 24]. The replacement of oxygen atoms by sulfur atoms can lead to the two following situations: two six-membered heterocycles can be linked by both single and double C–C bonds; as a result, the molecule is bent in the former case and consists of S_4C_2 planar fragments in the latter case [18, 24]. It would be interesting to use a planar (unbent) donor for synthesizing new salts with a nitroprusside anion. Actually, this configuration leads to an increase in the probability of forming crystals with different packings of radical cation layers (as is the case with the *BEDT-TTF* donor), on the one hand, and to an increase in the number of peripheral sulfur atoms (as compared to that in the *BEDT-TTF* donor) capable of forming additional S···S contacts in conducting layers, on the other hand.

ACKNOWLEDGMENTS

Table 2. Shortened contacts S···S ($r \leq 3.70$ Å), S···C ($r \leq 3.65$ Å), S···O ($r \leq 3.35$ Å), and C···O ($r \leq 3.30$ Å) in the radical cation layer (interactions *A–G* in Fig. 3)

	S···S, Å	S···C, Å	S···O, Å	C···O, Å
A	3.675(×2), 3.601(×2)	3.62(×2), 3.42(×2)		
B	3.646(×2), 3.633(×2)	3.61(×2), 3.60(×2)		
C		3.55		3.25, 3.07, 3.12
D	3.591, 3.504, 3.650			
E	3.677(×2)			
F	3.685	3		
G	3.656, 3.560, 3.649, 3.537	3.59, 3.36	3.23	

REFERENCES

1. J. M. Williams, J. R. Ferraro, R. J. Thorn, *et al.*, *Organic Superconductors (Including Fullerenes): Synthesis, Structure, Properties, and Theory* (Prentice Hall, Englewood Cliffs, N.J., 1992).
2. T. Ishiguro, R. Yamaji, and G. Saito, *Organic Superconductors*, 2nd ed. (Springer-Verlag, Berlin, 1998).
3. H. Taniguchi, M. Miyashita, K. Uchiyama, *et al.*, J. Phys. Soc. Jpn. **72** (3), 468 (2003).
4. H. Kontani, Phys. Rev. B **67**, 180 503 (2003).
5. L. Kushch, L. Buravov, V. Tkacheva, *et al.*, Synth. Met. **102**, 1646 (1999).

6. M. Gener, E. Canadell, S. S. Khasanov, *et al.*, Solid State Commun. **111**, 329 (1999).

7. S. S. Khasanov, L. V. Zorina, and R. P. Shibaeva, Koord. Khim. **27** (4), 283 (2001).

8. S. V. Kapel'nitsky, É. B. Yagubskiĭ, L. A. Kushch, and I. Yu. Shevyakova, Pis'ma Zh. Éksp. Teor. Fiz. **76**, 199 (2002) [JETP Lett. **76**, 165 (2002)].

9. L. V. Zorina, S. S. Khasanov, R. P. Shibaeva, *et al.*, J. Mater. Chem. **10**, 2017 (2000).

10. L. V. Zorina, M. Gener, S. S. Khasanov, *et al.*, Synth. Met. **128**, 325 (2002).

11. L. V. Zorina, Candidate's Dissertation in Physics and Mathematics (Inst. of Solid State Physics, Russian Academy of Sciences, Chernogolovka, 2003).

12. I. Yu. Shevyakova, L. I. Buravov, L. A. Kushch, *et al.*, Koord. Khim. **28** (7), 520 (2002).

13. A. I. Kotov, L. I. Buravov, S. V. Konovalikhin, *et al.*, Synth. Met. **102**, 1630 (1999).

14. A. N. Gard and P. S. Goel, Inorg. Chem. **10** (7), 1344 (1971).

15. D. A. Stephens, A. E. Rehan, S. J. Compton, *et al.*, Inorg. Synth. **24**, 135 (1986).

16. G. M. Sheldrick, *SHELXS97: A Program for Automatic Solution of Crystal Structures* (Univ. of Göttingen, Germany, 1997), Release 97-2.

17. G. M. Sheldrick, *SHELXL97: A Program for Crystal Structure Refinement* (Univ. of Göttingen, Germany, 1997), Release 97-2.

18. J. Yamada, S. Tanaka, J. Segawa, *et al.*, J. Org. Chem. **63**, 3952 (1998).

19. C. Faulmann, P. Cassoux, A. I. Kotov, and E. B. Yagubskii, Acta Crystallogr., Sect. C: Cryst. Struct. Commun. **51**, 149 (1995).

20. V. V. Gritsenko, O. A. D'yachenko, A. I. Kotov, *et al.*, Koord. Khim. **27** (6), 432 (2001).

21. J. Yamada, S. Tanaka, H. Anzai, *et al.*, J. Mater. Chem. **7** (8), 1311 (1997).

22. A. I. Kotov, L. I. Buravov, V. V. Gritsenko, *et al.*, Synth. Met. **120**, 861 (2001).

23. O. A. D'yachenko, A. A. Bardin, A. I. Kotov, *et al.*, Izv. Ross. Akad. Nauk, Ser. Khim., No. 2, 359 (2003).

24. J. Yamada, Y. Nishimoto, S. Tanaka, *et al.*, Tetrahedron Lett. **36** (52), 9509 (1995).

Translated by O. Borovik-Romanova

LATTICE DYNAMICS
AND PHASE TRANSITIONS

Switching of SBN Crystals: Comparison with the Model Case (DTGS)

N. R. Ivanov*, T. R. Volk*, L. I. Ivleva**, S. P. Chumakova*, and A. V. Ginzberg*

* Shubnikov Institute of Crystallography, Russian Academy of Sciences,
Leninskiĭ pr. 59, Moscow, 119333 Russia
** Institute of General Physics, Russian Academy of Sciences,
ul. Vavilova 38, Moscow, 117942 Russia

Received September 18, 2003

Abstract—It is shown that a number of specific features of the electric-field induced polarization reversal and transition to the single-domain state observed in ferroelectric crystals of SBN-0.61 and DTGS (the model object)—delayed or incomplete transition to the single-domain state in strong fields, hysteresis loop degradation, and time dependence and the memory effect of the residual domain density—are due to the pinning of forward motion (intergrowth) of dynamic domains with charged inclined walls in the absence of lateral motion. © 2004 MAIK "Nauka/Interperiodica".

INTRODUCTION

Crystals of $Sr_xBa_{1-x}Nb_2O_6$ (SBN-x) solid solutions are tetragonal uniaxial ferroelectrics with a diffuse displacive phase transition accompanied by a change in the point symmetry ($4/mmm \longrightarrow 4mm$). They belong to the structural type of "unfilled" partially disordered tungsten bronzes; have high values of spontaneous polarization and dielectric, pyroelectric, piezoelectric, electro-optical, and nonlinear optical coefficients in the ferroelectric phase [1, 2]; and demonstrate relaxor dielectric behavior near and above the phase transition [1, 3]. In this context, SBN crystals are interesting objects for both fundamental and applied research. However, such conventional aspects of ferroelectricity of SBN crystals as the domain structure and the polarization reversal (switching) have been studied only for a relatively short time, in particular, in view of the perspectives of formation and use of regular (periodic) domain structures for efficient transformation of laser frequency in the mode of quasi-phase matching. Investigations of the two-dimensional (2D) cross sections of the static domain structure of SBN by scanning electron microscopy [4], X-ray topography [5], and chemical etching [6] revealed a characteristic feature of the domain structure of SBN crystals (independent of composition)—the existence of elongated (needle-shaped) domains with a cross section of ~10 μm and a length of ~1 mm. This relatively large static domain structure was characterized as sharp tetrahedral pyramidal needles grating from the surface into the crystal bulk [7]. However, the dynamic, shallower domain structure (which is formed and moves in the electric field during the crystal switching) has not been reliably established and adequately studied for real SBN crystals.

In this study, the fatigue phenomena (degradation of the hysteresis loop in the course of successive switching cycles [8, 9]) and the memory effect (recording and subsequent reproduction of a specified polarization of a crystal) observed in SBN crystals are considered in context of the specific features of switching caused by the motion of inclined (charged) domain walls along with defects in a crystal. Within this approach, an attempt is made to compare the switching in SBN with the switching in ferroelectrics of the model group of triglycine sulfate (TGS), in particular, in deuterated triglycine sulfate (DTGS). This comparison is justified, first of all, by the qualitative similarity of switching in SBN and DTGS: as will be shown below, the switching in both crystals is caused by the motion of inclined charged domain walls rather than lateral motion of neutral walls of cylindrical static domains, as has been assumed for all ferroelectrics until now [10–12]. There are some other reasons for choosing DTGS as an analog: (i) this material, as well as SBN, is a ferroelectric uniaxial solid solution characterized by the dependence of the transition point on composition (isotopic substitution); (ii) DTGS and SBN have comparable piezoelectric coefficients and coercive fields and their transition points differ from room temperature by comparable values; and (iii) both materials are characterized by hysteresis loops of similar shape, which contain, along with a "fast" portion, a "slow" portion corresponding to saturation (the phenomenon we are interested in). The domain dynamics in these crystals have been studied by different supplementing methods. The dynamic pattern of switching in SBN (the domain density and its change with time) was ascertained mainly by the electro-optical method of measuring electro-optical hysteresis loops. The nematic liquid crystal (NLC) method, which is promising for dynamic visualization of domains in

crystals of the TGS group [10], turned out to be insufficiently informative for visualization of fine features of fast domain motion in SBN due to the weak orientational contrast of an NLC on the lateral surfaces of SBN crystals [7]. In contrast, in DTGS, where the electro-optical method is not efficient due to the small magnitude of the electro-optical effect and more inhomogeneous (on the scale of the electro-optical method resolution) polarization distribution, the NLC method makes it possible to visualize with good contrast the state of the domain structure and its dynamics in two main nonpolar cuts and make video recording in real time. In the case of DTGS, direct investigation of the domain density by the electro-optical hysteresis loop (which is used for SBN), was replaced by more sensitive indirect investigation of the domain contribution to the low-frequency reciprocal permittivity with averaging of results.

Two stages—fast (main) and slow (final)—can be distinguished in switching of SBN crystals. In this study, we restrict our consideration to the final stage— an approach to the saturated (single-domain) state, when the sample-averaged residual domain density is lower than 5%. The new results on the collective fast stage of the polarization reversal will be published separately.

Despite the important differences in the shape and localization of residual domains in DTGS and SBN, the similarity of the switching processes in both types of crystals manifests itself mainly in the motion of charged domain walls and, accordingly, in the switching of both DTGS and SBN by the forward intergrowth of domains (for example, from electrode to electrode in relatively thick plates). Moreover, without detailed visual investigation and understanding of the three-dimensional (3D) structural dynamics of domains in DTGS, it would be difficult to understand the situation in SBN crystals, which are more symmetric, damaged, layered, and small-domain as compared with DTGS crystals.

CRYSTAL GROWTH AND SAMPLES

Single crystals of SBN-0.61 solid solutions $12 \times 24 \times 110$ mm^3 in size were grown in the form of profiled boules by the modified Stepanov method from a congruent melt with the use of an oriented seed [13]. It is well known that, growing SBN crystals by the Czochralski method, it is hardly possible to avoid growth striation (dependent on the pulling rate [2]) in the region of stable growth. Since striation is related to composition fluctuations [14], in particular, the Ba/Sr ratio [2], Czochralski-grown crystals may have macroscopically modulated polarization and bound charges interacting with the domain structure. The samples studied here also showed growth striation (with a period of 24 μm). However, the growth method we used made it possible to significantly reduce the fringe contrast, i.e., the amplitude of modulation of the composition and birefringence almost to the limiting possibili-

ties of the phase-contrast microscopy [15]. On the whole, the growth technique we used made it possible to obtain crystals of high optical quality.

Large DTGS crystals with a temperature of ferroelectric transition of 59°C were obtained by single crystallization upon cooling a 96% deuterated solution. Samples were cut from one of four large growth pyramids of the *m* type; therefore, the planes of growth layers with deposition defects were inclined with respect to the polar axis *b*. The presence of these layers cannot be revealed by measuring the density or refractive indices, as in the case of SBN, but they could be detected by NLC topography of polar-cut switching. The advantage of DTGS over other ferroelectrics characterized by the same type of domain motion that we consider here is in the efficiency of anisotropic molecular interaction of the NLC with the main nonpolar surfaces of DTGS; the chemical purity of these surfaces was obtained by oriented cleavage.

EXPERIMENTAL METHODS

The hysteresis loops in SBN were investigated by the dynamic electro-optical method with a high phase sensitivity ($2\pi \times 10^{-6}$). Electro-optical signals were excited by an ac measuring field with an effective strength of 6 V/cm and a frequency of 1000 Hz (the case of a mechanically free crystal). Polarization reversal was performed by applying a saw-tooth field E with a period of 27 min and an amplitude of $|\pm 5.6 \text{ kV/cm}| > |E_c| \approx 2$–2.5 kV/cm, where E_c is the coercitive field of the main switching process. The use of a single-mode He–Ne laser ($\lambda = 633$ nm) with almost parallel thin (0.1 mm in diameter) beam made it possible to measure the quasi-local electro-optical response of a sample to an external electric field and obtain the spatial distribution of the electro-optical coefficient during the sample scanning [16]. Since the photosensitivity of undoped SBN-0.61 in the vicinity of $\lambda = 633$ nm is low, the field distribution can be considered uniform at a low laser power. When the transverse geometry is used ($E \parallel z$, $k \perp z$), the measurable value is the linear electro-optical coefficient

$$r_0 = |r_{33} - (n_o/n_e)^3 r_{13}|. \qquad (1)$$

As is known, all linear electro-optical coefficients are obtained by linearization of the quadratic coefficients [17]. In particular, r_{33} can be written as follows:

$$r_{33} = 2g_{33}P_s\varepsilon_3\varepsilon_0, \qquad (2)$$

where P_s is the spontaneous polarization and g_{33} is the coefficient of the electro-optical effect that is quadratic with respect to polarization in the centrosymmetric phase. It follows from (2) that the effective coefficient $r < r_0$ in a multidomain crystal; the dependence $r(E)$ is a hysteresis loop. The loop $r(E)$ can be normalized to ± 1 by dividing r by $r_0(E = 0)$. As will be shown below, the shape of the "saturated" branches of the electro-optical hysteresis loop normalized by a constant differs

from the shape of saturated dielectric hysteresis loops $P(E)$. This difference is due to the dielectric nonlinearity $\varepsilon_3(E)$ and is interpreted as the contribution of the electro-optical effect in the ferroelectric phase (quadratic in field), which leads to the falloff (almost linear far from the Curie point) in the dependence $r_0(E)$. In principle, introduction of the correction for the quadratic effect would make the electro-optical loop more rectangular; however, we will present "as-recorded" loops below. In recording, at a fixed field, processes changing with time, the correction was introduced as a constant. Taking into account (i) problems with obtaining a complete transition to the single-domain state in SBN and (ii) unipolarity and time dependence of the polarization, the value of r_0 was assumed to be the value in absolute maximum at $E = 0$, which was obtained at least once and at least one point of the sample (either at a bipolar transition to the single-domain state or in the first measurement with the crystal transformed to the single-domain state from the paraelectric phase by cooling in the presence of a field). At 20°C, the half-wave voltage $V_\pi = (\lambda/r_0 n_e \varepsilon_3)d/l$ (where d and l are the sample sizes with respect to the field and light, respectively) is 220 V and $E_c = 2.5$ kV/cm (at $d/l = 1$), which is in agreement with the published data for SBN-0.61 [2].

When considering loops and when performing visual monitoring of domains, it is often convenient to use the concept of domain density (its definition—bulk or surface density—depends on the physical method of measuring). For the volumes of (+) and (–) domains, in the case of thin walls ($v_w = 0$), we have $v^+ + v^- = v$, where v is the volume of the crystal under study (a cylinder 0.1 mm in diameter with a length l). The positive domain density in the negative matrix $D^+ = v^+/v$, and the electro-optical signal is related to the bulk polarization of the cylinder outlined by the laser beam: $r/r_0 = (v^- - v^+)/v$; i.e., the relation between these quantities is linear: $r/r_0 = 1 - 2D^+$. Any (corrected to the quadratic effect, if the field is not fixed) isothermal changes in r, which are not related to the change in r_0, are treated as a result of a change in the domain density. Scanning a laser beam over the front surface of a sample in the form of a parallelepiped oriented parallel and perpendicular to the crystallographic directions yields one-dimensional (1D) and 2D distributions of D^+ and D^-.

When the dynamic NLC method [10] was used to investigate domains in SBN [7] and DTGS [16], mixtures of diphenyls with positive dielectric anisotropy were chosen. In the longitudinal observation geometry, the domain structure was observed by applying an ac field to a crystal along its polar axis, which provided visualization of oscillating walls. When studying DTGS, we used the transverse dynamic NLC method, in which an NLC layer is deposited on nonpolar ((ba') and (bc)) cleavages of the crystal and the observation is performed in the corresponding nonpolar direction. As a rule, only fragments of domain walls moving both forward (in a constant switching field) and backward (in a weak ac field) are visualized on these cleavages, whereas the quasi-static NLC contrast observed on polar ($a'c$) cleavages of TGS is either absent or very low [10].

EXPERIMENT AND DISCUSSION OF RESULTS

Distribution of an Electro-Optical Signal and Residual Domain Density in SBN

The general character of the distribution of an electro-optical signal from an SBN sample incompletely transformed into the single-domain state by switching in a bipolar electric field can be seen from Figs. 1 and 2. The sample was cut in the form of a parallelepiped $3 \times 1 \times 1.73$ mm³ in size; the scanning was performed along the principal axes (z and x') of the (110) cross section. Circles indicate the experimental data and the solid lines show the results of independent linear regression. In particular, it follows from Fig. 1 that the total range of the switched (in the fast mode) part of the loop is almost independent of z, whereas the residual domain density depends heavily on this coordinate. In this case, the lowest domain density and the largest electro-optical signal are observed near the positive electrode. The character of the distribution of the residual domain density is in qualitative agreement with the needle-like shape of domains if their tips are directed to the positive electrode. In contrast, the tips of the domains switched in the fast stage are directed to the negative electrode. This means that the displacement current is mainly due to the motion of positively charged domain walls.

Figure 2 shows the distribution of the domain density in the transverse (with respect to the polar axis) direction for the two polarities and three z coordinates. Here, against the background (dashed lines) of the small-scale beam-diameter averaged domain structure, one can easily see peaks of domain density correlated over the z coordinate. Based on their characteristic sizes and orientations, these peaks can be attributed to known macrodefects of striation type [2].

Until now, only a needle-like static structure with relatively large (with a transverse size of about 12 μm) and very sharp (with an angle at the tip of about 0.5°) domains penetrating deep into the sample bulk (up to 1 mm from the surface) was observed in SBN crystals The occurrence of this quasi-periodic structure with a 2D checkerboard order of localization of domain nuclei can be explained qualitatively taking into account the shear character of the distribution of piezoelectric strains in a tetragonal crystal with a growth periodicity of layers of 24 μm [7]. When trying to extrapolate the DTGS approach (see below) to SBN, one might expect that the zigzag formed (the switching front), which is 2D in a tetragonal crystal (in contrast to 1D zigzags in anisotropic monoclinic DTGS crystals), will rapidly pierce the samples (that are relatively thin for sharp domains) and then relax mechanically on the surface,
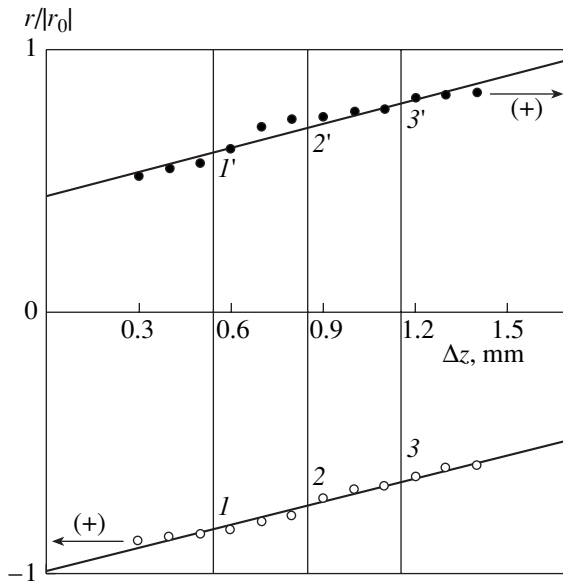
Fig. 1. Distributions (for both polarization directions) of an electro-optical signal along the z axis passing through the center of an SBN-0.61 sample ($x' = 1.5$ mm; see Fig. 2). The arrow with a "+" sign under/above it points (over the z coordinate) to the electrode with a positive switching potential.

Fig. 2. Distributions of an electro-optical signal and the domain density in SBN-0.61 for the upper (primed numbers) and lower (unprimed numbers) branches of the hysteresis loop for three fixed values of the z coordinate (see Fig. 1) for scanning along the [110] direction.

imitating the lateral motion within the checkerboard cellular structure, after which merging (clusterization) of filled cells should occur. The wall motion may be strongly pinned by microcracks formed in preceding switching cycles, which are typical of SBN crystals [2]. These microcracks, serving as mechanical traps for walls, may provide indefinitely long relaxation times for residual domains. This pattern is in good agreement with the results of investigation of the (001) surface [7].

In studying the switching on (110) surfaces by the dynamic NLC method [7], it was found that switching fronts may become closed at some internal layers. This closing requires either a sharp increase in the tilt angle of domain walls with conservation of the period (which is observed in part) or occurrence of a new type of switching with shallow domains. The second situation is also implemented. A cut of the crystal by a surface deviated from the (001) plane by a small angle (about 7°) is shown in Fig. 3 (left). In this case, the cleavage plane intersects several periodic growth layers (four periods in Fig. 3; recall that their periodicity is 24 µm along the c axis), which demonstrate a small-scale domain structure. Its average transverse size is 2.5 µm and the height is of the same order of magnitude as the layer thickness, i.e., about 12 µm or somewhat larger if we take into account the emergence of the domain tip from the layer plane; therefore, the angle at the vertex is ~10°, which exceeds that for sharp domains by a factor of 20. Hence, this structure is strongly electrically compensated and has low mobility. Based on the intensity distribution (Fig. 3), we can suggest that the small-scale domain structure belongs to the same checker-
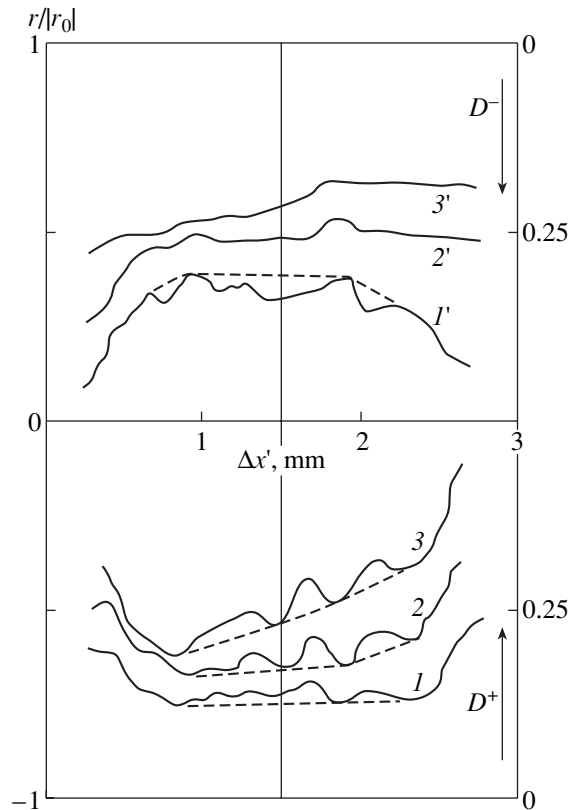
board cellular type as the large-scale one [7]. Both types of the domain structures are observed (not simultaneously) on the (001) surface in the form of scarce spots with a transverse size of about 0.3–0.5 mm, which is also characteristic of striations. The two types of the domain structure may be related to different mechanisms of dynamic wall pinning by defects responsible for the hypothetical bond: compensation–inclination–mobility.

Recently, we revealed this residual small-scale domain structure on (110) surfaces of SBN crystals. Observation is possible in a polarization microscope in the extinction mode due to combined action of the local electro-optical and piezooptic effects in a strong field (from 3 to 10 kV/cm). Mechanical traps of domains, accumulating during successive switching cycles or surface treatment, are also clearly visualized in a strong field. Small domains with low mobility turned out to be uniaxial and needle-shaped, with angles 2φ from 3° to 10°, and based on an irregular zigzag-shaped switching front of a larger scale. The elements of the latter introduce high local stresses (which are proportional to the field). Their observation can be regarded as confirmation of the validity of the electromechanical approach
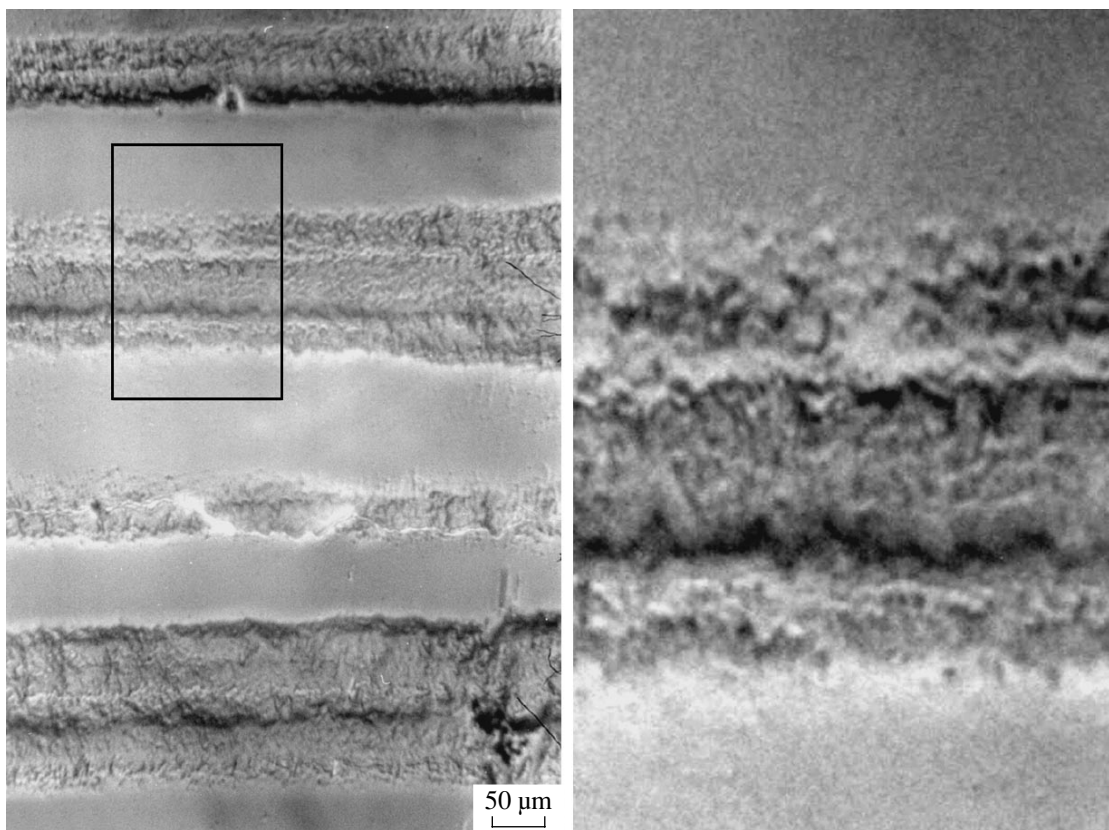
Fig. 3. Alternation of single-domain and multidomain growth layers (growth modulation of the domain density with a period of 24 μm along the *c* axis) in SBN-0.61 revealed by the combined phase-contrast method (NLC decoration in combination with contrast enhancement using a Bekke strip [7] with photographing in a film and subsequent contrast enhancement in digital processing) in a cleavage with a deviation of about 7° from the (001) plane.

and analogy with DTGS crystals. Unfortunately, small transverse sizes of these domains (and, accordingly, weak phase contrast), on the one hand, and the significant decrease in the resolution caused by the stresses and overlap of domains, on the other hand, significantly impede their direct optical investigation.

FATIGUE EFFECTS AND DOMAIN MEMORY OF SBN CRYSTALS

Electro-Optical Hysteresis Loops in SBN

Figure 4 shows how the shape and size of electro-optical hysteresis loops observed in SBN change during successive half-cycles (*1–19*) of switching by a sawtooth voltage and with a change in the voltage amplitude from $\sim E_c$ to $\sim 2E_c$ (groups 1–5 and 11–19). The loop segments *a–b* and *d–e* demonstrate fast switching and the segments *b–c* and *e–f* show slow switching. Irregularities on the *c–d* and *f–a* branches are due to the local reverse switching. In general, the loop height decreases during cycling both in weak ($E \simeq E_c$) and strong ($E > E_c$) fields (where E_c is the coercive field, which is not constant in SBN [8], although the fast switching stage has a pronounced threshold character).

The degradation (fatigue) of a loop in a strong field (curves *11–19*), as can be seen from the change in the loop shape, is related mainly to the occurrence of a domain subsystem that either is switched very slowly or loses switching ability at all (becomes frozen) and is only partly due to the decrease in the volume that is rapidly switched (in this case, the average rate of the fast process decreases). However, the frozen region may be polarized for a rather long time (the settling time may be as long as several hours). An example is the transition from curve *19* to curve *19'* (Fig. 4), which occurs only over the course of time (in a constant field). The record of this process is shown in Fig. 5. It should be noted that the optical quality of samples decreases during multiple long-term cycling in a strong field, which manifests itself in scattering and depolarization of light due to the formation of optical inhomogeneities and an increase in noise in electro-optical measurements. A possible reason for this is that, at piezoelectrical fixing of internal domains, the elastic-strain limit is locally exceeded (in strong pulsed fields—up to the loss of continuity). Indeed, we observed in [7] that pulsed switching resulted in a formation of a network of microcracks in orthogonal (110) planes—"easy-cleavage planes" (the real cleavage is absent), which coin-
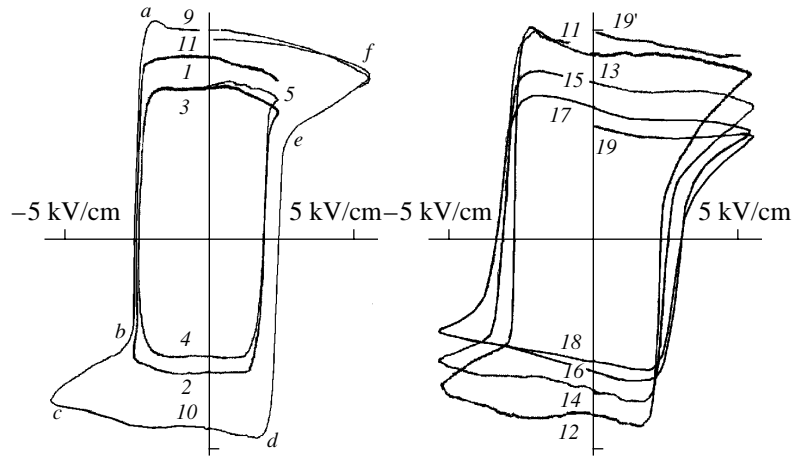
Fig. 4. Degradation of a hysteresis loop observed for SBN-0.61 during switching by a saw-tooth voltage (some curves are omitted, numeration by half-cycles). $T = 296$ K and $V_\pi = 220$ V.

cide with the planes of preferred orientation of domain walls. Some microcracks are not healed over the course of time. In slowly changing fields (up to ~5 kV/cm), no microcracks were revealed by visual monitoring.

Time Dependences of the Degree of Polarization of SBN

The curve in Fig. 5 represents a slow transition process between two levels (19 and 19' in Fig. 4) of an electro-optical signal (the degree of polarization or the domain density) from the area of the crystal outlined by the laser beam. Obviously, the derivative of this function (the current dependence) is a dome-shaped curve with a wide maximum in the central part of the time interval. However, the accuracy of our experiment is insufficient to analyze the form of the quasi-local displacement current. Anomalously long polarization times were also observed for SBN crystals of different composition in with fields $E > E_c$ in measurements by electrical methods [8].

The curve in Fig. 5 characterizes not only the transition process between the two levels of the degree of polarization but also the memory effect. Let us illustrate this effect for both polarities; in this case, the necessary condition is that the crystal should be aged in a special way.

Figure 6 shows the history of aging process for the bottom branch of the hysteresis loop. Before measuring each curve of the slow time dependence of an electro-optical signal (the fast switching stage was not measured), the sample was switched by a positive field to the opposite polarization state for 10 s. As soon as the upper limit of the domain density D^+ in the preliminary aging process reached saturation or a level sufficiently high for reliable measurements, we performed the final

recording of the settling curve during a much longer time (see the curve in Fig. 6 corresponding to the last measurement time). As a rule, each previous and subsequent aging curves are in a certain relation: the level of the domain density (or the signal) given by the previous curve coincides with the level at which the maximum of the derivative of the subsequent curve is observed (provided that the latter was recorded for a sufficiently long time). This situation can be classified as the memory effect of the domain density (and, therefore, the domain configuration) during switching. In this case, the last curve is the "reproduction curve" and the next to the last one is the "record curve." Similar behavior is observed for the other loop polarity (Fig. 7). The difference in the amplitudes and the number of aging cycles indicates the crystal unipolarity. Note that the first curve (it is assumed that the crystal was "at rest" for a long time before recording) often demonstrates anomalous behavior during aging, which can be explained by the effect of reverse switching. Due to the inhomogeneity of the crystals studied, this effect can be much more pronounced for some local loops rather than for integrated loops.
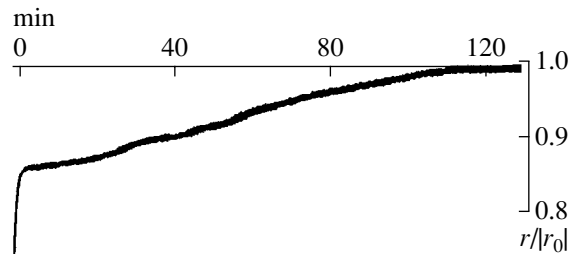

Fig. 5. An example of settling the paramagnetic single-domain state in SBN 0.61 in the course of time.
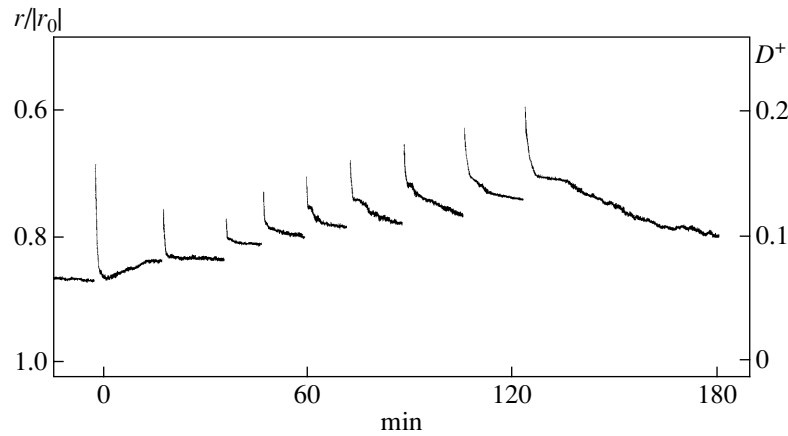
Fig. 6. Change (time in minutes) in a relative electro-optical signal (scale on the left; bar stands for minus) and the positive domain density (scale on the right) in SBN-0.61 for the lower branch of the hysteresis loop during the pulsed switching.

Comparison with Switching in DTGS

It will be shown below that the memory effect is characteristic of ferroelectrics switched due to the forward motion of charged dynamic domain walls (the intergrowth of domains along the polar axis). Let us consider dynamic domain walls in crystals of the TGS group, which are well-studied model ferroelectrics in other aspects. Using the method of decoration of nonpolar (i.e., parallel to the polar axis) crystallographic cuts by an NLC, we showed that the electric-field switching in isomorphous crystals of this group occurs mainly due to the formation and intergrowth of wedges with inclined (i.e., charged) walls rather than the lateral motion of ordinary (neutral and parallel to the ferroelectric axis) walls. Merz was the first who observed this mechanism in barium titanate [17]. In crystals of the TGS group, wedges are formed from nuclei at external surfaces under the electrodes. They form a quasi-periodic structure in the (ac) plane and, during the intergrowth along the polar b axis, merge into 1D zigzags, ridges and valleys of which are elongated perpendicular to the c axis (along a'). The zigzags have opposite charges (at interfaces, they correspond to the head-to-head and tail-to-tail orientations of the spontaneous-polarization vectors) and move in opposite directions in the field until they are annihilated (the case of complete switching). Let us consider a zigzag when the switching is unipolar and incomplete. The observation is carried out by the NLC method in the (bc) plane. In this case, we omit the stage of merging of separate wedges into a zigzag, which is valid when the thickness of a crystal plate greatly exceeds the amplitude of the zigzag. When the field pulse is over at the instant t_1, the zigzag remains in some intermediate position between the electrodes. Let us change the field direction and apply a pulse of duration $t_2 < t_1$ to the crystal. The crystal is switched again by a new zigzag-shaped wall of the same shape and localization (but with the opposite charge). The instant at which the new wall stops is determined by the time t_2. It is noteworthy that the velocity of the zigzag motion decreases with increasing the distance from the nucleation surface (the wall pinning), while the localization of nuclei on the nucleation surface is rigidly determined and independent of polarity. This makes the switching process reproducible and controlled, allowing only insignificant backward displacement of the first zigzag towards the second one with changing polarity. As a result, an internal domain layer elongated in the $(a'c)$ plane and limited by two surfaces with a zigzag-shaped profile is formed. After switching off the field, such a corrugated layer should collapse due to the electrostatic instability. However, it turned out to be metastable with a rather long lifetime (we observed its degradation for more than an hour since the instant when it was formed). The zigzag (1D corrugation) is the collective form of the internal dynamic domain wall. By analogy, taking into account the tetragonal symmetry, one might expect the occurrence of 2D pyramidal corrugation in thick SBN plates.

Figure 8 shows the only internal domain layer formed by the double-pulse method (dark against the gray background of the matrix; the contrast is exaggerated). Note that the source of zigzag initiation (the nucleation surface) is in the bottom part (beyond the figure); therefore, the lower zigzag is somewhat more mobile than the upper one. Estimation based on the ratio of the average layer thickness to the sample thickness (1 mm) gives an average residual domain density of about 5%, i.e., the value in the range of slow saturation of the hysteresis loop (it is convenient to investigate the electro-optical hysteresis in crystals of the TGS group in the longitudinal geometry). Thus, the slow transition to the single-domain state of a crystal is due to the degradation of zigzag-shaped domains.

The degradation occurs irreversibly, first by gradual thinning and stepwise collapse of the narrowest and longest parallel segments of the double zigzag (the formation of discontinuities) and then by lateral narrowing
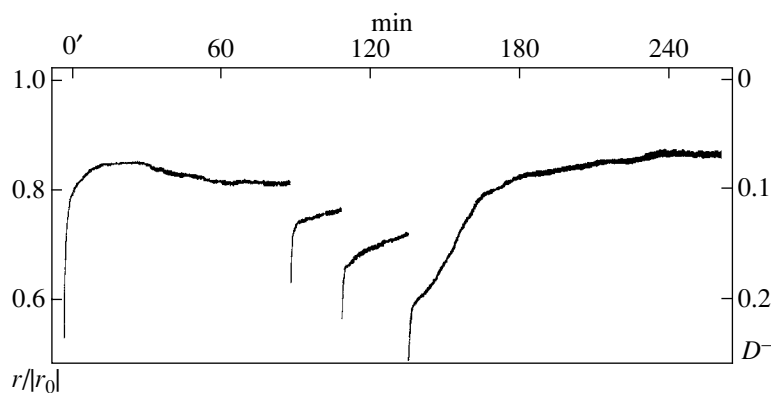
Fig. 7. Change (time in minutes) in an electro-optical signal (scale on the left) and the negative domain density (scale on the right) in SBN-0.61 for the upper branch of the hysteresis loop for successive switching pulses.

of residual (asymmetric with respect to the twofold axis) parallelograms and their transformation to a symmetric form (fusiform in the (*bc*) cross section) by a small displacement of the bottom end strictly under the top end with simultaneous smoothing of lateral sides. One domain of this type can be seen on the right-hand side of Fig. 8 against the dark background of the initial domain. Chainoves was the first to reveal these domains in crystals of the TGS group by etching [17]; however, the process of their formation has not been described. We should also add that the image of the large dark domain in Fig. 8 contains a bright image of smaller size, which is obtained by contrast inversion and corresponds to the image of the noted dark domain degraded for some time (in this case, 20 s). The difference contour characterizes the significant spread in the velocities of different segments (walls), while the difference in the tilt angles can be explained by the difference in the degree of electric compensation of the walls by defects.

In the perpendicular cross section (*ba'*) (where $a' = a \sin\beta$), these residual internal domains have parabolic rather than sharp vertices; thus, in the 3D reconstruction, the final shape of a separate domain looks like a disk significantly extended along the *b* axis rather than a spindle. The major axes of the disk are oriented parallel to the principal axes of the dielectric tensor. This shape is close to ellipsoidal and, apparently for this reason, is most stable electrostatically. Therefore, the process of degradation of a residual dynamic domain to a static state upon switching off the external field can be described as the result of relaxation of elastic stresses at zigzag elements. It should also be noted that, although the residual disk-shaped internal domains are more mobile in an electric field than cylindrical ones and can even oscillate in a weak ac field, they do not serve as nuclei for the domains involved in the main (fast) switching process, which is restored in each subsequent cycle from the same nucleation points on a certain surface. As a result, the old pattern is substituted each time

by a new one and is reproduced for the most part after aging.

The new pattern of switching described above and the difference in the static and dynamic domains indicate an important role of the piezoelectric effect as a factor that not only facilitates domain fixing but also affects their shape and the switching process itself. Therefore, particular attention should be paid to the piezoelectric-coefficient matrix, considering the motion of domains as the phase growth and domain walls as interfaces requiring lattice coherence [14]. Analysis of the reference data on the piezoelectric properties of a large number of ferroelectrics (nonferroelastics) shows that, most often, one of the three coefficients entering the volume (hydrostatic) piezoelectric modulus has a sign different from those of the other two coefficients, thus indicating the only particular piezoelectric (and, at convolution with polarization, strain)
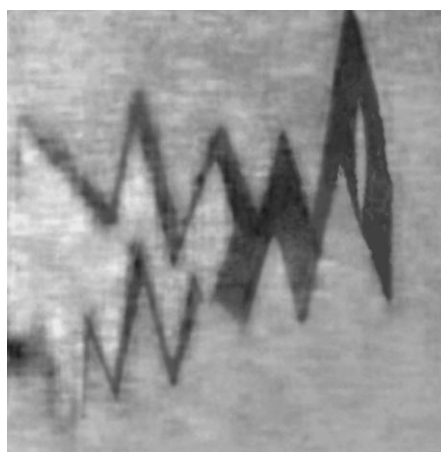

Fig. 8. Residual zigzag-shaped domain (dark) in a DTGS crystal (0.2×0.2 mm^2 segment of the (*bc*) cut, the polar axis is vertical) formed during incomplete switching by a double-pulse technique and its state (bright in the dark contour) as a result of slow (after 20 s) transformation in the absence of the external field (the electrodes are closed).

direction in the crystal. Obviously, in tetragonal crystals, this direction coincides with the ferroelectric direction. However, in crystals with lower symmetry (orthorhombic and monoclinic), such a coincidence is not dictated by the symmetry and, therefore, is not necessary. Examples are crystals of the TGS group, in which the particular piezoelectric direction (with an error of about 3° since these crystals are monoclinic) is the *c* axis and the ferroelectric direction is the *b* axis. From all contributions to the elastic energy of a domain wall in a field, let us select the main contribution related to the strain along its largest length. Using indicating surfaces of the strain tensor [18], one can easily find that (only) at different signs of piezoelectric strains along the crystallophysical axes, two real symmetric solutions for the orientation of an unstrained domain wall exist. These solutions depend only on the ratio of piezoelectric coefficients (or electrostriction coefficients, from which they are derived by linearization similar to that noted for the electro-optical tensor) and have the form

$$\varphi_{1,2} = \pm \arctan \left| (-x_\parallel / x_\perp)^{1/2} \right|. \qquad (3)$$

For these solutions, the longitudinal piezoelectric strain becomes zero, which means an efficient minimization of the corresponding main elastic contribution to the energy of a dynamic wall upon its rotation around a'. (The above considerations refer also to any nonpolar cross section in SBN. For large domains, further identification of orientation can be obtained considering the elasticity rosette in the basal plane.) However, at a deviation from the vertical direction, the electrostatic energy of the wall increases; therefore, the total energy becomes minimum at smaller angles of the wall rotation (the higher the polarization, the smaller the angle of deviation of the wall from the polar axis). If the wall is electrically compensated by defects, the angle of its deviation in the corresponding cut may increase, tending to the value calculated from the piezoelectric coefficients. It is convenient to characterize inclined walls by the angle at wedge vertex 2φ. For sharp domains in SBN, $2\varphi < 1°$, while, for zigzag-shaped and surface domains in DTGS, the angle $2\varphi > 10°$ and may be as large as 60°. Thus, there arises the possibility of using a change in the shape and dynamics of slow dynamic walls for visual finding of clusters of defects (mainly charged ones, which can partially compensate the polarization charge of the walls). When passing through clusters of defects, extended walls are bent and the intergrowth rate of shallow wedges decreases.

Now, when the domain dynamics in the slow stage of approaching the single-domain state is qualitatively clear from the direct observations and estimations performed, we will consider Fig. 9, which illustrates the memory effect by an example of the domain contribution to the permittivity of DTGS. Five pairs of curves *A* and *B* are shown. In order to avoid a superposition of close curves from the set *A*, only the curve A_5 is left, while the four others are represented by their end points. Arrows emerging from these points and pointing to left indicate the corresponding curves from the set *B*. Each curve *A* (recorded at some field polarity selected with regard to the crystal unipolarity) always precedes the corresponding curve *B* (reproduction at opposite field polarity). The initial instant of time coincided with the instant of switching the polarity of a 4.7-kV/cm field. The logarithmic time scale in Fig. 9 is used only for scale compression. However, it also allows one to reveal empirically some (averaged and approximate) characteristics of the processes under consideration: the logarithmic recording; two logarithmic reproduction rates, the second of which (i.e., corresponding to the later record) exceeds the first one; and the presence of the maximum time of the effect existence, which, according to approximate extrapolation, is about 7 h.

The domain-layer degradation observed suggests the following domain–structural interpretation of the memory effect. During the recording process, we leave the charged dynamic walls (zigzag) at some position in the crystal in metastable equilibrium with the fields of stresses and defects formed. During the reproduction, an oppositely charged, "almost parallel" and somewhat faster moving, zigzag is formed. Its total annihilation with the first (less mobile) zigzag, which begins with the narrowest portions, manifests itself as a sharp increase in the rate of transition to the single-domain state, specifically in the same position (and, therefore, at the same domain density) at which the first zigzag was left. The zigzag slows nonuniformly due to the interaction with defects. As a result, the elements of the double zigzag-shaped domain layer in the regions with higher defect density have not only a larger tilt angle but also a larger thickness. Specifically in these regions,
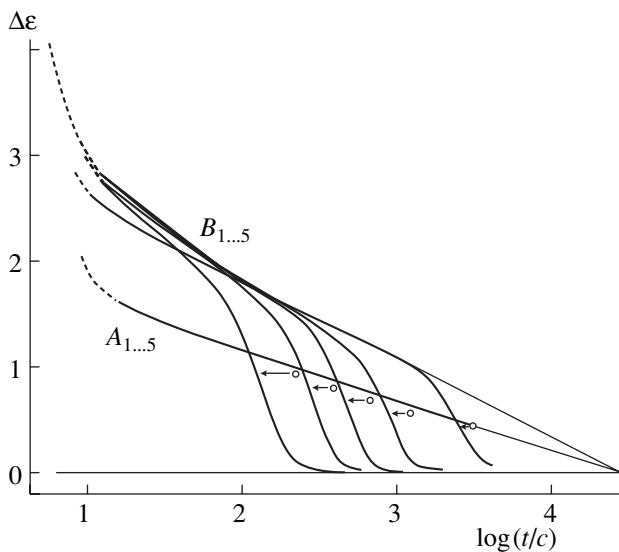

Fig. 9. Time dependences of the domain contribution to the permittivity of DTGS (record and reproduction curves for successive switching cycles). $t = 24°C$, $E = 4.7$ kV/cm, $E_\sim = 3$ V/cm, and $\varepsilon_{min} = 20.3$.

disk-shaped domains are formed, which, obviously, are additionally stabilized by a cloud of defects. Similar (only longer) domains may arise due to the long-term degradation of "normal" cylindrical static domains (the so-called pyroelectric domains) obtained in the absence of a field by pulsed superheating.

CONCLUSIONS

Until now, in comparing the switching behavior of SBN and DTGS at room temperature, we tried to clarify qualitatively and stress only some general features related to the presence of charged internal dynamic domain walls, in particular, the long final stage of the transition to the single-domain state and the memory effect of small levels of residual domain density. Visual investigation of the state of the internal domain structure demonstrates its complex inhomogeneous transformation during switching by an electric field. Along with the fact that it is impossible to control the conditions at the internal interfaces of damaged regions, this method does not allow us to propose some uniform or simple quantitative model with regard to the electromechanical properties and the role of growth defects, especially as the analogy between SBN and DTGS can hardly be extended due to the differences in the symmetry, polarization, and inclination of domain walls; shape of domains; and the role of microcracks and growth defects. For SBN, it would be desirable to continue the study of dynamic domain structures. At present, the NLC method remains almost the only direct method for observing fast dynamics of domains in an electric field in nonpolar cuts of ferroelectrics. Attempts have been made to improve the efficiency of this method for SBN crystals.

ACKNOWLEDGMENTS

REFERENCES

1. M. E. Lines and A. M. Glass, *Principles and Applications of Ferroelectrics and Related Materials* (Oxford Univ. Press, Oxford, 1977; Mir, Moscow, 1981).
2. Yu. S. Kuz'minov, *Ferroelectric Crystals for Laser Radiation Control* (Nauka, Moscow, 1982), p. 400 [in Russian].
3. J. Dec, W. Kleemann, Th. Woike, and R. Pankrath, Eur. Phys. J. B **14**, 627 (2000).
4. L. A. Bursill and P. J. Lin, Philos. Mag. B **54**, 157 (1986).
5. G. Fogarty, B. Steiner, M. Cronin-Golomb, *et al.*, J. Opt. Soc. Am. B **13**, 2636 (1996).
6. J. Romero, D. Jaque, J. Garcia-Sole, and A. A. Kaminskii, Appl. Phys. Lett. **78** (14), 1961 (2001).
7. N. R. Ivanov, T. R. Volk, L. I. Ivleva, *et al.*, Kristallografiya **47** (6), 1065 (2002) [Crystallogr. Rep. **47**, 1023 (2002)].
8. V. V. Gladkiĭ, V. A. Kirikov, S. V. Nekhlyudov, *et al.*, Fiz. Tverd. Tela (St. Petersburg) **42** (7), 1296 (2000) [Phys. Solid State **42**, 1334 (2000)].
9. T. Granzow, U. Dorfler, Th. Woike, *et al.*, Phys. Rev. B **63**, 174101 (2001).
10. N. A. Tikhomirova, L. I. Dontsova, S. A. Pikin, and L. A. Shuvalov, Pis'ma Zh. Éksp. Teor. Fiz. **29**, 37 (1979) [JETP Lett. **29**, 34 (1979)].
11. J. C. Burfoot, *Ferroelectrics: an Introduction to the Physical Principles* (Van Nostrand, New York, 1967; Mir, Moscow, 1970).
12. A. S. Sonin and B. A. Strukov, *Introduction to Ferroelectricity* (Vysshaya Shkola, Moscow, 1970), p. 272 [in Russian].
13. L. I. Ivleva, N. V. Bogodaev, N. M. Polozkov, and V. V. Osiko, Opt. Mater. **4**, 168 (1995).
14. A. G. Khachaturyan, *The Theory of Phase Transformations and the Structure of Solid Solutions* (Nauka, Moscow, 1974), p. 384 [in Russian].
15. R. E. Stoiber and S. A. Morse, *Microscopic Indentification of Crystals* (Ronald, New York, 1972; Mir, Moscow, 1974).
16. N. R. Ivanov, S. P. Chumakova, A. V. Ginzberg, and V. V. Dolbinina, Kristallografiya **45** (6), 1061 (2000) [Crystallogr. Rep. **45**, 979 (2000)].
17. F. Jona and G. Shirane, *Ferroelectric Crystals* (Pergamon Press, Oxford, 1962; Mir, Moscow, 1965).
18. W. A. Wooster, *Tensors and Group Theory for the Physical Properties of Crystals* (Clarendon Press, Oxford, 1973; Mir, Moscow, 1977).

Translated by Yu. Sin'kov

LATTICE DYNAMICS
AND PHASE TRANSITIONS

Low-Temperature X-ray Diffraction Studies
of [(CH$_3$)$_2$NH$_2$]$_5$Cd$_3$Cl$_{11}$ Crystals

A. U. Sheleg*, E. M. Zub*, A. Ya. Yachkovskiĭ*, and L. F. Kirpichnikova**

* Institute of Solid State and Semiconductor Physics, National Academy of Sciences of Belarus,
ul. Brovki 17, Minsk, 220072 Belarus
e-mail: sheleg@ifttp.bas-net.by
** Shubnikov Institute of Crystallography, Russian Academy of Sciences,
Leninskiĭ pr. 59, Moscow, 119333 Russia
Received March 16, 2004

Abstract—[(CH$_3$)$_2$NH$_2$]$_5$Cd$_3$Cl$_{11}$ crystals are grown by the method of isothermal evaporation from saturated aqueous solutions containing dimethylamine and cadmium chlorides, [(CH$_3$)2NH$_2$]Cl and CdCl$_{2.5}$H$_2$O. The crystal grown are studied by the X-ray diffraction method. It is established that the crystals are orthorhombic with the unit-cell parameters at room temperature $a = 18.115 \pm 0.004$ Å, $b = 11.432 \pm 0.002$ Å, and $c = 15.821 \pm 0.003$ Å. The unit-cell parameters a, b, and c of the [(CH$_3$)$_2$NH$_2$]$_5$Cd$_3$Cl$_{11}$ crystals are measured as functions of temperature in the temperature range 100–320 K. The data obtained were used to determine the thermal expansion coefficients along the main crystallographic axes. The temperature curves of the unit-cell parameters and thermal expansion coefficients showed pronounced anomalies in the vicinity of the temperatures $T_1 = 120$, $T_2 = 150$, and $T_3 = 180$ K corresponding to the phase transitions in the [(CH$_3$)$_2$NH$_2$]$_5$Cd$_3$Cl$_{11}$ crystals. The crystals are also characterized by a pronounced anisotropy of thermal expansion. © 2004 MAIK "Nauka/Interperiodica".

INTRODUCTION

Crystals containing dimethylammonium (DMA) cations, which belong to the family described by the general formula [(CH$_3$)$_2$NH$_2$]$_2$*Me*Cl$_4$ (*Me* = Cu, Co, Zn, and Cd), are of great interest since most of these crystals undergo a number of phase transitions in the low-temperature range because of ordering of hydrogen bonds and changes in cation dynamics [1–7].

Growth of new crystals with dimethylammonium cations described by the chemical formula [(CH$_3$)$_2$NH$_2$]$_5$Cd$_3$Cl$_{11}$ (DMA))$_5$Cd$_3$Cl$_{11}$) was first reported by Czapla *et al.* [8], who studied these crystals by the X-ray diffraction method at room temperature and also measured the dielectric constant ε along the main crystallographic axes as a function of temperature in the temperature range 127–300 K. It was shown [8, 9] that the crystals are orthorhombic (sp. gr. C_{mcm}) with the unit-cell parameters $a = 18.108 \pm 0.015$ Å, $b = 11.413 \pm 0.008$ Å, and $c = 15.789 \pm 0.010$ Å, $Z = 4$. The anomalies on the curves of the temperature dependence of the dielectric constant measured along the *c* axis showed the occurrence in these crystals of phase transitions at $T_1 = 127$, $T_2 = 180$, and $T_3 = 260$ K. The phase transformation at $T_1 = 127$ K is a first-order phase transition during which sample cracking was observed. At $T_2 = 180$ K, a second-order phase transition takes place The dilatometric and dielectric measurements made on these crystals [10] showed the occurrence of the phase transition also at $T_2 = 179$ K. Birefringence measure-

ments [11] confirmed the existence in (DMA)$_5$Cd$_3$Cl$_{11}$ crystals of phase transitions at $T_1 = 127$ and $T_2 = 178.5$ K. Gezi and Czapla [12] studied the influence of pressure on dielectric properties of these crystals. In the absence of pressure ($P = 0$), the curve of the temperature dependence of the dielectric constant showed a maximum in the vicinity of 280 K.

Below, we present the results of an X-ray study of the temperature dependence of the unit-cell parameters and thermal expansion of a [(CH$_3$)$_2$NH$_2$]$_5$Cd$_3$Cl$_{11}$ crystal in the temperature range 100–320 K undertaken with the aim of refining the temperatures of the phase transitions and their sequence.

EXPERIMENTAL

Single crystals of the composition [(CH$_3$)$_2$NH$_2$]$_5$Cd$_3$Cl$_{11}$ were grown from a saturated aqueous solution containing dimethylamine and cadmium chlorides, [(CH$_3$)$_2$NH$_2$]Cl and CdCl$_2$ · 2.5H$_2$O, by the method of isothermal evaporation. A subsequent X-ray diffraction study showed that the crystals belong to the orthorhombic system with the unit-cell parameters at room temperature $a = 18.115 \pm 0.004$, $b = 11.432 \pm 0.002$, and $c = 15.821 \pm 0.003$ Å. The transparent colorless $10 \times 20 \times 10$-mm-large crystals thus grown had the shape of rhombic prisms. The two largest growth faces had the shape of rhombuses and were (001) crystallographic planes, whereas the four side
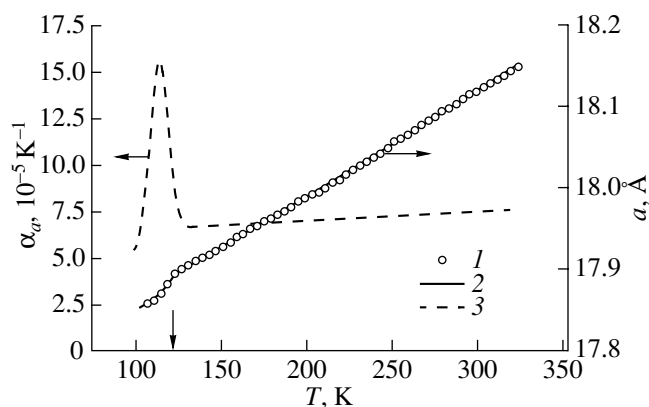
Fig. 1. Temperature dependences of the unit-cell parameter a and the thermal-expansion coefficient: (*1*) experimental dots, (*2*) approximation of the experimental data, (*3*) thermal expansion coefficient α_a.

Fig. 2. Temperature dependence of the unit-cell parameter b and the thermal expansion coefficient: (*1*) experimental dots, (*2*) approximation of the experimental data, (*3*) thermal expansion coefficient α_b.

faces coincided with the crystallographic (110), ($\bar{1}$10), (1$\bar{1}$0), and ($\bar{1}\bar{1}$0) planes. Some crystals also had additional (100) planes.

The $[(CH_3)_2NH_2]_5Cd_3Cl_{11}$ crystals grown were studied by X-ray diffraction method on a TUR-M62 diffractometer (CuK_α radiation) and in a Rigaku low-temperature X-ray diffraction chamber. The measurements were made in the temperature range 100–320 K. The samples were ~$5 \times 4 \times 2$ mm plates cut from single crystals with the reflecting faces being the natural growth (001) and (110) faces. The (010) and (100) planes were checked by the X-ray diffraction method within an accuracy of ±7'. The temperature dependences of the unit-cell parameters were constructed using the measured value of the Bragg angles of the 00.18. 17.00. and 0 10.0 reflections. The diffraction spectra were recorded by continuous θ and 2θ scanning with recording of reflection intensity profiles at a rate of (1/4) deg/min at a step of 2K.

The sample temperature was set by a special control block based on a VRT-3 temperature regulator and was controlled by a copper–constantan thermocouple. This system maintained the sample temperature with an accuracy of ±2 K in the temperature range 100–320 K. Prior to each run, the sample was thermostated within 10–15 minutes at the given temperature. Using the experimental temperature dependences of the unit-cell parameters and volume $a = f(T)$, $b = f(T)$, $c = f(T)$, and $V = f(T)$, we determined the corresponding thermal expansion coefficients $\alpha_a = f(T)$, $\alpha_b = f(T)$, and $\alpha_c = f(T)$ along the main crystallographic axes and also the volume expansion coefficient $\alpha_V = f(T)$ in the temperature range 100–320 K. The experimental $a = f(T)$, $b = f(T)$, $c = f(T)$, and $V = f(T)$ curves were then approximated by polynomials of the form $L = A + \sum_i^n (-1)^i B_i T^i$. The approximation curves were divided into temperature 1–3 K segments within which the ther-

mal expansion coefficients were calculated by the formula $\alpha_L = \Delta L/(L\Delta T)$, where L are the a, b, c, and V values at the middle point of the ΔT segment for which the thermal expansion coefficient is determined and ΔL is the change of the parameter within this segment.

RESULTS AND DISCUSSION

Figures 1–4 show the temperature dependences of the a, b, and c unit-cell parameters and the unit-cell volume V and the temperature dependences of the thermal expansion coefficient $\alpha_a = f(T)$, $\alpha_b = f(T)$, $\alpha_c = f(T)$, and $\alpha_V = f(T)$ of a $[(CH_3)_2NH_2]_5Cd_3Cl_{11}$ crystal. It is seen that the unit-cell parameters a, b, and c and the unit-cell volume V of this crystal increase with the temperature in the whole temperature range studied. However, the characters of the variation of the a, b, and c unit-cell parameters with the temperature are somewhat different (Fig. 1–3). The variation of parameter a in the temperature range 120–320 K (Fig. 1) and parameter c in the range 180–320 K (Fig. 3) are of the linear nature. The temperature dependence of the experimental values of parameter b (Fig. 2) in the range 102–189 K is described by a third-degree polynomial; in the vicinity of $T_1 = 180$ K, the curve shows a kink; with a further increase in temperature it acquires a linear character. Moreover, at $T_2 = 150$ K, the tangent of the slope of the $b = f(T)$ curve changes, which manifests itself as a well-pronounced maximum at 150 K on the temperature dependence of the thermal expansion coefficient. It should be indicated that the curve $a = f(T)$ shows an anomaly (a kink) at $T_1 = 120$ K (Fig. 1). It is seen from Fig. 3 that the $c = f(T)$ curve also has kinks at $T_1 = 124$, $T_2 = 149$. and $T_3 = 181$ K. The temperature dependences of the thermal expansion coefficient, $\alpha_a = f(T)$ and $\alpha_c = f(T)$, in the vicinities of these temperatures also have anomalies (extrema). The kinks at $T_1 = 120$ and

Fig. 3. Temperature dependence of the unit-cell parameter c and the thermal-expansion coefficient: (*1*) experimental dots, (*2*) approximation of the experimental data, (*3*) thermal expansion coefficient α_c.
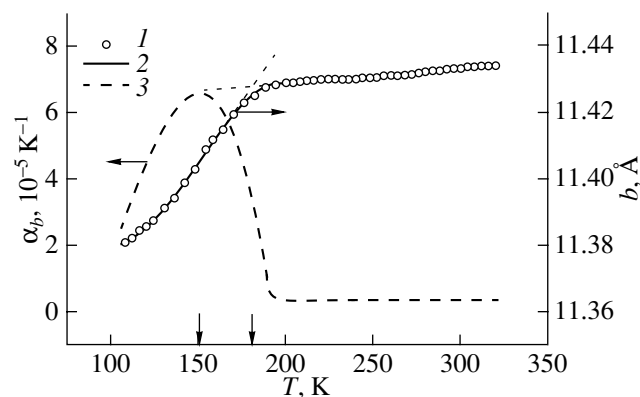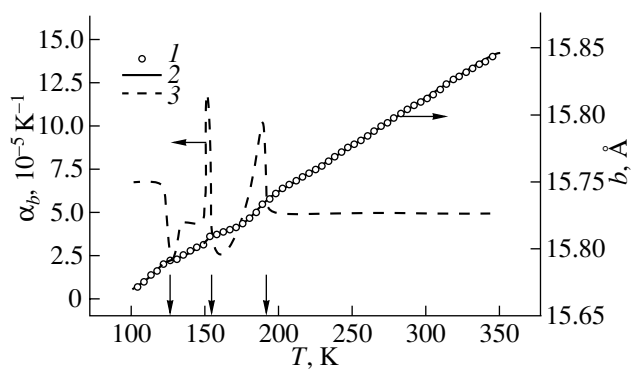

Fig. 4. Temperature dependence of the unit-cell volume V and the thermal-expansion coefficient: (*1*) experimental dots, (*2*) approximation of the experimental data, (*3*) thermal expansion coefficient α_V.

$T_3 = 183$ K are also observed at the $V = f(T)$ curve (Fig. 4).

The anomalies observed at $T_1 = 120$, $T_2 = 150$, and $T_3 = 180$ K indicate that, at these temperatures, the $[(CH_3)_2NH_2]_5Cd_3Cl_{11}$ crystals undergo phase transitions. It can be seen from the figures that the crystal under study is characterized by anisotropy of thermal expansion such that $\alpha_b \ll \alpha_c \approx \alpha_a$. It is interesting that the thermal expansion coefficients α_a, α_b, and α_c in the temperature ranges 120–320, 200–320, and 180–320 K, respectively, are practically temperature-independent. The α_b value is less than α_a and α_c by an order of magnitude. The α_b values in the range 180–320 K are equal to $\sim 4 \times 10^{-6}$ K^{-1}, whereas the values of α_a and α_c are equal to $\sim 6 \times 10^{-5}$ K^{-1}. Thermal expansion of this crystal was studied by the dilatometric method in the temperature range 160–300 K [10]; the thermal expansion coefficient α_a along the c axis at room temperature satisfactorily agrees with our data, whereas the α_a and α_b values and the character of their temperature dependences considerably differ from our data. Moreover, contrary to the results obtained in [10] (negative α_b values at temperatures above $T_1 = 179$ K), the thermal expansion coefficients α_a, α_b, and α_c along all the three crystallographic axes obtained in this study are positive in the whole temperature range studied. It should also be indicated that our $[(CH_3)_2NH_2]_5Cd_3Cl_{11}$ samples started cracking not at 127 K (as in [8]), but at $T = 102$ K.

Such a character of thermal expansion of the crystal seems to be associated with the typical features of its structure [9]. The $[(CH_3)_2NH_2]_5Cd_3Cl_{11}$ structure is built by two layers parallel to the (001) plane. One of these layers consists of dimethylammonium cations $[(CH_3)_2NH_2]^+$, whereas the other layer consists of anions of cadmium chloride complexes $[Cd_3Cl_{11}]^{5-}$.
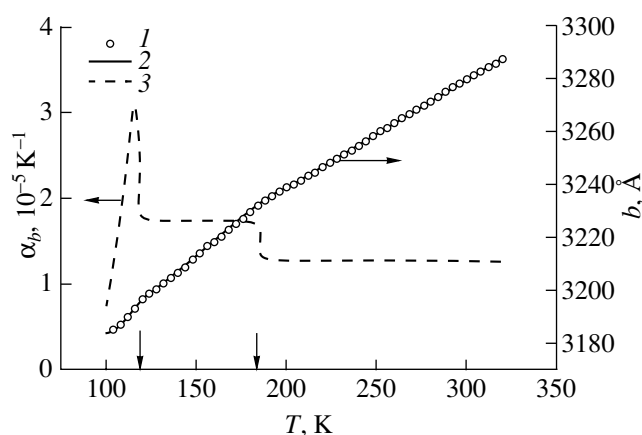
These layers are linked by comparatively weak N–H···Cl hydrogen bonds [9]. Considering the chemical bonds in the layer of dimethylammonium cations, we see that these cations are bound by weak van der Waals bonds. The $[Cd_3Cl_{11}]^{5-}$ complexes in the layer of cadmium chloride anions are linked by ammonium groups. In the $[Cd_3Cl_{11}]^{5-}$ anion, three cadmium atoms and three chlorine atoms with double bonds lie in the same plane and form a hexagon whose angles are alternatively occupied by Cd and Cl atoms [9]. The interatomic forces in this hexagon are much stronger than the interaction forces between the layers. The layers in the crystal lattice are arranged in such a way that, along the a axis, the atomic interactions characteristic of the layers of dimethylammonium cations prevail, whereas along the b axis, the stronger interactions characteristic of the $[Cd_3Cl_{11}]^{5-}$ complexes prevail. This may be explained by the fact that the thermal expansion coefficients along the a and c axes are approximately equal, whereas along the b axis, this coefficient is lower by an order of magnitude.

Attention is attracted to the fact that the anomalies corresponding to the phase transitions manifest themselves differently along different crystallographic directions. Curve $a = f(T)$ has only one kink at $T_1 = 120$ K, whereas curve $c = f(T)$ shows all three phase transitions and curve $b = f(T)$ shows two phase transitions at $T_2 = 150$ and $T_3 = 180$ K. This seems to be associated with the sequence of phase transitions in this crystal, which is determined by the anisotropic reorientational motion of dimethylammonium cations [8].

It should be indicated that small differences in the temperatures of phase transitions determined from different curves, $a = f(T)$, $b = f(T)$, and $c = f(T)$, seem to explained by the use of the samples cut out from different crystals with different defect densities. As is well known, the physical properties of crystals with hydrogen bonds (such as $[(CH_3)_2NH_2]_5Cd_3Cl_{11}$), including

the phase-transition temperatures, are very sensitive to the crystal history and defects and stresses in the crystal lattice.

Thus, the X-ray diffraction study of $[(CH_3)_2NH_2]_5Cd_3Cl_{11}$ crystals confirmed the occurrence of the phase transition at $T_3 = 180$ K and also showed the occurrence of new phase transitions at $T_1 = 120$ and $T_2 = 150$ K. It is difficult to uniquely establish the order of these phase transitions solely from the character of the anomalies on the temperature dependences of the unit-cell parameters and the thermal expansion coefficients. Therefore, we will measure also heat capacity of this crystal in the same temperature range. We also established the anisotropy of thermal expansion of this crystal.

REFERENCES

1. Z. A. Bobrova and V. M. Varikash, Dokl. Akad. Nauk BSSR **30** (6), 510 (1986).

2. V. E. Vasil'ev, V. M. Rudyak, Z. A. Bobrova, and V. M. Varikash, Fiz. Tverd. Tela (Leningrad) **29** (5), 1539 (1987) [Sov. Phys. Solid State **29**, 882 (1987)].

3. O. T. Vlokh, V. B. Kapustyanyk, and I. I. Mykhalina, Kristallografiya **37** (3), 766 (1992) [Sov. Phys. Crystallogr. **37**, 403 (1992)].

4. O. T. Vlokh, V. B. Kapustyanyk, and I. I. Polovinko, Zh. Prikl. Spektrosk. **52** (5), 785 (1990).

5. A. U. Sheleg, E. M. Zub, A. Ya. Yachkovskiĭ, and L. F. Kirpichnikova, Kristallografiya **47** (4), 634 (2002) [Crystallogr. Rep. **47**, 577 (2002)].

6. A. U. Sheleg, T. I. Dekola, and N. P. Tekhanovich, Fiz. Tverd. Tela (St. Petersburg) **45** (5), 901 (2003) [Phys. Solid State **45**, 946 (2003)].

7. A. U. Sheleg, E. M. Zub, and A. Ya. Yachkovskiĭ, Poverkhnost: Rentgen. Sinkhron. Neĭtron. Issled., No. 6, 83 (2003).

8. Z. Czapla, S. Dacko, U. Krzewska, and A. Waskowska, Solid State Commun. **71** (2), 139 (1989).

9. A. Waskowska, T. Lis, U. Krzewska, and Z. Czapla, Acta Crystallogr. **46**, 1768 (1990).

10. H. Pykach and Z. Czapla, Ferroelectr. Lett. Sect. **24**, 141 (1998).

11. Z. Czapla, J. Pzeslawski, and H. Schlembach, Solid State Commun. **91** (12), 981 (1994).

12. K. Gesi and Z. Czapla, Ferroelectrics **159**, 37 (1994).

Translated by L. Man

Selective Optical Properties of a Multilayered Periodic Gyrotropic Structure at an Arbitrary Angle of Incidence of Waves

I. V. Semchenko and V. E. Kaganovich

Gomel State University, ul. Sovetskaya 14, Gomel, 246019 Belarus
e-mail: isemchenko@gsu.unibel.by
Received April 28, 2003

Abstract—A multilayered periodic gyrotropic structure consisting of an arbitrary number of unit cells is considered. The gyrotropic properties of this multilayered structure are due to the external magnetic field. A matrix is calculated on the basis of the boundary conditions for waves in each layer, which relates a wave incident at an arbitrary angle with the transmitted and reflected waves. The complex amplitude transmittance and reflectance are found for the entire multilayered structure from the calculated matrix elements. The optimal parameters of a structure consisting of layers of potassium dihydrogen phosphate and europium-doped glass are calculated. The dependences of the intensity, ellipticity, and the angle of rotation of the major axis of the polarization ellipse of reflected and transmitted waves on the number of cells, light frequency, and magnetic field at an arbitrary angle of incidence of waves are obtained in graphical form. The structure considered is characterized by selective reflection of electromagnetic waves and can be used as a polarization converter controlled by a magnetic field. © 2004 MAIK "Nauka/Interperiodica".

INTRODUCTION

Multilayered composite materials have attracted the interest of researchers studying electromagnetic properties of materials for many years [1–11]. It was shown in [1–3] that, in the thin-film limit, the magneto-optical Kerr effect obeys the additivity law for a system consisting of an arbitrary number of magnetic films. This conclusion was verified experimentally and by numerical calculation by an example of a three-layer Fe/Cu/Fe structure grown on a Pb substrate. An elementary formula for the magneto-optical Kerr effect was derived based on the superlattice model. The specific features of interaction of light with a periodic bigyrotropic medium were investigated in [4]. The values of the reflectance and transmittance, the ellipticity, and the angle of rotation of the plane of polarization of a light wave at resonant and nonresonant frequencies were obtained. To describe the propagation of electromagnetic waves in bianisotropic chiral layered structures, it was proposed in [5] to use the 4×4 matrix method. The dependences of the amplitude and polarization characteristics of reflected and transmitted waves on the angle of incidence were also studied in [5]. The reflection and transmission of light in periodic anisotropic structures containing layers that interact coherently and incoherently with transmitted waves were considered in [6]. Formulas for the intensity and polarization of reflected and transmitted light were derived for a three-layer system in [7]. The system considered in [7] was formed of a ferromagnetic film and two adjacent nonmagnetic layers. The effects of interference and absorption of light were taken into account. Expressions for the Fresnel coefficients for a wave incident on a semi-infinite composite were obtained in [8]. The properties of a layered ferromagnetic insulator on the surface of a material in a microwave device placed in a static magnetic field were investigated in [9–11].

However, the optical properties of multilayered periodic structures, selective with respect to frequency and polarization, were not considered in detail in the noted studies. The selectivity of optical properties is most pronounced when resonant reflection of one of natural circularly polarized light waves is observed in the gyrotropic layer.

In this study, we consider an electromagnetic wave incident on a multilayered structure consisting of an arbitrary number of repetitive unit cells in an external magnetic field. It is assumed that the first layer in the unit cell is isotropic and nongyrotropic. The second layer is also isotropic but, at the same time, magneto-optically active, which manifests itself in the circular birefringence of waves in this layer.

To determine the parameters of a wave reflected from a multilayered structure and a wave passed through it, we used a matrix method based on the linearity of the equations describing the propagation of light. Therefore, the continuity of the tangential components of the electric and magnetic fields of a light wave at the interface between two isotropic media can be described using a linear matrix transformation [12, 13].

A uniaxial potassium dihydrogen phosphate (KDP) crystal (the symmetry class $\bar{4}2m$) with the optical axis directed perpendicular to the interface is chosen as the first layer of the unit cell. This layer is optically isotropic and nongyrotropic. A europium glass is taken as the material of the second (gyrotropic) layer.

In this study, we determined the reflectance and transmittance of light for a multilayered periodic structure. The dependences of the amplitude and polarization characteristics of reflected and transmitted waves on the thicknesses of layers, magnetic field, and the angle of incidence of a wave are obtained in the graphical form for the case of selective reflection from the structure.

NORMAL INCIDENCE OF WAVES

Let us consider the case of normal incidence of waves on a multilayered periodic structure. Figure 1 schematically shows this structure in an external magnetic field. The material equations for the magnetoactive layer of the structure under consideration have the form [14, 15]

$$\begin{cases} \mathbf{D} = \varepsilon_0 \varepsilon \mathbf{E} + i\varepsilon_0 \mathbf{g} \times \mathbf{E}, \\ \mathbf{B} = \mu_0 \mu \mathbf{H} \end{cases}, \quad (1)$$

where ε and μ are the relative dielectric and magnetic permittivities, respectively, and $\mathbf{g}$ is the gyration vector, which depends on the crystallographic symmetry of the medium and the vector of the magnetic field strength. As follows from the solution to the Maxwell equations, the refractive index for natural waves of an isotropic gyrotropic medium is

$$n_\pm = \sqrt{\mu(\varepsilon \pm g)}, \quad (2)$$

where the subscripts "+" and "–" denote the left-hand and right-hand circularly polarized wave components, respectively.

Using the boundary conditions for waves in each layer, one can calculate the scattering matrix M, which relates the incident wave with the transmitted and reflected waves [16, 17]:

$$M = I_{21} D_1 I_{12} D_2, \quad (3)$$

where

$$I_{ij} = \frac{1}{t_{ij}} \begin{pmatrix} 1 & r_{ij} \\ r_{ij} & 1 \end{pmatrix}, \quad D_j = \begin{pmatrix} e^{-ik_j d_j} & 0 \\ 0 & e^{ik_j d_j} \end{pmatrix},$$

I_{ij} is the transmission matrix for the interface between the ith and jth layers, D_j is the propagation matrix for the jth layer, t_{ij} is the amplitude transmittance for the interface between the ith and jth layers, r_{ij} is the amplitude reflectance for the interface between the ith and jth layers, $k_j = \dfrac{\omega n_j}{c}$ is the wave number for the jth layer, ω
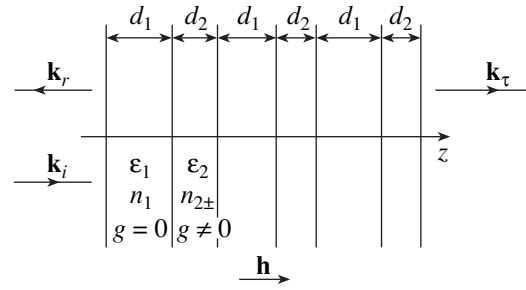
Fig. 1. Schematic diagram of a multilayered periodic structure for the case of normal incidence of waves.

is the circular wave frequency, $c = (\sqrt{\varepsilon_0 \mu_0})^{-1}$ is the speed of light in vacuum, n_j is the refractive index of light in the jth layer, and d_j is the thickness of the jth layer.

In the case of a multilayered periodic structure consisting of N unit cells, the matrix M must be raised to the Nth power. The matrix M^{eff} for the entire multilayered periodic structure can be written as the product

$$M^{\text{eff}} = I_a M^N I_b, \quad (4)$$

where I_a is the transmission matrix for the interface between two adjacent layers in the structure and I_b is the transmission matrix for the structure–environment interface.

The matrix M^{eff} thus obtained relates the wave incident on the multilayered periodic structure and the transmitted wave. The complex amplitude transmittance and reflectance of the entire multilayered periodic structure are expressed in terms of the elements of this matrix:

$$T = \frac{1}{M^{\text{eff}}_{(1, 1)}}, \quad R = \frac{M^{\text{eff}}_{(2, 1)}}{M^{\text{eff}}_{(1, 1)}}. \quad (5)$$

In order to observe the maximum reflection of waves from each cell, selective with respect to polarization, the layer thicknesses d_1 and d_2 should satisfy the following relations:

$$2k_1 d_1 = (2m_1 + 1)\pi,$$
$$2k_{2+} d_2 = (2m_{2+} + 1)\pi, \quad (6)$$
$$2k_{2-} d_2 = m_{2-}\pi,$$

where m_1 and m_2 are integers, k_1 is the wave number for the nongyrotropic layer, and $k_{2\pm}$ are the wave numbers of the right- and left-hand polarized waves for the gyrotropic layer. Choosing the thicknesses of the layers corresponding to the frequency of electromagnetic waves and the external magnetic field strength, one can obtain the maximum reflection for one of the circularly polarized waves and, simultaneously, the minimum reflection for the wave of opposite polarization (Fig. 2).

It can be seen from Fig. 2 that, with an increase in the number of cells, the intensity of the left-hand polar-

Fig. 2. Dependence of the normalized intensity I_r of the reflected wave on a number of cells N for the cases of incidence of a left- and right-hand circularly polarized waves (I_{r_p} and I_{r_m}, respectively): $h = 16 \times 10^5$ A/m, $\lambda = 500$ nm, $\varepsilon_1 = 2.161$, $\varepsilon_2 = 2.56$, $\mu_1 = 1$, $\mu_2 = 1$, $g_z = -1.882 \times 10^{-4}$, $d_1 = 1.90 \times 10^{-5}$ m, and $d_2 = 1.06 \times 10^{-3}$ m.

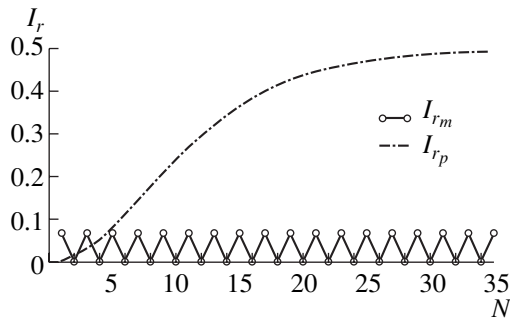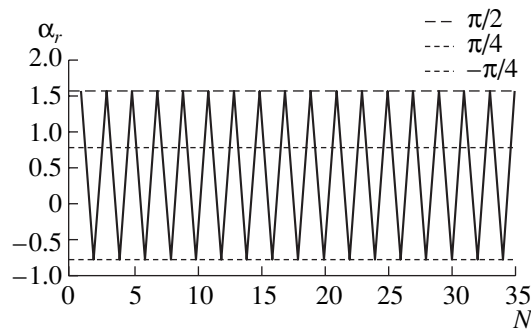**Fig. 3.** Dependence of the angle of rotation α_r of the major axis of the polarization ellipse of the reflected wave on the number of cells N. The calculation parameters are the same as in Fig. 2.
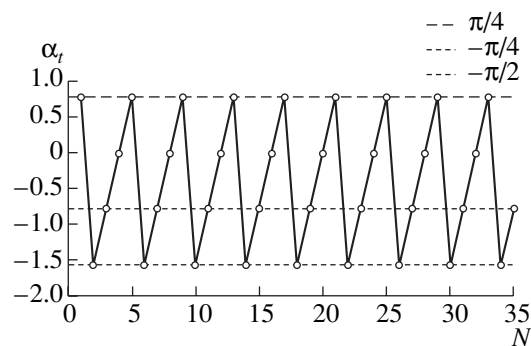

Fig. 4. Dependence of the angle of rotation α_t of the major axis of the polarization ellipse of the transmitted wave on the number of cells N. The calculation parameters are the same as in Fig. 2.

ized reflected wave steadily increases and reaches saturation, while the intensity of the right-hand polarized reflected wave oscillates, periodically approaching zero. This makes it possible to obtain the polarization of the reflected wave close to circular [16, 17].

An electromagnetic wave can be represented as a superposition of two circular waves with the wave numbers k_+ and k_-. Then, the specific angle of rotation of the plane of polarization can be found by the formula

$$\alpha = \frac{1}{2}(k_+ + k_-). \qquad (7)$$

It can be seen from Figs. 3 and 4 that, for an odd number of cells, the polarization ellipse of the reflected wave is rotated by $\pi/2$. The polarization ellipse of the transmitted wave can be rotated by either $\pi/4$ or $-\pi/4$ at an odd number of cells and by either 0 or $-\pi/2$ at an even number of cells. Systems consisting of 10 or 11 cells are most interesting since the intensities of both reflected and transmitted wave are sufficiently high for such systems. For a multilayered periodic structure consisting of ten unit cells, the plane of polarization of the transmitted wave is rotated by $-\pi/2$. In this case, the reflected wave is circularly polarized and the transmitted wave is linearly polarized. In the case of a system consisting of 11 cells, the reflected wave is elliptically polarized and its polarization ellipse is rotated by $\pi/2$, while the transmitted wave is linearly polarized and its the plane of polarization is rotated by $-\pi/4$. A system consisting of 11 cells can be used as a polarization switch.

Analysis of the dependences obtained shows that, at a small deviation of the thickness of the unit-cell layers from the resonance value, the character of the dependences changes: the saturation intensity of the reflected wave significantly decreases and, with further deviation from the resonance thickness, the intensity of the reflected wave oscillates with a long period with a change in the total number of cells (the total thickness of the structure). The case of significant deviation of the layer thickness from the resonance value is of interest only for consideration of the transmitted wave since the intensity of the reflected wave is very low in this case.

The complex amplitudes obtained by the matrix method make it possible to calculate the ellipticity of the reflected and transmitted waves for the entire multilayered periodic structure:

$$\rho = \frac{|E_+| - |E_-|}{|E_+| + |E_-|}, \qquad (8)$$

where E_+ and E_- are the amplitudes of the left- and right-hand circularly polarized waves, respectively.

Figures 5 and 6 show that the range of the external magnetic field strength $h \sim 16.7 \times 10^5 – 18.1 \times 10^5$ A/m is of primary interest, since the reflected wave is elliptically polarized in this range. With a change in the magnetic field, the polarization ellipse of the reflected wave continuously rotates by $\pi/2$. The same change in the azimuth of the polarization ellipse in this range is also characteristic of the transmitted wave.
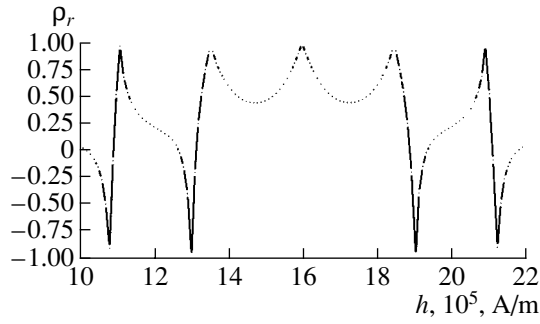
Fig. 5. Dependence of the ellipticity ρ_r of the reflected wave on the external magnetic field strength **h** for $N = 26$. The calculation parameters are the same as in Fig. 2.

Fig. 6. Dependence of the azimuthal angle α_r of the reflected wave on the external magnetic field strength h. The calculation parameters are the same as in Fig. 2.

INCIDENCE OF WAVES AT AN ARBITRARY ANGLE

In the case of oblique incidence of waves on a multilayered periodic structure, a wave in the gyrotropic layer has two modes propagating at different angles (Fig. 7). Hence, 4×4 matrices should be used in the matrix method [18].

The elements of the matrix I_{ik}, which relates the incident wave with the transmitted and reflected waves at the interface between the nongyrotropic and gyrotropic layers, can be derived from the continuity equations for the tangential components of the electric and magnetic field vectors and the solutions to the Maxwell equations:

$$I_{11} = A_+^{(2)}, \quad I_{12} = \alpha_- \cos(\theta_-) A_-^{(2)}, \quad I_{13} = -A_+^{(1)},$$

$$I_{14} = \alpha_- \cos(\theta_-) A_-^{(1)}, \quad I_{21} = \frac{B_+^{(2)}}{\alpha_+ \cos(\theta_+)}, \quad I_{22} = B_-^{(2)},$$

$$I_{23} = -\frac{B_+^{(1)}}{\alpha_+ \cos(\theta_+)}, \quad I_{24} = B_-^{(1)}, \quad I_{31} = I_{13}, \tag{9}$$

$$I_{32} = -I_{14}, \quad I_{33} = I_{11}, \quad I_{34} = -I_{12}, \quad I_{41} = -I_{23},$$

$$I_{42} = I_{24}, \quad I_{43} = -I_{21}, \quad I_{44} = I_{22},$$

where

$$A_\pm^{(p)} = \frac{\mu_2 n_1 \cos(\theta_1) + (-1)^p \mu_1 n_\pm \cos(\theta_\pm)}{2\mu_2 n_1 \cos(\theta_1)},$$

$$B_\pm^{(p)} = \frac{\mu_2 n_1 \cos(\theta_\pm) + (-1)^p \mu_1 n_\pm \cos(\theta_1)}{2\mu_2 n_1 \cos(\theta_1)},$$

$$\alpha_\pm = \frac{i\mu_2 g_z}{(n_\pm)^2 - \mu_2 \epsilon_2};$$

$p = 1, 2$; the subscripts "+" and "−" of the parameters refer to the left- and right-hand circularly polarized wave components; θ_+ and θ_- are the angles between the z axis and the wave vectors of the left- and right-hand circular wave components in the gyrotropic layer; θ_1 is the angle between the z axis and the wave vector of the wave in the nongyrotropic layer; μ_1, ϵ_1, and $n_1 = \sqrt{\epsilon_1 \mu_1}$ are the magnetic permittivity, the dielectric permittivity, and the refractive index of the nongyrotropic layer, respectively; μ_2, ϵ_2, and $n_\pm = ((2\mu_2\epsilon_2^2 - \mu_2 g_z^2 \sin^2(\theta_\pm) \mp (\mu_2^2 g_z^4 \sin^4(\theta_\pm) + 4\mu_2^2\epsilon_2^2 g_z^2 \cos^2(\theta_\pm))^{1/2}/2\epsilon_2)^{1/2}$ are the magnetic permittivity, the dielectric permittivity, and the refractive indices of the gyrotropic layer, respectively; and g_z is the z component of the gyration vector.

The elements of the matrix J_{ik} which relates the incident wave with the transmitted and reflected waves at the interfaces between a gyrotropic and nongyrotropic layers, are expressed similarly and can be written as

$$J_{11} = -D_+ - C_+ \cos(\theta_1),$$

$$J_{12} = D_+\alpha_- \cos(\theta_1) + C_+ \cos^2(\theta_-)\alpha_-,$$

$$J_{13} = D_+ - C_+ \cos(\theta_1),$$

$$J_{14} = D_+\alpha_- \cos(\theta_1) - C_+ \cos^2(\theta_-)\alpha_-,$$

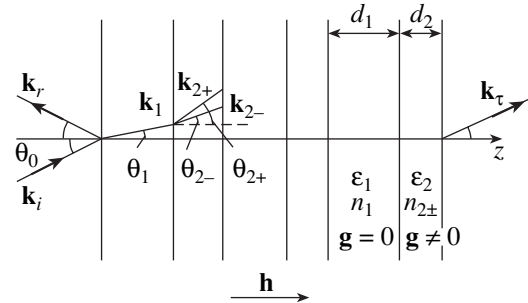**Fig. 7.** Schematic diagram of a multilayered periodic structure for the case of oblique incidence of waves at an arbitrary angle.
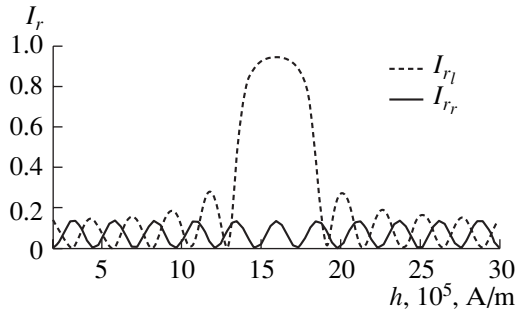
Fig. 8. Dependence of the normalized intensity I_r of the reflected wave on the external magnetic field strength h for the cases of incidence of a left- and right-hand circularly polarized waves (I_{r_p} and I_{r_m}, respectively): $\theta_0 = 15°$, $N = 25$, $d_1 = 1.93 \times 10^{-5}$ m, and $d_2 = 1.06 \times 10^{-3}$ m.
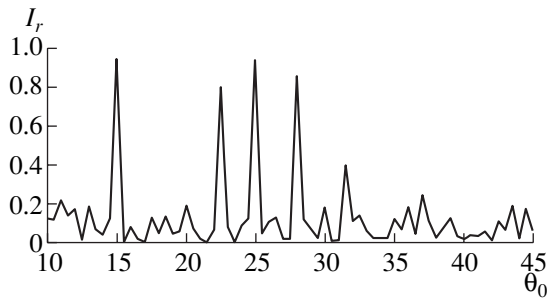
Fig. 9. Dependence of the normalized intensity I_r of the reflected wave on the angle of incidence θ_0 in the case of incidence of a left-hand polarized wave: $N = 25$, $d_1 = 1.93 \times 10^{-5}$ m, and $d_2 = 1.06 \times 10^{-3}$ m.
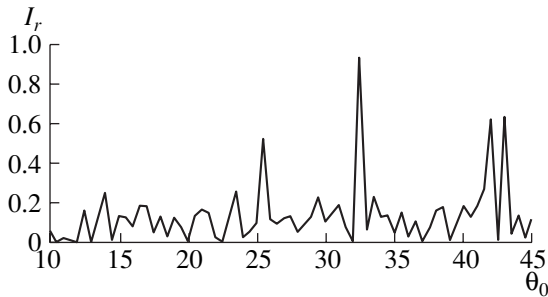
Fig. 10. Dependence of the normalized intensity I_r of the reflected wave on the angle of incidence θ_0 in the case of incidence of a right-hand polarized wave.

$$J_{21} = \frac{D_- + C_- \cos(\theta_1)}{\alpha_- \cos(\theta_-)},$$

$$J_{22} = \frac{-D_+ \alpha_- \cos(\theta_1) - C_- \cos^2(\theta_+)\alpha_+}{\alpha_- \cos(\theta_-)}, \quad (10)$$

$$J_{23} = \frac{-D_- + C_- \cos(\theta_1)}{\alpha_- \cos(\theta_-)},$$

$$J_{24} = \frac{-D_+ \alpha_- \cos(\theta_1) + C_- \cos^2(\theta_+)\alpha_+}{\alpha_- \cos(\theta_-)},$$

$$J_{31} = J_{13}, \quad J_{32} = -J_{14}, \quad J_{33} = J_{11}, \quad J_{34} = -J_{12},$$

$$J_{41} = -J_{23}, \quad J_{42} = J_{24}, \quad J_{43} = -J_{21}, \quad J_{44} = J_{22},$$

where

$$D_\pm = \frac{1}{2}\frac{\alpha_\pm}{\alpha_- - \alpha_+},$$

$$C_\pm = \frac{1}{2}\frac{\mu_2 n_1}{n_\pm \mu_1}\frac{\cos(\theta_\pm)\alpha_\pm}{\cos^2(\theta_-)\alpha_- - \cos^2(\theta_+)\alpha_+}.$$

The matrix D_j, which describes the wave propagation in the jth layer, has a standard diagonal form [12]. The resulting matrix M_{ik} for the entire unit cell, as in the case of normal incidence, is obtained by multiplication:

$$M = JD_1ID_2. \quad (11)$$

To obtain the maximum reflection of the wave from each cell, the thicknesses of the layers should satisfy the relations [13]

$$2k_1d_1\cos(\theta_1) = (2m_1 + 1)\pi,$$
$$2k_2d_2\cos(\theta_2) = (2m_2 + 1)\pi, \quad (12)$$

where m_1 and m_2 are integers and k_1 and k_2 are the wave numbers of the right- or left-hand circularly polarized wave in the first and second layers, respectively. Similarly, the condition for the maximum transmission of the wave passed through the cell can be written as

$$k_1d_1\cos(\theta_1) = m_1\pi,$$
$$k_2d_2\cos(\theta_2) = m_2\pi. \quad (13)$$

When conditions (12) and (13) are satisfied, the intensity of the reflected wave for the calculated value of the external magnetic field strength 16×10^5 A/m is maximum in the case of incidence of a left-hand circularly polarized wave and close to zero when a right-hand circularly polarized wave is incident on the structure (Fig. 8).

Figures 9 and 10 show the dependences of the reflected-wave intensity on the angle of incidence θ_0 for left- and right hand circularly polarized incident waves, respectively. The dependence of the normalized intensity of the transmitted wave on the angle of incidence was also calculated for left- and right-hand polarized waves. The calculation showed that the relation $I_r = 1 - I_t$ holds true, as one would expect for the nonabsorbing structure under study.

It can be seen from Fig. 9 that, for the layer parameters under consideration, at an angle of incidence of 15°, a local maximum of the intensity of the reflected wave is observed for a left-hand polarized wave and, accordingly, a minimum of the transmitted wave. At the same time, in the case of incidence of a right-hand

polarized wave (Fig. 10), the intensity of the reflected wave is maximum at other angles of incidence.

Analysis of the dependences obtained shows that, in the case of incidence of electromagnetic waves on a gyrotropic multilayered periodic structure in an external magnetic field, the reflection of the waves is selective not only with respect to the wave frequency but also with respect to the wave polarization. A change in the magnetic field strength, or the angle of incidence, or the wave frequency leads to a change in the polarization characteristics of both transmitted and reflected waves. Hence, such a multilayered periodic structure showing selective reflection of light can be used as a polarization converter controlled by a magnetic field.

REFERENCES

1. J. Zak, E. R. Moog, C. Liu, and S. D. Bader, J. Magn. Magn. Mater. **88**, L261 (1990).

2. J. Zak, E. R. Moog, C. Liu, and S. D. Bader, J. Magn. Magn. Mater. **89**, 107 (1990).

3. J. Zak, E. R. Moog, C. Liu, and S. D. Bader, Appl. Phys. Lett. **58** (11), 1214 (1991).

4. O. V. Ivanov and D. I. Sementsov, Kristallografiya **41** (5), 791 (1996) [Crystallogr. Rep. **41**, 749 (1996)].

5. O. V. Ivanov and D. I. Sementsov, Kristallografiya **45** (3), 534 (2000) [Crystallogr. Rep. **45**, 487 (2000)].

6. O. V. Ivanov and D. I. Sementsov, Kristallografiya **45** (5), 899 (2000) [Crystallogr. Rep. **45**, 827 (2000)].

7. V. M. Maevskiĭ, Fiz. Met. Metalloved. **59** (2), 213 (1985).

8. O. Acher, A. L. Adenot, and F. Duverger, Phys. Rev. B **62** (20), 13748 (2000).

9. O. Acher, P. Le Gourriérec, G. Perrin, *et al.*, IEEE Trans. Microwave Theory Tech. **44** (5), 674 (1996).

10. O. Acher, P. Baclet, G. Perrin, *et al.*, J. Magn. Magn. Mater. **157–158**, 480 (1996).

11. A. L. Adenot, O. Acher, T. Taffary, *et al.*, J. Appl. Phys. **87** (9), 6914 (2000).

12. R. M. Azzam and N. M. Bashara, *Ellipsometry and Polarized Light* (North-Holland, Amsterdam, 1977; Mir, Moscow, 1981).

13. A. Yariv and P. Yeh, *Optical Waves in Crystals: Propagation and Control of Laser Radiation* (Wiley, New York, 1984; Mir, Moscow, 1987).

14. F. I. Fedorov, *Theory of Gyrotropy* (Nauka i Tekhnika, Minsk, 1976) [in Russian].

15. A. F. Konstantinova, B. N. Grechushnikov, B. V. Bokut', and E. G. Valyashko, *Optical Properties of Crystals* (Nauka i Tekhnika, Minsk, 1995) [in Russian].

16. I. V. Semchenko and V. E. Kaganovich, Proc. SPIE **4358**, 303 (2001).

17. I. V. Semchenko and V. E. Kaganovich, in *Proceedings of 8th International Conference on Electromagnetics of Complex Media* (2000), p. 317.

18. I. V. Semchenko and V. E. Kaganovich, Izv. Gomel. Gos. Univ. im. F. Skoriny, No. 6 (9), 39 (2001).

Translated by Yu. Sin'kov

Growth, Structure, and Magnetic Properties of CuFeTe$_2$ Single Crystals[1]

A. I. Dzhabbarov, S. K. Orudzhev, G. G. Guseĭnov, and N. F. Gakhramanov

Institute of Physics, Academy of Sciences of Azerbaijan,
pr. Dzhavida 33, Baku, 370143 Azerbaijan

e-mail: semic@lan.ab.az

Received June 17, 2002; in final form, March 18, 2004

Abstract—CuFeTe$_2$ single crystals were grown and the temperature dependence of their magnetic susceptibility in the temperature range 1.8–400 K was investigated. It is found that the magnetic susceptibility shows anomalies at temperatures $T_s = 65$ and $T_N = 125$ K. At $T > 125$ K, the crystal is in the paramagnetic state controlled by Fe^{2+} and Cu^{2+} ions with an effective magnetic moment of 1.44 μB. © *2004 MAIK "Nauka/Interperiodica".*

INTRODUCTION

It is known that the spins of 3d metals are coupled by Coulomb forces and long-range relativistic interactions in chalcogenides of these metals. It should be noted that the character of many physical properties (magnetic susceptibility, specific heat, and so on) depend strongly on the dimension of the magnetic structure and the character of exchange interactions. In this context, ternary chalcogenides of 3d metals are interesting, although complex, objects of study.

This study deals with the growth of CuFeTe$_2$ single crystals and investigation of the magnetic susceptibility of this material. CuFeTe$_2$ is of interest because it forms, as do other chalcogenides of 3d metals, into various crystal structures, depending on the valence state. In some cases, this circumstance facilitates the low-dimensional ordering of magnetic ions.

Many studies [1–7] have been devoted to the growth of CuFeTe$_2$ single crystals and investigation of their structural, magnetic, and electrical characteristics. Some results of these studies and the new data obtained by us are analyzed and discussed here.

GROWTH AND STRUCTURE OF SINGLE CRYSTALS

Single crystals were grown by the Bridgman method from melts prepared from previously synthesized stoichiometric ingots. We should note that growth of single crystals of chalcopyrite and its Se and Te analogs is a complex problem due to the change in the valence

states of Cu and Fe atoms during their interaction with chalcogens.

We used polycrystalline ingots of three different compositions: stoichiometric CuFeTe$_2$ and nonstoichiometric Cu$_{1.13}$Fe$_{1.22}$Te$_2$ (Vaipolin composition) and Cu$_{1.1}$Fe$_{1.2}$Te$_2$. Independent of composition, we obtained similar results by the end of experiments: a smaller part of the sample transformed into the single-crystal phase and the larger part remained polycrystalline. The single-crystal part has a layered structure with a perfect cleavage; it can be easily split into thin plates with mirror surfaces.

Analysis of the X-ray rocking curves and diffraction patterns in the range $10° < 2θ < 70°$ on a DRON-3 diffractometer (CuK_α radiation, Ni filter) revealed that the grown single crystals belong to the tetragonal system with the cell parameters $a = 4.02$ Å; $c = 6.03$ Å; sp. gr. $P4/nmm$; and $Z = 1$, which is in complete agreement with the data of [1, 2]. Polycrystalline parts show identical X-ray diffraction patterns and form an imperfect tetragonal structure of the chalcopyrite type with a primitive lattice [8].

Chemical analysis performed in [1] and in this study showed that the single crystals grown have an excess of metal atoms in comparison with the CuFeTe$_2$ composition. This fact could be attributed to the self-doping. However, repeated growth experiments with all three initial ingot compositions showed the appearance of cracks on the ampoule walls, through which vapor emerges to be crystallized in the form of a wire in the cold zone of the furnace. X-ray diffraction analysis of the wire composition showed it to be pure tellurium. Therefore, further crystallization experiments were performed in double-wall ampoules and tellurium was weighted each time after the growth cycle (its weight turned out to be ~12–16%). Chemical analysis of the

---

[1] The theses of this study were presented at the IX National Conference on Crystal Growth (NCCG 2000, 266).

single crystals on an RA-2 X-ray analyzer showed that their composition corresponds to the calculated data within experimental error.

Taking into account that the single crystals grown by us have similar unit-cell parameters and the same symmetry as the mineral rickardite $Cu_{4-x}Te_2$ [9], we can suggest that the valence of metals changes during the crystallization of $CuFeTe_2$ ingots, due to which some part of Te atoms precipitate to form an excess of metal. Undergoing a phase transition, the composition with an excess of metal forms a tetragonal structure of rickardite type described by the formula $Cu_{1.15}Fe_{1.23}Te_2$. With regard to the valence balance, this formula can be written as $Cu^{1+}Cu^{2+}_{0.15}Fe^{2+}Fe^{3+}_{0.23}Te_2$.

The formula of rickardite can be written as $Cu_2Cu_{2-x}Te_2$ ($x = 0.5$–0.6). However, in this formula, the valence balance is not satisfied for all values of x. The appropriate variant is the composition $Cu^{1+}_3Cu^{2+}_{0.5}Te_2$. It is ascertained that some fraction of Cu^{1+} ions occupy the twofold position $2a$: $(0\,0\,0)$. Other Cu^{1+} ions, along with Cu^{2+} ions, statistically occupy the $2c$ position $(0, 1/2, 0.269)$; two Te atoms are located in the $2c$ position with the coordinate $z = 0.774$.

One might expect Cu and Fe atoms to be distributed statistically over the $2a$ and $2c$ positions in the crystals under study.

We should note again that a specific feature of the rickardite structure is that a strictly stoichiometric composition cannot be implemented in it. According to the data of [9], the rickardite structure consists of a single-stack layer of empty octahedra formed by four Cu and two Te atoms. Such a representation crystallochemically does not characterize the structure (Fig. 1a). An idealized scheme of distribution of atoms in the (001) plane for $Cu_{1.15}Fe_{1.23}Te_2$ is shown in Fig. 1b. It can be clearly seen that Cu atoms are surrounded by eight (4 Te + 4 Fe) atoms forming a tetragonal prism. Each such prismatic layer is located at a distance of ~3 Å from neighboring similar layers, which makes the structure layered and ensures perfect cleavage. In other words, prismatic copper layers alternate with empty prismatic layers along the c axis.

MAGNETIC SUSCEPTIBILITY

The statistical magnetic properties of the crystals grown were investigated using SQUIDs and Domenicali pendulum magnetometers in magnetic fields up to 10 kOe in the temperature range 2–400 K.

The results of measurements of the temperature dependences of the magnetic susceptibility of a $Cu_{1.15}Fe_{1.23}Te_2$ crystal in magnetic fields of 100, 500, and 1000 Oe directed perpendicular to the tetragonal axis (parallel to the xy plane) are shown in Fig. 2. As can be seen, the susceptibility has an anomaly. At $T_N = 125$ K, a jump of susceptibility is observed in the
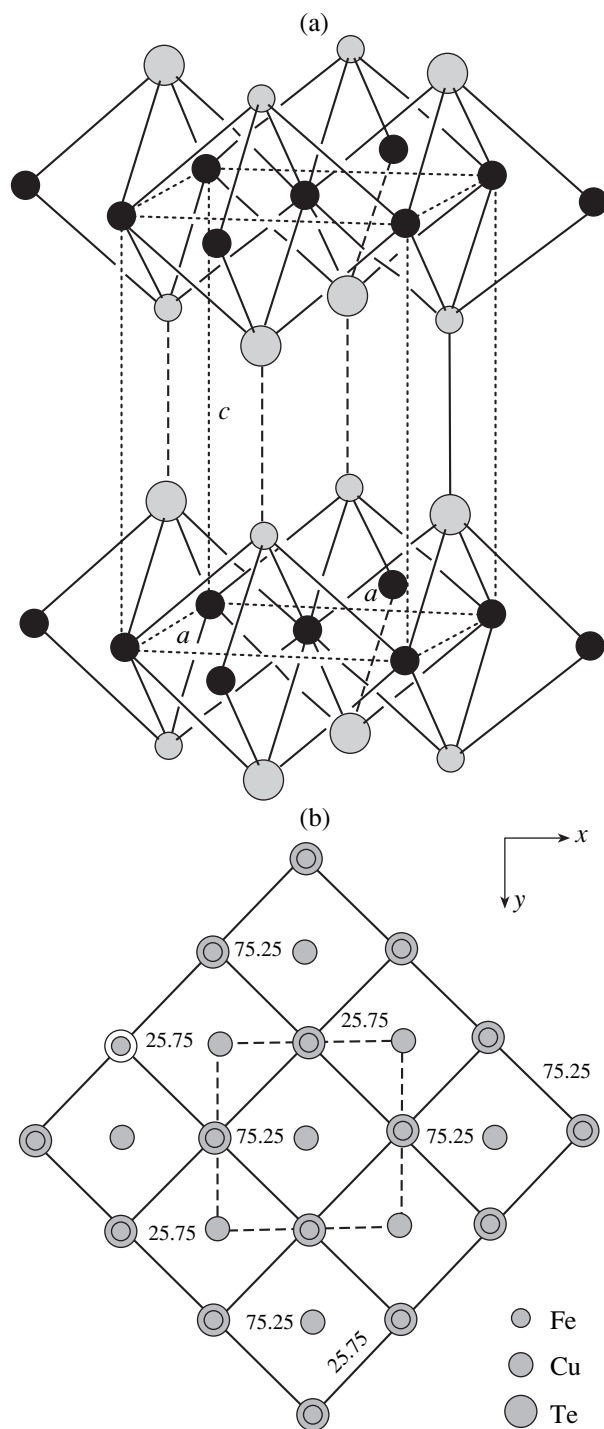
Fig. 1. (a) Crystal structure of $Cu_{1.15}Fe_{1.23}Te_2$ and (b) idealized schematic diagram of the location of atoms in the xy plane.

dependence $\chi(T)$. With a further decrease in temperature, the susceptibility increases. The noted jump is related to the formation of a long-range magnetic order; T_N is the Néel temperature. At $T_s = 65$ K, the susceptibility shows a kink and remains almost constant with
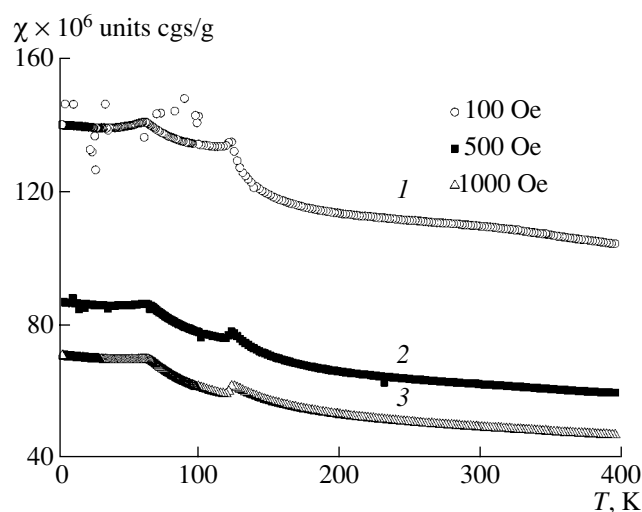
Fig. 2. Temperature dependences of the magnetic susceptibility of $Cu_{1.15}Fe_{1.23}Te_2$ in the direction parallel to the xy plane in magnetic fields of 100, 500, and 1000 Oe.

Fig. 3. Temperature dependences of the ZFC and FC magnetic susceptibilities of $Cu_{1.15}Fe_{1.23}Te_2$ in the direction perpendicular to the xy plane at 10 kOe.

further decrease in temperature. As can be seen from the dependences $\chi(T)$ in Fig. 2, the susceptibility decreases with increasing the magnetic field. The asymptotic Néel temperatures and the effective magnetic moments corresponding to the three noted values of magnetic field are, respectively, $\theta_1 = -2700$ K, $\theta_2 = -1450$ K, and $\theta_3 = -950$ K; $\mu_{eff_1} = 0.283$ µB, $\mu_{eff_2} = 0.493$ µB, and $\mu_{eff_3} = 0.566$ µB.

The temperature dependences of the magnetic susceptibility along the tetragonal axis (perpendicular to the xy plane) of the crystal cooled in the absence of a magnetic field and in a field of 10 kOe (zero-field cooling (ZFC) and field cooling (FC), respectively) are shown in Fig. 3. In the high-temperature range ($T >$ 200 K), the change in the susceptibility obeys the Curie–Weiss law with the parameters $\theta = -392$ K and $\mu_{eff} = 1.44$ µB. Below $T_s = 65$ K, both magnetic susceptibilities ($\chi_{ZFC}(T)$ and $\chi_{FC}(T)$) become irreversible.

RESULTS AND DISCUSSION

The analysis of the crystal structure of $Cu_{1.15}Fe_{1.23}Te_2$ showed the possibility of forming several antiferromagnetic phases allowing for the location of the spontaneous magnetic moment in the basal plane (001) of the crystal [10]. The exchange interaction between Cu and Fe ions in the crystal occurs in $1/2c$-thick layers parallel to the (001) plane. The Néel temperature is 125 K.

The characteristic feature of this compound is the irreversibility of the temperature dependence of the ZFC and FC magnetic susceptibilities below $T_s = 65$ K. A similar behavior of the magnetic susceptibility is most often observed in unordered magnetic systems (including spin glasses) [11–14]. We can suggest that

the spin-glass ordering in $Cu_{1.15}Fe_{1.23}Te_2$ can be related to a random arrangement of paramagnetic ions (Cu, Fe).

Note that the difference in the energies of exchange interaction of Cu and Fe ions with their neighbors in different crystallographic directions is due to the difference in the interatomic distances. According to the values of these distances, Cu and Fe atoms in sublattices are bound to each other more strongly than Cu and Fe atoms with atoms of the same type: the average Cu–Fe distance is ~2.5 Å, whereas the Cu–Cu and Fe–Fe distances are 2.82 and 3.6 Å, respectively.

In our opinion, the reason for the inconsistency between some experimental data on the physical properties of $CuFeTe_2$ crystals obtained by different researches [1, 2, 4] is due to that the objects under study had different chemical compositions of the $Cu_{1+x}Fe_{1+x}Te_2$ type.

REFERENCES

1. A. A. Vaĭpolin, V. D. Prochukhan, Yu. V. Rud', and V. E. Skoryukin, Neorg. Mater. **20** (4), 578 (1984).

2. L. V. Kradinova, A. M. Polubotko, V. V. Popov, *et al.*, Semicond. Sci. Technol., No. 8, 1616 (1993).

3. T. Nomiyama, H. Kuriyaki, and K. Hirakawa, Synth. Met., No. 7, 2237 (1995).

4. A. M. Lamarche, J. C. Woolley, G. Lamarche, *et al.*, J. Magn. Magn. Mater., No. 186, 121 (1998).

5. F. Gonzalez-Jimenez, E. Saimes, A. Rivas, *et al.*, Physica B (Amsterdam) **259–261**, 987 (1999).

6. F. Yu. Aliev, G. G. Guseĭnov, A. I. Dzhabbarov, and S. K. Orudzhev, Fiz. Nats. Akad. Nauk Azerb. **4** (2), 58 (2000).

7. A. A. Vaipolin, S. A. Kijaev, L. V. Krandinova, *et al.*, J. Phys.: Condens. Matter, No. 4, 8035 (1992).

8. A. I. Nadzhafov, O. Z. Alekperov, G. G. Guseĭnov, and S. K. Orudzhev, Izv. Nats. Akad. Nauk Azerb., No. 5, 81 (2002).

9. S. A. Forman and M. A. Peacock, Am. Mineral., Nos. 5–6, 44 (1949).

10. E. A. Turov, *Physical Properties of Magnetically Ordered Crystals* (Akad. Nauk SSSR, Moscow, 1983; Academic, New York, 1965).

11. J. M. D. Coey, Can. J. Phys. **65** (10), 1210 (1987).

12. K. P. Belov, *Ferrites in Strong Magnetic Fields* (Nauka, Moscow, 1972), p. 200 [in Russian].

13. K. P. Belov, L. I. Koroleva, N. A. Tsvetkova, *et al.*, Fiz. Tverd. Tela (Leningrad) **23** (8), 2477 (1981) [Sov. Phys. Solid State **23**, 1452 (1981)].

14. M. Nogues, M. Hamedoun, J. L. Dormann, and A. Saifi, J. Magn. Magn. Mater. **54–57**, 85 (1986).

Translated by Yu. Sin'kov

Hysteresis Loops of a Periodic Multilayered Structure with Antiferromagnetic Coupling

D. I. Sementsov and A. M. Shutyi

Ul'yanovsk State University, ul. L'va Tolstogo 42, Ul'yanovsk, 432700 Russia

e-mail: sementsovdi@ulsu.ru

Received April 28, 2003

Abstract—The hysteresis loops of 180° in-plane magnetization reversal in a system of magnetic films with cubic crystallographic anisotropy coupled by the interlayer antiferromagnetic exchange interaction are plotted. The loops correspond to different orientations of the switching field with respect to crystallographic axes. Wasp-waisted loops, loops collapsing in weak fields, and bistable (bifurcation) loops are found. © *2004 MAIK "Nauka/Interperiodica".*

INTRODUCTION

In recent years, much attention has been given to multilayered structures consisting, as a rule, of thin magnetic-metal layers separated by nonmagnetic metallic spacers [1–4]. The most typical representatives of these structures are $(Fe/Cr)_n$ periodic structures (n is the number of periods). Unique static and dynamic properties of these structures are determined primarily by the character of coupling of magnetic moments of neighboring layers. This coupling is due to the indirect exchange interaction and results in ferromagnetic, antiferromagnetic, or noncollinear ordering of the magnetic moments of neighboring layers [5, 6]. Detection and analysis of the specific features in the excitation of dynamical regimes (sensitive to minor variations in structure parameters and switching fields) require one, first of all, to determine the character of equilibrium states of the system. Antiferromagnetic coupling is most interesting for the implementation of different equilibrium orientational states and various dynamical regimes [7, 8]. An important characteristic of a magnetic thin-film sample (which can be obtained in experiment rather easily) is a hysteresis loop corresponding to the 180° magnetization reversal of the sample. The shape of the hysteresis loop is strongly connected with many structural parameters, which can be obtained by measuring the loop parameters. In this study, based on the energy approach, we found the equilibrium states and plotted the hysteresis loops (corresponding to several characteristic orientations of the switching field and the constants of interlayer exchange coupling) for a multilayered system consisting of a large number of pairs of layers of magnetic and nonmagnetic metals with antiferromagnetic ordering of the magnetic moments of the layers.

STATEMENT OF THE PROBLEM

We assume that the structure under study consists of a large number ($n \gg 1$) of magnetic metal layers with a magnetization $\mathbf{M}_i$ and thickness d_i (where i is the number of a magnetic layer) separated by nonmagnetic spacers, whose thickness corresponds to antiferromagnetic exchange coupling between magnetic layers. In accordance with the available experimental data on $(Fe/Cr)_n$ structures [9], we also assume that the magnetic anisotropy of the magnetic layers is the sum of the induced uniaxial easy-axis anisotropy and the cubic anisotropy. The [100] and [010] axes lie in the layer plane, while the easy-magnetization axis of induced anisotropy is normal to the layers. In this case, the free energy of the system (per unit area) has the form

$$
E = \sum_{i=1}^{n} d_i \left[-\mathbf{HM}_i + \frac{K_{1i}}{4}(\sin^2 2\psi_i + \cos^4\psi_i \sin^2 2\varphi_i) \right.
$$

$$
+ \frac{K_{2i}}{16}\sin^2 2\psi_i \cos^2\psi_i \sin^2 2\varphi_i \tag{1}
$$

$$
\left. + (K_{ui} - 2\pi M_i^2)\cos^2\psi_i \right] + J\sum_{i=1}^{n} \frac{\mathbf{M}_i\mathbf{M}_{i+1}}{M_i M_{i+1}},
$$

where J is the constant of bilinear coupling due to the indirect exchange interaction of the magnetic moments of nearest-neighbor layers (this constant depends, generally, on the thickness, composition, and structural characteristics of the spacer); $K_{1,2i}$ are, respectively, the first and second cubic-anisotropy constants of the ith layer; K_{ui} is the growth-anisotropy constant; $\mathbf{H}$ is the static bias field; φ_i is the azimuthal angle counted from the [100] axis (this angle specifies the orientation of the magnetic moment of the ith layer); and ψ_i is the angle at which the magnetization vector $\mathbf{M}_i$ outgoes from the layer plane. Further, the magnetic layers are assumed to

be identical, that is, $M_i = M$, $d_i = d$, $K_{ui} = K_u$, and $K_{1,\,2i} = K_{1,\,2}$. The coupling constant J is assumed to be positive, which should ensure antiferromagnetic coupling of the magnetic moments of neighboring layers (i.e., opposite directions of these moments in the absence of a bias field). In this case, the entire set of magnetic layers is divided into two subsystems ($j = 1, 2$) with identical behavior of the layers of each subsystem. Since demagnetizing fields for structures realized in practice are high ($4\pi M \gg 2K_u/M$, JM), for the in-plane switching field **H**, the magnetic moments lie in the layer plane. Therefore, the equilibrium angles $\psi_j = 0$. To determine the equilibrium azimuthal angles $\varphi_j(H)$, we use the equilibrium conditions $\partial E/\partial\varphi_j = 0$ and $\partial^2 E/\partial\varphi_j^2 > 0$. Taking into account (1), these conditions yield the system of equations

$$2HM\sin(\varphi_j - \varphi_H) + K_1\sin 4\varphi_j$$
$$- 2\bar{J}\sin(\varphi_j - \varphi_{3-j}) = 0,$$
$$HM\cos(\varphi_j - \varphi_H) + 2K_1\cos 4\varphi_j \qquad (2)$$
$$- \bar{J}\cos(\varphi_j - \varphi_{3-j}) > 0,$$
$$j = 1, 2,$$

where φ_H is the azimuthal angle counted from the [100] axis and determining the in-plane direction of the field **H** and $\bar{J} = 2J/d$.

ANALYSIS OF THE HYSTERESIS-LOOP SHAPE

In order to find the equilibrium states of the system of magnetic moments of the layers and plot the hysteresis loops, we will analyze numerically Eqs. (2) using the parameters of a real structure. For Fe layers, the magnetization $M = 1620$ G; the anisotropy constants are $K_1 = 4.6 \times 10^5$ erg/cm^3, $K_2 = 1.5 \times 10^5$ erg/cm^3, and $K_u = 2.06 \times 10^6$ erg/cm^3; and the thickness $d = 21.2 \times 10^{-8}$ cm. The parameters of Cr layers do not appear in Eq. (1) explicitly but determine the coupling constant J [3].

Figure 1 shows the field dependences of the normalized projection of the total magnetic moment of both sublattices $(\mathbf{M}_1 + \mathbf{M}_2)/M$ on the direction of the switching field for the initial orientation of the magnetic moments specified by the angles $\varphi_j = \pm\pi/2$; the external-field orientation specified by the angles $\varphi_H = 0$, $\pi/4$, and (c) $\pi/8$; and the coupling constants $J = 0.05$, 0.15, and 0.25 erg/cm^2 (curves *1–3*, respectively). These dependences demonstrate that the hysteresis loops for the structure under consideration, as a rule, collapse in low fields. As the coupling constant increases, the loop width decreases and the collapse region increases.

Based on the equilibrium conditions, one can obtain for $\varphi_H = 0$ the expressions for the outer boundaries of
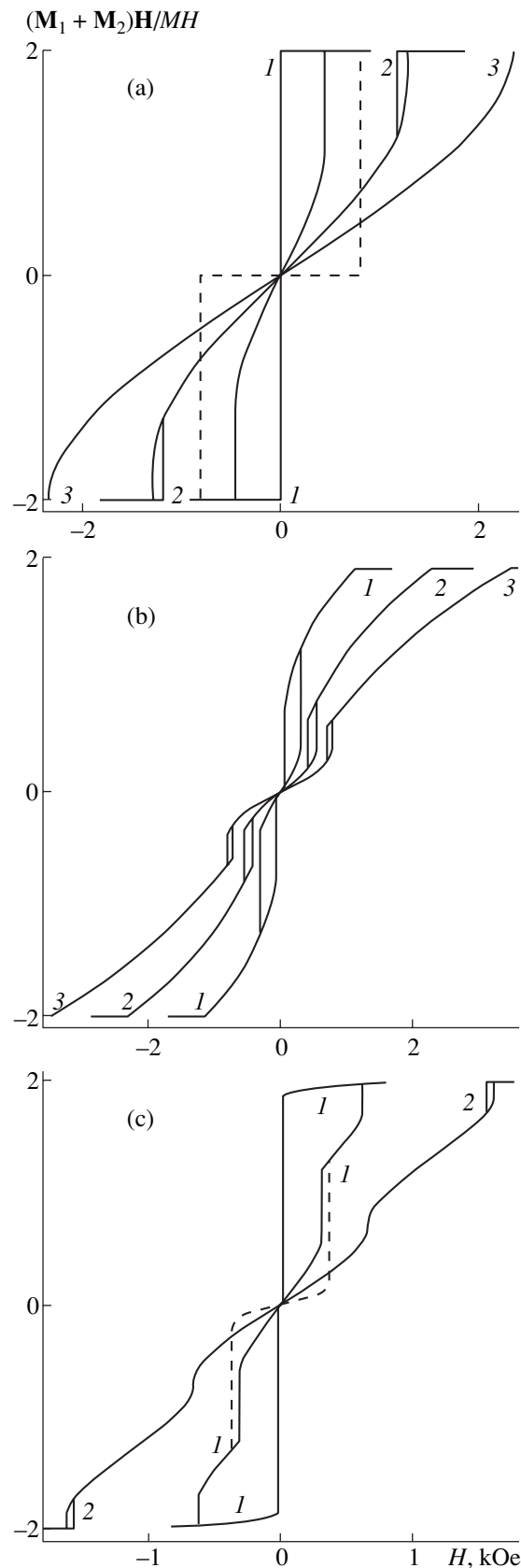
$(\mathbf{M}_1 + \mathbf{M}_2)\mathbf{H}/MH$

Fig. 1. Hysteresis loops of the multilayered structure having a collapse region: $\varphi_H =$ (a) 0, (b) $\pi/4$, and (c) $\pi/8$; $J =$ (*1*) 0.05, (*2*) 0.15, and (*3*) 0.25 erg/cm^2.

the hysteresis loop (the critical field H_a at which the noncollinear orientation of the magnetic moments becomes unstable) and the boundaries of the collapse region (the critical field H_b at which the codirectional phase becomes unstable)

$$H_a = \pm\frac{4}{3M}\sqrt{\frac{\bar{J}+K_1}{6K_1}}(\bar{J}+K_1),$$
$$H_b = \pm\frac{2}{M}(\bar{J}-K_1). \tag{3}$$

In this case, H_a is also the saturation field. For $J > J_{ab}$, where J_{ab} corresponds to the equality $H_a = H_b$, the hysteresis loop collapses completely and transforms into a magnetization-reversal curve. The loop has the only point of collapse at $H = 0$ if $J = J_b$ ($J_b = K_1 d/2$ is the value at which the field H_b becomes zero). For $J < J_b$, the loop does not collapse. For small values of H_b, the orientational phase transition occurring when the field approaches this critical value is of bifurcation type and can result not only in the orientation of magnetic moments similar to the initial one ($\varphi_j \approx \pm\pi/2$) but also in the orientation with the angles $\varphi_{1,2} = \pi, 0$. The reason for this is that, in the early stage of the phase transition, due to the significant change in the azimuthal angle, the magnetic moments of the structure execute up to a few revolutions in the film plane during high-amplitude chaotic oscillations. Therefore, any possible stationary orientation can be implemented. Thus, two hysteresis loops will occur with some probabilities. The first one is shown in the Fig. 1a by a solid line and the differing part of the second loop is shown by a dotted line. The outer boundaries of the second loop are determined by the field values at which the opposite orientation of the magnetic moments of the neighboring layers is no longer stable:

$$H_c = \pm\frac{2}{M}\sqrt{K_1(\bar{J}+K_1)}. \tag{4}$$

In the second case considered here ($\varphi_H = \pi/4$), the magnetization continues to increase after the collapse of the hysteresis loop, becoming saturated when the field reaches the value

$$H_a^{(\pi/4)} = \pm\frac{2}{M}(\bar{J}+K_1). \tag{5}$$

The field values that specify the boundaries of the hysteresis loop collapse can be found only numerically. For the external field oriented along the [110] axis, the collapse of the hysteresis loop occurs at the coupling constants exceeding those for the field oriented along the [100] axis. After the orientational phase transition at the boundary of the collapse region, the two possible equilibrium configurations of the magnetic moments prove to be equivalent; therefore, a single loop is observed.

When the switching-field direction differs from those considered above (in particular, $\varphi_H = \pi/8$, an extra bend (sharp or smooth, depending on the coupling constant) is observed in the hysteresis loop. In addition, with an increase in the field, the magnetization asymptotically approaches the maximum value. However, these hysteresis loops have some features similar to those observed in case (a) (when the field is directed along the [100] axis). At small coupling constants, two loops can be realized due to the bifurcation phase transition. One of them (solid line) is similar to that observed in case (a) and the other (dotted line) is similar to that typical of case (b) (the field is directed along the [110] axis). The direction of the magnetization reversal can be affected by (1) various fluctuations of the system parameters and (2) the parameters determining the character of the decay of the field H. The shape of the loops shown in Fig. 1 is in good agreement with the shape of the experimentally observed hysteresis loops of real films [9, 10].

Figure 2 shows the hysteresis loops corresponding to the coupling constant $J = 0.035$ erg/cm² and the orientations of the switching field specified by the angles $\varphi_H = 0$ and $\pi/8$ (dotted and solid lines, respectively). A specific feature of these loops is the presence of wasp waists (narrowings) in their central parts. The orientational phase transition occurring in the waist region results in a significant change in the azimuthal angles of the magnetic moments. Therefore, as in the above cases, the hysteresis loops are of bifurcation type and the probability of implementing a particular loop can be affected by external perturbations. For $\varphi_H = 0$, a double bifurcation hysteresis loop arises, while a triple loop occurs when the field is oriented along the [100] axis. The third possible loop is not shown in Fig. 2; it is due to the implementation of the antiparallel configuration of the magnetic moments of layers and is similar to the
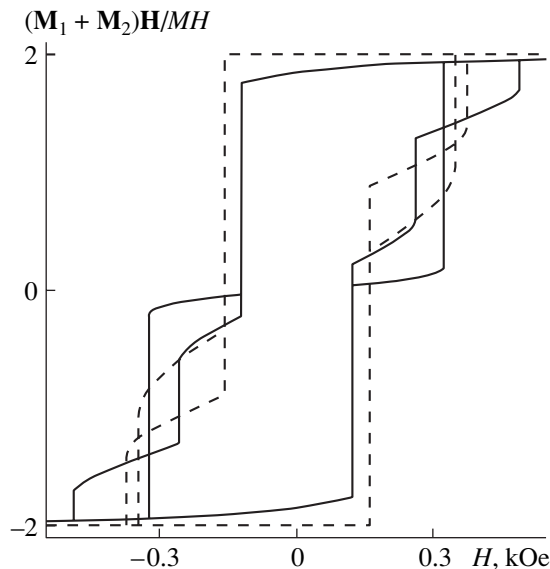
Fig. 2. Bifurcation hysteresis loops at $J = 0.035$ erg/cm² and $\varphi_H = 0$ (dotted line) and $\pi/8$ (solid line).

dotted loop shown in Fig. 1a. The outer boundaries of this loop are set by the fields $H_c \approx \pm 744$ Oe.

CONCLUSIONS

The analysis performed shows that, in the case of the 180° magnetization reversal, hysteresis loops are typical of the multilayered $(Fe/Cr)_n$ structure with the antiferromagnetic coupling caused by indirect exchange coupling. The shape of the loops depends strongly on the direction of the switching field with respect to the crystallographic axes to which the direction of the magnetic cubic anisotropy is related. Wasp-waist loops or loops with a collapse region are observed. In addition, the possibility of implementing double and triple bifurcation hysteresis loops is demonstrated. When comparing the reported hysteresis loops with the experimental ones, one should bear in mind that the crystallographic structure was considered idealized in this study. In actual thin-film systems, there always exists a certain spread of crystallographic directions throughout the sample volume [11]. This spread must result in an angular dispersion of the magnetic anisotropy, which, in turn, must lead to smoothing the hysteresis loops [12].

ACKNOWLEDGMENTS

REFERENCES

1. V. V. Ustinov, M. M. Kirilova, I. D. Lobov, *et al.*, Zh. Éksp. Teor. Fiz. **109** (2), 477 (1996) [JETP **82**, 253 (1996)].
2. V. V. Kostyuchenko and A. K. Zvezdin, Phys. Rev. B **57** (10), 5951 (1998).
3. N. G. Bebenin and V. V. Ustinov, Fiz. Met. Metalloved. **84** (2), 29 (1997).
4. A. K. Zvezdin and V. V. Kostyuchenko, Fiz. Tverd. Tela (St. Petersburg) **41** (3), 461 (1999) [Phys. Solid State **41**, 413 (1999)].
5. A. Schreyer, J. F. Ankner, Th. Zeidler, *et al.*, Phys. Rev. B **52** (12), 16 066 (1995).
6. G. S. Patrin, N. V. Volkov, and V. P. Kononov, Pis'ma Zh. Éksp. Teor. Fiz. **68** (4), 287 (1998) [JETP Lett. **68**, 307 (1998)].
7. D. I. Sementsov and A. M. Shutyĭ, Pis'ma Zh. Éksp. Teor. Fiz. **74** (6), 339 (2001) [JETP Lett. **74**, 306 (2001)].
8. D. I. Sementsov and A. M. Shutyĭ, Fiz. Met. Metalloved. **93** (4), 5 (2002).
9. M. A. Milyaev, L. N. Romashev, V. V. Ustinov, *et al.*, in *Abstracts of International School–Seminar on New Magnetic Materials in Microelectronics, NMMM-XVIII* (Moscow, 2002), p. 102.
10. P. N. Stetsenko, S. D. Antipov, G. E. Goryunov, *et al.*, in *Abstracts of International School–Seminar on New Magnetic Materials in Microelectronics, NMMM-XVIII* (Moscow, 2002), p. 510.
11. A. V. Semerikov, T. P. Krinitsina, V. V. Popov, *et al.*, in *Abstracts of International School–Seminar on New Magnetic Materials in Microelectronics, NMMM-XVI* (Moscow, 1998), Part 1, p. 33.
12. A. P. Abramova, E. N. Afanas'eva, and T. M. Sementsova, Fiz. Met. Metalloved. **89** (4), 43 (2000).

Translated by A. Zolot'ko

SURFACE
AND THIN FILMS

Dedicated to the 80th Birthday of L.A. Shuvalov

Size Effect in Displacive Ferroelectrics

O. G. Vendik and S. P. Zubko

Electrotechnical University, St. Petersburg, 197376 Russia
e-mail: OGVendik@mail.eltech.ru
Received June 11, 2003

Abstract—It is ascertained that the size effect in thin ferroelectric films is related to the spatial correlation of ferroelectric polarization, depending on boundary conditions. The influence of the size effect on the permittivity of displacive ferroelectrics is described. It is shown that the size effect manifests itself differently for different orientations of the polarization vector with respect to the boundaries of a ferroelectric layer. © *2004 MAIK "Nauka/Interperiodica".*

INTRODUCTION

When the characteristic size of a sample of some material (the thickness of a single-crystal film [1] or the size of polycrystalline granules [2]) turns out to be smaller than some critical value, the properties of the material change significantly. This phenomenon is referred to as the size effect. The dependence of the permittivity of a ferroelectric sample on its size (especially the thickness of a ferroelectric film) is of primary interest (Fig. 1) [3, 4]. The dependence of the permittivity of a ferroelectric film on its thickness has been known for a long time. Various reasons have been considered in order to explain this phenomenon: the formation of a thin subelectrode layer of a nonferroelectric material [5], the contribution of the semiconductor Schottky barrier near the electrode to the field distribution [5, 6], and the correlation of the ferroelectric polarization and freezing of the dynamic polarization on the electrode surface [7, 8]. The estimations in [7] show that the most adequate explanation is the spatial correlation of the ferroelectric polarization and freezing of the dynamic polarization on the electrode surface [7]. The most convincing confirmation of this mechanism is the experimentally found suppression of the size effect in thin ferroelectric films. This suppression occurs when the ferroelectric polarization can penetrate an electrode, i.e., when the polarization on the electrode surface is not frozen [7–9]. Thus, we suggest that ferroelectric polarization may occur in a nonferroelectric material due to the similarity of the crystal structures of the ferroelectric and the electrode material (like the proximity effect in superconductors).

The above-mentioned spatial correlation is directly related to the spatial dispersion of the ferroelectric mode [10, 11]. To explain the anomalously small value of the eigenfrequency and the spatial dispersion of the ferroelectric mode, one need not use the concepts based

on the characteristic size of the same order of magnitude as the lattice constant. Therefore, all the main characteristics of the ferroelectric mode can be described within continuous representations and the symmetry of the medium can be represented by the tensors of corresponding physical quantities [11].

SPATIAL DISPERSION OF THE FERROELECTRIC MODE AND SPATIAL CORRELATION

The parameter responsible for the manifestation of the size effect is the correlation radius. The correlation radius is generally found from the dispersion relation for the ferroelectric mode, which is determined by neutron inelastic scattering. The experimental dependences of the frequencies of the longitudinal and transverse optical modes on the wave vector, obtained at different temperatures [12], are shown in Fig. 2.
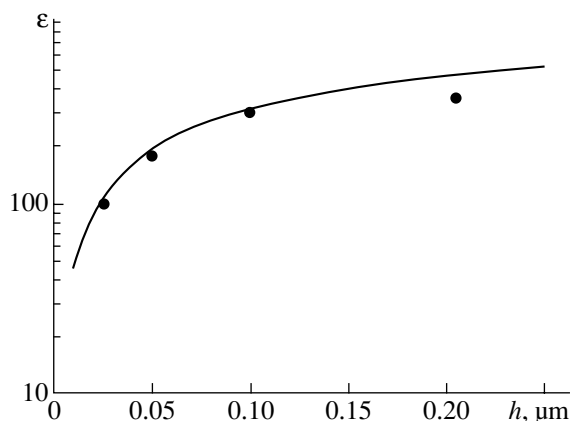

Fig. 1. Dependence of the permittivity of a $Ba_{0.5}Sr_{0.5}TiO_3$ film on the film thickness.

As follows from the equation of motion of the ion-polarization vector, the spatial dispersion of the longitudinal and transverse modes in a medium of arbitrary symmetry is determined by the correlation tensor of rank 4 [11]. The correlation tensor for a medium with a cubic structure (to which a ferroelectric crystal in the paraelectric phase belongs) has only three nonzero components:

$$\lambda_{xxxx} = \lambda_{yyyy} = \lambda_{zzzz} = \lambda_1,$$

$$\lambda_{xxzz} = \lambda_{yyxx} = \lambda_{zzyy} = \lambda_{zzxx} = \lambda_{xxyy} = \lambda_{yyzz} = \lambda_2,$$

$$\lambda_{xyxy} = \lambda_{yzyz} = \lambda_{zxzx} = \lambda_3.$$

The components λ_1, λ_2, and λ_3 are referred to as the correlation parameters of a medium.

The dispersion equation for optical modes in a cubic medium has the form [11, 13]

$$\{[\omega_{OT}^2(0, T) - \omega^2 + s_t](a_t k^2 - \omega^2) - k^4 v_t^2\}^2$$
$$\times \{[\omega_{OL}^2(0, T) - \omega^2 + s_L](a_L k^2 - \omega^2) - k^4 v_L^2\} = 0, \quad (1)$$

where

$$s_t = \frac{1}{A(T)}\lambda_3\omega_{OT}^2(0, T),$$

$$s_L = \frac{3\varepsilon_\infty(\varepsilon(T) - \varepsilon_\infty)}{\varepsilon(T)(\varepsilon_\infty + 2)}\lambda_1\omega_{OL}^2(0, T),$$

$$v_t^2 = \frac{1}{A(T)}\frac{\varepsilon_0}{\rho_r}\omega_{OT}^2(0, T)\theta_3^2, \quad (2)$$

$$v_L^2 = \frac{3\varepsilon_\infty(\varepsilon(T) - \varepsilon_\infty)}{\varepsilon(T)(\varepsilon_\infty + 2)}\frac{\varepsilon_0}{\rho_r}\omega_{OL}^2(0, T)\theta_1^2,$$

$$a_t = \frac{c_3}{\rho_r}, \quad a_L = \frac{c_1}{\rho_r}, \quad A(T) = \frac{(\varepsilon_\infty + 2)}{3(\varepsilon(T) - \varepsilon_\infty)}. \quad (3)$$

Here, T is temperature; $\varepsilon(T)$ and ε_∞ are the values of permittivity corresponding to the frequencies $\omega \ll \omega_i$ and $\omega \gg \omega_i$, respectively (ω_i is the eigenfrequency of the ionic component of polarization); ε_0 is the permittivity of vacuum; ρ_r is the density of the medium; θ_1 and θ_3 are the tensor components responsible for the relationship between nonuniform mechanical displacements and polarization; and c_1 and c_2 are the elasticity-tensor components.

Excluding the relation between the acoustic and optical branches [11, 13] from formulas (1)–(3), we obtain the dispersion relations for the transverse and longitudinal optical modes for the [100] direction of the wave vector **k**:

$$\omega_{OT}(kT) = \sqrt{\omega_{OT}^2(0, T) + \omega_{OT}^2(0, T)A^{-1}(T)\lambda_3 k^2} \quad (4a)$$
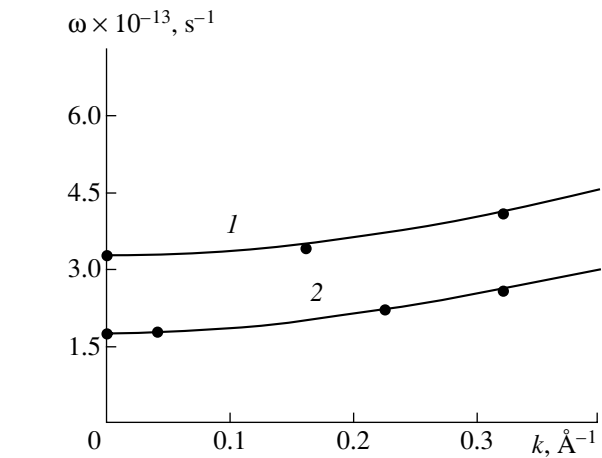
Fig. 2. Dependences of the frequencies of the (*1*) longitudinal and (*2*) transverse optical modes on the wave vector k in the [100] direction for $SrTiO_3$.

(the transverse mode) and

$$\omega_{OL}(k, T) = \sqrt{\omega_{OL}^2(0, T) + \omega_{OL}^2(0, T)A^{-1}(T)\varepsilon_\infty\varepsilon_s^{-1}\lambda_1 k^2} \quad (4b)$$

(the longitudinal mode).

The curves in Fig. 2 are plotted by formulas (4a) and (4b). The values of the correlation parameters for the longitudinal (λ_1) and transverse (λ_3) waves used in the calculation were determined by processing the experimental data on the dependence of the transverse mode frequency on the wave vector [12] (circles in Fig. 2) and the temperature dependence of the permittivity ε of the single-crystal displacive ferroelectric $SrTiO_3$ [14]. The value of ε_∞ was determined from the refractive index n. At optical frequencies, $n \simeq 3.5$ [1] and $\varepsilon_\infty = n^2 \simeq 12$. Comparison of the calculated curves (4) and experimental points [12] yields $\lambda_1 \simeq 3.5$ Å^2 (the longitudinal mode) and $\lambda_3 \simeq 0.17$ Å^2 (the transverse mode) for $SrTiO_3$. The values of the correlation parameters for the ferroelectric $KTaO_3$ were reported in [15]: $\lambda_1 \simeq 53.7$ Å^2 and $\lambda_3 \simeq 0.47$ Å^2.

CORRELATION FUNCTION OF THE FERROELECTRIC MODE IN AN INTEGRAL REPRESENTATION

The spatial distribution of polarization in a ferroelectric layer is described by a second-order differential equation derived from the expansion of the thermodynamic potential in the order parameter (polarization in the case under consideration) [16–18]. In the one-dimensional approximation (the physical quantities vary along the x axis), this equation has the form

$$-2\lambda\frac{d^2 P(x)}{dx^2} + \frac{1}{\varepsilon(T)}P(x) + \frac{1}{D_N^2}P^3(x) = \varepsilon_0 E(x), \quad (5)$$
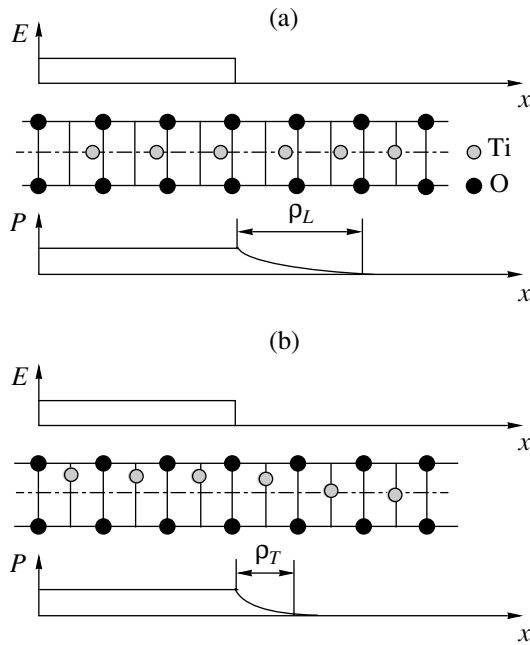
Fig. 3. Spatial distributions of the bias field and the polarization: the polarization vector and the polarization gradient are directed (a) similarly (analog of a longitudinal wave) and (b) oppositely (analog of a transverse wave).

where P is the polarization, $\varepsilon(T)$ is the permittivity of the bulk material in the case of uniform polarization, and E is a bias field.

A solution to the Eq. (5) for a medium infinite in the direction x, i.e., with the boundary conditions

$$\left.\frac{dP(x)}{dx}\right|_{x \to +\infty} = \left.\frac{dP(x)}{dx}\right|_{x \to -\infty} = 0, \qquad (6)$$

can be written in the integral form:

$$P(x) = \int_{-\infty}^{+\infty} K(x - x')E(x')dx' \qquad (7)$$

with the kernel

$$K(x - x') = K\exp\left(-\frac{|x - x'|}{\rho(T)}\right), \qquad (8)$$

where $K = \varepsilon_0\varepsilon(T)/2\rho(T)$ and $\rho(T)$ is the correlation radius:

$$\rho(T) = \sqrt{\varepsilon(T)\lambda}. \qquad (9)$$

Figure 3 shows the mutual shift of the titanium and oxygen sublattices, which is responsible for the ferroelectric polarization in displacive ferroelectrics. The relative shift of the sublattices is associated with the formation of a soft mode since the elasticity of the structure formed due to the relative shift of the sublattices is small. The rigidity of the sublattices themselves is much higher than the rigidity counteracting their

mutual shift. Unfortunately, we only have data on the crystal rigidity rather than the rigidity of the sublattices. Hence, we will restrict ourselves to qualitative estimates. The rigidity of the sublattices determines the spatial correlation of the polarization and, accordingly, the correlation radius. The correlation radius for a transverse wave $\rho_T(T) = \sqrt{\varepsilon(T)\lambda_3}$ is significantly smaller than that for a longitudinal wave $\rho_L(T) = \sqrt{\varepsilon(T)\lambda_1}$). Apparently, the reason is that the rigidity of the titanium and strontium sublattices with respect to the compression and extension (Fig. 3a) is much higher than their rigidity with respect to shear strains (Fig. 3b).

BOUNDARY CONDITIONS FOR THE DYNAMIC FERROELECTRIC POLARIZATION

The permittivity in the presence or absence of a dc bias is measured in a weak ac field, i.e., represented as the ratio of the dynamic ferroelectric polarization $P_\sim$ to the applied ac field $E_\sim$.

The size effect manifests itself differently at different orientations of the ferroelectric-polarization vector with respect to the boundaries of the ferroelectric layer [19].

Figure 4 shows the ferroelectric structures with different orientations of an external field. In the structures shown in Figs. 4a and 4b, the dynamic polarization can be represented by a standing longitudinal wave and a transverse wave, respectively.

To calculate the size effect in a plane-parallel capacitor (Fig. 4a), the correlation parameter for a longitudinal wave, λ_1, is used.

Different boundary conditions for the dynamic polarization can be implemented at the ferroelectric-layer–electrode interface, depending on the electrode material. It was shown in [20] that the dynamic polarization becomes zero at the interface between a ferroelectric and normal metal, which corresponds to the zero boundary conditions

$$P_\sim(x)|_{x = \pm h/2} = 0. \qquad (10)$$

Solution of Eq. (5) for the dynamic component of the polarization with zero boundary conditions (10) yields the polarization distribution across the ferroelectric layer [8]:

$$P_\sim(x) = P_{\max}\left(1 - \cosh\left(\frac{x}{\sqrt{2}\lambda_1}\right)\bigg/\cosh\left(\frac{h}{2\sqrt{2}\lambda_1}\right)\right), \quad (11)$$

$$P_{\max}(x) = \frac{Q_\sim}{S}\left[1 - \frac{1}{\varepsilon(T)} - 3\left(\frac{Q_{dc}}{D_N S}\right)^2\right], \qquad (12)$$

where $Q_\sim$ and Q_{dc} are, respectively, the ac and constant components of the charge at the capacitor electrodes; S is the electrode area; h is the thickness of the ferroelectric layer; and D_N is the normalizing displacement (for
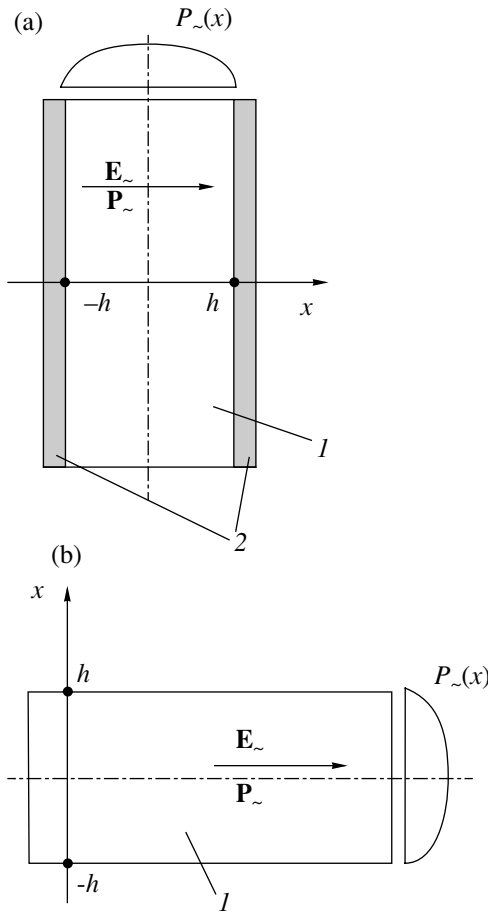
Fig. 4. (a) Capacitor structure with a longitudinal standing wave and (b) a thin ferroelectric layer with a transverse standing wave: (*1*) ferroelectric and (*2*) electrodes.
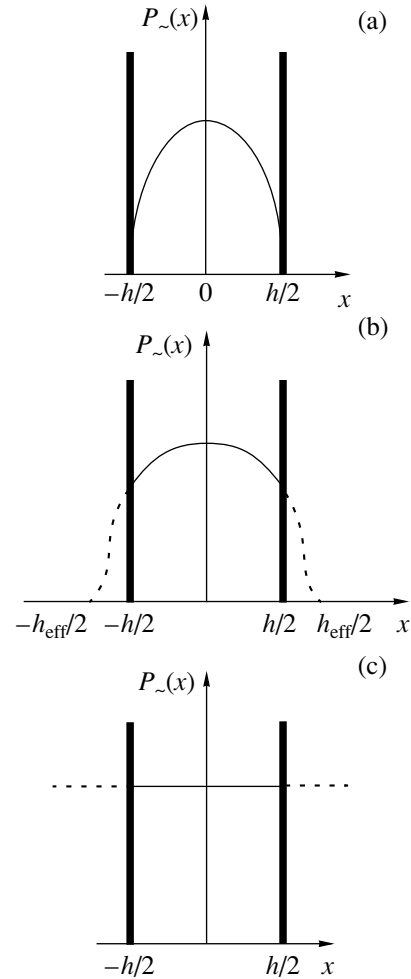
Fig. 5. Distribution of the dynamic polarization in a ferroelectric layer for (a) zero, (b) intermediate, and (c) free boundary conditions.

SrTiO$_3$, $D_N \simeq 4.2$ C/m^2). Thus, in the case of zero boundary conditions, the coordinate dependence of the polarization is described by the hyperbolic cosine (Fig. 5a). Due to the absence of space charges in the bulk of the material, the electric displacement D is constant in the capacitor bulk and is related to the charge at the capacitor plates as follows:

$$D_\sim = \frac{Q_\sim}{S}. \tag{13}$$

The effect of elastic waves in the crystal is disregarded as well.

The displacement, polarization, and bias-field strength are related to each other by the expression

$$P_\sim(x) = D_\sim - \varepsilon_0 E_\sim(x). \tag{14}$$

From (11), with regard to (13) and (14), we obtain the coordinate dependence of the bias field. Then, integrating the field strength over the coordinate x from $-h/2$ to $h/2$, taking into account that $\varepsilon(T) \gg 1$ and $h/\sqrt{2\lambda_1} \gg 1$

for SrTiO$_3$, we obtain the expression relating the ac component of the bias applied to the capacitor to the charge induced on its plates:

$$U_\sim = \frac{Q_\sim h}{\varepsilon_0 S}\left[\frac{1}{\varepsilon(T)} + 3\left(\frac{Q_{dc}}{D_N S}\right)^2 + \frac{2}{\alpha h}\right]. \tag{15}$$

Formula (15) contains the size-effect parameter α:

$$\alpha = \frac{1}{\sqrt{2\lambda_1}}. \tag{16}$$

Based on expression (15), the effective permittivity of the capacitor material can be written in the form

$$\frac{1}{\varepsilon_{\text{eff}}(U, T)} = \frac{1}{\varepsilon(U, T)} + \frac{2}{\alpha h}. \tag{17}$$

Boundary conditions (10) are not always satisfied: for example, in the structure in which a ferroelectric is adjacent to a high-temperature superconductor YBa$_2$Cu$_3$O$_{7-\delta}$ (YBCO), polarization can partially penetrate the electrode (Fig. 5b). The penetration depth of

$\alpha, \mu m^{-1}$
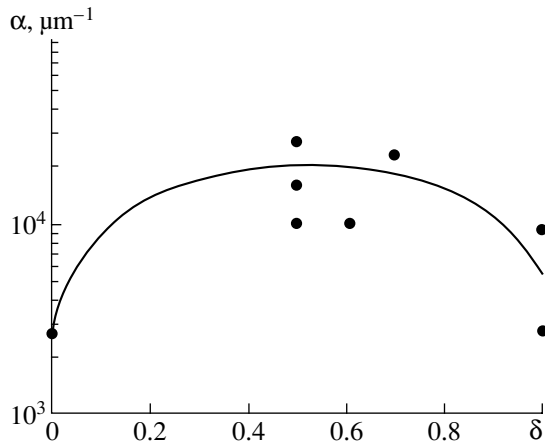
Fig. 6. Dependence of the size-effect parameter on Ba concentration in $Ba_\delta Sr_{1-\delta} TiO_3$ films.

ε
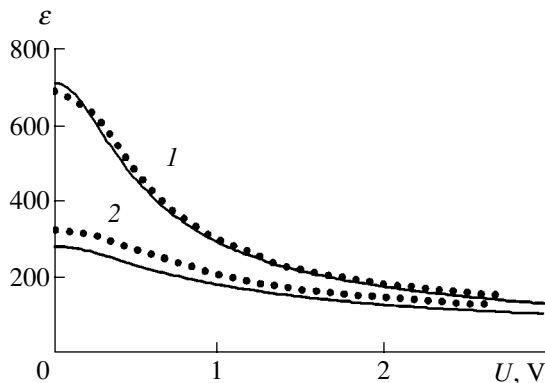
Fig. 7. Suppression of the size effect in a thin layer of $Ba_{0.12}Sr_{0.88}TiO_3$ in (*1*) SRO/BSTO/SRO and (*2*) SRO/BSTO/Pt structures at $T = 300$ K.

$\varepsilon \times 10^{-3}$
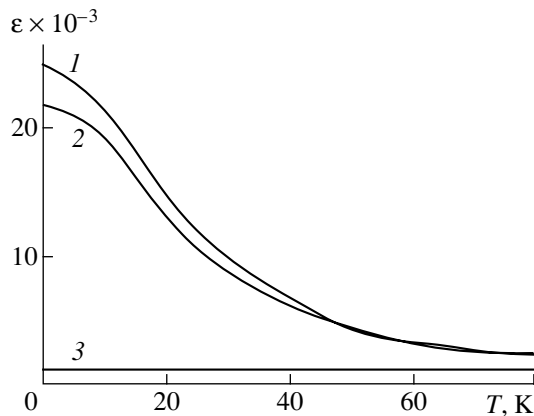
Fig. 8. Temperature dependence of the effective permittivity of $SrTiO_3$ for (*1*) the bulk material and a film of thickness $h = 1$ μm with (*2*) YBCO and (*3*) metal electrodes.

polarization in the YBCO electrode is determined by the YBCO permittivity and the correlation parameter. For example, for a longitudinal wave, the penetration

depth of polarization in the electrode is about 20 nm [7]. This case corresponds to the so-called intermediate boundary conditions.

When the polarization at the interfaces between the ferroelectric layer and the electrodes is nonzero and can penetrate the material of electrodes (Fig. 5b), the effective thickness of the ferroelectric layer h_{eff} is introduced

Finally, when a ferroelectric comes in contact with a material with the same crystal structure, for example, $SrRuO_3$ (SRO) [8, 21, 22], free boundary conditions (6) are implemented, which correspond to a uniform distribution of polarization in the film, independent of its thickness. The spatial distribution of polarization in a ferroelectric satisfying these boundary conditions is shown in Fig. 5.

Obviously, the relationship between the effective (h_{eff}) and geometric (h) thicknesses of the ferroelectric layer depends on the boundary conditions. For zero, free, and intermediate boundary conditions, $h_{eff} = h$, $h_{eff} \longrightarrow \infty$, and $h < h_{eff} < \infty$, respectively.

The size-effect parameter α of the displacive ferroelectric $Ba_\delta Sr_{1-\delta} TiO_3$ (BSTO), which is most widely used at present, depends on its composition. Figure 6 shows the dependence of α on Ba concentration δ [18].

SUPPRESSION OF THE SIZE EFFECT

The temperature behavior of the permittivity of $SrTiO_3$ for different electrodes and layers of different thickness is shown in Figs. 7 and 8. These data clearly demonstrate the effect of boundary conditions for the dynamic polarization on the size effect. The strongest suppression of the size effect occurs when electrodes are made of materials with a structure most similar to the ferroelectric structure. Plane-parallel capacitors based on a thin $Ba_{0.12}Sr_{0.88}TiO_3$ film of thickness $h = 20$ nm with electrodes made of either Pt or $SrRuO_3$ were investigated in [21]. $SrRuO_3$ has a perovskite structure (as well as displacive ferroelectrics) with a lattice constant close to that of $SrTiO_3$. As can be seen from Fig. 7, in the structure with $SrRuO_3$ electrodes, the tunability (determined by the ratio $\varepsilon(0)/\varepsilon(U_{max})$) is about 5 at room temperature, whereas the tunability of the capacitor with Pt electrodes (for the same thickness of the ferroelectric film) is smaller by a factor of 1.5. We can conclude that the size effect does not affect the film permittivity in this case and free boundary conditions for the polarization are implemented. Thus, the use of $SrRuO_3$ as an electrode material or fabrication of structures with a $SrRuO_3$ sublayer will make it possible to design ferroelectric thin-film capacitors with high capacitance and tunability.
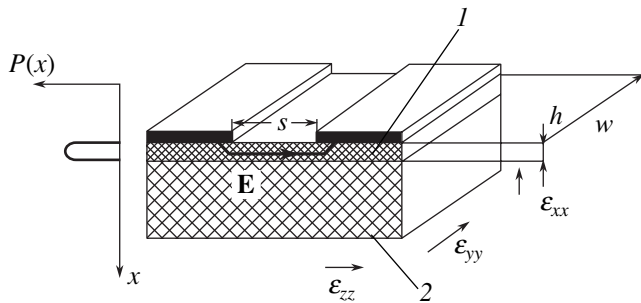
Fig. 9. Schematic mechanism of the formation of the effective anisotropy of a ferroelectric layer in a planar capacitor due to the size effect: (*1*) ferroelectric and (*2*) substrate.

THE SIZE EFFECT IN A PLANAR CAPACITOR

Let us consider a planar capacitor with a ferroelectric layer (Fig. 9). We assume that the ferroelectric polarization is zero at both boundaries of the layer, i.e., zero boundary conditions for the dynamic polarization are implemented. Due to this, a gradient of ferroelectric polarization arises across the layer exists. In the capacitor gap, the electric field is directed perpendicular to the polarization gradient. In this case, the size effect may manifest itself only when the layer thickness $h < 10^{-2}$ μm. Hence, we assume that, with respect to the field components parallel to the interface (E_z), the ferroelectric permittivity is not influenced by the size effect, i.e., independent of the layer thickness (in contrast to the field components E_x).

The effective anisotropy of the ferroelectric layer caused by the size effect is described by the diagonal permittivity tensor with the components $\varepsilon_{zz} = \varepsilon_{yy} = \varepsilon(U, T)$ and $\varepsilon_{xx} = \varepsilon_{eff}(U, T)$. The diagonal representation of the permittivity tensor is valid in the coordinate system related to the crystallographic axes of the structure.

Using the formula for the capacitance of a planar capacitor with an anisotropic dielectric layer [23], we obtain the expression for the capacitance of the ferroelectric layer:

$$C(U, T) = \varepsilon_0 w \frac{\varepsilon(U, T)}{s/h + (4/\pi)\ln 2 \sqrt{\varepsilon(U, T)/\varepsilon_{eff}(U, T)}}, \quad (18)$$

where s, h, and w are the geometric sizes of the capacitor (see Fig. 9).

Using (17) and taking into account the size effect in terms of the partial-capacitance method, we can write the capacitance of the ferroelectric layer in a planar capacitor in the form [24]

$$C(U, T) = \varepsilon_0 w \frac{\varepsilon(U, T) - \varepsilon_S}{s/h + (4/\pi)\ln 2 \sqrt{1 + 2\varepsilon(U, T)/\alpha h}}, \quad (19)$$

where ε_S is the substrate permittivity.

The numerical estimates of the capacitance of a planar capacitor showed that it is almost not influenced by the size effect. Therefore, when the film thickness exceeds 10^{-2} μm, the size effect in a planar capacitor can be disregarded.

CONCLUSIONS

The size effect in displacive ferroelectrics is directly related to the spatial correlation of the ferroelectric polarization. The spatial correlation is characteristic of not only ferroelectrics but also other materials undergoing phase transitions (for example, superconductors).

The spatial correlation, together with the boundary conditions for the dynamic ferroelectric polarization, leads to the dependence of the effective permittivity of a material on its sizes in thin-film capacitors. In this context, the spatial correlation is of interest not only for physicists studying the specific features of ferroelectrics near the phase transition but also from the practical point of view (design and application of thin-film structures based on ferroelectrics).

In some particular cases (for example, ferroelectric liquid crystals and ferroelectric copolymers), the models proposed here require additional analysis.

The anisotropy of the size effect and the possibility of its suppression in the case of particular boundary conditions for dynamic ferroelectric polarization are of particular interest.

In summary, we note that, in order to describe the size effect, spatial dispersion, and spatial correlation, we introduced the three interrelated parameters: the correlation parameter λ_1, the size-effect parameter α, and the correlation radius ρ.

This study is dedicated to the 80th birthday of Professor L.A. Shuvalov. Note that the first two books [1, 2] we refer to were edited by Shuvalov and published in the Soviet Union. These books played an important role in the development of the physics of ferroelectricity. We remember with great pleasure the congratulations to Shuvalov on the occasion of his 75th birthday from the editorial board of *Kristallografiya* (*Crystallography Reports*) [25] and we hope that, in the future, we will mark more than one jubilee of this remarkable scientist.

REFERENCES

1. F. Jona and G. Shirane, *Ferroelectric Crystals* (Pergamon Press, Oxford, 1962; Mir, Moscow, 1965).

2. J. C. Burfoot and I. G. W. Taylor, *Polar Dielectrics and Their Applications* (Univ. of California Press, Berkeley, 1979; Mir, Moscow, 1981).

3. J. C. Burfoot and J. R. Slack, J. Phys. Soc. Jpn. **28** (Suppl.), 417 (1970).

4. P. Padmini, T. R. Taylor, M. J. Lefevre, *et al.*, Appl. Phys. Lett. **75**, 3186 (1999).

5. A. G. Chynoweth, Phys. Rev. **102**, 705 (1956).

6. S. Triebwasser, IBM J. Res. Dev. **2**, 212 (1958).

7. O. G. Vendik and L. T. Ter-Martirosyan, Fiz. Tverd. Tela (St. Petersburg) **36** (11), 3343 (1994) [Phys. Solid State **36**, 1778 (1994)].

8. O. G. Vendik, S. P. Zubko, and L. T. Ter-Martirosyan, Appl. Phys. Lett. **73**, 37 (1998).

9. B. Desu Seshu and O. G. Vendik, Integr. Ferroelectr. **28**, 175 (2000).

10. O. G. Vendik, S. P. Zubko, and L. T. Ter-Martirosyan, Fiz. Tverd. Tela (St. Petersburg) **38** (12), 3654 (1996) [Phys. Solid State **38**, 1991 (1996)].

11. O. G. Vendik and I. G. Mironenko, Fiz. Tverd. Tela (Leningrad) **16** (11), 3445 (1974) [Sov. Phys. Solid State **16**, 2230 (1974)].

12. R. A. Cowley, Phys. Rev. **134**, A981 (1964).

13. V. G. Vaks, *Introduction to the Microscopic Theory of Ferroelectrics* (Nauka, Moscow, 1973) [in Russian].

14. K. Bethe, Philips Res. Rep. Suppl., No. 2, 1 (1970).

15. S. P. Zubko, Pis'ma Zh. Tekh. Fiz. **24** (21), 23 (1998) [Tech. Phys. Lett. **24**, 839 (1998)].

16. A. F. Devonshir, Philos. Mag. **40**, 1040 (1949); Philos. Mag. **42**, 1065 (1951).

17. V. L. Ginzburg, Zh. Éksp. Teor. Fiz. **19**, 36 (1949).

18. O. G. Vendik and S. P. Zubko, J. Appl. Phys. **88**, 5343 (2000).

19. O. G. Vendik, I. G. Mironenko, and L. T. Ter-Martirosyan, Fiz. Tverd. Tela (Leningrad) **26** (10), 3094 (1984) [Sov. Phys. Solid State **26**, 1864 (1984)].

20. O. G. Vendik and L. A. Rosenberg, J. Phys. Soc. Jpn. **28** (Suppl.), 413 (1970).

21. M. Izuha, K. Abe, and N. Fukushima, Jpn. J. Appl. Phys., Part 1 **36**, 5866 (1997).

22. M. Izuha, K. Abe, M. Koike, *et al.*, Appl. Phys. Lett. **70**, 1405 (1997).

23. V. I. Lavrik and V. N. Savenkov, *Conformal Mapping: A Handbook* (Naukova Dumka, Kiev, 1970) [in Russian].

24. O. G. Vendik, S. P. Zubko, and M. A. Nikol'skiĭ, Zh. Tekh. Fiz. **69** (4), 1 (1999) [Tech. Phys. **44**, 349 (1999)].

25. Kristallografiya **44** (1), 5 (1999) [Crystallogr. Rep. **44**, 1 (1999)].

Translated by Yu. Sin'kov

CRYSTAL
GROWTH

A Variational Approach to Cellular Crystal Growth

V. N. Kanishchev

Institute of Single Crystals, National Academy of Sciences of Ukraine, Kharkov, Ukraine
e-mail: kanishchev@isc.kharkov.com
Received March 4, 2003

Abstract—The variational method is applied to the study of crystal growth from melt under the condition that the boundary between the liquid and solid phases has a cellular structure. The surface energy of the interface is taken into account. © *2004 MAIK "Nauka/Interperiodica"*.

As is well known, the interface between the liquid and solid phases in some modes of growth from melt acquires a cellular structure [1]. Cellular crystal growth was studied by the method of integral functional with an indefinite integration domain [2]. The efficiency of this method was demonstrated on simple examples with the use of the simplest solidification model of a binary melt. In particular, the surface energy of the interface was ignored [2]. The aim of the present study is to take into account this energy in the variational approach to cellular crystal growth. Consider the classical model of solidification of a binary melt in the two-dimensional case with the crystallization direction coinciding with the x axis and take into account the surface energy of the interface. The impurity concentration in the melt, $C(x, y)$, is measured in the $C_0(1 - k)/k$ units from the level C_0, where C_0 is the impurity concentration in the melt at an infinitely large distance from the crystallization front and k is the coefficient of impurity distribution. The coordinate x is measured in the D/V units from the position which would have been possessed by a plane crystallization front, where D is the diffusion coefficient of the impurity in the melt and V is the crystallization rate. The coordinate y is measured in the L units, where L is the half-width of the cells or a half-period of the crystallization-front line determined by the equation $x = x(y)$.

Introduce the dimensionless coefficients

$$\kappa = \frac{D}{VL}, \tag{1}$$

$$B = \frac{kGD}{(k-1)mVC_0}, \tag{2}$$

$$\gamma = \frac{kT_m V\Gamma}{(k-1)mDC_0}, \tag{3}$$

where G is the temperature gradient, m is the slope of the liquidus line on the phase diagram of a binary system, T_m is the solidification temperature of pure melt,

and Γ is the capillary constant proportional to the surface energy of the interface.

Now, the problem of two-dimensional diffusion of the impurity toward the melt crystallizing at a constant rate may be formulated as

$$C_{xx} + C_x + \kappa^2 C_{yy} = 0, \tag{4}$$

$$\begin{aligned} C_x(x(y)) - \kappa^2 x_y(y)C_y(x(y)) \\ + (1-k)C(x(y)) + k = 0, \end{aligned} \tag{5}$$

$$C(x(y)) = 1 - Bx(y) + \gamma\kappa^2 x_{yy}(1 + \kappa^2 x_y^2)^{-3/2}, \tag{6}$$

$$C(\infty, y) = 0, \quad C_y(x, 0) = C_y(x, 1) = 0. \tag{7}$$

Above, we used the index notation of partial derivative of $C(x, y)$ with respect to x and y and also of the derivatives of $x(y)$ with respect to y. Equation (5) is the condition for the impurity conservation at the crystallization front. Equation (6) relates the impurity concentration at the interface to the thermodynamic characteristics of this interface. This equation is derived based on the phase diagram, the Gibbs–Thomson condition, and the assumption that the temperature field is plane and linearly depends on x.

Limiting the consideration to small amplitudes δ of the cell bulges, the solution of the above problem in the second approximation with respect to δ may be represented as [3]

$$\begin{aligned} C(x, y) = \exp(-x) + A_1\delta\exp(-q_1 x)\cos\pi y \\ + \delta^2[A_0\exp(-x) + A_2\exp(-q_2 x)\cos 2\pi y], \end{aligned} \tag{8}$$

$$x(y) = \delta\cos\pi y + \delta^2(\alpha_0 + \alpha_2\cos 2\pi y), \tag{9}$$

where

$$q_i = 0.5 + \sqrt{0.25 + (i\pi\kappa)^2}. \tag{10}$$

Now, substitute solution (8), (9) into each of the conditions at the interface, expand the exponents into a Taylor series, and equate the sums of the common factors

L, cm

0.04

0.02

0

2   3   4   5

V, 10^{-4} cm/s

1

2
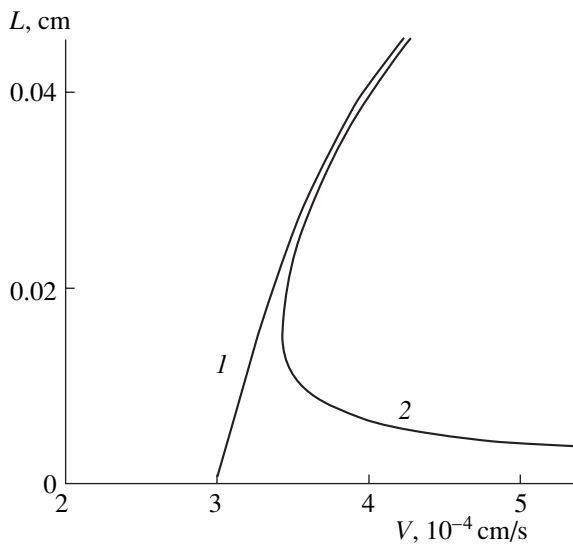
Half-width L of the cell as a function of the crystallization rate V (*1*) without and (*2*) with allowance for the surface energy of the interface.

before $\delta\cos\pi y$, δ^2, and $\delta^2\cos2\pi y$ to zero. Thus, we arrive at a system of six equations that yields

$$B + \pi^2\kappa^2\gamma = \frac{q_1 - 1}{q_1 + k - 1}, \qquad (11)$$

$$A_1 = 1 - B - \pi^2\kappa^2\gamma, \quad A_0 = \frac{1}{2}\left(A_1 q_1 - \frac{1}{2}\right),$$

$$A_2 = \frac{A_\gamma(kA_0 + \pi^2\kappa^2 A_1) - kA_0}{A_\gamma(q_2 + k - 1) - k}, \quad \alpha_0 = 0, \qquad (12)$$

$$\alpha_2 = \frac{A_2 - A_0}{A_\gamma},$$

where $A_\gamma = 1 - B - 4\pi^2\kappa^2\gamma$.

It is seen from the above solution that the amplitude of the cell bulges in problem (4)–(7) is an independent parameter, whereas the coefficient κ is not independent. This coefficient may be determined from Eq. (11) using the set of k, B, and γ values. According to Eqs. (1)–(3) and (10), the same equation also relates the cell half-width L to each of the growth parameters. Figure shows the dependences of L on the crystallization rate constructed for the following typical values of the parameters: G = 9 K/cm, m = –3 K/at %, k = 0.5, D = 10^{-5} cm², C_0 = 0.1 at % [1], T_m = 1000 K, Γ = 0 cm (curve *1*) and Γ = 10^{-8} cm (curve *2*) [4]. It is seen from this figure that the curves are located to the right of the line V = V_c. Thus, for curves *1* and *2*, we have V_c = 3 × 10^{-4} and 3/43 × 10^{-4} cm/s. This signifies that, at V > V_c, the solution can be only plane (δ = 0) and, at δ ≠ 0, it becomes two-dimensional. It is essential that the solution of

problem (4)–(7) does not lead to the cellular interface in the supercritical crystallization mode (V > V_c).

The situation dramatically changes with the transition from the differential formulation of the problem to the variational one [2]. One can readily see that Eq. (4) is the Euler equation for the following integral functional with an unknown integration domain:

$$I\{C(x, y), x(y)\} = \int_0^1 dy \int_{x(y)}^\infty \exp(x)(C_x^2 + \kappa^2 C_y^2)dx. \quad (13)$$

Then the solution of the problem of two-dimensional impurity diffusion in the melt crystallizing at a constant rate reduces to a search for the functions C(x, y) and x(y) minimizing functional (13) if conditions (5)–(7) are fulfilled, as well as the continuity condition for the function x in the whole range of its definition.

In such a formulation, the problem is far from being a simple mathematical problem. Considering it is beyond the scope of the present study. However, it is possible to draw some important conclusions without invoking complex calculations.

Substituting Eqs. (8) and (9) into functional (13) and using Eqs. (11) and (12), we obtain, within the second order of smallness with respect to δ, the following equation:

$$I = 1 - \frac{\delta^2}{4}\{1 - 2(1 - B_\gamma)[1 - B_\gamma(1 - k)]\}, \qquad (14)$$

where $B_\gamma = B + \pi^2\kappa^2\gamma$. It is seen from (14) that, at least at sufficiently low values of $1 - B_\gamma$, the value of functional (13) for a curved interface decreases in comparison with the plane case.

As is shown in [2], the value of integral (13) is proportional to the energy scattered during impurity diffusion in the melt, in accordance with the well-known principle of nonequilibrium thermodynamics. It should have the minimum value at the given external constraints [5]. Then, from the condition I < 1, it follows that the state of the crystal–melt system with the cellular crystallization front is more advantageous than with the plane one. Thus, under the condition V > V_c, one should observe a spontaneous bending of the crystallization front.

As is seen from figure, the effect of the surface energy of the interface manifests itself in an increase of the V_c value, which is consistent with the data obtained by an independent method in one of the pioneering theoretical works of the theory of cellular crystal growth [4]. Another important feature of the L(V) dependence observed at Γ ≠ 0 (curve *2*) is that the L(V) function at V > V_c is two-valued. One can readily see that the more general function $\kappa(1/B)$ (determined by Eq. (11)) at γ ≠ 0 also possesses this property. It turned out that in the critical mode, the cellular structure of the interface may develop with an increase in V by one of the two possible scenarios—either with a decrease or an increase in the

cell widths, which, according to Eq. (1), corresponds either to an increase or a decrease in the κ value. Now, the dilemma, which cannot be solved within the framework of the problem (4)–(7), arises again. According to the variational principle, the first scenario seems to be more advantageous, since a decrease in the scattering energy [see Eq. (14)] without an increase in κ would be more noticeable than with a decrease in it.

Thus, when using the two-dimensional model of solidification of a binary melt at a constant rate, the allowance for the surface energy of the interface along with the well-known effect of the displacement of the critical values of the growth parameters results in the problem of of having to choose one of the two tendencies in the development of the cellular surface of the interface. The results obtained in the present study demonstrate the efficiency of the variational method in solving similar problems of solidification theory.

REFERENCES

1. W. A. Tiller, in *The Art and Science of Growing Crystals*, Ed. by J. J. Gilman (Wiley, New York, 1963; Metallurgizdat, Moscow, 1968).
2. V. N. Kanischev, Funct. Mater. **8** (3), 450 (2001).
3. V. N. Kanischev, Funct. Mater. **9** (3), 402 (2002).
4. W. W. Mullins and R. F. Sekerka, J. Appl. Phys. **35** (2), 444 (1964).
5. I. Gyarmati, *Non-Equilibrium Thermodynamics. Field Theory and Variational Principles* (Springer, Berlin, 1970; Mir, Moscow, 1974).

Translated by L. Man

CRYSTAL
GROWTH

Effect of Surface Kinetics on the Dendritic Growth of Ice in Supercooled Water

A. A. Shibkov, M. A. Zheltov, A. A. Korolev, A. A. Kazakov, and A. A. Leonov

Tambov State University, ul. Internatsional'naya 33, 392622 Tambov, Russia

e-mail: shibkov@tsu.tmb.ru

Received June 24, 2003

Abstract—The dendritic growth of ice in supercooled water was investigated experimentally. It has been found that, with an increase in the degree of initial supercooling of water, the data of measuring the growth rate of the dendrite tip v_t, the average distance between the tip and the first side branch $\bar{z}_{SB}$, and the fractal dimension d_f of the dendrite contour diverge from the analytically and numerically calculated parameters of dendritic growth. It is shown that the discrepancy between experiment and theory is due to the transition from the diffusional growth to the growth controlled by the surface kinetics. The nature of the anisotropic surface kinetics of ice growth in supercooled water is discussed. © *2004 MAIK "Nauka/Interperiodica"*.

INTRODUCTION

It is well known that dendritic crystallization is a typical example of formation of a structure in nonequilibrium systems, the macroscopic dynamics of which is determined by diffusion fields [1–19]. It has been suggested that, with an increase in the driving force of a phase transition (supercooling of a melt or supersaturation of a solution), diffusional growth should be replaced with growth determined by processes of molecular rearrangement at the interface, i.e., the surface kinetics. In contrast to diffusional growth, crystal growth controlled by the molecular attachment kinetics at the interface is less studied, mainly because it is difficult to obtain deeply supercooled liquids.

In this study, we report the results of experimental investigation of the transition from the diffusional to kinetic ice growth in bidistilled water at atmospheric pressure. The ice–water system is used as simple model system, which is convenient for studying the crystal growth under highly nonequilibrium conditions. At the same time, this system plays a very important role in nature. Experiments were performed in the range of supercoolings from 0.1 to 30°C, in which both diffusional and kinetic regimes of ice growth occur. For comparison with the diffusion theories of dendritic growth, we measured the parameters that allow such comparison: the growth rate of the dendrite tip v_t, the position of the first side branch $\bar{z}_{SB}$ (measured in radii of curvature of the tip in the basal plane), and the fractal dimension d_f of the entire dendrite. It has been found that, for deeply supercooled water, there is a significant discrepancy between the experimental data and the theories of diffusional growth. The reason is that ice growth is transformed from the diffusional to kinetic regime at large supercoolings.

EXPERIMENTAL

Taking into account the fact that ice crystals are planar due to the high anisotropy [20–22], we used samples in the form of a horizontal water film (free membrane), 200 μm thick, spanned over a wire ring 30 mm² in area. To measure the crystallization temperature, the ring was made of two different conductors (copper and Manganin) forming a thermocouple. Water was redistilled with subsequent filtration and had a resistivity of ~10^7 Ω cm. Crystallization was initiated by bringing the surface of the supercooled water near the thermocouple junction into contact with a crystal seed. The temperature jump at the thermocouple junction caused by the evolution of latent crystallization heat made it possible to measure the degree of initial supercooling of water with accuracy of 0.05°C. The evolution of the shapes of growing ice crystals was video recorded in polarized light using a microscope (see for details [23−25]). Using this technique, we obtained earlier [26, 27] a complete morphological diagram of nonequilibrium patterns of ice growth in the range of supercoolings from 0.1 to 30°C, which covers almost the entire range of heterogeneous ice nucleation in bidistilled water at atmospheric pressure.

RESULTS AND DISCUSSION

Temperature Dependence of the Growth Rate of a Dendrite Tip

In the diffusion approximation, the problem of finding the equation of motion of the crystallization front in a one-component melt (the Stefan problem) is reduced to the solution of the heat-conduction equation with boundary conditions at a moving interface taking into account the dependence of its temperature on the front curvature (due to the Gibbs–Thomson effect) and the

growth rate (due to the kinetic effects related to the finite rate of molecular attachment at the interface). The analytical solution to this problem was first obtained by Ivantsov [1]. He neglected the Gibbs–Thomson effect and the kinetic effects at the interface and found a steady-state solution for a crystal in the form of a paraboloid of revolution that grows with a constant velocity of its tip v_t, which is inversely proportional to the radius of curvature of the tip r_t. In the Ivantsov solution, the dimensionless supercooling $\Delta = \Delta T(L/c_p)/L$ is related to the Peclet number $p = v_t r_t/2D$ by the Ivantsov function

$$\Delta = Iv(p) = p\exp(p)E_1(p), \qquad (1)$$

where

$$E_1(p) = \int_p^\infty \frac{\exp(-x)}{x}dx. \qquad (2)$$

Here, $\Delta T = T_m - T$ is the initial supercooling of the melt, T_m is the melting temperature, T is the temperature of the melt far from the crystallization front, L is the latent heat of phase transition, c_p is the isobaric specific heat of a unit volume of the melt, D is the thermal diffusivity of the melt, and $E_1(p)$ is an integral exponential function. The Ivantsov solution determines only the product $v_t r_t$ rather than values of v_t and r_t separately, whereas experiment shows single values of the radius of the dendrite tip and its growth rate at a specified supercooling [28].

A more appropriate theory of dendritic growth was developed by Langer and Muller-Krumbhaar [29]. They proposed using marginal stability as a criterion for selection of the growth rate of the dendrite tip and analysis of stability, considering the surface tension γ of the crystal–melt interface a perturbation. Based on this approach, it was shown that a continuous set of Ivantsov solutions is divided into stable and unstable regions, and the selected dendrite corresponds to the point of marginal stability separating these regions when the dendrite-tip radius r_t becomes equal to the minimum wavelength of the interface-strain wave λ_s. According to [2], the value of λ_s is determined by the expression

$$\lambda_s = 2\pi(2Dd_0/v_t)^{1/2} = 2\pi d_0/V^{1/2}, \qquad (3)$$

where $d_0 = \gamma c_p T_m/L^2$ is the capillary length, which characterizes the radius of action of the surface tension forces, and $V = v_t d_0/2D$ is the dimensionless growth rate of the dendrite tip. The other dimensionless parameter of this theory $\sigma = 2Dd_0/(v_t r_t^2)$ is equal to

$$\sigma = \sigma^* = (\lambda_s/2\pi r_t)^2 = \frac{1}{4\pi^2} \approx 0.0253 \qquad (4)$$

at the point of marginal stability.

The parameter σ^*, referred to as the stability constant, is an invariant of dendritic growth, since it is independent of the time of dendrite evolution and initial melt supercooling. Formulas (3) and (4) yield the relation between the dimensionless parameters of the Stefan problem that satisfy the criterion for marginal stability of the tip of a growing needle-shaped crystal:

$$V = \sigma^* p^2. \qquad (5)$$

Relation (5), along with Eq. (1), yields the dependence of the dimensionless growth rate of the dendrite tip V on the dimensionless supercooling Δ. The dependence $V(\Delta)$ ("the universal law of dendritic growth" [29, 30]) makes it possible to compare the dendritic crystallization rates of different materials. The Langer–Muller-Krumbhaar theory was experimentally verified for a number of simple model materials [31–33].

Figure 1 shows the temperature dependence $V(\Delta)$ for an ice crystal in double logarithmic coordinates in comparison with the experimental data obtained previously [34–39] and with the theoretical curve $V(\Delta)$ calculated in the diffusion approximation in [29]. The values of the corresponding parameters were taken from [30]: $T_m = 273.15$ K, $c_p = 4.18$ J/(cm^3 K), $L = 333$ J/cm^3, $D = 1.34 \times 10^{-3}$ cm^2/s, $\gamma = 2.8 \times 10^{-6}$ J/cm^2, and $d_0 = 0.288$ nm. It can be seen from Fig. 1 that the data obtained over the last forty years and the results of this study are in good agreement with the theoretical curve of dendritic growth in the supercooling range $0.006 < \Delta < 0.05$. At the same time, at larger supercoolings ($\Delta > (5–6) \times 10^{-2}$, which corresponds to $\Delta T > 4$°C), the results obtained by us and the data of [30, 39] show a systematic deviation from the Langer–Muller-Krumbhaar theory to lower growth rates. Our measurements confirm this tendency up to $\Delta_{max} \approx 0.37$ ($\Delta T_{max} \sim 30$°C), when the growth rate becomes as high as 60 cm/s, which is lower by a factor of 3.3 than the corresponding value calculated in terms of the diffusion model.

The reason for the discrepancy between the diffusion theory of dendritic growth and the experimental data in the range of large supercoolings is in the following. The Langer–Muller-Krumbhaar theory assumes that there is local thermal equilibrium at the moving crystallization front, which does not hold true at high growth rates. In this case, the finite rate of penetration of H$_2$O molecules through the interface must be taken into account. As a result, the slow surface kinetics leads to the decrease in the growth rate in comparison with the value calculated in the diffusion model, in which the surface kinetics is assumed to be infinitely fast. Transition from the diffusional growth to the growth determined by the surface kinetics occurs at supercoolings of 4–5°C; therefore, at larger supercoolings, the growth rate of the ice-crystal tip is determined predominantly by the molecular attachment kinetics at the ice–water interface.
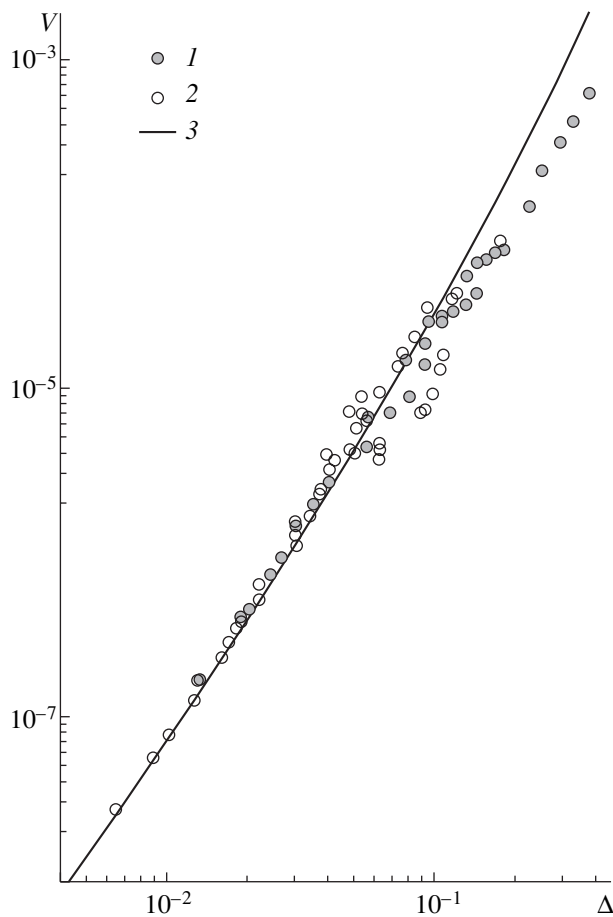
Fig. 1. Dimensionless growth rate V of an ice crystal tip as a function of dimensionless supercooling of water Δ: (*1*) data of this study, (*2*) data of [34–39], and (*3*) theoretical dependence $V(\Delta)$ according to the Langer–Muller-Krumbhaar diffusion model [29].

Position of the First Side Branch

The occurrence of side branches of dendrites is related to the Mullins–Sekerka diffusional instability [2]: with an increase in the velocity of the atomically rough crystallization front, the latter becomes unstable with respect to infinitely small strains with wavelengths exceeding the stability wavelength $\lambda_s = 2\pi(d_0 l)^{1/2}$, where $l = 2D v^{-1}$ is the diffusion length. The origin of initial perturbations that are necessary to form side branches has been discussed for a long time. Generally, two main scenarios of occurrence of an initial perturbation are considered: dendrite-tip splittings, which include oscillations of the tip velocity [4, 40, 41], and selective amplification of the thermal noise acting on the dendrite tip [42–44]. The tip splitting during the dendritic ice growth was investigated experimentally in [20–22]. It was ascertained that the tip splitting is due to the action of natural convection, which significantly affects the shape of ice crystals in regions of supercoolings smaller than 0.35°C.

The theory of dendrite sidebranching, based on the mechanism of selective thermal-noise amplification, was developed by Langer [43] for the case of isotropic surface tension at the crystal–melt interface and by Brener and Temkin [44] for anisotropic surface tension. In the Langer theory, the equation for a crystallization front in cylindrical coordinates is written as

$$Z = -r^2/2 + \xi_0(r) + \xi_1(r, t). \qquad (6)$$

This shape differs from the Ivantsov paraboloid by the sum of two corrections: time-independent smooth-shape correction $\xi_0(r)$, which is due to nonzero surface tension at the interface, and the time-dependent perturbation $\xi_1(r, t)$. In [43, 45], the average distance between the dendrite tip and the coordinate at which side branches have a mean-square amplitude $\langle \xi_1^2(r) \rangle^{1/2}$ equal to the tip radius of curvature r_t was chosen as a quantitative measure of the growth rate of side branches. The theories of dendrite sidebranching based on the mechanism of selective amplification of thermal fluctuations were experimentally verified in the studies of the growth of NH_4Br dendrites from a supersaturated aqueous solution [46, 47] and xenon dendrites grown from a pure melt [45].

In order to find out whether the selective amplification of thermal noise is responsible for the sidebranching in ice dendrites, we measured the distance Z_{SB} between the dendrite tip and the position at which the side branches have the mean-square amplitude equal to the radius of curvature of the dendrite tip in the basal plane (R_2) (Fig. 2). According to [22], R_2 was calculated by the formula $R_2 = x^2/8Z$, where $2x$ is the crystal width at a distance Z from the dendrite tip in the part without side branches; i.e., $Z < Z_{SB}$ (we use the generally accepted designations [20–24]). Figure 3 shows the dependence of the average value of the dimensionless position of the first side branch $\bar{z}_{SB} = \langle Z_{SB}/R_2 \rangle$ on absolute supercooling ΔT and dimensionless supercooling Δ. As can be seen from Fig. 3, with an increase in supercooling ΔT from 0.5 to 3.8°C, the value of $\bar{z}_{SB}$ increases from 2.7 to 500 (see also Fig. 4). Such behavior of growing ice dendrites ice differs significantly from the results of theoretical investigations of the dendrite sidebranching [43, 44].

According to the Langer theory [43], the dimensionless position of the first side branch is given by the expression

$$\bar{z}_{SB} \approx \frac{\sigma^2}{2}\left(\frac{3}{2}\right)^6 \ln^4(\bar{S}\bar{C}) \qquad (7)$$

for dendrites with cylindrical symmetry. Here, $\bar{S}$ is the dimensionless noise intensity:

$$\bar{S} = \left(\frac{T}{T_0}\right)\sigma^{3/2} p, \qquad (8)$$

where

$$T_0 = \left(\frac{L^2 d_0^3}{k_B c_p}\right)^{1/2}, \qquad (9)$$

p is the Peclet number, and k_B is the Boltzmann constant. The constant σ is determined in the same way as in the Langer–Muller-Krumbhaar theory of formation of needle-shaped crystals [29]:

$$\sigma = \frac{d_0 v_t}{2 D p^2}. \qquad (10)$$

Brener and Temkin [44] analyzed sidebranching taking into account that the shape of real dendrites does not have cylindrical symmetry due to the anisotropy of surface tension. In accordance with the Brener–Temkin theory, the position of the first side branch is given by the expression

$$\bar{z}_{SB} \approx \frac{(27\sigma)^{5/4}}{2^{5/2}\left(\frac{5}{3}\right)^{9/4}}\left|\ln(\bar{S}\bar{C})\right|^{5/2}. \qquad (11)$$

To calculate the temperature dependence of the position of the first side branch for ice dendrites from Eqs. (7)–(11), one needs an expression relating the tip velocity v_t to the supercooling ΔT. The best approximation of the results of our measurements of the tip velocity in the supercooling range $0.4 < \Delta T < 4°C$ (which corresponds to dendritic growth) is given by the formula

$$v_t = 1.72 \times 10^{-2}(\Delta T)^2 \text{ cm/s}. \qquad (12)$$

Substituting (12) for v_t into Eq. (10), we obtain an expression for the temperature dependence of the Peclet number:

$$p = 0.21\Delta. \qquad (13)$$

The theoretical values are $\bar{C} = 1$ [43] and $\sigma = 0.025$ [29]. Substituting the values of the corresponding parameters into (7) and (11), we obtain

$$\bar{z}_{SB} \approx 3.55 \times 10^{-3}\left|\ln(0.001\Delta)\right|^4 \qquad (14)$$

for a symmetric dendrite in the Langer model and

$$\bar{z}_{SB} \approx 3.41 \times 10^{-2}\left|\ln(0.001\Delta)\right|^{5/2} \qquad (15)$$

for a dendrite having no cylindrical symmetry in the Brener–Temkin model.

Figure 3 shows the dependence of $\bar{z}_{SB}$ on supercooling according to the Langer theory (curve 1) and the Brener–Temkin theory (curve 2). It can be seen that the temperature dependence of the position $\bar{z}_{SB}$ of the first side branch of ice dendrites is inconsistent with the diffusion theories of sidebranching based on selective noise amplification: with an increase in supercooling in the range 0.4–4°C, the value of $\bar{z}_{SB}$ significantly (by
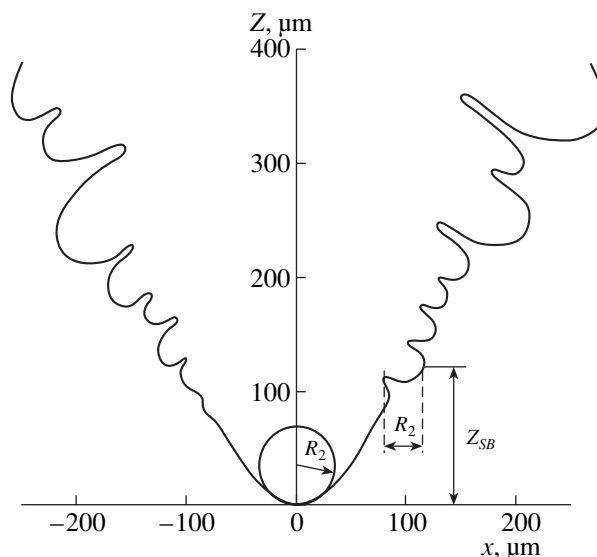
Fig. 2. Contour $Z(x)$ of an ice dendrite in the basal plane. The Z axis is directed along the growth direction of the dendrite tip $\langle 11\bar{2}0\rangle$ direction); Z_{SB} is the distance between the tip and the position at which the mean-square amplitude of side branches $\langle \xi_1^2(x)\rangle^{1/2} = R_2$.
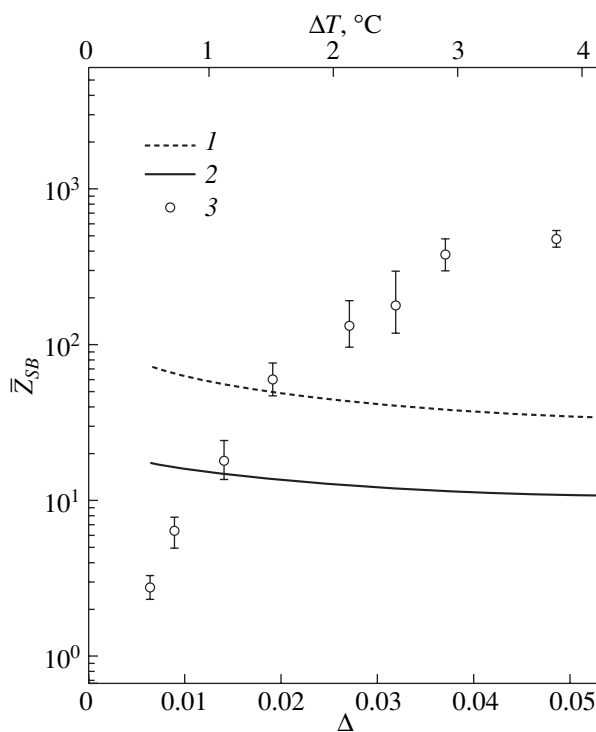
Fig. 3. Dependence of the dimensionless position of the first side branch $\bar{z}_{SB}$ on dimensionless supercooling Δ (the bottom abscissa axis) and absolute supercooling ΔT (the top abscissa axis): (1) the Langer theory, (2) the Brener–Temkin theory, and (3) experimental values of $\bar{z}_{SB}$ for ice dendrites.
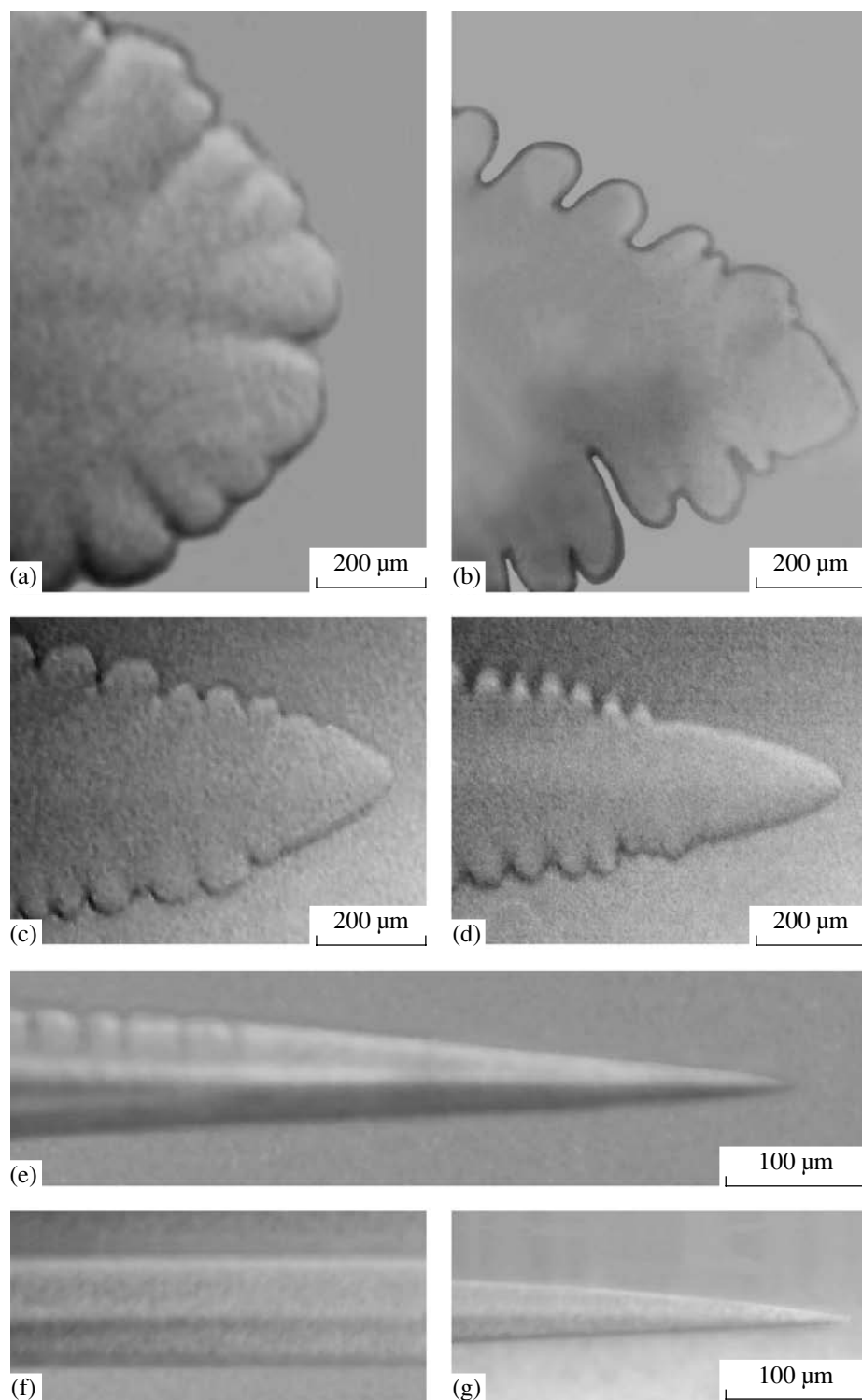
Fig. 4. Shape of ice crystals freely growing in supercooled water in the supercooling range $0.3 < T < 4.2$°C:(a) dendrite with a split tip, $\Delta T = 0.3$°C, (b–e) dendrites growing at different supercoolings: (b) $\Delta T = 0.5$°C, $\bar{z}_{SB} = 2.7$; (c) $\Delta T = 0.7$°C, $\bar{z}_{SB} = 6.4$; (d) $\Delta T = 1.1$°C, $\bar{z}_{SB} = 18$; (e) $\Delta T = 3.8$°C, $\bar{z}_{SB} \approx 500$; (f) needle-shaped crystal, a region far from tip, $\Delta T = 4.2$°C; and (g) region near the tip of a needle-shaped crystal, $\Delta T = 4.2$°C.

more than two orders of magnitude) increases rather than decrease logarithmically in accordance with the theory [43, 44]. This is indicative of gradual stabilization of the interface. The observed discrepancy between the experiment and theory may be caused by the following reasons: with an increase in the initial supercooling of water, (i) the intensity of the noise acting on the dendrite tip (which initiates the sidebranching) decreases; (ii) kinetic smoothing of the ice–water interface occurs, i.e., the degree of its roughness gradually decreases; and (iii) the role of thermal conductivity in the mechanism of dendrite formation decreases due to the increase in the velocity of the interface motion. It follows from formulas (8) and (13) that, at $\Delta T \ll T_0$, the thermal noise intensity $\bar{S}$ increases linearly with increasing supercooling ΔT; therefore, the suppression of the lateral growth instability, which manifests itself in the increase in $\bar{z}_{SB}$, can only be due to factors (ii) and (iii), i.e., the increase in the effect of the surface kinetics and decrease in the effect of thermal conductivity on the growth rate of side branches of ice dendrites.

Let us consider in more detail the evolution of ice crystals in this supercooling range. Observations show that the increase in the position of the first side branch with increasing the initial supercooling is accompanied by a decrease in the average distance between side branches and the ratio $\bar{v}_{s_1}/\bar{v}_1$, where $\bar{v}_{s_1}$ is the average growth rate of the tip of the first side branch. As a result, a dendrite with developed side branches is continuously transformed into an optically smooth needle-shaped crystal (Fig. 4). In contrast to the generally accepted concept of a needle-shaped crystal as a paraboloid of revolution, the needles observed exhibit pronounced faceting (Figs. 4f, 4g).

At the same time, when supercooling becomes as low as 0.4°C, $\bar{z}_{SB} \longrightarrow 1$, $\bar{v}_{s_1}/\bar{v}_1 \longrightarrow 1$, and dendrite-tip splitting occurs. Figure 4a shows a dendrite with a split tip. This observation is consistent with the results of [20–22], where it was ascertained that the reason for tip splitting is the enhancing effect of natural convection in the region of very small water supercoolings, which initiates morphological instability in the basal plane due to the low surface-tension anisotropy.

Fractal Analysis

The fractal dimension d_f of the ice-dendrite contour determined by the Mandelbrot formula $P \approx A^{d_f/2}$ [48], where P is the perimeter of the dendrite contour and A is the area limited by this contour. Figure 5 shows the dependence of P on A in double logarithmic coordinates for the dendrites growing at $\Delta T_1 = 1.5$ and $\Delta T_2 = 2.8$°C. It can be seen that these dependences can be approximated by linear functions. This circumstance means that ice dendrites are fractals with a scaling of about two orders of magnitude on the linear scale. The
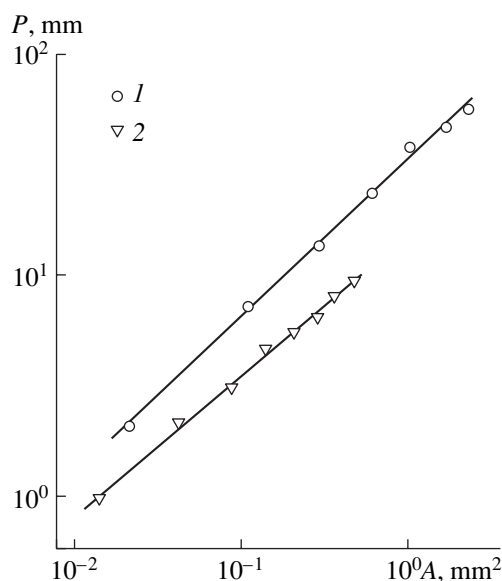
Fig. 5. Dependence of the perimeter P of the ice-dendrite contour on the area A limited by this contour: (*1*) $\Delta T_1 = 1.5$°C and (*2*) $\Delta T_2 = 2.8$°C. The slope coefficients correspond to the fractal dimensions $d_{f1} = 1.45 \pm 0.01$ and $d_{f2} = 1.31 \pm 0.01$.

scaling region is limited from below and above by the average distance between side branches and the size of the entire dendrite, respectively.

The fractal dimension of dendrites turned out to be dependent on the degree of water supercooling: in the range $0.3 < \Delta T < 4$°C, the fractal dimension of the dendrite d_f steadily decreases from 1.6 ± 0.07 to 1 (Fig. 6), which corresponds to a gradual extension of the dendrite with developed side branches (a fractal shape) into a needle-shaped crystal (an Euclidean shape). At the same time, analytical, numerical, and experimental investigations of dendritic growth under controlled diffusion growth conditions show that the fractal dimension of the dendrite contour is independent of supercooling. For different substances, the diffusion values of d_f vary from 1.42 to 1.73 [3, 15, 45, 48]. The pronounced discrepancy between the fractal dimension of dendrites calculated on the basis of the diffusion models and the fractal dimension of real ice dendrites is observed in the supercooling range $2 < T < 4$°C, where d_f continuously decreases from 1.4 to 1.0. The found discrepancy is an additional evidence of a gradual decrease in the effect of thermal conductivity on the lateral growth of ice dendrites in this supercooling range.

Anisotropy of the Kinetic Effect

Let us consider in more detail the fact that the temperature ranges characterized by the discrepancy between experimental data and predictions of diffusion models of dendritic growth are different for different growth directions. First, the temperature dependence of
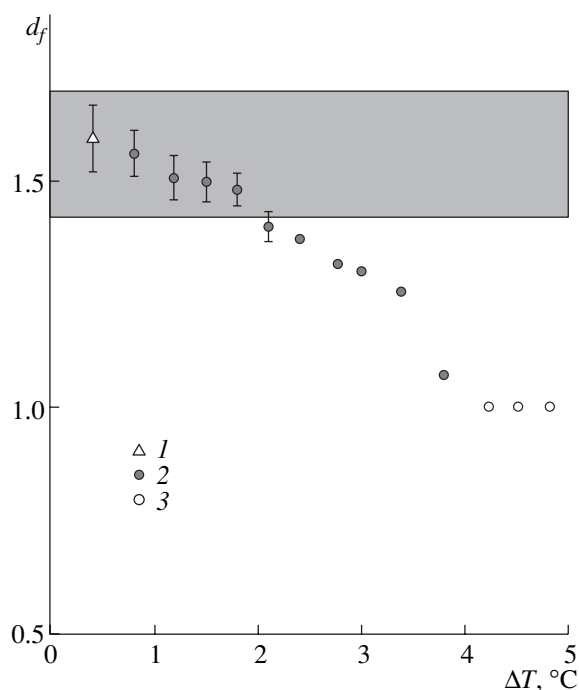
Fig. 6. Temperature dependence of the fractal dimension d_f of the ice-crystal contour: (*1*) dense branch structure formed as a result of multiple processes of "finger"-tip splitting, (*2*) dendrite, and (*3*) needle. Shaded band indicates the range of values of d_f corresponding to the diffusion growth: $1.42 < d_f < 1.73$ [3, 15, 45, 48].

by the expectation time for the appearance of 2D nuclei on the crystal surface, whereas the normal growth on a molecularly rough surface does not require nucleation. Therefore, the growth rate for a rough surface is significantly higher than that for a smooth surface at the same value of the driving force of the phase transition (supercooling or supersaturation).

Numerical simulation of the ice growth kinetics [50] shows that the interface is molecularly smooth for the basal system and rough for the prismatic system. At the same time, it is the rough interface that is morphologically unstable, which leads to dendrite sidebranching. This is consistent with the experimental data [51] on the growth of ice crystals in supercooled water at relatively low supercoolings (lower than 1°C). We can suggest that, with an increase in supercooling up to 4°C, a continuous transition occurs from a molecularly rough to smooth interface for the prismatic system of planes, except for the region near the crystal tip, which remains molecularly rough. As a result, sidebranching is suppressed and the crystal is continuously transformed from a dendrite into a long smooth needle due to the large difference in the growth rates for rough and smooth surfaces.

Thus, the observed anisotropy of growth kinetics suggest the following: (i) the molecular attachment at the interface occurs much faster along the $\langle 11\bar{2}0 \rangle$ direction (the growth direction of the dendrite trunk) than in other directions; (ii) at supercoolings T exceeding 4°C, the growth rate of the crystal tip is mainly determined by the rate of molecular rearrangement at the ice–water interface (this conclusion is qualitatively in agreement with the results of theoretical investigations of the crystal growth under highly nonequilibrium conditions [11, 52], which showed that the growth rate and the crystal shape at a large melt supercooling should be determined mainly by the anisotropic surface kinetics); and (iii) the experimental dependence of the position of the first side branch $\bar{z}_{SB}$ on supercooling is inconsistent with the theories of dendritic growth based on the mechanism of selective amplification of thermal noise acting on the dendrite tip [43, 44]. Therefore, study of alternative mechanisms of ice dendrite sidebranching should be continued.

the growth rate of the dendrite tip v_t, which characterizes the growth of the dendrite trunk (i.e., the growth in the $\langle 11\bar{2}0 \rangle$ direction), differs significantly from that predicted by the diffusion Langer–Muller-Krumbhaar theory of dendritic growth at supercoolings exceeding 4–5°C. At the same time, in the supercooling range from 0.4 to 4°C, the measurements of the growth rate of dendrite tips are in good agreement with diffusion theory. This circumstance means that, in the range $0.4 < T < 4$°C, the main assumptions of the Langer–Muller-Krumbhaar theory are valid only for the region near the dendrite tip. According to [29], these assumptions are as follows: the shape of the crystal is a paraboloid of revolution; the interface is molecularly rough and moves according to the normal mechanism; and the surface kinetics is infinitely fast.

Second, the experimental temperature dependences of $\bar{z}_{SB}$ and d_f, which characterize the sidebranching, differ significantly from the corresponding theoretical dependences in the range from 2 to 4°C, i.e., the range where a continuous morphological transition between a dendrite and a faceted needle occurs. It is well known that faceted crystals are formed as a result of layer-by-layer growth, which requires the presence of two-dimensional (2D) nuclei on a molecular smooth surface [49, 50]. The rate of such growth is mainly determined

ACKNOWLEDGMENTS

REFERENCES

1. G. P. Ivantsov, Dokl. Akad. Nauk SSSR **58**, 567 (1947).
2. W. W. Mullins and R. S. Sekerka, J. Appl. Phys. **34**, 323 (1963).

3. T. A. Witten and L. M. Sander, Phys. Rev. Lett. **27**, 5686 (1983).

4. D. A. Kessler, J. Koplik, and A. Levine, Adv. Phys. **37**, 255 (1988).

5. D. E. Temkin, Kristallografiya **32**, 1331 (1987) [Sov. Phys. Crystallogr. **32**, 782 (1987)].

6. D. E. Temkin, Kristallografiya **32**, 1336 (1987) [Sov. Phys. Crystallogr. **32**, 785 (1987)].

7. E. A. Brener, S. É. Esipov, and V. I. Mel'nikov, Pis'ma Zh. Éksp. Teor. Fiz. **45**, 595 (1987) [JETP Lett. **45**, 759 (1987)].

8. E. A. Brener, M. B. Geĭlikman, and D. E. Temkin, Zh. Éksp. Teor. Fiz. **94** (5), 241 (1988) [Sov. Phys. JETP **67**, 1002 (1988)].

9. E. A. Brener, S. É. Esipov, and V. I. Mel'nikov, Zh. Éksp. Teor. Fiz. **94** (3), 236 (1988) [Sov. Phys. JETP **67**, 565 (1988)].

10. E. A. Brener, S. V. Iordanskiĭ, and V. I. Mel'nikov, Zh. Éksp. Teor. Fiz. **94** (12), 320 (1988) [Sov. Phys. JETP **67**, 2574 (1988)].

11. E. A. Brener and V. I. Mel'nikov, Adv. Phys. **40**, 53 (1991).

12. E. Ben-Jacob, P. Garik, T. Mueller, and D. Grier, Phys. Rev. A **38**, 1370 (1988).

13. E. Ben-Jacob and P. Garik, Nature **343**, 523 (1990).

14. E. Brener, H. Muller-Krumbhaar, and D. Temkin, Phys. Rev. E **54**, 2714 (1996).

15. H. Muller-Krumbhaar, M. Zimmer, T. Ihle, and Y. Saito, Physica A (Amsterdam) **224**, 322 (1996).

16. E. Brener, H. Muller-Krumbhaar, D. Temkin, and T. Abel, Physica A (Amsterdam) **249**, 73 (1998).

17. L. M. Martyushev and V. D. Seleznev, Dokl. Akad. Nauk **371**, 466 (2000) [Dokl. Phys. **45**, 129 (2000)].

18. L. M. Martyushev, V. D. Seleznev, and I. E. Kuznetsova, Zh. Éksp. Teor. Fiz. **118**, 149 (2000) [JETP **91**, 132 (2000)].

19. L. M. Martyushev, I. E. Kuznetsova, and V. D. Seleznev, Zh. Éksp. Teor. Fiz. **121**, 363 (2002) [JETP **94**, 307 (2002)].

20. S. H. Tirmizi and W. N. Gill, J. Cryst. Growth **85**, 488 (1987).

21. S. Tirmizi and W. N. Gill, J. Cryst. Growth **96**, 277 (1989).

22. K. K. Koo, R. Ananth, and W. N. Gill, Phys. Rev. A **44**, 3782 (1991).

23. A. A. Shibkov, Yu. I. Golovin, M. A. Zheltov, *et al.*, Kristallografiya **46**, 549 (2001) [Crystallogr. Rep. **46**, 496 (2001)].

24. A. A. Shibkov, Yu. I. Golovin, M. A. Zheltov, *et al.*, J. Cryst. Growth **236**, 434 (2002).

25. A. A. Shibkov, Yu. I. Golovin, M. A. Zheltov, *et al.*, Physica A (Amsterdam) **319**, 65 (2003).

26. A. A. Shibkov, M. A. Zheltov, A. A. Korolev, and A. A. Leonov, Dokl. Akad. Nauk **389**, 94 (2003).

27. A. A. Shibkov, Yu. I. Golovin, M. A. Zheltov, *et al.*, Materialovedenie, No. 11, 15 (2002).

28. M. E. Gliksman, R. J. Schaefer, and J. D. Ayers, Metall. Trans. A **7**, 1747 (1976).

29. J. S. Langer and H. Muller-Krumbhaar, Acta Metall. **26**, 1681 (1978).

30. J. S. Langer, R. F. Sekerka, and T. Fujioka, J. Cryst. Growth **44**, 414 (1978).

31. S. C. Huang and M. E. Glicksman, Acta Metall. **29**, 701 (1981).

32. E. R. Rubinstein and M. E. Glicksman, J. Cryst. Growth **112**, 84 (1991).

33. E. R. Rubinstein and M. E. Glicksman, J. Cryst. Growth **112**, 97 (1991).

34. C. S. Lindenmeyer, G. T. Orrok, K. A. Jackson, and B. Chalmers, J. Chem. Phys. **27**, 822 (1957).

35. J. Hallet, J. Atmos. Sci. **21**, 671 (1964).

36. H. R. Pruppacher, Pure Appl. Geophys. **68**, 186 (1967).

37. W. C. Macklin and B. F. Ryan, Philos. Mag. **17**, 83 (1968).

38. J. P. Kallungal and A. Barduhn, AIChE J. **23**, 294 (1977).

39. K. Ohsaka and E. H. Trinh, J. Cryst. Growth **194**, 138 (1998).

40. D. A. Kessler, J. Koplik, and A. Levine, Phys. Rev. A **30**, 3161 (1984).

41. O. Martin and N. Goldenfeld, Phys. Rev. A **35**, 1382 (1987).

42. R. Pieters and J. S. Langer, Phys. Rev. Lett. **56**, 1948 (1986).

43. J. S. Langer, Phys. Rev. A **36**, 3350 (1987).

44. E. Brener and D. Temkin, Phys. Rev. E **51**, 351 (1995).

45. U. Bisang and J. H. Bilgram, Phys. Rev. E **54**, 5309 (1996).

46. A. Dougherty, P. D. Kaplan, and J. P. Gollub, Phys. Rev. Lett. **58**, 1652 (1987).

47. A. Dougherty and J. P. Gollub, Phys. Rev. A **38**, 3043 (1988).

48. J. Feder, *Fractals* (Plenum, New York, 1988; Mir, Moscow, 1991).

49. A. A. Chernov, E. I. Givargizov, Kh. S. Bagdasarov, *et al.*, in *Modern Crystallography*, Vol. 3: *Crystal Growth*, Ed. by B. K. Vaĭnshtein, A. A. Chernov, and L. A. Shuvalov (Nauka, Moscow, 1980; Springer, Berlin, 1984).

50. H. Nada and Y. Furukava, J. Cryst. Growth **169**, 587 (1996).

51. P. V. Hobbs, *Ice Physics* (Clarendon Press, Oxford, 1974).

52. E. A. Brener, J. Cryst. Growth **99**, 165 (1990).

Translated by Yu. Sin'kov

===== **JUBILEES** =====

Lyubov' Fedorovna Kirpichnikova
(On the Occasion of Her 60th Birthday)

On December 5, 2004, Lyubov' Fedorovna Kirpichnikova, Doctor of Physics and Mathematics, will celebrate her 60th birthday. Kirpichnikova came to the Institute of Crystallography in 1967 as a student to do her diploma work. Later, she conducted all stages of her scientific carrier from junior researcher to the head of the Laboratory of Crystal Optics.

Kirpichnikova started her carrier quite successfully—she began her work at a laboratory headed by Academician A.V. Shubnikov, the founder of the Institute of Crystallography. After looking closely at his new student, Shubnikov presented her with the reprint of his article "Problems of Crystal Chemistry and Endogeneous Formation of Minerals" with a warm inscription and good wishes, which she has cherished to the present day. Her scientific interests were formed under the influence of Professor L.A. Shuvalov, a well known expert in crystal physics of ferroelectrics, and N.R. Ivanov, a knowledgeable and experienced scien-

tist. In 1972, Kirpichnikova successfully defended her candidate's dissertation, dedicated to the study of dielectric properties and phase transitions of some crystals of the alkali trihydrogen selenite family. She studied the phase transitions in sodium trideuterium selenite and revealed and studied the ferroelectric properties of rubidium trihydrogen selenites, and the phenomenon of isotopic nonisomorphism of various mixed crystals of the alkali trihydrogen selenite family. Almost immediately after the introduction of the notion of ferroelastics by K. Aizu, Kirpichnikova revealed and studied the ferroelastic properties of a $K_2Ba(NO_2)_4$ crystal. Later, she also investigated the influence of carbamide impurity on the ferroelectric properties of Rochelle salt, and studied the influence of various external factors on the ferroelectric–ferroelastic phase transition in lithium ammonium sulfate crystals. She also was engaged in numerous applied studies.

Kirpichnikova's main scientific interest is the search for new crystals with ferroelectric and ferroelastic properties. She was the first to study dimethylammonium aluminum sulfate hexahydrate (DMAAS) and reveal the ferroelectric and ferroelastic properties of these crystals, their anomalously high spontaneous deformation, and their anomalously high plasticity at room temperature. Later, she studied the effect of high partly reversible plasticity of ferroelastics. Kirpichnikova also studied specific features of the domain structure of other ferroelastics. The results of her investigations formed the basis of her Doctoral Dissertation, "Anomalous Properties and Phase Transitions in Ferroelastics," successfully defended in 1998.

Kirpichnikova also studied phase transitions in crystals of double chlorides with organic cations and the domain structure in double sulfates and selenates during superprotonic–ferroelectric phase transitions.

Her successful recent studies have been determined, to a large extent, by her close scientific and friendly relations with Polish colleagues within the Agreement on Cooperation between the Russian and Polish Academies of Sciences. She works in cooperation with the Institute of Molecular Physics of the Polish Academy of Sciences in Poznan and the Institute for Low Temperatures and Structure Research of the Polish Academy of Sciences in Wroclaw.

In 1999, Kirpichnikova became the head of a sector at the Shubnikov Institute of Crystallography, and then the head of the Laboratory of Crystal Optics, headed

earlier by Professor B.N. Grechushnikov, an honorary scientist of the Russian Federation. Kirpichnikova proved to be a leader of the classical academic school. She always supports the initiatives of her colleagues, cherishes their scientific potential, appreciates their achievements, and preserves respectful relations with all, regardless of their official position. This style has proved to be very efficient. The colleagues and all the members of the laboratory continue to carry out a high level of fruitful activity. As a result, the laboratory performs research oriented to the study and prediction of physical properties of new promising materials at a high scientific level. This is reflected in several grants received, participation in national and international conferences, and a large number of annual publications, including those in the leading national and international journals and books. Kirpichnikova is always ready to encourage and help her colleagues. She is highly respected by all the members of the laboratory staff, who highly appreciate her invariably good attitude toward people.

The Editorial Board of *Kristallografiya* and her colleagues and friends congratulate Lyubov' Fedorovna Kirpichnikova on her 60th birthday and wish her good health and further success and achievements in her research.

Translated by L. Man

Vladimir Mikhaĭlovich Fridkin
(On the Occasion of His 75th Birthday)

Doctor of Physics and Mathematics Professor Vladimir Mikhailovich Fridkin has gained prominence with his research in several fields of solid state physics. He started his scientific carrier with research in the physics of photoelectrets for application to electrophotography that is widely used in xerography in Russia. The logical continuation of these ideas was the development by Fridkin of a new area—physics of the so-called photoferroelectric phenomena associated with the influence of nonequilibrium electron subsystems on ferroelectric properties of crystals. This wide class of phenomena, which has been discovered and studied in a large number of photosensitive ferroelectrics, includes photoinduced shift of the Curie temperature, photohysteresis and photodomain effects, the bulk photovoltaic effect in noncentrosymmetric media, and the effect of photorefraction (photoinduced variation of the refractive indices). Fridkin made a considerable contribution to the study of all these phenomena. Among the other studies of fundamental importance performed by Fridkin are the first experimental observation of the critical Curie point (the so-called tricritical point) in ferroelectrics and recent studies of two-dimensional ferroelectricity in superthin ferroelectric Langmuir–Blodgett films.

Fridkin's life in science is closely related to the Shubnikov Institute of Crystallography of the Russian Academy of Sciences. After graduation with distinction from the Physics Faculty of Moscow State University in 1952 and a short period of work at the Research Institute of the Printing Industry, where Fridkin started his pioneering works in physics of photoelectrets, Fridkin became a postgraduate at the Institute of Crystallography under the supervision of Academician A.V. Shubnikov in 1955. In 1958 he defended his candidate's dissertation on electrophotography and, in 1964, a doctoral dissertation on photoelectrets. He published more than 250 scientific articles, including those in journals one can only dream about, such as *Uspekhi Fizicheskikh Nauk*, *Nature*, etc. He also published six monographs and presented an enormous number of papers at various conferences dedicated to the most diverse topics of solid state physics. Fridkin has numerous students and followers. He supervised the candidate's dissertations of 65 students, six of whom also defended their doctoral dissertations. There is little doubt that he managed to create a scientific school.

In his long scientific life, Fridkin managed to cooperate with many international teams. Recently, he has been working in close cooperation with the University of Trento (Italy) and Lincoln University (United States). His fruitful scientific activity is highly regarded, and he was awarded (unfortunately only abroad) with the Kozar Medal of the Photographic Society of America for the development of silver-free photographic methods and with the Berg Prize for creating xerography. Fridkin's six monographs have not lost their importance, and translations of them are published in Germany and the United States. These are *Photoelectrets and Photographic Process* in (cooperation with I.S. Zheludev) (1960), *Physical Foundations of the Photographic Process* (1966), *Ferroelectrics–Semiconductors* (1976), *Photoferroelectrics* (1979), *Ferroelectrics of the ABC Type* (in cooperation with E.I. Gerzanich) (1982), and *The Photogalvanic Effect in Noncentrosymmetric Media* (in cooperation with B.I. Sturman (1992).

Fridkin has an artistic nature, and the sphere of his interests is very large. As fate willed it, about twenty years ago he became acquainted with Pushkin's archives and remains fascinated by his works. His natural scientist's approach also helped him to find his way in this enormous field. Readers and TV viewers know Fridkin as an author of fascinating historical investigations and essays, travel notes, and amusing memoirs published in seven books by prestigious publishing houses. Fridkin's recent hobby is literary translation—he translated from German (which he knows excel-lently) into Russian a novel written by N.A. Pushkina, Pushkin's youngest daughter, about her life in Russia.

The Editorial Board of *Kristallografiya* and his colleagues and friends wish Vladimir Mikhailovich Fridkin good health (about which he has been so anxious for the last fifty years) and success in his creative activity, as well as happiness in his family and personal relationships.

Translated by L. Man

OBITUARIES

Renata L'vovna Kayushina
(December 16, 1926–February 18, 2004)

Renata L'vovna Kayushina, a leading researcher at the Institute of Crystallography of the Russian Academy of Sciences, where she had worked since 1957, died suddenly on February 18, 2004.

Kayushina was born on December 16, 1926 in Leningrad, but soon after that her family moved to Moscow. In 1944, Kayushina entered the Faculty of Physics of Moscow State University. She graduated from the university in June 1949, having worked as a technician for a few years. Her working life began in the tragic period of our history—in the years of the Great Patriotic War. Together with all people of our country, she contributed her work to the victory over fascism and was awarded the title of Veteran of Labor. From 1950 to 1953, she worked at the Central Aerological Observatory. Although Kayushina worked very fruitfully, she was fired because her father was subjected to repression at the beginning of the 1950s.

From 1953 to 1957, Kayushina worked as a engineering researcher at the All-Union Institute for Problems of Fine Grinding of Building Materials (VNIITISM), where she investigated the dispersion structure of organic dyes and developed methods for studying the dispersivity of powders and gels of various nature.

In 1957, Kayushina went to work at the Institute of Crystallography of the Academy of Sciences of the Soviet Union and became the first post-graduate student of B.K. Vaĭnshteĭn, who was then a young promising researcher (later, he became an academician). The subject of her study—structural analysis of biological systems—was new for the Institute of Crystallography. To master this field, Kayushina had to complement her knowledge of physics by studying the new problems of structural biology and biochemistry, which were little-known at that time. She successfully did this on her own by mastering the latest methods of computer calculations, the application of which in structural crystallography had only just started then. Based on the results obtained, she defended her candidate's dissertation in physics and mathematics, titled "Electron-Diffraction Study of the Structure of L-Proline" (proline is one of 20 amino acids—components of all protein molecules). Her further research work at the Institute of Crystallography dealt with the development of X-ray methods for studying the structure of biological molecules in solutions. She obtained many very important data on the structure of many protein molecules and carried out one of the pioneer X-ray studies of the structure of ribosomal particles. Kayushina made a great contribution to the solution of the problem that arose again in the 1980s—packing of protein molecules in combination with low-molecular compounds by the Langmuir–Blodgett method and according to the scheme of polyionic condensation of polymers.

During her last years, she performed an intensive and very successful investigation of the structure of molecules of various immunoglobulins, which are of much interest for medicine. Kayushina, along with the group of researchers under her guidance, obtained pioneer data on the structure of immunoglobulins and rheumatic factor in solutions.

Being an active and sociable person, Kayushina did not limit himself to scientific research alone. She was always at the center of public life in any group of people where she studied or worked. For many years. Kayushina was Scientific Secretary of the Institute of Crystallography for international scientific relations. She

performed these duties (rather delicate at that time) humanely and benevolently with respect to all her colleagues. Due to her active position, a number of new scientific contacts between the Institute of Crystallography and various organizations and people in socialist and capitalist countries has arisen. Until 1983 she helped Vaĭnshteĭn to deal with all foreign relations of the Institute. A quick mind and cheerfulness helped Kayushina to simultaneously manage a lot of information, successfully solve many administrative problems at hand, and find enough time for research work.

Kayushina's distinctive feature was the ability and need to learn continuously, improve her knowledge, and be involved with new achievements in the fields of her interest. She generously shared her knowledge with her colleagues. Until her last days, when a serious ill-ness finally overcame her, she continuously looked through the latest scientific literature, searched for the latest developments in bionanotechologies using Internet tools, coordinated the studies supported by the Russian Foundation for Basic Research, and made plans for future scientific research.

The death of Kayushina was an irreplaceable loss for the staff of the Institute of Crystallography; her colleagues from the Small-Angle Scattering Laboratory, where she worked for many years; and the editorial board of *Kristallografiya* (Crystallography Reports). We will always remember her in our hearts.

Translated by Yu. Sin'kov

$$==\text{ERRATA}==$$

Erratum: "Comparative Analysis of Two Methods of Calculation of the Orientation of Domain Walls in Ferroelastics" [*Crystallogr. Rep.* 49, 828 (2004)]

V. A. Nepochatenko

On page 828, the last line in the left column should read "$Pb_3(PO_4)_2$ and $BiVO_4$."

On page 830 in the left column the beginning of the sentence in the 20th line from the bottom should read "Bismuth vanadate $BiVO_4$ …"

On page 830 in the right column line 9 from the top should read:

"where $K = -(2e_{12} + \sqrt{4e_{12}^2 + (e_{11} - e_{22})^2})/(e_{11} - e_{22})$."

== **ERRATA** ==

Erratum: "Algorithms for Solving Atomic Structures of Nanodimensional Clusters in Single Crystals Based on X-ray and Neutron Diffuse Scattering Data" [*Crystallogr. Rep*. 49, 863 (2004)]

N. M. Andrushevskiĭ, B. M. Shchedrin, and V. I. Simonov

On page 865 in the right column the sentence in lines 12–14 from the bottom should read "Therefore series (7) is the superposition function $\hat{\rho}(x)$ with the period $T = L/n$".

Electrons of *l* Shells of Free Atoms As a Regular System of Points on a Sphere:
II. Some Manifestations of the Symmetry of Electron Shells of Ions of Transition Metals in Ordered Media

T. F. Veremeĭchik and R. V. Galiulin

Shubnikov Institute of Crystallography, Russian Academy of Sciences,
Leninskiĭ pr. 59, Moscow, 119333 Russia
e-mail: tomver@online.ru
Received April 2, 2004

Abstract—Manifestations of the spatial symmetry of *d* and *f* shells formed by equivalent electrons of transition-metal ions in crystals and other ordered media are considered. It is shown that sizes of crystals and the rare coordination number of ions can be explained in terms of the noncrystallographic symmetry of these shells. The symmetry of the *d* shell may cause manifestations of elements of fivefold symmetry in the crystal faceting and the structure of molecules and affect the properties dependent on matching of the intrinsic symmetry of the shell and the translational symmetry of a crystal. © *2004 MAIK "Nauka/Interperiodica"*.

INTRODUCTION

Groups of equivalent electrons of free ions—*l* shells—are closed stable systems of identical interacting particles. Hence, they should be characterized by a certain position in space. For example, *d* and *f* shells are modeled, respectively, by pentagonal and heptagonal antiprisms with fivefold and sevenfold axes [1–5]. In a crystal structure, the fivefold and sevenfold symmetries may manifest themselves as a result of competition of the intrinsic symmetry of the *d* and *f* shells and the translational symmetry of the crystal, since the translational symmetry forbids the existence of fivefold and sevenfold axes in the three-dimensional Euclidean space. The symmetry of *d* and *f* shells may also manifest itself in crystals because the symmetry of the free state of a shell is retained near the ion core in a crystal lattice [6].

The chemical bond formed by a *d* shell stronger (in comparison with the bond formed by an *f* shell) due to the absence of external screening shells. Therefore, one might expect that the nontrivial symmetry of the valent electron shells of transition metals can be found, first of all, in ordered media containing *d* ions. In this study, we consider some structural characteristics and properties of such media in the context of the noncrystallographic symmetry of *d* and *f* shells.

INCORPORATION OF A PENTAGONAL ANTIPRISM INTO A CRYSTAL

Different ways of incorporation of a pentagonal antiprism into the crystalline field of symmetry of cubic groups are related to the derivation of isohedra with fivefold symmetry—pentagonal tritetrahedron, pentagonal dodecahedron, or pentagonal trioctahedron—from a tetrahedron, dodecahedron, and cube (octahedron). Figure 1 shows examples of incorporation of a pentagonal antiprism into a cube. From the five vertices of the base, which also form the face of the pentagonal dodecahedron, one pair (Figs. 1a, 1b) is located on the three-fold axes, another pair lies in the plane of symmetry perpendicular to the cube face, and the fifth vertex is in the plane of symmetry that is perpendicular to the plane above. In a strong crystal field of cubic symmetry, the vertices of an antiprism are transformed into the vertices of an octahedron and tetrahedron, which corresponds to the reduction of a *d* shell into t_2 and *e* subshells of the strong field (Fig. 2). These examples show that the vertices of an antiprism lose their equivalence in a crystal. Therefore, only subgroups of the $\bar{5}m$ group, in particular, the 5-order cyclic group, can
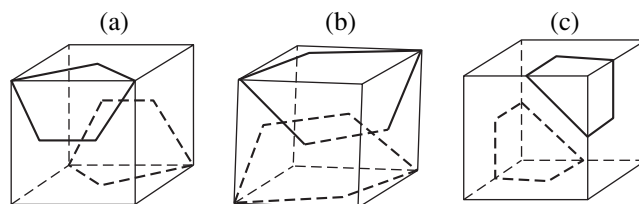
Fig. 1. Different incorporations of a pentagonal antiprism into a cubic field: (a) the most harmonic, (b) corresponding to the orientation of electron densities along the threefold axes and the coordinate axes *x*, *y*, and (c) corresponding to the dumbbells of electron density with one spin direction.
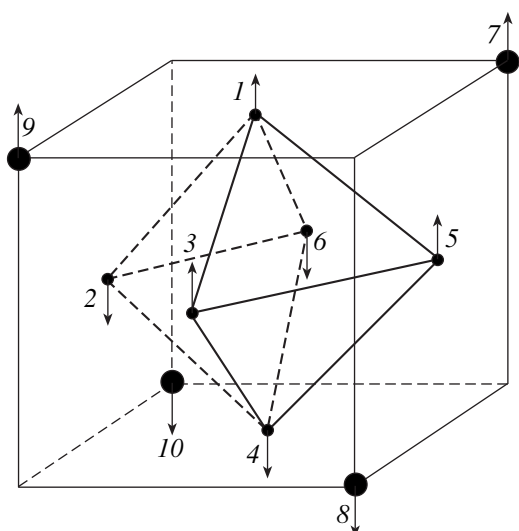
Fig. 2. Juxtaposition of the vertices of an octahedron and a tetrahedron with the electrons of the t_2 and e subshells of a strong cubic crystal field: points *1–6* and *7–10*, respectively.

locally manifest themselves in a crystal. The pentagon in the antiprism base may become irregular or transform into another polyhedron, but the trend to the implementation of the fivefold symmetry may remain due to the topological equivalence.

CHEMICAL BOND AND THE SYMMETRY OF THE d SHELL

The representation of the electron-density probability for an ion, accepted in quantum mechanics, is based on the arbitrary choice of such linear combinations of spherical functions that are real and allow pictorial description. If we refuse selection of one direction in space, the tori of the electron density of the d shell of a free ion are distributed over four tetrahedral (three-

fold) and three octahedral (coordinate) axes [7]. When a direction in space is selected, the angular part of the density of one electron in the d shell of a free ion is modeled by dumbbells, which are related to the projection m_l of the orbital momentum l on the z axis as follows: $d_{z^2} \longrightarrow m_l = 0$; $d_{xz} \longrightarrow m_l = 1$ (-1); $d_{yz} \longrightarrow m_l = -1$ (1); $d_{x^2-y^2} \longrightarrow m_l = 2$ (-2); $d_{xy} \longrightarrow m_l = -2$ (2) (Fig. 3).

The chemical bond is formed by the electron shell of an ion in the ground state, which has the maximum total spin for a free ion (the Hund rule). The maximum spin is retained in a crystal field: for the d^1, d^2, d^8, and d^9 shells it is retained in any field; for the d^3 and d^7 shells it is retained in fields of octahedral and tetrahedral symmetry, respectively; and for the d^4–d^6 shells it is retained in weak fields. The vertices of one base of the antiprism correspond to the states of maximum spin multiplicity, since the two antiprism bases correspond to the opposite $(+1/2, -1/2)$ projections of the m_s spin on the z axis (Fig. 4).

In order to determine the chemical-bond properties in the quantum model of the d shell of a free ion, we will select the dumbbells with the same values of m_s in Fig. 3 (as in Fig. 1c). This system has the $2m_v^2$ symmetry and its cross section by the plane perpendicular to the three-fold axis is a pentagon. To obtain a pentagon (for example, in the plane perpendicular to the z axis), at least one dumbbell should be somewhat displaced.

Thus, the quantum-mechanical model for the probability of the d-electron density does not exclude a local manifestation of the fivefold symmetry for certain combinations of shells and characteristics of the crystal
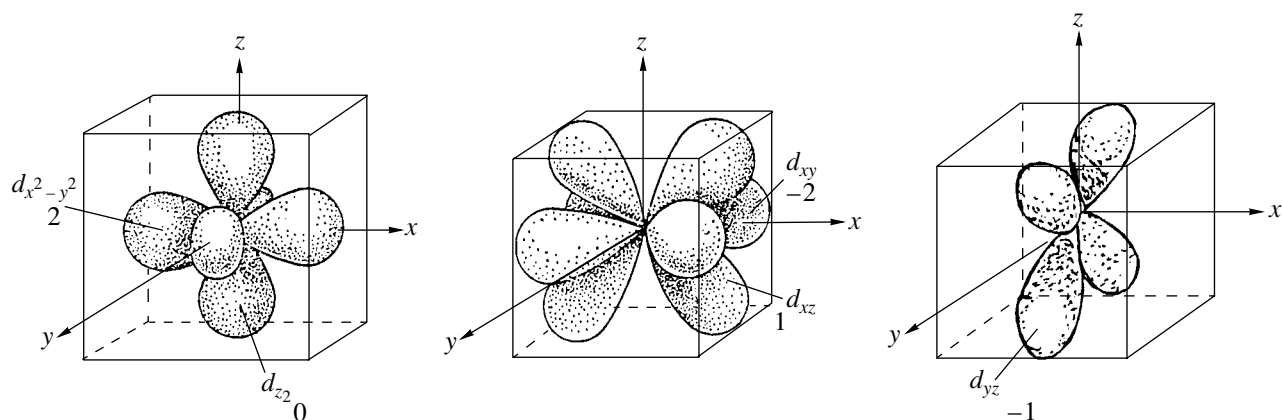
Fig. 3. Electron-density probabilities for the t_2 and e subshells of a strong cubic crystal field, expressed in terms of spherical functions $Y_{lml}(\theta, \varphi)$. Numbers are the values of m_l (the projection of the orbital momentum l on the z axis).

field, for example, such combinations that lead to removal of the spin degeneracy in the ground state or some displacement of one dumbbell.

SYMMETRY OF THE d AND f SHELLS AND SIZES OF CRYSTALS. IDEAL CRYSTAL

Since five- and sevenfold axes are noncrystallographic, the tendency of the d and f shells to their formation should impede the growth of large crystals, since polyhedra with such axes, when incorporated into the crystal structure, loosen it. According to vast mineralogical data [8], large single crystals of transition metals do not exist. Moreover, there are no data on large crystals containing transition-metal ions in the matrix. In contrast, the largest among the known single crystals is, apparently, the single crystal of spodumene LiAl[Si$_2$O$_6$], which is as large as 13 m in length and ~1 m in cross section [8]. The chemical elements entering its composition have only s and p shells: $1s^22s$ for Li, (Li)$2s2p^4$ for O, (O)$2p^23s^23p$ for Al, and (Al)$3p$ for Si. In this case, the antiprisms modeling the s and p shells have only crystallographic axes and are covered by the translational symmetry [1].

It may be established that the structural nonideality impedes the formation of large crystals. A crystal that contains ions with d and f shells cannot be considered ideal due to the inconsistency of these shells with the translational symmetry and the nonequivalence of combinations of N' electrons of the unfilled $l^{N'}$ shell taken all $N = 2(2l + 1)$ vertices of the antiprism at a time. The latter factor leads to different angular distributions of the electron-density probability at any instant of time. Thus, the definition of ideal crystal itself is to be refined and should contain the characteristics of the electron shells of ions, i.e., be formulated in terms of quantum crystallography [2].

COORDINATION POLYHEDRA OF IONS WITH d AND f SHELLS

Apparently, due to the noncrystallographic symmetry of the d and f shells of transition-metal ions, the latter should tend to be located in general positions of the structure and pass from general and particular positions to the positions having common symmetry elements with the corresponding antiprisms. Indeed, in an overwhelming number of crystals, including cubic ones, the local symmetry of the activating transition-metal ion is described by a low-symmetry group [9, 10].

Both the central ion and repulsion of ligands contribute to the formation of a coordination polyhedron [11–13]. In the first case, the valence-bond direction, the shell hybridization, and the overlap of atomic orbitals are of importance. Analysis of the dependence of the coordination on the angular distribution of hybrid elec-
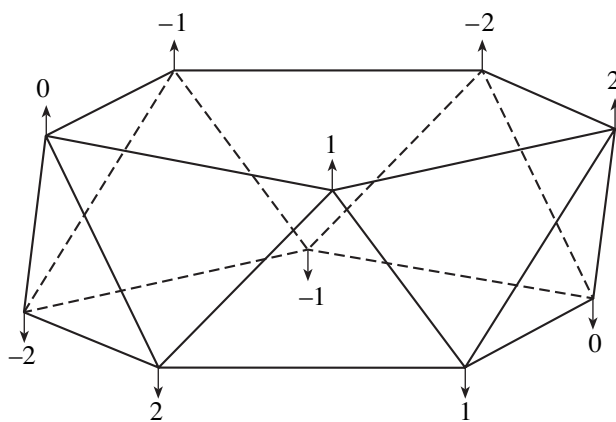
Fig. 4. Modeling of the d shell by a pentagonal antiprism. Arrows indicate the spin orientation and the numbers are the values of m_l.

tron densities [12] showed that sevenfold and fivefold coordinations correspond to the electron-density distribution over the vertices of polyhedra of the icosahedron group. It can be easily seen that the icosahedron models the hybridization of d and s shells since it is the sum of a pentagonal antiprism and a dumbbell [1].

Another manifestation of the fivefold symmetry in transition metals is that, although the content of elements with valent d shells in the periodic table is ~30%, about 70% of examples of fivefold coordination correspond to these ions [14–18]. Different polyhedra with fivefold coordination (Fig. 5) correspond to different variants of matching of the fivefold symmetry of the d shell with the crystal structure. The other ~30% cases of fivefold coordination are related to the ions in the oxidation state corresponding to the external d^{10} shell or the $1s^22s^22p^6$ shell. The $1s^22s^22p^6$ shell allows diverse hybridization. These 30% include, for example, Ga^{3+} and Sn^{4+} ions with the external shells (Ar shell)$3d^{10}$ and (Kr shell)$4d^{10}$, respectively, and Na$^+$ and Mg^{2+} ions with the $1s^22s^22p^6$ shell. In addition, ions with d and f shells demonstrate, in total, about 80% of the examples of sevenfold coordination. The specific feature of this coordination is that (i) it can be easily transformed into the fivefold coordination, for example, by shifting the central ion towards the pyramid (Fig. 5c) and (ii) the fivefold symmetry directly manifests itself in this case. For example, the five equivalent vertices of the pentagonal bipyramid in Fig. 5l are occupied, as rule, by ions of one type, whereas the other two vertices are occupied by ions of another type [15, 16].

The shapes of polyhedra with fivefold and sevenfold coordinations and polyhedra with other rare coordination numbers for the most dense packing were determined by Belov (Figs. 5a–5j) [17]. Most examples are ions with d shells (Fig. 5) [17, 18]. The fivefold symmetry directly manifests itself in the shapes of the polyhedra with the coordination numbers 8 and 12 (Figs. 5f, 5j).
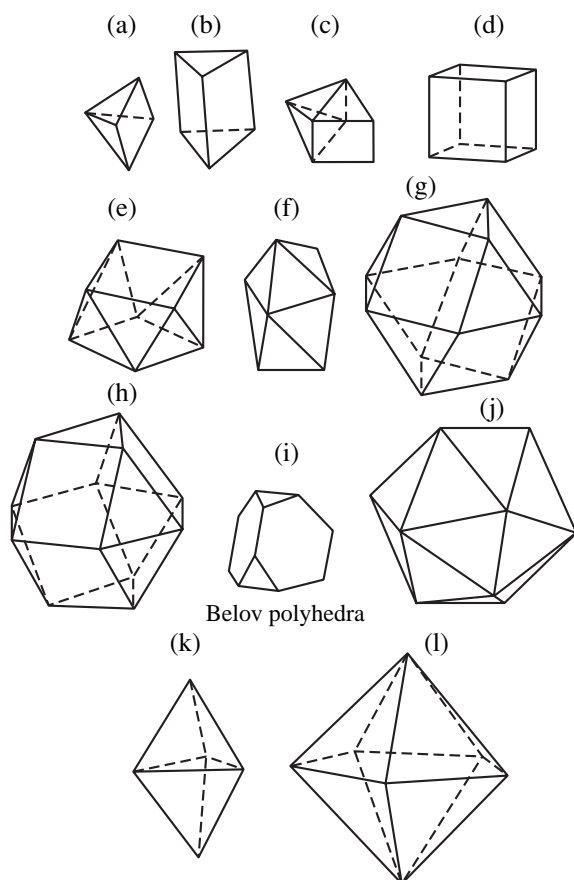
Belov polyhedra

Fig. 5. Coordination polyhedra with rare coordination numbers with the densest packing—Belov polyhedra: (a) NiS, (b) MoS_2, (c) Sb_2S_3 (Sb has a $4d^{10}5s^2$ shell), (e) $CuAl_2$, (f) $ZrSiO_4$, and (j) $K_3[Co(NO_2)_6]$; some (k) five- and (l) seven-coordination polyhedra in molecules.

For example, the Ir ion in the nitrite $K_3Ir(NO_2)_6$ is surrounded by 12 O ions forming an icosahedron. In this case, the icosahedron is distorted by the crystal to the "mineralogical icosahedron" [17] with two rather than one types of faces.

Fivefold symmetry often manifests itself in the structure of molecules because the ions surrounding the central ion make its d shell tend to the fivefold symmetry by reducing to zero some overlap integrals for this shell and orbitals of the environment ions. For example, the fivefold symmetry manifests itself in the structure of a large number of cyclic sandwich compounds of transition metals, for example, organometallic compounds, which may contain the entire series of the ions of the iron group ($3d$ shell) (Fig. 6) and some ions of the actinide group ($4d$ shell) [19]. The most striking example are the compounds structures of which directly reproduce a pentagonal antiprism, for example, structures of ferrocene $M(C_5H_5)_2$, where M is a transition metal attached to the center of the ring via a d–π bond (Figs. 6a, 7).
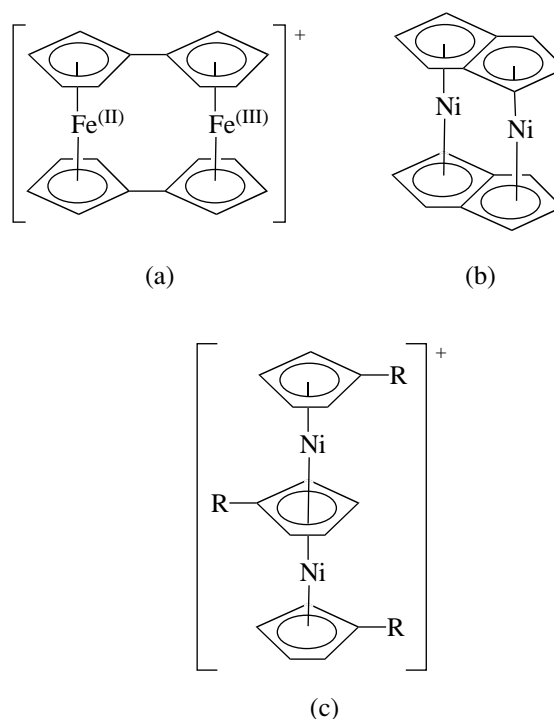
Fig. 6. Structures of some organometallic compounds containing (a) Fe^{2+} and Fe^{3+} ions (diferrocene) and Ni^{2+} ions ((b) picrate and (c) bis-pentalenyl).

EFFECT OF THE d SHELL ON CRYSTAL FACETING

Faceted polyhedra are complementary to coordination polyhedra. The pentadodecahedron is complimentary to the icosahedron modeling hybrid d and s shells. In addition, a face of a polyhedron can be a pentagon if five edges converge to a vertex of the coordination polyhedron. Coordination polyhedra of such type are characteristic of some transition-metal ions (Fig. 5).

Generally speaking, the crystals containing ions with d shells constitute a significant part among the crystal's faceting of which shows the fivefold symmetry. Cobaltite CoAsS is an example of icosahedral faceting (Fig. 8a). Pyrite FeS_2 is faceted in three shapes, two of which are a mineralogical icosahedron and a pentadodecahedron (Fig. 9) [8]. The variety of pentagons in the crystal faceting is illustrated in Fig. 8 by examples of calamine $Zn_2(OH)_2SiO_3$ (Fig. 8b), sphalerite ZnS (Fig. 8c), hematite Fe_2O_3 (Fig. 8d), and many other crystals [6, 8]. Note that faceting of calamine demonstrates what is probably a maximum number, equal to four, of pentagons of different shape, whereas its symmetry $2m_v^2$ is equivalent to the symmetry of the system of dumbbells with one value of m_s (Fig. 3).

SPECIFIC FEATURES OF IONS
WITH DIFFERENT NUMBERS OF ELECTRONS
IN THE *d* SHELL

In quantum mechanics, the term ^1S of the highest spherical symmetry of the shell atomic model corresponds to the ground states of the semifilled shell $l^{N/2}$ and the filled shell l^N, where $N = 2(2l + 1)$. In the crystallographic model, taking into account that an antiprism should completely correlate with the partially filled $l^{N'}$ shell at any N' [1, 3], the highest symmetry of this model is most adequately described by the $l^N - d^{10}$ shells (and the similar d^9 shell) and the $l^{N/2} - d^5$ shells. The ground states of these shells correspond to equal electron-density probabilities at the vertices of the antiprism. Obviously, when these shells are incorporated into a crystal, they undergo maximum distortion. At the same time, the ground states of the d^2 and d^3 shells are modeled, respectively, by combinations of two and three vertices of the antiprism base: *2, 1* and *0, 2, 1* (Fig. 4). These vertices of the antiprism, when the latter is incorporated into a strong crystal field, are naturally transformed into two and three vertices of a tetrahedron and an octahedron, respectively (Fig. 2). One might expect that d^2 and d^3 shells will be more readily incorporated into the crystal structure as compared with d^5 and d^{10} shells.

The stabilization energy E_{st} of the crystal field characterizes the decrease in the energy of the ground state of an ion in a crystal with respect to the ion free state. The significantly different values of E_{st} for the d shells under comparison can be explained by different possibilities of matching the symmetry of the d^2 and d^3 shells and the d^5 and d^{10} (d^9) shells with the translational symmetry of the crystal. For the d^5 and d^{10} shells, the value of E_{st}, as one would expect, is minimum. At the same time, this energy is maximum for the d^2 and d^3 shells (Table 1).

The coordination polyhedra in crystals are also different for the d shells compared. For example, the ions with d^5 and d^{10} (d^9) shells are characterized by a large variety of coordination numbers, which accounts for different possibilities of matching for the pentagonal and translational symmetries. This variety includes also the fivefold coordination (Table 2). According to the data of [20], the average values of the coordination numbers for ions with d^5 shells (Mn^{2+}, Fe^{3+}) are 5.98 and 5.69, respectively; with d^9 shells (Cu^{2+}) it is 5.10; and with d^{10} shells (Ag^+, Zn^{2+}, Hg^{2+}, Cd^{2+}) they are 5.10, 4.98, 5.5, and 6.14, respectively.

Ions with d^2 and d^3 shells (according to [14, 20]) have mainly sixfold coordination (Table 3). These ions form the strongest clusters [21].

In contrast, the stereochemistry of molecules and coordination compounds containing ions with both d^2 and d^3 shells and d^5 and d^{10} (d^9) shells exhibits a large variety of coordinations, including rare ones [16].
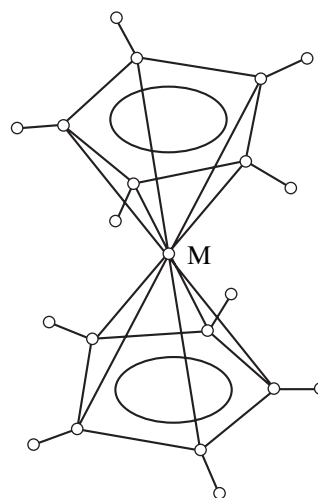
Fig. 7. Ferrocene structure $M(C_5H_5)_2$ (M is an iron-group ion).
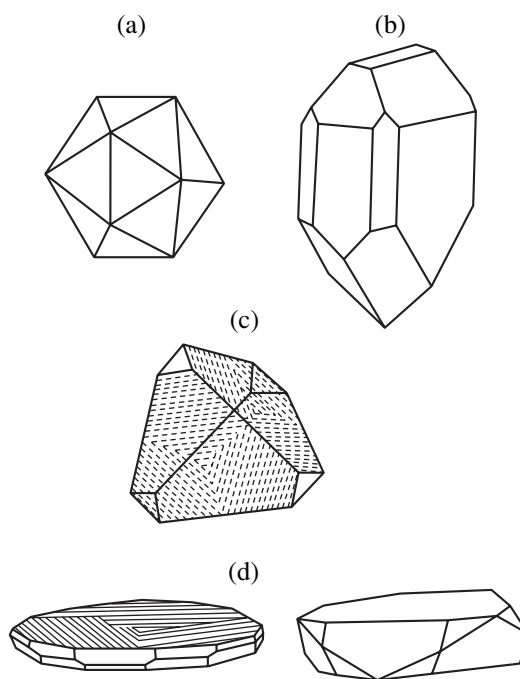
Fig. 8. Faceting of crystals of (a) cobaltite CoAsS, (b) calamine $Zn_2(OH)_2SiO_3$, (c) sphalerite ZnS, and (d) hematite Fe_2O_3.
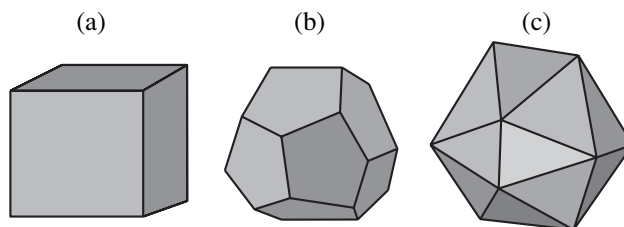
Fig. 9. Faceted crystals of pyrite FeS_2: (a) cube, (b) dodecahedron, and (c) mineralogical icosahedron.

Table 1. Stabilization energies E_{st} (in Dq units) of the $^{2s+1}$ state and the $\Gamma(t_2^{n_1}e^{n_2})$ states of a cubic crystal field

Shell	^{2s+1}L	$\Gamma(t_2^{n_1}e^{n_2})$	E_{st}
d^1	^2D	$^2T_2(t_2)$	$-2/5$
d^2	^3F	$^3T_1(t_2^2)$	$-4/5$
d^3	^4F	$^4A_2(t_2^3)$	$-6/5$
d^4	^5D	$^5E(t_2^3e)$	$-3/5$
d^5	^6S	$^6A_1(t_2^3e^2)$	0
d^6	^5D	$^5T_2(t_2^4e^2)$	$-2/5$
d^7	^4F	$^4T_1(t_2^5e^2)$	$-4/5$
d^8	^3F	$^3A_2(t_2^6e^2)$	$-6/5$
d^9	^2D	$^2E(t_2^6e^3)$	$-3/5$
d^{10}	^1S	$^1A_1(t_2^6e^4)$	0

Table 2. Coordination numbers of transition-metal ions with d^5, d^9, and d^{10} shells

Ion	Coordination number	Ion	Coordination number
	$3d^5$		$3d^{10}$
Mn^{2+}	4, 5, 6, 7, 8	Cu^+	2, 4, 6,
Fe^{3+}	4, 5, 6, 8	Zn^{2+}	4, 5, 6, 8,
Co^{4+}	4, 6	Gd^{3+}	4, 5, 6,
	$4d^5$		$4d^{10}$
Ru^{3+}	6	Ag^+	2, 4, 5, 6, 7, 8
Rh^{4+}	6	Cd^{2+}	4, 5, 6, 7, 8, 12
	$5d^5$	In^{3+}	4, 6, 8
Ir^{4+}	6	Sn^{4+}	4, 5, 6, 7, 8
Pt^{5+}	6	Sb^{5+}	6
	$3d^9$		$5d^{10}$
Cu^{2+}	4, 5, 6	Au^+	6
	$4d^9$	Hg^{2+}	2, 4, 6, 8
Pd^+	2	Tl^{3+}	4, 6, 8
Ag^{2+}	4, 6	Pb^{4+}	4, 5, 6, 8
		Bi^{5+}	6

Location in the positions that have common symmetry elements with antiprisms also differently manifests itself for the shells compared. For example, it was shown in [22] that, for two isomorphic positions with the plane of symmetry C_s and the inversion center C_i, the distributions of ions over these positions depend on the shell type: ions with d^5 and d^{10} shells are distributed predominantly over the C_s positions, while ions with d^2 (d^8) and d^3 (d^7) shells are distributed over the C_i positions. From the point of view of different density distributions over the vertices of a pentagonal antiprism for these shells of a free ion, this fact can be explained as follows. The ground states of the d^5 shells (in a weak field) and d^{10} shells correspond to the plane of symmetry with respect to the modulus $|l|$ (Fig. 4). The energy minimum in the ground states of the d^2 and d^3 shells can be reached only when electrons are located at the most remote vertices of the antiprism. Taking into account the maximum value of L in the ground state (Fig. 4, Table 1) and the equal probability of location of electrons at both bases of the antiprism, we can conclude that these positions have only the inversion center.

The melting temperatures of transition metals serve as an example of the effect of different possibilities of incorporation of d^2 and d^3 shells and d^5 and d^{10} shells into the crystal structure on the crystal properties. As was shown above, such a possibility is lower for the latter pair. Therefore, for example, d^{10} metals have

Table 3. Coordination numbers of transition-metal ions with d^2 and d^3 shells

Ion	Coordination number	Ion	Coordination number
	$3d^2$		$3d^3$
V^{3+}	6	V^{2+}, Cr^{3+}	6
Cr^{4+}	4, 6		
	$4d^2$		$4d^3$
Nb^{3+}, Mo^{4+}	6	$Nb^{2+}, Mo^{3+}, Tc^{4+}$	6
	$5d^2$		$5d^3$
W^{4+}, Re^{5+}	6	Re^{4+}, Os^{5+}	6

Table 4. Melting temperatures t_{melt} (in °C) of some metals

Ion	t_{melt}	Ion	t_{melt}
		$3d$	
$Cr^{3+}(d^3)$	1877	$Zn^{2+}(d^{10})$	419.5
$V^{3+}(d^2)$	1917	$Ga^{3+}(d^{10})$	29.78
		$4d$	
$Mo^{3+}(d^3)$	2620	$Cd^{2+}(d^{10})$	320.9
$Nb^{3+}(d^2)$	2469	$In^{3+}(d^{10})$	156.4
		$5d$	
$W^{3+}(d^3)$	3420	$Hg^{2+}(d^{10})$	−38.89
$Ta^{3+}(d^2)$	2996	$Tl^{3+}(d^{10})$	303.5

Note: The data for the most stable oxidation states of the ions.

lower melting temperatures (Table 4) [23]. A striking example is mercury, which exists in the liquid state even at room temperature.

QUASICRYSTALS

Quasicrystals illustrate the symmetry properties of the electron shells of transition-metal ions. In the overwhelming majority of cases, these structures contain transition-metal ions with *d* shells, for example, in the form of such alloys as Al–Mn, Ga–Mg–Zn, Al–Cu–Fe, and Al–Pd–Re. If quasicrystals are composed of possible local configurations of a small number of ions, the configuration with the lowest energy (the optimal one) may have noncrystallographic fivefold and tenfold axes of symmetry. When optimal configurations fill space densely, gaps between them are filled with matching configurations, which minimize energy loss at joints of optimal configurations. This makes it possible to get along without translational symmetry [24]. The possibility of implementing noncrystallographic axes is due to the fivefold symmetry of *d* shells.

CONCLUSIONS

Based on the tendency of *d* and *f* electron shells to give rise to the fivefold and sevenfold symmetries in ordered media, we explained a number of structural characteristics and features of some physical properties of ordered media. The nontrivial and noncrystallographic symmetry of *d* and *f* shells manifests itself to the greatest extent when these shells are either semifilled or completely filled.

The particular symmetry of the *d* and *f* shells is also topical in studying new materials, including (along with the noted structures) clusters, nanoparticles, nanocrystals in thin films and discrete alloys, and other nanosystems. The above-considered property of the *d* and *f* shells may be especially pronounced in nanocrystals. Due to small sizes, nanocrystals may have metrics of non-Euclidean spaces. These spaces contain regular systems with fivefold and sevenfold symmetry [25].

We reported our first results on the problem under consideration in 2001 [2]. Later publications confirmed the manifestation of the fivefold and sevenfold symmetries in *d* and *f* shells. The presence of clusters of Cu atoms with a pentagonal crystal structure in thin copper films and in bulk molten copper has been ascertained. Their volume content is about 10%. The same phenomenon was also predicted for other *d* ions [26].

The noncrystallographic symmetry of *d* and *f* shells of transition metals also provides deeper insight into their role in organic matter. Apparently, these ions impede crystallization—transition to the state characterized by a global potential minimum—in organic

materials. This suggestion is confirmed by the relative content of ions with d^2 and d^3 shells and d^5 and d^{10} shells in organic materials [27].

REFERENCES

1. T. F. Veremeĭchik and R. V. Galiulin, Kristallografiya **49** (5) (2004) [Crystallogr. Rep. **49**, 847 (2004)].

2. T. F. Veremeĭchik and R. V. Galiulin, *Crystallogenesis and Mineralogy* (S.-Peterb. Gos. Univ., St. Petersburg, 2001), p. 409 [in Russian].

3. T. F. Veremeĭchik and R. V. Galiulin, in *Proceedings of VI International Conference on Crystals: Growth, Properties, Structure, and Application* (Aleksandrov, 2003), p. 201.

4. T. F. Veremeĭchik and R. V. Galiulin, in *Proceedings of International Conference Dedicated to the 150th Birth Anniversary of E. S. Fedorov* (Gornyĭ Inst., St. Petersburg, 2003), p. 12.

5. R. V. Galiulin, Kristallografiya **48** (6), 965 (2003) [Crystallogr. Rep. **48**, 899 (2003)].

6. B. F. Ormont, *Introduction to Physical and Crystal Chemistry of Semiconductors* (Vysshaya Shkola, Moscow, 1968) [in Russian].

7. M. M. Protod'yakonov and I. L. Gerlovin, *Electronic Structure and Physical Properties of Crystals* (Nauka, Moscow, 1975) [in Russian].

8. A. G. Betekhtin, *Course on Mineralogy* (NTI lit. po Geologii i Okhrane Nedr, Moscow, 1956) [in Russian].

9. A. A. Kaminskiĭ, *Laser Crystals* (Nauka, Moscow, 1975) [in Russian].

10. D. T. Sviridov, R. K. Sviridova, and Yu. F. Smirnov, *Optical Spectra of Transition-Metal Ions in Crystals* (Nauka, Moscow, 1976) [in Russian].

11. L. Pauling, *The Nature of the Chemical Bond* (Itaca, New York, 1950).

12. L. A. Aslanov, *Structure of Atoms, Molecules, Crystals* (Mosk. Gos. Univ., Moscow, 1985) [in Russian].

13. L. A. Aslanov, *Structures of Materials* (Mosk. Gos. Univ., Moscow, 1989) [in Russian].

14. V. S. Urusov, *Theoretical Crystal Chemistry* (Mosk. Gos. Univ., Moscow, 1987) [in Russian].

15. A. Wells, *Structural Inorganic Chemistry*, 5th ed. (Clarendon Press, Oxford, 1984; Mir, Moscow, 1998), Vols. 1–3.

16. D. Kepert, *Inorganic Stereochemistry* (Springer, Berlin, 1982; Mir, Moscow, 1985).

17. N. V. Belov, *Structure of Ionic Crystals and Metal Phases* (Akad. Nauk SSSR, Moscow, 1947) [in Russian].

18. G. B. Bokiĭ, *Crystal Chemistry* (Nauka, Moscow, 1971) [in Russian].

19. K. Nakamoto, *Infrared and Raman Spectra of Inorganic and Coordination Compounds* (Wiley, New York, 1986; Mir, Moscow, 1991).

20. I. D. Brown, Acta Crystallogr., Sect. B: Struct. Sci. **44**, 545 (1988).

21. S. S. Batsanov, *Experimental Fundamentals of Structural Chemistry* (Izd. Standartov, Moscow, 1986) [in Russian].

22. T. F. Veremeĭchik and R. V. Galiulin, Neorg. Mater., No. 9, 1110 (2002).

23. *Physical Values: Handbook*, Ed. by I. S. Grigor'ev and E. Z. Meĭlikhov (Énergoatomizdat, Moscow, 1991) [in Russian].

24. V. F. Gantmakher, Usp. Fiz. Nauk **172** (11), 1283 (2002) [Phys. Usp. **45**, 1165 (2002)].

25. R. V. Galiulin, Zh. Vychisl. Mat. Mat. Fiz. **43** (6), 791 (2003).

26. A. Di Cicco, A. Tarapanant, S. Faggiony, and A. Filipony, Phys. Rev. Lett. **91**, 135505 (2003).

27. T. F. Veremeĭchik, I. A. Yamskov, and Z. S. Klemenkova, in *Abstracts of X National Conference on Crystal Growth (NKRK-2002)* (Inst. Kristallografii Ross. Akad. Nauk, Moscow, 2002), p. 581.

Translated by Yu. Sin'kov

STRUCTURE
OF INORGANIC COMPOUNDS

Synthesis and Structural Study of $Rb_2FeZr(PO_4)_3$ Phosphate with Langbeinite Structure

I. G. Trubach*, A. I. Beskrovnyĭ**, A. I. Orlova*, V. A. Orlova*,
and V. S. Kurazhkovskaya***

* *Nizhni Novgorod State University, pr. Gagarina 23, Nizhni Novgorod, 603950 Russia*
** *Joint Institute for Nuclear Research, Dubna, Moscow oblast, 141980 Russia*
*** *Moscow State University, Vorob'evy gory, Moscow, 119992 Russia*
Received July 8, 2003

Abstract—A new orthophosphate of rubidium, iron, and zirconium, crystallizing in the langbeinite structure (cubic system, sp. gr. $P2_13$, $Z = 4$), was synthesized and investigated by X-ray powder diffraction and IR spectroscopy. The structure of the $Rb_2FeZr(PO_4)_3$ phosphate was refined by the Rietveld method using the neutron powder diffraction data (DN-2 time-of-flight diffractometer; Joint Institute for Nuclear Research, Dubna). This structure is characterized by a mixed framework $[FeZr(PO_4)_3]$ with Rb atoms located in large cavities. Fe^{3+} and Zr^{4+} cations are distributed statistically over two independent crystallographic positions. © *2004 MAIK "Nauka/Interperiodica".*

INTRODUCTION

Many inorganic compounds with tetrahedral anions XO_4 are characterized by $[T_2(XO_4)_3]^{n-}$ frameworks, where elements with valences from 1 to 5 may serve as T cations (n is the framework charge). Such frameworks are characterized by several structure types.

One of the types of the $[T_2(XO_4)_3]^{n-}$ framework is implemented in the langbeinite structure of double potassium–magnesium sulfate (cubic system, sp. gr. $P2_13$) [1].

In the set of structural analogs of langbeinite, sulphates with the general formula $M_2^I M_2^{II}(SO_4)_3$, where M^I = K, Rb, Cs, Tl, or NH_4 and M^{II} = Mg, Ca, Mn, Co, Ni, Zn, Cd, or Fe, are dominant [1, 2]. These compounds contain small atoms of a divalent element M^{II} in the frameworks and large (mainly alkali) M^I cations in cavities.

The known phosphates with langbeinite structure have the following compositions: (i) $AM_2(PO_4)_3$ (A = H, K; M = Ti, Zr) [3–5]; (ii) $K_2RM(PO_4)_3$ (R = Cr, Fe, Ga, Y, Yb, Er, Gd, Ti; M = Ti, Zr, Hf) [6–11], (iii) $KBaR_2(PO_4)_3$ (R = Cr, Fe) [12, 13]; and (iv) $Na_2RTi(PO_4)_3$; (R = Cr, Fe) [14]. Potassium cations serve as compensators in many of these compounds. The question of incorporation of alkali cations (exceeding K cations in size) into extraframework positions in phosphates remains open. Investigation of such compounds, along with the scientific interest (determination of the possibility of incorporation of large cations into cavities in the langbeinite structure), is also important from the practical point of view. Rubidium and cesium cations are reliably retained in cavities of a langbeinite structure containing narrow channels, which is important in solving ecological problems of radioactive waste disposal.

The purpose of this study was to synthesize a new phosphate $Rb_2FeZr(PO_4)_3$ with langbeinite structure and refine its structure by the full-profile analysis based on the neutron powder diffraction data.

EXPERIMENTAL

The sample was synthesized by the sol–gel method. One-molar aqueous solutions of RbCl, $FeCl_3$, $ZrOCl_2$, and H_3PO_4 were used as starting reagents. In the initial stage of the synthesis, a calculated amount of orthophosphoric acid was slowly, with stirring, added to the solutions of metal salts taken in the stoichiometric ratio. The gel obtained was dried at 95°C and then heated successively at 400, 600, 800, 1000, and 1100°C with intermediate dispersion in each stage.

The samples were investigated by X-ray powder diffraction, IR spectroscopy, and neutron powder diffraction. X-ray diffraction analysis was performed on a DRON-2.0 diffractometer in CoK_α filtered radiation (Fe filter, $\lambda = 1.78892$ Å) in the range of reflection angles 2θ from 14° to 60°. IR spectra were recorded on a SPECORD 75IR spectrophotometer in the range of wave numbers 1400–400 cm^{-1} (samples were prepared in the form of thin films on a KBr substrate). The neutron diffraction pattern of a powder sample placed in a cylindrical container (d = 10 mm) was measured at room temperature on a DN-2 time-of-flight diffractometer installed in the IBR-2 pulsed fast neutron reactor (Joint Institute for Nuclear Research, Dubna) [15]. The structure of the compound synthesized was refined by
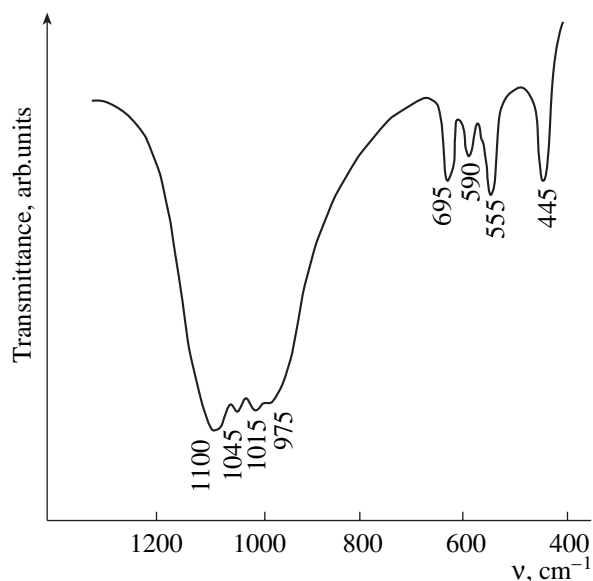
Fig. 1. IP spectrum of the $Rb_2FeZr(PO_4)_3$ phosphate.

Fig. 2. Experimental ($\circ$), theoretical (solid line), and difference (experiment minus calculation), normalized of the standard deviation at point, profiles of the neutron diffraction pattern of the $Rb_2FeZr(PO_4)_3$ phosphate. Vertical bars are the calculated positions of diffraction peaks.

the Rietveld method using the MRIA program [16]. The background was modeled by a fourth-order polynomial.

RESULTS AND DISCUSSION

The sample synthesized was a light brown powder. According to the X-ray powder diffraction data, the compound studied crystallizes at $t = 800°C$. A further increase in temperature leads to the increase in crystallinity and makes it possible to obtain a sample without impurities. X-ray powder diffraction analysis showed that the compound obtained crystallizes in a cubic system, sp. gr. $P2_13$ (langbeinite structure).

The IR spectrum of the compound synthesized indicates that it belongs to orthophosphates (Fig. 1). The

spectrum contains all absorption bands that can be predicted by the factor-group analysis for the P tetrahedron with the positional symmetry C_1 in a structure described by the sp. gr. $P2_13$ (the factor group T) [11]. Asymmetric stretching and bending vibrations, ν_3 and ν_4, of the P tetrahedron are responsible for the three bands in the frequency ranges 1085–990 and 645–555 cm^{-1}, respectively. The band at 930 cm^{-1} is due to the symmetric stretching vibration ν_1, and the weak band at 450 cm^{-1} is due to the symmetric bending vibration ν_2. In comparison with the isostructural potassium phosphate [11], an insignificant red shift of the absorp-

Table 1. Unit-cell parameters and refinement data for the structure of $Rb_2FeZr(PO_4)_3$

Space group	$P2_13$
a, Å	10.1199(2)
V, Å^3	1036.40
Z	4
Color	light brown
d interval, Å	0.726–3.792
Number of reflections	297
R_{exp}	2.77
R_{wp}	2.75
R_p	3.86
χ^2	3.33
Number of parameters in refinement	40

Table 2. Position occupancies (w), coordinates, and thermal parameters B_{iso} for the structure of $Rb_2FeZr(PO_4)_3$

Atom	Position	w	x	y	z	B_{iso}
Rb(1)	4a	1	0.2896(4)	0.2896(4)	0.2896(4)	3.2(2)
Rb(2)	4a	1	0.0657(4)	0.0657(4)	0.0657(4)	3.2(2)
(Fe/Zr)(1)	4a	0.5	0.8578(3)	0.8578(3)	0.8578(3)	1.2(1)
(Fe/Zr)(2)	4a	0.5	0.5841(3)	0.5841(3)	0.5841(3)	1.4(1)
P	12b	1	0.6257(4)	0.4577(3)	0.2702(6)	0.10(8)
O(1)	12b	1	0.6457(5)	0.5044(4)	0.4132(4)	1.0(1)
O(2)	12b	1	0.7503(5)	0.4759(4)	0.1915(5)	1.5(1)
O(3)	12b	1	0.5815(5)	0.3114(4)	0.2678(4)	1.6(1)
O(4)	12b	1	0.5202(4)	0.5439(5)	0.2017(5)	1.8(1)

tion bands is observed in the spectrum of the compound under study, which is related to the larger size of Rb atoms.

The coordinates of the basis atoms in the structure of the $Rb_2FeZr(PO_4)_3$ phosphate were refined by neutron powder diffraction analysis. We used the values of the coordinates of atoms in the $K_2FeZr(PO_4)_3$ phosphate obtained by us previously [11] as a starting model to refine the structural characteristics. The unit-cell parameters and the refinement data for the crystal structure of $Rb_2FeZr(PO_4)_3$ are listed in Table 1. The experimental and theoretical profiles of the neutron diffraction pattern of the sample and the difference curve (experiment minus calculation), normalized to the standard deviation at point, are shown in Fig. 2. The calculated positional and thermal parameters are listed in Table 2, and the corresponding values of interatomic distances and bond angles are listed in Table 3.

A fragment of the structure of the $Rb_2FeZr(PO_4)_3$ phosphate is shown in Fig. 3. It is based on the mixed anionic framework $\{[FeZr(PO_4)_3]^{2-}\}_{3\infty}$ constructed from discrete FeO_6, ZrO_6, and PO_4 polyhedra. A characteristic fragment of this framework is the group (dimer) $\{M_2(PO_4)_3\}$ formed of two octahedra linked by three bridge tetrahedra. Sharing oxygen atoms, these dimers form a three-dimensional network with large interframework cavities.

Calculations showed that Fe^{3+} and Zr^{4+} cations are statistically distributed over two nonequivalent structural positions $4a$, being located in distorted MO_6 octahedra. The disordered distribution of Fe and Zr ions is also confirmed by the close values of Me–O bond lengths in Me(1)–O_6 and Me(2)–O_6 octahedra. Rubidium cations completely occupy interframework cavities ($4a$ positions); each Rb cation is coordinated by nine O atoms.

Table 3. Selected interatomic distances (Å) and bond angles (deg) in the structure of $Rb_2FeZr(PO_4)_3$

Rb(1)O_9 polyhedron		Rb(2)O_9 polyhedron	
Rb(1)–O(2)	3.20(1)	Rb(2)–O(1)	2.99(1)
Rb(1)–O(3)	3.14(1)	Rb(2)–O(2)	3.23(1)
Rb(1)–O(4)	2.98(1)	Rb(2)–O(4)	2.96(1)
⟨Rb–O⟩	⟨3.11⟩	⟨Rb–O⟩	⟨3.06⟩
MO_6 octahedron			
(Fe/Zr)(1)–O(1)	2.013(6)	(Fe/Zr)(2)–O(3)	2.008(6)
(Fe/Zr)(1)–O(2)	2.034(6)	(Fe/Zr)(2)–O(4)	2.088(6)
⟨(Fe/Zr)–O⟩	⟨2.02⟩	⟨(Fe/Zr)–O⟩	⟨2.05⟩
PO_4 tetrahedron			
		O(1)–P–O(2)	110.6(8)
P–O(1)	1.536(6)	O(1)–P–O(3)	109.9(7)
P–O(2)	1.503(7)	O(1)–P–O(4)	110.3(6)
P–O(3)	1.547(5)	O(2)–P–O(3)	105.9(7)
P–O(4)	1.543(8)	O(2)–P–O(4)	110.6(6)
⟨P–O⟩	⟨1.53⟩	O(3)–P–O(4)	109.5(7)
		⟨O–P–O⟩	⟨109.5⟩

The average bond lengths in the coordination polyhedra of $Rb_2FeZr(PO_4)_3$ and its analog $K_2FeZr(PO_4)_3$ are rather close: 2.04 Å in Fe/Zr–O_6 octahedra and 1.53 Å in PO_4 tetrahedra (in $K_2FeZr(PO_4)_3$, 2.03 and 1.52 Å, respectively).

The distortions of the framework-forming polyhedra, estimated by the maximum spread Δ in bond lengths, are somewhat different in the compound studied and its analog. In the structures of $Rb_2FeZr(PO_4)_3$ and $K_2FeZr(PO_4)_3$, phosphorus tetrahedra are distorted similarly: $\Delta = 0.04$ Å. The values of the O–P–O bond
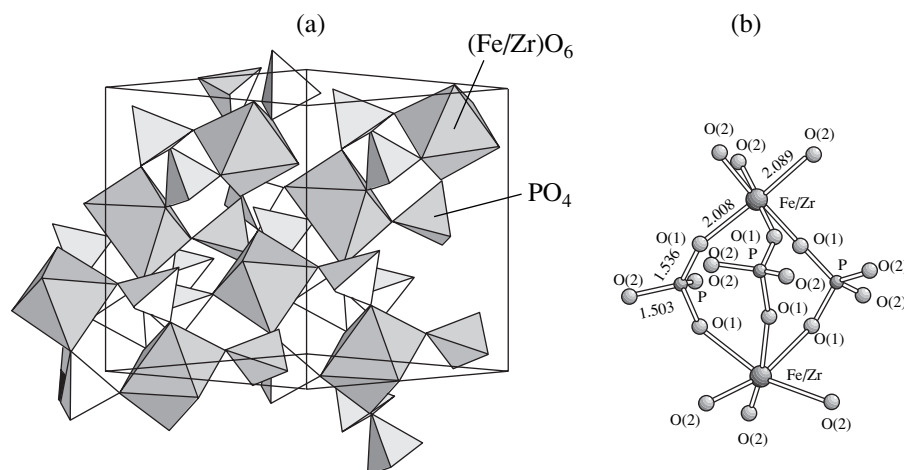
Fig. 3. (a) Fragment of the $Rb_2FeZr(PO_4)_3$ structure and (b) pattern of bonds in the structural fragment $\{M_2(PO_4)_3\}$.

angles are close to the calculated value: 109.5°. Somewhat larger distortions are observed in the metal–oxygen $(Fe/Zr)O_6$ octahedra ($\Delta = 0.08$ and 0.02 Å, respectively), which can be explained by higher strains of the framework caused by the incorporation of large Rb cations into interframework cavities.

The results of the structural investigation performed here show that an increase in the size of alkali cations in interframework cavities of phosphates with langbeinite structure is accompanied by an insignificant increase in the structural distortions.

In summary, it should be noted that the phosphate with langbeinite framework, in which Rb cations serve as compensating cations, was synthesized for the first time.

ACKNOWLEDGMENTS

REFERENCES

1. A. Zemann and J. Zemann, Acta Crystallogr. **10**, 409 (1957).

2. A. Guelylah, G. Madariaga, and T. Breczewski, Acta Crystallogr., Sect. C: Cryst. Struct. Commun. **52** (12), 2954 (1996).

3. R. Masse, A. Durif, J. C. Guitel, and I. Tordjman, Bull. Soc. Fr. Mineral. Cristallogr. **95**, 47 (1972).

4. A. Leclaire, A. Benmoussa, M. M. Borel, *et al.*, J. Solid State Chem. **78**, 227 (1989).

5. O. Akira and Y. Yoshiyuki, Bull. Chem. Soc. Jpn. **59**, 2761 (1986).

6. H. Wulff, U. Guth, and B. Loescher, Powder Diffr. **7** (2), 103 (1992).

7. R. Perret, J. Less-Common Met. **144**, 195 (1988).

8. E. R. Losilla, S. Bruque, M. A. G. Aranda, *et al.*, Solid State Ionics **112**, 53 (1998).

9. S. T. Norberg, Acta Crystallogr., Sect. B: Struct. Sci. **58**, 743 (2002).

10. E. S. Lunezheva, B. A. Maksimov, O. K. Mel'nikov, and L. A. Murad'yan, Kristallografiya **34**, 611 (1989) [Sov. Phys. Crystallogr. **34**, 363 (1989)].

11. A. I. Orlova, I. G. Trubach, V. S. Kurazhkovskaya, *et al.*, J. Solid State Chem. **173**, 314 (2003).

12. P. D. Battle, A. K. Cheetham, W. T. A. Harrison, and G. J. Long, J. Solid State Chem. **62**, 16 (1986).

13. P. D. Battle, T. C. Gibb, S. Nixon, and W. T. A. Harrison, J. Solid State Chem. **75**, 21 (1988).

14. J. Isasi and A. Daidouh, Solid State Ionics **133**, 303 (2000).

15. http://nf8.jinr.ru/userguide-97//dn-2.htm.

16. V. B. Zlokazov and V. V. Chernyshev, J. Appl. Crystallogr. **25**, 447 (1992).

Translated by Yu. Sin'kov

<div align="center">

STRUCTURE
OF INORGANIC COMPOUNDS

</div>

Study of the Effects of Isotopic Substitution ^{16}O $\longrightarrow$ ^{18}O in Sm$_{1-x}$Sr$_x$MnO$_3$-type ($x = 0.45$ and 0.50) Manganites by Powder Neutron Diffraction

A. I. Kurbakov*, V. A. Trunov*, and G. André**

* St. Petersburg Institute of Nuclear Physics, Russian Academy of Sciences, Gatchina,
Leningradskaya oblast, 188300 Russia
e-mail: kurbakov@pnpi.sspb.ru
** Laboratoire Léon Brillouin, CE Saclay, Gif-sur-Yvette, 91191 France
Received January 4, 2004

Abstract—The results of neutron diffraction studies of the effect of the isotopic substitution ^{16}O $\longrightarrow$ ^{18}O in Sm$_{1-x}$Sr$_x$MnO$_3$-type ($x = 0.45$ and 0.50) manganites are considered. The parameters of the crystal and magnetic structures of the samples are determined in the temperature range 1.4–300.0 K. It is shown that the isotopic substitution considerably changes the phase diagram of manganites. The results of the earlier macroscopic studies of the same samples are confirmed. © 2004 MAIK "Nauka/Interperiodica".

INTRODUCTION

Recent theoretical and experimental studies showed [1] that the tendency to phase layering and formation of inhomogeneous states resulting in coexistence of antiferromagnetic and ferromagnetic regions is an important factor for the description of the properties of manganites over the wide temperature range and understanding of fine thermodynamic properties of the system, which is associated with complex interactions between the atomic and spin degrees of freedom [2]. To reveal and identify possible mechanisms of such interactions, the samples were subjected to the action of various external factors such as temperature, magnetic fields, and pressure. One of such factors is also the isotopic substitution ^{16}O $\longrightarrow$ ^{18}O. It was shown [3, 4] that the isotopic effect manifests itself most pronouncedly in the vicinity of magnetic transformations, which indicates that isotopic substitution may serve as a sensitive probe for studying the most interesting regions of the phase diagram of various manganites in the vicinity of the critical temperatures. It was revealed that in the $(\text{La}_{1-y}\text{Pr}_y)_{0.7}\text{Ca}_{0.3}\text{MnO}_3$ manganite with the critical y value $y = 0.75$ the isotopic substitution ^{16}O $\longrightarrow$ ^{18}O gives rise to the metal–insulating transition (giant isotopic effect). The changes of the electrical properties correlate with the changes of magnetic characteristics obtained in neutron diffraction measurements [5].

We have studied Sm$_{1-x}$Sr$_x$MnO$_3$-type manganites for quite a long time. In particular, we considered the concentration region $0.25 \le x \le 0.55$ by the method of powder neutron diffraction. In this region, the Sm, Sr manganites manifest the effect of colossal magnetoresistance [6–11]. However, at the composition $x = 0.55$, this effect disappears. The most interesting results were

obtained in the concentration region of the phase diagram $0.4 \le x \le 0.5$. At $x = 0.4$ and temperatures lower than T_C (Curie temperature), the material manifests the metallic phase-separated magnetic ground state with one main ferromagnetic phase and two antiferromagnetic phases of the A and CE types [8]). These magnetic phases have close parameters of the atomic structure (indistinguishable for diffraction methods) which correspond to the orthorhombic phase with the sp. gr. *Pnma* (or, in another setting, *Pbnm*). The manganite of the composition Sm$_{0.6}$Sr$_{0.4}$MnO$_3$ shows unusual magnetic behavior above T_C associated with the formation of antiferromagnetic domains in the paramagnetic matrix. This behavior is associated mainly with pronounced coherent Jahn–Teller (JT) distortions arising below $T_{JT} \sim 180$ K and preserved also in the ferromagnetic phase.

In the ground state and temperatures below T_C, the compounds with $x = 0.5$ show the coexistence of several crystalline and magnetic phases, with the antiferromagnetic A phase prevalent over the ferromagnetic one.

However, it was revealed that at $x = 0.45$, the ground state is homogeneous, ferromagnetic, and metallic [9]. At the same time, the paramagnetic phase of the Sm$_{0.55}$Sr$_{0.45}$MnO$_3$ compound turned out to be inhomogeneous and had local inclusions of antiferromagnetic regions of the CE type, which showed weak Dzyaloshinski–Moriya ferromagnetism and ferromagnetic domains [10].

We studied various methods of synthesis of ceramic manganites and, as a result, managed to synthesize identical samples by different methods in order to exclude possible "synthetic" effects.
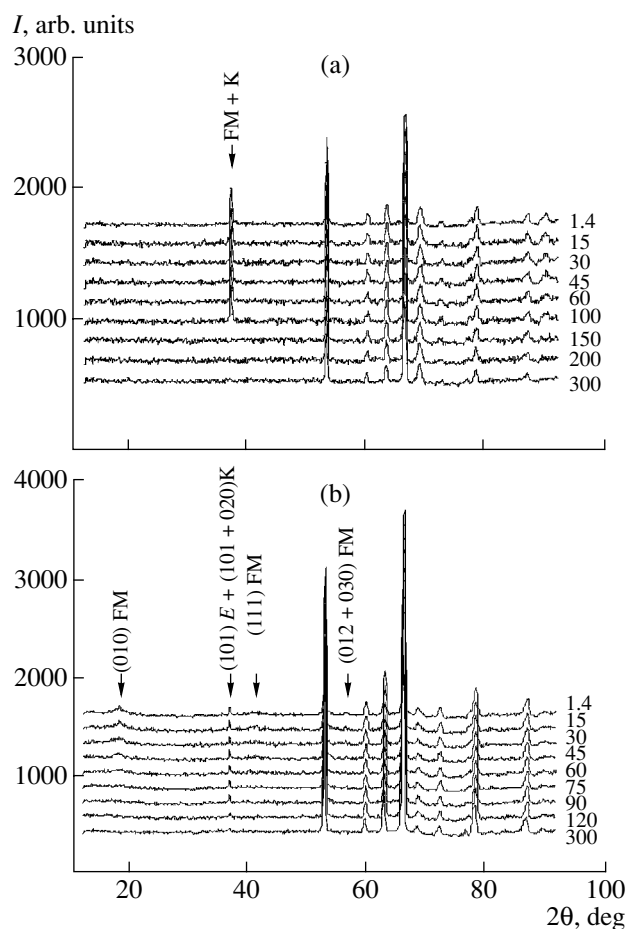
Fig. 1. Experimental powder neutron diffraction patterns of (a) $^{152}Sm_{0.55}Sr_{0.45}Mn^{16}O$ and (b) $^{152}Sm_{0.55}Sr_{0.45}Mn^{18}O$ obtained in the heating mode at different temperatures (K). Arrows indicate the angular positions of the strongest magnetic reflections.

It was interesting to study the effects of the $^{16}O \longrightarrow$ ^{18}O substitution on Sm–Sr manganites in this most interesting and complicated region of the phase diagram. Below, we present the results of neutron diffraction studies and the parameters of the crystal and magnetic structures of all the samples with $x = 0.45$ and 0.50 in the temperature range 1.4–300.0 K. The data obtained by neutron diffraction are compared with the known data of macroscopic studies performed on the same samples [12].

EXPERIMENTAL

Samples and methods of measurements. Two samples of the compositions $Sm_{0.55}Sr_{0.45}MnO_3$ and $Sm_{0.5}Sr_{0.5}MnO_3$ were synthesized by the already tested technology [13] at the Chemistry Department of the Moscow State University. The samples for neutron diffraction studies were synthesized with the use of the ^{152}Sm isotope in order to decrease too-high neutron absorption by the ^{149}Sm isotope contained in natural

Sm. The ^{152}Sm isotope for synthesis of samples was supplied by the St. Petersburg Institute of Nuclear Physics of the Russian Academy of Sciences. The process of sample enrichment with the oxygen isotope ^{18}O was similar to that described in [14] and was performed at the Institute of Molecular Physics of the Russian Research Center *Kurchatov Institute*. Altogether, we studied four samples of the compositions $^{152}Sm_{0.55}Sr_{0.45}Mn^{16}O_3$ (**I**), $^{152}Sm_{0.55}Sr_{0.45}Mn^{18}O_3$ (**II**), $^{152}Sm_{0.5}Sr_{0.5}Mn^{16}O_3$ (**III**), and $^{152}Sm_{0.5}Sr_{0.5}Mn^{18}O_3$ (**IV**).

Neutron diffraction experiments were performed in the Léon Brillouin Laboratory (Saclay, France) on a G4.1 high-intensity powder diffractometer ($\lambda = 2.4266$ Å) with the aim to follow the temperature evolution of the crystal and its magnetic structure. As was indicated above, the use of the ^{152}Sm isotope allowed us to considerably decrease neutron absorption by natural Sm and enhance the contrast of the diffraction experiment because of the negative coherent-scattering amplitude of ^{152}Sm ($b = -0.5 \times 10^{-12}$ cm). Prior to measurements, the powder samples were placed into a vanadium cylindrical container with a diameter of 2 mm. The container with the samples was placed into a standard cryostat for neutron diffraction measurements. The samples were cooled to the temperature 1.4 K. Neutron diffraction patterns were measured during heating at $T = 1.4, 15.0,$ $30.0, 45.0, 60.0, 100.0, 150.0, 200.0,$ and 300.0 K for sample **I**; $T = 1.4, 15.0, 30.0, 45.0, 60.0, 75.0, 90.0,$ $120.0,$ and 300.0 for sample **II**; $T = 1.4, 45.0, 70.0,$ $80.0, 90.0, 105.0,$ and 120.0 K for sample **III**; and at $T = 1.4, 45.0, 70.0, 80.0, 90.0, 105.0, 150.0,$ and 185.0 K for sample **IV**. These heating modes were selected proceeding from the specific features of the temperature dependence of magnetic susceptibility $\chi_{ac}(T)$ preliminarily measured for these samples.

Crystal structure. Figures 1 and 2 show neutron diffraction patterns obtained from these samples. The neutron diffraction patterns were subjected to Rietveld analysis [15] using the FULLPROF program [16]. It was revealed that the diffraction profiles of all the patterns at high temperatures (where no magnetic ordering is observed) corresponded to the sp. gr. *Pnma*. No structural phase transitions were revealed below T_C down to the temperature 1.4 K.

Tables 1–4 list the main parameters of the crystal structures determined from neutron diffraction patterns. It should be noted that some discrepancies in the error bars of the parameters and different numbers of the samples should be replaced by different amounts of the samples used and different times of collection of the diffraction reflections. We believe that the most interesting and important results are presented in Figs. 3 and 4. Figure 3 shows the temperature dependences of the lattice parameters, and Fig. 4 shows the temperature dependences of interatomic distances in a MnO_6 octahedron.
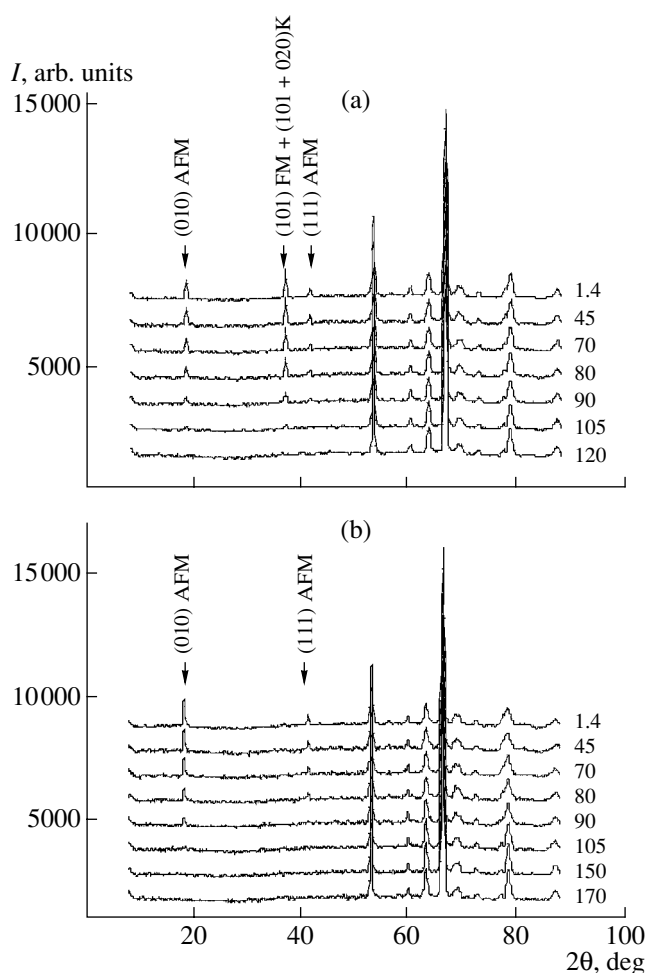
Fig. 2. Experimental powder neutron diffraction patterns of (a) $^{152}Sm_{0.5}Sr_{0.5}Mn^{16}O_3$ and (b) $^{152}Sm_{0.5}Sr_{0.5}Mn^{18}O_3$ obtained in the heating mode at different temperatures (K). Arrows indicate the angular positions of the strongest magnetic reflections.

Fig. 3. Temperature dependences of the lattice parameters. Black symbols connected by solid lines correspond to the samples with ^{16}O, light symbols not connected by lines correspond to the samples with ^{18}O.

The lattice parameters obtained indicate that in the temperature range from 1.4 K to room temperature the lattice parameters of all the samples obey the inequality $c > a > b/\sqrt{2}$. Compound **I** shows the characteristic increase in the parameters a and c with the corresponding jump in the unit-cell volume in the vicinity of the temperature of ferromagnetic ordering, $T_C \sim 120$ K. We have already observed this phenomenon in the samples with the natural oxygen having the similar composition. This phenomenon is associated with the giant spontaneous magnetostriction observed for Sm,Sr manganites in the vicinity of the concentration $x = 0.45$ [13, 17]. As has already been indicated, the space group in this case remains the same, *Pnma*. For sample **II** having the same composition, the temperature dependences of the unit cell parameters after the isotopic oxygen substitution become quite different. With an increase in the temperature in the region showing no magnetic ordering, the a and c parameters have close

values; i.e., the orthorhombicity in the equatorial plane becomes weak, and the unit cell of the compound is close to cubic. A similar phenomenon was also observed for both samples with concentration $x = 0.5$.

The analysis of the Mn–O distances (Fig. 4) indicates the existence of noticeable Jahn–Teller distortions of MnO_6 octahedra in samples **II** and **III** and their almost complete absence in two other samples. The Jahn–Teller samples show different values of the equatorial Mn–O(2) bond lengths and also dramatic temperature variations, whereas the apical Mn–O(1) bond demonstrates considerably less changes in the Jahn–Teller transition, which, generally speaking, is characteristic of undoped $LaMnO_3$. These distortions are reduced in the region of the transition to the magnetically ordered state, but do not attain their high-temperature values.

Thus, these compounds may have unusually pronounced coherent distortion of octahedra even in the

KURBAKOV *et al.*

Table 1. Lattice parameters and interatomic distances (Å) in a MnO_6 octahedron according to neutron diffraction data for $^{152}Sm_{0.55}Sr_{0.45}Mn^{16}O_3$

T, K	a	$b/\sqrt{2}$	c	Mn–O(1)	Mn–O(2)
1.4	5.4337(8)	5.4277(10)	5.4415(9)	1.947(2)	1.933(7)
					1.945(9)
15	5.4340(9)	5.4280(10)	5.4411(8)	1.948(2)	1.932(7)
					1.944(7)
30	5.4342(9)	5.4285(9)	5.4415(9)	1.948(2)	1.935(7)
					1.943(9)
45	5.4340(9)	5.4290(10)	5.4425(8)	1.948(2)	1.932(6)
					1.942(9)
60	5.4345(10)	5.4277(11)	5.4427(9)	1.948(2)	1.933(7)
					1.944(9)
100	5.4369(8)	5.4270(8)	5.4447(8)	1.947(3)	1.937(6)
					1.945(8)
150	5.4385(9)	5.4300(9)	5.4447(8)	1.953(2)	1.931(7)
					1.955(6)
200	5.4387(9)	5.4303(8)	5.4462(10)	1.942(2)	1.932(6)
					1.953(6)
250	5.4396(10)	5.4326(9)	5.4485(9)	1.942(2)	1.934(6)
					1.952(6)
300	5.4429(9)	5.4360(9)	5.4506(9)	1.946(2)	1.940(6)
					1.950(6)

Table 2. Lattice parameters and interatomic distances (Å) in a MnO_6 octahedron according to neutron diffraction data for $^{152}Sm_{0.55}Sr_{0.45}Mn^{18}O_3$

T, K	a	$b/\sqrt{2}$	c	Mn–O(1)	Mn–O(2)
1.4	5.4351(6)	5.4238(9)	5.4426(7)	1.952(3)	1.83(3)
					2.06(2)
15	5.4356(8)	5.4235(10)	5.4427(9)	1.953(4)	1.84(3)
					2.05(3)
30	5.4347(7)	5.4225(10)	5.4424(8)	1.950(4)	1.85(3)
					2.04(3)
45	5.4357(7)	5.4243(10)	5.4418(9)	1.953(4)	1.87(3)
					2.03(3)
60	5.4361(11)	5.4251(12)	5.4431(10)	1.947(6)	1.87(4)
					2.03(4)
75	5.4366(6)	5.4249(8)	5.441(8)	1.954(3)	1.80(4)
					2.09(3)
90	5.4365(7)	5.4270(10)	5.4405(9)	1.954(4)	1.74(5)
					2.13(5)
120	5.4368(10)	5.4262(13)	5.4419(13)	1.956(5)	1.75(5)
					2.12(5)
300	5.4435(9)	5.4320(13)	5.4487(13)	1.961(4)	1.77(5)
					2.11(4)

Table 3. Lattice parameters and interatomic distances (Å) in a MnO_6 octahedron according to neutron diffraction data for $^{152}Sm_{0.5}Sr_{0.5}Mn^{16}O$

T, K	a	$b/\sqrt{2}$	c	Mn–O(1)	Mn–O(2)
1.4	5.4307(9)	5.4029(12)	5.4467(9)	1.941(2)	1.83(4)
					2.05(3)
45	5.4303(10)	5.4056(15)	5.4468(10)	1.937(2)	1.81(5)
					2.07(4)
70	5.4295(10)	5.4098(15)	5.4477(9)	1.934(2)	1.82(5)
					2.07(5)
80	5.4322(9)	5.4101(14)	5.4477(9)	1.934(2)	1.84(4)
					2.05(4)
90	5.4306(10)	5.4060(16)	5.4469(10)	1.933(2)	1.79(3)
					2.09(4)
105	5.4312(10)	5.4094(10)	5.4455(9)	1.935(2)	1.77(3)
					2.11(3)
120	5.4289(11)	5.4065(15)	5.4408(10)	1.930(2)	1.78(3)
					2.10(3)

Table 4. Lattice parameters and interatomic distances (Å) in a MnO_6 octahedron according to neutron diffraction data for $^{152}Sm_{0.5}Sr_{0.5}Mn^{18}O_3$

T, K	a	$b/\sqrt{2}$	c	Mn–O(1)	Mn–O(2)
1.4	5.4379(12)	5.3972(17)	5.4518(11)	1.930(3)	1.92(4)
					1.97(3)
45	5.4390(15)	5.3977(22)	5.4509(15)	1.931(5)	1.91(5)
					1.98(5)
70	5.4390(15)	5.4034(21)	5.4514(14)	1.935(5)	1.90(4)
					1.99(3)
80	5.4328(14)	5.3987(21)	5.4471(13)	1.933(5)	1.90(4)
					2.02(3)
90	5.4348(14)	5.4060(21)	5.4500(13)	1.943(5)	1.87(3)
					1.98(4)
105	5.4314(18)	5.4087(25)	5.4431(16)	1.936(6)	1.91(4)
					1.98(4)
150	5.4400(11)	5.4116(22)	5.4243(14)	1.934(3)	1.92(4)
					1.98(4)
170	5.4452(11)	5.4147(21)	5.4288(13)	1.935(4)	1.94(4)
					1.95(4)

metallic magnetically ordered state. Earlier, we observed this phenomenon, which is rather surprising for doped manganites, in $Sm_{0.6}Sr_{0.4}MnO_3$ [8, 18]. We explained this behavior by the adiabatic (above T_C) and nonadiabatic (below T_C) motion of charges. This scenario is quite admissible since electron mobility in the insulating state is lower than the frequencies of active JT phonons. If $Mn^{3+}O_6/Mn^{4+}O_6$ octahedra are either pronouncedly distorted or are undistorted in the insulating state, then they completely relax during electron hopping from the position Mn^{3+} into the position Mn^{4+}. In the metal phase, the charges are more mobile and the octahedra cannot relax completely. The local distortions of $Mn^{3+}O_6$ octahedra may be reduced in the metal state, whereas the distortion of $Mn^{4+}O_6$ octahedra becomes more pronounced, so that, on the average, the lattice has the resulting distortion.

Analyzing the results associated with the isotopic $^{16}O \longrightarrow {}^{18}O$ substitution, one has to pay attention to the
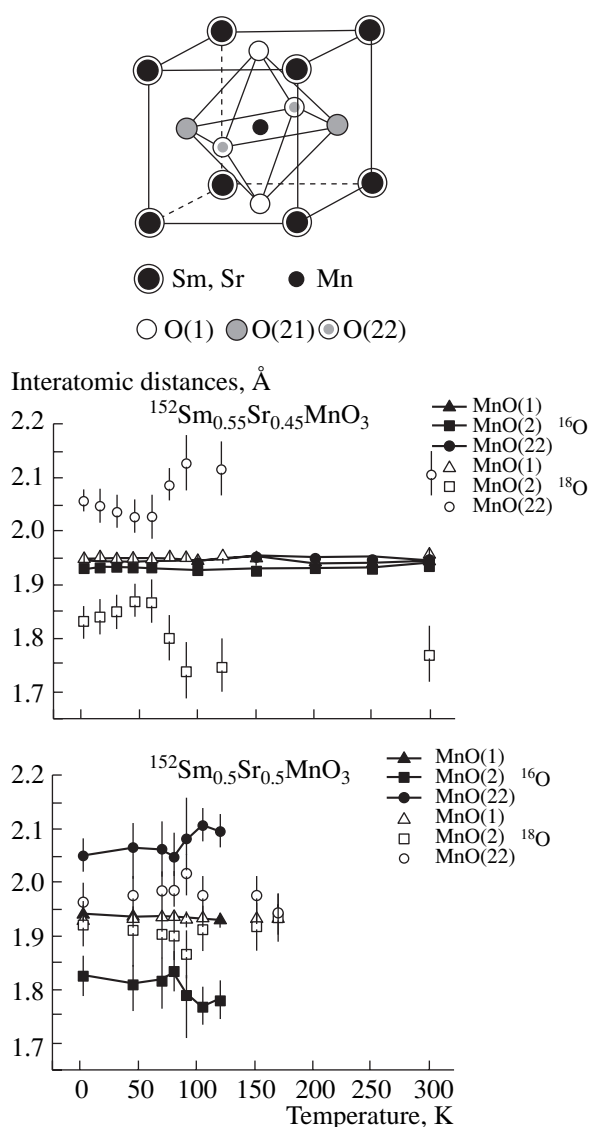
Fig. 4. Temperature dependences of Mn–O distances. Black symbols connected by lines correspond to the samples with ^{16}O; light symbols not connected by lines correspond to the samples with [18]O. The unit cell is also shown.

changes in the Jahn–Teller effect, because these changes are different at $x = 0.45$ and $x = 0.50$ and depend on the type of the oxygen isotope. This seems to be indicative of the fact that the changes in the structural parameters (atomic and magnetic) and physical characteristics are due to the interference of two effects: the change in the isotopic composition and the change in the doping level. Such a strong influence of the doping level on the isotopic effect seems to be determined by the close values of the parameter x to a certain "magic" critical value [10]. In the vicinity of this value, doping with strontium may dramatically change the isotopic effect.

Magnetic structure. Rietveld analysis of the magnetic contribution to the neutron diffraction patterns at low temperatures was also performed using the FULL-PROF program. We considered only the one-phase homogeneous model for the Mn sublattice within the sp. gr. *Pnma*.

In sample **I**, we observed only the transition to the homogeneous ferromagnetically ordered state at $T_C \sim$ 125 K, which is consistent with data [9–11] obtained on samples with natural oxygen. The direct confirmation of the formation of the inhomogeneous state and both ferromagnetic and antiferromagnetic ordering in the samples of the same composition but with [18]O was obtained from neutron diffraction patterns from sample II measured at low temperatures (Fig. 1b).

The regions of antiferromagnetic ordering (of the *A* type) arise in the sample with [18]O above T_C (since the antiferromagnetic peaks are noticeably broadened, it is difficult to determine the temperature of the beginning of antiferromagnetic ordering). However, the antiferromagnetic regions do not extend over the whole sample and are of the mesoscopic character (hundreds of angstroms). On the neutron diffraction patterns, this corresponds to the appearance of broad maxima in the region where antiferromagnetic peaks corresponding to the *A*-type ordering would have been located. In the *A*-type magnetic, Mn ions are ferromagnetically ordered in one plane, whereas in the neighboring planes they are ordered antiferromagnetically with respect to one another. With lowering of the temperature, the volume of these regions increases. At $T_C \sim 100$ K, ferromagnetic regions start arising. At lower temperatures, the long-range antiferromagnetic state is formed. These long-range antiferromagnetic regions are formed from small mesoscopic antiferromagnetic regions, so that, in the final analysis, both types of antiferromagnetic ordering coexist at the lowest temperatures. The neutron diffraction patterns show narrow Bragg peaks on strongly diffuse bases with the widths corresponding to the diffractometer resolution at the positions corresponding to the *A*-type magnetic ordering. This is especially well seen for the first most intense antiferromagnetic reflection 010. The fact that the long-range antiferromagnetic regions are formed from the short-range regions is confirmed by the total antiferromagnetic moment ($m_{AF} = 1.70(7)$ μ_B/Mn), which remains constant in the temperature range 1.4–75.0 K. Thus, contrary to the sample with [16]O and $x = 0.45$, the sample with [18]O cannot attain the homogeneous ferromagnetic state and, thus, cannot prevail in the sample. The ferromagnetic moment ($m_F = 0.80(9)$ μ_B/Mn) at the lowest attained temperature 1.4 K and the magnetic susceptibility at low temperatures also have lower values than in the sample with [16]O.

Neutron diffraction studies of the samples **III** and **IV** (Fig. 2) also provided the unambiguous determination of the types of magnetic ordering and their temperature evolution for each composition. Thus, the neutron diffraction patterns show that the ground magnetic state for sample **III** is the mixture of the ferromagnetic and *A*-

type antiferromagnetic phases with prevalent ferromagnetism. The ferromagnetic moment obtained in the Rietveld analysis of the neutron diffraction pattern at the lowest temperature (1.4 K) is $m_F = 2.13(7)$ μ_B/Mn, whereas the antiferromagnetic moment is $m_{AF} = 1.04(4)$ μ_B/Mn. At the same time, the ground state for the sample $^{152}Sm_{0.5}Sr_{0.5}Mn^{18}O_3$ is A-type antiferromagnetic with the antiferromagnetic moment at $T = 1.4$ K equal to $m_{AF} = 1.84(5)$ μ_B/Mn.

Thus, the above consideration allows us to state that, in terms of homogeneity of the ground magnetic state, the isotopic substitution $O^{16} \longrightarrow O^{18}$ resulted in different effects for different (although close) compositions. Thus, the $O^{16} \longrightarrow O^{18}$ substitution in the samples with $x = 0.45$ results in the transformation of the homogeneous magnetic state into the inhomogeneous one, whereas in samples with $x = 0.5$, the inhomogeneous state is transformed into the homogeneous one. These states also have completely different physical nature.

As an example of Rietveld analysis of neutron diffraction patterns, Fig. 5 shows the results obtained on sample **III** at $T = 1.4$ K. The samples studied also have different temperatures of magnetic ordering. Figure 6 shows the temperature dependences of the ordered magnetic moments for the sample with $x = 0.5$. In sample **III**, the formation of the ordered ferromagnetic and antiferromagnetic phases takes place almost simultaneously at $T \sim 112$ K, whereas in sample **IV**, the formation of the ordered ferromagnetic phase starts only at 108 K. However, this temperature difference is unimportant in comparison with the 20 K difference observed for samples with the composition $x = 0.45$.

We should like to emphasize the low values of magnetic moments obtained. These moments and the character of the their temperature dependences (no plateaux at low temperatures) indicates that, even at the temperature $T = 1.4$ K, no complete magnetic ordering is attained.

All the consequences of the isotopic oxygen substitution in manganites of the $Sm_{1-x}Sr_xMnO_3$ system are in good qualitative agreement with the macroscopic studies of the same samples with the natural Sm performed in the heating mode [12].

Thus, for samples with $x = 0.45$, the change in electrical conductivity (ρ) showed that in the $^{16}O \longrightarrow {}^{18}O$ substitution the temperature corresponding to the maximum resistivity (T_{MI}) in the metal–insulating transition is shifted by 20 K to the region of low temperatures, with the resistivity at the maximum being increased by a factor of about 30 in comparison with the resistivity in the sample with ^{16}O. The measurements of magnetic susceptibility (χ) also showed that the sample with ^{16}O has a sharper transition to the ferromagnetic state, which takes place at the temperature higher by 20 K. The T_{MI} and T_C values turned out to be practically equal: 120 and 100 K for the samples with ^{16}O and ^{18}O, respectively. In other words, these temperatures coin-
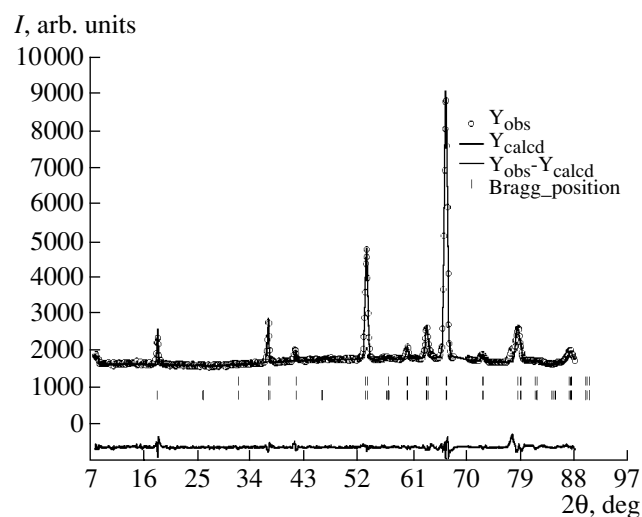
Fig. 5. Neutron diffraction pattern of the $^{152}Sm_{0.5}Sr_{0.5}Mn^{16}O_3$ sample at $T = 1.4$ K. One can see the experimental points and the calculated and difference curves. The positions of the Bragg reflections are indicated by vertical bars. The first row corresponds to the nuclear and ferromagnetic structures; the second row corresponds to the antiferromagnetic structure.
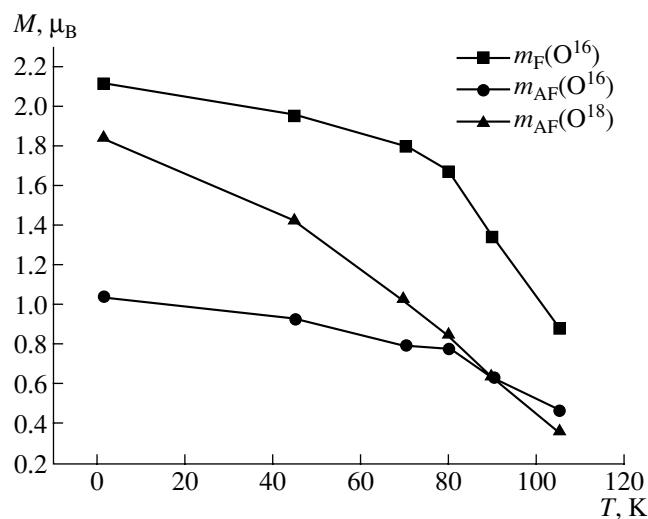
Fig. 6. Temperature dependences of ordered magnetic moments of the $^{152}Sm_{0.5}Sr_{0.5}Mn^{16}O_3$ and $^{152}Sm_{0.5}Sr_{0.5}Mn^{18}O_3$ compounds.

cide with the temperatures of the beginning of magnetic ordering established from our neutron diffraction data. The direct proof of the formation of an inhomogeneous magnetic state in the sample with ^{18}O and its existence along with ferromagnetic and antiferromagnetic ordering obtained from the neutron diffraction data also explains the dramatic increase in resistivity and the temperature behavior of magnetic susceptibility with a decrease of resistivity.

Resistivity and magnetic-susceptibility measurements on the samples with $x = 0.5$ [12] are interpreted

in a similar way [12]. The formation of a homogeneous antiferromagnetic state revealed from our neutron diffraction data for the sample with ^{18}O results in the transition from the metal to the insulating state with a dramatic decrease in χ observed earlier in [12].

Comparing the data obtained at $x = 0.45$ and 0.50, we have to emphasize that the effects observed seem to result from the complex interference of two factors: the doping level, i.e., the change in the Mn^{+4}/Mn^{+3} ion ratio in the vicinity of the critical doping level, and the renormalization of the phonon degree of freedom in the oxygen subsystem because of the changes in the isotopic composition. The nature of these phenomena is associated with the complex electron–phonon interactions including the spin degrees of freedom. It has not been completely understood as yet and requires a further more detailed study. It is also necessary to investigate the differences in the thermodynamics caused by the incorporation of ^{16}O and ^{18}O oxygen into the samples [2].

ACKNOWLEDGMENTS

REFERENCES

1. E. Dagotto, Springer Ser. Solid-State Sci. **136**, 456 (2003).
2. E. L. Nagaev, Phys. Rev. B **64**, 144409 (2001).
3. G.-M. Zhao, H. Keller, J. Hoffer, *et al.*, Solid State Commun. **104** (2), 57 (1997).
4. N. A. Babushkina, L. M. Belova, O. Yu. Gorbenko, *et al.*, Nature **391**, 159 (1998).
5. A. M. Balagurov, V. Yu. Pomjakushin, D. V. Sheptyakov, *et al.*, Phys. Rev. B **60** (1), 383 (1999).
6. S. M. Dunaevskiĭ, A. I. Kurbakov, V. A. Trunov, *et al.*, Fiz. Tverd. Tela (St. Petersburg) **40**, 1271 (1998) [Phys. Solid State **40**, 1158 (1998)].
7. V. V. Runov, D. Yu. Chernyshov, A. I. Kurbakov, *et al.*, Zh. Éksp. Teor. Fiz. **118**, 1174 (2000) [JETP **91**, 1017 (2000)].
8. I. D. Luzyanin, V. A. Ryzhov, D. Yu. Chernyshov, *et al.*, Phys. Rev. B **64**, 094432 (2001).
9. J. M. De Teresa, M. R. Ibarra, P. Algarabel, *et al.*, Phys. Rev. B **65**, 100403(R) (2002).
10. A. V. Lazuta, V. A. Ryzhov, A. I. Kurbakov, *et al.*, J. Magn. Magn. Mater. **258–259**, 315 (2003).
11. A. M. Aliev, Sh. B. Abdulvagidov, A. B. Batdalov, *et al.*, Fiz. Tverd. Tela (St. Petersburg) **45**, 124 (2003) [Phys. Solid State **45**, 130 (2003)].
12. N. A. Babushkina, E. A. Chistotina, O. Yu. Gorbenko, *et al.*, Phys. Rev. B **67**, 100410 (2003).
13. A. Abramovich, L. Koroleva, A. Michurin, *et al.*, Physica B (Amsterdam) **293**, 38 (2000).
14. N. A. Babushkina, L. M. Belova, V. I. Ozhogin, *et al.*, J. Appl. Phys. **83** (11), 7369 (1998).
15. H. M. Rietveld, J. Appl. Crystallogr. **2**, 65 (1969).
16. J. Rodriguez-Carvajal, Physica B (Amsterdam) **192**, 55 (1993).
17. A. I. Abramovich, L. I. Koroleva, A. V. Michurin, *et al.*, Fiz. Tverd. Tela (St. Petersburg) **42**, 1451 (2000) [Phys. Solid State **42**, 1494 (2000)].
18. D. Yu. Chernyshov, A. I. Kurbakov, and V. A. Trounov, Physica B (Amsterdam) **276–278**, 318 (2000).

Translated by L. Man

STRUCTURE
OF INORGANIC COMPOUNDS

Structural Characteristics of Peroxo Complexes of Group IV and V Transition Metals. Review

V. S. Sergienko

Kurnakov Institute of General and Inorganic Chemistry, Russian Academy of Sciences,
Leninskiĭ pr. 31, Moscow, 199991 Russia
Received February 6, 2003

Abstract—Structural characteristics of peroxo complexes of transition metals of Groups IV and V (Ti, V, Nb, and Ta) with the ratios $M : O_2 = 1 : 1$, $1 : 2$, $1 : 3$, and $1 : 4$ and alkyl peroxo complexes of Ti, Hf, and V have been considered. The structural manifestation of the *trans* effect of η^2-coordinated peroxo ligand in pseudooctahedral Ti, Nb, and V monoperoxo complexes is characterized. The structural manifestations of the *trans* effect of multiply bonded peroxo and oxo ligands in monooxomonoperoxo complexes of vanadium(V) are compared. © 2004 MAIK "Nauka/Interperiodica".

INTRODUCTION

The structures of peroxo compounds of Group IV (Ti, Zr, and Hf) and V (V, Nb, and Ta) transition metals in the highest oxidation degree (d^0 electron configuration) have been studied to different extents (Table 1). The best studied are the crystal structures of peroxo compounds of vanadium(V) (about 60 structures) and to a considerably lesser degree, the structures of peroxo complexes of titanium(IV) (13 structures) and nio-

Table 1. Total number of structurally characterized peroxo complexes of Group IV and V transition metals

M	Total	$M : O_2 = 1 : 1$	$M : O_2 = 1 : 2$	$M : O_2 = 1 : 3$	$M : O_2 = 1 : 4$
Ti	13 + 1*	12 + 1*	1		
Zr					
Hf	0 + 1*	0 + 1*			
V	60** + 1*	34 + 1*	24		2
Nb	13	8	2	2	1
Ta	5	4	1		
Altogether	91 + 3*	58 + 3*	28	2	3

* Number of structurally characterized *tert*-butylperoxo complexes of Group IV and V metals.
** Of the total number of 60 peroxo complexes of vanadium(V), 58 are related to oxoperoxo compounds containing VO(O$_2$)$_n$ complexes, $n = 1, 2$.

$M(O_2)A_5$ $M(O_2)_2A_4$ $M(O_2)A_4$

$M(O_2)_3A_2$ $M(O_2)_4$ $(\eta^5\text{-}Cp)_2M(O_2)A$
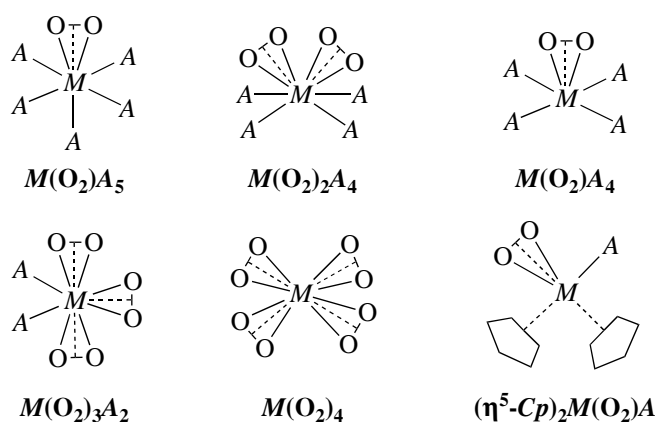
Scheme 1

bium(5) (13 structures). Structural chemistry of tantalum(IV) compounds with dioxygen ligands is represented only by five examples, whereas for the zirconium(IV) and hafnium(IV) compounds no X-ray diffraction data were obtained at all.[1]

The crystal structures of mono-, di-, tri-, and tetraperoxo complexes of the Group IV and V metals are also studied to different extents (Table 1): the compounds with the $M : O_2$ ratio equal to 1 : 1 and 1 : 2 (58 and 28 examples) are studied in full detail, whereas the $M(O_2)_3$ and $M(O_2)_4$ complexes are studied only on 2 and 3 examples.

The structural data for peroxo compounds of Group V transition metals (M^{5+} = V, Nb, and Ta) studied before 1986 are reviewed in the monograph by Vol'nov [1]. Butler *et al.* [2] summarized in their review the V–O (oxo), V–O(peroxo), and O–O distances for 26 oxoperoxo complexes of vanadium(V) structurally characterized by 1994. Review [2] is dedicated mainly to the chemistry of peroxo complexes of vanadium (V), whereas only a quarter of a page is devoted to the characterization of the structures of this class of compounds. Numerous structural data on peroxo compounds of Group IV and V transition metals accumulated and published for the last fifteen years have not been analyzed as yet.

It should be indicated that the vanadium(V) compounds occupy a special place among the structurally characterized peroxo complexes of the Group IV and V metals. The majority of the structurally studied vanadium(V) compounds of this class (58 of total 60) contain, in addition to dioxygen ligands, a multiply bonded oxo ligand. None of the other five metals of groups IV and V have structures containing oxo peroxo $MO(O_2)_n$ fragments—all these structures belong to peroxo compounds $M(O_2)_n$ (M = Ti, Mb. Ta, n = 1–4). Since the structural characteristics of oxoperoxo complexes of

vanadium(V) with the coordination sites $VO(O_2)_nA_m$ (where A are the donor atoms of mono and polydentate ligands, n = 1, 2, m = 1–4) were analyzed in detail for 58 compounds of this class that were structurally characterized before 2002 in [3, 4], the structures of vanadium(v) oxo peroxo complexes are only briefly considered in our article.

In all the peroxo compounds of Group IV and V metals considered in the present review, the dioxygen ligands coordinate M atoms in the bidentate–chelating mode.[2] In these cases, the peroxo complexes are characterized by eightfold (dodecahedral), sevenfold (pentagonal-bipyramidal or, in some rare cases, one-capped trigonal-prismatic), or sixfold coordination (tetragonal–pyramidal with a split axial vertex).[3] A particular location is occupied by the complexes of the $(\eta^5\text{-}Cp)_2M(O_2)A$ type ($\eta^5\text{-}Cp$ = C_5H_5 and C_5Me_5; where A is a monodentate ligand) in which the coordination number of a metal atom equals five or nine, depending on the interpretation of the Cp ligand as either a mono- or tridentate one.

If one assumes that the O_2 ligand bonded to a metal in the η^2-mode occupies one coordination site, then the $V(O_2)_nA_m$ complexes may have four variants of the coordination site: pseudooctahedral (n = 1, m = 5; n = 2, m = 4), pseudotetragonal–pyramidal (n = 1, m = 4), pseudotrigonal–bipyramidal (n = 3, m = 2), and pseudotetrahedral (n = 4, m = 0) (scheme 1).[4]

1. TITANIUM(IV) PEROXO COMPLEXES WITH Ti : O_2 = 1 : 1

Table 2 lists the geometrical parameters of twelve structurally studied titanium(IV) peroxo compounds (**I–XII**) [5–15].[5]

1.1. Pseudooctahedral Mononuclear Peroxo Complexes of Ti(IV)

Mononuclear complexes of titanium(IV) with the pseudooctahedral coordination of the metal atom are represented by seven examples (**I–VII**) in Table 2.

In three compounds (**I–III**), the coordination sphere of the Ti atom includes, in addition to the peroxo ligand, four donor atoms (2 N, 2 O, N, and 3 O or 4 N) from two equivalent or different bidentate–chelating ligands in the *cis* positions with respect to each another and one donor atom (O or N) of the monodentate

---

[1] The only exception is the structure of one hafnium *tert*-butylperoxide [$(\eta^5\text{-}C_5Me_5)_2$Hf(*tert-Bu*OO)(*Et*)] (see Sect. 9).

[2] In the dimer and polymer oxoperoxo complexes of vanadium(V), the O_2 ligand in a number of cases coordinates metal atoms in the bidentate–chelating–bridging mode(η^2, μ-mode) [4].

[3] The $VO(O_2)_2$ complexes may also have the sixfold pentagonal–pyramidal coordination.

[4] The complexes of the $(\eta^5\text{-}Cp)_2M(O_2)A$ type may also be considered as pseudotetrahedral if one assumes that the Cp ligand occupies one site in the coordination polyhedron of the metal.

[5] The $(NH_4)_3[Ti(O_2)F_5]$ structure is considered in Sect. 2.1 together with the structures of pentafluoroperoxoniobates(V) and pentofluorotantalates(V), $[M(O_2F_5)]^{2-}$, M = Nb, Ta.

ligand. In all the cases, the nitrogen atom of a bidentate–chelating ligand is *trans* to the O_2-ligand.

In the $[Ti(O_2)(Pic)_2(HMPT)]$ structure (**I**) [5] (Fig. 1a), the Ti atom is coordinated with in addition to the O_2-ligand, two O and two N atoms of two approximately plane monoanions of the pyridine-2-carboxylic acid, H*Pic* and NC_5H_4COOH, and the O atom of hexamethylphosphortriamide (HMPT, OPN_3Me_6). The two Ti–N(*Pic*) bonds are not equivalent. The Ti–N(2) bond with the nitrogen atom *trans* to the peroxo ligand is longer by 0.133 Å than the Ti–N(1) bond to the O atom (HMPT) in the *trans* position (the structural manifestation of the *trans* effect of the peroxo ligand is considered in detail in Sect. 5).

Mimoren *et al.* [5] indicate the high stability of complex **I** and its hydroxyquinoline and hydroxymate analogues, which hinders oxygen transfer in reactions with olefins, allyl alcohols, cyclic ketones, and sulfides. As a rule, dioxygen complexes of transition metals are active carriers of molecular oxygen to organic substrates [16]. In particular, under similar conditions, molybdenum and tungsten complexes analogous to **I** and other titanium peroxides oxidize these substrates in the presence of an excess of allyl alcohol and cyclohexane to α,β-epoxy alcohol [17] and lactone [18]. The specific features of the behavior of Ti(IV) peroxo complexes in the reactions of oxygen transfer is explained in [5] by saturation of the metal atom, which only weakly coordinates (at a large distance) even such a strong donor as HMPT. On the other hand, according to [5], Ti peroxo complexes (**I** and its analogues) oxidize triphenylphosphine and tetracyanoethylene, potential agents of direct incorporation along metal–peroxide bonds.

Analogous high stability of the Ti(IV) peroxo compound, hindering oxygen transfer to the organic substrates, was also observed for the structurally characterized $[Ti(O_2)(2,3-HPzdc)(Acac)(HMPT)] \cdot HMPT$ complex (**II**) [6]. Indicating a certain propensity to bridging of the anions of the pyrazine and pyridine carboxylic acids, Postel *et al.* [6] emphasize an unusual character of the mononuclear structure **II** in which an almost plane monoprotonated 2,3-H*Pzdc*⁻ ligand (where 2,3-H_2Pzdc is the pyrazine-2,3-dicarboxylic acid) plays the bidentate–chelating (N,O) role (Fig. 1b). The coordination polyhedra of each of the two independent metal atoms in structure **II** also include three oxygen atoms of the bidentate–chelating acetylacetonate (*Acac*) and monodentate HMPT ligands. Structures **I** and **II** are similar with only one difference: the Ti(O_2) fragment in the former is approximately perpendicular to both Ti(*Pic*) fragments, whereas in the latter this fragment is approximately coplanar to the 2,3-H*Pzdc* ligand. Like in most other complexes of transition metals with HMPT [19], the Ti–O–P fragments are not rigorously linear (the TOP angle equals 154.5(2)° and 168.6(4)° ± 1.0° in **I** and **II**, respectively).

Contrary to **II**, the dianions of the 2,5-pyrazine- and 2,5-pyridine carboxylic acids (2,5-H_2Pzdc and 2,5-
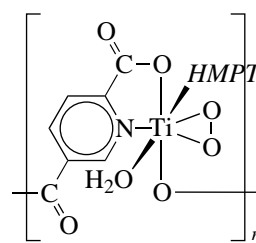
Scheme 2

H_2Pydc, respectively) in the three $[Ti(O_2)(2,5-Pzdc)(HMPT)(H_2O)] \cdot H_2O$ (**II′**), $[Ti(O_2)(2,5-Pydc)(HMPT)(H_2O)]$ (**II″**), and $[Ti(O_2)(2,5-Pydc)(HMPT)_2] \cdot H_2O$ (**III‴**) complexes [6] act in a more typical way than tridentate–chelating–bridging ones: the O atoms of both deprotonated carboxyl groups unite the pairs of metal atoms into a polymer chain (**II″**, scheme 2).[6] Unlike monocomplex **II**, polymers **II′**–**II‴** epoxidize tetramethylethylene. Postel *et al.* [6] indicate that olefin epoxidation may proceed only in the presence of a vacant position in the coordination polyhedron of the metal atom. This vacancy may be formed if one of the bridging Ti–O bonds break (2,5-*Pzdc* and 2,5-*Pzdc*) in complexes **II′**–**II‴** in the solution, and the coordination of olefin to the metal is broken by its subsequent oxidation.

In the $[Ti(O_2)(Tspa)_2(Py)]$ (**III**) structure [7], the Ti atom is coordinated in addition to a peroxo ligand also with four nitrogen atoms of two bidentate–chelating ligands—*N,N′*-bis(trimethylsilyl)-phenylamidinate monoanions (H*Tspa*, $PhC(NSiMe_3)_2$) and one nitrogen atom of the monodentate pyridine (*Py*) ligand (Fig. 1c). As usual, the Ti–N(2) 2.286(3) Å bond with the nitrogen atom of the *Tspa* ligand in the *trans* position to the peroxo ligand is longer (on the average, by 0.153 Å) than the Ti–(*Tspa*)$_{cis}$ bonds. The latter also have nonequal lengths: the Ti–N(3) bond to the nitrogen atom of the *Tspa* ligand in the *trans* position to the N(5) atom of the pyridine ligand is longer (on the average by 0.055 Å) than the Ti–N(*Tspa*) bonds in the *trans* position with respect to Ti–N(*Tspa*) to the N(1, 4) (2.170(3)) and 2.115(3) ± 0.012 Å, respectively).

In four compounds (**IV**–**VII**, Table 1), the pseudooctahedral mononuclear peroxo complexes contain in the coordination sphere of the metal atom, in addition to the O_2 ligand, one tridentate–chelating and two monodentate ligands.

In the two modifications of the $[Ti(O_2)(Dipic)(H_2O)_2] \cdot 2H_2O$ compounds—triclinic (**IV**) [8] and orthorhombic (**V**) [9]—a double-charged

---

[6] The polymer structure of microcrystalline **II′**–**II‴** samples was suggested in [6] based on the IR spectra and insolubility of the compounds (nonelectrolytes) in conventional organic solvents.
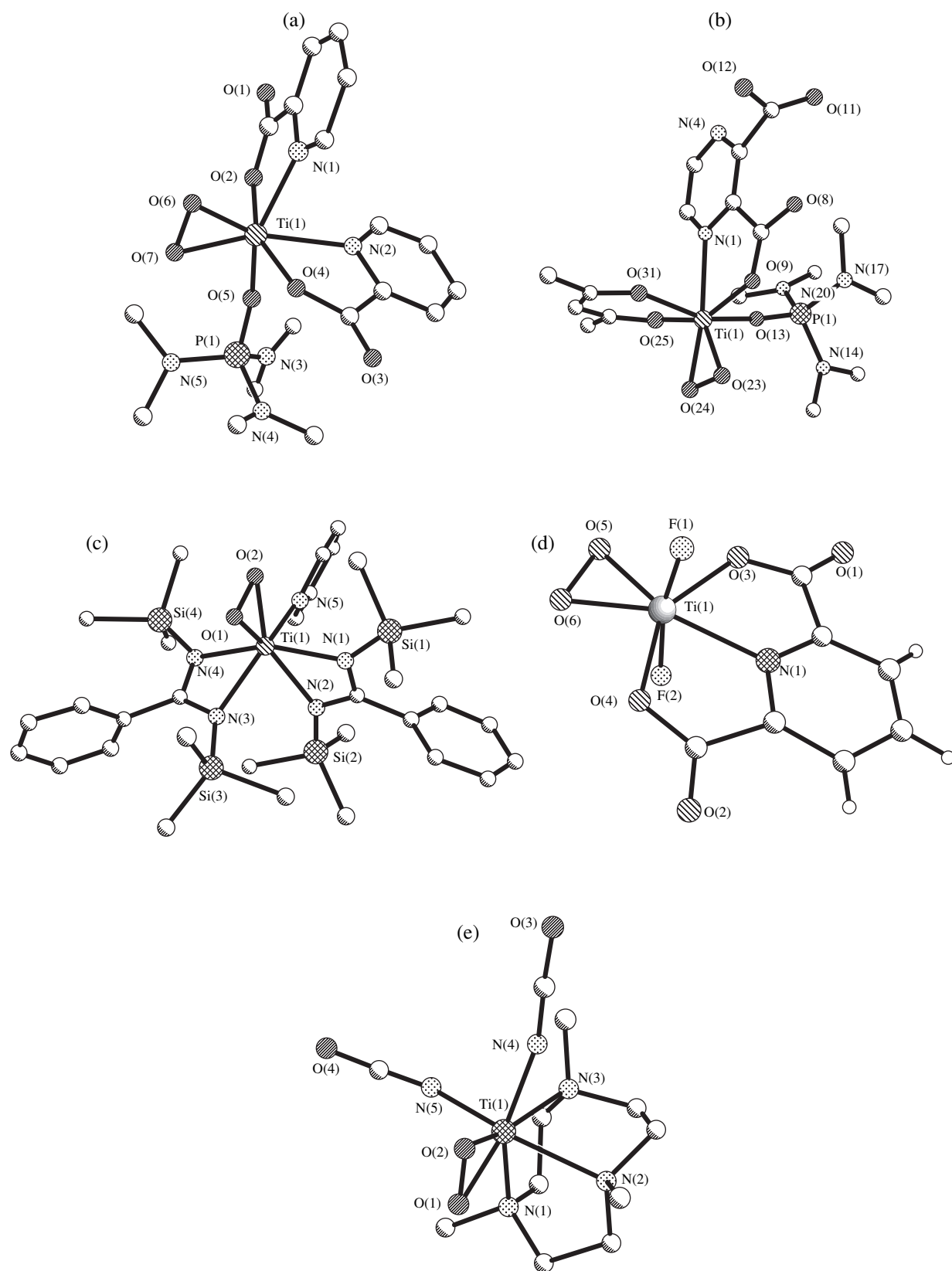
Fig. 1. Structures of pseudooctahedral mononuclear peroxo complexes of titanium(IV): (a) [Ti(O$_2$)(*Pic*)$_2$(HMPT)], (b) [Ti(O$_2$)(2,3-H*Pzdc*)(*Acac*) (HMPT)], (c) [Ti(O$_2$)(*Tspa*)$_2$(*Py*)], (d) [Ti(O$_2$)(*Dipic*)F$_2$]$^{2-}$, (e) [Ti(O$_2$)(*TacnMe*$_3$)(NCO)$_2$].

Table 2. Geometrical parameters (Å) for peroxo complexes of titanium (IV) (Ti : O_2 = 1 : 1)

No.	Compound	Ti–O(O_2)	O–O(O_2)	Ti–L_e	Ti–L_a	Δ(O_2)*	Reference
I	[Ti(O_2)(*Pic*)$_2$(HMPT)]	1.848(4) ± 0.006	1.419(6)	2.207(4) N(*Pic*) 1.977(3) ± 0.009 O(*Pic*) 2.042(4) O(HMPT)	2.340(4) N(*Pic*)	0.133	[5]
II	[Ti(O_2)(2.3-H*Pzdc*)(*Acac*)(HMPT)] · HMPT	1.850(4) ± 0.002	1.437(8) ± 0.000	2.028(5) ± 0.002 O(*Pzdc*) 2.025(5) ± 0.026 O(*Acac*) 2.013(5) ± 0.011 O(HMPT)	2.358(4) ± 0.006 N(*Pzdc*)		[6]
III	[Ti(O_2)(*Tspa*)$_2$(*Py*)]	1.853(3) ± 0.003	1.465(3)	2.133(3) ± 0.037 N(*Tspa*) 2.260(3) N(*Py*)	2.286(3) N(*Tspa*)	0.153	[7]
IV	[Ti(O_2)(*Dipic*)(H_2O)$_2$] · 2H_2O (*t*)**	1.846(2) ± 0.012	1.464(2)	2.096(2) ± 0.001 O(*Dipic*) 2.041(2) ± 0.017 O(H_2O)	2.146(2) N(*Dipic*)		[8]
V	[Ti(O_2)(*Dipic*)(H_2O)$_2$] · 2H_2O (*o*)**	1.833(1)	1.458(2)	2.073(1) O(*Dipic*) 2.018(1) O(H_2O)	2.164(5) N(*Dipic*)		[9]
VI	K$_2$[Ti(O_2)(*Dipic*)F$_2$] · 2H_2O	1.854(5) ± 0.008	1.463(6)	2.101(5) ± 0.007 O(*Dipic*) 1.870(5) ± 0.017 F	2.148(5) N(*Dipic*)		[8]
VII	[Ti(O_2)(*TacnMe*$_3$)(NCO)$_2$]	1.818(5) ± 0.003	1.348(5)	2.259(3) ± 0.028 N(*Tacn*Me$_3$) 2.041(4) ± 0.029 N(NCO)	2.372(3) N(*Tacn*Me$_3$)	0.113	[10]
VIII	K$_2$[{Ti(O_2)(*Dipic*)(H_2O)}$_2$(μ-O)] · 3H_2O	1.889(7) ± 0.017	1.45(1)	2.073(6) ± 0.001 O(*Dipic*) 2.183(7) O(H_2O) 1.825(2) O$_m$	2.172(7) N(*Dipic*)		[11]
IX	Na$_4$[{Ti(O_2)(*Nta*)}$_2$(μ-O)] · 11H_2O	1.891(2) ± 0.002	1.469(3)	2.074(2) ± 0.009 O(*Nta*) 1.819(2) O$_m$	2.271(2) N(*Nta*)		[12]
X	[{Ti(*tert*-BuOO)(μ-*Toea*)}$_2$] · 3CH$_2$Cl$_2$	1.913(3) 2.269(2) (*tert*-BuO)	1.469(3)	1.994(2) O$_{xm}$(*Toea*) 1.866(3) ± 0.016 O$_x$(*Toea*) 2.299(3) N(*Toea*)	2.048(2) O$_{xm}$(*Toea*)	0.054	[13]
XI	(NH$_4$)$_8$[{Ti(O_2)(μ-*Cit*)}$_4$] · 8H_2O	1.878(2) ± 0.021	1.464(2) ± 0.001	2.016(1) ± 0.006 O$_{xm}$(*Cit*) 2.050(1) ± 0.035 O$_x$(*Cit*)	2.052(1) ± 0.006 O$_{xm}$(*Cit*)	0.036	[14]
XII	[Ti(O_2)(*OEP*)]	1.825(4) ± 0.003	1.445(5)	2.109(4) ± 0.024 N(*OEP*)			[15]

Note: For ligand notation see Sect. 1.

   * Δ(O_2) is the difference between the Ti–L_a and Ti–L_e distances to the atoms of the same species in the *trans* and *cis* positions to peroxo ligand.

   ** *t* is triclinic and *o* is orthorhombic modifications of the [Ti(O_2)(*Dipic*)(H_2O)$_2$] · 2H_2O compound.

anion of the 2,6-pyridinedicarboxylic acid (H$_2$*Dipic*, NC$_5$H$_3$(COOH)$_2$) in the neutral [Ti(O$_2$)(*Dipic*)(H$_2$O)$_2$] complex coordinates the metal with the nitrogen atom of pyridine in the *trans* position to the dioxygen ligand in two oxygen atoms of two deprotonated acetate groups in *trans* positions with respect to one another. The coordination pseudooctahedron of the titanium atom is built up by two oxygen atoms of the water molecules. The Ti–O(*Dipic*) bonds in structures **IV** and **V** are longer (on the average by 0.055 Å) than the Ti–O(H$_2$O) bonds (2.085 and 2,030 Å, respectively). In orthorhombic modification **V**, water molecules are located along the axis 2 passing through the Ti and N atoms and the *para*atom C of a pyridine ring.

Two modifications, **IV** and **V**, have close parameters of the complexes but different packing of structural units in the crystals. In the triclinic phase, **IV**, all the molecules are parallel to one another and bonded by hydrogen bonds, which determines pleochroism of this complex, whereas the neighboring rows of molecules in the orthorhombic modification, **V**, are tilted by an angle 79.2° to one another, which explains the absence of pleochroism in the orthorhombic modification.[7] The neighboring molecules in the rows of structure **V** are spaced by large distances, so that the intermolecular distance between the middle of the O···O(peroxo) bond and the atom H(*Py*) is 4.59 Å. As a result, structure **V** has channels surrounded with hydrophylic oxygens and hydrophobic *Py* groups. Hydrogen bonds with the participation of coordinated and terminal O atoms of the acetate groups (O···O 2.622–2.911 and O–H 0.65–0.92, and H···O 1.74–2.02 Å) form zigzag chains and link the complex molecules into a three-dimensional framework. Complex **V** acts rather as a free acid than as a hydroxonium salt.

The dianionic [Ti(O$_2$)(*Dipic*)F$_2$]$^{2-}$ complex (Fig. 1d) in the K$_2$[Ti(O$_2$)(*Dipic*)F$_2$] · 2H$_2$O (**VI**) has a structure similar to that of **IV** and **V** [8] with the only difference being that two *trans* positions in the Ti pseudooctahedron are occupied by the F$^-$ ligands and not the O(H$_2$O) atoms.

In the [Ti(O$_2$)(*TacnMe$_3$*)(NCO)$_2$] structure (**VII**) [10], the metal atom is coordinated, in addition to the O$_2$ ligand, with five nitrogen atoms: three from the tridentate–chelating macrocyclic ligand of 1,4,7-trimethyl-1,4,7-triazacyclononane (*TacnMe$_3$*, N$_3$C$_6$H$_{12}$*Me$_3$*) and two from monodentate NCO$^-$ ligands (Fig. 1e). It should be noted that the O–O distance is unrealistically short, 1.348(5) Å, in structure **VII** and falls outside the rather narrow interval of distances, 1.42–1.47 Å, in the structures of Ti peroxo complexes in **I**–**XII** (Table 1).

Jeske *et al.* [10] explain this anomaly by the disordered nature of the peroxo group: according to the vibrational spectroscopy[8] and electrochemistry data, crystal **VII** also contain [TiO(*TacnMe$_3$*)(NCO)$_2$] molecules not identified in the course of X-ray diffraction analysis.

Jeske *et al.* [10] obtained some data on the [Ti(O$_2$)(*TacnMe$_3$*)Cl$_2$] crystal structure also containing an impurity of the oxo complex of similar composition [TiO(*TacnMe$_3$*)Cl$_2$]. In the crystal with the disordered structure, the oxygen atoms occupy five positions with different occupancy factors corresponding to two Ti(O$_2$) groups (the total occupancy for four O atoms is about 50%) and one TiO whose occupancy is also about 50%.

1.2. Pseudooctahedral Binuclear Peroxo Complexes of Ti(IV)

Two binuclear peroxo complexes of titanium(IV), **VIII** and **IX**, are structurally characterized. On these complexes, metal atoms are connected by the bridging oxo ligand in the special position on the twofold axis (the TiOTi angle equals 178.1(8)° and 167.59(6)° in **VIII** and **IX**, respectively).

In the K$_2$[{Ti(O$_2$)(*Dipic*)(H$_2$O)}$_2$(μ-O)] · 3H$_2$O compound (**VIII**) [11], the structure of the independent half of the dimer in the binuclear complex anion (Fig. 2a) is similar to the structures of mononuclear complexes **IV** and **V** with only one difference: one of two oxygen atoms of the coordinated water molecule is replaced by a bridging oxo ligand.

In the Na$_4$[{Ti(O$_2$)(*Nta*)}$_2$(μ-O)] · 11H$_2$O structure (**IX**) [12], each Ti atom in the four-charged complex dimer anion (Fig. 2b) is coordinated, in addition to μ-oxo and peroxo ligands, by four (N and 3O) atoms of the anion of nitriletriacetic acid (H$_3$*Nta*, N(CH$_2$COOH)$_3$). In structures **VIII** and **IX**, the nitrogen atoms of the *Dipic* and *Nta* ligands are in *trans*-positions to peroxo ligands. The Ti–(μ-O) bonds in **VIII** and **IX** (1.825(2) and 1.819(2) Å, respectively) are double bonds. In this case, the Ti–O(H$_2$O) bond to the oxygen atom in the *trans*-position to the μ-oxo ligand in **VIII** is considerably longer (on the average by 0.153 Å) than the analogous Ti–O(H$_2$O) bonds *trans* to Ti–O(H$_2$O) bonds in structures **IV** and **V** (2.183 and 2.030 ± 0.012 Å, respectively). On the other hand, the Ti–O(*Nta*) bond to the oxygen atom in the *trans* position to the μ-oxo ligand in structure **IX** is not longer but even somewhat shorter (on the average, by 0.014 Å) than the length of the Ti–O(*Nta*) bonds *trans* to Ti–O(*Nta*) (2.065 and 2.079 ± 0.003 Å, respectively).

---

[7] The existence of the shortest and most symmetric hydrogen bond in complex IV between the coordinated and solvation water molecules (O···O 2.580, O–H(1) 0.95, H(1)···O 1.64 Å) allowed Schwarzenbach *et al.* [8] to consider the H(1) atom as an proton of the acid and to consider complex IV as an intermediate one in the transition to the hydroxonium salt.

[8] The IR spectra of VII and the analogous Cl$_2$ complex (see below) in addition to the ν(O–O) = 907 cm^{-1} bands also have intense bands at 938 and 933 cm^{-1}, respectively, which correspond to the vibrations of the Ti=O(oxo) bonds.
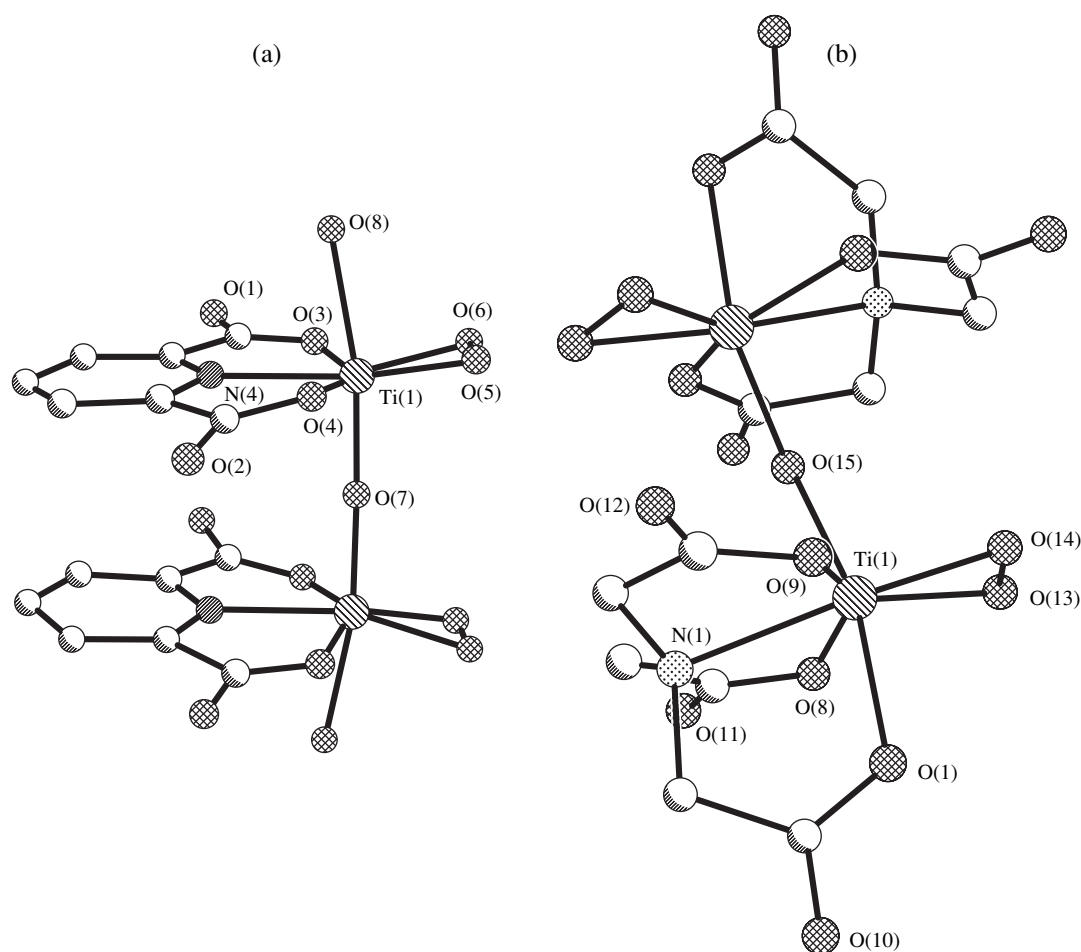
Fig. 2. Structures of pseudooctahedral binuclear peroxo complexes of titanium (**IV**): (a) [{Ti(O$_2$)(*Dipic*)(H$_2$O)}$_2$(μ-O)]$^{2-}$ and (b) [{Ti(O$_2$)(*Nta*)}$_2$(μ-O)]$^{4-}$.

Schwarzenbach *et al.* [8, 9, 12] considered five mono- and binuclear titanium(IV) complexes—**IV–VI**, **VIII**, and **IX**—and indicated the relation between the basicity of the axial ligands, complex color, and the lengths of the Ti–O(peroxo) and Ti–*L*(axial) bonds, with the O–O distance being constant. An increase in the activity of axial ligands in the H$_2$O ⟶ F ⟶ (μ-O) row results in the change of the color from dark red for **IV** and **V** (2O(H$_2$O)$_{axial}$) to yellowish–orange for **VI** (2F$_{axial}$), yellow for **VIII** ({O(H$_2$O), (μ-O)}$_{axial}$), and pale yellow for **IX** ({O(*Nta*), (μ-O)}$_{axial}$). In the same row, the V–O(peroxo) bonds increase (1.846 ± 0.012, 1.833, 1.854 ± 0.008, 1.889 ± 0.017, and 1.891 ± 0.002 Å for **IV**, **V**, **VI**, **VIII**, and **IX**, respectively). The V–*L*$_{axial}$ bond becomes shorter (for O(H$_2$O), 2.039 ± 0.017 Å in **IV** and 2.018 Å in **V**; for F$_{axial}$, 1.870 ± 0.017 in **VI** and 1.819 in **VIII**, and for (μ-O)$_{axial}$, 1.825 Å in **IX**). This conclusion is confirmed by the electron-density distribution on difference Fourier syntheses. The maxima of the residual electron density for structures **IV** and **V** are located between the maxima of the Ti atom and the O$_2$ group; for structure **VI**, they are located in the vicinity of the Ti–F$_{axial}$ bond, and for structure **IX**, in the vicinity of the Ti–(μ-O)$_{axial}$ bond. On the whole, the electron-density distribution for bonds in **IV–VI** and **IX** structures agree with the pentagonal–bipyramidal sp^3d^3 hybridization of titanium(IV).

In the centrosymmetric complex dimer molecule of (*tert*-butylperoxo)titanatrane, [{Ti(*tert*-BuOO)(μ-*Toea*)}$_2$] (Fig. 3) exists in a structure of solvate 1 : 3 with dichloromethane (**X**) [13]; its Ti atoms are linked by two tetradentate (N, 3O) tris(chelate)-bridging N,N,N-tris(2-oxyethyl)amine ligands (*Toea*, N(O*Et*)$_3$). Each of two *Toea* ligands acts as tetradentate–chelating one to the first metal atom and as monodentate-chelating-bridging one to the second metal atom. The coordination polyhedron of titanium is built up to a pseudooctahedron by an η^2-coordinated *tert*-butylperoxo group. Structure **X** is considered in more detail in Sect. 9.
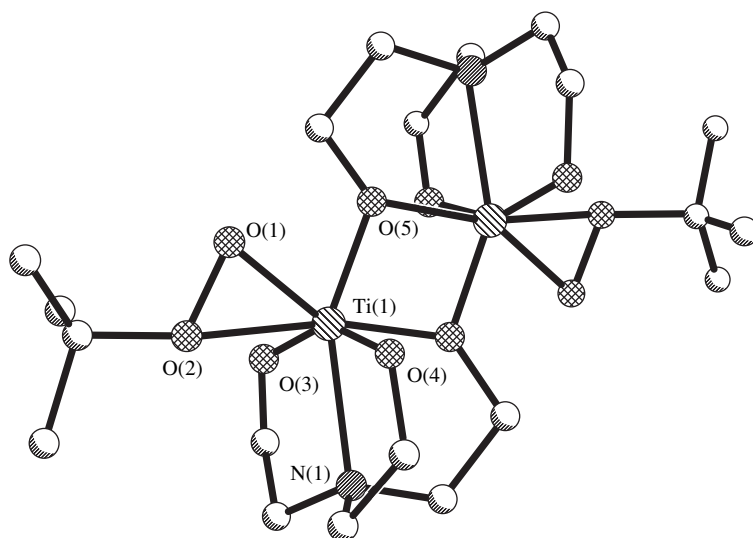
Fig. 3. Structure of a binuclear (*tert*-butylperoxo)-titanatrane[{Ti(*tert-Bu*OO)(μ-*Toea*)}$_2$]] complex.

1.3. Pseudooctahedral Tetranuclear [{Ti(O$_2$)(μ-Cit)}$_4$]$^{8-}$ Complex

The structure of the (NH$_4$)$_8$[Ti(O$_2$)$_4$ · (C$_6$H$_4$O$_7$)$_4$] · 8H$_2$O compound (**XI**) [14] is based on the centrosym-
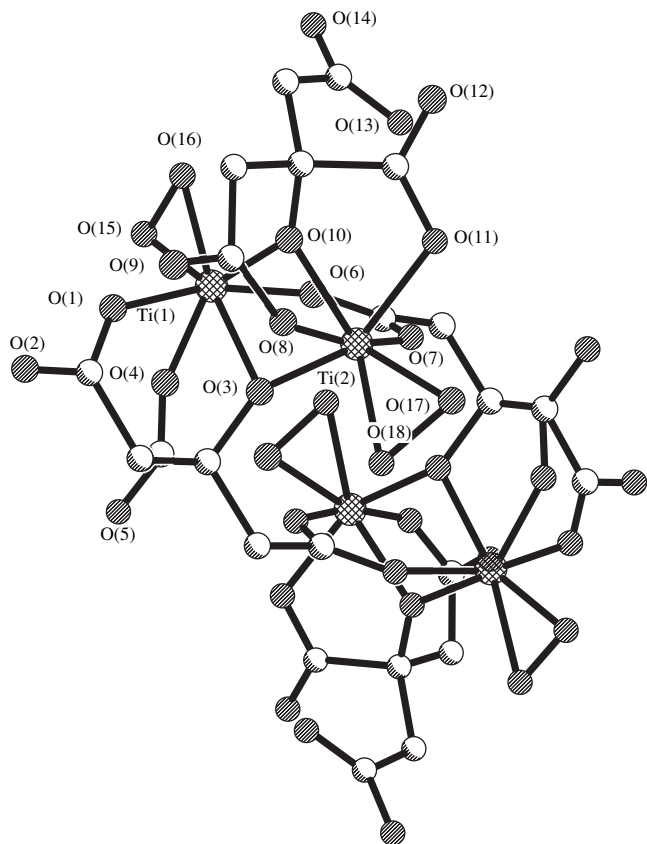
Fig. 4. Structure of a tetranuclear [{Ti(O$_2$)(μ-*Cit*)}$_4$]$^{8-}$] complex.

metric tetranuclear [{Ti(O$_2$)(μ-*Cit*)}$_4$]$^{8-}$ anion (Fig. 4). Two binuclear fragments [{Ti(O$_2$)(μ-*Cit*)}$_2$]$^{4-}$ of the complex anion are linked by chelating-bridging carboxylate O(6)–C–O(7) groups of two symmetrically bonded anions of the citric acid (H$_4$*Cit*, (CH$_2$)$_2$(COOH)$_3$(COH)). Two *Cit*$^{4-}$ (*Cit*$_1$ and *Cit*$_2$) ligands coordinate metal atoms in different ways. The *Cit*$_1$ ligand coordinates, in addition to O(6) and O(7) atoms of one carboxylate group, the Ti(1) atom through the O(1) and O(4) atoms of two remaining COO groups and also through the O(3) atom of the deprotonated chelating–bridging alcohol group. Thus, the *Cit*$_1$ ligand acts as pentadentate chelating–bridging one. The *Cit*$_2$ ligand coordinates the Ti(2) atom with O(8) and O(11) atoms of two chelating COO groups and the O(10) atom of the chelate–bridging alcohol group. Thus, the *Cit*$_2$ ligand acts as a tridentate chelating-bridging one. On the whole, four of the six COO groups participate in the coordination of metal atoms with one oxygen atom, whereas the fifth COO group coordinates the Ti(1) and Ti(2) atoms with the O(6) and O(7) atoms, respectively, and thus is the chelating–bridging group. Oxygen atoms of the sixth COO group (O(13)–C–(O(14)) do not participate in the coordination of a metal atom. The O(3) and O(10) atoms of deprotonated alcohol groups in both *Cit* ligands *trans* to the peroxo O(15, 16) and O(17, 18) ligands, respectively, act as chelating–bridging atoms. Kakihana *et al.* [14] indicate an important stabilizing role played by the coordinated O$_2$ ligands preventing further polymerization of the tetranuclear anion because of the nucleophilic attack on the equatorial position (occupied by the peroxo group) and hydrolysis, which also increase the negative charge of the complex and make possible the formation of the ammonium salt **XI** stable in an aqueous solution. Hydrolysis-stable compound **XI**, is a very promising

starting material for cheap and convenient synthesis of practically important titanium-based materials.

1.4. Pseudotetragonal–Pyramidal Mononuclear [Ti(O₂)(OEP)] Complex

The metal atom in the [Ti(O$_2$)(OEP)] complex (**XII**) [15] is characterized by the pseudotetragonal–pyramidal coordination with four nitrogen atoms of macrocyclic dianionic 2, 3,7,8,12,13,17,18-octaethylporphyrin ligand (OEP^{2-}, N$_4$C$_{36}$H$_{44}$) in the equatorial plane and the peroxo ligand in the axial position (Fig. 5). The peroxo ligand has the eclipsed conformation relative to two N(22, 24) atoms of a macroring. The Ti–N(22, 24) bonds are longer (on the average by 0.038 Å) than the remaining two Ti–N(21, 23) bonds (2.128 ± 0.005 and 2.090 ± 0.004 Å, respectively). The Ti atom is displaced by 0.620 Å from the equatorial plane of four nitrogen atoms. The structure similar to that of **XII** also has an isostructural oxo analogue [TiO(OEP)] (**XII**) [15]. In the transition from structure **XII** to **XII'**, the local symmetry of the molecule C_{2v} becomes higher, C_{4v}. Guilard *et al.* believe that the conformation formed in crystal XII is preferable and confirmed this opinion by the dynamic NMR data [15]. This conformation is sterically advantageous because it minimizes the O(O$_2$)···C(Et) repulsion. This eclipsed conformation observed in a number of structures of other peroxo complexes of transition metals (in particular, in the structure of the *trans*-Mo^{VI}(O$_2$)$_2$ with tetraarylporphyrin [20]). The molecular–orbital calculations show [21] that the eclipsed conformation of the O$_2$ ligand and two N atoms, N(22, 24), maximizes the bonds between the Ti, N(OEP), and O(O$_2$) atoms. The study by the method of dynamic ^{1}H and ^{13}C NMR of complexes **XII** and Ti(O$_2$)(TPP) (**XII''**) [15] (H$_2$TPP = 5, 10, 15, 20-tetraphenylporphyrin) shows that, in the temperature range from room temperature to –50°C, the peroxo ligand in solution undergoes fast exchange between two equivalent sites, where two oxygen atoms eclipse two equivalent pairs of opposite *trans*-nitrogen atoms, N(22), N(24) and N(21), N(23). The rotation barrier for an O$_2$ ligand is 10.8 ± 0.5 and 9.9 ± 0.5 kcal mole at the coalescence temperatures t_c –50 and –65°C for **XII** and **XII''**, respectively. According to [15], peroxotitanium(IV) porphyrin complexes undergo three successive electron-transfer reactions at the Pt cathode in the dichloromethane solution. The first step is bielectronic and irreversible and leads to the corresponding oxotitanium(IV) complex by reductive cleavage of the O–O bond.

2. PSEUDOOCTAHEDRAL PEROXO COMPLEXES OF NIOBIUM(V) AND TANTALUM (V) WITH M : O$_2$ = 1 : 1

Table 3 lists the geometric parameters of nine structurally characterized pseudooctahedral peroxo com-
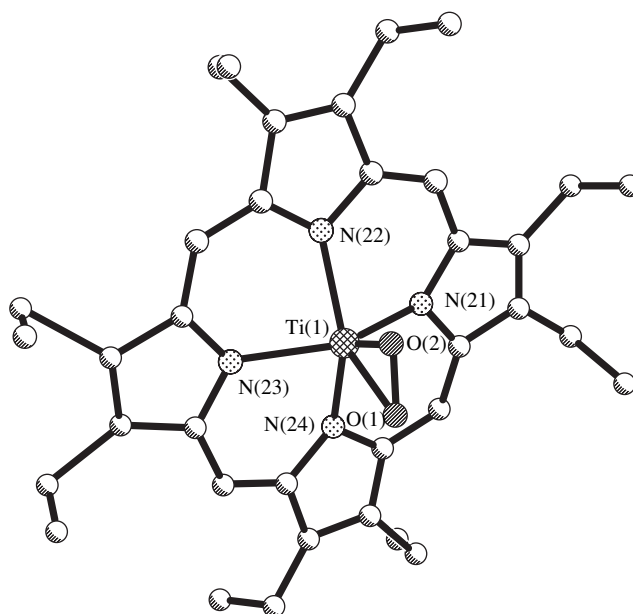
Fig. 5. Structure of a pseudotetragonal–pyramidal mononuclear [Ti(O$_2$)(OEP)] complex.

pounds of niobium(V) (**XIII–XVII**) [22–27], tantalum(V) (**XVIII–XX**) [28–30], and titanium(IV) (**XXI**) [31–33] with M : O$_2$ = 1 : 1.

2.1. Mononuclear Pentafluoroperoxoniobates(V), [Nb(O₂)F₅]²⁻

Five of compounds **XIII–XVII** contain pseudooctahedral complex [Nb(O$_2$)F$_5$]$^{2-}$ cation with the noncrystallographic symmetry C_{2v}.[9]

Two sodium salts, Na$_2$[Nb(O$_2$)F$_5$] · nH$_2$O, n = 1 (**XIII**) [22] and n = 2 (**XIV**) [23] differ only by complex anions statistically disordered with respect to peroxo ligand with two equiprobable orientations.

In the Na$_3$[Nb(O$_2$)F$_5$][HF$_2$] structure (**XV**) [24], two independent hydrogen fluoride anions have almost a linear structure with the FHF angles 176(12)° and 179(10)°. The F···F distance in the HF$_2^-$ anions of structure **XV** (2.838(4) and 2.292(4) Å) agree with the neutron-diffraction value 2.292 Å [35] in the KHF$_2$ structure [35]. Crystals **XV** are not isomorphous to K$_3$[Ta(O$_2$)F$_5$][HF$_2$] crystals (**XVIII**) [28] which are isostructural to the Nb analogue, K$_3$[Nb(O$_2$)F$_5$][HF$_2$].

In the phenanthrolinium salt (N$_2$C$_{12}$H$_{10}$)[Nb(O$_2$)F$_5$] (**XVI**) [25], the complex anion is disordered between two orientations with the site occupancy factors (SOF) 0.6 and 0.4. Three equatorial F$_e$ and two O(peroxo) atoms are disordered; the Nb and two axial F$_a$ atoms

---

[9] The crystallographic data for seven potassium salts of isostructural oxo-, dioxo-, oxoperoxo- and peroxo complexes of Mo(VI), Nb(VI), and Ta(V), including the data for [K$_2$[M(O$_2$)F$_5$] · H$_2$O with M = Ta and Nb are given in [34].

Table 3. Geometric parameters (Å) of pseudooctahedral peroxo complexes of niobium(V) and tantalum(V) (M : O = 1 : 1 and 1 : 2)

No.	Compound	M–O(O_2)	O–O(O_2)	M–L_e	M–L_a	$\Delta(O_2)$*	Reference
XIII	$Na_2[Nb(O_2)F_5] \cdot H_2O$	1.928(4)	1.476(7)	1.949(4) ± 0.043 F	2.037(4) F	0.088	[22]
XIV	$Na_2[Nb(O_2)F_5] \cdot 2H_2O$	1.95(1) ± 0.02	1.46(3) ± 0.05	1.937(4) ± 0.001 F	1.987(7) F	0.050	[23]
XV	$Na_3[Nb(O_2)F_5] \cdot [HF_2]$	1.932(2) ± 0.008	1.481(4)	1.951(2) ± 0.045 F	2.019(2) F	0.068	[24]
XVI	$(H_2Phen)[Nb(O_2)F_5]$**	1.878(1) ± 0.006	1.483(8)	1.947(4) ± 0.034 F	2.127(3) F	0.180	[25]
		1.904(9) ± 0.021	1.44(2)	1.943(6) ± 0.030 F	1.963(3) F	0.020	
XVII	$(HQu)_2[Nb(O_2)F_5] \cdot 3H_2O$ (295K)	1.93(6) ± 0.02	1.17(9)	1.93(4) ± 0.09 F	1.94(2) F	0.01	[26]
XVIIa	$(HQu)_2[Nb(O_2)F_5] \cdot 3H_2O$ (275K)	1.94 ± 0.05	1.32	1.94 ± 0.05 F	1.92 F	−0.02	[27]
XVIIb	$(HQu)_2[Nb(O_2)F_5] \cdot 3H_2O$ (170K)	1.96 ± 0.01	1.45	1.95 ± 0.06 F	1.94 F	−0.01	[27]
XVIII	$K[Ta(O_2)(F_5)][HF_2]$	2.035(12) ± 0.015	1.6(2)	1.93(7) ± 0.04 F	1.91(3) F	−0.02	[28]
XIX	$(NEt_4)[Ta(O_2)F_4(OPyMe)]$	1.92(5) ± 0.08	1.55(7) ± 0.12	1.94(3) ± 0.12 F	2.20(4) ± 0.06 O(OPyMe)		[29]
XX	$K_6[Ta(O_2)F_5][\{Ta(O_2)F_4\}_2(\mu\text{-}O)] \cdot H_2O$***	1.93(1)	1.39(3)	1.93(2) ± 0.04 F;	1.99(2) F	0.06	[30]
		1.97(1) ± 0.02	1.69(3) ± 0.05	1.97(2) ± 0.02 F; 1.89(10) ± 0.03 O_m	2.00(2) F	0.03	
XXI	$(NH_4)_3[Ti(O_2)F_5]$	1.90(2)	1.64	1.881(6)	1.881(6)		[31]
XXIa	$(NH_4)_3[Ti(O_2)F_5]$	1.82	1.421	1.91(1) F	1.91(1) F		[32]
XXIb	$(NH_4)_3[Ti(O_2)F_5]$	1.95(2) ± 0.01****		1.95(2) ± 0.01 F,O(O_2)****	1.95(2) ± 0.01 F,O(O_2)****		[33]
XXII	$(NH_4)_3[Ta(O_2)_2F_4]$	2.07(4)	1.45	1.91(4) F	1.91(4) F		[32]
XXIIa	$(NH_4)_3[Ta(O_2)_2F_4]$	2.03(2)	1.50	1.94(2) F	1.94(2) F		[36]
XXIII	$(NH_4)_3[Nb(O_2)_2F_4]$	1.94(2)	1.45	1.95(2) F	1.95(2) F		[32]
XXIV	$(NH_4)_3[Nb(O_2)_2(Ox)_2]_2 \cdot H_2O$	1.972(4) ± 0.011	1.483(6) ± 0.003	2.130(3) ± 0.007 O($Ox)_{Ts}$*****	2.145(4) ± 0.014 O($Ox)_T$*****	0.015	[37]
XXV	$Cs_6[PW_9\{Nb(O_2)\}_3O_{37}] \cdot HCl \cdot 6.5H_2O$	1.955 ± 0.035	1.494 ± 0.024	2.490 ± 0.024 μ_4-O	1.834 ± 0.014, 2.037 ± 0.009 μ_2-O (Nb, Nb) 2.064 ± 0.024 μ_2-O (Nb, W)		[38]
XXVI	$H_3Cs_{5.6}K_{3.1}Li_{0.3}[P_2W_{12}\{Nb(O_2)\}_6] \cdot 11H_2O$******	1.93(3)	1.43(4)	2.35(2) μ_4, μ_3-O	1.95(2) μ_2-O (Nb, Nb) 2.04(2) μ_2-O (Nb, W)		[41]

* $\Delta(O_2)$ is the difference between the M–L_a and M–L_e distances to the atoms of the same species in the *trans* and *cis* positions to the peroxo ligand.

** For structure **XVI**, the data are given for two orientations of a disordered anion with the site occupancy factors 0.6 (the upper line) and 0.4 (the lower line).

*** For structure **XX**, the geometrical parameters of the $[Ta(O_2)F_5]^{2-}$ complexes (the upper line) and the $[\{Ta(O_2)F_4\}_2(\mu\text{-}O)]^{4-}$ complex (the lower line) are indicated.

**** In the refinement of **XXIb** structure, the light (F, O, and O_2) atoms were set as fluorine atoms.

***** For structure **XXIV**, *Ts* and *T* are the Nb–O(*Ox*) distances to oxygen atoms *cis* and *trans* to peroxo ligand, respectively.

****** For structure **XXVI**, the geometrical parameters for metal atoms are given 5/6 Nb + 1/6 W (Nb(3, 8, 9, 14, 15, 18) in Fig. 8b).

occupy, within error, the ordered positions. The planes of the two orientations of the approximately plane Nb, $3F_e$, 2O (peroxo) fragment are tilted by 3.3° to one another and are rotated around the F_a–Nb–F_a axis by 61° with respect to one another.

In the structure of 8-hydroxyquinolinium (HQu_4^+) salt $(C_9H_8NO)_2[Nb(O_2)F_5] \cdot 3H_2O$ (**XVII**) determined by the photographic method at room temperature [26] and refined by the diffractometric data at 275 and 170 K [27], the (HQu_4^+) cations, complex anions, and water molecules of crystallization are linked by a branched net of hydrogen O–H···F, O–H···O, N–H···F, and N–H···O bonds. Ružic-Toroš *et al.* [26] and Stomberg [27] indicate positional disorder in the complex anion in structure **XVII**. In particular, the unrealistically short O–O distance 1.17(9) Å and rather low accuracy are explained by the crystal decomposition under X-rays and partial removal of peroxo groups [26]. For one of two O(peroxo) atoms, the refined site occupancy factor was as low as 0.3 (in the refinement of the other O(per-oxo) atom, the occupancy did not deviate from the ideal value, 1.0).

One more type of disorder was established in the ammonium pentafluoroperoxotitanate, $(NH_4)_3[Ti(O_2)F_5]$ (**XXI**) [31–33]. The compound is crystallized in the cubic system ($Z = 4$, sp. gr. $Fm3m$). According to [31, 32], fluorine and oxygen atoms occupy their positions only partially: the F atom occupies $24e$ position by 0.833, and the O atom occupies the $96j$ position by 0.083. Thus, the peroxo ligand has 12 orientations and statistically occupies two orientations in each of the six vertices of a pseudooctahedron with equal probabilities.

Stomberg and Svenson [33] describe structure **XXI** somewhat differently. They interpret light atoms (F and $O(O_2)$) as fluorine atoms in two $96j$ positions in the ratio 2.5 : 1; in other words, the site occupancy factors of F(1) and F(2) positions are 0.208 and 0.083.

The coordination polyhedra of metal atoms in the $[M(O_2)F_5]^{-2-n}$ complexes (M = Nb, Ta, n = 0, M = Ti, n = 1) in structures **XIII–XXI** are described either as pseudooctahedra (the peroxo ligand occupies one vertex) or as pentagonal bipyramids with two oxygen atoms of the O_2 ligand in the equatorial positions [22–33]. As a rule, the Nb–F_{trans} bond to the fluorine atom in the *trans* position to the peroxo ligand in a pseudoocta-hedron is longer than the Nb–F_{cis} bond (for details see Sect. 5). Moreover, usually, Nb–F_{cis} bonds have different lengths: Nb–F_a bonds to fluorine atoms in the axial vertices of a pentagonal bipyramid are often shorter than the Nb–F_e bonds to fluorine atoms in the equatorial positions. Thus, in structures **XIII**, **XV**, and **XVI**, the Nb–F_a bonds (1.922 ± 0.016, 1.921 ± 0.015, and 1.922 ± 0.009 Å, respectively) are shorter (on the average, by 0.054, 0.061, and 0.046 Å) than the *cis*-bonds
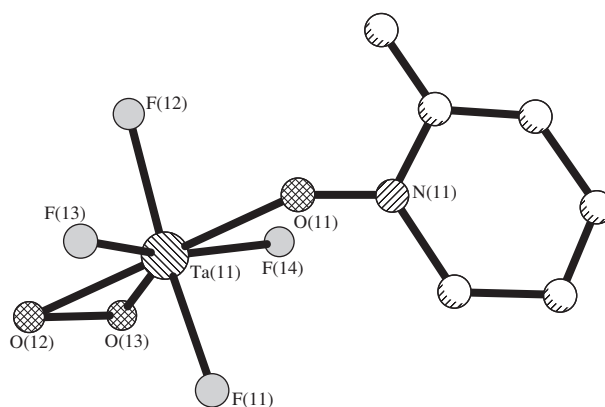
Fig. 6. Structure of a pseudooctahedral per-oxo[$Ta(O_2)F_4(OPyMe)$]⁻ complex.

Nb–F_e (1.976 ± 0.000, 1.982 ± 0.007, and 1.968 ± 0.022 Å, respectively). This may be explained by the fact that the fluorine atoms located at the longest and shortest distances from the metal participate in the minimum and maximum numbers of contacts with the counterions, respectively. In particular, in structure **XV**, the F(3) atom contacts with only one metal atom, whereas each of the F(1) and F(2) atoms contact with three Na atoms (Nb–F(3) 1.906 is the shortest bond, and Nb–F(1) 1.988 and Nb–F(2) 2.019 Å are the long-est bonds in the structure).

2.2. Mononuclear [Ta(O₂)F₄(OPyMe)]⁻ Complex

In each of the two independent complex anions in the $(NEt_4)[Ta(O_2)F_4(C_6H_7NO)]$ structure (**XIX**) [29], the *trans* position to the peroxo ligand is occupied by the oxygen atom of the 2-methylpyridine-*N*-oxide ligand (O*PyMe*). In the pentagonal bipyramid TaO_3F_4, the axial Ta–F bonds are, on the average, 0.02 Å shorter than the equatorial ones (Ta–F_a 1.93(3) ± 0.03 and Ta–F_e 1.95(3) ± 0.11 Å). The average Ta–O(O*PyMe*) bond length is 2.20(4) ± 0.06 Å.

2.3. Pseudooctahedral Mono- and Binuclear Fluoroperoxotantalate Anions in K₆Ta₃(O₂)₃OF₁₃ · H₂O Compound

In the $K_6Ta_3(O_2)_3OF_{13} \cdot H_2O$ structure (**XX**) [30], there are two types of complex anions: mononuclear $[Ta(O_2)F_5]^{2-}$ and binuclear $[\{Ta(O_2)F_4\}_2(\mu\text{-}O)]^{4-}$ ones with an approximately linear Ta–(μ-O)–Ta bridge (TaOTa angle 171.5(9)°). As usual, the Ta–F_{trans} bonds from the atoms in the *trans* positions to the O_2 ligand in the $Ta(O_2)F_5$ and $Ta(O_2)F_4(\mu\text{-}O)$ octahedra are some-what longer than the Ta–F_{cis} bonds (on average, by 0.05_5 and 0.03_5 Å in the mono- and binuclear anions, respectively). The average Ta–(μ-O) bond length is $1.89_5(10) ± 0.03_5$ Å. Massa and Pausewang [30] indi-

cate a considerable difference in the O–O(peroxo) bond lengths in mono- and binuclear anions (1.39(3) and 1.70(3) ± 0.06 Å, respectively), which correlates with the IR- and Raman-spectroscopy data. In particular, to the O–O bonds in mono- (A) and binuclear (B) anions there correspond the following frequencies in the IR spectrum of compound **XX**: $\nu(O–O) = 887$ (A) and 833 (B), $\nu_s(Ta–O_2) = 577$ (A) and 533 (B), $\nu_{as}(Ta–O_2) = 490$ cm^{-1} ($A + B$).

3. PSEUDOOCTAHEDRAL MONONUCLEAR PEROXO COMPLEXES OF NIOBIUM(V) AND TANTALUM(V) WITH $M : O_2 = 1 : 2$

Table 3 lists the geometrical parameters of three pseudooctahedral peroxo complexes of Nb(V) and Ta(V) with $M : O_2 = 1 : 2$ (**XXII–XXIV**).

Crystals of the two compounds with the general formula $(NH_4)_3[M(O_2)_2F_4]$, M = Ta (**XXII**) [32, 36] and M = Nb (**XXIII**) [32] are isostructural to crystals of compound **XXI** [31–33] considered in Sect. 2.1 with only one difference: different values of site occupancy of positions of light atoms. In **XXII** and **XXIII**, the occupancies of the positions occupied by fluorine and oxygen atoms are 0.667 and 0.167, respectively.[10] In the $[M(O_2)_2F_4]^{3-}$ pseudooctahedron, the peroxo groups are located in the neighboring vertices (in the *cis* positions). The M–F bonds for fluorine atoms in the *trans* and *cis* positions to the peroxo ligands have the same lengths, because all the fluorine atoms are located in one crystallographic position 96*j*.

Depending on the conditions of crystal synthesis, the $K_3[Ta(O_2)_2F_4]$ compound may have, in addition to the cubic phase [32, 36] isostructural to **XXII** and **XXIII**, the monoclinic phase whose parameters are indicated in [36]. According to [36], cooling of the **XXII** crystal to 120 K gave no rise to a phase transition.

In the $(NH_4)_3[Nb(O_2)_2(Ox)_2] \cdot H_2O$ structure (**XXIV**) [37], the Nb atom in the complex anion (Fig. 7) is coordinated with two peroxo ligands *cis* to one another and to four oxygen atoms in two bidentate–chelating dianion ligands of the oxalic acid H_2Ox, $H_2C_2O_4$. On the average, the Nb–O(Ox) bonds to the oxygen atoms *trans* to the O_2 ligand are by 0.015 Å longer than the Nb–O(Ox)$_{cis}$ bonds to the O(Ox) atoms in *trans* positions to one another (2.145(4) ± 0.014 and 2.130(3) ± 0.007 Å, respectively).

Considering O_2 as a bidentate–chelating ligand, one may describe the coordination polyhedron of a $M(O_2)_2F_4$ complex as a dodecahedron [37].

---

[10]According to [32], the positions of oxygen atoms localized from the difference Fourier syntheses of structures **XXII** and **XXIII** were not refined.

4. PSEUDOOCTAHEDRAL $Nb(O_2)O_5$ COMPLEXES IN POLYTUNGSTOPHOSPHATE HETEROPOLYANIONS

Two compounds containing polytungstophosphate heteropolyanions in which several terminal oxotungsten groups are replaced by peroxoniobium fragments are of special interest.

In the $Cs_6[PW_9\{Nb(O_2)\}_3O_{37}] \cdot HCl \cdot 6.5H_2O$ structure (**XXV**) [38] containing heteropolyanion 1 : 12 of the Keggin type [39], three terminal WO groups are replaced by the $Nb(O_2)$ fragments. In the $[PW_9\{Nb(O_2)\}_3O_{37}]^{6-}$ structure with heteropolyanions (Fig. 8a), the A,α-PW_9 isomer is formed instead of the expected A,β-PW_9 isomer. Three Nb atoms are located in three different $NbW_2O_{12}(O_2)$ triads containing WO_6 octahedra sharing the edges and $Nb(O_2)O_5$ pseudooctahedra. In this case, the Nb atoms share the vertices (A-type positional isomer). The fourth W_3O_{13} triad is rotated around axis 3 with respect to the initial α isomer by an angle of 60° and, thus, forms the β isomer. The $Nb(O_2)$ fragments are oriented in such a way that peroxo groups lie in the planes of the corresponding atoms of Nb_2W_4, whereas the relative orientation of three Nb_2W_4 at angles of about 120° determines the heteropolyanion symmetry close to C_3. In **XXV**, the Cs^+ cations and the water molecules of crystallization are partially disordered.

Similar to structure **XXV**, in the heteropolyanion 2 : 18 of the Dawson α type (Fig. 8b) [40] of the $H_3Cs_{5.6}K_{3.1}Li_{0.3}[[P_2W_{12}\{Nb(O_2)\}_6O_{56}] \cdot 11H_2O$ structure (**XXVI**) [41], six terminal WO groups (one in each of two "caps" and two in each of two "belts") are replaced by $Nb(O_2)$ fragments whose orientation with respect to the Nb_2W_4 belts is such that the Nb(9)O(21, 22) and Nb(15)O(53, 54) groups are perpendicular to the belt, whereas Nb(8)O(19, 20) and Nb(14)O(51, 52) are approximately coplanar to the Nb_2W_4. Judd *et al.* [41] believe that the distribution of the O_2 groups in a heteropolyanion is partly determined by the cation–anion interaction: in particular, the Cs–O(22) and Cs–O(53) distances are less than the sum of the van der Waals radii of Cs and O. The orientation of the $Nb(O_2)$ groups lowers the symmetry of a heteropolyanion in **XXVI** to C_1. In distinction from an ordered heteropolyanion in structure **XXV**, the positions of Nb and W atoms in a heteropolyanion in structure **XXVI** are mixed in the ratio 5/6 Nb + 1/6 W for the Nb(3, 8, 9, 14, 15, 18) atoms and 5/6 W + 1/6 Nb for the W(1, 4, 5, 10, 11, 16) atoms.

The Nb atoms in **XXV** and **XXVI** structures are coordinated over the vertices of pseudooctahedra by the terminal η^2-peroxo group, four equatorial μ_2-bridging O atoms (in *cis* position to the O_2 ligand), and the axial μ_4 O atom in **XXV** (in the cap position in **XXVI**) or the μ_3-bridging O atom in the belt position in **XXVI** (*trans* to O_2). In structures **XXV** and **XXVI**, the equatorial
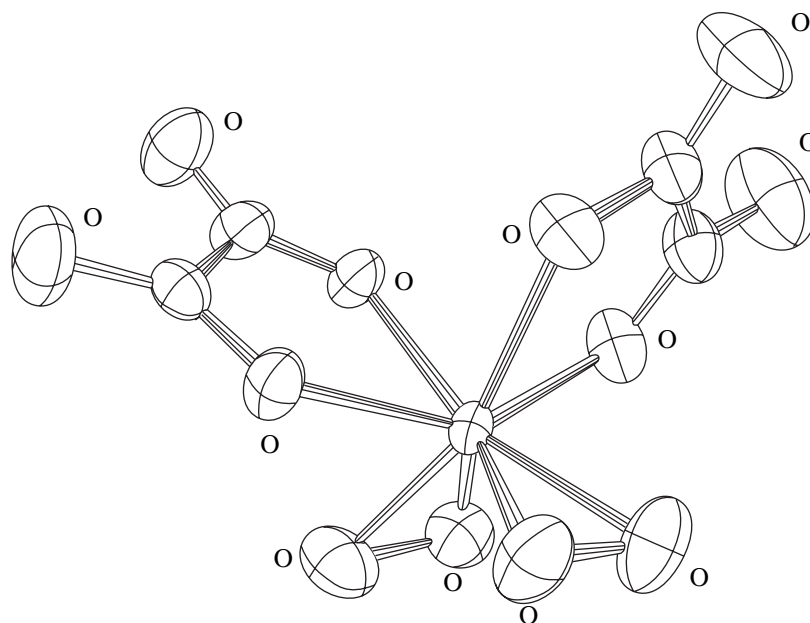
Fig. 7. Structure of a pseudooctahedral mononuclear $[Nb(O_2)_2(Ox)_2]^{3-}$ complex.

Nb–O bonds differ depending on the nature of metal atoms bonded by μ_2-O atoms. In structure **XXV**, the μ_2-bridges that link two niobium atoms (μ_2-atoms O(31), O(38), and O(39)) are strongly asymmetric: in each triad, one Nb–(μ_2-O) bond is shorter, on the average, by 0.203 Å than the other bonds (1.834 ± 0.014 and 2.037 ± 0.009 Å, respectively). On the other hand, the μ_2 bridges that link the niobium and tungsten atoms (μ_2 atoms (O(15), O(19), O(21), O(23), O(28), O(29)) are symmetric (2.064 ± 0.024 Å). The Nb–(μ_2-O)$_{Nb, Nb}$ bonds are shorter, on the average, by 0.13 Å than the Nb–(μ_2-O)$_{Nb, W}$ bonds (1.936 and 2.064 Å, respectively). The equatorial Nb–(μ_2-O)$_{Nb, Nb}$ bonds in structure **XXVI** (only the averaged distances are indicated in [41]) are shorter, on the average, by 0.09 Å than the Nb–(μ_2-O)$_{Nb, W}$ bonds (1.95(2) and 2.04(2) Å, respectively).

Table 3 does not list rather large $\Delta(O_2)$ parameters for compounds **XXV** and **XXVI** (equal, on the average, to 0.355 and 0.490, respectively), because the oxygen atoms in *trans* and *cis* positions to peroxo ligands act in different bridging modes: μ_3, μ_4 in the former case and μ_2 in the latter).

5. STRUCTURAL MANIFESTATION OF *trans* EFFECT OF THE PEROXO LIGAND IN COMPLEXES OF GROUP IV AND V TRANSITION METALS

One of the characteristic features of structures of pseudooctahedral peroxo complexes of transition metals of Groups IV and V is the structural manifestation of the *trans* effect of peroxo groups: elongation of the M–L_{trans} bond to the ligand (or the donor atoms of the ligand) *trans* to the O$_2$ ligand in comparison with the length of the M–L_{cis} to an atom or a ligand of the same species. The quantitative measure of the structural effect of peroxo ligands is its parameter $\Delta(O_2)$.

The structural manifestation of the structural manifestation of the *trans* effect (SMTE) of the O$_2$ ligand is rather clearly seen in all the five Ti(IV) complexes with the same donor atoms (N or O) of organic polydentate ligands (Table 2). In monomer $[Ti(O_2)(Pic)_2(HMPT)]$ (**I**) [5], $[Ti(O_2)(Tcpa)_2(Py)]$ (**III**) [7], and $[Ti(O_2)(TacnMe_3)(NCO)_2]$ (**VII**) [10] complexes, the $\Delta(O_2)$ values for the Ti–N bonds of the chelating *Pic*, *Tcpa*, and *TacnMe$_3$* ligands are equal to 0.133, 0.153, and 0.113 Å, respectively. For the Ti–O bonds of chelate–bridging *Toea* and *Cit* ligands in the bi- and tetranuclear $[\{Ti(tert\text{-}BuOO)(\mu\text{-}Toea)\}_2]$ (**X**) [13] and $[\{Ti(O_2)(\mu\text{-}Cit)\}_4]$ (**XI**) [14] complexes, respectively, the structural manifestation of the *trans* effect of a peroxo ligand is also observed, although to a considerably lesser degree, $\Delta(O_2) = 0.054$ and 0.036 Å.

The structural manifestation of the *trans* effect of a peroxo ligand is also observed in four pentafluoroperoxoniobates, $[Nb(O_2)F_5]^{2-}$, (**XIII–XVI**, Table 3) [22–25] with the average value ranging within $\Delta(O_2) = 0.050$–0.100 Å, similar to the structural *trans* effect of the mono- $[Ta(O_2)F_5]^{2-}$ and binuclear $[\{Ta(O_2)F_4\}_2(\mu\text{-}O)]^{4-}$ complexes of structure **XX** [30] equal to $\Delta(O_2) = 0.05_5$ and 0.03_5 Å, respectively.[11]

---

[11]In terms of the structural manifestation of the *trans* effect of the O$_2$ ligand, the more or less disordered $[M(O_2)F_5]$ complexes in structures **XVII**, **XVIII**, and **XXI–XXIII** are not discussed here.

(a)   (b)
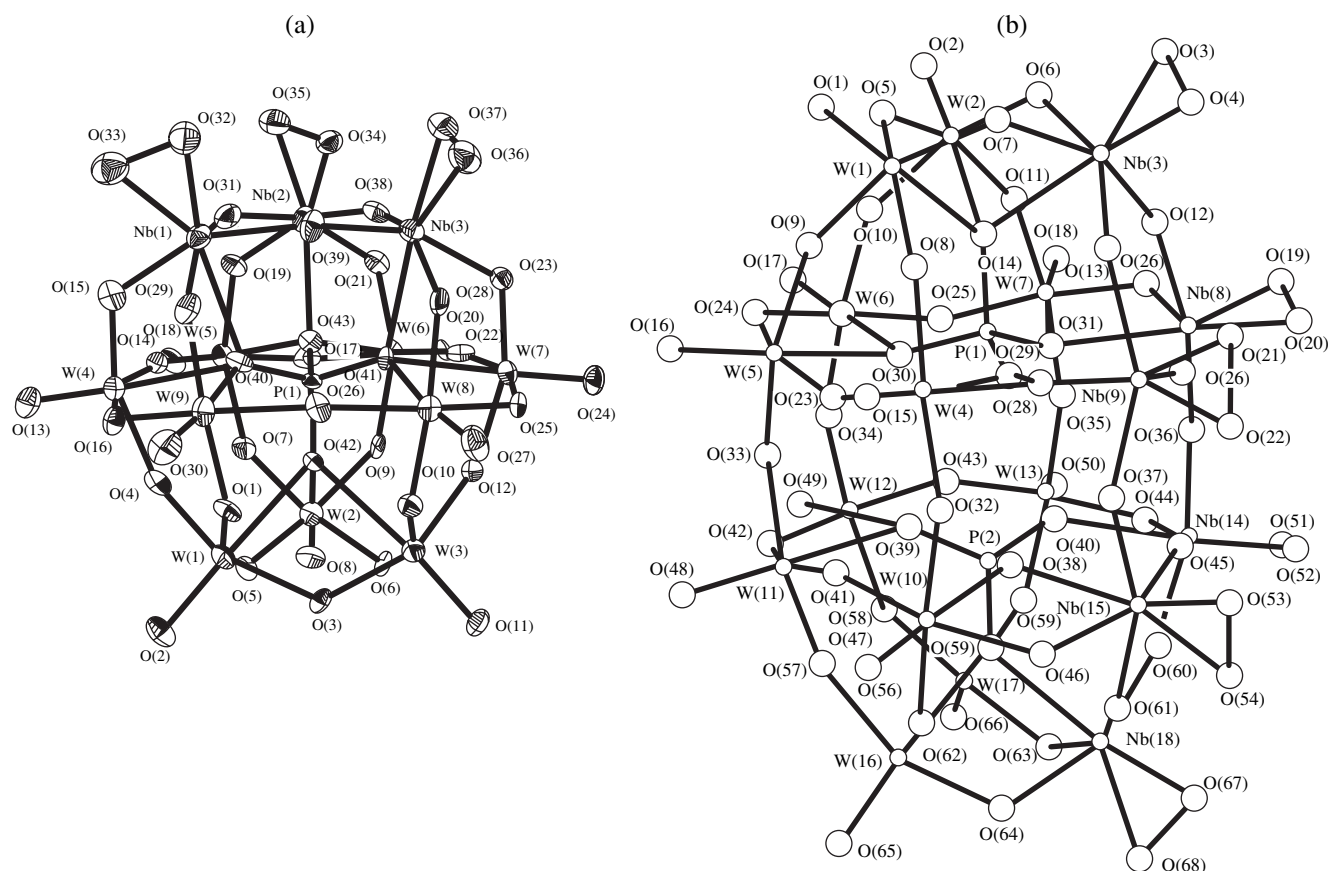
Fig. 8. Structure of heteropolyanions containing Nb(O$_2$)O$_5$ fragments: (a) [PW$_9${Nb(O$_2$)}$_3$O$_{37}$]$^{6-}$ and (b) [P$_2$W$_{12}${Nb(O$_2$)}$_6$O$_{56}$]$^{12-}$.

A considerably weaker structural manifestation of the *trans* effect of the O$_2$ ligand is observed in the diperoxo [Nb(O$_2$)$_2$(*Ox*)$_2$]$^{3-}$ complex in **XXIV** (Table 3) [37] (Δ(O$_2$) = 0.015 Å), which seems to be quite natural if one takes into account that the structural manifestation of the *trans* effect of any multiply bonded ligands (in particular, O$_{oxo}$) is reduced with an increase of the number of these ligands in the structure, Δ(O$_{oxo}$) > Δ(O$_{oxo}$)$_2$ > Δ(O$_{oxo}$)$_3$ [42] and Δ(O$_2$) > Δ(O$_2$)$_2$.

It is interesting to compare the structural manifestation of the *trans* effect of peroxo and oxo ligands in monoperoxo and monooxo complexes with close compositions. Thus, in peroxo complex **VII** mentioned above (Table 2) and in the analogous [TiO(*TacnMe*$_3$)(NCO)$_2$] (**VII'**) oxo compound [43], the Ti–N(*TacnMe*$_3$)$_{trans}$ bond to the nitrogen atom *trans* to the O$_2$ ligand is somewhat shorter than to the O$_{oxo}$ atom (2.372 and 2.413 Å, respectively), where, on the contrary, the Ti–N(*TacnMe*$_3$)$_{cis}$ bond in structure **VII** is somewhat longer than in **VII'** (2.259 and 2.236 Å, respectively). Naturally, the value of the Δ(O) parameter in structure **VII'** is considerably higher than Δ(O$_2$) in **VII** (0.177 and 0.113 Å, respectively). The length of the Ti=O$_{oxo}$ bond in **VII'** equals 1.638 Å.

An even more pronounced difference in the Δ(O) and Δ(O$_2$) parameters is observed in a [NbOF$_5$]$^{2-}$ complex of the Na$_2$[NbOF$_5$] structure (**VIII'**) [44] and in a [Nb(O$_2$)F$_5$]$^{2-}$ complex of three sodium salts **XIII–XV** [22-24]: the length of the Nb–F$_{trans}$ bond equals 2.095 in **VIII'** and 2.014 ± 0.027 Å in **XIII–XV**, the length of the Nb–F$_{cis}$ bond equals 1.946 ± 0.028 and 1.946 ± 0.009 Å, respectively; Δ(O) = 0.149 Å in **VIII'** and Δ(O$_2$) = 0.069 ± 0.019 Å in **XIII–XV**. The Nb = O$_{oxo}$ distance in structure **VIII'** equals 1.765 Å.

The structural manifestation of the *trans* effect of a multiple *M*–O bond in oxo complexes of d^0 metals of Groups V–VII is well studied and described, e.g., in [42–45]. One can state that elongation of a bond which is *trans* to the η^2-dioxo ligand is the structural manifestation of the weakening *trans* effect of this ligand and is comparable with the effect of a multiply bonded oxo ligand.

Now, consider in brief the structural manifestation of the *trans* effect of multiply bonded ligands in pseudooctahedral oxoperoxo complexes of vanadium(V) of the VO(O$_2$) type described in detail elsewhere [3, 4]. These complexes may be considered as analogues of sixfold-coordinated dioxo complexes of d^0 metals (in

particular, $V(O)_2$). In this case, oxo and peroxo ligands or two oxo ligands are always in *cis* positions with respect to one another in the coordination polyhedra of both types.

Table 4 lists the main bond lengths for thirteen pseudooctahedral $VO(O_2)$ complexes in which the *trans* and *cis* positions to the O_2 ligand are always occupied by the same donor atoms of polydentate organic ligands (**XXVII**–**XXXIX**) [46–57].

In the general case, the choice of a concrete geometric isomer in octahedral oxo compounds of the d^0 metals of Groups V–VI in the presence of competing donor atoms in heteroligand complexes is determined by the self-consistency rule [58]: the *trans* position to multiply a bonded ligand is usually occupied by an atom or a ligand, the bond with which may be more easily weakened (in particular a neutral–donor ligand rather than an acido ligand). The self-consistency rule works, practically without any exceptions, being applied to an oxo ligand and, in its general features, also to an O_2 ligand.

As is seen from Table 4, the structural manifestation of the *trans* effect of a peroxo ligand is usually weaker than of an oxo ligand. Indeed, of the total number of nine structures in which both *trans* and *cis* positions in oxo and peroxo ligands are occupied by the same donor atoms of organic ligands, the $\Delta(O_2)$ and $\Delta(O)$ parameters are comparable (0.115–0.126 and 0.112–0.121 Å, respectively) only in three structures: $[VO(O_2)(L)_2]^+$ [50], $L = Bipy$ (**XXXI**), *Phen* (**XXXII**); and $[VO(O_2)(Ox)_2]$ (**XXXIII**) [51]. In the remaining six structures (Table 4), the $\Delta(O_2)$ value ranges within $\Delta(O_2) = -0.048$ to $+0.081$, whereas $\Delta(O) = 0.099$–0.548 Å. The quantitative value of the structural manifestation of the *trans* effect of a peroxo ligand depends more pronouncedly on the nature of the opposite ligand. Thus, the complexes containing asymmetric chelating ligands (anions of carboxylic acids, *Pyanaph*, *Ida*, etc.) with the donor N and O atoms *trans* to O_2 usually exist in the range of weak or absent structural manifestation of the *trans* effect ($\Delta(O_2) = -0.08$ to $+0.08$ Å, Table 4 and Table 1 in [3]). Based on the accumulated structural data, one may assume that a dioxygen ligand manifests no *trans* effect in those occasions where the accompanying chelating ligand contains nonequivalent atoms that may be potential donors (N, O).

6. MONONUCLEAR PEROXO COMPLEXES OF NIOBIUM(V) AND VANADIUM(V) WITH $M : O_2 = 1 : 3$

Table 5 lists the geometrical parameters of two triperoxo compounds: $K[Nb(O_2)_3(Phen)] \cdot 3H_2O$ (**XL**) [59] and $K[Nb)O_2)_3(Phen)] \cdot 3H_2O \cdot H_2O_2$ (**XLI**) [59]. In a complex $[Nb(O_2)_3(Phen)]^-$ anion (Fig. 9) with the local symmetry C_s, the Nb atom is coordinated over the dodecahedron vertices with six oxygen atoms of three peroxo ligands and two nitrogen atoms of a *Phen*
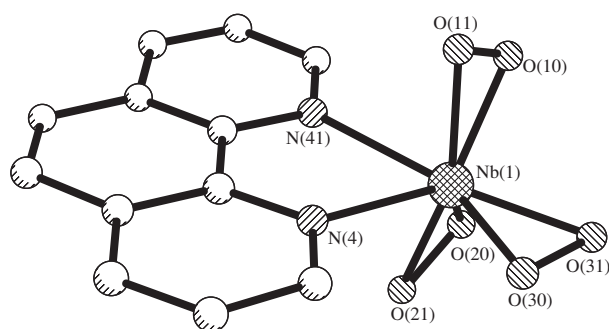
Fig. 9. Structure of a pseudotrigonal–bipyramidal mononuclear $[Nb(O_2)_3(Phen)]^-$ complex.

ligand. If one assumes that the O_2 ligand occupies one vertex, then the coordination polyhedron of a metal in structures **XL** and **XLI** may be described as a strongly distorted pseudotrigonal bipyramid with the N(*Phen*) atoms in the equatorial positions and the peroxo ligands, O(10, 11) and O(20, 21), in the axial positions. The dihedral angle between the pseudoequatorial and pseudoaxial planes of the pseudotrigonal bipyramid (O(30), O(31), N(4), N(41)/O(10), O(11), O(20), O(21)) equals 89.9° and 89.8° in structures **XL** and **XLI**, respectively. The average bond lengths in the two structures are Nb–$O(O_2)$ 1.986 Å, O–$O(O_2)$ 1.499 Å, and Nb–N 2.310 Å; the $O(O_2)NbO(O_2)$ angle equals 44.4°. The O–O bond length in the water molecule of crystallized H_2O_2 of the **XLI** structure equals 1.425(10) Å.

The short communication [60] describes the $(NMe_4)_2[V(OH)(O_2)_3] \cdot 4H_2O$ structure (**XLII**) with an unusual geometry: a one-capped trigonal–prismatic seven-vertex coordination polyhedron of a metal atom. The symmetry axis 3 passes in the complex anion of the trigonal crystal through the capped hydroxoligand and the central vanadium atom; the local symmetry of the complex is 3*m*. The V atom is displaced from the trigonal plane of the prism by 0.17 Å. All the hydrogen atoms in the structure are disordered. One may assume that the coordination seven-vertex polyhedron of a metal in structure **XLII** is reduced to a pseudotetrahedron with three η^2-peroxo and one σ hydroxoligands at the vertices.

The one-capped trigonal–prismatic geometry characteristic of structure **XLII** is also possessed by a complex anion in the $(NH_4)_2[V(O_2)_3F] \cdot H_2O$ compound [61] whose structure is determined with a very low accuracy ($R = 25\%$).

7. MONONUCLEAR PEROXO COMPLEXES OF NIOBIUM(V) AND VANADIUM(V) WITH $M : O_2 = 1 : 4$

Table 5 lists the geometrical parameters of three mononuclear tetraperoxo complexes of Nb(V) and V(V) with $M : O_2 = 1 : 4$ (**XLIII**–**XLV**).

Table 4. The basic bond lengths (Å) in pseudooctahedral oxomonoperoxo complexes of vanadium(V)

No.	Compound	V–O(peroxo) V–O(oxo)	V–L, *trans* to O₂ V–L, *trans* to O(oxo)	V–L_{cis}	Δ(O₂) Δ(O)	Reference
XXVII	K[VO(O₂)(*DL-Cmhis*)] · H₂O	1.878(1) ± 0.004 1.598(1)	2.169(2) N(*Cmhis*) 2.144(1) O(*Cmhis*)	2.156(2) N(*Cmhis*) 2.045(1) O(*Cmhis*)	0.013 0.099	[46]
XXVIII	[VO(O₂)(*Bpg*)] · H₂O	1.867(2) ± 0.002 1.615(1)	2.217(2) N(*Bpg*) 2.085(2) O(*Bpg*)	2.143(2) ± 0.005 N(*Brg*)	0.074	[47]
XXIX	[VO(O₂)(*Py*)(*Pyanaph*)]	1.853 ± 0.006 1.708	2.124 N(*Pyanaph*) 2.439 N(*Py*)	2.124 N(*Pyanaph*) 2.001 O(*Pyanaph*)	0.000	[48]
XXX	[VO(O₂){HB(*Pz*)₃}(*Pz*H)] · Tgf	1.875(1) ± 0.013 1.603(4)	2.203(5) 2.324(5) } N(HB(*Pz*)₃)	2.122(5) N(HB)(*Pz*)₃) 2.165(5) N(PzH)	0.081 0.202	[49]
XXXI	[VO(O₂)(*Bipy*)₂]ClO₄	1.840(5) ± 0.028 1.625(3)	2.247(4) 2.243(5) } N(*Bipy*)	2.131(4) ± 0.005 N(*Bipy*)	0.116 0.112	[50]
XXXII	[VO(O₂)(*Phen*)₂]ClO₄	1.85(2) ± 0.02 1.60(1)	2.24(2) 2.24(2) } N(*Phen*)	2.12(2) ± 0.01 N(*Phen*)	0.12 0.12	[50]
XXXIII	K₃[VO(O₂)(*Ox*)₂] · 0.5H₂O	1.876(6) ± 0.006 1.625(6)	2.147(3) 2.142(3) } O(*Ox*)	2.021(3) ± 0.003 O(*Ox*)	0.126 0.121	[51]
XXXIV	[VO(O₂)(*Phen*)(H₂O)₂]Cl · 0.38H₂O	1.876(2) ± 0.011 1.589(2)	2.201(2) N(*Phen*) 2.209(3) O(H₂O)	2.157(2) N(*Phen*) 2.075(2) O(H₂O)	0.044 0.134	[52]
XXXV	(NH₄)[VO(O₂)(*Bipy*)F₂] · 2H₂O	1.88(2) ± 0.03 1.602(9) ± 0.006	2.20(1) ± 0.02 N(*Bipy*) 2.223(8) ± 0.030 F	2.21(1) ± 0.01 N(*Bipy*) 1.891(9) ± 0.015 F	−0.01 0.332	[53]
XXXVI	(NH₄)₂[VO(O₂)(μ-*Mal*H)]₂ · 2H₂O	1.878(1) ± 0.007 1.602(1) ± 0.001	2.000(1) ± 0.009 O$_{xm}$(*Mal*H) 2.286(1) ± 0.016 O$_x$(*Mal*H)	2.030(1) ± 0.000 O$_{xm}$(*Mal*H) 2.036(1) ± 0.001 O$_x$(*Mal*H)	−0.030 0.250	[54]
XXXVII	K₂[VO(O₂)(μ-*Cit*H₂)]₂ · 2H₂O	1.880(1) ± 0.008 1.601(1)	1.991(1) O$_{xm}$(*Cit*H₂) 2.561(1) O$_x$(*Cit*H₂)	2.039(1) O$_{xm}$(*Cit*H₂) 2.013(1) O$_x$(*Cit*H₂)	−0.048 0.548	[55]
XXXVIII	K₂[VO(O₂)(μ-*Tart*H₂)₂(μ-H₂O)] · 0.5H₂O	1.882(5) ± 0.021 1.586(5) ± 0.002	2.018(5) ± 0.008 O$_{xm}$(*Tart*H₂) 2.394(6) ± 0.004 O$_m$(H₂O)	2.009(5) ± 0.006 O$_{xm}$(*Tart*H₂) 2.002(6) ± 0.005 O$_x$(*Tart*H₂)	0.009	[56]
XXXIX	(N*Et₄*)₂[VO(μ-O₂)(*GlyGly*)]₂ · 3.16H₂O	1.893(4) ± 0.016 1.593(4) ± 0.008	2.034(5) ± 0.001 N$_x$(*GlyGly*) 2.617(4) ± 0.04 O$_m$(O₂)	2.114(4) ± 0.003 N$_x$(*GlyGly*) 2.010(1) ± 0.001 O$_x$(*GlyGly*)	−0.080	[57]

Note. We used the following notations: m—bridging atom, x—chelating atom, and xm—chelate-bridging atom. Notation of acids and other ligands: H₂O*x*—oxalic acid, H₃*Mal*—malonic acid, H₄*Cit*—citric acid, H₄*Tart*—tartric acid, H₂*Cmhis*—*N*-carboxymethylhistidine, H*Bpg*—*N*,*N*-bis(2-pyridyl-2-methyl)glycine, H*Pyanaph*—1-(2-pyridine-2-naphthalene), H₂B(*Pz*)₃—hydrotris(3,5-diisopropyl-1-yl)borate, *Pz*H—3,5-diisopropylpyrazole, *Bipy*—2,2'bipyridyl, *Phen*—1,10-phenanthroline, H₂*GlyGly*—glucylglycine.

Table 5. Geometrical parameters (Å) of the peroxo complexes of the d^0 metals of Groups IV and V (Ti, V, Nb, Ta) with $M : O_2 = 1 : 3$ and $1 : 4$

No.	Compound	M–O(O_2)	O–O(O_2)	M–L	Reference
XL	K[Nb(O_2)$_3$(*Phen*)] · 3H$_2$O	1.987(7) ± 0.027	1.489(9) ± 0.019	2.307(8) ± 0.026 N(*Phen*)	[59]
XLI	K[Nb(O_2)$_3$(*Phen*)] · 3H$_2$O · H$_2$O$_2$	1.985(6) ± 0.020	1.509(6) ± 0.015	2.314(6) ± 0.007 N(*Phen*)	[59]
XLIII	KMg[Nb(O_2)$_4$] · 7H$_2$O	2.026(3) ± 0.040	1.500(4) ± 0.005		[62]
XLIV	Na$_3$[V(O_2)$_4$] · H$_2$O$_2$ · 10.5H$_2$O	1.918(1) ± 0.016	1.470(2) ± 0.003		[63]
XLXLV	Na$_3$[VO(O_2)$_4$] · 14H$_2$O	1.915(2) ± 0.045	1.500(4) ± 0.031		[63]

The metal atom in the complex $[M(O_2)_4]^{3-}$ anions (M = Nb and V) with the local symmetry D_{2d} is coordinated over the vertices of a dodecahedron (pseudotetrahedron) with eight atoms of four peroxo ligands coordinated in an η^2-fashion.

In the KMg[Nb(O_2)$_4$] · 7H$_2$O structure (**XLIII**) [62], the [Mg(H$_2$O)$_6$]$^{2+}$ cations are linked by hydrogen O–H···O bonds into layers with the K$^+$, [Nb(O_2)$_4$]$^{3-}$, and H$_2$O molecules of water of crystallization in between.

The structures of two tetraperoxovanadates of Na$_3$[V(O_2)$_4$] · 10.5H$_2$O · H$_2$O$_2$ (**XLIV**) [63] and Na$_3$[V(O_2)$_4$] · 14H$_2$O (**XLV**) [63] are partly disordered. In structure **XLIV**, one of the Na atoms occupies the position with occupancy 0.5, whereas the positions of three oxygen atoms (from one water molecule of crystallization and an H$_2$O molecule) with occupancy 0.5 are overlapped. In structure **XLV**, four disordered O$_2$ ligands uniquely determine two equally probable orientations of the centrosymmetric [V(O_2)$_4$]$^{3-}$ complex (Fig. 10 shows only one orientation; the site occupancy factors of the O(2A), O(2B), O(4A0, and O(4B) atoms are equal to 0.5). In the [M(O_2)$_4$] dodecahedra of the opposite peroxo groups, the O(1)VO(2)- and O(2A)VO(2B)-type angles (Fig. 10) are close to 180 and 88°, respectively, 177.81(5)° and 87.76(5)° in **XLIV**, and 180° and 87.7(1)° in **XLV**, whereas in diperoxovanadates these angles are close to 150° and 90°, respectively.

The synthesis of tri- and tetraperoxo compounds is rather difficult [63] since the alkali solutions used for obtaining [M(O_2)$_4$] and [M(O_2)$_3$] complexes are rather unstable because of hydroperoxide decomposition. It is also indicated [63] that the complex color (pale yellow for [V(OH)(O_2)$_3$]$^{2-}$ and [VO(O_2)$_3$]$^{3-}$ and blue or purple for K$_3$[V(O_2)$_4$] powders) is not the sign that allows one to uniquely identify (and distinguish) tri- and tetraperoxo complexes of vanadium(V).

8. PSEUDOTETRAHEDRAL MONONUCLEAR MONOPEROXO COMPLEXES OF NIOBIUM(V) AND TANTALUM(V) WITH CYCLOPENTADIENYL LIGANDS

Table 6 lists the geometrical parameters of two mononuclear complexes of the metals of Group V described by the general formula [(η^5-Cp)$_2$$M$($O_2$)L], Cp = C$_5H_5$, M = Nb, L = Cl (**XLVI**) [64]; and Cp = C$_5$$Me_5$, M = Ta, L = CH$_2$Ph (**XLVII**) [65] (Fig. 11)

The bent sandwich **XLVI**, **XLVII** structures contain two O(peroxo) atoms, a metal atom, and the σ atom of the L ligand (Cl in **XLVI**, C(benzyl) in **XLVII**) which lie in one plane (A) intersecting the plane Cp_2M (B) (the average value of the dihedral A/B angle in **XLVI** structure equals 26.4° ± 0.5°).

Bkouche–Waksman *et al.* [64] describe a coordination polyhedron of Nb atoms in two independent molecules in **XLVI** as a pseudotetrahedron with the centroid (Ctr) of two Cp ligands, the midpoint (MP) of the peroxo ligand, and the Cl atom at the vertices. In a NbCt$_2$(MP)Cl pseudotetrahedron, the average values of
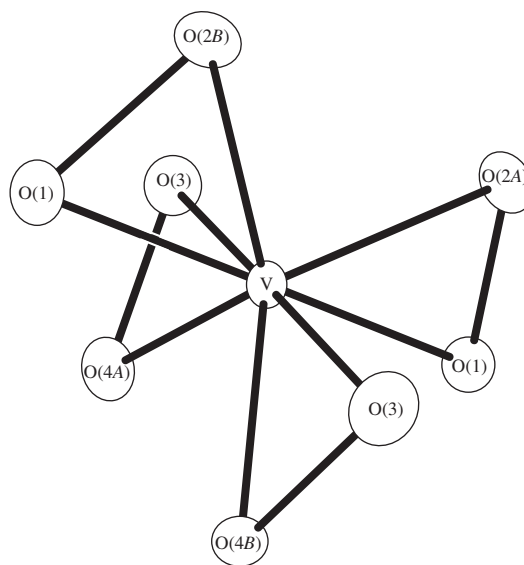
Fig. 10. Structure of a pseudooctahedral mononuclear [V(O_2)$_4$]$^{3-}$] complex.

Table 6. Geometrical parameters (Å) of peroxo complexes with cyclopentadienyl ligands and alkyl-peroxo complexes of the d^0 metals of Groups IV and V

No.	Compound	M–O(O₂)	O–O(O₂)	M–L	Reference
XLVI	[(η⁵-C₅H₅)₂Nb(O₂)Cl]	1.985(10) ± 0.015	1.47(1) ± 0.00	2.482(3) ± 0.002 Cl 2.13(1) ± 0.00 *Ts* 2.44(1) ± 0.03 C(*Cp*)	[64]
XLVII	[(η⁵-C₅*Me*₅)₂Ta(O₂)(CH₂*Ph*)]	1.976(6) ± 0.021	1.477(8)	2.323(9) C(CH₂*Ph*) 2.20(1) ± 0.01 *Ctr* 2.51(1) ± 0.05 C(*Cp*)	[65]
XLVIII	[(η⁵-C₅*Me*₅)₂Hf(*tert-Bu*OO)(*Et*)]	1.970 (O)	1.487	2.278(3) C(*Et*) 2.249 ± 0.003 *Ctr* 2.554 ± 0.026 C(*Cp*)	[67]
XLIX	[VO(*tert-Bu*OO)(*Dipic*)(H₂O)]	1.872(3) (O) 1.999(3) (O(C))	1.436(5)	1.574(3) O(*okco*) 2.058(4) N(*Dipic*) 1.990(3) ± 0.007 O(*Dipic*) 2.234(3) O(H₂O)	[68]

Note: *Ctr* is the center of the cyclopentadienyl ring; *Cp* are the C₅H₅ and C₅*Me*₅ ligands.

the angles at the metal atom are Ctr–Nb–Ctr 128.4(4)° ± 0.3°, Ctr–Nb–MP 109.6(4)° ± 0.9°, Cl–Nb–MP 100.2(3)° ± 0.2°, and Cl–Nb–Ctr 102.4(4)° ± 1.2°.

The bent sandwich structure (and the staggered conformation of *Cp* ligands) of a **XLVI** crystal is consistent with the structures of other Cp_2Nb complexes: the Ctr–Nb–Ctr angles for six similar compounds range within 129°–143° (Table 4 in [64] and references there). The Ctr–Ta–Ctr angle in **XLVII** structure (134.6°) also lies within this range.

Van Asselt *et al.* [65] describe synthesis of a number of complexes with the general formula (η⁵-C₅*Me*₅)₂Ta(O₂)R, where $R = $ CH₂*Ph* (**XLVII**), *Me*,

Scheme 3

Ph, CH₂*Me*, and CH₂CH₂*Me*, which are remarkably stable, especially in the solid state (for several days in range from room temperature to –30°C). A crystal of benzyl peroxide derivative **XLVII** is isostructural and isoelectronic to (η⁵-C₅H₅)₂Nb(η⁵-C₂H₄)(CH₂*Me*) [66].

Van Asselt *et al.* [65] indicate that the electrophilic attack of the Cp_2Ta(O₂)R complexes at the exo-oxygen atom enhances the heterolysis of the O–O bond in the migration of the alkyl or Ph group (scheme 3). In a similar way, the nucleophilic attack of phosphines or SO₂ at the endo-oxygen atom should be enhanced if the Lewis acids are coordinated to endo-oxygen atom. The acid-catalyzed rearrangement mechanism Cp_2Ta(O₂)(R) ⟶ Cp_2Ta(O)(OR) is similar to the mechanism suggested for rearrangement of the isoelectronic Cp_2Hf(*tert-Bu*OO)(R) ⟶ Cp_2Hf(*tertBu*O)(OR), where [*tert-Bu*]⁺ formally serves the role of the electrophile [E]⁺ (scheme 3).

In the Cp_2Hf(O₂)(*Et*) complex, where $Cp = $ C₅*Me*₅ [67], described in Sect. 9, oxidation of the ethyl to the ethoxy ligand takes place at 33°C.

9. MONONUCLEAR HF(IV), Ti(IV), AND V(V) COMPLEXES WITH *tert*-BUTYLPEROXO LIGANDS

The bent sandwich Cp_2Hf(*tert-Bu*OO)(*Et*) complex (**XLVIII**) [67] (Fig. 12) is the only example of the compounds of transition metals of Group IV and V in which the peroxo ligand, in this case, the alkylperoxo group OOR (R = C*Me*₃), coordinates the metal in the σ monodentate and not the η² or η²,μ mode. In this case, the Hf–O and O–O bond lengths typical of the η²-coordinated O₂ ligands are equal to 1.970 and 1. 487, respec-
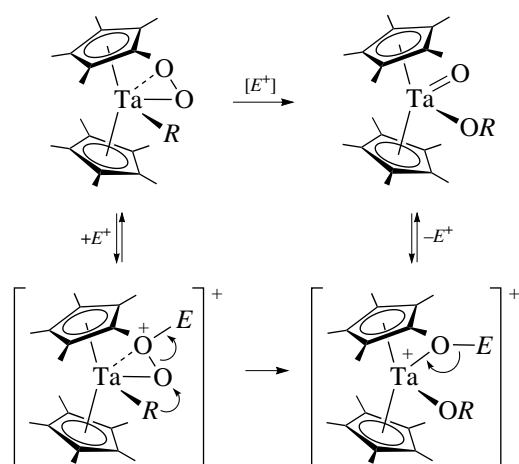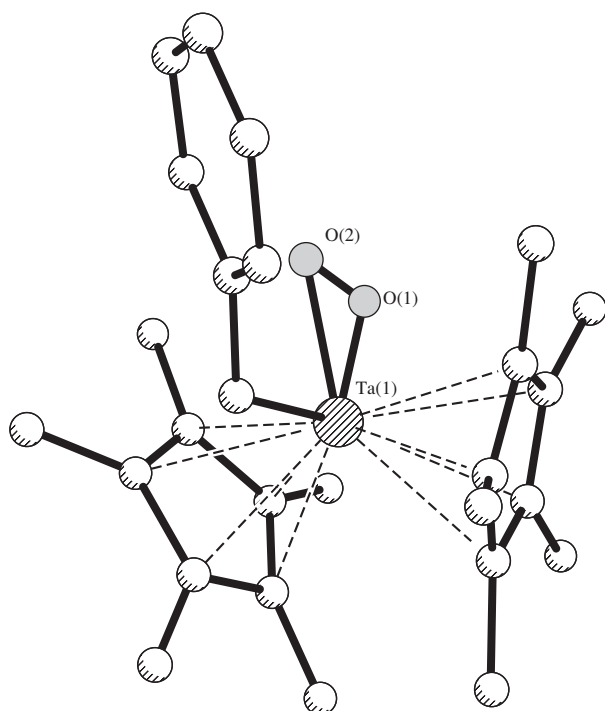
Fig. 11. Structure of a $(C_5Me_5)_2Ta(O_2)(CH_2Ph)$ complex.
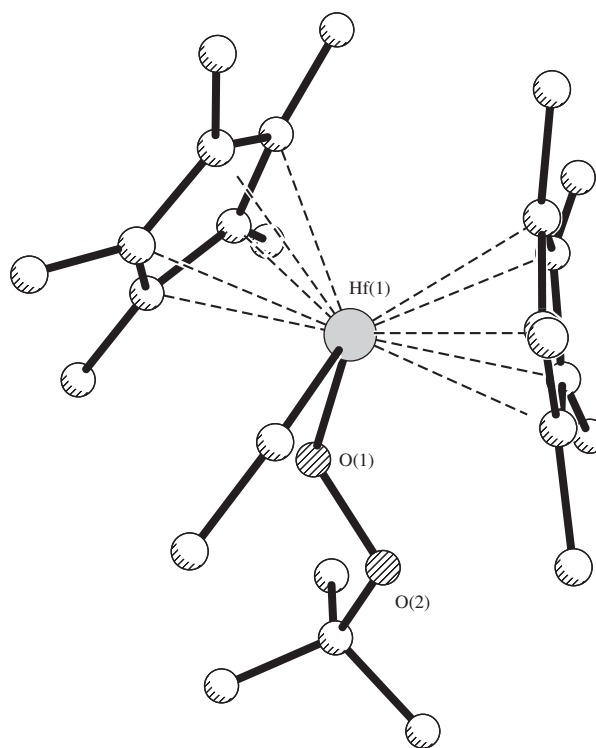
Fig. 12. Structure of a $(C_5H_5)_2Hf(tert\text{-}BuOO)(Et)$ complex.

tively. The O–C bond equals 1.436 Å, the OOC angle equals 108.5°.

In two pseudooctahedral *tert*-butylperoxo complexes—mononuclear [VO(*tert*-)*Bu*OO)(*Dipic*)(H$_2$O)] (**XLIX**) [68] (Fig. 13) and binuclear [Ti(*tert*-)*Bu*OO)(μ-*Toea*)}$_2$] (**X**) described above [13] (Fig. 3, Table 2)—the alkyl-peroxo ligand is coordinated in the η^2 mode. The most pronounced difference between the geometries of the η^2-coordinated OO*R* and O$_2$ ligands is the essentially nonequivalent *M*–O and *M*–O*R* bonds in the first case. In structure **XLIX**, the V–O(6) bond to the O(C) atom is longer by 0.127 Å than the V–O(5) one (1.999(3)) and 1.872(3) Å, respectively). In structure **X**, this difference (0.356 Å) is much more pronounced (Ti–O(2) 2.269(2), Ti–O(1) 1.913 Å). Other geometrical parameters of alkyl-peroxo ligands in structures **XLIX** and **X** have usual values: O–O(C) 1.436(5) and 1.469(3) Å, respectively. In structure **XLIX**, the O(6)–C bond length is equal to 1.503(6) Å and the angles are equal to O(5)VO(6) 43.4(1)° and O(5)O(6)C 114.9(3)°.

The X-ray diffraction data for crystal **X** are consistent with the quantum chemical calculations [69]; the calculated Ti–O and Ti–O(C) distances are equal to 1.906 and 2.294 Å, respectively.

10. GEOMETRICAL PARAMETERS OF $M(O_2)_n$ FRAGMENTS IN PEROXO COMPLEXES OF GROUP IV AND V METALS

The O–O distances in peroxo groups coordinated in the bidentate (dihapho) mode range within a large interval (for transition metals of Groups IV–VI, from 1.36 to 1.54 Å [70]). In pseudotrigonal bipyramidal and pseudotetrahedral oxodiperoxovanadates(V), the O–O distances in 23 structures range within a narrow interval: 1.44–1.49 Å ([4], Tables 5 and 6). The transition to pseudooctahedral oxomonoperoxovanadates(V) results in shortening of the O–O bonds. In most of the compounds (31 from total 34) ([4], Table 4), the O–O distances range within 1.35–1.46 Å. The anomalously short O–O bonds inconsistent with the conventional interval of their variation were observed in [VO(O$_2$)L_2]ClO$_4$ structures, where $L = Bipy$ (**XXXI**) [50], *Phen* (**XXXII**) [50], and [VO(O$_2$)(*Pic*)$_2$] · 2.5H$_2$O (**L**) [52] and are equal to 1.24, 1.30, and 1.29 Å, respectively. Although this shortening of the O–O bonds (in particular, in structure **L**) seems to be a result of the statistical mixing of the positions of the oxo and peroxo ligands in the crystal, the O–O bonds in pseudooctahedral VO(O$_2$) complexes vary within the wide range, 1.24–1.46 Å ([4], Table 4) and, in fact, are beyond the lower boundary of the narrow range of O–O bond lengths (1.46–1.47 Å) for 14 formally also-seven-fold coordinated VO(O$_2$) complexes having quite different geometry: pseudotrigonal–bipyramidal ([4], Tables 5
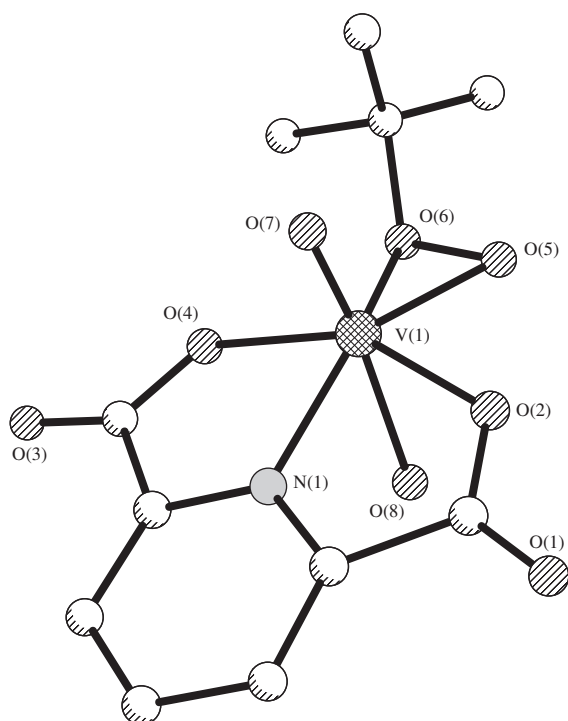
Fig. 13. Structure of a [VO(*tert-Bu*OO)(*Dipic*)(H$_2$O)] complex.

and 6). In this case, the pseudooctahedral VO(O$_2$) complexes show a certain correlation of the O–O bond lengths and the parameters Δ and Δ'(O$_2$): the weak structural manifestation of the *trans* effect of the peroxo group and its absence (Δ, Δ'(O$_2$) = –0.05…+0.08 Å) is characteristic of the complexes with relatively large O–O distances (1.41–1.46 Å). Strong structural manifestation of the *trans* effect (Δ, Δ'(O$_2$) = +0.08…+0.26 Å) is characteristic of the compounds with short O–O bond lengths (1.24–1.43 Å).[12] The average Δ, Δ'(O$_2$) and O–O values in the first group are equal to +0.028 and 1.434 Å and in the second group are +0.137 and 1.342 Å, respectively ([4], Fig. 8). Shortening of the O–O bond in the VO(O$_2$) complexes is accompanied by a decrease in the OVO angle in the dioxygen ligand ([4], Fig. 9, Table 4).

In the Ti(IV) and Nb(V) peroxo complexes, the O–O distances lie within the characteristic range, 1.42–1.51 Å (Tables 2, 3, 5 in the present article).[13]

---

[12] Δ'(O$_2$) is the difference between the V–L_{trans} bond length and the average statistical (standard) V–L_{stand} distance formed by an atom of the same species (in the absence of the same ligands and also in the *trans* and *cis* positions to O2): V–L_{stand} = 2.136, 2.027, and 2.060 Å for the L_{stand} = N(neutro), O(acido), and O(H$_2$O), respectively.

[13] The deviations from this range to both sides in the Ti(IV), Nb(V) and Ta(V) peroxo complexes (O–O 1.17–1.35 and 1.55–1.70 Å) are explained by disorder in the O$_2$ ligand, a low accuracy of the photographic method, or by both these factors.

In principle, shortening of the O–O bond in η^2-dioxygen ligand, which signifies the intensified transfer of the electron density from this ligand to the central atom, should be accompanied by shortening of the three-center multiple O$_2$–M bond [71]. As a general tendency, this correlation may be followed on an example of pseudooctahedral oxomonoperoxovanades ([4], Fig. 10, Table 4). To the interval of the O–O distances 1.36–1.46 Å calculated for 27 VO(O$_2$) structures there correspond the V–O(peroxo) distances ranging within 1.85–1.89 Å, whereas to the shortest O–O bonds in structures **XXXI** [50], **XXXII** [50], and **L** [52] and K$_2$[{VO(O$_2$)}$_2$(μ-*Lact*)$_2$] (**LI**) [72] (1.24, 1.30, 1.29, and 1.35 Å, respectively) there correspond relatively short V–O(peroxo) bonds (1.84 Å in all the four structures).

Practically in all the psedooctahedral VO(O$_2$) complexes (with only one exception[14]), the η^2-peroxo ligand is coordinated symmetrically with respect to the metal: the difference between the lengths of two V–O(O$_2$) bonds usually does not exceed Δ(V–O$_2$) = ±0.015 Å ([4], Table 4). The O$_2$ ligand in pseudooctahedral monoperoxo complexes of Ti(IV) and Nb(V) is also symmetrically coordinated (within Δ(V–O$_2$) = ±0.02 Å) (Table 2 and 3 of the present article).

One cannot uniquely state the type of coordination of the O$_2$ ligands either for Nb(V) complexes with Nb : O$_2$ = 1 : 3 (**XL, XLI**) [59] or for the Nb(V) and V(V) compounds with M : O$_2$ = 1 : 4 (**XLIII–XLV**) [62, 63]. Each of the five structures has both symmetrically (Δ(V–O$_2$) = ±0.001–0.014 Å) and asymmetrically (Δ(V–O$_2$) = ±0.020–0.036 Å) coordinated η^2-peroxo groups.

The most obvious asymmetry in the orientation of peroxo groups caused by steric hindrances in the contacts of the equatorial ligands is seen in both (O$_2$)$_e$ groups of diperoxo complexes of transition metals and, in particular, of vanadium(V) with the coordination polyhedra either of the type of a pseudotrigonal bipyramid (pentagonal bipyramid) or of a pseudotetrahedron (pentagonal pyramid). In this case, the M–O(O$_2$)$_{cis}$ bonds close to the equatorial donor atoms of the heteroligand L are longer than the M–O(O$_2$)$_{trans}$ bonds to neighboring oxygen atoms remote from this L_e atom. The interval of the average V–(O$_2$)$_{cis}$ bond lengths in 15 compounds ranges within 1.89–1.95 Å; the range of the V–(O$_2$)$_{trans}$ bond lengths is 1.86–1.89 Å; the difference between these values $\Delta_{cis–trans}$ ranges within 0.02–0.07 Å ([4], Table 5). Of course, the L_eVO$_{cis}$ angles are considerably less than the L_eVO$_{trans}$ angles (84.8°–90.0° and 128.6°–134.3°, respectively), and the VO$_{cis}$O$_{trans}$ angles

---

[14] In the (NH$_4$)$_{1.5}$[VO(O$_2$)(*Edta*H)] structure [73], the peroxo group is oriented pronouncedly asymmetrically with respect to the metal atom: V–O(O2) 1.74(1) and 1.88(1) Å and O–O 1.39(2) Å.

Table 7. Valence O*M*O and *M*OO angles (deg) in the $M(O_2)$ fragments of peroxo complexes of titanium(IV) and niobium(V)*

No**	Angle		Reference
	O*M*O	*M*OO	
I	45.2(2)		[5]
II	45.7(2) ± 0.0	67.1(2) ± 0.1	[6]
III	46.6(1)	66.5(1)	[7]
IV	46.72(6)	65.64(6) ± 0.14	[8]
V	46.88(6)	66.56(5)	[9]
VI	46.5(2)	66.8(2) ± 0.6	[8]
VII	43.5(2)	68.3(2) ± 0.3	[10]
VIII	45.2(4)	67.4(4) ± 1.2	[11]
IX	45.72(6)	67.14(6) ± 0.12	[12]
XI	45.8(1)	67.9(1) ± 0.3	[14]
XII	46.7(2)	66.7(2) ± 0.2	[15]
XIII	45.0(2)		[22]
XIV	44.0(9) ± 1.8		[23]
XV	45.1(1)		[24]
XVI	45.0(4) ± 0.6		[25]
XXIV	44.1(2) ± 0.0	68.0(2) ± 0.8	[37]
XXV	44.9 ± 1.2	67.5 ± 1.8	[38]
XXVI	44(1)		[41]
XL	44.0(3) ± 0.5	68.0(4) ± 1.3	[59]
XLI	44.7(3) ± 0.5	67.7(3) ± 1.1	[59]
XLIII	43.5(1) ± 0.5	68.3(1) ± 2.6	[62]
XLVI	43.6(3) ± 0.0	68.2(7) ± 1.3	[64]

* The OVO and VOO angles for oxoperoxo complexes of vanadium(V) are given in [4] (Tables 4–6).

** Formulas of compounds **I–IX**, **XI**, and **XII** are given in Table 2; those of complexes **XIII–XVI** and **XXIV–XXVI**, in Table 3; those of **XL**, **XLI**, and **XLIII**, in Table 5, and that of **XLVI**, in Table 6.

$(65.2°–66.7°)$ are less than $VO_{trans}O_{cis}$ angles $(67.5°–69.7°)$.[15]

As has already been noted, on the average, the $V–O_2$ bonds in oxoperoxo complexes $(V : O_2 = 1 : 1)$ are shorter than in oxodiperoxo compounds $(V : O_2 = 1 : 2)$; they range within 1.81–1.89 and 1.87–1.92 Å, respectively ([4], Tables 4 and 5). This elongation is quite natural if one takes into account the weakened transfer of the electron density from peroxo groups to metal with an increase in the number of multiply bonded ligands (competition of two and more peroxo groups in donating electrons to a metal). The similar elongation of the $M–O_2$ bonds with an increase the $M : O_2$ ratio is

_____

[15] The asymmetry of the V–O(peroxo) bonds in oxoperoxo complexes of transition metals is discussed in more detail elsewhere [71, 74].

observed in peroxo complexes of niobium(V): 1.88–1.96, 1.97, 1.99, and 2.03 Å at Nb : O_2 = 1 : 1, 1 : 2, 1 : 3, and 1 : 4, respectively.

The position of a transition metal in the periodic table also affects the length of a metal–peroxo ligand bond. An increase in the covalent radius of a metal downward from the 4th to the 6th period in the V ⟶ Nb ⟶ Ta row results in the elongation of the $M–O_2$ bond length at the $M : O_2$ = 1 : 1 within 1.81–1.89 Å for M = V ([4], Table 4), 1.88–1.96 Å for M = Nb, and 1.93–1.97 Å for M = Ta (Table 3). In principle, a certain decrease in the covalent radius of a metal from left to right should result in shortening of the $Ti–O_2$ bonds in comparison with the $V–O_2$ bonds. However, the intervals of these values at $M : O_2$ = 1 : 1 are practically the same: 1.82–1.89 and 1.81–1.89 Å, respectively (Tables 2 and 3).

Table 7 lists the valence angles O*M*O and *M*OO in the $M(O_2)$ fragments of peroxo complexes of Ti(IV) and Nb(V). The ranges of the O*M*O $(43.5°–46.9°)$ and *M*OO $(65.6°–68.3°)$ angles in these compounds agree with the ranges of the corresponding angles in oxo peroxo complexes of vanadium(V) ([4], Tables 4 and 5).

CONCLUSIONS

Summarizing all considered above, we should like to emphasize the following characteristics of the structures of the peroxo complexes of the transition metals of Groups IV and V.

The formation of one or another geometry of the coordination polyhedron is determined, first and foremost, by the metal : peroxo ligand ratio equal to 1 : 1, 1 : 2, 1 : 3, or 1 : 4.

Two multiply bonded ligands, $2(O_2)_{peroxo}$ or $(O_2)_{peroxo}(O)_{oxo}$, are always located in *cis* positions to one another.

The structural manifestation of the *trans* effect of the peroxo ligand in oxomonoperoxo complexes of V(V) is comparable with this effect in the oxo ligand.

The geometrical parameters of peroxo ligands (lengths of the $V–O_2$ and O–O bonds and values of the OVO angles) in the $VO(O_2)_n$ complexes depend on the type of the coordination seven-vertex polyhedron (pseudooctahedron, $n = 1$ or pseudotrigonal bipyramid, $n = 2$).

In order to compare the structures of peroxo complexes of various metals, it is necessary to accumulate more experimental data on the compounds of this class (in particular, on peroxo complexes of zirconium(IV) and hafnium(IV)).

REFERENCES

1. I. I. Vol'nov, *Peroxocomplexes of Vanadium, Niobium, and Tantalum* (Nauka, Moscow, 1987) [in Russian].

2. A. Butler, M. J. Clague, and G. E. Meister, Chem. Rev. **94** (3), 625 (1994).

3. V. S. Sergienko, Russ. J. Inorg. Chem. **48** (Suppl. 1), S55 (2003).

4. V. S. Sergienko, Kristallografiya **44** (3), 467 (2004).

5. H. Mimoren, M. Postel, F. Casabianca, *et al.*, Inorg. Chem. **21** (4), 1303 (1982).

6. M. Postel, F. Casabianca, Y. Gauffreteau, and J. Fisher, Inorg. Chim. Acta **113** (2), 173 (1986).

7. J. R. Hagadorn and J. Arnold, Inorg. Chem. **36** (14), 2928 (1997).

8. D. Schwarzenbach, Helv. Chim. Acta **55** (8), 2990 (1972).

9. H. Manohar and D. Schwarzenbach, Helv. Chim. Acta **57** (4), 1086 (1974).

10. P. Jeske, G. Haselhorst, T. Weyhermüller, *et al.*, Inorg. Chem. **33** (11), 2462 (1994).

11. D. Schwarzenbach, Inorg. Chem. **9** (11), 2391 (1970).

12. D. Schwarzenbach, Helv. Chim. Acta **58** (8), 2391 (1975).

13. G. Boche, K. Möbus, K. Harms, and M. Marsh, J. Am. Chem. Soc. **118** (11), 2770 (1996).

14. M. Kakihana, M. Tada, M. Shiro, *et al.*, Inorg. Chem. **40** (5), 891 (2001).

15. R. Guilard, J.-M. Latour, C. Lecomte, *et al.*, Inorg. Chem. **17** (5), 1228 (1978).

16. H. Mimoun, J. Mol. Catal. **7** (1), 1 (1980).

17. H. Tomioka, K. Takai, K. Oshima, and H. Nozaki, Tetrahedron Lett. **21** (20), 4843 (1980).

18. S. E. Jacobson, R. Tang, and F. Mares, J. Chem. Soc. Chem. Commun., No. 20, 888 (1978).

19. L. Hubert-Pfalzgraf, A. A. Pinkerton, and J. G. Riess, Inorg. Chem. **17** (3), 663 (1978).

20. B. Chevrier, T. Diebold, and R. Weiss, Inorg. Chim. Acta **19** (1), L57 (1976).

21. R. Hoffmann, M. M. L. Chen, and D. L. Thorn, Inorg. Chem. **16** (3), 503 (1977).

22. R. Stomberg, Acta Chem. Scand. A **34** (3), 193 (1980).

23. R. Stomberg, Acta Chem. Scand. A **35** (7), 489 (1981).

24. R. Stomberg, Acta Chem. Scand. A **35** (6), 389 (1981).

25. R. Stomberg, Acta Chem. Scand. A **36** (1), 101 (1982).

26. Ž. Ružic-Toroś and B. Kojić-Prodić, Acta Crystallogr., Sect. B: Struct. Crystallogr. Cryst. Chem. **33** (3), 692 (1977).

27. R. Stomberg, Acta Chem. Scand. A **37** (7), 523 (1983).

28. Ž. Ružic-Toroś, B. Kojić-Prodić, and M. Šljukić, Acta Crystallogr., Sect. B: Struct. Crystallogr. Cryst. Chem. **32** (4), 1096 (1976).

29. J. C. Dewan, A. J. Edwards, J. Y. Calves, and L. E. Guerchais, J. Chem. Soc. Dalton Trans., No. 10, 981 (1977).

30. W. Massa and G. Pausewang, Z. Anorg. Allg. Chem. **456** (9), 169 (1979).

31. W. Massa and G. Pausewang, Mater. Res. Bull. **13** (4), 361 (1978).

32. Ž. Ružic-Toroś, B. Kojić-Prodić, and M. Šljukić, Inorg. Chim. Acta **86** (3), 205 (1984).

33. R. Stomberg and I.-B. Svenson, Acta Chem. Scand. A **31** (8), 635 (1977).

34. D. Grandjean and R. Weiss, Bull. Soc. Chim. Fr., No. 8, 3040 (1967).

35. H. L. Carrell and J. Donohue, Isr. J. Chem. **10** (2), 195 (1972).

36. R. Schmidt, G. Pausewang, and W. Massa, Z. Anorg. Allg. Chem. **488** (5), 108 (1982).

37. G. Mathern and R. Weiss, Acta Crystallogr., Sect. B: Struct. Crystallogr. Cryst. Chem. **27** (8), 1572 (1971).

38. M. K. Harrup, G.-S. Kim, H. Zeng, *et al.*, Inorg. Chem. **37** (21), 5550 (1998).

39. J. F. Keggin, Proc. R. Soc. London, Ser. A **144** (1), 75 (1934).

40. B. Dawson, Acta Crystallogr. **6** (1), 113 (1953).

41. D. A. Judd, Q. Chen, C. F. Campana, and C. L. Hill, J. Am. Chem. Soc. **119** (23), 5461 (1997).

42. E. M. Shustorovich, M. A. Porai-Koshitz, and Y. A. Buslaev, Coord. Chem. Rev. **17** (1), 1 (1975).

43. A. Bodner, P. Jeske, T. Weyhermüller, *et al.*, Inorg. Chem. **31** (18), 3737 (1992).

44. R. Stomberg, Acta Chem. Scand. A **38** (8), 603 (1984).

45. M. A. Poraǐ-Koshits and V. S. Sergienko, Usp. Khim. **59** (1), 86 (1990).

46. K. Kanamori, K. Nashida, N. Miyata, and K. Okamoto, Chem. Lett., 1267 (1998).

47. G. J. Copas, B. J. Hamstra, J. W. Kampf, and V. L. Recoraro, J. Am. Chem. Soc. **118** (14), 3469 (1996).

48. M. Shao, X. Dong, and J. Tang, Sci. Sin., Ser. B (Engl. Ed.) **31**, 789 (1988).

49. M. Kosugi, S. Hikichi, M. Acita, and Y. Morooka, J. Chem. Soc. Dalton Trans., No. 9, 1369 (1999).

50. V. S. Sergienko, V. K. Borzunov, and M. A. Poraǐ-Koshits, Zh. Neorg. Khim. **37** (5), 1062 (1992).

51. R. Stomberg, Acta Chem. Scand. A **40** (2), 168 (1986).

52. V. S. Sergienko, M. A. Poraǐ-Koshits, B. K. Borzunov, and A. B. Ilyukhin, Koord. Khim. **19** (10), 767 (1993).

53. V. S. Sergienko, V. K. Borzunov, and M. A. Poraǐ-Koshits, Dokl. Akad. Nauk SSSR **301** (5), 1141 (1988).

54. C. Djordjevic, M. Lee-Renslo, and E. Sinn, Inorg. Chim. Acta **233** (1), 97 (1995).

55. C. Djordjevic, M. Lee, and E. Sinn, Inorg. Chem. **28** (4), 719 (1989).

56. P. Shwendt, P. Švančárek, L. Kuchta, and L. Marek, Polyhedron **17** (13–14), 2166 (1998).

57. F. W. B. Einstein, R. J. Batcheloz, S. J. Angus-Dunne, and A. S. Tracey, Inorg. Chem. **35** (6), 1680 (1996).

58. M. A. Poraǐ-Koshits and L. O. Atovmyan, Koord. Khim. **1** (9), 1271 (1975).

59. G. Mathern and R. Weiss, Acta Crystallogr., Sect. B: Struct. Crystallogr. Cryst. Chem. **27** (8), 1582 (1971).

60. R. E. Drew, F. W. B. Einstein, J. S. Field, and D. Begin, Acta Crystallogr., Sect. A: Cryst. Phys., Diffr., Theor. Gen. Crystallogr. **31** (3), S135 (1975).

61. K. Westermann, M. Leimkuehler, and R. J. Mattes, J. Less-Common Met. **137** (2), 181 (1988).

62. G. Mathern and R. Weiss, Acta Crystallogr., Sect. B: Struct. Crystallogr. Cryst. Chem. **27** (8), 1598 (1971).

63. T. J. Won, L. Barnes, O. Shlemper, and R. C. Thompson, Inorg. Chem. **34** (17), 4499 (1995).

64. I. Bkouche-Waksman, C. Bois, J. Sala-Pala, and J. E. Guerchais, J. Organomet. Chem. **195** (2), 307 (1980).

65. A. van Asselt, M. S. Trimmer, L. M. Henling, and J. E. Bercaw, J. Am. Chem. Soc. **110** (24), 8254 (1988).

66. L. J. Guggenberger, P. Meakin, and F. N. Tebbe, J. Am. Chem. Soc. **96** (17), 5420 (1974).

67. A. van Asselt, B. D. Santasiero, and I. E. Bercaw, J. Am. Chem. Soc. **108** (26), 8291 (1986).

68. H. Mimoun, P. Chaumette, M. Mignard, and L. Saussine, Nouv. J. Chim. **7** (8–9), 467 (1983).

69. Y.-D. Wu and D. K. W. Lai, J. Am. Chem. Soc. **117** (45), 11327 (1995).

70. R. Stomberg, Acta Chem. Scand. **24** (6), 2024 (1970).

71. P. Schwendt, K. Volka, and M. Suchanek, Spectrochim. Acta A **44** (5), 839 (1998).

72. F. Demartin, M. Biagoli, L. Strinna-Erre, *et al.*, Inorg. Chim. Acta **299** (1), 123 (2000).

73. A. E. Lapshin, Yu. I. Smolin, Yu. F. Shepelev, *et al.*, Kristallografiya **37** (6), 1415 (1992) [Sov. Phys. Crystallogr. **37**, 764 (1992)].

74. R. Stomberg and H. Szentivanyi, Acta Chem. Scand. A **38** (2), 121 (1984).

75. F. H. Allen and O. Kennard, Chem. Design. Autom. News **8** (1), 31 (1993).

Translated by L. Man

STRUCTURE
OF INORGANIC COMPOUNDS

Magnetic Properties and Crystal Structure of β-Ta

V. F. Shamraĭ*, J. K. Warhulska**, A. V. Arakcheeva*, and V. V. Grinevich*

* Baikov Institute of Metallurgy, Russian Academy of Sciences,
Leninskiĭ pr. 49, Moscow, 119991 Russia
e-mail: shamray@ultra.imet.ac.ru
** International Laboratory of High Magnetic Fields and Low Temperatures,
Wroclaw, 53-529 Poland
Received May 29, 2003

Abstract—Polycrystalline samples of β-Ta with Frank–Kasper σ-phase structure prepared by electrolysis are studied. The atomic parameters are determined by the Rietveld method. The magnetic susceptibility is measured in the temperature range $4.2 < T < 273$ K and the dependence of the magnetization on the magnetic field strength is measured at 4.2 and 77 K. The analysis of interatomic distances and the results of magnetic measurements indicate that clusters with a localized excess charge exist in β-Ta. The data obtained in this study suggest structural changes in β-Ta at $T < 77$ K. © 2004 MAIK "Nauka/Interperiodica".

INTRODUCTION

Polycrystalline tetragonal β-Ta was first obtained by magnetron sputtering [1]. It was shown that the single-phase β-Ta samples can be prepared by electrodeposition from molten fluorides at temperatures ~1000 K [2]. β-Ta in the form of thin (~30 nm) layers begins to transform into the α-Ta phase at ~1100 K [3]. The synthesis of β-Ta single crystals 5–20 μm in size by electrolytic crystallization made it possible to refine their crystal structure by single-crystal X-ray diffraction analysis at room temperature (sp. gr. $P\bar{4}2_1m$, $a = 10.211(3)$ Å, $c = 5.3064(10)$ Å) [4].

As was shown in [4], the crystal structure of β-Ta can be described by a packing of Kagome nets $3636 + 3^26^2$ located at the levels $z = 1/4$ and $3/4$ of the unit-cell size and the 3^2434 nets with the coordinates $z \simeq 0$ and $1/2$ (Fig. 1). The atoms of the 3^2434 nets are located on the axes of channels formed by atoms of Kagome nets. Tantalum atoms may be intercalated on the channel axes at the levels $z = 1/4$ and $3/4$, which is confirmed by the maxima on the residual electron-density maps [4]. The Kagome and 3^2434 nets are regarded in [4] as host and guest sublattices, respectively. β-Ta has the structure of the Frank–Kasper σ-phase type. Coordination polyhedra of all atoms are slightly deformed Frank–Kasper polyhedra FKP12, FKP14, and FKP15. The structural channels centered by tantalum and penetrating the lattice along the c axis (Fig. 1) are characteristic of the structure type of hexagonal tantalum bronzes [5]. Depending on the oxidation state of tantalum, these compounds can change their properties including the magnetic susceptibility and the temperature dependence of resistivity [6].

Magnetic properties of β-Ta have not been studied. The temperature dependence of the magnetic suscepti-bility χ of β-Ta in the temperature range $100 < t < 1600°C$ has a paramagnetic character. This dependence follows the Curie–Weiss law within rather wide temperature ranges. However, good agreement between the measured and calculated from the Curie–Weiss law values of χ was not observed [7].

EXPERIMENTAL

Polycrystalline β-Ta samples with grains from 2 to 20 μm in size were obtained by electrolysis. The ternary eutectic LiF–NaF–KF was used as solvent and K_2TaF_7 or K_2TaOF_5 were used as tantalum-containing components. Electrolysis was carried out at temperatures $900 < T < 1200$ K, and the cathode-current density J_c was in the range $0.1 < J_c < 0.3$ A/cm². Along with β-Ta (the main electrolysis product), second-phase impurities can be present on the cathode: α-Ta and cubic ($KTaO_3$) or tetragonal ($K_{0.4}TaO_{2.4}F_{0.6}$) bronzes. The content of ferromagnetic impurities (Fe, Co, Ni) in β-Ta samples did not exceed 0.002%. The oxygen and fluorine contents were evaluated by two methods: measuring the increase in the sample weight after complete oxidation and carrying out X-ray spectral microanalysis. It was established that both oxygen and fluorine contents in these samples did not exceed 0.01 at %.

The X-ray diffraction patterns were recorded on a URD6 diffractometer (CuK_α radiation). The diffraction data for the Rietveld refinement were obtained using a rotating sample on an STOE diffractometer with CuK_α radiation in transparent geometry. A full-profile analysis of the β-Ta structure was performed using the Simref program complex [8].

Magnetic characteristics were measured at $4.2 < T < 293$ K by the Faraday method on a Khan-1000 electrobalance with a sensitivity of 0.5 μg in magnetic fields
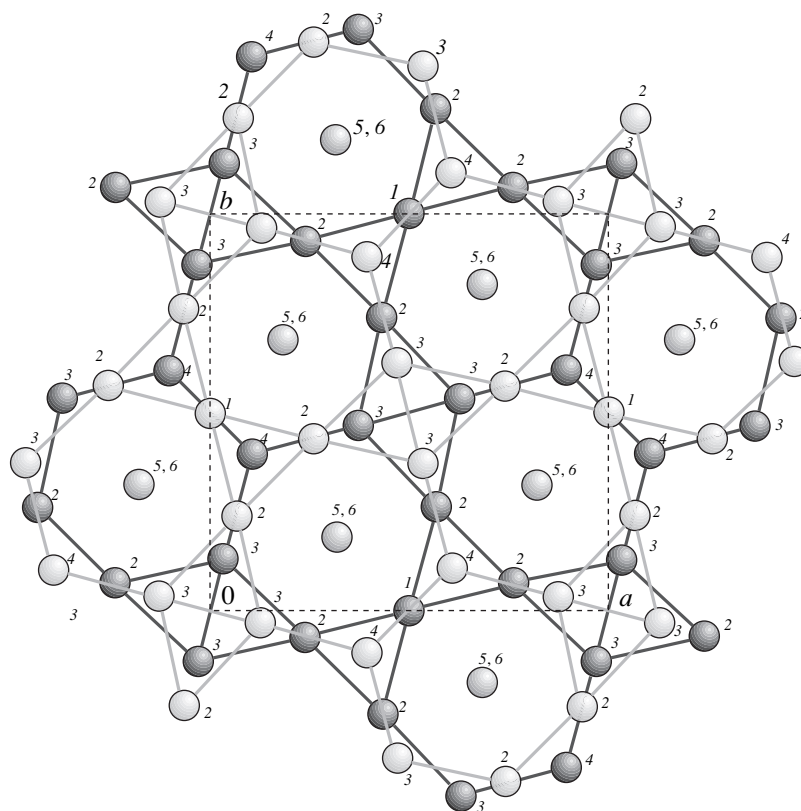
Fig. 1. The projection of the β-Ta structure onto the (001) plane. Atomic nets of different levels are marked by different shades of gray color: $z = 1/4$ (light-gray), $z = 0$ (dark-gray), and $z = 3/4$ (black). Independent atomic positions are denoted by numbers.

up to 4.28 kOe. During the measurements, the temperature was maintained with an accuracy of 0.1 K.

RESULTS

X-ray diffraction analysis and magnetic susceptibility measurements were carried out with β-Ta samples containing α-Ta impurities (less than 5 vol %). The main refinement characteristics and structure parameters are listed in Table 1. In the initial stage of the structure refinement by the least-squares method (sp. gr. $P\bar{4}2_1m$), we used the atomic parameters reported in [4]. During the refinement, 36 parameters were optimized, including the position of the zero point, the coefficient of reduction to the absolute scale, the lattice periods, and the parameters determining the profiles of X-ray reflections described by the pseudo-Voigt function. The experimental and difference X-ray patterns of a β-Ta sample are shown in Fig. 2.

The coordinates and isotropic thermal displacements of atoms obtained from the refinement are listed in Table 2. Their values are close to those reported in [4], where the β-Ta structure was studied by a single-crystal X-ray analysis (Table 2). Thus, it was confirmed that the β-Ta phase in polycrystals studied is structurally identical to that studied previously [4].

The results of measurements of the magnetic susceptibility $\chi(T)$ in the temperature range $4 < T < 273$ K are shown in Fig. 3. Figure 4 shows the dependence of the magnetic moment M on the magnetic field H at $T = 4.2$ and 77 K. As can be seen from Fig. 3, χ changes only slightly in this temperature range. Upon cooling from 273 K down to ~150 K, it is almost constant. In the temperature range $65 < T < 150$ K, the magnetic susceptibility increases smoothly following the Curie–Weiss law. At $T = 65$ K, χ drops stepwise to a value a little smaller than that at 273 K and then decreases

Table 1. Unit-cell parameters of β-Ta and main characteristics of the Rietveld refinement

a, Å	10.184(3)
c, Å	5.306 (1)
Range of 2θ angles, deg	25–95
Step in 2θ, deg	0.01
Number of experimental points	7001
Number of reflections	169
Number of refined parameters	36
S	2.06
R_{wp} (%)	9.46
R_B (%)	6.45
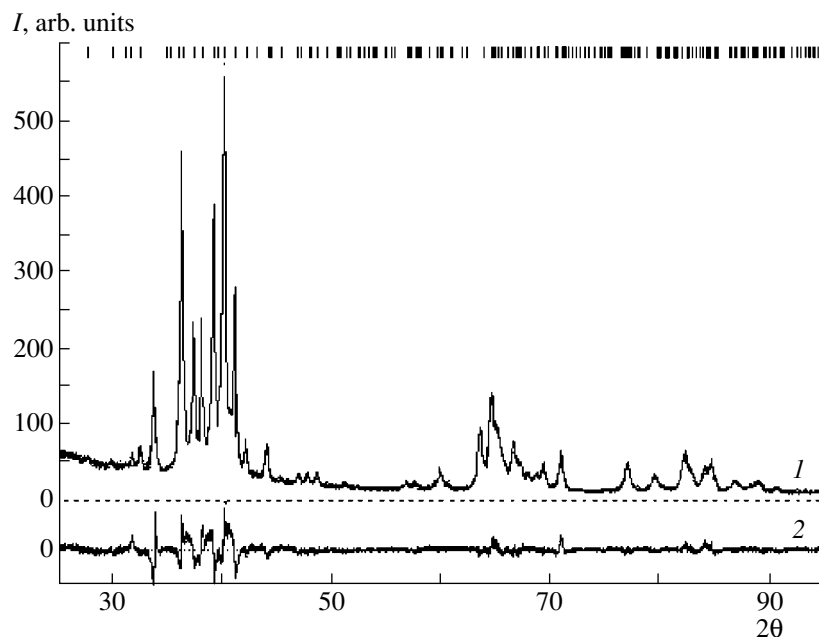
Fig. 2. (*1*) Experimental (circles) and calculated (solid line) diffraction patterns of β-Ta and (*2*) their difference.

smoothly below 65 K. The character of the dependence of the magnetic moment on magnetic field, *M*(*H*), is radically different at *T* < 65 K and *T* > 65 K (Fig. 4). In the former case, the deviation from a linear dependence is only slightly pronounced, whereas, in the latter case, this deviation is pronounced fairly well.

DISCUSSION

The magnetic susceptibility of transition metals of the IV–VI groups was studied in a wide temperature range in [7]. The temperature dependence of χ was expressed as

$$\chi(T) = \chi_{\text{pauli}}(T) + \chi_{\text{dia}} + \chi_{vV}(T), \qquad (1)$$

where $\chi_{\text{pauli}}(T)$, χ_{dia}, and $\chi_{vV}(T)$ are the contributions of the Pauli susceptibility, the diamagnetic susceptibility of core electrons, and the Van Vleck susceptibility, respectively [7].

Some regularities in the dependence of the magnetic susceptibility of transition metals on their position in the periodic table of elements and atomic coordination have been established. The transition metals of the

Table 2. Coordinates and thermal displacements of atoms in the β-Ta structure

Atom	Position	x	y	z	$U_{\text{equi}} \times 10^2 \, (\text{Å}^2)$
Ta(1)	2*c*	0.5	0.0	0.240(5)	1.3(2)
				0.228(2)*	1.3(1)*
Ta(2)	8*f*	0.760(1)	0.068(1)	0.233(3)	1.8(1)
		0.7598(3)*	0.0677(3)*	0.235(1)*	1.52(7)*
Ta(3)	8*f*	0.034(1)	0.127(1)	0.252(5)	2.6(2)
		0.0343(3)*	0.1267(4)*	0.255(2)*	2.9(1)*
Ta(4)	4*e*	0.604(1)	0.105(1)	0.751(5)	2.3(1)
		0.6033(4)*	0.1033(4)*	0.764(2)*	2.79(7)*
Ta(5)	4*e*	0.821(1)	0.308(1)	0.006(3)	1.9(2)
		0.8142(6)*	0.3142(6)*	0.003(1)*	2.0(1)*
Ta(6)	4*e*	0.321(1)	0.184(1)	0.490(3)	2.1(2)
		0.3196(5)*	0.1804(5)*	0.491(1)*	1.9(2)*

* The values were obtained by the single-crystal method in [4].

χ, 10^{-6}, G cm^3/g
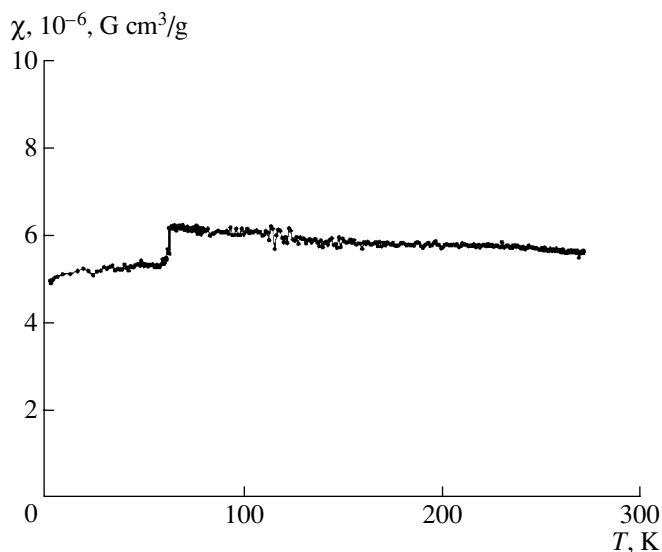
Fig. 3. Temperature dependence of the magnetic susceptibility $\chi(T)$ of β-Ta at $4.2 < T < 280$ K.

M, 10^{-2}, G cm^3/g
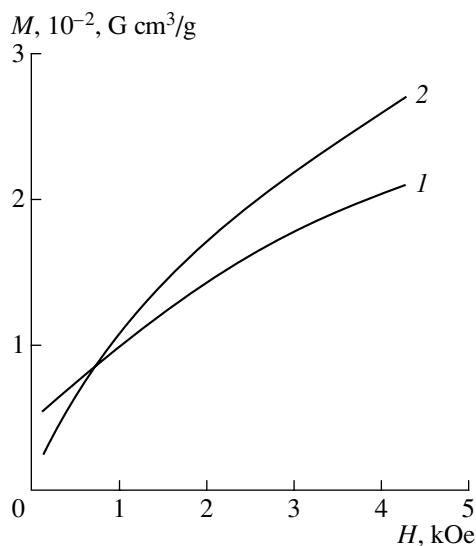
Fig. 4. Dependence of the magnetization M on the magnetic field strength H at (*1*) 4.2 and (*2*) 77 K.

Fig. 5. Schematic diagram of distances that do not exceed 2.99 Å in the β-Ta structure at (a) 293 and (b) 120 K. Independent atomic positions are denoted by numbers. Hexagons in the *xy* plane of one net ($z = 3/4$) are shown by thick lines; light-gray circles indicate the atoms of this net. The distances in Ta(1) clusters and between them are shown by thin lines. Black circles indicate Ta(5) and Ta(6) atoms located under each other at the levels $z = 0$ and 0.5 and dark-gray circles indicate Ta(4) atoms located at the level $z = 1/4$.

same group reveal the same type of the temperature dependence of the magnetic susceptibility (the derivative $d\chi/dT$ has the same sign for transition metals of the same group). The dependence $\chi(T)$ of transition metals of the fifth group (V, Nb, Ta) has a shape characteristic of paramagnets with a magnetic susceptibility smoothly increasing upon cooling. When a phase transition is not associated with a change in the atomic coordination (*fcc* lattice $\longleftrightarrow$ *hcp* lattice), the magnetization changes insignificantly. At the same time, the phase transformations associated with a significant change in the coordination (*bcc* lattice $\longleftrightarrow$ *hcp* lattice) lead to noticeable changes in magnetic properties.

As was noted above, β-Ta has a structure of the Frank–Kasper σ-phase type. The crystal structure of σ-phase is usually considered consisting of intergrown 12-, 14-, and 15-vertex Frank–Kasper polyhedra (FKP) faceted with triangular faces. It is generally assumed that the Frank–Kasper polyhedra in the σ-phase structure are slightly deformed, and the coordination factor is responsible for their stability. The *bcc* structure, into

Table 3. Interatomic distances (in Å), which do not exceed the average value (2.99 Å) in the first coordination spheres of atoms in the β-Ta structure at 293 and 120 K

Ta–Ta distances	293 K; $a = 10.211(3)$, $c = 5.3064(10)$ Å (according to [4])	120 K; $a = 10.1815(5)$, $c = 5.2950(1)$ Å (according to [9])
Ta(1)–Ta(2)	2.74 × 4	2.73 × 2, 2.76 × 2
Ta(1)–Ta(4)	2.88 × 2	(3.025 × 2)
Ta(1)–Ta(5)	2.95 × 2	2.95 × 2
Ta(1)–Ta(6)	2.96 × 2	2.92 × 2
Ta(2)–Ta(1)	2.74	2.76
Ta(2)–Ta(2)	2.77	2.79
Ta(2)–Ta(3)	2.96	2.89
Ta(2)–Ta(4)	2.99	(3.09)
Ta(2)–Ta(5)	2.86, 2.98	2.93, 2.99
Ta(2)–Ta(6)	2.99 × 2	2.93, 2.98
Ta(3)–Ta(2)	2.87 × 2	2.85, 2.88
Ta(3)–Ta(2)	2.89	2.88
Ta(3)–Ta(2)	2.96	2.89
Ta(3)–Ta(3)	2.68	2.74
Ta(3)–Ta(4)	2.85	2.78
Ta(4)–Ta(1)	2.88	(3.025)
Ta(4)–Ta(2)	2.98 × 2	(3.09, 3.12)
Ta(4)–Ta(3)	2.85 × 2	2.78, 2.82
Ta(4)–Ta(4)	2.98	(3.04)
Ta(5)–Ta(1)	2.95	2.95
Ta(5)–Ta(2)	2.85 × 2	2.93, 2.98
Ta(5)–Ta(2)	2.98 × 2	2.94, 2.96
Ta(5)–Ta(6)	2.62, 2.68	2.65 × 2
Ta(6)–Ta(1)	2.96	2.92
Ta(6)–Ta(2)	2.99 × 2	2.92, 2.95
Ta(6)–Ta(2)	(3.017)	2.96
Ta(6)–Ta(5)	2.62, 2.68	2.65 × 2

which α-Ta crystallizes, is often regarded as a structure formed by 14-vertex polyhedra with orthorhombic faces. It can be assumed in the first approximation that these structures are similar from the standpoint of atomic coordination. Indeed, the interatomic distances in β-Ta (2.74–3.25 Å in FKP12 and 2.85–3.40 Å in FKP14 and FKP 15, with the average value ⟨2.93⟩ Å) are close to the distances in 14-vertex polyhedra of α-Ta: eight distances of 2.86 Å and six distances of 3.30 Å, with the average value ⟨3.05⟩ Å.

At the same time, the analysis performed with due regard for the differentiation of Ta–Ta distances into shortened and lengthened ones indicates a significant difference in the first coordination sphere of the atoms of the two modifications of metallic tantalum under comparison. As can be seen from Fig. 5, where the

interatomic distances no larger than 2.99 Å (the average value for α and β-Ta) are indicated, the atoms with shortened Ta–Ta distances form groups in the β-Ta structure, which are somewhat different at 293 and 120 K. All the interatomic distances listed in Table 3 were obtained by us from single-crystal structure studies at 293 [4] and 120 K [9], respectively. Table 3 contains the values to two decimal places since the standard deviations reported in [4] and [9] do not exceed 0.0007 Å. The Ta(5)–Ta(6) chains with the shortest interatomic distances, penetrating the lattice along the z axis (normal to the drawing plane), characterize the structure at both temperatures. At 293 K, Ta(3) and Ta(4) atoms form hexagons shown in Fig. 2 by thick lines with distances equal to 2.68 Å for Ta(3)–Ta(3), 2.85 Å for Ta(3)–Ta(4), and 2.98 Å for Ta(4)–Ta(4) pairs. At 120 K, the Ta(4)–Ta(4) link with a distance of 3.04 Å is "lost" in these hexagons (located in the xy plane) and they transform into infinite corrugated chains (Fig. 5b). At 293 K, Ta(1) atoms (located at the hexagon centers) and Ta(2), Ta(4), Ta(5), and Ta(6) atoms form clusters with an average interatomic distance of 2.86 Å (Fig. 5a). The centers of these clusters (Ta(1) atoms) are located at two levels: z = 1/4 and 3/4. At each level, Ta(1) clusters are connected with hexagons by short bonds in Ta(3)–Ta(3)–Ta(2) triangles. The clusters of two neighboring levels are connected by short bonds in the Ta(5)–Ta(6) chains. At 120 K, Ta(4) atoms are excluded from these clusters (Fig. 5b), and the Ta(1)–Ta(4) distances become equal to 3.03 Å (instead of 2.88 Å at 293 K) despite the thermally-induced decrease in the unit-cell parameters (Table 3). Thus, if we take into account only Ta–Ta distances (which do not exceed the average value 2.99 Å), the coordination numbers (CNs) for the β-Ta structure differ significantly from the CNs for α-Ta, as well as from the CNs considered generally for the σ-phase. For Ta(1) and Ta(2), CN = 10 and 8 at 120 and 293 K, respectively; for Ta(3) and Ta(4), CN = 6 at 293 K (for (Ta(4), CN becomes as low as 2 at 120 K); for Ta(5), CN = 7 at both temperatures: and, for Ta(6), CN = 5 and 6 at 293 and 120 K, respectively (Table 3). In α-Ta, short distances of 2.86 Å correspond to CN = 8.

The presence of the group with anomalously short distances distinguishes the β-Ta phase from of the α-Ta phase. These are the distances in infinite Ta(5)–Ta(6) chains elongated along the z axis and some distances in the above-considered Ta(1) clusters and hexagons located in xy planes. The selection of these distances, which do not exceed 2.78 Å, suggests the presence of low-dimensional clusters with a finite number of atoms in the β-Ta structure. Note that the formation of low-dimensional Ta-clusters (chains or triangles) in inorganic compounds was considered in some publications [10].

The occurrence of clusters in the structures formed involving transition metals is usually associated with localization of charges at these clusters, which depends on the electronic state and size of a cluster. Mass-spec-

trometric studies of vapor phase formed upon laser heating of tantalum showed that the charge of isolated tantalum clusters may vary from 1 to 4 [11]. If we assume that the crystal lattice of β-Ta contains charged clusters with magnetic moments, an additional contribution to the magnetic susceptibility should be expected (see Eq. (1)). The dependence of the magnetic moment on magnetic field $M(H)$ for this contribution is defined by the Langevin equation. Since the nonlinearity of this type is pronounced on the $M(H)$ dependences obtained for β-Ta samples at 77 K (Fig. 4), they were approximated by the equation

$$M = M_0\{\coth(m_{cl}H/T) - T/m_{cl}H\},$$

where $M_0 = Nm_{cl}$ (N is the number of clusters per unit volume and m_{cl} is the magnetic moment accounted per cluster). Satisfactory agreement between the experimental and calculated dependences $M(H)$ was obtained for $N \simeq 10^{20}$ mol^{-1} and $m_{cl} \simeq 1000\mu_B$. However, it is difficult to associate these values of N and m_{cl} with any specific elements of the β-Ta lattice on the basis of the data obtained to date.

At 4.2 K, the dependence $M(H)$ is close to linear in the range $1 < H < 4$ kOe (Fig. 3). Evaluation of the magnetic susceptibility at 4.2 K from the relation $M = \chi H$ gives $\chi = 3.5 \times 10^{-6}$ m^3/kg. This value is much larger than that for α-Ta (~10^{-6} m^3/kg), is close to the magnetic susceptibility of Nb (2.4×10^{-6} m^3/kg), and is smaller than the magnetic susceptibility of V (5.5×10^{-6} m^3/kg).

These evaluations are rather relative since the separation of the contributions to the magnetic susceptibility of transition metals is ambiguous. In this case, as was noted in [7], difficulties arise in determination of the diamagnetic and Pauli components of the susceptibility. A change in the atomic coordination generally leads to a pronounced change in the Pauli magnetic susceptibility. Evaluation of the Pauli susceptibility requires a correct approximation of the shape of the d band. An additional contribution to the susceptibility may occur due to the localization of charges and magnetic moments at clusters, which complicates this problem even more.

Along with the fact that the magnetic susceptibility of β-Ta is much higher than that of α-Ta, their temperature dependences $\chi(T)$ are also substantially different. The dependence $\chi(T)$ of α-Ta is characteristic of paramagnets and close to the dependence following the Curie–Weiss law. For β-Ta, this similarity is violated by a significant decrease in the susceptibility upon cooling from $T \sim 65$ K, which, in the first approximation, is likely to be the diamagnetic contribution.

The temperature dependence of the magnetic susceptibility of β-Ta different from that of the transition metals of group V, and the difference in the dependences $M(H)$ at liquid-nitrogen and liquid-helium temperatures indicate the possibility of structural variations in the temperature range $4.2 < T < 77$ K. This suggestion is confirmed by the data of X-ray single-crystal analysis, according to which a phase transition related to the formation of a two-component composite structure occurs in β-Ta with decreasing temperature from 293 to 120 K [9].

REFERENCES

1. D. J. Mills, J. Can. Ceram. Soc. **35**, 48 (1966).
2. P. T. Moseley and H. Seabrook, Acta Crystallogr., Sect. B: Struct. Crystallogr. Cryst. Chem. **29**, 1170 (1973).
3. H.-J. Lee, K. W. Kwon, C. Ryu, *et al.*, Acta Mater. **47**, 3965 (1999).
4. A. Arakcheeva, G. Shapuic, and V. Grinevitch, Acta Crystallogr., Sect. B: Struct. Sci. **58**, 1 (2002).
5. M. Vlasse, A. Boukhari, and J. P. Chaminade, Mater. Res. Bull. **14**, 101 (1979).
6. A. V. Arakcheeva, V. V. Grinevich, A. V. Mitin, *et al.*, Kristallografiya **46** (2), 221 (2001) [Crystallogr. Rep. **46**, 182 (2001)].
7. H. Kojima, R. S. Tebble, and D. E. Williams, Proc. R. Soc. London, Ser. A **260**, 237 (1961).
8. C. Rebmann, H. Ritter, and J. Ihringer, Acta Crystallogr., Sect. A: Found. Crystallogr. **54**, 225 (1998).
9. A. Arakcheeva, G. Shapuic, H. Birkedal, *et al.*, Acta Crystallogr., Sect. B: Struct. Sci. **59**, 324 (2003).
10. V. E. Fedorov, *Chalcogenides of Refractory Transition Metals* (Nauka, Novosibirsk, 1988) [in Russian].
11. S. Naoaki, K. Kazuyoshi, and T. Mitsumori, Chem. Phys. Lett. **300**, 262 (1999).

Translated by T. Dmitrieva

Crystal Structure of a New Synthetic Ca,Li Pentaborate: CaLi₄[B₅O₈(OH)₂]₂

A. P. Kantor, N. A. Yamnova, Yu. K. Egorov-Tismenko, and O. V. Dimitrova

Geology Faculty, Moscow State University, Vorob'evy gory, Moscow, 119992 Russia
e-mail: natalia_yamnova@mail.ru
Received May 7, 2003

Abstract—When studying the phase formation in the CaO–Li_2O–B_2O_3–H_2O system, a new Ca,Li pentaborate was synthesized under hydrothermal conditions. The structure of a new compound with the crystallochemical formula $CaLi_4[B_5O_8(OH)_2]_2$ (sp. gr. $Pb2n$, $a = 8.807(7)$, $b = 9.372(7)$, $c = 8.265(6)$ Å, $V = 682.2(9)$ Å^3, $Z = 2$, $d_{calcd} = 2.43$ g/cm^3, automated SYNTEX-$P\bar{1}$ diffractometer, 2690 reflections, $2\theta/\theta$ scan, λMo) is refined up to $R_{hkl} = 0.0557$ in the anisotropic approximation of atomic thermal vibrations with allowance for the localized H atoms. The structure of the Ca,Li pentaborate is formed by (010) open boron–oxygen layers formed by two independent $[B_5O_8(OH)_2]^{3-}$ pentagroups, with each of them being formed by three B tetrahedra and two B triangles. The structure framework consists of the above boron–oxygen layers bound by isolated Li tetrahedra. The Ca cations are localized in the centers of eight-vertex polyhedra located in the [001] channels of the Li,B,O framework. Comparative crystallochemical analysis of the new Ca,Li pentaborate and Li pentaborate of the composition $Li_3[B_5O_8(OH)_2]$-II showed that the anionic matrices of both compounds are completely identical, whereas some of the cationic positions are different. © *2004 MAIK "Nauka/Interperiodica".*

INTRODUCTION

During the study of phase formation in the CaO–Li_2O–B_2O_3–H_2O system, the crystals of a new synthetic Ca,Li borate were synthesized under hydrothermal conditions ($t = 270°C$, $P = 20$ atm). The weigh ratios of the main compound components are 1:1:2. In addition, we also added to the solution the Cl^- and CO_3^{2-} mineralizers. The crystals grown were colorless, isometric, well-faceted crystals with a size up to 1–2 mm. The crystal faceting has four simple forms: bipyramid, two rhombic prisms, and two pinacoids (Fig. 1). The qualitative X-ray spectral analysis of the crystals performed on a CamScan 4DV scanning electron microscope with a Link energy-dispersive attachment (analyst E.V. Guseva) showed the presence of only Ca atoms. The comparison of the powder diffraction pattern of the compound studied with the ICSD database revealed no analogues of the new crystals synthesized. The IR spectrum (Fig. 2) obtained by V.S. Kurazhkovskaya on a Specord 75 IR spectrophotometer by the method of a fine disperse film on a KBr substrate had vibration bands of condensed B triangles (1380–1315 cm^{-1}) and B tetrahedra (1085–915 cm^{-1}), with the latter band having a much higher intensity. The low intense bands in the low-frequency range of the spectrum were identified with the deformation vibrations of B triangles and B tetrahedra. The band 1655 cm^{-1} corresponds to the deformation vibrations of H_2O, but its extremely weak intensity indicates a very low H_2O content in the struc-

ture. In the vicinity of 3600 cm^{-1}, a very weak doublet of OH$^-$ vibrations is observed (3640–3600 cm^{-1}).

EXPERIMENTAL. STRUCTURAL MODEL AND ITS REFINEMENT

The experimental material for X-ray diffraction study was obtained on an automated single crystal SYNTEX $P\bar{1}$ diffractometer. The main crystallographic data and the characteristics of the experiment and structure refinement are listed in Table 1. Analysis of the diffraction pattern allowed us to establish the extinction rules for the $hk0$ ($h + k = 2n$) and $0kl$ ($k = 2n$) reflections, which indicated two possible space groups: $Pbmn$ and $Pb2n$.

The structure model was obtained by the direct method and was refined within the noncentrosymmetric sp. gr. $Pb2n$ (C_{2v}^6) in the full matrix anisotropic approximation with the use of the AREN complex of programs [1]. The division of the anionic part of the structure into oxygen ions and (OH)$^-$ groups was based on the calculation of the local balance of valences with due regard for the cation–anion distances in [2] (Table 2). The concluding value of the reliability factor $R = 0.0557$ for the formula $CaLi_4[B_5O_8(OH)_2]_2$ ($Z = 2$, $d_{calcd} = 2.43$ g/cm^3) was obtained based on 2617 structure factors after the rejection of 73 weak reflections with large differences (Table 1) and the refinement of the positional parameters of hydrogen atoms. The coor-
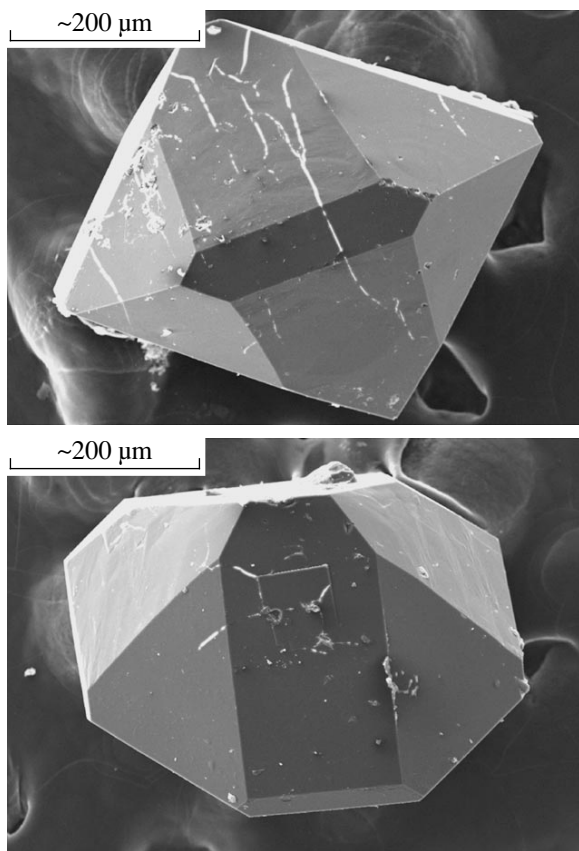
Fig. 1. Synthesized crystals. Photographs were taken in a JSM-5300 analytical scanning electron microscope by A.V. Mokhov (Institute of Geology of Ore Deposits, Petrography, Mineralogy, and Geochemistry of the Russian Academy of Sciences).

Fig. 2. IR spectrum of the synthetic Ca,Li pentaborate.
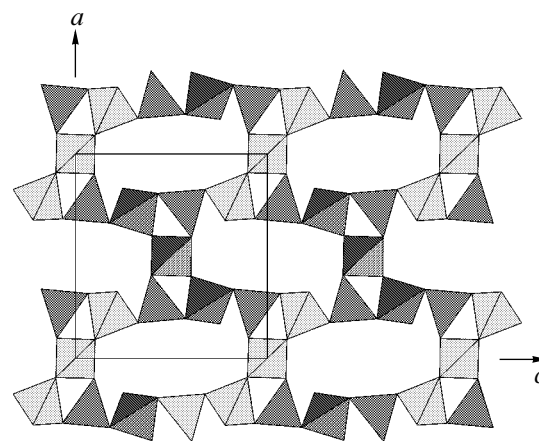
Fig. 3. Fragment of a boron–oxygen layer in the structure of the Ca,Li pentaborate. All the B triangles are located at the same level along the b axis. The triads of B tetrahedra of the pentagroups located above and below the level of B triangles are showed as light and dark tetrahedra.

dinates of the basis atoms and the geometric characteristics of hydrogen bonds are indicated in Tables 3 and 4, respectively.

The analysis of the model showed the absence of the mirror symmetry plane m normal to the y axis. The arrangement of all the structure atoms (except for Ca) is consistent with the centrosymmetric sp. gr. *Pbcn*. A weak maximum with a height comparable with the heights of hydrogen atoms on the difference electron-density map corresponds to the position centrosymmetric to the position of Ca atom. Taking into account the IR spectroscopy data, we assumed that this position has an additional O atom from the H_2O molecule which do not belong to the coordination sphere of any cation. The refinement of the positional and thermal parameters and position occupancy showed that it is filled about 15%. With due regard for this fact, the general formula of this borate should have been written as $CaLi_4[B_5O_8(OH)_2]_2 \cdot xH_2O$ ($x \sim 0.15$); however, taking into account the extremely low content of H_2O molecules in the crystal which could affect the reliability factor, we did not change the above structural formula.

DESCRIPTION OF THE STRUCTURE

The structure of the new Ca,Li pentaborate consists of open boron–oxygen (010) layers formed by two independent $[B_5O_8(OH)_2]^{6-}$ pentagroups, each of which consists of three B tetrahedra and two B triangles (with the average B–O distances in the B tetrahedra and B triangles being 1.473 and 1.366 Å, respectively) (Fig. 3). All the B triangles are localized in the central part of layers, whereas the triads of B tetrahedra are located above and below these triangles, which results in layer corrugation. There are two such layers with the "opposite corrugation" (Fig. 4a) per the unit-cell period b. The boron–oxygen layers are connected via isolated Li tetrahedra into a framework (Fig. 5a). The Ca cations localized in the [001] channels at the level $z = 0$ are coordinated with four O^{2-} ions and four $(OH)^-$ groups. They form isolated eight-vertex polyhedra with the average cation–anion distance 2.527 Å and connect boron–oxygen layers. Similar positions in the frame-
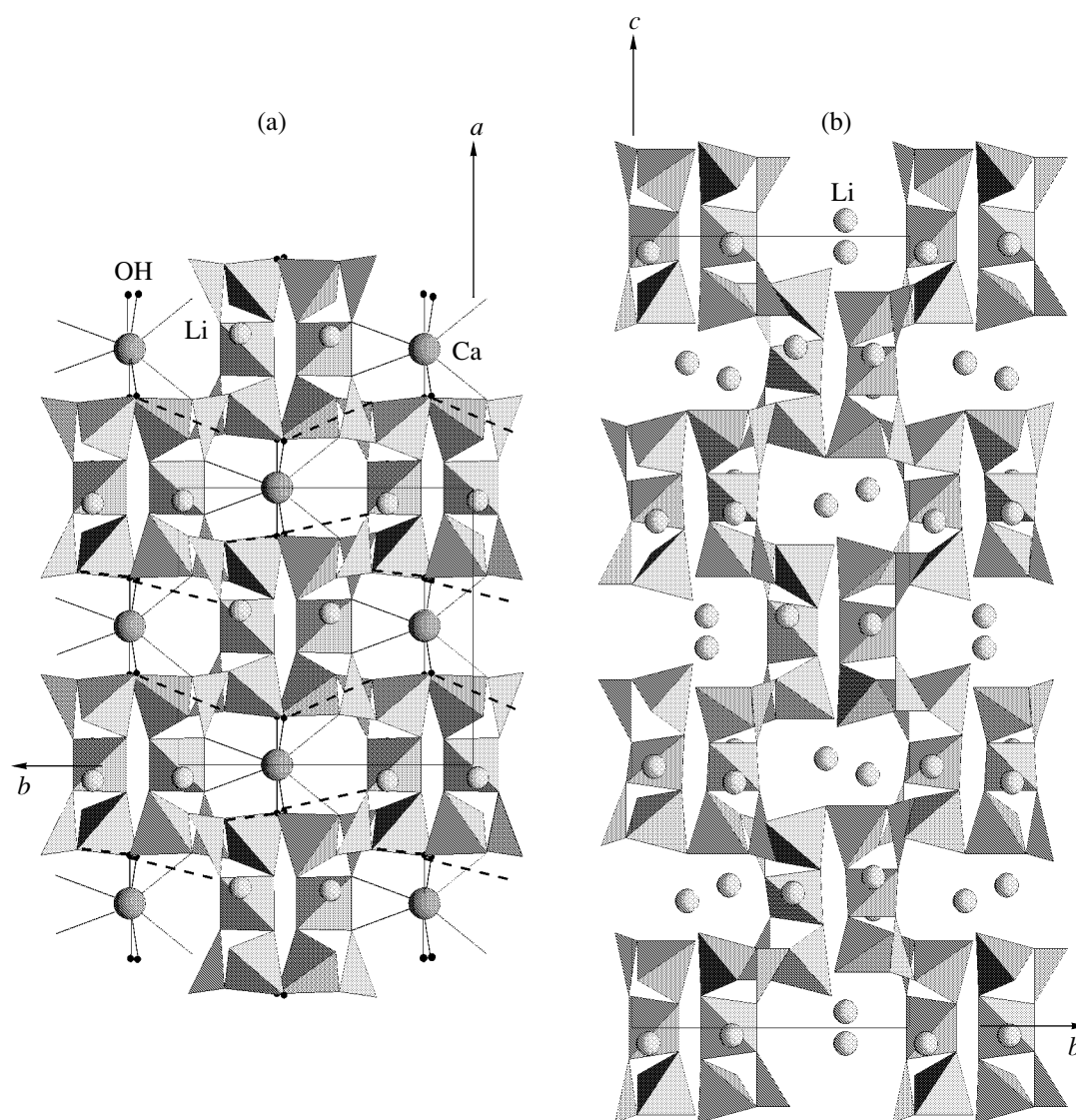
Fig. 4. (a) Ca,Li pentaborate of the composition $CaLi_4[B_5O_8(OH)_2]_2$ projected onto the (001) plane and (b) Li pentaborate of the composition $Li_3[B_5O_8(OH)_2]$-II projected onto the (100) plane. The neighboring pentagroups consisting of three B tetrahedra and two B triangles located along the *b* axis are displaced by *T*/2 in the direction normal to the drawing plane. The Li atoms are located (a) above and under the central B tetrahedra of the pentagroups and (b) in the [100] channels. The Ca–O(OH) bonds in Fig. 4a are shown by solid lines; hydrogen bonds are indicated by dashed lines.

work voids lying at the level $z = 0.5$ and related to Ca cations by a pseudocenter of inversion may be occupied by H_2O molecules. The dangling vertices of the B tetrahedra of the pentagroup are represented by (OH)⁻ ions coordinating an eight-vertex Ca polyhedron. The additional rigidity of the framework is provided by hydrogen bonds localized between the boron–oxygen layers (Fig. 4a).

Comparing the structures of the new Ca,Li pentaborate and Li pentaborate of the composition $Li_3[B_5O_8(OH)_2]$-II ($a = 8.449(5)$, $b = 9.308(3)$, $c = 26.52(1)$ Å, $Z = 12$, sp. gr. *Pn2b*) [2] showed that both structures have the same boron–oxygen motif consist-

ing of $[B_5O_8(OH)_2]^{6-}$ pentagroups. The structures have almost equal translations along the *a* axis: $a = 8.807$ Å in the Ca,Li pentaborate (Fig. 4a) and $c/3 = 8.84$ Å in the Li pentaborate (Fig. 4b). It is obvious that the anionic matrices of these structures are identical, and the lattice parameters and the unit-cell symmetries are similar; so the only difference may be reduced to the replacement of Ca^{2+} cations by Li^+ cations according to the scheme $Ca^{2+} \Leftrightarrow 2Li^+$. But in the actual fact, some of the Li positions in the structure of the Li pentaborate $Li_3[B_5O_8(OH)_2]$-II differ from the cationic positions in the Ca,Li pentaborate structure (Figs. 5a and 5b). These are the Li tetrahedra participating in the formation of the Li, B, O framework similar to the framework of the
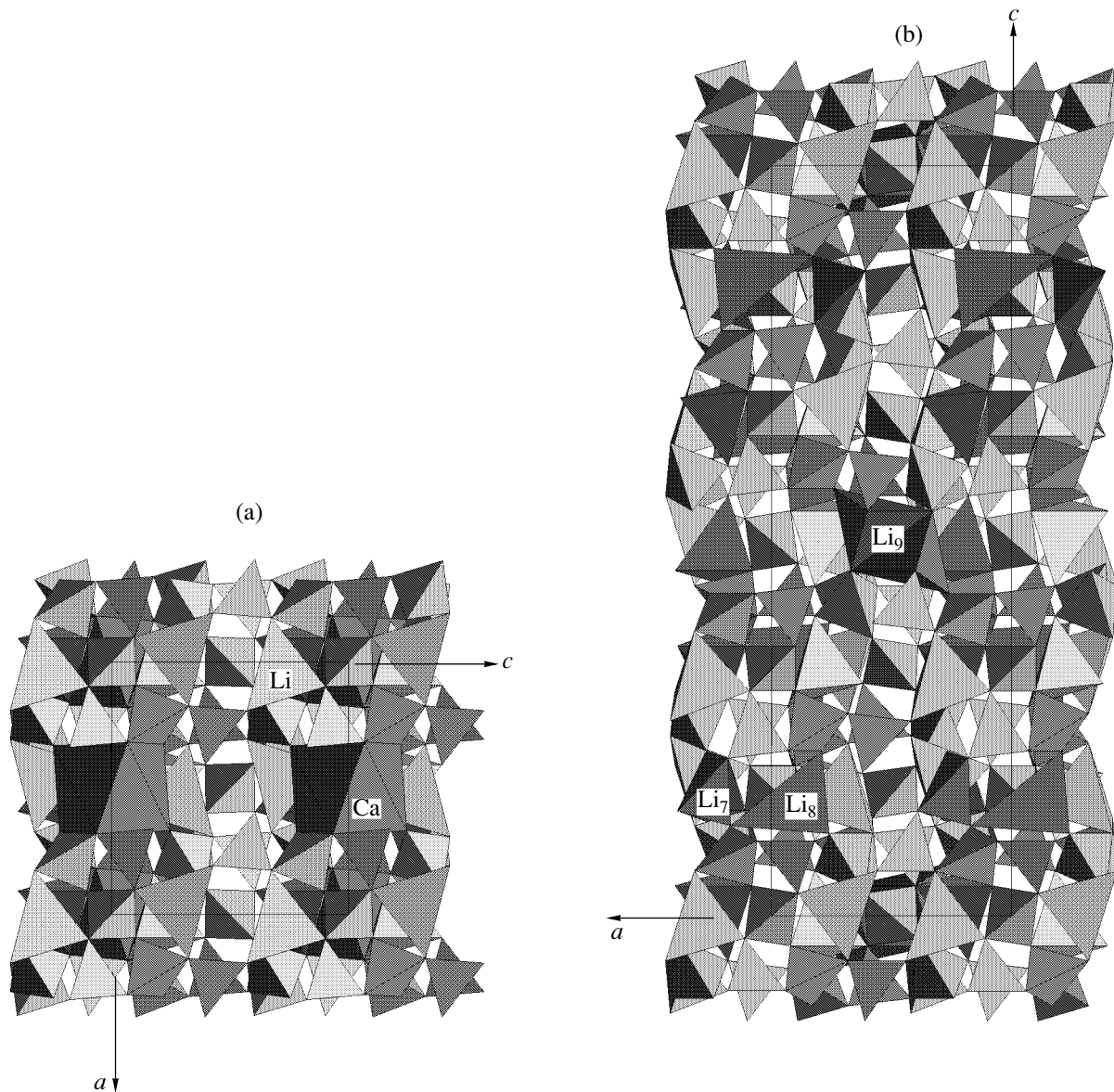
Fig. 5. (a) Ca,Li-pentaborate and (b) Li-pentaborate projected onto the (010) plane. The Ca atoms at the level $y \sim 0.17$ and the Li_7, Li_8, and Li_9 atoms at the levels $y \sim 0.15$, 0.30, and 0.73 are indicated.

Ca,Li pentaborate, two Li tetrahedra [Li(7) and Li(8)] replacing the eight-vertex Ca polyhedra, and also Li(9) tetrahedra sharing the edges and replacing vacant positions or, probably, the positions statistically filled with H_2O molecules in the structure of the Ca,Li pentaborate. Taking into account that localization of light (such as Li) atoms in the structure of Li pentaborate is always rather difficult, the reliable determination of the positional parameters of this part of Li atoms in the Li pentaborate is somewhat ambiguous, because of an unreliable balance of valence strengths at the anions (unfortunately, no corresponding calculations are given in [2]) and also because of an anomalously short distance between the Li atoms (~1.7 Å) whose tetrahedra share

the edges. It is these Li atoms that violate [2] the obvious pseudoperiodicity ($c' = c/3$) of the Li borate structure. Possibly, the correct localization of these positions would eliminate this pseudoperiodicity. The reduction of the parameter $c = 26.52$ Å by a factor of three would have lead to the formula $Li_6[B_5O_8(OH)_2]_2$ ($Z = 2$) comparable with the formula of the Ca,Li pentaborate $CaLi_4[B_5O_8(OH)_2]_2$ ($Z = 2$) studied in this work. We cannot exclude the existence of hypothetical compounds with the general formula $M_6^+[B_5O_8(OH)_2]_2$, which are the analogues of the $CaLi_4[B_5O_8(OH)_2]_2$, where the monovalent cations also occupy the Ca-position and the position related to it by a center of inversion. In this

Table 1. Main crystallographic characteristics and experimental data for the $CaLi_4[B_5O_8(OH)_2]_2$ structure

System	Orthorhombic	Minimum and maximum $\sin\theta/\lambda$, $Å^{-1}$	0.06, 1.08
Sp. gr.	*Pb2n*	Scanning rate, deg/min	4–24
Z	2	Scanning region	$0 \le h \le 18$
a, Å	8.807(7)		$0 \le k \le 20$
b, Å	9.372(7)		$0 \le l \le 17$
c, Å	8.265(6)	Number of measured reflections with $I \ge 1.96\sigma\,(I)$	2690
V, $Å^3$	682.2(9)	Number of reflections used at the concluding stage of the LS refinement	2617
d_{calc}, g/cm^3	2.43	Complex of programs used	AREN
μ, mm^{-1}	0.59	Concluding reliability factor (anisotropic approximation)	
Linear dimensions of crystal, mm	$0.20 \times 0.20 \times 0.25$	$R\,(2617F)$	0.0557
Radiation wavelength	MoK_α, 0.71069	$R\,(2690F)$	0.0602
Diffractometer	SYNTEX $P\bar{1}$	Number of parameters in the refinement	166
Scanning	$2\theta : \theta$		

Table 2. Local balance of valences at the anions in the $CaLi_4[B_5O_8(OH)_2]_2$ structure

Anion	Cations											
	Ca	B(1)	B(2)	B(3)	B(4)	B(5)	B(6)	Li(1)	Li(2)	H(1)	H(2)	ΣV_{ij}
O(1)						0.84	$0.86 \times 2\downarrow$	0.29				1.99
O(2)		1.03		$0.73 \times 2\downarrow$				0.28		0.02		2.06
O(3)			1.05		0.72			0.27				2.04
O(4)		1.03				0.78			0.26			2.07
O(5)				$0.79 \times 2\downarrow$	0.83				0.28			1.90
O(6)	$0.18 \times 2\downarrow$		0.98			0.67		0.19				2.02
O(7)		0.99			0.71				0.21	0.01	0.02	1.94
(OH)(8)	$0.33 \times 2\downarrow$					0.77				0.97		2.07
(OH)(9)	$0.22 \times 2\downarrow$				0.75						0.98	1.95
O(10)	$0.18 \times 2\downarrow$		1.01				$0.68 \times 2\downarrow$		0.21			2.08
Total	1.82	3.05	3.04	3.04	3.01	3.07	3.07	1.02	0.97	1.00	1.00	20.12

case, the symmetry of this structure would have been described by the sp. gr. *Pbcn*.

Concluding the article, we should like to note that pentaborate groups formed by B tetrahedra and B triangles in various ratios are among the most widespread structural units in natural and synthetic borate compounds. The Ca,Li pentaborate of the composition $CaLi_4[B_5O_8(OH)_2]_2$ and Li-pentaborate of the composition $Li_3[B_5O_8(OH)_2]$-II should be related to the group of layer borates (the symbol 6.EC.25 [4, 5]), namely, to that part of these compounds whose boron–oxygen motif consists of the layers formed by pentagroups of two B triangles and three B tetrahedra ($5[2\Delta + 3T]$ blocks). According to the pentaborate classification given in [6], this group includes the minerals heidornite $Na_2Ca_3[B_5O_8(OH)_2]_2 \cdot SO_4 \cdot Cl$, tuzlaite $NaCa[B_5O_8(OH)_2] \cdot 3H_2O$, and two synthetic borates $Ba_2[B_5O_8(OH)_2](OH)$ and $Na_3[B_5O_8(OH)_2] \cdot H_2O$. However, the structure of the Ca,Li and Li pentaborates differ from other layer pentaborates by the symmetry of the pentagroup and the configuration and symmetry of boron–oxygen layers.

Table 3. Coordinates of basic atoms and equivalent thermal corrections in the $CaLi_4[B_5O_8(OH)_2]_2$ structure

Atom	Position multiplicity	x/a	y/b	z/c	B_{eq} (Å^2)
Ca	2	0.0000	0.6653	0.0000	0.86(2)
O(1)	4	0.0930(1)	0.0995(1)	0.1025(1)	0.60(2)
O(2)	4	0.0925(1)	0.3576(2)	0.3949(2)	0.81(2)
O(3)	4	0.8383(1)	0.3273(1)	0.1773(2)	0.80(2)
O(4)	4	0.3255(1)	0.4657(2)	0.3255(2)	0.81(2)
O(5)	4	0.9011(1)	0.1756(1)	0.3984(1)	0.63(2)
O(6)	4	0.1818(1)	0.4538(2)	0.0662(1)	0.76(2)
O(7)	4	0.6932(1)	0.3434(2)	0.4278(2)	0.94(2)
(OH)(8)	4	0.3257(1)	0.1651(2)	0.2203(2)	1.17(3)
(OH)(9)	4	0.6687(2)	0.1413(1)	0.2456(2)	1.04(3)
O(10)	4	0.5976(1)	0.4120(1)	0.0978(2)	0.72(2)
B(1)	4	0.2396(2)	0.3882(2)	0.4310(2)	0.73(3)
B(2)	2	0.7507(3)	0.4009(2)	0.0717(2)	0.67(3)
B(3)	4	0.0000	0.2619(3)	0.5000	0.58(2)
B(4)	4	0.7765(2)	0.2446(2)	0.3167(2)	0.62(3)
B(5)	4	0.2251(2)	0.0438(2)	0.1820(2)	0.66(3)
B(6)	2	0.0000	0.0132(3)	0.0000	0.54(4)
Li(1)	4	0.0567(6)	0.2911(6)	0.1753(7)	1.27(8)
Li(2)	4	0.5471(6)	0.4850(6)	0.3237(7)	1.25(8)
H(1)	4	0.38(1)	0.15(2)	0.30(1)	
H(2)	4	0.63(1)	0.09(2)	0.32(1)	

Note: Only positional parameters at the fixed values of the thermal correction 5 Å^2 were refined for hydrogen atoms.

Table 4. Geometric characteristics of hydrogen bonds in the $CaLi_4[B_5O_8(OH)_2]_2$ structure

D–H$\cdots A$	D–H, Å	H$\cdots A$, Å	D–A, Å	DHA angle, deg
O(8)–H(1)$\cdots$O(2)	0.8(1)	2.8(1)	3.091(2)	114.0(9)
O(8)–H(1)$\cdots$O(7)	0.8(1)	2.9(1)	3.358(2)	112.0(9)
O(9)–H(2)$\cdots$O(7')	0.8(1)	2.8(1)	3.397(2)	118.0(9)

REFERENCES

1. V. I. Andrianov, Kristallografiya **32** (1), 228 (1987) [Sov. Phys. Crystallogr. **32**, 130 (1987)].

2. N. E. Brese and M. O'Keeffe, Acta Crystallogr., Sect. B: Struct. Sci. **47**, 192 (1991).

3. E. V. Sokolova, N. A. Yamnova, and N. V. Belov, Kristallografiya **25** (4), 716 (1980) [Sov. Phys. Crystallogr. **25**, 411 (1980)].

4. H. Strunz, Eur. J. Mineral. **9**, 225 (1997).

5. H. Strunz and E. H. Nickel, *Strunz Mineralogical Tables* (Schweizerbart, Stuttgart, 2001).

6. E. L. Belokoneva, T. A. Korchemkina, and O. V. Dimitrova, Zh. Neorg. Khim. **45** (11), 1838 (2000).

Translated by L. Man

Refinement of the Crystal Structure of Zn-Containing Greifensteinite

A. V. Barinova*, R. K. Rastsvetaeva*, N. V. Chukanov**, and A. Pietraszko***

* Shubnikov Institute of Crystallography, Russian Academy of Sciences,
Leninskiĭ pr. 59, Moscow, 119333 Russia

e-mail: rast@ns.crys.ras.ru

** Institute of Problems of Chemical Physics, Russian Academy of Sciences,
Chernogolovka, Moscow oblast, 142432 Russia

*** Trzebiatowski Institute for Low Temperature and Structure Research,
Polish Academy of Sciences, PO Box 1410, 50-950 2 Wroclaw, Poland

Received May 11, 2004

Abstract—The crystal structure of Zn-containing greifensteinite from the Pirineus Mine (Minas Gerais, Brazil) was refined ($R = 0.045$, 562 reflections with $|F| > 2\sigma(F)$). The unit-cell parameters are $a = 15.941(3)$ Å, $b = 11.877(3)$ Å, $c = 6.625(2)$ Å, $\beta = 95.09(2)°$; $V = 1249.4$ Å^3; sp. gr. $C2/c$; and $Z = 2$. The idealized formula is $[Mn(Fe^{2+},Zn)_4]Ca_2Be_4(PO_4)_6(OH)_4 \cdot 6H_2O$. The mineral is isostructural with the previously studied monoclinic representatives of the roscherite group from different deposits and differs from these representatives in that it contains Zn in one of two octahedral positions. © *2004 MAIK "Nauka/Interperiodica".*

Roscherite (beryllium phosphate) from the Greifenstein Rocks (Germany) was first described in [1, 2] as a monoclinic mineral (sp. gr. $C2/c$) with the formula $(Ca,Mn,Fe)_3Be_3(PO_4)_3 \cdot 2H_2O$. Later on, a magnesium-rich analogue of this mineral from the Lavra da Ilha pegmatite (Minas Gerais, Brazil) [3, 4] was studied by X-ray diffraction analysis. The study of a manganese-rich specimen from the Foote Mine (North Carolina, USA) demonstrated [5] that a triclinic modification of roscherite (sp. gr. $C\bar{1}$) exists along with a monoclinic modification. Recently, the Fe^{2+}-dominant representative of the roscherite group from the Greifenstein Rocks (Saxony, Germany) [6, 7] has been approved under the name greifensteinite by the Commission on New Minerals and Mineral Names of the International Mineralogical Association. Later, we studied its triclinic magnesium-rich analogue (sp. gr. $P\bar{1}$) from the Galileia Mine (Minas Gerais, Brazil) [8]. Thus, the roscherite group includes three isostructural minerals: roscherite, zanazziite, and greifensteinite, which differ in the dom-

inating octahedral cation, and triclinic modifications of roscherite and greifensteinite.

In this study, we investigated an analogue of greifensteinite containing about 4% of ZnO, which was discovered in the Pirineus Mine (Minas Gerais, Brazil). It was of interest to study the structure of this new specimen, because an anomalously high zinc content is sometimes indicative of special structural features. The replacement of iron or manganese with zinc is untypical of some minerals (for example, minerals of the eudialyte and labuntosivite groups). The presence of zinc in a mineral of the labuntosivite group is a reliable indication that this mineral belongs to a structural type other than labuntosivite (for example, to the kuzmenkoite subgroup).

The chemical composition of the new mineral was determined by electron-microprobe (EDX) analysis. Variations in the local composition within one grain associated with growth zoning correspond to the following empirical formula:

$$(Fe_{2.2-2.4}Mn_{1.0-1.4}Zn_{0.5-0.7}Mg_{0.2-0.8}Al_{0.3-0.5})Ca_2Be_4(PO_4)_6(OH)_4 \cdot nH_2O.$$

X-ray diffraction data were collected from an irregularly shaped chip of a single crystal on a Kuma-4 CCD diffractometer. The parameters of the triclinic unit cell were determined and refined on the same diffractometer. The structural parameters and characteristics of X-ray diffraction study are given in Table 1.

The structure was refined using the atomic coordinates of greifensteinite [7] as the starting model. The cations were distributed over two independent octahedral positions, $M(1)$ and $M(2)$, taking into account the mixed atomic scattering curves for the $M(2)$ position, whereas the $M(1)$ position was assumed to be partially vacant and occupied exclusively by Mn.

Table 1. Structural data and characteristics of X-ray diffraction study

Characteristic	Data and conditions
Generalized chemical formula	$(Fe, Mn, Zn)_5Ca_2Be_4(PO_4)_6(OH)_4 \cdot 6H_2O$
Unit-cell parameters; Å, deg	$a = 15.941(3)$
	$b = 11.877(3)$
	$c = 6.625(2)$
	$\beta = 95.09(2)$
Unit-cell volume, V, Å^3	1249.4
Space group; Z	$C2/c$; 2
Calculated density ρ, g/cm^3	2.96
Absorption coefficient μ, mm^{-1}	35.12
Molecular weight	2225.8
Diffractometer	Kuma-4 CCD
Radiation, wavelength	MoK_α, 0.71073
Crystal dimensions, mm	$0.25 \times 0.25 \times 0.125$
Maximum $\sin\theta/\lambda$, Å^{-1}	0.69
Ranges of the indices of measured reflections	$-21 < h < 21$; $-16 < k < 15$; $-9 < l < 8$
Total number of reflections	14074
Number of independent reflections	7126
Number of reflections with $|F| > 2\sigma(F)$	562
R_{int} for equivalent reflections	0.085
Program for structure calculations	AREN [9]
R_{hkl} factor upon anisotropic refinement	0.046
Extinction parameter E	0.0000026

The hydrogen atoms of one water molecule were revealed from a difference electron-density map. The anisotropic refinement converged to an R factor of 4.5%. The positional and equivalent thermal parameters of the atoms corresponding to this R factor are given in Table 2. The interatomic distances in M octahedra and hydrogen-bond lengths are listed in Table 3.

The structure of Zn-containing greifensteinite, like the structures of other representatives of the roscherite group studied earlier, can be described as a three-dimensional framework consisting of tetrahedra, octahedra, and Ca seven-vertex polyhedra (figure). Be and P tetrahedra form infinite chains linked by M octahedra into a mixed framework. M octahedra, in turn, share edges to form octahedral chains. Ca atoms occupy cavities in the framework. Generally, the octahedra in the lattice sites are occupied only partially. Hence, the total number of M cations decreases from six to five, and the chains statistically break down into pairs of octahedra.

The crystal-chemical formula of the mineral can be represented as follows ($Z = 2$): $[Mn^{2+}_{0.68} \square_{0.32}] \cdot [(Fe^{2+},Fe^{3+})_{2.35}Zn_{0.72}Mn_{0.46}Al_{0.28}Mg_{0.19}]Ca_2Be_4(PO_4)_6 \cdot (OH)_4(H_2O,O)_2 \cdot 4H_2O$, where the compositions of independent octahedral positions are enclosed in brackets. The Ca polyhedron is formed by four oxygen atoms and three water molecules, one of which is shared with

Table 2. Atomic coordinates and equivalent thermal parameters

Atom	x/a	y/b	z/c	B_{eq}, Å^2
Ca	0	0.2571(2)	0.25	2.1(1)
$M(1)$	0	0	0	2.04(1)
$M(2)$	0.1713(1)	0.1616(1)	0.9960(2)	2.26(6)
P(1)	0.1880(2)	0.1173(2)	0.4779(4)	1.9(1)
P(2)	0	0.2740(3)	0.75	1.6(2)
Be	0.333(1)	0.178(1)	0.299(2)	2.6(6)
O(1)	0.3559(5)	0.4973(6)	0.498(1)	2.4(4)
O(2)	0.2824(4)	0.0999(6)	0.450(1)	2.1(4)
O(3)	0.1454(4)	0.1823(6)	0.299(1)	1.9(4)
O(4)	0.3188(4)	0.3136(5)	0.328(1)	1.6(4)
O(5)	0.4583(4)	0.2970(6)	0.074(1)	1.9(3)
O(6)	0.4338(4)	0.1505(5)	0.342(1)	2.1(4)
OH	0.3000(4)	0.1640(6)	0.062(1)	1.9(4)
$H_2O(1)$	0.0928(5)	0.4194(6)	0.219(1)	2.5(4)
$H_2O(2)$	0	0.041(1)	0.25	3.3(6)
H(1)	0.082(1)	0.488(1)	0.179(1)	3*
H(2)	0.150(1)	0.417(1)	0.180(1)	3*

Note: $M(1) = Mn_{1.36}$; $M(2) = Fe_{4.7}Zn_{1.44}Mn_{0.92}Mg_{0.38}Al_{0.56}$; $H_2O(2) = (H_2O, O)$.
* Isotropic thermal parameters (unrefined).
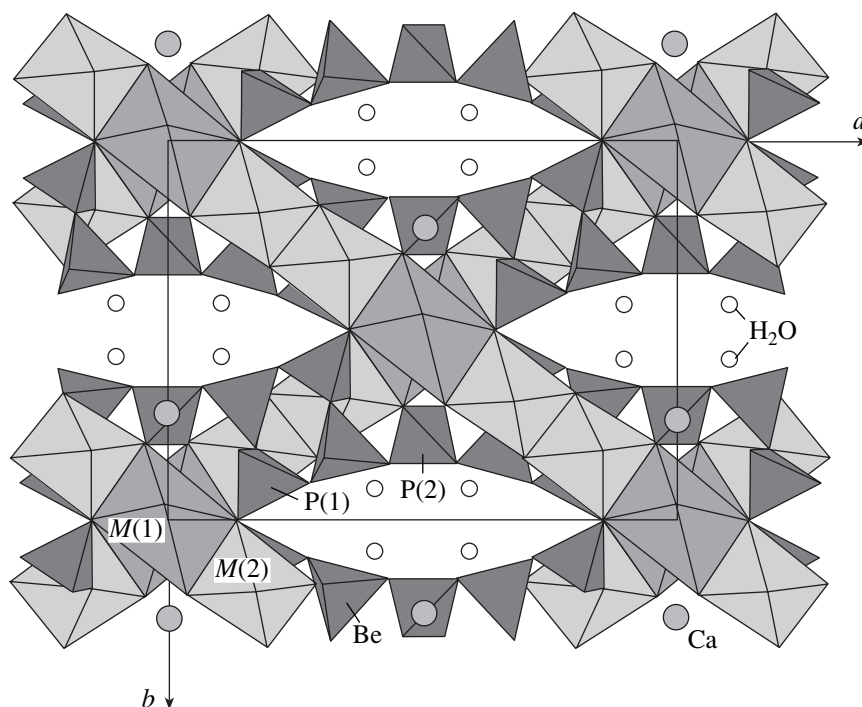
Structure of Zn-containing greifensteinite projected onto the (001) plane.

the strongly distorted $M(1)$ octahedron. According to the local bond-valence requirements [10] (Table 4), an excess of bond valences in the corresponding $H_2O(2)$ position indicates that the water molecules are partially replaced with oxygen atoms. Taking into account that the $M(1)$ position is vacant in the majority (2/3) of unit cells, we write the composition of the $H_2O(2)$ position as (H_2O, O). Previously, we found a similar partial substitution of water molecules with OH groups in the structure of the triclinic analogue of greifensteinite [8]. This substitution can occur also in other members of the group resulting in a decrease in the total number of H_2O molecules in the formulas of the minerals. However, this fact was not noted in the original studies.

The occurrence of Zn atoms in one of two octahedral positions is consistent with the smaller size of the $M(2)$ octahedron as compared to the $M(1)$ octahedron (interatomic distances of 2.106 and 2.194 Å, respec-

Table 3. Selected interatomic distances, Å

M octahedra			
$M(1)$–$H_2O(2)$	1.727(3) × 2	$M(2)$–O(1)	2.000(7)
O(1)	2.296(6) × 2	OH	2.059(7)
O(5)	2.559(7) × 2	O(3)	2.099(7)
	⟨2.194⟩	O(5)	2.133(7)
		OH	2.163(7)
		O(4)	2.183(7)
			⟨2.106⟩

H bonds			
H(1)–$H_2O(1)$	0.87(1)	∠H(1)–$H_2O(1)$–H(2)	97.0(1)
H(2)–$H_2O(1)$	0.97(2)	∠$H_2O(1)$–H(1)–O(6)	166.3(5)
H(1)–H(2)	1.63(1)	∠$H_2O(1)$–H(2)–O(2)	175.8(3)
H(1)···O(6)	1.94(1)		
H(2)···O(2)	2.09(2)		

Table 4. Bond valences according to [10]

Anion/cation	$M(1)$	$M(2)$	Ca	P(1)	P(2)	Be	Σ
O(1)	0.25	0.49		1.21			1.95
O(2)				1.21		0.52	1.73
O(3)		0.37	0.25	1.29			1.91
O(4)		0.30		1.23		0.50	2.03
O(5)	0.13	0.34	0.32		1.22		2.01
O(6)					1.21	0.50	1.71
OH		0.42				0.54	1.27
		0.31					0.27
$H_2O(1)$			0.27				2.58
$H_2O(2)$	1.19 × 2		0.20				

Note: The occupancy of the $M(1)$ position is 0.34; the composition of the $M(2)$ position was assumed to be Fe^{2+}.

Table 5. Structural data for minerals of the roscherite group

No.	Mineral	Unit-cell parameters; Å, deg	Sp. gr.	Formula	Mn : Fe : Mg	Reference
1	Roscherite*	$a = 15.90$, $b = 11.88$, $c = 6.69$ $\beta = 94.7$	$C2/c$	$(Mn, Fe)_5Ca_2Be_4(PO_4)_6(OH)_4 \cdot 6H_2O$	0.85 : 0.14 : 0.01	[2]
2	Zanazziite	$a = 15.874$, $b = 11.854$, $c = 6.605$ $\beta = 95.21$	$C2/c$	$(Mg, Fe)_5Ca_2Be_4(PO_4)_6(OH)_{3.4} \cdot 6.6H_2O$	0.05 : 0.33 : 0.62	[4]
3	Greifensteinite	$a = 15.903$, $b = 11.885$, $c = 6.677$ $\beta = 94.68$	$C2/c$	$(Fe, Mn)_5Ca_2Be_4(PO_4)_6(OH)_4 \cdot 6H_2O$	0.16 : 0.74 : 0.09	[7]
4	Zn-containing greifensteinite	$a = 15.941$, $b = 11.877$, $c = 6.625$ $\beta = 95.09$	$C2/c$	$(Fe, Mn, Zn)_5Ca_2Be_4(PO_4)_6(OH)_4 \cdot 6H_2O$	0.31 : 0.64 : 0.05	This study
5	Triclinic roscherite	$a = 15.921$, $b = 11.965$, $c = 6.741$ $\alpha = 91.04$, $\beta = 94.21$, $\gamma = 89.59$	$C\bar{1}$	$(Mn, Fe)_5Ca_2Be_4(PO_4)_6(OH)_4 \cdot 6H_2O$	0.90 : 0.09 : 0.01	[5]
6	Triclinic greifensteinite	$a = 9.883$, $b = 9.879$, $c = 6.668$ $\alpha = 86.93$, $\beta = 85.60$, $\gamma = 73.53$	$P\bar{1}$	$(Fe, Mg)_5Ca_2Be_4(PO_4)_6(OH)_4 \cdot 6H_2O$	0.04 : 0.51 : 0.45	[8]

Note: For uniformity, the unit-cell parameters a and b for triclinic greifensteinite are interchanged.
      * The structure was not studied.

tively). An analogous regular and compact Zn octahedron is observed, for example, in the alsakharovite-Zn structure (Zn–O = 2.04–2.26 Å; aver., 2.14 Å) [11, 12]. The idealized formula of the mineral can be written as $[Mn(Fe^{2+},Zn)_4]Ca_2Be_4(PO_4)_6(OH)_4 \cdot 6H_2O$.

Minerals of the roscherite group from different deposits differ in the cation content in octahedral positions, with the compositions in tetrahedral positions being invariant (Table 5). For example, Mg atoms predominate in the zanazziite structure (three of five atoms), whereas Mn and Fe cations predominate in roscherite and greifensteinite, respectively. In monoclinic minerals of the roscherite group, there is only one key ("specimen-forming") octahedral position (eightfold $M(2)$ position), whereas the second position (at the inversion center) tends to be vacant (greifensteinite) or contains the same dominating cation as that in the major position (zanazziite). In the triclinic mineral, three positions (except for the vacant one) are of importance from the viewpoint of classification [8].

To summarize, the mineral under study retains the structural type of the monoclinic representatives of the roscherite group and differs from them in that Zn atoms are present in the eightfold octahedral position.

ACKNOWLEDGMENTS

REFERENCES

1. F. Slavík, Akad. Ceska, Bull. Int. Acc. Sci. Bohéme, No. 4, 108 (1914).

2. M. L. Lindberg, Am. Mineral. **43** (9), 824 (1958).

3. L. Fanfani, A. Nunzi, P. F. Zanazzi, and A. R. Zanzari, TMPM Tschermaks Mineral. Petrogr. Mitt. **22**, 266 (1975).

4. P. B. Leavens, J. S. White, and J. A. Nelen, Mineral. Rec. **21**, 413 (1990).

5. L. Fanfani, P. F. Zanazzi, and A. R. Zanzari, TMPM Tschermaks Mineral. Petrogr. Mitt. **24**, 169 (1977).

6. N. V. Chukanov, Sh. Mékkel', R. K. Rastsvetaeva, and A. E. Zadov, Zap. Vseros. Mineral. O–va, No. 4, 47 (2002).

7. R. K. Rastsvetaeva, O. A. Gurbanova, and N. V. Chukanov, Dokl. Akad. Nauk **383** (3), 354 (2002).

8. R. K. Rastsvetaeva, A. V. Barinova, N. V. Chukanov, and A. Petrashko, Dokl. Akad. Nauk **398** (4) (2004).

9. V. I. Andrianov, Kristallografiya **32** (1), 228 (1987) [Sov. Phys. Crystallogr. **32**, 130 (1987)].

10. N. E. Brese and M. O'Keeffe, Acta Crystallogr., Sect. B: Struct. Sci. **47**, 192 (1991).

11. K. A. Rozenberg, R. K. Rastsvetaeva, I. V. Pekov, and N. V. Chukanov, Dokl. Akad. Nauk **383** (5), 657 (2002).

12. I. V. Pekov, N. V. Chukanov, A. E. Zadov, *et al.*, Zap. Vseros. Mineral. O–va, No. 1, 52 (2003).

Translated by T. Safonova

STRUCTURE
OF INORGANIC COMPOUNDS

Structure of the New Mineral Paratsepinite-Na and Its Place in the Labuntsovite Group

N. I. Organova*, S. V. Krivovichev**, Z. V. Shlyukova*, A. E. Zadov***, I. V. Rozhdestvenskaya**, and T. I. Ivanova**

* Institute of Geology of Ore Deposits, Petrography, Mineralogy, and Geochemistry,
Russian Academy of Sciences, Staromonetnyĭ per. 35, Moscow, 119017 Russia
** St. Petersburg State University, Universitetskaya nab. 7/9, St. Petersburg, 199034 Russia
*** Regenerator Research and Production Association, Moscow, Russia
Received November 18, 2002

Abstract—X-ray diffraction study of high-strontium Ti-nenadkevichite showed that it is a new mineral, which was given the name paratsepinite-Na, sp. gr. $C2/m$, a double value of the parameter c, and a different distribution of the non-framework cations in comparison with tsepinite-Na. In particular, strontium is located not only in the hexagonal window of the small channel, but also in three positions of the large channel. The characteristics of the mosaic blocks constituting the crystal are studied. It is assumed that polysynthetic twinning in these crystals and many other representatives of this family is associated with the phase transformation occurring in this hydrothermal mineral during its cooling after formation. The comparison of all the three structures of the vuoriyarvite subgroups of the labuntsovite group allows us to explain the disability of vuoriyarvite to absorb strontium from the aqueous solution by its smaller unit-cell volume and higher framework charge in comparison with those of tsepinites. © 2004 MAIK "Nauka/Interperiodica".

INTRODUCTION

Recently, an ever increasing interest in new microporous crystals that may absorb and retain harmful radioactive wastes resulted in numerous publications on possible use of mineral labuntsovite for this purpose [1]. The recent study of natural labuntsovites of different compositions in aqueous solutions at room temperature [2] showed that the highest absorption of Na, K, and Cs is observed in the minerals of the vuoriyarvite group, whereas Sr is absorbed only by tsepinite.

In the recent decade, Russian researchers achieved considerable progress in the structural and mineralogical study of the labuntsovite–nenadkevichite group. They also developed new nomenclature according to which all the 18 minerals of this group were divided into 8 subgroups [3].

The structures of the minerals of the labuntsovite group consist of the chains of Ti–Nb octahedra connected by four-member silicon–oxygen rings. The framework thus formed (Fig. 1) has a zeolite-like structure and two kinds of channels: those with a large diameter along the y axis and those with a small diameter along the [101] and [10$\bar{1}$] directions.

The pseudoorthorhombic framework is negatively charged and its channels are filled with cations. The large channels are occupied by Na, K, and Ba, and, sometimes, also with Sr and Ca and water molecules. Some minerals of the labuntsovite group also contain oxonium ions [4]. Small channels are occupied by Mg, Fe, Zn, Na, Ca, and Sr ions. Similar to zeolites, the dis-

tribution of atoms over all or some positions may be both ordered and disordered and may or may not have vacancies.

The well-known minerals of the labuntsovite group are crystallized in one of four possible space groups: $Pbam$, Cm, $C2/m$, and $I2/m$. The first, orthorhombic, space group is characterized by the minimum unit-cell parameters ($a_p \sim 7$, $b_p \sim 7$, $c_p \sim 14$ Å (Fig. 1a). The monoclinic unit cells may be divided into three types: the C-cell with small dimensions ($a \sim 14$, $b \sim 14$, $c \sim 8$ Å, $\beta' \sim 117^o$), the doubled C-cell ($a_m \sim 14$, $b_m \sim 14$, $c_m \sim 16$ Å, $\beta'' \sim 117^o$), and the I-cell ($a \sim 14$, $b \sim 14$, $c \sim 16$ Å, $\beta \sim 117^o$). It should be noted that the transition from the small c-cell to the large C-cell is caused not by doubling of the c parameter but, what is important, by the cell transformation described by the relationships $\mathbf{a}_m = -\mathbf{a}$, $\mathbf{b}_m = -\mathbf{b}$, and $\mathbf{c}_m = \mathbf{a} + 2\mathbf{c}$. The specific features of the diffraction pattern from labuntsovite with the doubled C-cell will be discussed later. The authors of the new nomenclature suggested to supply to the names of labuntsovites with the double cells the prefix "para-" in those cases where there exists a similar mineral with the conventional (not doubled) c parameter.

There are also other subgroups of the family having both para- and monoforms (e.g., kuzmenkoite and parakuzmenkoites [5]) and also minerals whose names have no prefix para- (e.g., organovaite-Zn and organovaite-Mn [6, 7]) because the latter have no varieties with the monoparameter c.
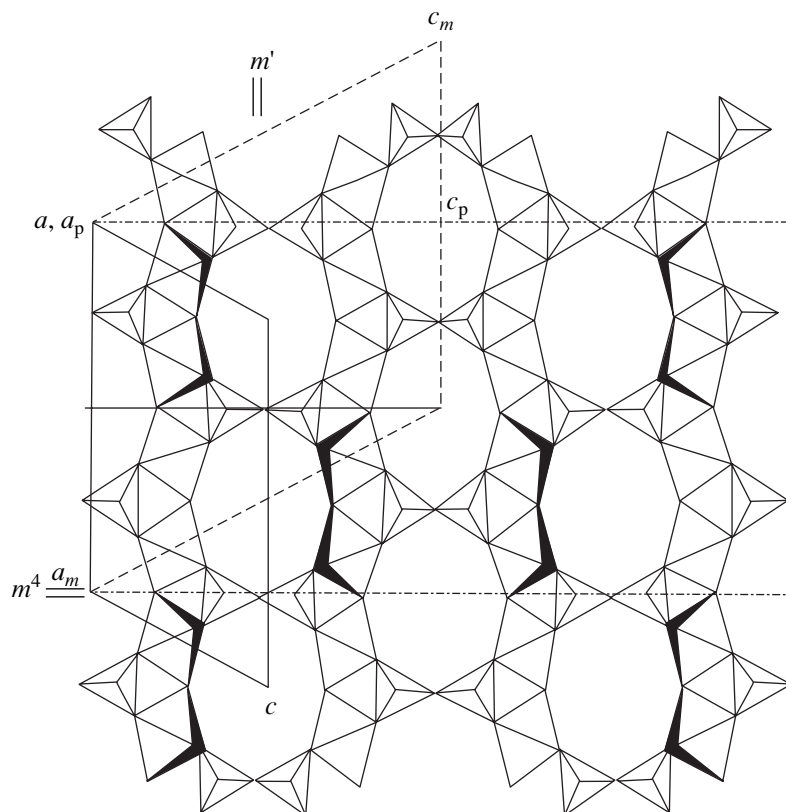
Fig. 1. Labuntsovite framework projected along the y axis (according to Rastsvetaeva) [4].

Earlier, we studied both mineralogically and structurally Ti-nenadkevichite from pegmatites of the Khibiny massif (mount Khibinpakhchorr) [8–10]. The microprobe analysis of these crystals epitaxially grown over the labuntsovite crystals ("caps") [10] showed not only the pronounced inhomogeneity in the distribution of the elements in both labuntsovite crystals and the caps, but also the presence of strontium "not seen" by the "wet" chemical analysis.

The structure determination of Sr-containing Ti-nenadkevichite (2.32% SrO) [4] allowed one to consider it as a new mineral tsepinite-Na [12]. The same pegmatites contained among small crystals of Ti-nenadkevichite epitaxially grown on labuntsovite also crystals with a high strontium content. One of these

crystals with 8% SrO was selected for structure refinement, which is the subject of the present article, which allowed us to consider it as a new mineral: paratsepinite-Na. Its existence was confirmed by the Commission on New Minerals and Mineral Names of the International Mineralogical Association on March 12, 2003.

EXPERIMENT AND STRUCTURE REFINEMENT

The study of the chemical composition of paratsepinite-Na was performed on a CAMEBAX-MBX microprobe setup. The chemical formula of the crystal corresponds to the empirical formula

$$(Na_{3.68}Sr_{1.73}K_{0.76}Ca_{0.51}Ba_{0.16}Mn_{0.03}Zn_{0.03})_{\Sigma7.99}(Ti_{5.03}Nb_{2.87}Fe_{0.09})_{\Sigma7.99}$$

$$[Si_{15..92}Al_{0.08}O_{48}](O_{4.01}OH_{3.99})_{\Sigma8.00} \cdot 7.75H_2O.$$
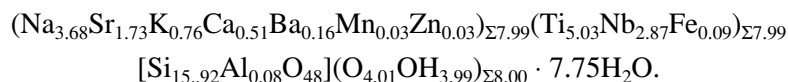
The X-ray diffraction experiment (Table 1) was performed at the University of Notre Dame, Indiana, USA. The set of diffraction-reflection intensities was obtained using a CCD detector (the exposure time of each pattern was 30 s). Altogether 1200 patterns were obtained by ω scanning at a step of 0.3°, which corresponds to the more than half of the diffraction sphere.

The set of structure factors was obtained using the SAINT program with the introduction of all the necessary corrections. The absorption correction was introduced by the semiempirical method of pseudo ψ scanning with the use of 1276 reflections with $I > 15\sigma(I)$. The crystal shape was modeled by an ellipsoid. After averaging symmetrically equivalent reflections, the

Table 1. Crystallographic characteristics and the refinement parameters for the paratsepinite-Na structure in the anisotropic approximation

a, Å	14.596(2)
b, Å	14.249(2)
c, Å	15.852(3)
β, deg	117.270(3)
V, Å^3	2930.55
Sp. gr., Z	$C2/m$, 4
Radiation, λ, Å	MoK_α, 0.70926
ρ_{calcd}, g/cm^3	2.76
Crystal dimensions, mm^3	$0.20 \times 0.35 \times 0.025$
Diffractometer	Bruker APEX 4K CCD
$\sin\theta/\lambda$	<1.245
Number of crystallographically independent reflections	2164 $|F| > 4\sigma(F)$
R	0.077

reliability factor was $R_{int} = 0.072$. The structure was refined in the anisotropic approximation up to $R_1 = 0.077$ using 2164 reflections with $|F_{hkl}| \geq 4\sigma|F_{hkl}|$ with due regard for the pseudomerohedral twinning in the (001) plane. Twinning was taken into account using the SHELXTL program with the use of the twinning matrix [100/010/101]. The refined ratio of the twinning components was 0.75 : 0.25.

In order to confirm that doubling of the unit cell is not an auxiliary effect of twinning [13], the diffraction data were reindexed for a small C-cell. It turned out that about 600 reflections with $|F_{hkl}| \geq 4\sigma|F_{hkl}|$ cannot be adequately indexed within the frameworks of the small C-cell. The structure of the paratsepinite-Na was solved anew in the small unit cell and was refined in the sp. gr. $C2/m$ up to $R = 0.125$ over 1518 reflections with $|F_{hkl}| \geq 4\sigma|F_{hkl}|$. All the attempts to refine the structure in the anisotropic approximation resulted in physically unreasonable thermal parameters, which usually indicates an inappropriate choice of the unit cell or the space group. The transition to the group Cm allowed us to refine the structure only to $R = 0.154$ and also deteriorated the thermal parameters. Thus, the unit-cell doubling is favored by the presence of about 600 strong reflections which could not be indexed in the small unit cell and the difficulties in structure refinement in this small unit cell. Thus, paratsepinite-Na really has the doubled unit cell, which determines its structural and mineralogical difference from tsepinite-Na. Structurally, doubling of the cell is explained by disorder of Sr^{2+} cations over the cavities of the titanium–silicate framework.

The high value of the R factor is explained, first and foremost, by the systematic broadening of some reflections and their approximate superposition.

Table 2. Coordinates and thermal parameters (Å^2) of structure atoms

Atom	x	y	z	U_{iso}
Ti(1)	0.2497(2)	0.73996(6)	0.2502(2)	0.0271(4)
Ti(2)	0.5000(2)	0.2500(2)	0.2503(2)	0.0277(4)
Si(1)	0.6937(3)	0.3892(2)	0.3823(2)	0.0139(7)
Si(2)	0.3051(3)	0.1114(2)	0.1174(2)	0.0149(8)
Si(3)	0.6953(3)	0.3886(2)	0.8957(2)	0.0136(7)
Si(4)	0.8055(3)	0.3882(2)	0.6043(2)	0.0159(8)
O(1)	0.4011(6)	0.2607(4)	0.3015(5)	0.022(2)
O(2)	0.6716(1)	1/2	0.8829(8)	0.030(3)
O(3)	0.7420(7)	0.3597(5)	0.6587(6)	0.025(2)
O(4)	0.7354(7)	0.3630(4)	0.4932(6)	0.028(2)
O(5)	0.8263(10)	1/2	0.6128(8)	0.033(4)
O(6)	0.5745(7)	0.3588(5)	0.3281(6)	0.028(2)
O(7)	0.0988(5)	0.7411(5)	0.1983(4)	0.0148(14)
O(8)	0.5871(7)	0.3340(5)	0.8566(5)	0.028(2)
O(9)	0.9136(6)	0.3350(5)	0.6441(6)	0.025(2)
O(10)	0.7642(8)	0.3626(4)	0.0074(7)	0.035(2)
O(11)	0.7635(6)	0.3357(4)	0.3442(6)	0.020(2)
O(12)	0.7600(6)	0.3612(4)	0.8399(6)	0.018(2)
O(13)	0.2361(6)	0.1655(5)	0.1559(6)	0.023(2)
O(14)	0.4242(6)	0.1404(5)	0.1744(6)	0.025(2)
O(15)	0.2913(9)	0	0.1282(8)	0.028(3)
O(16)	0.7038(10)	1/2	0.3684(9)	0.037(4)
H$_2$O(1)	0.561(1)	1/2	0.665(1)	0.063(4)
H$_2$O(2)	0.930(1)	1/2	0.830(1)	0.051(4)
H$_2$O(3)	0.074(2)	0	0.151(1)	0.147(11)
H$_2$O(4)	0.0716(13)	1/2	0.6540(11)	0.107(6)
H$_2$O(5)	0.4099(4)	0.2587(4)	0.4964(4)	0.020(2)
H$_2$O(6)	−0.0889(4)	0.7435(3)	−0.0033(4)	0.0194(15)
K(1)	1/2	0.3194(16)	1/2	0.154(12)
K(2)	0	0.6136(15)	0	0.148(12)
Na(1)	0.2511(48)	0	0.2532(43)	0.026(8)
Na(2)	−0.0327(23)	0.8701(14)	−0.0574(17)	0.185(14)
Sr(1)	0.7490(7)	1/2	0.7485(6)	0.0168(9)
Sr(2)	0.4667(21)	0.1232(13)	0.4366(16)	0.199(14)

The final model included the coordinates of all the atoms and the anisotropic thermal parameters for all these atoms with the position occupancy 100% (Table 2). The cation coordination is indicated in Table 3.

COMPARISON OF THE STRUCTURES OF THE VUORIYARVITE SUBGROUP

Figure 2 shows the tsepinite-Na and paratsepinite-Na structures. Table 4 lists the data for each of the struc-

Table 3. Characteristics of coordination polyhedra

Posi-tion	Composition	c.n.	Bond lengths, Å	
			range	average
Ti(1)	$0.6Ti + 0.4Nb$	6	1.954(8)–1.988(7)	1.97
Ti(2)	$0.6Ti + 0.4Nb$	6	1.959(8)–1.986(8)	1.97
Si(1)	Si	4	1.597(8)–1.619(9)	1.61
Si(2)	Si	4	1.595(9)–1.619(4)	1.61
Si(3)	Si	4	1.609(8)–1.628(10)	1.62
Si(4)	Si	4	1.581(8)–1.621(9)	1.60
Sr(1)	$0.2Sr + 0.2Ca$	6	2.345(2)–2.438(2)	2.41
Sr(2)	$0.1Sr + 0.1Ca$	7	2.17(2)–2.93(2)	2.60
K(1)	$0.2K + 0.05Ba$	6	2.920(9)–3.411(10)	3.21
K(2)	$0.2K + 0.2Sr$	7	2.27(5)–3.27(5)	2.67
Na(1)	0.2Na	8	2.321(6)–2.77(6)	2.52
Na(2)	0.6Na	6	2.27(2)–2.72(3)	2.53
$H_2O(4)$	$0.2Sr + 0.3H_2O$	6	2.46(2)–2.73(1)	2.60

tures and for vuoriyarvite. It is obvious that the large channel in tsepinite-Na is less occupied than in paratsepinite-Na. The character of the disorder in these channels is somewhat contradictory. On the one hand, the doubling of one of the parameters indicates a higher order, whereas an increase in the number of isomorphously substituting components in most of the cation positions is a sign of a more pronounced disorder. The more disordered cation distribution results in cell doubling.

SPECIFIC FEATURES OF MOSAICITY AND A PROBABLE PHASE TRANSFORMATION IN TSEPINITE

The specific character of mosaicity in crystals gives the information on crystal genesis and is reflected in the crystal properties, including the characteristics of their diffraction patterns.

The mosaicity in labuntsovites was first observed by Bulakh and Evdokimov [14] who also assumed that the microblock structure of these crystals is the result of submicroscopic intergrowth of two solid phases with similar structures but different compositions. In light of

Table 4. Some structural characteristics of minerals of the vuoriyarvite subgroup

	Paratsepinite-Na*	Tsepinite-Na**	Vuoriyarvite***
Sp. gr.	$C2/m$	Cm	Cm
Unit-cell parameters	$a = 14.596$, $b = 14.249$,	$a = 14.604$, $b = 14.276$,	$a = 14.692$, $b = 14.164$,
	$c = 15.952$ Å, $\beta = 117.27$	$c = 7.933$ Å, $\beta = 117.40$	$c = 7.859$ Å, $\beta = 117.87$
Unit-cell volume, Å^3	2948.9 (2 × 1474.5)	1468.2	1445.75
Twinning	(001)	(001), (–401)	(001), (–401)
Occupancy:			
Ti(1)	$Ti_{0.6}Nb_{0.4}$	$Ti_{0.7}Nb_{0.3}$	$Ti_{0.4}Nb_{0.6}$
Ti(2)	$Ti_{0.6}Nb_{0.4}$	$Ti_{0.4}Nb_{0.6}$	$Ti_{0.5}Nb_{0.5}$
Sr(1)	$Sr_{0.2}Ca_{0.2}\eta_{0.6}$****	$Sr_{0.22}\square_{0.78}$****	$Na_{0.58}\square_{0.42}$****
Sr(2)	$Sr_{0.1}Ca_{0.1}$		
K	$K_{0.2}Ba_{0.05}\eta_{0.75}$	$K_{0.6}\eta_{0.4}$	$K_{0.49}\eta_{0.51}$
Ba		$Ba_{0.08}\eta_{0.92}$	$K_{0.44}\eta_{0.56}$
Na(1)	$Na_{0.2}\eta_{0.8}$****	$Na_{0.47}\square_{0.53}$****	$Na_{0.49}\square_{0.51}$****
Na(2)$_P$	$Na_{0.6}\eta_{0.4}$	$Na_{0.62}\square_{0.38}$****	$(H_2O)_{0.32}\square_{0.68}$****
Na(2)$_O$	$K_{0.2}Sr_{0.1}\eta_{0.7}$		
Na(3)	$Ca_{0.1}Sr_{0.1}\eta_{0.8}$		
Na(4)	$Na_{0.6}\eta_{0.4}$		
$H_2O(4)$	$(H_2O)_{0.3}$, $Sr_{0.2}\eta_{0.5}$		
H_2O		$(H_2O)_{0.2}\eta_{0.8}$	

* $(Na, Sr, K, Ca, Ba)_{10}(Ti, Nb)_{16}[Si_4O_{12}]_8 12H_2O$.
** $(H_3O, Na, K, Sr)_{7.5}(Ti, Nb)_8[Si_4O_{12}]_4 5H_2O$.
*** $(K, Na)_8(Nb, Ti)_8[Si_4O_{12}]_4 6H_2O$.
**** The position between Ti(1) and Ti(2) is an analogue of the Na(1) position in the nenadkevichite and korobitsynite structures or the D position in labuntsovites with prevailing Ti components.

(a)

(b)
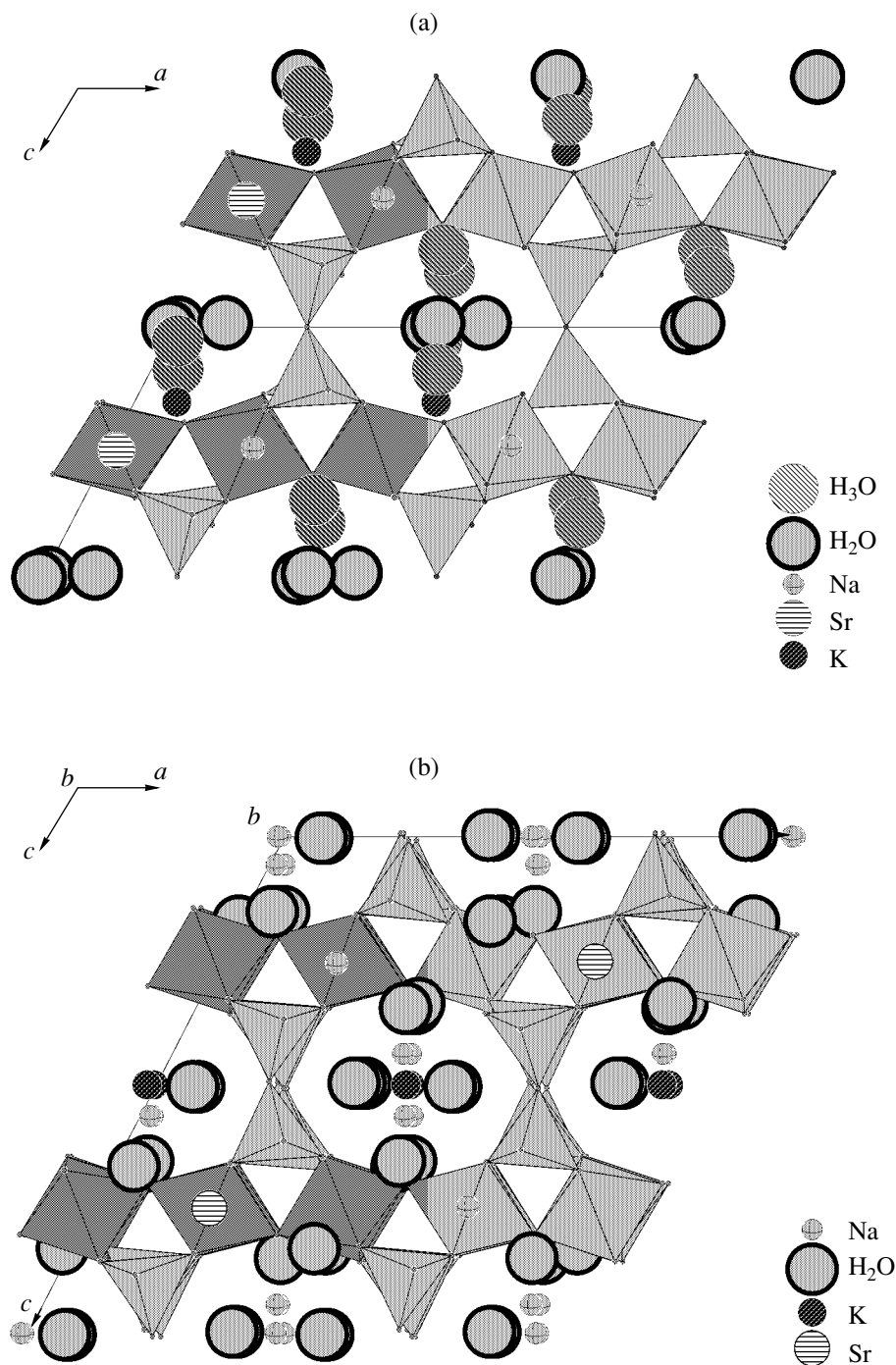
Fig. 2. (a) Tsepinite-Na and (b) paratsepinite-Na projected along the *y* axis.

the modern theories, the number of different phases can be even larger.

The structurally studied small paratsepinite-Na crystal was used to record the axial (*h*00) and (00*l*) reflections in the orthorhombic setting in order to perform profile analysis [15]. The experimental data obtained are shown in Fig. 3. The processing of these data showed that the average sizes of the coherent-scattering regions along *X* and *Z* are 300 and 1100 Å, respectively. The stresses along the former axis are seven-fold higher than the stresses along the latter axis.

The schematic drawing of the image of a tsepinite crystal in an optical microscope may be found in [9]. The blocks of mosaics of the crystals grown from
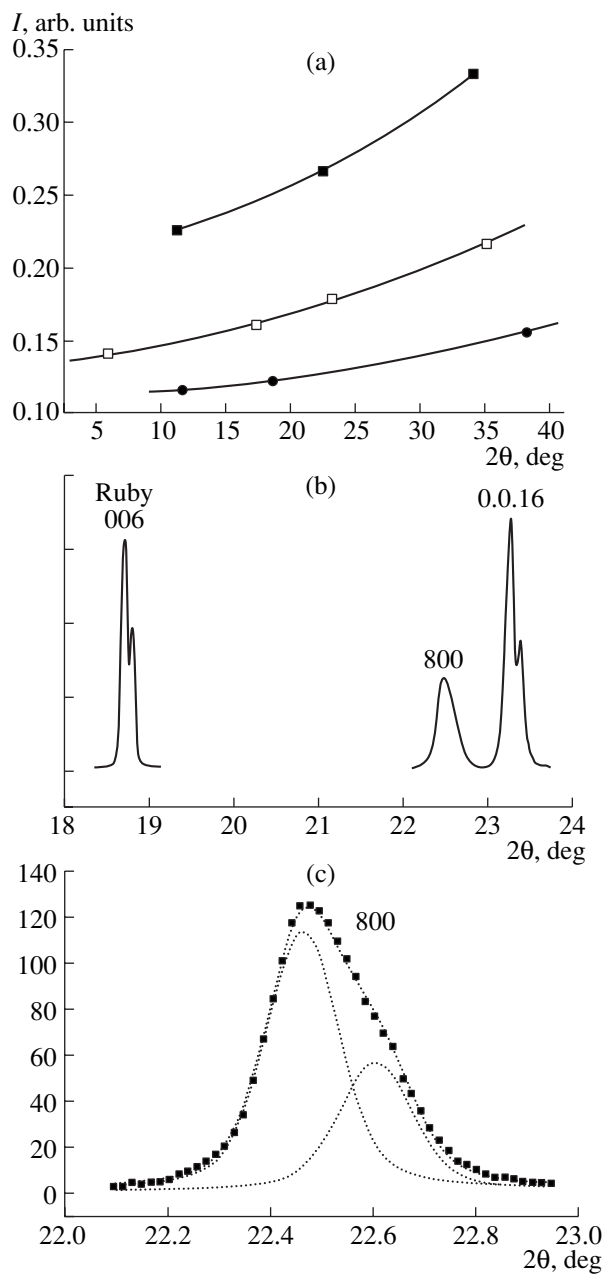
Fig. 3. Profiles of the basic ($h00$) and ($00l$) reflections of the paratsepinite-Na crystal in the orthorhombic setting: (a) integral half-widths of the □—$00l$ and ●—$h00$ reflections and ■—of the ruby standard, (b) reflections from the sample and the standard, (c) an example of the reflection decomposition into the $K_{\alpha1}$ and $K_{\alpha2}$ components.

Ti–O–Si bonds. The zero layer line of the paratsepinite-Na crystal recorded on the photographic film had diffuse ($h00$) and sharp ($00l$) reflections in full accordance with the shape of the coherent-scattering region.

Thus, the moderate-sized coherent-scattering region has the shape flattened along the X axis and intersects the structure normally to the direction of the elongation of the Ti–Nb octahedra. It is highly probable that the initial crystal growth starts with the formation of an individual blocks having orthorhombic symmetry and located with their side faces parallel to one another onto the (001) plane. Then, the "life" of tsepinite-Na and paratsepinite-Na may be considered as follows.

Small crystals grown from hydrothermal solutions have orthorhombic symmetry. All the positions between the chains of the Ti–Nb octahedra are filled as in korobitsynite. With lowering of the temperature, the crystals undergo a phase transition [16] as a result of which the orthorhombic symmetry changes to monoclinic. The resulting stresses give rise to a certain "discharge": polysynthetic twinning in the (001) or along (001) and ($\bar{4}01$) planes. Some atoms located between the octahedra migrate to larger channels. The structure at twin boundaries and inside these boundaries differs from the bulk structure. It is there that the atoms with small radii, and first of all Na atoms, may migrate [17].

The classical mineralogical example of such a transformation is albite which becomes twinned during the phase transition from monoclinic to triclinic modification.

The orthorhombic symmetry of the coherent-scattering regions confirms the assumption on the phase transformation. The distribution and redistribution of the framework cations takes place at the first stage of crystal growth. For non-framework cations, ordering processes may occur within their whole "life" and depend not only on the composition of the hydrothermal solution and its temperature, but also on the process kinetics.

Under certain conditions, the cations of one species may be localized within individual blocks. As a result, the order in such blocks may be higher than the average order over the whole diffracting volume.

The different space groups of the crystals from one pegmatite under similar conditions—Cm or $C2/m$—may be explained by the prevalence of one type of symmetry in the diffracting volume.

hydrothermal solutions contain the information on the growth conditions and growth mechanism and also reflect the symmetry of a growing crystal. Thus, flattening of the coherent-scattering regions in the x_{p} direction in the layer grown mainly along the y axis may be explained by breaking of the bonds in the chain of T–Nb octahedra often linked by the hydroxyl groups which weaken bonding in comparison with the

MAIN RESULTS

The paratsepinite-Na structure with the sp. gr. $C2/m$ and the double c parameter is refined.

It is shown that the Na-tsepinite has two modifications with sp. gr. Cm and $C2/m$ and with different values of the c parameter.

The polysynthetic microtwinning may be considered as a consequence of the phase transformation of

the initial orthorhombic structure into the monoclinic one which is accompanied by the displacements of the nonframework cations and water molecules.

It is assumed that two varieties may coexist within one crystalline volume.

The processes described seem to be characteristic of most of the monoclinic labuntsovites; some other minerals of this family considered in this article are also polysynthetic twins and obey the same twinning laws.

ACKNOWLEDGMENTS

REFERENCES

1. J. Rocha, P. Brandao, Zh. Lin, *et al.*, Chem. Commun., No. 5, 660 (1996).

2. I. E. Pekov, A. G. Turchkova, N. N. Kononkova, and N. V. Chukanov, in *Abstracts of Meeting on Geochemistry of Magmatic Rocks* (2002), p. 76.

3. N. V. Chukanov, I. V. Pekov, and A. P. Khomyakov, Eur. J. Mineral. **14**, 165 (2002).

4. R. K. Rastsvetaeva, N. I. Organova, I. V. Rozhdestvenskaya, *et al.*, Dokl. Akad. Nauk **371**, 336 (2000).

5. N. V. Chukanov, I. V. Pekov, E. I. Semenov, *et al.*, Zap. Vseross. Mineral. O–va **130** (6), 63 (2001).

6. N. V. Chukanov, I. V. Pekov, A. E. Zadov, *et al.*, Zap. Vseross. Mineral. O–va **130** (2), 46 (2001).

7. I. V. Pekov, N. V. Chukanov, A. E. Zadov, *et al.*, Zap. Vseross. Mineral. O–va **131** (1), 29 (2002).

8. Z. V. Shlyukova, M. N. Sokolova, T. A. Yakovlevskaya, *et al.*, Zap. Vses. Mineral. O–va, No. 4, 430 (1965).

9. N. I. Organova, Z. V. Shlyukova, N. I. Zabavnikova, *et al.*, Izv. Akad. Nauk SSSR **39** (2), 98 (1976).

10. N. I. Organova, D. K. Arkhipenko, Yu. P. Dikov, *et al.*, Mineral. Zh., No. 2, 49 (1981).

11. Z. V. Shlyukova, N. I. Organova, N. V. Chukanov, *et al.*, in *Mineralogical Society and Mineralogy at the Threshold of the 21st Century: Abstracts of the IX Meeting of the Russian Mineralogical Society* (St. Petersburg, 1999), p. 70.

12. Z. V. Shlyukova, N. V. Chukanov, I. V. Pekov, *et al.*, Zap. Vseross. Mineral. O–va, No. 3, 43 (2001).

13. R. K. Rastsvetaeva, R. A. Tamazyan, D. Yu. Pushcharovskiĭ, *et al.*, Kristallografiya **39** (6), 994 (1994) [Crystallogr. Rep. **39**, 908 (1994)].

14. A. G. Bulakh and M. D. Evdokimov, Vestn. Leningr. Univ., No. 24, 15 (1973).

15. T. I. Ivanova and O. V. Frank-Kamenetskaya, Zh. Strukt. Khim. **42** (1), 151 (2001).

16. N. I. Organova and Z. V. Shlyukova, Izv. Ross. Akad. Nauk, Ser. Fiz. **65**, 822 (2001).

17. E. K. Salie, U. Bismayer, S. A. Hayward, *et al.*, Miner. Mag. **64** (2), 201 (2000).

Translated by L. Man

STRUCTURE
OF INORGANIC COMPOUNDS

Crystal Structure of the Na-, Ca-, Be-Cordierite and Crystallochemical Regularities in the Cordierite–Sekaninaite Series

O. V. Yakubovich*, V. Massa**, I. V. Pekov*, P. G. Gavrilenko*, and N. V. Chukanov***

* Moscow State University, Vorob'evy gory, Moscow, 119992 Russia
** Philipps University, Marburg, Germany
** Institute of Problems of Chemical Physics, Russian Academy of Sciences,
Chernogolovka, Moscow oblast, 142432 Russia
Received May 26, 2003

Abstract—The crystal structure of the beryllium-rich cordierite $[(Na_{0.28}Ca_{0.19})(H_2O)_{0.92}](Mg_{1.86}Fe^{2-}_{0.14})$ · $\{Al_{3.39}Be_{0.61}Si_5O_{18}\}$ was established by X-ray diffraction analysis (IPDS Stoe diffractometer, λMoK_α radiation, graphite monochromator, $2\theta_{max} = 65°$, $R = 0.0186$ for 1378 reflections): $a = 16.850(3)$, $b = 9.729(2)$, and $c = 9.298(2)$ Å; $V = 1524.3(4)$ Å^3, sp. gr. *Cccm*, $Z = 4$, and $\rho_{calcd} = 2.655$ g/cm^3. The numbers of Mg and Fe atoms isomorphously occupying the octahedral positions, Al and Be atoms in tetrahedra, and Na and Ca atoms and H_2O molecules in the framework cavities are refined. The hydrogen atom is localized and its coordinates and thermal displacement parameters are refined. Based on the comparative crystallochemical analysis of cordierites from different locations and origins, the regularities relating the unit-cell parameters *b* and *c* and the distortion index to the features of the chemical composition of the minerals under study are shown. © *2004 MAIK "Nauka/Interperiodica".*

INTRODUCTION

Cordierite is a framework magnesium aluminosilicate described by the idealized formula $Mg_2Al_4Si_5O_{18}$. The crystal structure of this mineral has been widely studied. Investigations of samples of different origins were aimed at finding correlations between the structure and chemical composition, since the latter changes in a fairly wide range. Variations in the chemical composition within this structure type are related, in particular, to the isomorphous incorporation of Fe^{2+}, Mn^{2+}, and Li^+ cations into the octahedral position, which is occupied predominantly by magnesium. The micropore structure of cordierite allows mobile alkali (Na^+, K^+) and alkaline-earth (Ca^{2+}) cations, as well as water molecules (under certain conditions), to migrate through channels of the crystal structure, due to which the chemical composition of the mineral changes. An interesting specific feature of cordierite is that Be^{2+} cations can be involved in the formation of the mixed Si,Al tetrahedral framework: the basis of the cordierite structure. One of the crystallochemical problems that have not been solved unambiguously is the question of localization of the hydrogen atoms of the water molecule in the cordierite structure.

Beryllium-, sodium-, and calcium-rich cordierite was found in tourmaline–amphibole aggregates and at places of their contact with andesine–calcite clusters in the vein of desilicated granite pegmatite in the Lipovka

pegmatite field (Central Urals). Cordierite forms irregular transparent bright orange grains up to 2 cm in size in cross section, with no signs of cleavage or separation. The chemical composition of cordierite determined by electron microprobe analysis is as follows (wt %): Na_2O (1.42), CaO (1.80), MgO (12.16), FeO (2.30), Al_2O_3 (28.36), and SiO_2 (51.03); 97.07 in total; the content of K, Mn, Cr, and Ti was below the detection limit. Laser spectral semiquantitative analysis showed the content of Be to be 1–2 wt %. The content of water was not determined directly because the number of experimental samples was limited.

HISTORY OF STUDYING THE CRYSTAL CHEMISTRY OF CORDIERITES

The crystal structure of aluminosilicate with composition $(Mg,Fe)_2[Al_4Si_5O_{18}] \cdot nH_2O$, is based on a tetrahedral framework formed of Si and Al tetrahedra with shared vortices. This compound exists in nature in the form of two polymorphic modifications: indialite (hexagonal structure, disordered with respect to the distribution of Si and Al atoms over tetrahedral positions) and cordierite (ordered orthorhombic structure). Indialite is a very rare mineral, whereas cordierite is widely spread and can be found in rocks of different geological formations, mainly in metamorphits and granite pegmatites.

To analyze the deviation of the orthorhombic *C* lattice of cordierite from the hexagonal lattice of indialite, it was proposed in [1] to use the distortion index, which is defined by the relation $\Delta = 2\theta_{131} - (2\theta_{511} + 2\theta_{421})/2°$ (Cu$K_{\alpha 1}$ radiation; $c < b < a$, Å; θ_{hkl} is the angle of reflection from the *hkl* plane). In [1], cordierites are interpreted as a continuous series of structures, the final terms of which are completely disordered indialite ($\Delta \approx 0°$) and ordered cordierite ($\Delta \approx 0.30°$). Using the modified formula $\Delta = 1.094(a - b\sqrt{3})$, where *a* and *b* are the parameters of the orthorhombic unit cell, one can easily estimate the value of deviation of the lattice from the hexagonal geometry [2].

The variable chemical composition of cordierites is primarily related to variations in the contents of Mg^{2+} and Fe^{2+} cations in the octahedral position: the Fe content may change from 4 to 96%. The wide range of isomorphism of Mg and Fe suggest the existence of a continuous isomorphic series cordierite $(Mg,Fe)_2[Al_4Si_5O_{18}] \cdot nH_2O$–sekaninaite $(Fe,Mg)_2[Al_4Si_5O_{18}] \cdot nH_2O$ within this structure type. The effect of the character of occupation of octahedra by Mg and Fe atoms on the unit-cell geometry of cordierites was studied in [2–4]. It was shown that a relative increase in the iron content leads to an increase in the unit-cell parameters *a* and *b*.

The more complex chemical composition of cordierite may be due to Be atoms involved in the formation of its structure. Incorporation of Be into the cordierite structure occurs according to the scheme $Na^+ + Be^{2+} \Rightarrow Al^{3+}$, which is implemented when Be partially substitutes Al in the tetrahedral position and Na compensates the deficit of positive charges by incorporating into channels of the tetrahedral framework [5]. A positive linear correlation between the contents of Na and Be in cordierite was noted in [6].

A characteristic feature of Be-containing cordierites is a fairly small value of Δ, which ranges from 0.06° to 0.17° [7]. The results of structural analysis of the Be-cordierite [7] confirmed the suggestion [5] about "dilution" of aluminum in the tetrahedral position with beryllium. It was shown that Be atoms are incorporated isomorphously only into one of two independent Al tetrahedra, decreasing the size of the corresponding polyhedron. Unfortunately, quantitative relations between Al and Be in the tetrahedral position were not refined in interpreting the structure [7] but taken as known from the data of chemical analysis. X-ray diffraction analysis of cordierites with low distortion indices Δ showed 100% ordering of Al^{3+} and Si^{4+} cations in tetrahedra [7]. This fact confirmed the suggestion [2, 6] that the value of Δ is determined by the features of the chemical composition of a specific compound rather than depends on the degree of ordering of Al and Si in the tetrahedral framework. As was correctly reasoned in [8], the value of Δ (and $a - b\sqrt{3}$) can be zero, which corresponds to the hexagonal geometry of the unit cell of the crystal, although its real symmetry is orthorhombic.

Heterovalent isomorphism of the $Na^+ + Li^+ \Rightarrow Mg^{2+}$ type (Li occupies octahedra along with Mg and Fe) was established [7] for the Li-containing cordierite, for which Δ is also rather small (0.12°) and the tetrahedral framework is ordered; i.e., it contains neither mixed (Si,Al) nor (Al,Be) tetrahedra.

In this study, we analyzed the crystal structure of the Na-, Ca-, Be-cordierite. This analysis is reasoned by the following factors: the specific features of the chemical composition of cordierites from the Lipovka pegmatite field, the lack of structural data on Be-containing mineral modifications of cordierite, and the unsolved problems related to the determination of the crystallochemical hydrogen-bond function.

X-RAY EXPERIMENT AND STRUCTURE REFINEMENT

The unit-cell parameters and the orthorhombic symmetry were determined and refined with a crystal $0.08 \times 0.05 \times 0.05$ mm^3 in size. The measurements were performed on a diffractometer with a highly sensitive imaging plate (Stoe detector) [9] using MoK_{α} radiation (graphite monochromator). The reflection intensities recorded on the same diffractometer were corrected taking into account the Lorentz factor and the polarization effect. A semiempirical absorption correction was introduced based on the analysis of equivalent reflections. The crystallographic characteristic of the cordierite and the experimental and refinement parameters are listed in Table 1.

The optical properties and the ratio of the unit-cell parameters of the mineral under study were such that, until the last moment, it was not clear whether it was cordierite or indialite. All calculations in the interpretation and refinement of the structure were performed using the SHELX97 program package [10, 11]. The values of the atomic scattering functions and anomalous dispersion corrections were taken from [12]. The structure was refined within the sp. gr. *Cccm* based on F^2 to $R = 0.0186$ (for 1378 reflections with $I \geq 2\sigma(I)$) in the anisotropic approximation. The refinement of the occupancies of the *M* position by Mg and Fe atoms was carried out assuming identical thermal displacement parameters of these atoms. The Al and Be contents in the *T* tetrahedral position was refined in the same way. The occupancy of the cation position in the framework cavities was determined by analyzing the corresponding electron densities taking into account the requirement for electroneutrality of the crystal. The contents of Ca and Na atoms in this position and their thermal displacement parameters were refined assuming that the latter have the same values. The ratio of independently refined contents of cations and water molecules in the framework cavities is 1: 2 (within experimental error). The hydrogen atom is localized and its coordinates and thermal displacement parameters are refined in the isotropic approximation. The obtained values of the coor-

Table 1. Crystallographic data and the details of X-ray data collection and refinement

Chemical formula	$[(Na_{0.28}Ca_{0.19})(H_2O)_{0.92}](Mg_{1.86}Fe^{2+}_{0.14})\{Al_{3.39}Be_{0.61}Si_5O_{18}\}$
Absorption coefficient μ, mm^{-1}	1.05
Space group, Z	$Cccm$, 4
a, Å	16.850(3)
b, Å	9.729(2)
c, Å	9.298(2)
V, $Å^3$	1524.3(4)
ρ, g/cm^3	2.655
Diffractometer	IPDS Stoe
Radiation	MoK_α (graphite monochromator)
T, K	293
Range of collection: θ_{max}, deg	32.50
Number of independent/collected with $I > 1.96\sigma(I)$ reflections	1438/1378
Refinement method	on F^2
Number of parameters in refinement	92
Absorption correction	semiempirical, using equivalents
T_{max}, T_{min}	0.848, 0.631
R_{int}	0.040
Extinction coefficient	0.0036(5)
Reliability factors:	
R (for collected reflections)	0.0186
wR_2 (for all independent reflections)	0.0520
S	1.154
Residual electron density, $e/Å^3$	$\rho_{max} = 0.37$, $\rho_{min} = -0.35$

dinates of the basis atoms and the temperature corrections are listed in Table 2. The results of calculation of the local valence balance are listed in Table 3.

ANALYSIS OF INTERATOMIC DISTANCES

The values of cation–oxygen distances in five independent tetrahedra forming a three-dimensional anionic framework indicate ordered distribution of Si^{4+} and Al^{3+} cations over structural positions. For example, in the Si(1) and Si(3) tetrahedra with the intrinsic symmetry C_s, the Si–O distances are in the range 1.5888(9)–1.6209(6) Å (the average values of the Si(1)–O and Si(3)–O distances are 1.610 and 1.612 Å, respectively). Si(2) tetrahedra, which are more symmetric (the symmetry of the D_2 position) are somewhat larger; they are characterized by four identical Si(2)–O bond lengths equal to 1.6207(5) Å. Aluminum atoms (the symmetry of the C_s position) in the tetrahedral coordination are surrounded by oxygen atoms located at distances in the range 1.7074(9)–1.7548(6) Å (the average is 1.733 Å). T tetrahedra at the twofold axis with mixed occupation by Al^{3+} and Be^{2+} cations in the ratio 0.7 : 3 are described by interatomic cation–oxygen

distances of 1.7204(6) and 1.7221(7) Å (the average is 1.721 Å).

In M octahedra, which are occupied by Mg^{2+} and Fe^{2+} cations (93 and 7%, respectively), the M–O distance ranges from 2.0659(6) to 2.1345(7) Å. Na^+ and Ca^{2+} cations, which are larger in size, are disordered in channels of the tetrahedral framework; they statistically occupy the same (A) position at the inversion center (55 and 38% for Na^+ and Ca^{2+}, respectively). These cations are coordinated by the framework oxygen atoms and interstitial water molecules, which form an eight-vortex polyhedron with an average A–O distance of 2.565 Å. The A–H_2O bond lengths in the polyhedron (2.3245(5) Å) are shorter than the A–O bond lengths, which range from 2.4671(9) to 2.8568(10) Å.

COMPARATIVE CRYSTAL CHEMISTRY OF CORDIERITES

One independent AlO_4 tetrahedron and two SiO_4 vortex-oriented tetrahedra share oxygen atoms to form six-member rings at $z = 0$ and 1/2 along the c axis of the cordierite unit cell (Fig. 1). Four such rings with the coordinates of the centers $\{1/2\ 0\ 0\}$ restrict the chan-

Table 2. Coordinates of the basis atoms and equivalent thermal displacement parameters

Atom	Notation according to [14]	Position symmetry	Wyckoff position	Number of atoms per position	x	y	z	U_{eq}
Si(1)	$T_2 1$	m	$8l$	0.5	0.30764(2)	0.07956(3)	0	0.00635(8)
Si(2)	$T_1 6$	222	$4a$	0.25	0	0	0.25	0.00638(9)
Si(3)	$T_2 3$	m	$8l$	0.5	0.13756(2)	0.26233(3)	0.5	0.00646(8)
Al	$T_2 6$	m	$8l$	0.5	0.05072(2)	0.18985(3)	0	0.00626(8)
T	$T_1 1$	2	$8k$	0.347(2)Al + 0.153 Be	0.25	0.25	0.25019(4)	0.00693(14)
M	M	2	$8h$	0.456(1)Mg + 0.035 Fe	0.16630(2)	0	0.25	0.01085(14)
A	$Ch0$	$2/m$	$4d$	0.048(2)Ca + 0.069(2)Na	0	0.5	0.5	0.0259(6)
O(1)	$O_1 1$	1	$16m$	1.0	0.25400(3)	0.10655(6)	0.14193(6)	0.00977(11)
O(2)	$O_2 3$	m	$8l$	0.5	0.33655(5)	−0.07803(8)	0	0.01343(16)
O(3)	$O_2 1$	m	$8l$	0.5	0.38338(5)	0.17683(9)	0	0.01417(16)
O(4)	$O_1 6$	1	$16m$	1.0	0.06272(3)	0.08363(5)	0.15097(6)	0.00890(11)
O(5)	$O_2 6$	m	$8l$	0.5	−0.04311(5)	0.25765(8)	0	0.01228(15)
O(6)	$O_1 3$	1	$16m$	1.0	0.17424(3)	0.19051(6)	0.35748(6)	0.00977(11)
O(7)(H$_2$O)	$Ch1/4$	222	$4b$	0.232(2)	0.5	0	0.25	0.0419(5)
H*		1	$16m$	0.464	0.491(5)	0.055(5)	0.317(7)	0.12(3)

* Isotropic thermal displacement parameter is given for the H atom.

Table 3. Local balance of valences

	Si(1)	Si(2)	Si(3)	Al	T(Al,Be)	M(Mg,Fe)	A(Na,Ca)	H	Σ	Δ
O(1)	1.008				0.695	0.368			2.071	0.071
O(2)	1.041		1.030				0.015		2.086	0.086
O(3)	1.099			0.860			0.030		1.989	0.011
O(4)		1.008		0.755		0.306			2.069	0.069
O(5)			1.090	0.846			0.045	0.05	2.031	0.031
O(6)			1.008		0.697	0.326			2.031	0.031
O(7)							0.065	0.95	2.030	0.030
							0.065	0.95		
Σ	4.156	4.032	4.136	3.216	2.784	2.000		1.000		

nels parallel to the c axis, in which Na$^+$ and Ca^{2+} cations and water molecules are located. Edge-oriented tetrahedra of two types (SiO$_4$ and (AlBe)O$_4$) at $z = 1/4$ and 3/4 link six-member rings into a framework. Each oxygen vertex in the anionic framework of the composition $\{Si_5Al_{3.39}Be_{0.61}O_{18}\}_{\infty\infty\infty}^{4.6-}$ is shared by two tetrahedra. Octahedral voids are occupied by (Mg,Fe)$^{2+}$ cations. M(Mg,Fe) octahedra share edges with SiO$_4$ and (Al,Be)O$_4$ tetrahedra to form rings from alternating octahedra and tetrahedra at $z = 1/4$ and 3/4. Thus, the framework of cordierite can be interpreted as a quasi-layered structure formed of layers of tetrahedra linked

into rings by sharing vertices ($z = 0$ and 1/2) and octahedra and tetrahedra sharing edges ($z = 1/4$ and 3/4), which alternate along the c axis (Fig. 2).

Crystallographic and some crystallochemical characteristics of cordierites of different composition and origin with known crystal structures are listed in Table 4. It can be seen that ordered distribution of Si and Al atoms over structural positions is typical of all cordierite modifications, although the value of Δ changes significantly. Obviously, the distortion index of the orthorhombic unit cell, as was shown in [2], is determined by the chemical composition of cordierite rather than the
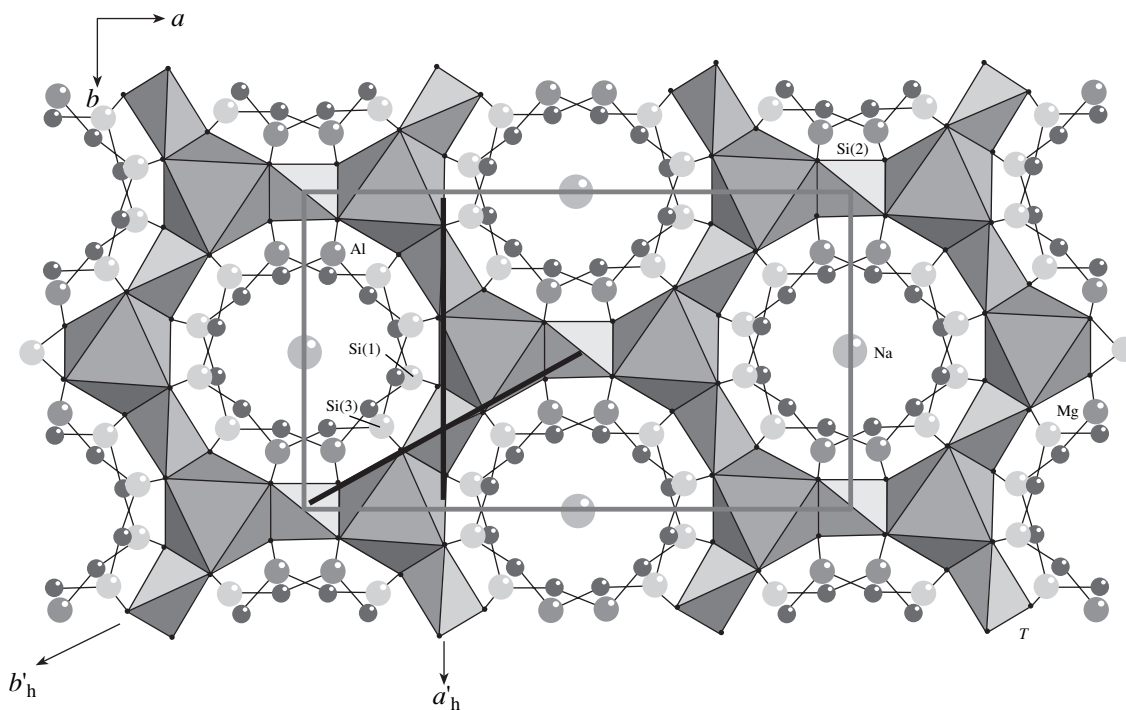
Fig. 1. Projection of the cordierite crystal structure onto the *ab* plane. Quasi-layers composed of edge-shared octahedra and tetrahedra, located at $c = 1/4$ and $3/4$, can be easily seen.
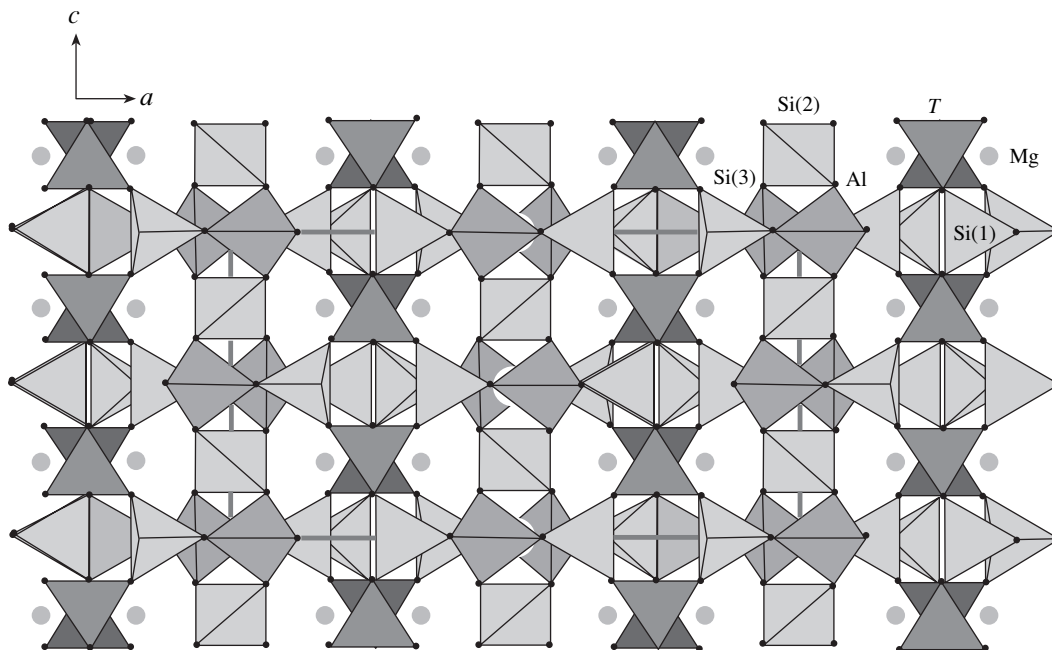
Fig. 2. Crystal structure of cordierite along the *b* axis of the unit cell.

degree of ordering of Si and Al atoms in the tetrahedral framework.

The data of Table 4 confirm also the previously noted [2–4] correlation between the number of Fe^{2+} cations ($r Fe^{VI} = 0.78$ Å) in octahedra in the cordierite structure and the unit-cell parameter *b*. The average values of the M(Mg,Fe)–O bond lengths in octahedra increase with decreasing the content of Mg^{2+} cations ($r Mg^{VI} = 0.72$ Å) [13]. Accordingly, the period of alteration along the *b* axis increases as well. For example,

Table 4. Crystallographic and crystallochemical characteristics of mineral species in the isomorphic series cordierite–sekaninaite (sp. gr. *Cccm*, Z = 8)

Location	Unit-cell parameters a, b, c, Å	V, Å³	Δ	Composition of the M octahedron	$(M-O)_{av}$, Å	Composition of the T tetrahedron	$(T-O)_{av}$, Å	O(1)–O(6), Å	O(1)–O(6'), Å	Composition of the cation position in a channel	Content of water in a channel	References
Dolbni Bori, West Moravia	17.230(5) 9.835(3) 9.314(3)	1578.3	0.214	0.12Mg + 0.83Fe +0.04Mn	2.158	1.00Al	1.748	2.616	3.068	0.075Na + 0.025Ca	0.3	[15]
Bergel, Central Alps	17.044(4) 9.716(3) 9.334(2)	1545.7	0.239	0.93Mg + 0.07Fe	2.106	1.00Al	1.754	2.582	3.123	0.06Na	0.37	[3]
White Well, West Australia	17.079(3) 9.730(2) 9.356(2)	1554.8	0.247	0.95Mg + 0.04Fe + 0.01Mn	2.109	1.00Al	1.758	2.616	3.132	0.03Na + 0.01Ca + 0.01K	0.28	[14]
Central Man, the United States	17.056(3) 9.783(2) 9.335(2)	1557.6	0.122	0.53Mg + 0.29Fe + 0.18Li	2.134	1.00Al	1.751	2.607	3.093	0.18Na	0.43	[7]
Alpe Sponda, Switzerland	17.060(2) 9.759(1) 9.322(2)	1552.0	0.172	0.70Mg + 0.30Fe	2.120	0.92Al + 0.08Be	1.746	2.585	3.097	0.13Na	0.3	[7]
Haddom, Connecticut, the United States	17.054(1) 9.759(2) 9.324(1)	1551.8	0.165	0.66Mg + 0.29Fe + 0.05Li	2.123	0.92Al + 0.08Be	1.746	2.587	3.094	0.14Na	0.38	[7]
Kemio, Finland	17.0.65(2) 9.797(2) 9.293(2)	1553.7	0.105	0.38Mg + 0.55Fe + 0.07Li	2.139	0.80Al + 0.20Be	1.730	2.581	3.051	0.24Na*	0.4*	[7]
Lipovka, Central Urals	16.850(3) 9.729(2) 9.298(2)	1524.3	–0.001	0.93Mg* + 0.07Fe*	2.103	0.694Al* + 0.306Be*	1.721	2.548	3.062	0.138Na* + 0.096Ca*	0.464*	This study

* Refined during the structure interpretation.
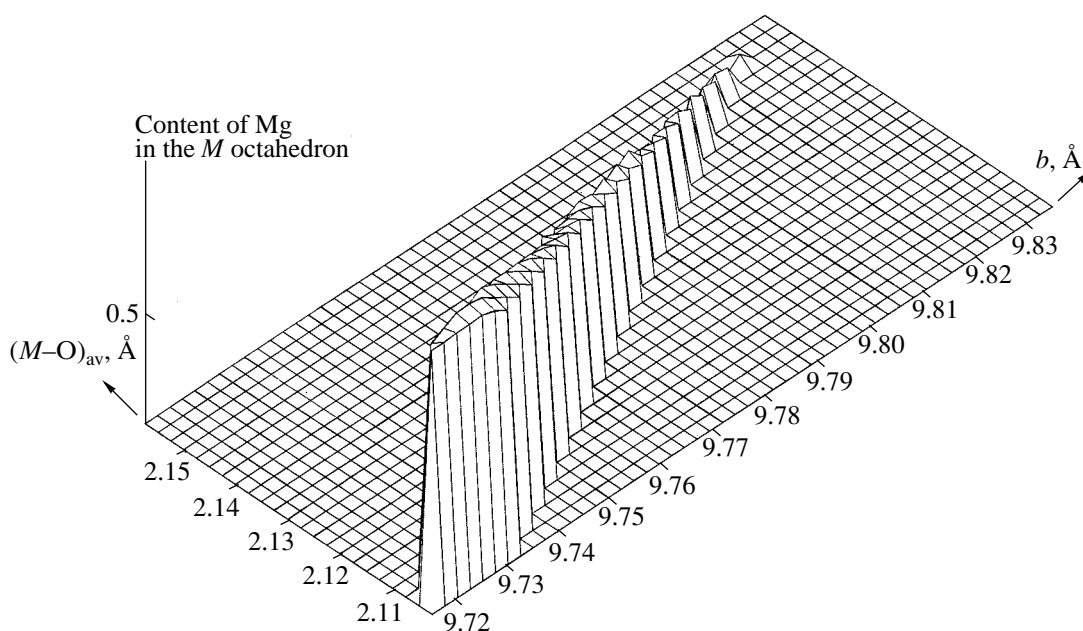
Fig. 3. Relation between the content of Mg in the M octahedron, average M–O distance, and the parameter b of the cordierite unit cell.

the decrease in the Mg content from 93–95 to 12% is accompanied by the increase in the average cation–oxygen distance in the octahedron from 2.106 to 2.158 Å, and the parameter b increases from 9.716 to 9.835 Å (Fig. 3, Table 4).

Another regularity following from the analysis of the data of Table 4 is that the number of Be atoms in T(Al,Be) tetrahedra, the tetrahedron size, and the unit-cell parameter c are related to each other. The systematic decrease in the tetrahedron size upon dilution of Al^{3+} cations ($rAl^{IV} = 0.39$ Å) occupying the tetrahedron with smaller Be^{2+} cations ($rBe^{IV} = 0.27$ Å) was noted in [7]. Our interpretation of the crystal structure of cordierite as quasi-layered (with layers alternating along the c axis) turns out to be useful for finding the dependence between the length of this axis and the tetrahedron composition. Since the composition of the Si,Al,O rings at $z = 0$ and 0.5 does not change upon incorporation of Be into T tetrahedra, it is important to trace the change in the sizes of layers located at $z = 1/4$ and 3/4. In these layers, the unit of constant composition is the Si(2) tetrahedron, which shares two opposite edges O(4)–O(4') with M octahedra. Comparison of the corresponding edge lengths for cordierites with different contents of M polyhedra shows that the O(4)–O(4') edge length remains relatively constant and, therefore, does not affect the parameter c. In contrast, the lengths of the O(1)–O(6) edges (shared with M octahedra) and O(1)–O(6') edges of the T tetrahedron vary significantly (Table 4), following the variations in the numbers of Al and Be atoms in the tetrahedron. We should note that the length of the O(1)–O(6) edge (shared by the T and M polyhedra) depends on the chemical composition of

not only the tetrahedron but also the octahedron and, therefore, there is no direct correlation between the length of this edge, the tetrahedron composition, and the value of the alteration period along the c axis. However, such a correlation can be observed if we compare the O(1)–O(6') edge lengths of T tetrahedra in cordierites of different composition and their parameters c (Table 4, Fig. 4): the larger the Be content in the tetrahedron, the shorter its O(1)–O(6') edge and the smaller the parameter c.

A particular feature of the mineral from the Lipovka pegmatite field is the zero value of the distortion index $\Delta = 1.094(a - b\sqrt{3})$ (where a and b are the orthorhombic unit-cell parameters), which determines the deviation of the orthorhombic lattice of cordierite from the hexagonal geometry. According to the type of the crystal structure, a change in the chemical composition affects the composition of polyhedra in cellular layers at $z = 1/4$ and 3/4. In the layers formed of octahedra and tetrahedra with shared edges, a bent column composed of M and T polyhedra, extended along the b axis, can be distinguished. Linking with each other through SiO_4 tetrahedra along the a axis, these columns are closed into a two-dimensional ring construction. As can be easily seen from Fig. 1, the parameter of the orthorhombic unit cell b_o of cordierite (equal to the parameter of the pseudohexagonal unit cell a'_h) can be approximately represented as a sum of the two O(1)–O(1') edge lengths of the T tetrahedron and two O(1)'–O(1') edge lengths of the M octahedron projected onto the ab plane. At the same time, the value of the pseudohexag-
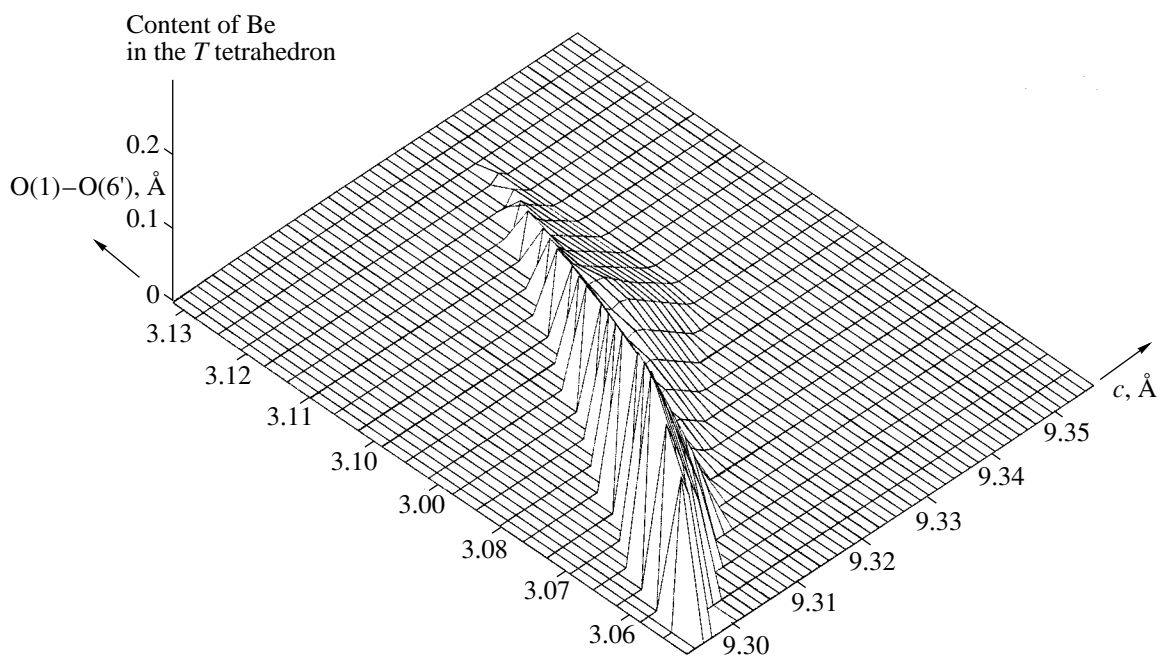
Fig. 4. Relation between the content of Be in the *T* tetrahedron, O(1)–O(6') edge length of the tetrahedron, and the parameter *c* of the cordierite unit cell.

onal unit-cell parameter b'_{h} (equal to the half diagonal of the (001) plane of the orthorhombic cell) is a sum of the projection of two O(6)–O(4') edges of the *M* octahedron, the O(6)–O(6) edge of the *T* tetrahedron, and the O(4)–O(4') edge of the Si tetrahedron on the (001) plane. The sizes of the *M* and *T* polyhedra of the cordierite from the Lipovka pegmatite field are such that the parameters of the pseudohexagonal unit cell turn out to be approximately equal:

$$a'_{\mathrm{h}} = 2 \cdot 2.794[\mathrm{O}(1)\text{–}\mathrm{O}(1')]$$

$$+ 2 \cdot 2.118[\text{projection O}(1')\text{–}\mathrm{O}(1')] \approx 9.7 \text{ Å},$$

$$b'_{\mathrm{h}} = 2 \cdot 2.037[\text{projection O}(6)\text{–}\mathrm{O}(4')]$$

$$+ 2.803[\mathrm{O}(6)\text{–}\mathrm{O}(6)] + 2.668\,[\mathrm{O}(4)\text{–}\mathrm{O}(4')] \approx 9.7 \text{ Å}.$$

Hence, the degree of hexagonality of the unit cell of cordierite is determined by the topology of the columns composed of *M* octahedra and *T* tetrahedra parallel to the *b* axis. The variable composition of the polyhedra determines variations in the sizes of polyhedra and the degree of curvature of the columns, which are directly related to the values of the parameters $a'_{\mathrm{h}} = b_{\mathrm{o}}$ and $a'_{\mathrm{h}} = a - b_{\mathrm{o}}\sqrt{3}$ of the pseudohexagonal unit cell.

A particular problem in the crystal chemistry of cordierite is the orientation of water molecules in interstices of the tetrahedral framework. According to the spectroscopic data [8], two types of water molecules may exist in channels of the cordierite structure, which differ by the orientation of the H–H vector. Orientation of the H–H vector parallel to the *c* axis is typical of

water molecules of type I. For water molecules of type II, the H–H vector is parallel to the *b* axis. In both cases, the plane of a water molecule is parallel to the (100) plane. A correlation between the content of water molecules of type II and the content of cations in channels was also established in [8]; their ratio was estimated as approximately 2 : 1. Localization of cations and water molecules in the framework cavities on the basis of X-ray and neutron diffraction experiments [14] showed disordering of the oxygen atom of the water molecule between two positions near the point with symmetry 222. Cohen *et al.* [14] believed that the plane of the H_2O molecule is parallel to the (001) plane, which is inconsistent with the spectroscopic data. In accordance with the later interpretation of the results of [14], the plane of the water molecule makes an angle of 29° with the (100) plane, and the H–H vector makes an angle of 19° with the *c* axis [15].

According to our data, the oxygen atoms of water molecules occupy statistically 93% of the particular position {0 1/2 1/4} (the symmetry D_2). Using difference electron-density maps, we managed to localize the hydrogen atom in the general position and refine its coordinates and thermal displacement parameters in the isotropic approximation (Table 2). The geometric characteristics of the hydrogen bond formed by this atom are as follows:

D–H$\cdots A$	$d(D\text{–H})$, Å	$d(\mathrm{H}\cdots A)$, Å	Angle DHA, °	$d(D\text{–}A)$, Å
O(7)–H$\cdots$O(5)	0.83(6)	2.56(6)	173(6)	3.3897(9).
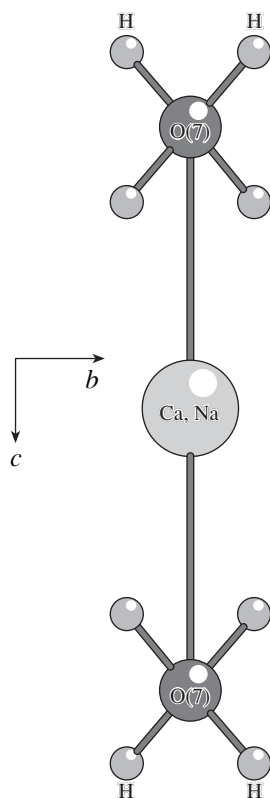
Fig. 5. Location of Ca and Na atoms and water molecules in the channels of the cordierite crystal structure. Two possible variants of localization of H atoms of the water molecules are shown.

Fig. 6. IR spectra of cordierites, sekaninaite, and indialite. Numbering of the curves is the same as for the minerals in Table 5.

Independent refinement of the contents of Na and Ca atoms and water molecules in framework cavities showed that cation positions are occupied approximately by half, while H_2O positions are almost completely occupied. This distribution of atoms is in good agreement with the model, according to which H_2O–Na and Ca–OH_2 groups are oriented in channels parallel to the c axis of the unit cell and alternate with empty cation positions. A small number of empty $O(7)(H_2O)$ and Na,Ca positions leads to a disorder in the distribution of linear groups H_2O–Na and Ca–OH_2, due to which the positions of metal atoms with the coordinates $z = 0$ and 0.5 are occupied statistically.

The data above indicate that the hydrogen bond O(7)–O(5) is very weak. This is in agreement with the conclusions drawn by Langer and Schreyer [16], who found from spectroscopic experiments that the water molecule forms rather weak hydrogen bonds with the oxygen atoms of the framework. The presence of such bonds is unlikely to significantly change the topology of cordierite quasi-layers, and, apparently, the effect of the water molecule on the distortion index should be considered only as mediated within the scheme of heterovalent substitution: $Al^{3+} \longrightarrow Be^{2+} + Na^+ + H_2O$.

The plane of the water molecule is parallel to the [001] direction and makes a dihedral angle of 12.8° with the (100) plane. In the H_2O–Na,Ca–OH_2 fragment, which is parallel to the c axis (Fig. 5), both hydrogen atoms of each water molecule should be oriented in the directions from the metal atoms (otherwise, the A–H distance will be intolerably short (1.8 Å)). Thus, the H–H vector of the water molecule is parallel to the [010] direction in the case under consideration, which corresponds to the orientation of water molecules of type II (revealed in the spectroscopic study of cordierite [8]). The forbidden angle H–O–H = 82.8° indicates that the water molecule either has an oscillating orientation or is disordered between two (or more) positions. The electron density of neighboring equivalent positions can be summed due to the high-symmetry operation 222, and it is possible that we observe in X-ray experiment an averaged position characterized by overestimated symmetry. One should also bear in mind that, within the same model, the direction of the H–H vector may be parallel to [001] (water molecules of type I), provided that metal cations are absent in channels of the tetrahedral framework.

The IR spectrum of the mineral from the Lipovka pegmatite field differs significantly from the IR spectra

Table 5. Wave numbers (cm^{-1}) of the bands in the IR spectra of minerals from the cordierite group

Mineral				Band type
Na-, Ca-, Be-cordierite[1]	Cordierite[2]	Indialite[3]	Sekaninaite[4]	
	3692		3655	ν(OH)
3575	3570		3572	ν(H$_2$O)
1628	1635 sh		1630 sh	δ(H$_2$O)
1161	1173	1162	1171	ν(Si, Al–O)
1138	1140		1140 w	
1098	1088	1100	1092	
	1025	1050	1024	
971	955	1000	959	
918	906	948	910	
895 w				
773	768	779	763	mixed vibrations of the tetra-hedral framework (including resonance vibrations involving Be–O bonds)
720 w	750 w	690	740 w	
	705 w		695 w	
	676		670 sh	
657	617	607	599	
596	582		577	mixed vibrations of the frame-work and octahedral cations
	570 w	553	561	
520 sh				ν(^{VI}Al–O)
475 w	485	473	483	ν(Mg, Fe–O) + δ(Si–O–Al)
			445 w	
463	442	430	430	
407	418		410	

Note: The wave number in the maxima of the strongest Si–O stretching vibration bands are underlined. Designations: (sh) shoulder, (w) weak band, (ν) stretching vibrations, and (δ) bending vibrations.
[1] Lipovka, Urals.
[2] Cordierite-3 Mine, East Pamir.
[3] According to the data of Povarennykh, 1979.
[4] Eveslogchorr mountain, Khibiny massif (iron-rich species).

of other types of cordierite and sekaninaite with a low beryllium content (Fig. 6, Table 5). Powder samples for spectroscopic analysis (Specord 75 IR spectrophotometer) were pressed into a KBr matrix and studied using polystyrene and gaseous ammonia as references. As one would expect, the minerals belonging to the isomorphic series (beryllium-free) cordierite–sekaninaite are characterized by almost identical spectra in the range of oscillations of the tetrahedral framework (650–1200 cm^{-1}) but have different frequencies of vibrations involving octahedrically coordinated cations (442 and 418 cm^{-1} for cordierite and 430 and 410 cm^{-1} for sekaninaite). Obviously, this discrepancy is related to the differences in the reduced masses for the Mg–O and Fe–O pairs. In contrast, for beryllium-rich cordierites, strong perturbation of the IR spectrum is observed, which manifests itself primarily in the blue shifts of the bands due to the framework vibrations in the range

600–1000 cm^{-1}. The values of these shifts range from 5 to 40 cm^{-1}.

Generally, three bands with a poorly resolved fine structure are present in the range of O–H stretching vibrations in the IR spectra of cordierite and sekaninaite. The positions of two of these bands (at 3630–3633 and 3570–3575 cm^{-1}), which are due to the vibrations of water molecules of type II in structural channels, are almost independent of the Mg : Fe ratio, and the ratio of the intensities of these bands varies weakly from sample to sample [17]. The third O–H stretching vibration band, which is absent in the spectrum of Lipovka cordierite, behaves quite differently. It is peaked at about 3690 cm^{-1} in the spectrum of the cordierite and is shifted to 3655 cm^{-1} in the spectra of iron-rich sekaninaites. Such a strong dependence of the position of the third band on the iron content in a mineral casts doubt on the correctness of the assignment of this band to vibrations of water molecules in zeolite

channels. The intensity of this band changes significantly from sample to sample: it may be the strongest O–H stretching vibration band in one sample and absent in the spectrum of other samples. Although this band was assigned to water molecules of type I in [17], it was noted that the absence of the second stretching vibration band due to vibrations of water molecules of this type, which is intolerable for the weakly bound symmetric H_2O molecule, can hardly be explained and requires further study (we should add that this is also intolerable for the asymmetric H_2O molecule). The most likely explanation of the above facts is the assumption about the existence of $[Fe^{2+}\cdots OH^-]$ and $[Mg^{2+}\cdots OH^-]$ complexes in the channels of the structure. The positions of the bands at 3692 and 3655 cm^{-1} are quite consistent with the vibrational frequencies of the OH groups coordinated to Mg and Fe ions, respectively. The possibility of the presence of iron in zeolite channels in iron-containing members of the cordierite–sekaninaite series was proved experimentally by Mössbauer spectroscopy [8].

The Be-containing cordierite from the Lipovka pegmatite field can be considered a typomorphic mineral from beryllium-rich desilicated granite pegmatites cutting magnesium-rich rocks. To estimate the maximum possible beryllium content in cordierite, we must first take into account the scheme of heterovalent isomorphism $Be^{2+} + Na^+ + H_2O \longrightarrow Al^{3+}$, according to which the dilution of framework Al tetrahedra with Be atoms is accompanied by the incorporation of Na^+ (K^+, Ca^{2+}) cations and water molecules into the channels. Since the ratio of the number of alkali and alkaline-earth cations to the number of water molecules in channels, which coordinate these cations, is equal to 1 : 2 and the maximum number of H_2O molecules cannot exceed unity (because the H_2O molecule occupies the {0 1/2 1/4} position), the maximum number of cations in zeolite channels cannot exceed 0.5 (per 18 oxygen atoms). In the case of our consideration, this number is 0.468(8); i.e., it is close to maximum. The beryllium content in the framework can be increased by increasing the ratio $Ca^{2+} : Na^+$ in the {0 1/2 0} position. In the limiting case, when the position at the inversion center is completely occupied by Ca^{2+} cations, we obtain a formula for cordierite, which corresponds to the maximum possible Be content for this isomorphic scheme: $(Mg,Fe)_2[Si_5Al_2(Al_{0.5}Be_{0.5})O_{18}](Ca_{0.5}H_2O)$.

As was shown in [7], Li in cordierite is incorporated into M octahedra with simultaneous capture of alkali (alkaline-earth) cations and the molecules into the channels. This circumstance means that both Li and Be contents are controlled by cations in framework cavities. Hence, the larger number of Li atoms is accumulated by the structure, the smaller number of Be atoms (at the maximum number of cations in the A position) can occupy tetrahedra isomorphously with aluminum.

A particular feature of the crystal structure of cordierite that gives grounds to interpret it as a zeolite-like mineral is the variable content of atoms of alkali (and alkaline-earth) metals and water molecules in framework cavities. Another feature is that, in contrast to zeolites, the composition of cavities and the framework of cordierite are not independent of each other, which makes it possible to consider this mineral intermediate between ring silicates of the beryl type and zeolites.

REFERENCES

1. A. Miyashiro, Am. J. Sci. **255**, 43 (1957).
2. K. R. Selkregg and F. D. Bloss, Am. Mineral. **65**, 522 (1980).
3. J. H. Wallace and H.-R. Wenk, Am. Mineral. **65**, 96 (1980).
4. Th. Armbruster, Contrib. Mineral. Petrol. **91**, 180 (1985).
5. P. Černý and P. Povodra, Neues Jahrb. Mineral. Monatsh., No. 44, 36 (1966).
6. W. Schreyer, C. E. Gordillo, and G. Werding, Coutrib. Mineral. Petrol. **70**, 421 (1979).
7. Th. Armbruster, Am. Mineral. **71**, 746 (1986).
8. D. S. Goldman and G. P. Rossman, Am. Mineral. **62**, 1144 (1977).
9. *IPDS (Imaging Plate Diffraction System) Software. Ver. 2.87* (Stoe, Darmstadt, Germany).
10. G. M. Sheldrick, *SHELXS97. Program for the Solution of Crystal Structures* (Univ. of Göttingen, Germany, 1997).
11. G. M. Sheldrick, *SHELXL97. Program for the Refinement of Crystal Structures* (Univ. of Göttingen, Germany, 1997).
12. *International Tables for Crystallography*, Ed. by T. Hahn, 8th ed. (Kluwer, Dordrecht, 1995), Vol. A.
13. R. D. Shannon, Acta Crystallogr., Sect. A: Cryst. Phys., Diffr., Theor. Gen. Crystallogr. **32**, 751 (1976).
14. J. P. Cohen, F. K. Ross, and G. V. Gibbs, Am. Mineral. **62**, 67 (1977).
15. H. F. Hochella, Jr., G. E. Brown, Jr., F. K. Ross, and G. V. Gibbs, Am. Mineral. **64**, 337 (1979).
16. K. Langer and W. Schreyer, Am. Mineral. **61**, 1036 (1976).
17. É. V. Sokol, V. N. Stolpovskaya, and G. G. Lepezin, Dokl. Akad. Nauk **359** (5), 671 (1998).
18. A. S. Povarennykh, Mineral. Zh. **1** (2), 3 (1979).

Translated by Yu. Sin'kov

STRUCTURE
OF INORGANIC COMPOUNDS

Crystal Structure of Byelorussite-(Ce) NaMnBa$_2$Ce$_2$(TiO)$_2$[Si$_4$O$_{12}$]$_2$(F,OH) · H$_2$O

N. V. Zubkova*, D. Yu. Pushcharovskiĭ*, G. Giester**, E. Tillmanns**, I. V. Pekov*, and O. D. Krotova*

* Department of Geology, Moscow State University, Vorob'evy gory, Moscow, 119992 Russia
e-mail: nata-zubkova@rambler.ru; dmitp@geol.msu.ru
** Institute for Mineralogy and Crystallography, Geozentrum, University of Vienna, Althanstrasse 14, A-1090 Vienna, Austria

Abstract—The crystal structure of the mineral byelorussite-(Ce) NaMnBa$_2$Ce$_2$Ti$_2$Si$_8$O$_{26}$(F,OH) · H$_2$O belonging to the joaquinite group was solved and refined to $R = 0.033$ based on 4813 reflections with $I > \sigma2(I)$. The parameters of the orthorhombic unit cell are $a = 22.301(4)$ Å, $b = 10.514(2)$ Å, $c = 9.669(2)$ Å, $V = 2267.1(8)$ Å^3, sp. gr. $Ama2$, and $Z = 4$. The structure is composed of three-layer sheets, which consist of dimers of edge-sharing Ti octahedra located between isolated four-membered [Si$_4$O$_{12}$] rings. The sheets are linked to each other by Mn 5-vertex polyhedra to form a heteropolyhedral framework. Large cavities in the framework are occupied by Na 6-vertex polyhedra, Ba 11-vertex polyhedra, and REE 9-vertex polyhedra. © *2004 MAIK "Nauka/Interperiodica".*

INTRODUCTION

The joaquinite group includes seven monoclinic and orthorhombic minerals with the general formula A_6Ti$_2$Si$_8$O$_{24}$(O,OH,F)$_{2-3}$ · (0–1)H$_2$O, where A = Ba, Sr, Na, rare-earth element (REE), Fe, and Mn. These minerals are joaquinite-(Ce), orthojoaquinite-(Ce), orthojoaquinite-(La), byelorussite-(Ce), strontiojoaquinite, strontioorthojoaquinite, and barioorthojoaquinite [1]. However, in spite of the wide diversity of types, the complete crystal-structure data were published only for the monoclinic joaquinite-(Ce) with the composition Ba$_2$Ce$_2$NaFe^{2+}Ti$_2$Si$_8$O$_{26}$(OH) · H$_2$O, which is a representative of a unique structure type [2, 3]. In [2], the structure of joaquinite was solved within the sp. gr. $C2/m$ ($R = 0.160$). More recently, the structure of joaquinite was established independently [3]. The results of the latter study confirmed, on the whole, the model found earlier [2]. However, the structure was solved within sp. gr. $C2$ ($R = 0.075$). In 1991, Malinovskiĭ described a model of the crystal structure of byelorussite-(Ce) within the orthorhombic space group $C2cm$ ($a = 9.640(2)$ Å, $b = 10.492(2)$ Å, $c = 22.266(3)$ Å, $R = 0.024$ for 1587 reflections) [4]; however, the atomic coordinates, thermal parameters, and interatomic distances were not reported. All other minerals were assigned to the joaquinite group based on the similarity of their chemical compositions, stereochemistry, powder X-ray diffraction patterns, and properties. These minerals were characterized only by the symmetry and unit-cell parameters.

In this study, the crystal structure of byelorussite-(Ce) with the formula Ba$_2$Ce$_2$NaMn^{2+}Ti$_2$Si$_8$O$_{26}$(F,OH) · H$_2$O was established. This mineral is an orthorhombic Mn,F-dominant analogue of joaquinite-(Ce). The specimen under study was found in the Diabazovoe occurrence (Zhitkovichi District, Belarus), where this mineral was discovered for first time. This mineral occurrence is related to alkaline metasomatites of the rare-metal mineralization. A single-crystal grain was isolated from a large pale yellow tabular individual. Byelorussite-(Ce) was discovered in association with magnesioriebeckite, aegirine, microcline, albite, leucophanite, and titanite in a marginal part of a quartz vein crosscutting microclinized, albitized, and silicificated granosyenites. The average chemical composition of the mineral was determined by electron-probe X-ray microanalysis on Camebax and Superprobe-733 microanalyzers (wt %): Na$_2$O, 2.08; K$_2$O, 0.40; SrO, 0.43; BaO, 20.58; MgO, 0.15; MnO, 2.58; FeO, 0.82; ZnO, 1.58; La$_2$O$_3$, 8.33; Ce$_2$O$_3$, 12.13; Pr$_2$O$_3$, 0.58; Nd$_2$O$_3$, 2.30; Sm$_2$O$_3$, 0.10; Gd$_2$O$_3$, 0.15; TiO$_2$, 11.35; SiO$_2$, 33.98; F, 0.98; H$_2$O$_{calcd}$, 1.45; –O=F$_2$, 0.41; and in total, 99.56. The empirical formula is (Na$_{0.95}$K$_{0.12}$)$_{\Sigma 1.07}$ · (Mn$_{0.52}$Zn$_{0.27}$Fe$_{0.16}$Mg$_{0.05}$)$_{\Sigma 1.00}$(Ba$_{1.90}$Sr$_{0.06}$)$_{\Sigma 1.96}$REE$_{2.03}$ · Ti$_{2.01}$Si$_{8.00}$O$_{26}$[F$_{0.73}$(OH)$_{0.27}$] · H$_2$O [5].

EXPERIMENTAL

X-ray diffraction data were collected from a byelorussite-(Ce) single crystal of 0.10 × 0.14 × 0.17 mm^3 in size. The three-dimensional set of X-ray

Table 1. Principal crystallographic characteristics and experimental data

Idealized formula	NaMnBa$_2$Ce$_2$Ti$_2$Si$_8$O$_{26}$(F, OH) · H$_2$O
Unit-cell parameters, Å	$a = 22.301(4)$ $b = 10.514(2)$ $c = 9.669(2)$
Space group; Z	$Ama2$; 4
Unit-cell volume V, Å^3	2267.1(8)
Calculated density ρ, g/cm^3	4.08
Measured density ρ, g/cm^3*	3.92
Absorption coefficient μ, mm^{-1}	9.01
Molecular weight	1391.3
F_{000}	2567
Crystal dimensions, mm	$0.10 \times 0.14 \times 0.17$
Diffractometer	Nonius Kappa CCD
Radiation; wavelength, Å	MoK_α; 0.71073
Scan ranges	$-36 \le h \le 36$, $-17 \le k \le 17$, $-15 \le l \le 16$
Number of nonequivalent reflections	5155
Number of nonequivalent reflections with $I > 2\sigma(I)$	4813
Program package	SHELX97
Number of parameters in refinement	213
R_F	0.033
$wR(F^2)$	0.081
GOF	1.12
$\Delta\rho_{max}$, e/Å^3	2.78
$\Delta\rho_{min}$, e/Å^3	−2.04

* The measured density is taken from [5].

Table 2. Atomic coordinates and atomic displacement parameters for the crystal structure of byelorussite-(Ce)

Atom	x	y	z	U_{eq}^*
Mn	0.5	0.5	0	0.0165(3)
REE	0.52267(1)	0.18439(2)	0.1269(1)	0.01638(7)
Ba(1)	0.75	−0.07387(4)	0.3615(1)	0.0202(1)
Ba(2)	0.75	−0.04209(4)	−0.1267(1)	0.0187(1)
Ti	0.68617(3)	0.19084(6)	0.1336(1)	0.0125(1)
Na	0.5	0.5	0.3203(5)	0.0283(7)
Si(1)	0.62861(5)	0.4743(1)	0.1345(2)	0.0128(2)
Si(2)	0.60320(6)	0.2019(1)	−0.1689(2)	0.0135(2)
Si(3)	0.61373(6)	0.1771(1)	0.4339(2)	0.0129(2)
Si(4)	0.62760(6)	0.4057(1)	−0.3966(2)	0.0139(2)
O(1)	0.6824(1)	0.0055(3)	0.1150(5)	0.0168(6)
O(2)	0.75	−0.2997(5)	0.5028(6)	0.0147(8)
O(3)	0.4374(2)	0.0415(3)	0.0630(5)	0.0208(7)
O(4)	0.75	0.1792(4)	0.2640(5)	0.0136(8)
O(5)	0.5617(1)	0.4176(3)	0.1265(5)	0.0206(6)
O(6)	0.6357(2)	0.5758(4)	0.2638(4)	0.0191(7)
O(7)	0.6152(2)	0.1733(3)	0.2667(4)	0.0157(6)
O(8)	0.6232(2)	0.2081(4)	−0.0092(4)	0.0178(6)
O(9)	0.6822(1)	0.3743(3)	0.1579(4)	0.0165(6)
O(10)	0.6519(2)	0.3032(3)	−0.5138(4)	0.0175(6)
O(11)	0.6497(2)	0.0507(3)	0.4930(4)	0.0180(6)
O(12)	0.6302(2)	0.3273(4)	−0.2494(5)	0.0224(8)
O(13)	0.5493(2)	0.1752(3)	0.5065(4)	0.0184(6)
O(14)	0.5317(2)	0.1985(4)	−0.1781(5)	0.0244(8)
F, OH	0.5	0.5	−0.2031(7)	0.028(1)
H$_2$O	0.75	0.6968(8)	0.1761(9)	0.040(2)

* The parameters U_{eq} were calculated based on anisotropic atomic displacement parameters.

reflections was collected on a Nonius Kappa CCD diffractometer (MoK_α radiation, λ = 0.71073 Å). The parameters of the orthorhombic unit cell are a = 22.301(4) Å, b = 10.514(2) Å, c = 9.669(2) Å, and V = 2267.1(8) Å^3. The absorption correction was applied taking into account the crystal habitus (μ = 9.01 mm^{-1}). All calculations were carried out using the SHELX97 program package [6]. A total of 5155 independent nonzero reflections were obtained after standard processing of the X-ray diffraction data. The structure of byelorussite-(Ce) was solved by direct methods and refined within the sp. gr. $Ama2$ to $R(F)$ = 0.033 for 4813 reflections with $I > 2\sigma(I)$. The cation distribution was established based on the refinement of the electron contents of the cation positions and taking into account the requirements for retaining the positive values of thermal parameters, the electroneutrality of the chemical formula, and the valence balance. It turned out that large K cations replace Ba in the Ba(1) position, and Sr atoms partially replace Ba in the Ba(2) position. The Mn position, which has an electron content of 25.86e, is partially occupied by Zn, Fe, and Mg cations of similar sizes. Therefore, the structural formula of byelorussite-(Ce) can be written as NaMn(Ba$_{0.9}$K$_{0.1}$)(Ba$_{0.95}$Sr$_{0.05}$)Ce$_2$(TiO)$_2$[Si$_4$O$_{12}$]$_2$(F,OH) · H$_2$O. This formula is in good agreement with the results of electron-probe analysis. A small excess of negative charge (0.1e) in the formula above is compensated by possible partial oxidation of iron cations to the trivalent state.

The main characteristics of the crystal and details of X-ray diffraction study are listed in Table 1. The atomic coordinates and the atomic displacement parameters are listed in Table 2. The bond-valence balance for the anions in the byelorussite-(Ce) structure was calculated

Table 3. Bond-valence balance for the anions in the structure of byelorussite-(Ce)

	Mn	REE	Ba(1)	Ba(2)	Ti	Na	Si(1)	Si(2)	Si(3)	Si(4)	Σ
O(1)			0.17[×2]	0.24[×2]	0.68					1.02	2.11
O(2)			0.30	0.22	[×2]0.78						2.08
O(3)		0.39; 0.29				0.08[×2]				1.06	1.82
O(4)			0.23	0.11	[×2]0.78						1.90
O(5)	0.48[×2]	0.30				0.16[×2]	1.04				1.98
O(6)				0.14[×2]			0.93	0.94			2.01
O(7)		0.42			0.54				1.02		1.98
O(8)		0.29			0.64			1.05			1.98
O(9)			0.07[×2]	0.31[×2]	0.70		1.04				2.12
O(10)				0.17[×2]					0.93	0.92	2.02
O(11)			0.20[×2]				0.92		0.91		2.03
O(12)			0.12[×2]					0.96		0.93	2.01
O(13)	0.36[×2]	0.42							1.06		1.84
O(14)		0.33; 0.11				0.34[×2]		1.07			1.85
F, OH	0.58	[×2]0.30									1.18
H₂O			0.15	0.10							0.25
Σ	2.26	2.85	1.80	2.15	4.12	1.16	3.93	4.02	3.92	3.93	

Note: The left and right superscripts correspond to the bond valences that are doubled in calculations of the valence balance for the anions and cations, respectively. The bond valences for the Mn cation are given taking into account the presence of Zn in this position.

by the equations reported in [7]. The results of calculations (Table 3) allow us to unambiguously identify the positions occupied by the F atom or the OH group, which are located in the apical corners of Mn half-octahedra, and the water molecule involved in the formation of Ba polyhedra. The figures were drawn using the ATOMS program [8].

The ranges of the intermolecular distances in the coordination polyhedra in the byelorussite-(Ce) structure are close to the standard values: Mn–O, 1.963(6)–2.146(4) Å; REE–O, 2.469(4)–2.960(5) Å; Ba(1)–O, 2.740(5)–3.286(4) Å; Ba(2)–O, 2.719(4)–3.153(8) Å; Ti–O, 1.905(3)–2.049(4) Å; Na–O, 2.204(4)–2.765(6) Å; Si(1)–O, 1.608(3)–1.655(4) Å; Si(2)–O, 1.597(4)–1.646(4) Å; Si(3)–O, 1.599(4)–1.655(4) Å; and Si(4)–O, 1.602(4)–1.655(4) Å. The involvement of the O(14) atom in the Ce polyhedron (in spite of the increased distance, 2.960(5) Å) and the involvement of the O(3) atom in the Na polyhedron (Na–O(3), 2.765(6) Å) were confirmed by the results of calculation of the bond-valence balance (Table 3).

DESCRIPTION AND DISCUSSION OF THE BYELORUSSITE-(Ce) STRUCTURE

The structure of byelorussite-(Ce) is shown in Fig. 1. This mineral is structurally similar to joaquinite [3] and differs from the latter in that it contains Mn instead of Fe. Both structures are composed of three-layer sheets. The outer layers consist of isolated four-

membered Si_4O_{12} rings, which are typical of titanium silicates. The intermediate layer consists of Ti_2O_{10} dimers of the edge-sharing Ti octahedra (Fig. 2). In addition, the intermediate layer contains large Ba 11-vertex polyhedra. Ba atoms and the shared O(2)–O(4) edges of Ti octahedra lie in the mirror plane *m*. The mirror plane in the orthorhombic structure of byelorussite-(Ce) has been described for monoclinic joaquinite [3] as a pseudoplane, in which Ba atoms and water molecules are located. In the structure of monoclinic joaquinite, this plane is distorted by the Fe and Na polyhedra located between the layers. In byelorussite-(Ce), Mn 5-vertex polyhedra, distorted Na octahedra, and *REE* 9-vertex polyhedra are located symmetrically with respect to this plane.

The presence of edge-sharing Ti octahedra is typical of titanosilicates, in contrast to zirconosilicates, which contain predominantly isolated Zr octahedra. According to [9], more than a half of the known titanosilicates contain corner- or edge-sharing Ti polyhedra. Along with joaquinite and byelorussite-(Ce), edge-sharing Ti octahedra are also present in the structures of leucosphenite, neptunite, tinaksite, odintsovite, etc. In leucosphenite, pairs of Ti octahedra link Si, B-double layers, which are formed by four-membered rings like in byelorussite and joaquinite. In the structures of aluminum silicates, such as epidote, zoisite, pumpellyite, kyanite, and sillimanite, Ti and Al are brought together as a result of the edge sharing.

Fig. 1. Crystal structure of byelorussite-(Ce) projected along the [010] direction. The dimers of Ti octahedra and the SiO_4 tetrahedra are shaded in dark and light gray, respectively. The Na 6-vertex polyhedra and Mn half-octahedra are unshaded and shaded in dark gray, respectively.

Fig. 2. Three-layer sheet in the structure of byelorussite-(Ce) projected onto the (100) plane. For notations, see Fig. 1.

Si,O networks of six-membered rings, and the intermediate layers are formed by isolated Ce prisms. The variety of cation polyhedra and a high degree of disorder in the structures of ilimaussite-(Ce) and its Ti analogue [11] suggest different approaches to their description. However, the general structural features of byelorussite-(Ce) are similar to those of ilimaussite-(Ce). Both structure types contain three-layer sheets. The outer layers of the sheets are formed by the Si,O units (four-membered rings in byelorussite and networks of six-membered rings in ilimaussite). The intermediate layers are composed of dimers of Ti octahedra in byelorussite-(Ce) and isolated Ti octahedra in ilimaussite-(Ce). In ilimaussite-(Ce), these three-layer sheets are linked by Ce trigonal prisms, and the cavities between the layers are occupied by Ba, K, and Na cations. The structure of diversilite-(Ce) [12], which is compositionally similar to the Ti analogue of ilimaussite, has a number of differences from both ilimaussite-(Ce) and byelorussite-(Ce).

In the structure of byelorussite-(Ce), the three-layer sheets formed by Si tetrahedra and Ti octahedra are linked to each other through the Mn 5-vertex polyhedra to form a heteropolyhedral framework with large cavities occupied by Na, Ba, and REE cations. The framework density is 21.1 and, disregarding Na cations (characterized by a low force constant), there are 19.4 framework atoms per 1000 $Å^3$. Such framework densities are typical of microporous (zeolite-like) mixed-framework zirconium and titanium silicates, such as baotite, dalyite, and members of the eudialyte and vinogradovite–lintisite groups [13]. Hence, byelorussite-(Ce) and, apparently, all members of the joaquinite

The set of cations in byelorussite-(Ce) is similar to that in ilimaussite-(Ce) [10], which is also present in differentiates of alkali rocks. Both minerals are structurally similar. Ilimaussite-(Ce) also contains two symmetrically nonequivalent three-layer titanosilicate sheets. The outer layers in these sheets are formed by

group can be assigned to microporous heteropolyhedral-framework silicates. These minerals would be expected to exhibit zeolite properties.

REFERENCES

1. J. A. Mandarino and M. E. Back, *Fleischer's Glossary of Mineral Species* (Miner. Rec., Tucson, 2004).

2. E. Cannillo, F. Mazzi, and G. Rossi, TMPM Tschermaks Mineral. Petrogr. Mitt. **17**, 233 (1972).

3. E. Dowty, Am. Mineral. **60**, 872 (1975).

4. Yu. A. Malinovsky, Z. Kristallogr. Suppl., No. 4, 321 (1991).

5. E. P. Shpanov, G. N. Nechelyustov, S. V. Baturin, and L. S. Solntseva, Zap. Vseross. Mineral. O–va **118** (5), 100 (1989).

6. G. M. Sheldrick, *SHELX97. Program for the Solution and Refinement of Crystal Structures* (Siemens Energy and Automation, Madison, WI, 1997).

7. N. E. Brese and M. O'Keeffe, Acta Crystallogr., Sect. B: Struct. Sci. **42**, 192 (1991).

8. E. Dowty, *Atoms 5.0, Computer Program for Displaying Atomic Structures* (Kingsport, 1999), TN 37663.

9. Yu. A. Pyatenko, A. A. Voronkov, and Z. V. Pudovkina, *Mineralogical Crystal Chemistry of Titanium* (Nauka, Moscow, 1976) [in Russian].

10. G. Ferraris, A. Gula, N. V. Zubkova, *et al.*, Can. Mineral. (2004) (in press).

11. S. V. Krivovichev, V. N. Yakovenchuk, T. Armbruster, *et al.*, Z. Kristallogr. **218** (6), 392 (2003).

12. A. P. Khomyakov, G. N. Nechelyustov, R. K. Rastsvetaeva, and Ma Zeshen, Zap. Vseross. Mineral. O–va **132** (5), 34 (2003).

13. N. V. Chukanov, I. V. Pekov, and R. K. Rastsvetaeva, Usp. Khim. **73** (3), 227 (2004).

Translated by T. Safonova

X-ray and Neutron Diffraction Studies of $Rb_4LiH_3(XO_4)_4$ (X = S, Se) Single Crystals

S. I. Troyanov*, E. M. Snigireva*, and C. D. Ling**

* Chemistry Faculty, Moscow State University, Vorob'evy gory, Moscow, 119489 Russia
e-mail: troyanov@thermo.chem.msu.ru
** Institute Laue–Langevin, Grenoble, France
Received January 20, 2004

Abstract—$Rb_4LiH_3(SeO_4)_4$ single crystals (**1**) are studied by the X-ray diffraction method at 180 K and $Rb_4LiH_3(SO_4)_4$ single crystals (**2a–2c**) are studied by the neutron diffraction method at 298 K (**2a** and **2b**) and 480 K (**2c**). It is established that isostructural single crystals **1** and **2** (sp. gr. $P4_1$) have analogous systems of hydrogen bonds: chains of four XO_4 tetrahedra linked by three H bonds with the central bond (2.49 Å) being somewhat shorter than the terminal ones (2.52–2.54 Å). In the high-temperature **2c** phase, the amplitudes of atomic thermal vibrations and the degree of proton disorder in the central hydrogen bond have somewhat elevated values. © *2004 MAIK "Nauka/Interperiodica".*

INTRODUCTION

Earlier, it was established that the isostructural crystals described by the general formula $M_4^I LiH_3(XO_4)_4$ (M = K, NH_4, Rb and X = S, Se), hereafter denoted as *MLHX*, have a number of similar properties such as the occurrence of phase transitions at low and high temperature. Being cooled to 100–140 K, the tetragonal modifications of these crystals stable at room temperature undergo second-order phase transitions (at 234 K in *ALHS*, where A = NH_4) to monoclinic phases possessing ferroplastic properties [1, 2]. Some anomalies in their physical properties were established during their heating to 430–465 K and were interpreted as the transitions to the phases with high protonic conductivity [3]. Despite the intense studies of the structure and physical properties, many problems of the structures and phase transitions in these compounds are still unsolved. ZüNiga *et al.* [4] performed the first X-ray study of the crystal structure of $Rb_4LiH_3(SeO_4)_4$ (RLHS) single crystals at room temperature, but they did not manage to localize hydrogen atoms. Recently, Haznar and Pietraszko [5] performed the X-ray diffraction studies of $K_4LiH_3(SO_4)_4$ (KLHS) crystals at several temperatures, localized all the atoms, and analyzed a possible mechanism of proton conductivity in the high-temperature phase. Pietraszko and Lukaszewicz [6] reported the study of RLHSe single crystals but, unfortunately, no further publications appeared and no structural data were deposited. Mröz *et al.* [2] undertook a neutron diffraction study of an RLHS powder at 170 and 5 K [2] with the aim to determine the positions of hydrogen atoms (protons). The structural determination of the tetragonal phase at 170 K resulted in the localization of three independent protons, but, unfortunately,

this study is characterized by a rather low accuracy. The accuracy of the study of the monoclinic phase at 5 K was even lower because of the necessity of introduction of a large number of fixed parameters.

Below we consider the results of the low-temperature X-ray diffraction study of $Rb_4LiH_3(SeO_4)_4$ single crystals and the neutron diffraction study of $Rb_4LiH_3(SeO_4)_4$ single crystals at 298 and 480 K. Particular attention is given to the systems of hydrogen bonds in a number of *MLHX* structures.

EXPERIMENTAL

The RLHSe and RLHS single crystals were synthesized by slow concentration of aqueous solutions of the respective salts. The X-ray diffraction study of several RLHSe single crystals was performed on a four-circle STAD14 (Stoe) diffractometer and a diffractometer with an IPDS (Stoe) area detector (Mo radiation, λ = 0.71073 Å). The main difficulty in obtaining sufficiently accurate structural data was associated with the introduction of the absorption correction, because of a high Rb and Se content that resulted in a very high linear absorption coefficient in RLHSe, $\mu(MoK_\alpha)$ = 185.1 cm^{-1}. Upon taking into account absorption either by the empirical method based on the data of azimuthal scanning or by the numerical method with due regard for the crystal shape, the reliability factors for seven independent experiments ranged from 0.034 to 0.14. The best result was obtained for the data collected on an IPDS after the introduction of the absorption correction with due regard for the crystal shape and its refinement using the X-SHAPE program [7]. The positions of non-hydrogen atoms were determined by the direct methods (SHELXS-97) [8] and were refined in the anisotropic

Table 1. Crystallographic characteristics, experimental conditions, and details of the refinement of structures **1** and **2a** and **2b**

Parameter	$Rb_4LiH_3(SeO_4)_4$ **1**	$Rb_4LiH_3(SO_4)_4$ **2a**	$Rb_4LiH_3(SO_4)_4$ **2b**	$Rb_4LiH_3(SO_4)_4$ **2c**
Molecular weight	923.68	712.00	712.00	712.00
System	Tetragonal	Tetragonal	Tetragonal	Tetragonal
Sp. gr.	$P4_1$	$P4_1$	$P4_1$	$P4_1$
a, Å	7.818(1)	7.6316	7.6316(3)	7.6699(2)
c, Å	30.174(6)	29.500	29.500(2)	29.712(1)
V, Å^3	1844.3(5)	1718.1	1718.1(2)	1747.9(1)
Z	4	4	4	4
ρ_{calc}, g/cm^3	3.327	2.846	2.846	2.797
Temperature, K	180	298	298	480
Crystal dimensions, mm	$0.40 \times 0.22 \times 0.13$	$2.0 \times 1.5 \times 1.0$	$2.5 \times 2.5 \times 2.0$	$2.5 \times 2.5 \times 2.0$
Diffractometer	IPDS	VIVALDI	D19	D19
Radiation, λ, Å	MoK_α, 0.71073	Neutrons, 0.85–2.0	Neutrons, 1.3158	Neutrons, 1.3158
μ, cm^{-1}	185.14	0.458	0.458	0.448
θ_{max}, deg	24.7	30.5	30.1	26.0
Total number of reflections	11638	6632	3340	9203
Number of reflections with $I > 2\sigma(I)$	2647	1926	2057	3317
Number of reflections/parameters in LS refinement	3121/236	2553/254	2840/255	3845/255
R_1/wR_2	0.034/0.069	0.053/0.119	0.047/0.138	0.079/0.252

approximation (SHELXL-97) [9]. Hydrogen atoms were localized from difference Fourier syntheses and were refined in the isotropic approximation. The crystallographic parameters, experimental conditions, and the refinement parameters for the RLHSe (**1**) structure are listed in Table 1.

An RLHS crystal was cooled to 110 K, i.e., below the temperature of the phase transition at 134 K [2] or 130 K [3], directly in a STADI4 diffractometer. We observed considerable broadening of the initially narrow reflections caused by a phase transition. We also established a slight monoclinic distortion of the tetragonal unit cell: the angle γ deviated from 90°. The diffraction data were collected for the monoclinic unit cell with the parameters $a = 7.560(4)$, $b = 29.210(9)$, $c = 7.566(4)$ Å, $\beta = 90.32(3)°$, and $V = 1671$ Å^3. The determination and refinement of the crystal structure of the monoclinic modification of RLHS resulted in a relatively high reliability factor $R_1 = 0.077$, which seemed to be caused by crystal deformation and twinning due to the phase transformation. This did not allow us to reveal the details of the phase transition and the character of the displacements of individual groups in the structure.

One part of the neutron diffraction study was performed on a single-crystal four-circle D19 diffractometer with a germanium monochromator ($\lambda = 1.3158$ Å) and two ^{3}He area detectors of the "banana" and "square" types (Laue–Langevin Institute, Grenoble,

France). A single crystal was glued with a silicate glue on the rod of a heating device surrounded with two cylindrical Ge-foil shells and was placed into a sealed aluminum container. The data were collected on an RLHS single crystal (**2**) at three temperatures: 298 (**2b**), 480 (**2c**), and 500 K. In each neutron diffraction experiment performed at a given temperature, two partly overlapped sets of reflections were collected with the aid of two independent detectors in the small- and high-angle regions. Then the intensities of the crystallographically equivalent reflections in each region were averaged. The LS refinement was performed on the joint set of reflections with the refinement of the scaling factor for reflections from different regions. All the atoms, including hydrogens, were refined in the anisotropic approximation. Table 1 lists the data obtained in the diffraction experiments at 298 and 480 K.

The second part of the neutron diffraction study was performed on a VIVALDI Laue diffractometer using an intense flux ("white radiation") of nonmonochromatized neutrons and a cylindrical (image plate) detector (Laue–Langevin Institute, Grenoble, France) [10]. The data were collected from several diffraction "patterns" from a crystal at rest in several positions differed by its rotation by 20° around its axis. Upon indexing the reflections using the initial parameters known from other studies, we refined these data, integrated the intensities, and also determined the curve of intensity distribution I/λ in the neutron flux based on the compar-

Table 2. Interatomic distances (d, Å) in structures **1**, **2a**, **2b**, and **2c**

Bond	$d(\mathbf{1})$ (X=Se)	$d(\mathbf{2a})$ (X=S)	$d(\mathbf{2b})$ (X=S)	$d(\mathbf{2c})$ (X=S)
$X(1)$–O(1)	1.603(8)	1.440(5)	1.444(6)	1.450(5)
$X(1)$–O(2)	1.612(8)	1.447(5)	1.444(7)	1.456(5)
$X(1)$–O(3)	1.633(7)	1.452(5)	1.451(7)	1.423(5)
$X(1)$–O(4)	1.700(8)	1.556(6)	1.564(7)	1.550(5)
$X(2)$–O(5)	1.606(7)	1.445(5)	1.459(6)	1.462(5)
$X(2)$–O(6)	1.627(7)	1.452(6)	1.457(6)	1.463(5)
$X(2)$–O(7)	1.644(7)	1.470(6)	1.460(6)	1.456(4)
$X(2)$–O(8)	1.668(7)	1.511(5)	1.504(6)	1.494(5)
$X(3)$–O(9)	1.604(7)	1.430(6)	1.435(7)	1.439(5)
$X(3)$–O(10)	1.621(8)	1.451(6)	1.443(6)	1.435(5)
$X(3)$–O(11)	1.678(7)	1.527(5)	1.521(6)	1.515(5)
$X(3)$–O(12)	1.616(7)	1.448(6)	1.465(7)	1.444(5)
$X(4)$–O(13)	1.609(8)	1.452(5)	1.440(6)	1.442(5)
$X(4)$–O(14)	1.620(7)	1.436(5)	1.448(6)	1.434(5)
$X(4)$–O(15)	1.618(7)	1.446(5)	1.461(6)	1.447(5)
$X(4)$–O(16)	1.706(7)	1.563(6)	1.537(7)	1.560(5)
Li–O(3)	1.94(2)	1.906(9)	1.91(1)	1.919(7)
Li–O(6)	1.91(2)	1.900(8)	1.91(1)	1.921(7)
Li–O(10)	1.92(2)	1.904(8)	1.90(1)	1.894(7)
Li–O(15)	1.90(2)	1.938(8)	1.93(1)	1.936(7)
Rb–O	2.800–3.293(8)	2.835–3.247(4)	2.824–3.305(4)	2.843–3.291(4)

ison of the intensities of crystallographically equivalent reflections [1]. The VIVALDI diffractometer was extremely sensitive and allowed us to collect the data from small (1–2 mm) crystals for a comparatively short time (6–12 h). The RLHS (**2**) crystals were studied at both low and high temperatures. The exposures at 100 K revealed twinning caused by the phase transition, which did not allow us to index the Laue diffraction patterns. The measurements at 298 and 480 K were made to be able to compare the results of the neutron diffraction studies of the same structure with the data obtained by different methods of reflection recording. The LS refinement with the unit-cell parameters corresponding to the data for **2b** and **2c** crystals was performed in the anisotropic approximation for all the atoms of the RLHS crystals at 298 K (**2a**) and 480 K (Table 1). The structure studied at 480 K turned out to be almost identical to the structure **2c** (D19), but the accuracy of its determination by the experimental data obtained on the VIVALDI diffractometer was somewhat lower, $R_1 = 0.069$, and the scatter in the S–O distances was somewhat larger, 0.013–0.016 Å, because of a lesser number of the independent reflections used. Therefore, these results are not discussed here.

The most important interatomic distances for structures **1** and **2a**–**2c** are indicated in Table 2, and the characteristics of hydrogen bonds are indicated in Table 3.

The atomic coordinates and the coefficients of thermal displacements are deposited in the Database of Crystal Structures FIZ, Karlsruhe, D-76344, Eggenstein–Leopoldshafen (Germany), Nos. 000001, 000002, 000003, and 00004 (412716, 413717, 413718, and 413719).

RESULTS AND DISCUSSION

We studied two isostructural compounds by different methods, which allowed us to consider some methodological problems of the crystallographic studies. The X-ray diffraction studies were performed on several $Rb_4LiH_3(SeO_4)_4$ crystals possessing very high linear absorption coefficients. The use of a four-circle diffractometer requires the allowance for absorption and very accurate measurements of crystal shape and dimensions. In most cases, the authors who made such studies failed to make precision measurements, which resulted in unsatisfactory accuracy in the atomic coordinates determined and did not allow the authors to localize hydrogen atoms. The use of a diffractometer with an area detector allows one not only to perform relatively fast data collection for crystals with large unit-cell parameters but also to obtain the data sets based on the measurements of a large number of crystallographically equivalent reflections, which, in turn, is very important for the subsequent empirical refine-

Table 3. Hydrogen bonds in structures **1**, **2a**, **2b**, and **2c**

D–H⋯A bond	D–H, Å	H⋯A, Å	D⋯A, Å	D–H⋯A, deg
1				
O(4)–H(1)⋯O(7)	0.8(1)	1.7(1)	2.51(1)	176(16)
O(11)–H(2)⋯O(8)	1.2(1)	1.3(1)	2.485(8)	166(10)
O(16)–H(3)⋯O(12)	0.8(1)	1.8(1)	2.52(1)	153(13)
2a				
O(4)–H(1)⋯O(7)	1.018(5)	1.538(5)	2.536(4)	165.6(6)
O(11)–H(2)⋯O(8)	1.196(9)	1.289(9)	2.485(4)	179.7(6)
O(16)–H(3)⋯O(12)	0.997(5)	1.561(5)	2.548(3)	169.7(6)
2b				
O(4)–H(1)⋯O(7)	0.997(7)	1.547(7)	2.534(5)	169.3(6)
O(11)–H(2)⋯O(8)	1.190(10)	1.296(10)	2.486(4)	179.0(7)
O(16)–H(3)⋯O(12)	0.984(8)	1.565(8)	2.535(5)	167.5(5)
2c				
O(4)–H(1)⋯O(7)	0.964(7)	1.589(6)	2.538(4)	167.2(4)
O(11)–H(2)⋯O(8)	1.211(8)	1.301(8)	2.512(3)	179.6(7)
O(16)–H(3)⋯O(12)	0.988(6)	1.581(6)	2.557(4)	168.7(4)

ment of the crystal shape and dimensions (X-SHAPE [7]). In our case, the high (tetragonal) symmetry and, therefore, the presence in the data set of a large number of crystallographically equivalent reflections, allowed us to refine the shape of the RLHSe crystal so well that we managed to localize all the hydrogen atoms.

It is also worth to compare the use of the monochromatic and white radiations in neutron diffraction studies. The first method is traditional for obtaining accurate data on the proton (deuteron) positions. The record of the diffraction pattern with the aid of area and not point detectors allows one to considerably increase the speed of data acquisition. The second method, which combines the high intensity of the nonmonochromated neutron flux and the use of an area detector, has certain advantages. Along with the possible study of relatively small (1–2 mm) crystals, the exposure time is also considerably shorter, which makes the total time necessary for a neutron diffraction experiment comparable with the time of an X-ray diffraction experiment. The data presented in Tables 1 and 2 demonstrate that both neutron diffraction methods (used for **2a** and **2b** structures) yield almost the same accuracy.

On the whole, the results of the X-ray diffraction study of the RLHSe single crystal (**1**) confirmed that all the *MLHX* compounds have the same structure type [2, 4–6] (Fig. 1). In some structure determinations of RLHSe crystals, the enantiomorphous groups $P4_1$ and $P4_3$ were used. Crystal structure **1** (sp. gr. $P4_1$ with the Flack parameter 0.01(2)) has Rb cations coordinated with 7 or 8 O atoms from SeO$_4$ groups at distances 2.80–3.29 Å (Table 2). The structure contains zigzag

chains of four SeO$_4$ tetrahedra connected by three hydrogen bonds with the lengths 2.48–2.53 Å (Table 3). The longest Se–O distances (1.70–1.71 Å) correspond to the oxygen O(4) and O(16) atoms, which are donors of H atoms in hydrogen bonds. The shortest Se–O distances (1.60–1.63 Å) correspond to oxygen atoms not participating in hydrogen bonds. The Se–O bonds of the intermediate length (1.62–1.68(7) Å) are formed by the O atoms which, in addition, are either acceptors of H atoms in hydrogen bonds with O(7) and O(12) or act as both donors and acceptors in the bonds with O(8) and O(11) atoms. The oxygen atoms not participating in hydrogen bonds are characterized by short Se–O distances (1.60–1.63 Å). The same features are also characteristics of the Se–O bonds in the crystal structure of alkali-metal and alkaline-earth hydrogen selenates [12]. The central hydrogen bond O(11)⋯H(2)⋯O(8) (2.485 Å) is somewhat shorter than the terminal O(4)–H(1)⋯O(7) and O(16)–H(3)⋯O(12) (2.51–2.52 Å) bonds. The positions of hydrogen atoms are determined somewhat unreliably, but on the whole, they correspond to a more symmetric position of the H(2) atom of the hydrogen bond in comparison with the asymmetric arrangement of the H(1) and H(3) atoms. Lithium atoms have slightly distorted tetrahedral coordination of O atoms from four different chains with the Li–O distances ranging within 1.90–1.94(2) Å and the O–Li–O angles ranging within 104°–118°. Since the O(3), O(6), O(10), and O(15) oxygen atoms are coordinated with Li atoms, the corresponding Se–O distances are somewhat elongated (1.62–1.63 Å). Thus, unlike [6], where only the unit-cell parameters and R factors were reported without any further crystallographic information, the X-ray diffraction study performed allowed us to characterize the main modification of the RLHSe in good detail.

The neutron diffraction study of RLHS crystals (**2**) not complicated (as in the case of the X-ray diffraction study of RLHSe) by the problem of allowance for absorption ($\mu \approx 0.045$ mm^{-1}) allowed us not only to reliably localize protons, but also reveal the differences in the systems of hydrogen bonds at various temperatures. The structural results obtained by two methods with essentially different recording of reflections and their integration gave consistent results. Thus, most of the interatomic distances, including those of hydrogen bonds, turned out to be identical for structures **2a** (VIVALDI) and **2b** (D19) within 1σ, and only a few distances were consistent within 2σ (Table 2 and 3). For more convenient comparison of the results with the data for the RLHS structure at 480 K (**2c**), we considered the **2b** structure in more detail since both studies were performed on the same crystal.

On the whole, the RLHS (**2**) structure is analogous to the RLHSe (**1**) structure described above. The Rb–O distances range within 2.835–3.247 Å and the Li–O distances, within 1.90–1.93 Å. The main difference is the structures is explained by the smaller dimensions of
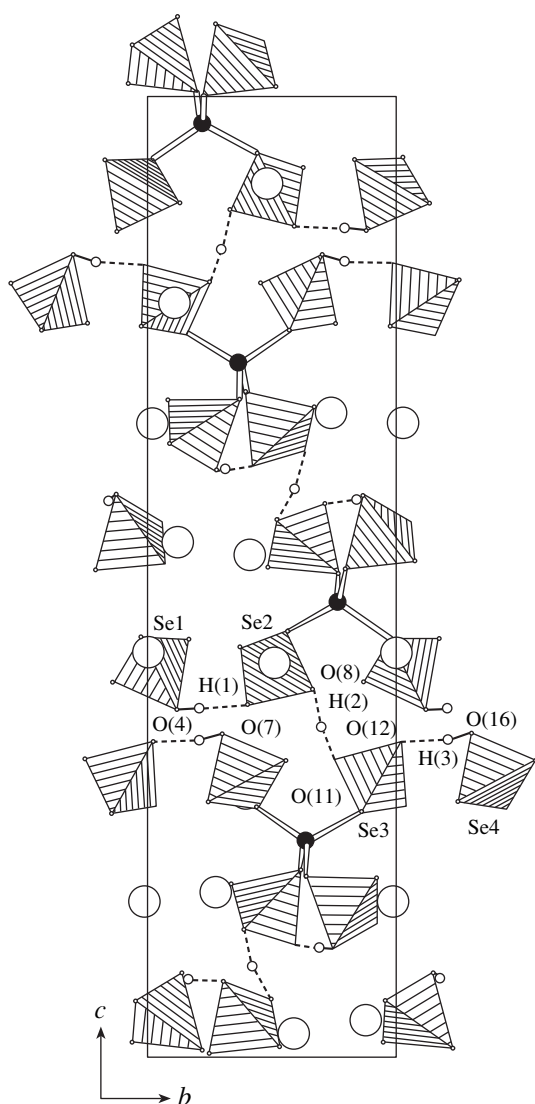
Fig. 1. Unit cell of the $Rb_4LiH_3(SeO_4)_4$ crystal structure (**1**) projected along the *a* axis. The SeO_4 groups are shown as Se(*n*) tetrahedra, Rb atoms are shown by large empty circles, Li atoms are depicted by filled circles, and H atoms are depicted by small empty circles.

Fig. 2. Chains of four SO_4 tetrahedra linked by hydrogen bonds in the $Rb_4LiH_3(SeO_4)_4$ crystal structure according to the neutron diffraction data at 298 K (**2b**, on the left and **2c**, on the right).

sulfate groups than those of the selenate groups. In the RLHS structure at 298 K (**2b**), the longest S–O distances (1.54–1.56 Å) are formed by the O(4) and O(16) atoms, which are donors of protons in hydrogen bonds, whereas the shortest distances (1.44–1.45 Å) are formed with the oxygen atoms not participating in hydrogen bonds and not coordinated with Li atoms. The tetrahedra forming four-member zigzag chains are connected by hydrogen bonds, whose geometrical characteristics are determined with a high accuracy. Two hydrogen bonds, O(4)–H(1)···O(7) and O(16)–H(3)···O(12), are longer (2.53–2.54 Å) than the central hydrogen bond O(11)···H(2)···O(8) (2.486 Å), which is in good quantitative agreement with the data for RLHSe (Table 3). Longer bonds are established for

conventional asymmetric hydrogen bonds with short O–H distances (1.00–1.02 Å) and considerably longer H···O distances (1.54–1.55 Å) and the O–H···O angle ranging within 166°–170°. The short central hydrogen bond is characterized by almost symmetric position of the H(2) atom with close H···O distances (1.19 and 1.29 Å) and the angle O(11)···H(2)···O(8) 179.0°. The ellipsoid of thermal vibrations of H(2) is slightly elongated along the bond (Fig. 2), which seems to indicate a certain disorder typical of short and symmetric hydrogen bonds. It should also be indicated that the systems of hydrogen bonds in the RLHS structure at 298 K and RLHSe structure at 180 K are identical within the estimated standard deviations. On the other hand, the results obtained for RLHS (**2a** and **2b**) complement the data of the X-ray diffraction study of this compound [4] in which no hydrogen atoms were localized.

In the *RLHS* crystal structure at 480 K (**2c**), i.e. at the temperature of the transition to the phase with a high protonic conductivity (455 K, according to [3]), the sp. gr. $P4_1$ is preserved and no essential structural changes in comparison with the structure at 298 K are

observed. Therefore, it is assumed that a second-order phase transition takes place. In fact, the Rb–O (2.843–3.291 Å) and Li–O (1.89–1.94 Å) distances remain unchanged and the maximum scatter in the S–O distances does not exceed $(1–2)\sigma$. These relationships remained unchanged after the introduction of the corrections for libration, because the latter did not exceed 0.001–0.002 Å.

Despite a considerable increase in the amplitudes of thermal vibrations (Fig. 2), the geometrical characteristics of hydrogen bonds remained almost unchanged. As earlier, the terminal tetrahedra of the chains are characterized by longer (2.538–2.557 Å) asymmetric hydrogen bonds with short O–H distances (0.964–0.988 Å) and long H⋯O distances (1.581–1.589 Å). The central (short) hydrogen bond (2.512 Å) is only slightly elongated in comparison with the bond in structure **2b** (2.486 Å). This bond also preserves its slight asymmetry, but the elongation of the ellipsoid of thermal vibrations along this bond shows a higher degree of proton disorder. The changes observed in the transition from the structures at room temperature to the structures at 480 K for the RLHS (the present study) and KLHS [5] structures are slightly different: the X-ray diffraction study of the high-temperature KLHS phase showed a noticeably dissymmetrization of the central hydrogen bond. However, none of these two structures showed the signs of a phase transitions characteristics, e.g., of the $MHXO_4$ or $M_3H(XO_4)_2$ phases, which manifest themselves in the phases with a high protonic conductivity in a pronounced disorder in the XO_4 tetrahedra [13, 14].

Thus, the X-ray diffraction method allowed us to obtain the reliable crystallographic data for $Rb_4LiH_3(SeO_4)_4$ and localize hydrogen atoms. The neutron diffraction study of $Rb_4LiH_3(SeO_4)_4$ single crystals allowed us to obtain the detailed information on the system of hydrogen bonds in the crystals at room temperature and in the high-temperature phase at 480 K. The space group and the main geometrical characteristics of hydrogen bonds are preserved, but the amplitudes of atomic thermal vibrations considerably increase, as well as the degree of proton disorder of the central hydrogen bond of the four-membered chains of SO_4 tetrahedra.

REFERENCES

1. J. Minge and T. Krajewski, Phys. Status Solidi A **109**, 193 (1988).
2. B. Mróz, S. M. Kim, B. M. Powell, *et al.*, Phys. Rev. B **55**, 11174 (1997).
3. A. Petrazhko, M. Polomska, and A. Pavlovski, Izv. Akad. Nauk SSSR, Ser. Fiz. **55** (3), 529 (1991).
4. F. J. Zúñiga, J. Etxebarria, G. Madariaga, and T. Breczewski, Acta Crystallogr., Sect. C: Cryst. Struct. Commun. **46**, 1199 (1990).
5. A. Haznar and A. Pietraszko, Solid State Chem. (2004) (in press).
6. A. Pietraszko and K. Lukaszewicz, Z. Kristallogr. **185**, 564 (1988).
7. *X-SHAPE: Crystal Optimization for Numerical Absorption Correction* (Stoe and Cie, Darmstadt, 1996).
8. G. M. Sheldrick, *SHELXS97. Program for the Solution of Crystal Structures* (Univ. of Göttingen, Germany, 1997).
9. G. M. Sheldrick, *SHELXL97. Program for the Refinement of Crystal Structures* (Univ. of Göttingen, Germany, 1997).
10. C. Wilkinson, J. A. Cowan, D. A. A. Myles, *et al.*, Neutron News **13**, 37 (2002).
11. J. W. Campbell, J. Appl. Crystallogr. **28**, 228 (1995).
12. E. Kemnitz and S. I. Troyanov, Adv. Mol. Struct. Res., JAI Press **4**, 79 (1998).
13. A. I. Baranov, B. V. Merinov, A. V. Tregubchenko, *et al.*, Solid State Ionics **36**, 279 (1989).
14. V. B. Merinov and L. A. Shuvalov, Kristallografiya **37** (3), 410 (1992) [Sov. Phys. Crystallogr. **37**, 211 (1992)].

Translated by L. Man

STRUCTURE
OF INORGANIC COMPOUNDS

Complex (Nonstandard) Six-Layer Polytypes of Lizardite Revealed from Oblique-Texture Electron Diffraction Patterns

A. P. Zhukhlistov*, N. N. Zinchuk**, and D. D. Kotel'nikov**

* Institute of Geology of Ore Deposits, Petrography, Mineralogy, and Geochemistry (IGEM),
Russian Academy of Sciences, Staromonetnyi per. 35, Moscow, 119017 Russia
** Yakutian Geological Enterprise of Exploration, Research, and Development CNIGRI ALROSA,
Chernyshevskoe sh. 7, Mirnyi, 678110 Russia
e-mail: anzhu@igem.ru

Abstract—Association of simple ($1T$ and $3R$) and two complex (nonstandard) orthogonal polytypes of the serpentine mineral lizardite from the Catoca kimberlite pipe (West Africa) association is revealed from oblique-texture electron diffraction patterns. A six-layer polytype with an ordered superposition of equally oriented layers (notation $3_2 3_2 3_4 3_4 3_6 3_6$ or $++--00$) belonging to the structural group A and a three-layer (336 or I,I,II) or a six-layer (336366 or I,I,II,I,II,II) polytype with alternating oppositely oriented layers and semi-disordered structure are identified using polytype analysis. © *2004 MAIK "Nauka/Interperiodica"*.

INTRODUCTION

Serpentine minerals are formed of trioctahedral two-story 1 : 1 OT layers composed of octahedral (O) and tetrahedral (T) sheets. The polytype variety of serpentines is determined by the features of mutual arrangement of layers. In derivation of theoretically possible polytypes of serpentines in [1, 2], intralayer displacements s between adjacent O and T sheets and interlayer displacements t between successive sheets of adjacent layers were used to describe the structures. In the orthogonal coordinate system a, $b = a\sqrt{3}$, the 1 : 1 layer may have six azimuthal orientations s_i ($i = 1, 2, \dots 6$), which are determined by displacements of tetrahedral sheets with respect to octahedral sheets when the a_i axis of the layer is oriented parallel to the a axis of the structure. Serpentine minerals are formed of layers with two opposite orientations s_3 and s_6 with the components along the a and b axes equal to [1/3, 0] and [−1/3, 0], respectively. Displacements t_k between successive T–O sheets of adjacent layers have nine values: six values of $t_k = s_i$ at $k = i$ (with different parities of k and the index i of the subsequent layer) and three additional values: $t_0 = [0, 0]$, $t_+ = [0, 1/3]$, and $t_- = [0, -1/3]$. The sequence of sheets and layers in the structures of serpentine minerals is described by the sequence of symbols s_i, t_k (or, briefly, ik). If the homogeneity condition (which means the equivalence of mutual arrangement of each pair of adjacent layers and the transition from the previous to subsequent layer) is satisfied, 12 possible serpentine polytypes are possible, which are divided into four groups: A (structures $1T$, $2T$, $3R$), B ($1M$, $2M_1$, $3T$), C ($2O$, $2M_2$, $6H$), and D ($2H_1$, $2H_2$, $6R$). In the structures of groups A and B, layers are equally oriented, whereas, in groups C and D, oppositely oriented layers alternate with each other. The structures belonging to these groups have identical projections onto the ac plane and their diffraction patterns are characterized by the $h0l$ and hkl reflections with $k = 3n$.

To describe serpentine polytypes, Bailey [3] used two possible systems of positions occupied by cations in octahedral sheets, denoted as I and II (equivalent to the two azimuthal orientations of layers), and interlayer displacements, counted between the T–T tetrahedral sheets of adjacent layers, equal to $t + s$. Serpentine polytypes are also divided into four groups (A, B, C, D). In groups A and B, the interlayer displacements are equal to $\pm a/3$ along three pseudohexagonal a axes. The structures of groups C and D are characterized by the displacements 0 or $\pm b/3$ (briefly denoted as 0, +, −), which are not mixed in the same structure (only + and − can alternate). Groups C, A, B, and D described in [3] correspond to groups A, B, C, and D considered in [1, 2].

In addition to the above 12 serpentine simple (standard) polytypes, there are complex (nonstandard) periodic structures, which do not obey the restrictions imposed in derivation of simple polytypes. The number of theoretically possible complex polytypes increases with increasing number of layers per repetition period. For example, in the case of equally oriented layers, the number of theoretically possible complex polytypes is 4, 5, 20, 44, 104, and 253 for periods of 3, 4, 5, 6, 7, and 8 layers, respectively [4].

In samples of natural serpentines, a relatively small number of complex polytypes have been identified. It is noteworthy that, except for one complex polytype, in

Table 1. Chemical composition of the kimberlite breccia

Components	wt %
SiO_2	37.21
TiO_2	0.98
Al_2O_3	1.93
Fe_2O_3	8.66
FeO	1.61
MnO	0.15
MgO	30.27
CaO	3.03
Na_2O	0.02
K_2O	0.12
P_2O_5	0.17
CO_2	2.99
H_2O^+	10.63
H_2O^-	2.42
Sum	100.19

which layers are displaced along the *a* and *b* axes [5], all other known complex polytypes are characterized by combinations of the interlayer displacements *b*/3 and –*b*/3 (according to a more complex law than a simple alternation of the +–+– type) or 0 and *b*/3 with alternation of oppositely oriented layers in a particular order. The most widespread is the complex six-layer polytype $6R_2$, in the structure of which the sequence of interlayer displacements 0–0–0– is combined with the opposite orientation of adjacent layers I and II, which is typical of group *D*. This polytype was identified for amesite [6–9] and cronstedtite [10, 11]. Another complex six-layer polytype with mixed displacements 0 and ±*b*/3 and oppositely oriented adjacent layers was revealed for the serpentine (polygonal chrysotile asbestos) from Unst [12]. For this serpentine, a –+–+00 model was proposed, which yielded the best coincidence of diffraction characteristics calculated for 24 theoretically possible models with experimental intensities of X-ray diffraction reflections with $k \neq 3n$. Later, high-resolution electron microscopy measurements showed that the Unst-type polygonal serpentine is a mixture of $6R_2$ and $2H_2$ polytypes [13]. A unique combination of simple and complex polytypes was revealed for lamellar serpentine (Cr-containing lizardite) from selected-area electron diffraction patterns [4, 13]. Banfield *et al.* [13] identified for the first time, along with the dominant simple $2T$, $2H_1$, $2H_2$, and $6R_1$ polytypes and the complex $6R_2$ polytype, an ordered three-layer 00– structure with the layer alternation of the I,I,II type; ordered four-layer 0–0+, 000–, – – – +, and 0 – – – structures with the layer alternation of the I,II type; and a semi-disordered structure with alternation of oppositely oriented layers: I,I,II; I,I,II,II; I,I,I,II; I,II,I,II,I; II,II,II,I,I,I; I,II,I,II,I,II,I; and I,II,I,II,I,I,I.

In view of the above considerations, the detection of an unusual association of simple ($1T$ and $3R$) and two complex six-layer orthogonal lizardite polytypes, identified from the oblique-texture electron diffraction patterns, is of particular interest. In this study, we analyze and interpret the diffraction features indicative of the presence of these polytypes.

RESULTS AND DISCUSSION

Electron diffraction study of lizardites from the Catoca kimberlite pipe (West Africa) [14, 15] revealed for most samples structural changes from the three-dimensionally ordered $1T$ polytype (in combination with an impurity structure of the *D* type) to semi-disordered structures of the *A* type. The oblique-texture electron diffraction pattern of a lizardite sample from the kimberlite breccia (well 0432, depth 124 m, fraction 0.001 mm) drew attention due to the unusual distribution of the intensities of the 02*l* and 11*l* reflections on the first ellipse (hereinafter, the indices are given for the orthogonal basis with $a = b/\sqrt{3}$). X-ray powder diffraction analysis showed that the sample consists mainly of lizardite with a semi-disordered structure of the *A* type with small impurities of saponite, phlogopite, and calcite. Based on the chemical analysis of the sample (Table 1), with regard to the low content of CaO, Na_2O, K_2O, and CO_2 (related to the presence of the noted mineral impurities), the following crystallochemical formula (per nine oxygen atoms) was obtained for lizardite: $(Mg_{2.37}Fe^2_{0.07}Fe^3_{0.34}Al_{0.08}Ti_{0.04}Mn_{0.01})_{2.91}(Si_{1.96}Al_{0.04})_{2.00} \cdot O_{5.27}(OH)_{3.73}$. This formula, in comparison with the ideal formula $Mg_3Si_2O_5(OH)_4$, shows a higher content of Fe^{3+} cations in the octahedral sheet of a serpentine layer and replacement of some fraction of $(OH)^{1-}$ ions with O^{2-} ions as a result of insignificant substitution of Si with Al in tetrahedra.

The oblique-texture electron diffraction pattern of this lizardite sample contained pronounced 02*l* and 11*l* reflections on the first ellipse, which correspond to the three-layer orthogonal cell. Very weak reflections corresponding to the six-layer orthogonal cell are located between these reflections (Table 2). The positions and intensities of stronger reflections correspond to the mixture of the $1T$ and $3R$ polytypes (with some dominance of $1T$) belonging to group *A*. It is noteworthy that the reflections in the positions with $l = 3n$ for the three-layer orthogonal cell are related to the $1T$ polytype, and the reflections in the positions with $l \neq 3n$ are related to the $3R$ polytype. The parameters of the base-centered lattices of the $1T$ and $3R$ lizardite polytypes are $a = 5.34$ Å, $b = 9.245$ Å, $c_{1T} = 7.27$ Å, and $c_{3R} = 21.81$ Å. The $3R$ polytype was identified for the first time for serpentines. The previous data on the detection of the $3R$ polytype in the serpentine mineral cronstedtite have not been confirmed subsequently [16].

Table 2. Sequence of the 02*l* and 11*l* reflections on the first ellipse of the oblique-texture electron diffraction patterns of simple (1*T*, 3*R*) and complex six-layer orthogonal (from Table 4) lizardite polytypes

l_6	d_{hkl}	I_{obs}	Values of $\Sigma |F| I^2_{hkl}$ for the 02*l* and 11*l* reflections																	
			1*T*	3*R*	1	2	3	4	5	6	7	8	9	10	11	12	13	14	15	16	17
0	4.622	s	861		0	72	72	72	0	72	287	215	215	0	72	215	215	72	502	215	287
1	4.597				71	71	71	107	178	214	71	107	71	214	178	71	178	286	71	286	214
2	4.522	mw		421	211	70	281	176	105	70	70	105	211	211	176	211	105	70	70	0	70
3	4.405	w			273	478	68	205	273	204	273	205	68	0	68	68	68	68	68	68	0
4	4.256	mw		395	198	66	263	165	99	65	66	99	198	198	165	198	99	66	66	0	66
5	4.085	vw			63	63	63	94	157	188	63	94	63	188	157	63	157	251	63	251	188
6	3.901	m	710		0	59	59	59	0	59	237	178	178	0	59	178	178	59	414	178	237
7	3.713	vw			55	55	55	82	138	165	55	83	55	165	138	55	138	220	55	220	165
8	3.526	mw		303	151	51	202	126	76	50	50	76	152	152	126	152	76	51	51	0	51
9	3.345	vw			183	321	46	138	184	137	184	138	46	0	46	46	46	46	46	46	0
10	3.172	mw		245	123	41	163	102	61	41	41	61	123	123	102	123	61	41	41	0	41
11	3.010	vw			36	36	36	53	90	107	36	54	36	108	90	36	90	144	36	144	108
12	2.857	mw	372		0	31	31	31	0	31	124	93	93	0	31	93	93	31	217	93	124
13	2.715				27	27	27	40	66	79	27	40	27	79	66	27	66	106	27	106	79
14	2.584			134	67	22	90	56	34	22	22	34	67	67	56	67	34	22	22	0	22
15	2.461				75	131	19	56	75	56	75	56	19	0	19	19	19	19	19	19	0
16	2.348			94	47	16	63	39	24	16	16	24	47	47	39	47	24	16	16	0	16
17	2.243				13	13	13	20	33	39	13	20	13	40	33	13	33	53	13	53	40
18	2.146		132		0	11	11	11	0	11	44	33	33	0	11	33	33	11	77	33	44

Table 3. Sequence of the 02*l* and 13*l* reflections on the second ellipse of the oblique-texture electron diffraction patterns of the polytypes of groups *A*, *D*, and *B* and complex three-layer 336 (I,I,II) and six-layer (from Table 5) orthogonal lizardite polytypes

l_6	d_{hkl}	I_{obs}	Values of ΣIFI^2_{hkl} for the 02*l*, 13*l* reflections								
			A	*D*	*B*	336	1	2	3	4	5
0	2.669	17	275	229		234	249	234	234	229	229
1	2.665						6	18	6	24	6
2	2.649				486	35	9	9	9	0	26
3	2.625			124			14	0	55	14	14
4	2.593				366	83	21	21	21	0	63
5	2.522						30	9	30	120	30
6	2.506	100	2379	2011		2052	2173	2052	2052	2011	2011
7	2.454						51	153	51	204	51
8	2.397	w			2256	243	61	61	61	0	182
9	2.338	w		619			69	0	275	69	69
10	2.277	vw			87	298	74	74	74	0	224
11	2.214						75	234	78	311	78
12	2.151	24	1229	505		585	825	585	585	505	505
13	2.089						81	244	82	326	81
14	2.027	vw			681	331	82	82	83	0	249
15	1.966	2		762			85	0	339	85	85
16	1.907	vvw			163	348	87	87	87	0	261
17	1.850						89	265	88	354	89
18	1.794	8	1061	256		345	611	345	345	256	256
19	1.741						87	261	87	348	87
20	1.689	vvw			1004	333	83	83	83	0	250
21	1.639	vw		698			77	0	310	77	78
22	1.592	vvw			408	282	70	70	70	0	211
23	1.546						62	188	62	51	63
24	1.502	10	1182	673		728	895	728	728	673	673
25	1.460						49	147	49	196	49
26	1.420				79	173	43	43	43	0	130

Note: Intensities of the most pronounced reflections are estimated from the electron diffraction patterns recorded on imaging plates [17].

However, there was much interest in the weak reflections on the first ellipse of the oblique-texture electron diffraction pattern, which indicated the presence of a complex six-layer orthogonal polytype ($c =$ 43.62 Å) in the lizardite sample (Table 2). A more careful preparation of specimens and measurements at different tilt angles of the sample holder (in the range 20°–60°) made it possible to obtain electron diffraction patterns of this lizardite sample, in which weak reflections, including those near the minor axis of the ellipses (with small values of *l*), were more pronounced. Weak reflections, also corresponding to an orthogonal period of three or six layers, were also revealed on the second ellipse near the separately located reflections of the *D*-group polytype (Table 3).

Analysis of the electron diffraction patterns obtained revealed structural (phase) inhomogeneity of the sample, due to which the weak reflections manifested themselves differently on the first and second ellipses of the electron diffraction patterns (in some patterns, these reflections were not observed at all). For example, the first-ellipse reflections related to the six-layer polytype are more pronounced in the electron diffraction patterns in which the second-ellipse reflections, corresponding to the structure type *D*, are weak and are also observed in the absence of the weak reflections 20*l* and 13*l* due to the structure with a period of three or six layers. In contrast, weak reflections arose on the second ellipse when the intensity of the reflections corresponding to group *D* increased somewhat. This gave grounds to suggest that two complex orthog-

onal polytypes are present in the lizardite under study. The one that manifests itself in weak reflections on the first ellipse belongs to the structure type *A* (as polytypes 1*T* and 3*R*) and is an ordered complex polytype. Equally oriented layers are typical of this polytype, as of simple polytypes of group *A*. Another complex lizardite polytype, which manifests itself in weak reflections on the second ellipse, is formed of oppositely oriented layers alternating according to a more complex law than a simple change in the orientations of adjacent layers, which is characteristic of group *D* (3636…). Obviously, this polytype belongs to semi-disordered structures, which are characterized by the displacement of adjacent layers by ±*b*/3.

To identify these structures, the intensities of the measured reflections 02*l*, 11*l*, and 20*l*, 13*l*, partially determined from the electron diffraction patterns recorded on imaging plates [17], were compared with the calculated values of $\Sigma|F|^2$ for 17 theoretically possible models of orthogonal six-layer structures belonging to group *A* (Table 2, 4), 5 variants of six-layer sequences of oppositely oriented layers differing in alternation order (Table 3, 5), and the only possible three-layer semi-disordered structure of the I,I,II (336) type. When the content of complex polytypes in a sample is low in comparison with simple polytypes, the choice of the model is based on the qualitative agreement between the distribution of weak reflections due to the six-layer polytypes and the corresponding calculated intensities characterized by the largest values of $\Sigma|F|^2$. To calculate the diffraction characteristics, we used an original program expressing the structure factors of an arbitrary sequence and any number of serpentine layers in terms of the scattering amplitude of separate layers and the phase factors in the orthogonal coordinate system.

In the models of complex polytypes formed of equally oriented layers (Table 4), the displacement of layers per alteration period of six layers in the projection onto the *ab* plane is zero. In these structures, the pairs of layers $s_3t_2s_3$, $s_3t_4s_3$ (structurally equivalent pairs) and $s_3t_6s_3$ (numbers 4, 5 and 6 in [2]), which are characterized by the *T–T* displacements equal to +, −, and 0, respectively, are represented by different alternation orders and different quantitative relations; i.e., they are distributed with violation of homogeneity. For example, the structures 1 and 2 (Table 4) are formed of mirror-equal pairs (as the simple 2*T* polytype), but their sequence order is ambiguous: ++, − − (as in the 3*R* polytype), and +− (as in the 2*T* polytype). In particular, in the structure 1, two mirror-equal 3*R* fragments (+++ and − − −) are separated by the 2*T* fragment (+−). Structures 13 and 14 are formed of structurally nonequivalent pairs (4, 6 in [2]); in other structures, all three pairs of layers and, respectively, the interlayer displacements 0, +, and − are represented.

Identification of the six-layer polytype was impeded by the superposition of the reflections 02*l* and 11*l* with

Table 4. Complex (nonstandard) six-layer orthogonal serpentine polytypes with equally oriented layers (structure type *A*)

Polytype	Notation according to [3]	Notation according to [1, 2]
1	+++−−−	$3_23_23_23_43_43_4$
2	++−−+−	$3_23_23_43_43_23_4$
3	++++−−0	$3_23_23_23_23_63_4$
4	+++0+−	$3_23_23_23_63_23_4$
5	++0++−	$3_23_23_63_23_23_4$
6	++−−00	$3_23_23_43_43_63_6$
7	+−+−00	$3_23_43_23_43_63_6$
8	+00+−−	$3_23_63_63_23_43_4$
9	+−0−+0	$3_23_43_63_43_23_6$
10	++0−−0	$3_23_23_63_43_43_6$
11	++−0−0	$3_23_23_43_63_43_6$
12	+−+0−0	$3_23_43_23_63_43_6$
13	+++000	$3_23_23_23_63_63_6$
14	+0++00	$3_23_63_23_23_63_6$
15	+−0000	$3_23_43_63_63_63_6$
16	+00−00	$3_23_63_63_43_63_6$
17	+000−0	$3_23_63_63_63_43_6$

Table 5. Complex (nonstandard) six-layer orthogonal sequences of oppositely oriented serpentine layers

Polytype	Notation according to [3]	Notation according to [1, 2]
1	I,I,I,I,I,II	333336
2	I,I,I,I,II,II	333366
3	I,I,I,II,I,II	333636
4	I,I,I,II,II,II	333666
5	I,I,II,I,II,II	336366

l = 2*n* with the corresponding reflections of the 1*T* and 3*R* polytypes. As can be seen from Table 2, the intensities of the 02*l* and 11*l* reflections due to the six-layer structure, which are observed separately in the oblique-texture electron diffraction patterns, most adequately describe structures 5 and 6. From these two, structure 6 should be preferred, the symbolic notation of which is $3_23_23_43_43_63_6$ or ++− −00. In this structure, fragments of two enantiomorphic 3*R* structures (++ and − −) and 1*T* structure (00), which are present in this sample in the form of dominant simple polytypes, alternate with each other. It is noteworthy that this is the first example of identification of a complex serpentine polytype composed of equally oriented layers.

The observed distribution of the intensities of weak 20*l* and 13*l* reflections grouped around the positions related to separate reflections of the *D*-type lizardite correspond to semi-disordered structures of three-layer

or six-layer orthogonal lizardite with alternating oppositely oriented layers: 336 (I,I,II) or 336366 (I,I,II,I,II,II) (Table 3). In the presence of a *D*-polytype impurity, these structures show identical oblique-texture electron diffraction patterns. The I,I,II structure is established for Cr-enriched lizardite [13]; the structure with alternating layers of the I,I,II,I,II,II type was revealed for the first time for serpentines.

The simple polytypes belonging to different groups [1, 2] are distinguished by the 20*l* and 13*l* reflections ($k = 3n$) and, within separate groups, by the 02*l* and 11*l* reflections ($k = 3n$). At the same time, the polytypes belonging to different groups *A* and *D* but having the same displacements of adjacent layers, $1T$ (0,0…) and $2H_1$ (0,0…), $2T$ (+−…) and $2H_2$ (+−…), and $3R$ (+)$_3$ and $6R$ (+)$_6$, are not distinguished by the 02*l* and 11*l* reflections (in the patterns of polycrystals and single crystals). The reason is that the layers with the orientations 3 and 6 have identical projections onto the planes perpendicular to the *a* axis and two other axes directed at angles of 120° to the *a* axis. This circumstance was used, in particular, in the identification of the $2H_1$ lizardite polytype mixed with the $1T$ polytype: the intensities of the reflections on the first ellipse were anomalously increased in comparison with the intensities of the reflections on the second ellipse in the electron diffraction patterns, which could not be explained by considering the sample a mixture of the $1T$ and *D* structures [18].

As applied to complex serpentine polytypes, the noted features of the projections of the structures of these minerals mean that ordered simple and complex polytypes differing in the orientation of layers and their number per repetition period but having the same displacements of the initial adjacent layers also cannot be distinguished by the 02*l* and 11*l* reflections. For example, it is possible theoretically that there exist ordered complex six-layer structures with alternation of layers of the 336366 type and interlayer displacements of the origins of coordinates of adjacent layers as in the $1T$(000…) or $3R$(+++…) structures, which are denoted (in the notation of [1, 2]) as $3_3 6_3 6_6 3_6 3_3 6_6$ or $3_1 6_1 6_2 3_2 3_1 6_2$, respectively. The intensities of the 02*l* and 11*l* reflections of these complex polytypes are the same as those of the simple $1T$ and $3R$ polytypes.

From the four structural groups of serpentine minerals, the polytypes of groups *A* and *D* are energetically most favorable and most widespread. For these polytypes, in contrast to the structures of groups *B* and *C*, neighboring octahedral and tetrahedral cations of adjacent layers do not overlap each other in the projection onto the *ab* plane [1, 2]. Note that octahedral cations of adjacent layers coincide in the projection onto the *ab* plane in structures of group *A*. In the case of statistical distribution of octahedral cations, the single-layer $1T$ polytype, which is most widespread for lizardites, turns out to be energetically most favorable in group *A*. When divalent Mg cations are substituted with trivalent Al and

Fe^{3+} cations in the lizardite structure, ordering in the distribution of cations of different valence in octahedral positions with a decrease in the structural symmetry may occur, which leads to dominant localization of positive charges in Al and Fe^{3+} octahedra. In this case, sources of positive charges in octahedral sheets of adjacent layers in structure $1T$ overlap in the projection onto the *ab* plane. Obviously, this is the reason why ordering of octahedral cations is not observed in $1T$ lizardite polytypes [19, 20]. Ordering of octahedral cations in the $2H$ and $3R$ structures (characterized by the displacement of adjacent layers by ±*b*/3) is accompanied by more uniform spatial distribution of sources of positive charges in the octahedral sheets of adjacent layers, which facilitates their structural stabilization. This possibly facilitated the formation of the $3R$ structure of lizardite in kimberlites. In this context, we should note the fact of identification of the rare $2H$ polytype in Cr-enriched lizardite [13].

CONCLUSIONS

Thus, for the first time in the practice of electron diffraction studies of serpentine minerals, the presence of two complex orthogonal polytypes in a mixture with two simple lizardite polytypes ($1T$ and $3R$) is established. Obviously, the formation of lizardite with an unusual polytype composition in one of the interlayers of the Catoca kimberlite pipe is related to the specific features of its chemical composition, which is determined by the processes accompanying the serpentization of the protomineral—olivine.

ACKNOWLEDGMENTS

REFERENCES

1. B. B. Zvyagin, K. S. Mishchenko, and V. A. Shitov, Kristallografiya **10** (5), 635 (1965) [Sov. Phys. Crystallogr. **10**, 539 (1965)].

2. B. B. Zvyagin, Izv. Akad. Nauk SSSR, Ser. Geol., No. 11, 106 (1981).

3. S. W. Bailey, Clays Clay Miner. **17**, 355 (1969).

4. S. W. Bailey and J. F. Banfield, Am. Mineral. **80**, 1104 (1995).

5. I. C. Jahanbagloo and N. Zoltai, Am. Mineral. **53**, 14 (1968).

6. R. Stedman and P. M. Nuttal, Acta Crystallogr. **15**, 510 (1962).

7. C. S. Anderson and S. W. Bailey, Am. Mineral. **66**, 185 (1981).

8. A. Wiewiora, J. A. Raysell-Colom, and T. Garsia-Gonzalez, Am. Mineral. **76**, 647 (1991).

9. H. Zheng and S. W. Bailey, Clays Clay Miner. **45** (3), 301 (1997).

10. R. Stedman and P. M. Nuttal, Acta Crystallogr. **16**, 1 (1963).

11. R. Stedman and P. M. Nuttal, Acta Crystallogr. **17**, 404 (1964).

12. S. Hall, S. Guggenheim, P. Moor, and S. W. Bailey, Can. Mineral. **14**, 314 (1976).

13. J. F. Banfield, S. W. Bailey, and W. W. Barker, Am. Mineral. **80**, 1116 (1995).

14. N. N. Zinchuk, S. F. Nosyko, V. B. Vasilenko, and A. Ya. Rotman, in *Problems of Prognosis, Search, and Study of Minerals at the Threshold of the XXI Century* (Voron. Gos. Univ., Voronezh, 2003), p. 70 [in Russian].

15. S. F. Nosyko and A. Ya. Rotman, in *Problems of Prognosis, Search, and Study of Minerals at the Threshold of the XXI Century* (Voron. Gos. Univ., Voronezh, 2003), p. 102 [in Russian].

16. S. W. Bailey, Rev. Mineral. **19**, 169 (1988).

17. A. P. Zhukhlistov, M. S. Nikolsky, B. B. Zvyagin, *et al.*, Z. Kristallogr. **219**, 224 (2004).

18. M. A. Litsarev, A. P. Zhukhlistov, and B. B. Zvyagin, Dokl. Akad. Nauk SSSR **277**, 188 (1984).

19. M. Mellini and C. Viti, Am. Mineral. **79**, 1194 (1994).

20. A. P. Zhukhlistov and B. B. Zvyagin, Kristallografiya **43** (6), 1009 (1998) [Crystallogr. Rep. **43**, 950 (1998)].

Translated by Yu. Sin'kov

STRUCTURE
OF ORGANIC COMPOUNDS

Crystal Structure and Vibrational Spectra of *N,N'*-Di(2,4-Dinitrophenyl)diaza-18-Crown-6 and *N,N'*-Di(tetrafluoropyridyl)diaza-18-Crown-6

L. Kh. Minacheva*, I. S. Ivanova*, E. N. Pyatova*, V. S. Sergienko*, G. A. Artamkina**, I. P. Beletskaya**, and A. Yu. Tsivadze*

* Kurnakov Institute of General and Inorganic Chemistry, Russian Academy of Sciences,
Leninskiĭ pr. 31, Moscow, 119991 Russia
** Moscow State University, Vorob'evy gory, Moscow, 119992 Russia

Received March 22, 2004

Abstract—Two new diaza-18-crown-6 derivatives, namely, *N,N'*-di(2,4-dinitrophenyl)diaza-18-crown-6 (**I**) and *N,N'*-di(tetrafluoropyridyl)diaza-18-crown-6 (**II**), are studied using X-ray diffraction. The vibrational spectra of these compounds are measured and analyzed. Crystals **I** are monoclinic, $a = 9.746(2)$ Å, $b = 12.117(4)$ Å, $c = 11.378(6)$ Å, $\beta = 98.90(3)°$, $V = 1327.5(4)$ Å^3, $Z = 2$, space group $P2_1/c$, and $R = 0.055$ for 1013 reflections with $I > 2\sigma(I)$. Crystals **II** are orthorhombic, $a = 8.225(4)$ Å, $b = 11.816(4)$ Å, $c = 24.626(5)$ Å, $V = 2393.3(9)$ Å^3, $Z = 4$, space group *Pbca*, and $R = 0.035$ for 451 reflections with $I > 2\sigma(I)$. Molecules **I** and **II** have a centrosymmetric structure and different conformations. It is demonstrated that the shape and size of the cavity and the conformation of the macrocycle depend substantially on the structure of the substituents at the nitrogen atoms of diaza-18-crown-6. © 2004 MAIK "Nauka/Interperiodica".

INTRODUCTION

This work is a continuation of systematic investigations into the structure and complexing properties of aza crown ethers and their derivatives. We performed the X-ray diffraction analysis of two new diaza-18-crown-6 derivatives, namely, *N,N'*-di(2,4-dinitrophenyl)diaza-18-crown-6 $N_6O_{12}C_{24}H_{30}$ (**I**) and *N,N'*-di(tetrafluoropyridyl)diaza-18-crown-6 $N_4O_4F_8C_{22}H_{24}$ (**II**), and studied their vibrational spectra.

EXPERIMENTAL

Compounds **I** and **II** were synthesized through the arylation of diaza-18-crown-6 ether with 2,4-dinitrofluorobenzene and pentafluoropyridine, respectively.

The experimental X-ray diffraction data for faceted crystals **I** and **II** were collected on an Enraf–Nonius CAD4 four-circle automated diffractometer (MoK_α radiation, $\lambda = 0.71073$ Å, graphite monochromator, $2\theta/\omega$ scan mode) at room temperature. No absorption correction was introduced.

Structures **I** and **II** were solved by direct methods (SHELXS86 [1]) and refined according to the full-matrix least-squares procedure on F^2 (SHELXL97 [2]). The positions of the hydrogen atoms were calculated from geometric considerations and refined within a riding-atom model ($U_H = 1.2U_J$ for the C atom bonded to the refined H atom).

The main crystal data, data collection, and refinement parameters for structures **I** and **II** are presented in

Table 1. The atomic coordinates and thermal parameters are listed in Table 2. The interatomic distances and bond angles are given in Table 3.

The IR absorption spectra (400–4000 cm^{-1}) were recorded on a Nicolet Nexus FTIR Fourier spectrometer. The samples were prepared as Nujol or hexachlorobutadiene mulls.

RESULTS AND DISCUSSION

The structural units in crystals **I** (Fig. 1) and **II** (Fig. 2) are individual centrosymmetric molecules.

The presence of different substituents at nitrogen atoms of the diaza-18-crown-6 ether, namely, dinitrophenyl in molecule **I** and tetrafluoropyridyl in molecule **II**, determines the difference between the structures of these compounds. The angles between the midplane of the crown ether macrocycle (the mean deviation Δ of the atoms is equal to 0.38 Å in molecule **I** and 0.22 Å in molecule **II**) and the planes of dinitro-substituted benzene in molecule **I** ($\Delta = 0.024$ Å) and tetrafluoro-substituted pyridine in molecule **II** ($\Delta = 0.033$ Å) are equal to 74.2° and 28.4°, respectively. The same angle in the structure of the related compound *N,N'*-di(perfluorotolyl)diaza-18-crown-6 (**III**) [3] is equal to 93.4°. The nitrogen atoms deviate from the plane passing through four O atoms of the macrocycle by ±0.878 Å in molecule **I**, ±0.337 Å in molecule **II**, and ±1.18 Å in molecule **III**. Therefore, the volume of the substituents at the nitrogen atoms of the diaza-18-crown-6 ether substantially affects the position of the benzene ring

Table 1. Crystal data, data collection, and refinement parameters for structures **I** and **II**

Parameter	I	II
Empirical formula	$C_{24}H_{30}N_6O_{12}$	$C_{22}H_{24}F_8N_4O_4$
M	594.54	560.45
Crystal system	Monoclinic	Orthorhombic
Space group	$P2_1/c$	$Pbca$
Unit cell parameters:		
a, Å	9.746(2)	8.225(4)
b, Å	12.117(4)	11.816(4)
c, Å	11.378(6)	24.626(5)
β, deg	98.90(3)	90
V, Å^3	1327.5(4)	2393.3(9)
Z	2	4
ρ_{calcd}, g/cm^3	1.487	1.555
μ_{Mo}, mm^{-1}	0.121	0.148
$F(000)$	624	1152
Color	yellow-brown	colorless
Crystal size, mm	$0.14 \times 0.25 \times 0.63$	$0.39 \times 0.42 \times 0.5$
θ range, deg	2.11 – 24.97	1.65 – 25.96
Index range	$-1 \le h \le 11, 0 \le k \le 14, -13 \le l \le 13$	$-1 \le h \le 10, 0 \le k \le 14, 0 \le l \le 30$
Number of reflections measured	2177	2666
Number of unique reflections	1853 [$R_{int} = 0.0292$]	2332 [$R_{int} = 0.2312$]
Number of reflections with $I > 2\sigma(I)$)	1013	413
Number of parameters refined	190	172
$GOOF$ on F^2	0.994	0.849
R_1, wR_2 ($I > 2\sigma(I)$)	0.0553, 0.1453	0.0351, 0.0660
R_1, wR_2 (for all reflections)	0.1167, 0.1752	0.3868, 0.1328
$\Delta\rho_{max}$ and $\Delta\rho_{min}$, eÅ^{-3}	0.325 and -0.248	0.183 and -0.211

with respect to the macrocycle plane and the deviation of the nitrogen atoms from the plane of four O atoms in the macrocycle.

The substituted diaza-18-crown-6 adopts different conformations in molecules **I** and **II**. All eight torsion angles around the C–O bonds in structure **II** are characterized by the most favorable *trans* conformation. In structure **I**, four bonds have a *trans* conformation and four bonds exhibit a *gauche* conformation. In both compounds, among six C–C bonds, four bonds have a *gauche* conformation and two bonds are characterized by a *trans* conformation. The *gauche* conformation is observed for two N–C bonds in molecule **II**. In structure **I**, one such bond has a *gauche* conformation and another bond exhibits an intermediate *S* conformation. The torsion angles in structures **I–III** are presented in Table 4. According to the torsion angles, the conformational formulas of the macrocycles in compounds **I–III**

and free diaza-18-crown-6 (**IV**) [4] are as follows:[1]

$$G_-GT_N\ G_+GT_O\ G_+TS_N\ G_-GT_N\ G_+GT_O\ G_+TS_N \text{ for } \mathbf{I},$$

$$GTT_{-N}\ T_-GT_{-O}\ TG_+G_{+N}\ GTT_{-N}\ T_-GT_{-O}\ TG_+G_{+N} \text{ for } \mathbf{II},$$

$$T_-TT_{-N}\ T_-GT_O\ T_-GG_{+N}\ T_-TT_{-N}\ T_-GT_O\ T_-GG_{+N} \text{ for } \mathbf{III},$$

$$TGT_N\ TG_+T_O\ TGT_N\ TGT_N\ TG_+T_O\ TGT_N \text{ for } \mathbf{IV}.$$

The conformation of the substituted diaza-18-crown-6 in compounds **I–III** differs from that of free diaza-18-crown-6. In the latter compound, both N–H bonds are directed inside the macrocycle; as a result, it takes a more symmetric conformation (symmetry C_{2h}). The replacement of the proton of the amino group in free diaza-18-crown-6 leads to a change in the orientation of the corresponding N–C bonds, and they are directed outward in structures **I–III**. Symmetry of the

---

[1] The subscripts N and O indicate the NCCO fragment containing the nitrogen atom and the OCCO fragment involving only the oxygen atoms, respectively.

Table 2. Atomic coordinates and thermal parameters U_{eq} for structures **I** and **II**

Atom	x	y	z	U_{eq}, Å^2
		I		
N(1)	0.0867(3)	−0.2320(3)	−0.0784(3)	0.0471(9)
N(2)	0.4827(4)	−0.5061(3)	0.1884(3)	0.0531(9)
N(3)	0.1392(4)	−0.4617(3)	−0.1605(3)	0.063(1)
O(1)	−0.1788(3)	−0.2350(3)	0.0083(3)	0.0677(9)
O(2)	−0.2212(3)	−0.0413(2)	0.1514(2)	0.0588(8)
O(3)	0.5646(4)	−0.4635(3)	0.2679(3)	0.081(1)
O(4)	0.4803(3)	−0.6059(3)	0.1687(3)	0.071(1)
O(5)	0.0940(5)	−0.5538(3)	−0.1561(3)	0.121(2)
C(6)	0.1403(4)	−0.4091(3)	−0.2515(3)	0.083(1)
C(1)	−0.0444(4)	−0.2763(4)	−0.1439(4)	0.057(1)
C(2)	−0.1737(5)	−0.2253(4)	−0.1116(4)	0.069(1)
C(3)	−0.3038(5)	−0.1994(4)	0.0413(4)	0.060(1)
C(4)	−0.3198(5)	−0.0810(4)	0.0562(4)	0.062(1)
C(5)	−0.2057(5)	0.0749(3)	0.1520(3)	0.053(1)
O(6)	−0.1019(5)	0.1125(3)	0.0740(3)	0.051(1)
C(7)	0.1906(4)	−0.2973(3)	−0.0236(3)	0.0399(9)
C(8)	0.2913(4)	−0.2556(3)	0.0693(3)	0.046(1)
C(9)	0.3857(4)	−0.3222(3)	0.1358(3)	0.045(1)
C(10)	0.3857(4)	−0.4348(3)	0.1149(3)	0.0416(9)
C(11)	0.2959(4)	−0.4791(3)	0.0214(3)	0.044(1)
C(12)	0.2049(4)	−0.4109(3)	−0.0476(3)	0.0411(9)
		II		
F(1)	0.0693(5)	0.2657(3)	0.2698(1)	0.059(1)
F(2)	0.0304(5)	0.3014(2)	0.1651(1)	0.072(1)
F(3)	−0.2968(5)	0.6011(3)	0.1925(1)	0.070(1)
F(4)	−0.2818(5)	0.5794(3)	0.2987(1)	0.063(1)
O(1)	−0.2123(5)	0.6063(3)	0.4543(1)	0.057(1)
O(2)	−0.1214(6)	0.6784(3)	0.5593(2)	0.057(1)
N(1)	−0.0887(6)	0.4074(3)	0.3470(2)	0.046(1)
N(2)	−0.1320(7)	0.4521(5)	0.1772(2)	0.053(2)
C(1)	−0.0886(8)	0.5036(5)	0.3848(2)	0.050(2)
C(2)	−0.2345(8)	0.5099(5)	0.4211(2)	0.060(2)
C(3)	−0.3187(8)	0.6095(5)	0.4985(2)	0.064(2)
C(4)	−0.2737(9)	0.7027(5)	0.5361(2)	0.065(2)
C(5)	−0.0898(8)	0.7376(5)	0.6076(2)	0.049(2)
C(6)	0.0735(8)	0.7058(4)	0.6287(2)	0.050(2)
C(7)	−0.1034(7)	0.4221(5)	0.2929(3)	0.038(2)
C(8)	−0.294(8)	0.3510(4)	0.2541(3)	0.042(2)
C(9)	−0.0473(8)	0.3700(5)	0.1999(3)	0.048(2)
C(10)	−0.2037(9)	0.5192(6)	0.2126(3)	0.051(2)
C(11)	−0.1943(8)	0.5082(5)	0.2677(3)	0.043(2)

Table 3. Selected bond lengths (d) and bond angles (ω) in structures **I** and **II***

Bond	d, Å	Bond	d, Å
		I	
N(1)–C(7)	1.359(5)	N(1)–C(6')	1.457(5)
N(1)–C(1)	1.476(5)	N(2)–O(3)	1.224(4)
N(2)–O(4)	1.229(4)	N(2)–C(10)	1.447(5)
N(3)–O(5)	1.204(5)	N(3)–O(6)	1.217(4)
N(3)–C(12)	1.479(5)	O(1)–C(2)	1.378(5)
O(1)–C(3)	1.397(5)	O(2)–C(4)	1.415(5)
O(2)–C(5)	1.416(4)	C(1)–C(2)	1.500(6)
C(3)–C(4)	1.457(6)	C(5)–C(6)	1.515(6)
C(7)–C(12)	1.414(5)	C(7)–C(8)	1.419(5)
C(8)–C(9)	1.362(5)	C(9)–C(10)	1.386(5)
C(10)–C(11)	1.377(5)	C(11)–C(12)	1.367(5)

Angle	ω, deg	Angle	ω, deg
C(7)N(1)C(6')	119.9(3)	C(7)N(1)C(1)	123.1(3)
C(6')N(1)C(1)	117.0(3)	O(3)N(2)O(4)	122.8(4)
O(3)N(2)C(10)	117.9(4)	O(4)N(2)C(10)	119.3(3)
O(5)N(3)O(6)	124.9(4)	O(5)N(3)C(12)	117.5(4)
O(6)N(3)C(12)	117.5(4)	C(2)O(1)C(3)	113.9(3)
C(4)O(2)C(5)	113.6(3)	N(1)C(1)C(2)	114.9(3)
O(1)C(2)C(1)	111.6(4)	O(1)C(3)C(4)	116.7(4)
O(2)C(4)C(3)	110.6(4)	O(2)C(5)C(6)	112.1(3)
N(1')C(6)C(5)	110.6(3)	N(1)C(7)C(12)	124.5(3)
N(1)C(7)C(8)	121.0(3)	C(12)C(7)C(8)	114.4(3)
C(9)C(8)C(7)	122.2(3)	C(8)C(9)C(10)	120.4(3)
C(11)C(10)C(9)	120.0(3)	C(11)C(10)N(2)	119.6(3)
C(9)C(10)N(2)	120.4(3)	C(12)C(11)C(10)	119.1(3)
C(11)C(12)C(7)	123.5(3)	C(11)C(12)N(3)	113.7(3)
C(7)C(12)N(3)	122.1(3)		

Bond	d, Å	Bond	d, Å
		II	
F(1)–C(8)	1.352(6)	F(2)–C(9)	1.341(6)
F(3)–C(10)	1.330(7)	F(4)–C(11)	1.344(6)
O(1)–C(3)	1.397(5)	O(1)–C(2)	1.413(6)
O(2)–C(5)	1.404(5)	O(2)–C(4)	1.407(7)
N(1)–C(7)	1.350(6)	N(1)–C(1)	1.469(5)
N(1)–C(6')	1.471(6)	N(2)–C(9)	1.319(7)
N(2)–C(10)	1.317(7)	C(1)–C(2)	1.500(7)
C(3)–C(4)	1.485(7)	C(5)–C(6)	1.489(7)
C(7)–C(11)	1.406(7)	C(7)–C(8)	1.410(7)
C(8)–C(9)	1.361(8)	C(10)–C(11)	1.366(7)

Angle	ω, deg	Angle	ω, deg
C(3)O(1)C(2)	113.0(5)	C(5)O(2)C(4)	114.0(5)
C(7)N(1)C(1)	121.7(4)	C(7)N(1)C(6')	121.7(4)
C(1)N(1)C(6')	116.6(4)	C(9)N(2)C(10)	113.5(6)
N(1)C(1)C(2)	114.6(5)	O(1)C(2)C(1)	106.3(5)
O(1)C(3)C(4)	110.5(5)	O(2)C(4)C(3)	108.9(5)
O(2)C(5)C(6)	109.8(5)	N(1')C(6)C(5)	116.6(5)
N(1)C(7)C(11)	125.1(6)	N(1)C(7)C(8)	123.6(6)
C(11)C(7)C(8)	111.2(6)	F(1)C(8)C(9)	118.0(6)
F(1)C(8)C(7)	120.6(6)	C(9)C(8)C(7)	121.3(6)
N(2)C(9)F(2)	115.2(7)	N(2)C(9)C(8)	126.4(6)
F(2)C(9)C(8)	118.4(6)	N(2)C(10)F(3)	116.7(6)
N(2)C(10)C(11)	125.1(7)	F(3)C(10)C(11)	118.1(7)
F(4)C(11)C(10)	118.3(7)	F(4)C(11)C(7)	119.2(5)
C(10)C(11)C(7)	122.4(6)		

* In Tables 3 and 4, the primed atoms N(1') and C(6') are related to the initial atoms through the inversion center (symmetry operations: $-x$, $-y$, $-z$ for **I** and $-x$, $-y + 1$, $-z + 1$ for **II**).
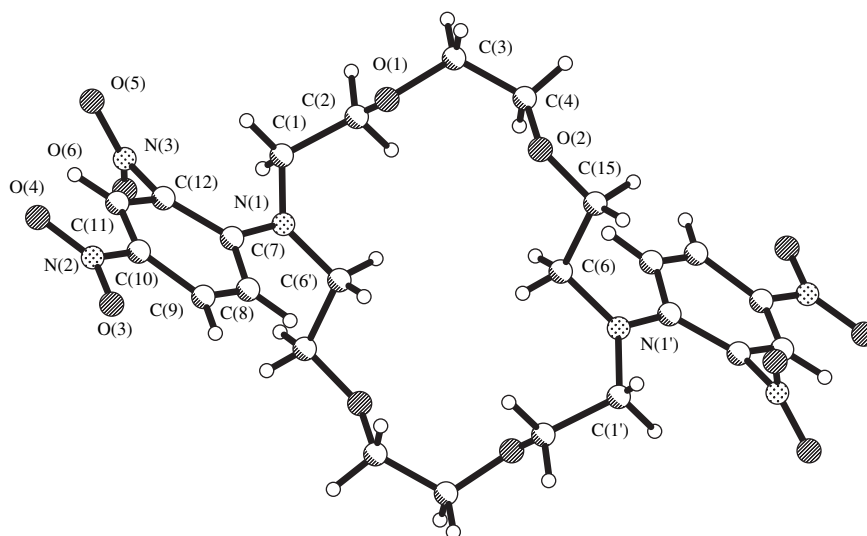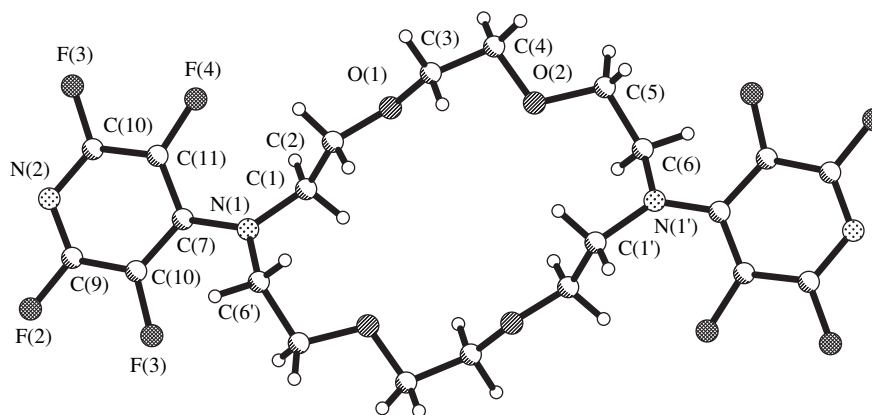
Fig. 1. Structure of molecule **I**.

Fig. 2. Structure of molecule **II**.

substituted diaza-18-crown-6 macrocycle is reduced to C_i.

The presence of the substituents in the diaza-18-crown-6 in compounds **I** and **II** also results in a change in the shape and size of the interior cavity of the macrocycle. In the heterocycle of free diaza-18-crown-6, the distances between the like donor atoms are close to each other: O···O, 5.61, 5.67 Å; N···N, 5.84 Å. The corresponding distances are equal to 6.69, 6.01, and 6.21 Å in molecule **I**; 4.86, 5.50, and 7.98 Å in molecule **II**; and 4.64, 6.67, and 6.90 Å in molecule **III**.

The mean geometric parameters of molecules **I** and **II** are close to each other. The bond lengths have the following values: C–O, 1.402(5) and 1.405(6) Å; C(sp^3)–N, 1.467(5) and 1.470(6) Å; C(sp^2)–N, 1.359(5) and 1.350(6) Å; C–C, 1.491(6) and 1.491(7) Å in the macrocycle and 1.388(5) and 1.386(7) Å in the benzene ring, respectively. The bond angles in the macrocycle are as follows: CCO, 112.8(4)° and 108.9(5)°; COC,

113.8(3)° and 113.5(5)°; CNC, 117.0(3)° and 116.6(4)°; and NCC, 112.8(3)° and 115.6(5)°, respectively.

Table 4. Torsion angles (τ) in structures **I**, **II**, and **III**

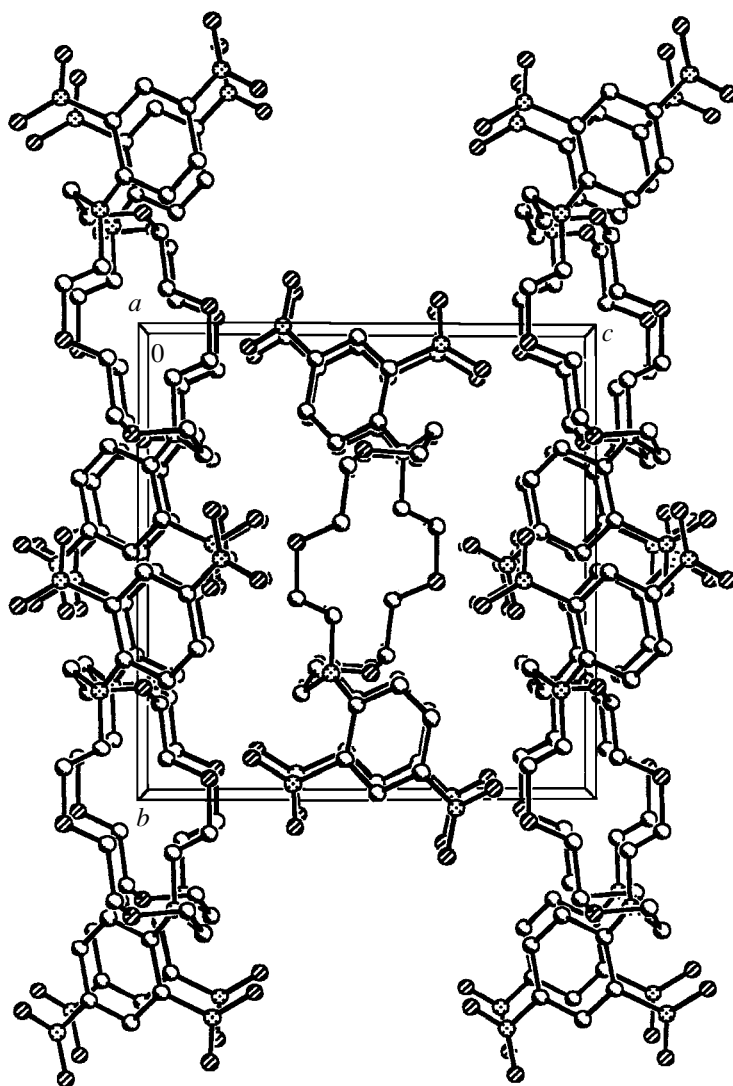| Angle	τ, deg		
	I	**II**	**III**
C(6')N(1)C(1)C(2)	−49.6	−67.2	158.4
N(1)C(2)C(2)O(1)	−56.5	179.6	−175.6
C(1)C(2)O(1)C(3)	−173.5	−166.3	168.9
C(2)O(1)C(3)C(4)	−80.9	171.6	−167.8
O(1)C(3)C(4)O(2)	−64.1	−66.1	69.4
C(3)C(4)O(2)C(5)	164.4	−159.9	−178.1
C(4)O(2)C(5)C(6)	−85.9	180.0	159.6
O(2)C(5)C(6)N(1')	−179.0	−73.1	−66.8
C(5)C(6)N(1')C(1')	107.9	73.5	80.0

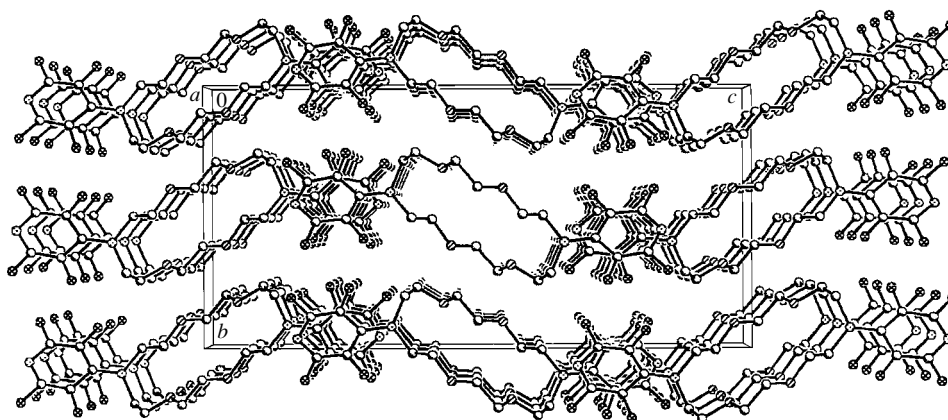**Fig. 3.** Packing of molecules in structure **I**.

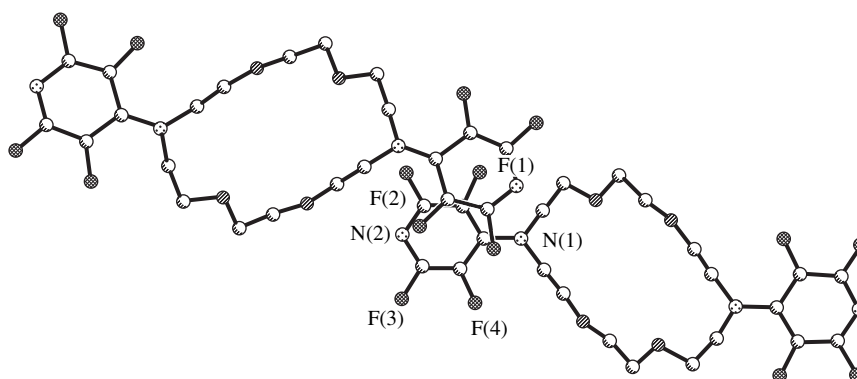**Fig. 4.** Packing of molecules in structure **II**.

Fig. 5. Superposition of the tetrafluoropyridyl rings of adjacent columns in structure **II**.

In molecule **I**, the nitro groups are rotated differently with respect to the benzene ring. The N(2)O(3)O(4) group and the benzene ring are nearly coplanar (the angle between their planes is 2.5°). The N(3)O(5)O(6) group is rotated through 66.2° with respect to the plane of the benzene ring. The dihedral angle between the planes of the NO$_2$ groups is equal to 44.7°. The mean parameters of the NO$_2$ groups are close to the standard parameters: N–O, 1.219(4) Å; and angle ONO, 123.9(4)°.

In structure **II**, the fluorine atoms lie virtually in the plane of the pyridine ring [the maximum deviation of the F(4) atom is equal to 0.08 Å]. The mean length of the C–F bond is equal to 1.342(6) Å in molecule **II** and 1.343(5) Å in molecule **III**.

The molecular packing in crystal **I** is similar to that in crystal **III** (Fig. 3). The translationally related molecules form columns parallel to the *a* axis, along which the unit cell parameters in all structures **I**–**III** are smallest, and are arranged in a face-centered manner. In crystal **II**, molecular columns are also formed along the *a* axis (Fig. 4). The columns are in contact through the fluorine-substituted pyridine rings. These rings are almost parallel to each other (the dihedral angle between their planes is 1°). The distance between the rings is equal to 3.22 Å. Although the rings do not overlap, a number of fluorine atoms appear to be above the ring plane. This suggests that they can interact with each other (Fig. 5).

The vibrational spectra of compounds **I** and **II** were interpreted by comparison with the IR absorption spectra of free diaza-18-crown-6, NiBr$_2$ · diaza-18-crown-6 [5, 6], and compound **III** [3]. The data obtained in [7, 8] were used to assign vibrations of the tetrafluoropyridyl and 2,4-dinitrophenyl groups. The assignment of the vibrational frequencies is presented in Table 5.

In the IR absorption spectra of compounds **I** and **II**, the stretching vibrations of the C–H bonds manifest themselves in the frequency range 2800–3100 cm^{-1}. In the IR spectrum of compound **I**, the low-intensity band with a maximum at a frequency of 3064 cm^{-1} is associated with the $\nu(CH)_{Ph}$ vibrations of the substituted benzene rings. The medium-intensity bands at 2954, 2915, and 2864 cm^{-1} are assigned to the $\nu(CH_2)$ vibrations of the methylene groups. The $\nu(CH_2)$ vibrations in the IR spectrum of compound **II** manifest themselves in the form of an intense complex band with a maximum at 2894 cm^{-1}.

The bands of the $\nu(CC)_{Ph}$ stretching vibrations of the substituted benzene rings are observed at 1601, 1571, and 1523 cm^{-1} for compound **I** and at 1644 and 1537 cm^{-1} for compound **II**.

The $\nu_{as}(NO_2)$ stretching vibrations of the nitro groups manifest themselves in the same spectral range (most likely, at 1506 cm^{-1}).

In the range of 1300 cm^{-1}, the IR spectrum of compound **I** contains a broad band with maxima at 1330, 1312, and 1301 cm^{-1}. According to [8, 9], the bands in this range are associated with the $\nu(Ph-NO_2)$ and $\nu_s(NO_2)$ stretching vibrations.

Compared to the spectrum of the diaza-18-crown-6 ether, the spectra of compounds **I** and **II** contain a new band at 1188 cm^{-1}. In our opinion, this band is attributed to the $\nu_{as}(Ph-N_{c.e.})$ stretching vibrations.

In our earlier work [3], we assigned the fundamental frequencies in the spectrum of compound **III**. The new data obtained in the present work on the spectra of the substituted diaza-18-crown-6 derivatives allow us to correct the previously proposed assignment. In particular, the intense asymmetric band at 1187 cm^{-1} in the IR spectrum of compound **III** was assigned to the $\nu(CF_3)$ stretching vibrations. Molecules **I** and **II** do not contain CF$_3$ groups; however, a similar band is observed in the spectra of these compounds. Consequently, the band at 1187 cm^{-1} in the IR spectrum of compound **III** has a different origin.

A comparison of the spectra of compounds **I**–**IV** allows us to make the inference that the band at ~1200 cm^{-1} is associated with the stretching vibrations of the *Ph*–N$_{c.e.}$ bond, which is observed in all three mol-

Table 5. Vibrational frequencies (cm^{-1}) in IR spectra of molecules **I** and **II** and their assignment

Assignment	I	Assignment	II
$\nu(CH)_{Ph}$	3064		
$\nu(CH_2)$	2954	$\nu(CH_2)$	2963
	2915		2894
	2864		2816
$\nu(CC)_{Ph}$,	1601	$\nu(CC)_{Py}$, $\nu(CN)_{Py}$	1644
$\nu_{as}(NO_2)$	1571		1537
	1523		
	1506		
$\delta(CH_2)$	1487	$\delta(CH_2)$	1484
	1472		1464
	1463		1449
	1443		1391
	1425		
$\omega(CH_2)$	1389	$\omega(CH_2)$	1373s
	1361		1351s
$\nu_s(NO_2)$,	1330		1292s
$\nu(Ph\text{-}NO_2)$	1312		
	1301		
$\tau(CH_2)$	1270	$\tau(CH_2)$	1242
	1247		
	1236		
$\nu(Ph\text{-}N_{c.e.})$	1188	$\nu(Py\text{-}N_{c.e.})$	1188
$\nu_{as}(CNC)$	1143	$\nu_{as}(CNC)$	1141
$\nu_{as}(COC)$	1124	$\nu_{as}(COC)$	1130
	1099		1112
$\nu(CC)_{c.e.}$	1068	$\nu(CC)_{c.e.}$	1082
$\delta(CH)_{Ph}$	1057	$\nu(CN)_{c.e.}$	1069
	1036		1039
	1022		
$\nu_s(COC)$	996	$\nu_s(COC)_{c.e.}$	982
$\nu_s(CNC)$	932	$\nu_s(CF)$	952
	915	$\nu_s(CNC)_{c.e.}$	934
$\delta(NO_2)$	850		
$\rho(CH_2) + \nu(CO) +$	827	$\rho(CH_2) + \nu(CO) +$	883
$\nu(CN) + \nu(CC)$	816	$\nu(CH) + \nu(CC)$	838
			795
$\delta(CC)_{Ph}^{np}$	784	other vibrations	738
	768		724
	757		666
	744		639
	721		601
other vibrations	661		560
	643		535
	607		407
	554		
	533		
	523		
	478		
	453		

ecules **I**–**III**. The molecule of free diaza-18-crown-6 does not contain such a bond, and a similar band is absent in the spectrum of this ether. Most likely, the bands of the $\nu_{as}(CF_3)$ and $\nu_{as}(Ph\text{–}N_{c.e.})$ vibrations overlap in the IR spectrum of compound **III**. Therefore, the band at 1331 cm^{-1} in the spectrum of compound **III**, which was previously assigned to the $\nu(Ph\text{–}N_{c.e.})$ vibrations, can be attributed to the $\omega(CH_2)$ bending vibrations of the methylene groups.

According to Desreux *et al.* [10], the bands of the $\nu(CNC)$ and $\nu(COC)$ bending vibrations of the NCCO and OCCO fragments are observed in the range 1000–1170 cm^{-1}. In this frequency range, the IR spectra contain three intense bands with maxima at 1143, 1124, and 1099 for compound **I** and at 1141, 1130, and 1112 cm^{-1} for compound **II**. As follows from our previous work [6], the bands at 1143 cm^{-1} for compound **I** and at 1141 cm^{-1} for compound **II** can be assigned to the $\nu_{as}(CNC)$ vibrations and the bands at 1124 and 1099 cm^{-1} for compound **I** and at 1130 and 1112 cm^{-1} for compound **II** can be attributed to the $\nu_{as}(COC)$ vibrations. In the IR spectrum of compound **III**, the intense band at 1142 cm^{-1}, which is associated with the stretching vibrations of the C–F bonds, apparently overlaps the band of the $\nu_{as}(CNC)$ vibrations.

The stretching–bending vibrations of the OCCO and NCCO fragments manifest themselves in the frequency range 800–1000 cm^{-1}. The bands observed at frequencies of 932 and 816 cm^{-1} for compound **I** and at 934 and 795 cm^{-1} for compound **II** are assigned to the stretching–bending vibrations of the NCCO fragment with the GGT_N conformation. This fragment is involved in both macrocycles. The bands at frequencies of 929 and 815 cm^{-1} in the IR spectrum of compound **III** can be attributed to the vibrations of the fragment with the same conformation. The difference between these frequencies in the IR spectra of compounds **I**–**III** can be explained in terms of different deviations of the torsion angles from the ideal value.

According to Kireeva *et al.* [5], the bands observed at 982 and 838 cm^{-1} in the IR spectrum of compound **II** (985 and 836, 828 cm^{-1} for **III** and 980 and 845, 835 cm^{-1} for **IV**) correspond to the vibrations of the OCCO fragment with the TGT_O conformation. Therefore, in the IR absorption spectrum of compound **I**, the band observed at 996 cm^{-1}, which is absent in the spectra of macrocycles **II**–**IV**, can be attributed to the fragment with the GTS_N conformation. This fragment is absent in the above ligands. It is quite possible that the intense band at 883 cm^{-1} in the IR absorption spectrum of compound **II** is associated with the NCCO fragment with the GTT_N conformation.

Structure **I** involves the OCCO fragment with the GGT_O conformation. A similar fragment is contained in the diaza-18-crown-6 macrocycle of the NiBr$_2 \cdot$ diaza-18-crown-6 complex [6]. Therefore, the bands

observed at frequencies of 932 and 785 cm^{-1} in the IR absorption spectrum of compound **I** can be assigned to the vibrations of this fragment with the GGT_O conformation.

The crystallographic data for compounds **I** and **II** have been deposited with the Cambridge Structural Database (CCDC nos. 234 069, 234 068).

ACKNOWLEDGMENTS

REFERENCES

1. G. M. Sheldrick, Acta Crystallogr., Sect. A: Found. Crystallogr. **46** (5), 467 (1990).
2. G. M. Sheldrick, *SHELXL97: Program for the Refinement of Crystal Structures* (Univ. of Göttingen, Germany, 1997).
3. L. Kh. Minacheva, I. S. Ivanova, E. N. Pyatova, *et al.*, Dokl. Akad. Nauk **389** (1), 1 (2003).
4. M. Herceg and R. Weiss, Bull. Soc. Chim. Fr., No. 2, 549 (1972).
5. I. K. Kireeva, N. B. Generalova, and A. Yu. Tsivadze, Zh. Neorg. Khim. **41** (5), 776 (1996).
6. L. Kh. Minacheva, N. B. Generalova, I. K. Kireeva, *et al.*, Zh. Neorg. Khim. **38** (10), 1666 (1993).
7. L. M. Sverdlov, M. A. Kovner, and E. P. Kraĭnov, *Vibrational Spectra of Polyatomic Molecules* (Nauka, Moscow, 1970; Wiley, New York, 1974).
8. L. J. Bellamy, *The Infra-Red Spectra of Complex Molecules,* 2nd ed. (Barnes and Noble, New York, 1958; Inostrannaya Literatura, Moscow, 1963).
9. K. Nakanishi, *Infrared Absorption Spectroscopy: Practical* (Holden-Day, San Francisco, 1962; Mir, Moscow, 1965).
10. J. F. Desreux, A. Renard, and G. Duyckaerts, J. Inorg. Nucl. Chem. **39**, 1587 (1977).

Translated by O. Borovik-Romanova

Crystal Structure of Zinc(II) Hydrated Trinuclear Complex with Monoprotonated Ethylenediaminetetraacetate Anion(3⁻), [Zn₃(H*Edta*)₂(H₂O)₆]

G. G. Sadikov*, A. S. Antsyshkina*, V. S. Sergienko*, and A. L. Poznyak**

* Kurnakov Institute of General and Inorganic Chemistry, Russian Academy of Sciences,
Leninskiĭ pr. 31, Moscow, 119991 Russia

e-mail: sadgg@igic.ras.ru

** Institute of Molecular and Atomic Physics, Belarussian Academy of Sciences,
pr. F. Skoriny 70, Minsk, 220072 Belarus

Received April 9, 2003

Abstract—The crystal structure of the $[Zn_3(HEdta)_2(H_2O)_6]$ complex (**I**) is determined by X-ray diffraction analysis. The crystals are orthorhombic, $a = 14.780$ Å, $b = 29.699$ Å, $c = 7.032$ Å, $Z = 4$, and space group $Pna2_1$. The structural units of crystals **I** are trinuclear linear molecules, in which the peripheral atoms $Zn(1)$ and $Zn(2)$ each coordinate two N atoms and three O atoms of the $HEdta^{3-}$ ligand and the $O(w)$ atom of the H_2O molecule, whereas the central $Zn(3)$ atom coordinates four $O(w)$ atoms of the H_2O molecules and two terminal O atoms of the two $HEdta^{3-}$ ligands. The $HEdta^{3-}$ ligand fulfills a hexadentate chelating–bridging function. The bond lengths are as follows: $Zn–O(HEdta)$, 2.006(4)–2.123(4) Å; $Zn–N$, 2.214(6) and 2.128(5) Å; and $Zn–O(w)$, 2.006(6)–2.225(5) Å. In structure **I**, there is a specific contact formed by hydrogen bonds, owing to which the distance between the central atoms of individual molecules appears to be shorter than that in covalently bonded complexes. © 2004 MAIK "Nauka/Interperiodica".

INTRODUCTION

Earlier structural studies of acid salts with monoprotonated ethylenediaminetetraacetate anions revealed that $Me_3(HEdta)_2 \cdot 10H_2O$ compounds have structures of two types, namely, structures with cation–anion units $[Me(H_2O)_6]^{2+}[Me(HEdta)(H_2O)]^-$ ($Me = Mg^{2+}$, Co^{2+}, Ni^{2+}; $Me : HEdta = 2 : 1$) [1, 2] and structures with trinuclear molecular complexes $[Me(HEdta)(H_2O)]_2 \cdot [Me(H_2O)_4]$ ($Me = Mn^{2+}$, Fe^{2+}, Cd^{2+}; $Me : HEdta = 3 : 2$) [2–5]. In trimers, the $Me(H_2O)_4$ centrosymmetric group plays the role of a linking unit, whereas the terminal oxygen atoms of the carboxyl groups in anionic complexes fulfill a bridging function and complete the coordination polyhedron of the central metal atom to an octahedron. This paper reports on the results of X-ray diffraction investigation of $Zn_3(HEdta)_2(H_2O)_6$ (**I**) crystals in which the metal : ligand ratio is 3 : 2.

EXPERIMENTAL

Synthesis. Compound **I** was synthesized from a solution of $ZnCl_2$ and $Na_2(H_2Edta)$. Single crystals suitable for the X-ray diffraction analysis were prepared by recrystallization of compound **I** from an aqueous solution upon slow evaporation at 60°C.

X-ray diffraction analysis. Colorless needle-shaped crystals **I** ($C_{20}H_{37}N_4O_{22}Zn_3$) are orthorhombic, $a = 14.780(5)$ Å, $b = 29.699(9)$ Å, $c = 7.032(6)$ Å, $V = 3086(3)$ Å^3, $M = 881.7$, $F(000) = 1804$, $\rho_{calcd} = 1.897$ g/cm^3, $\mu_{Mo} = 2.414$ mm^{-1}, $Z = 4$, and space group $Pna2_1$. The experimental data were collected on an Enraf–Nonius CAD4 diffractometer (λMoK_α, graphite monochromator, $\theta/2\theta$ scan mode, $2\theta_{max} = 56°$). Structure **I** was solved by direct methods. The hydrogen atoms were located from difference Fourier syntheses. The structure was refined by the least-squares procedure for all 5648 nonzero reflections ($R_{int} = 0.084$; $0 < h < 19$, $0 < k < 39$, $–9 < l < 4$). The non-hydrogen atoms were refined in the anisotropic approximation, and the hydrogen atoms were refined in the isotropic approximation. The final results of the refinement are as follows: $R_1 = 0.0375$ and $wR_2 = 0.0947$ for 4253 reflections with $F_0 \geq 4\sigma(F_0)$, $R_1 = 0.0701$ and $wR_2 = 0.1072$ for all reflections, and $GOOF = 1.105$ (the number of refined parameters was 590). The values of $\Delta\rho_{max}$ and $\Delta\rho_{min}$ are equal to 0.542 and –0.857 e/Å^3, respectively.

All the calculations were performed with the SHELX86 [6] and SHELXL93 [7] program packages. The crystal data have been deposited with the Cambridge Structural Database (no. 213 294). The bond lengths and bond angles are presented in Table 1.

Table 1. Bond lengths d (Å) and angles ω (deg) in compound **I**

| Bond	d, Å	Bond	d, Å	Bond angle	ω	Bond angle	ω
Zn(1)–N(1)	2.162(5)	Zn(1)–N(2)	2.214(6)	O(11)Zn(2)O(2w)	96.7(2)	O(13)Zn(2)O(2w)	93.1(2)
Zn(1)–O(1)	2.069(4)	Zn(1)–O(3)	2.063(4)	O(4)Zn(3)O(12)	100.0(2)	O(4)Zn(3)O(3w)	91.5(2)
Zn(1)–O(5)	2.090(4)	Zn(1)–O(1w)	2.050(4)	O(4)Zn(3)O(4w)	169.8(2)	O(4)Zn(3)O(5w)	93.8(2)
Zn(2)–N(3)	2.172(5)	Zn(2)–N(4)	2.218(5)	O(4)Zn(3)O(6w)	87.4(2)	O(12)Zn(3)O(3w)	88.0(2)
Zn(2)–O(9)	2.060(4)	Zn(2)–O(11)	2.123(4)	O(12)Zn(3)O(4w)	89.5(2)	O(12)Zn(3)O(5w)	165.4(2)
Zn(2)–O(13)	2.100(5)	Zn(2)–O(2w)	2.006(6)	O(12)Zn(3)O(6w)	87.4(2)	O(3w)Zn(3)O(4w)	92.5(2)
Zn(3)–O(4)	2.069(4)	Zn(3)–O(12)	2.080(4)	O(3w)Zn(3)O(5w)	96.3(2)	O(3w)Zn(3)O(6w)	175.0(2)
Zn(3)–O(3w)	2.104(6)	Zn(3)–O(4w)	2.225(5)	O(4w)Zn(3)O(5w)	76.4(2)	O(4w)Zn(3)O(6w)	89.3(2)
Zn(3)–O(5w)	2.069(4)	Zn(3)–O(6w)	2.103(6)	O(5w)Zn(3)O(6w)	88.6(2)	Zn(1)N(1)C(2)	104.6(3)
N(1)–C(2)	1.449(7)	N(1)–C(4)	1.479(7)	Zn(1)N(1)C(4)	107.0(4)	Zn(1)N(1)C(17)	105.2(3)
N(1)–C(17)	1.483(9)	N(2)–C(6)	1.483(8)	C(2)N(1)C(4)	112.9(5)	C(2)N(1)C(17)	114.6(5)
N(2)–C(8)	1.468(7)	N(2)–C(18)	1.498(7)	C(4)N(1)C(17)	111.7(5)	Zn(1)N(2)C(6)	106.9(4)
N(3)–C(10)	1.477(8)	N(3)–C(12)	1.482(7)	Zn(1)N(2)C(8)	109.6(4)	Zn(1)N(2)C(18)	103.8(3)
N(3)–C(19)	1.497(9)	N(4)–C(14)	1.474(8)	C(6)N(2)C(8)	111.6(5)	C(6)N(2)C(18)	111.7(5)
N(4)–C(16)	1.462(8)	N(4)–C(20)	1.493(7)	C(8)N(2)C(18)	112.7(5)	Zn(2)N(3)C(10)	105.1(4)
O(1)–C(1)	1.252(7)	O(2)–C(1)	1.255(7)	Zn(2)N(3)C(12)	106.3(4)	Zn(2)N(3)C(19)	106.0(4)
O(3)–C(3)	1.258(6)	O(4)–C(3)	1.251(6)	C(10)N(3)C(12)	112.3(5)	C(10)N(3)C(19)	113.2(5)
O(5)–C(5)	1.278(8)	O(6)–C(5)	1.244(7)	C(12)N(3)C(19)	113.2(5)	Zn(2)N(4)C(14)	108.2(4)
O(7)–C(7)	1.196(8)	O(8)–C(7)	1.314(7)	Zn(2)N(4)C(16)	107.1(4)	Zn(2)N(4)C(20)	103.2(3)
O(9)–C(9)	1.255(7)	O(10)–C(9)	1.250(7)	C(14)N(4)C(16)	113.9(5)	C(14)N(4)C(20)	111.0(5)
O(11)–C(11)	1.280(8)	O(12)–C(11)	1.262(6)	C(16)N(4)C(20)	112.8(5)	Zn(1)O(1)C(1)	113.1(4)
O(13)–C(13)	1.265(8)	O(14)–C(13)	1.248(8)	Zn(1)O(3)C(3)	116.3(4)	Zn(3)O(4)C(3)	128.9(4)
O(15)–C(15)	1.21(1)	O(16)–C(15)	1.319(8)	Zn(1)O(5)C(5)	115.7(4)	Zn(2)O(9)C(9)	115.6(4)
C(1)–C(2)	1.537(9)	C(3)–C(4)	1.522(8)	Zn(2)O(11)C(11)	111.0(4)	Zn(3)O(12)C(11)	121.9(4)
C(5)–C(6)	1.508(8)	C(7)–C(8)	1.527(9)	Zn(2)O(13)C(13)	118.3(4)	O(1)C(1)O(2)	124.6(5)
C(9)–C(10)	1.513(9)	C(11)–C(12)	1.517(9)	O(1)C(1)C(2)	118.7(5)	O(2)C(1)C(2)	116.6(5)
C(13)–C(14)	1.521(8)	C(15)–C(16)	1.517(9)	N(1)C(2)C(1)	110.9(5)	O(3)C(3)O(4)	125.5(5)
C(17)–C(18)	1.523(8)	C(19)–C(20)	1.536(8)	O(3)C(3)C(4)	118.8(5)	O(4)C(3)C(4)	115.7(5)
Bond angle	**ω**	**Bond angle**	**ω**	N(1)C(4)C(3)	113.6(5)	O(5)C(5)O(6)	123.7(5)
N(1)Zn(1)N(2)	83.8(2)	N(1)Zn(1)O(1)	78.8(2)	O(5)C(5)C(6)	119.4(5)	O(6)C(5)C(6)	116.8(5)
N(1)Zn(1)O(3)	81.4(2)	N(1)Zn(1)O(5)	94.9(2)	N(2)C(6)C(5)	115.6(5)	O(7)C(7)O(8)	124.3(6)
N(1)Zn(1)O(1w)	177.3(2)	N(2)Zn(1)O(1)	158.9(2)	O(7)C(7)C(8)	122.8(5)	O(8)C(7)C(8)	112.9(5)
N(2)Zn(1)O(3)	91.5(2)	N(2)Zn(1)O(5)	80.7(2)	N(2)C(8)C(7)	114.4(5)	O(9)C(9)O(10)	124.6(6)
N(2)Zn(1)O(1w)	96.6(2)	O(1)Zn(1)O(3)	97.5(2)	O(9)C(9)C(10)	118.8(5)	O(10)C(9)C(10)	116.6(5)
O(1)Zn(1)O(5)	89.0(2)	O(1)Zn(1)O(1w)	101.4(2)	N(3)C(10)C(9)	114.1(5)	O(11)C(11)O(12)	124.2(5)
O(3)Zn(1)O(5)	171.7(2)	O(3)Zn(1)O(1w)	95.9(2)	O(11)C(11)C(12)	119.8(5)	O(12)C(11)C(12)	116.0(5)
O(5)Zn(1)O(1w)	87.8(2)	N(3)Zn(2)N(4)	83.9(2)	N(3)C(12)C(11)	110.5(5)	O(13)C(13)O(14)	123.9(6)
N(3)Zn(2)O(9)	81.7(2)	N(3)Zn(2)O(11)	77.5(2)	O(13)C(13)C(14)	117.5(5)	O(14)C(13)C(14)	118.5(5)
N(3)Zn(2)O(13)	90.6(2)	N(3)Zn(2)O(2w)	172.8(2)	N(4)C(14)C(13)	114.2(5)	O(15)C(15)O(16)	124.3(6)
N(4)Zn(2)O(9)	92.3(2)	N(4)Zn(2)O(11)	155.8(2)	O(15)C(15)C(16)	126.2(6)	O(16)C(15)C(16)	109.5(5)
N(4)Zn(2)O(13)	79.0(2)	N(4)Zn(2)O(2w)	102.8(2)	N(4)C(16)C(15)	117.5(5)	N(1)C(17)C(18)	111.1(5)
O(9)Zn(2)O(11)	100.1(2)	O(9)Zn(2)O(13)	169.0(2)	N(2)C(18)C(17)	110.4(5)	N(3)C(19)C(20)	110.5(5)
O(9)Zn(2)O(2w)	95.4(2)	O(11)Zn(2)O(13)	85.8(2)	N(4)C(20)C(19)	111.0(5)		
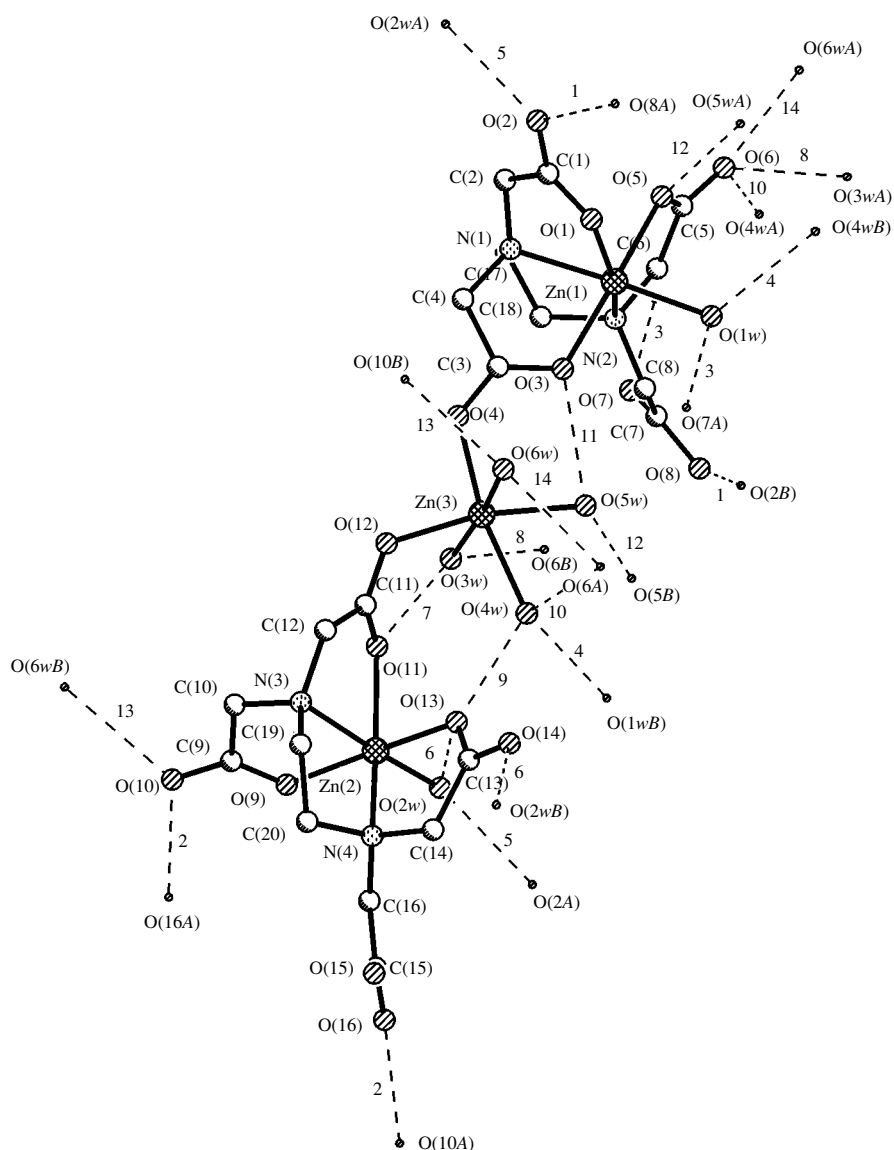
Fig. 1. Trinuclear molecular complex **I**. The numbering of the hydrogen bonds (dashed lines) corresponds to that in Table 2.

RESULTS AND DISCUSSION

Crystals **I** are built up of trinuclear linear molecular complexes (Fig. 1). All three Zn atoms in molecule **I** have an octahedral environment. The coordination spheres of the peripheral atoms [Zn(1) and Zn(2)] have an identical composition. The coordination sphere of each atom contains two N atoms and three O atoms of the H*Edta*$^{3-}$ ligand. The O(w) atom of the H$_2$O molecule completes the coordination polyhedron to an octahedron. The environment of the central Zn(3) atom involves four O(w) atoms of the H$_2$O molecules and two O atoms of two H*Edta*$^{3-}$ ligands coordinated by the Zn(1) and Zn(2) atoms.

Therefore, the H*Edta*$^{3-}$ ligands are coordinated by the peripheral Zn(1) and Zn(2) atoms in a pentadentate

chelating manner (2N + 3O). In this case, one acetate group remains free and the other three acetate groups participate in the coordination, thus closing the five-membered glycinate metallocycles: the N(1) and N(3) atoms are involved in the formation of the *G* and *R* cycles, whereas the N(2) and N(4) atoms participate only in the formation of the *R* cycles [8].

The Zn(1)–O(H*Edta*) bond lengths fall in the range 2.063(4)–2.090(4) Å. The Zn(2)–O(H*Edta*) distances vary over a wider range [2.060(4)–2.123(4) Å]. However, no correlation between the bond lengths is observed in both cases. The lengths of the Zn–N bonds with the nitrogen atoms of the cyclic acetate groups [Zn(1)–N(1), 2.162(5) Å; Zn(2)–N(3), 2.172(5) Å] and with the nitrogen atoms of the monocoordinated acetate groups [Zn(1)–N(2), 2.214(6) Å; Zn(2)–N(4),

Table 2. Geometric parameters of hydrogen bonds in structure **I**

Hydrogen bond no.	A–H$\cdots B$ bond	Distance, Å			AHB angle, deg	Position of the B atom
		$A\cdots B$	A–H	H$\cdots B$		
1	O(8O)–H(8O)$\cdots$O(2)	2.554(7)	0.8(2)	1.7(2)	163*	$0.5 + x, 1.5 - y, z{-}1$
2	O(16)–H(16O)$\cdots$O(10)	2.613(6)	0.97(11)	1.66(11)	167*	$2 - x, 1 - y, 0.5 + z$
3	O(1w)–H(1w1)$\cdots$O(7)	2.654(7)	0.77(7)	1.92(7)	160(7)	$x, y, z + 1$
4	O(1w)–H(2w1)$\cdots$O(4w)	2.858(7)	1.13(10)	1.74(9)	171(9)	$-0.5 + x, 1.5 - y, z$
5	O(2w)–H(1w2)$\cdots$O(2)	2.733(7)	1.03(7)	1.71(7)	168(6)	$1 + 1, y, z$
6	O(2w)–H(2w2)$\cdots$O(14)	2.633(8)	0.70(9)	1.94(9)	174(9)	$x, y, z - 1$
7	O(3w)–H(1w3)$\cdots$O(11)	2.726(7)	0.81(12)	2.11(13)	133*	x, y, z
8	O(3w)–H(2w3)$\cdots$O(6)	2.823(8)	0.82(11)	2.03(11)	163*	$0.5 + x, 1.5 - y, z$
9	O(4w)–H(1w4)$\cdots$O(13)	2.682(7)	0.64(7)	2.04(7)	177(9)	x, y, z
10	O(4w)–H(2w4)$\cdots$O(6)	2.790(7)	0.73(9)	2.10(10)	159(9)	$0.5 + x, 1.5 - y, 1 + z$
11	O(5w)–H(1w5)$\cdots$O(3)	2.709(6)	0.82(6)	2.10(8)	131(7)	x, y, z
12	O(5w)–H(2w5)$\cdots$O(5)	2.746(7)	0.81(8)	1.94(8)	178(5)	$0.5 + x, 1.5 - y, z$
13	O(6w)–H(1w6)$\cdots$O(10)	2.746(7)	0.83(7)	1.95(7)	161(7)	$1 - x, 1 - y, 0.5 + z$
14	O(6w)–H(2w6)$\cdots$O(6)	2.871(7)	0.64(8)	2.28(7)	154(9)	$0.5 + x, 1.5 - y, 1 + z$

* The error is larger than 10°.

2.218(5) Å] differ significantly. Running a little ahead, we should note that the lengths of the Zn(3)–O(H*Edta*) bonds with the central zinc atom [2.069(4), 2.080(4) Å] lie in the range of the Zn(1, 2)–O(H*Edta*) bond lengths and the Zn(1–3)–O(w) bond lengths vary over a rather wide range [2.006(6)–2.225(5) Å]. On the whole, the H*Edta*$^{3-}$ ligand in structure **I** fulfills a hexadentate chelating–bridging [(2N + 3O)$_c$ + O$_b$] function.

The main difference between the structures of the Zn(1) and Zn(2) complexes manifests itself in the formation of trinuclear molecules. The former complex participates in the coordination of the Zn(3) atom through the terminal O(4) atom of the *R* ring, whereas the latter complex is involved in the coordination through the terminal O(12) atom of the *G* ring. The second difference resides in the fact that the Zn(1) and Zn(2) complexes have different absolute configurations. In inverted molecules contained in the unit cell, the configurations of the Zn(1) and Zn(2) complexes are reversed. However, the Zn(1) complex does not become identical to the Zn(2) complex of the initial molecule, because these complexes coordinate the Zn(3) atom in different ways. Therefore, the structure involves complexes of four types, the crystal as a whole can be considered a racemic crystal, and its constituent molecules belong to the class of latent racemic molecules.

The trinuclear linear molecule in structure **I** is similar to that in the compound [Mn$_3$(H*Edta*)$_2$(H$_2$O)$_6$] ·

4H$_2$O (**II**) [4, 5] in many respects. In both compounds, the trinuclear molecules have the same ligands and identical central cationic units [*Me*(H$_2$O)$_4$]$^{2+}$ · 2O(H*Edta*). The peripheral anionic groups [*Me*(H*Edta*)(H$_2$O)]$^-$ are polar due to the presence of water molecules in the coordination sphere of the metal atom. Moreover, the chiralities of peripheral complexes are opposite in sign. However, despite the formal similarity, structures **I** and **II** differ substantially. In compound **II**, the peripheral groups in the trinuclear molecule have a tendency toward local symmetry C_2 and are related by the inversion center; i.e., they are mirror isomers. On the other hand, these groups in compound **I** differ significantly. In structure **II**, all three acetate groups of the H*Edta*$^{3-}$ ligand are involved in the coordination with the metal atom (the coordination number of the manganese atom is seven). At the same time, in structure **I**, one acetate group remains free (the coordination number of the zinc atom is six) and the anionic fragments of the molecule are asymmetric. The metal atom of the central unit is coordinated by the O(H*Edta*) atoms in different ways (the *cis* coordination in **I** and the *trans* coordination in **II**). Note that the linearities of the molecules are of different origin. In compound **II**, the linearity is associated with the *trans* arrangement of the O(H*Edta*) atoms, i.e., with the presence of the inversion center. In compound **I**, the pseudolinearity is provided by hydrogen bonds (see below). The acid proton in structure **I** is localized in the uncoordinated acetate
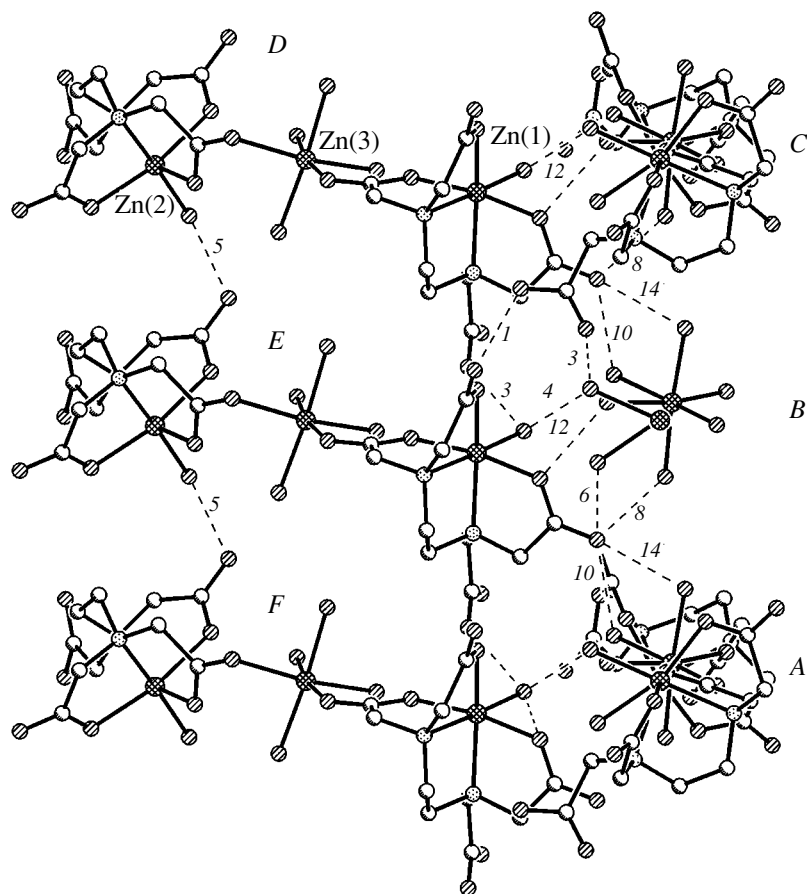
Fig. 2. Intermolecular hydrogen bonds in structure **I**. A fragment of the packing of trinuclear molecules inside a strongly puckered layer. Trinuclear complexes *A*, *B*, and *C* are oriented perpendicular to the figure plane. Molecule *B* is represented only by the Zn atoms and the O atoms of water molecules. Molecular complexes *D*, *E*, and *F* are nearly parallel to the figure plane.

group. A similar proton in structure **II** is located between two terminal O atoms of the coordinated acetate groups of the neighboring molecules and forms a statistically symmetric hydrogen bond.

Compared to compound **II**, compound **I** does not involve outer-sphere water molecules. This circumstance itself leads to the formation of different systems of hydrogen bonds in structures **I** and **II**. Moreover, the Zn(1) and Zn(2) complexes in crystal **I** are variously involved in the formation of intermolecular hydrogen bonds. The ratio between the numbers of hydrogen bonds formed with the participation of the Zn(1) and Zn(2) complexes is equal to 9 : 6. The geometric parameters of hydrogen bonds are listed in Table 2. Since the hydrogen bonds play a significant role in the formation of structure **I**, they are depicted, where possible, in all the figures.

According to the function and arrangement in local regions in the crystal, the hydrogen bonds can be separated into four groups, namely, intramolecular, intrachain, intralayer, and interlayer hydrogen bonds. The intramolecular hydrogen bonds (nos. 7, 9, 11) deter-

mine the shape of the trinuclear molecule. In the octahedron of the central Zn(3) complex, the O(H*Edta*) atoms of the peripheral Zn(1) and Zn(2) complexes coordinate the adjacent *cis* vertices and the anion–cation–anion fragment seemingly should have the shape of a corner, as is the case with the structure of the compound $Zn(Edta)_2Mg(H_2O)_4 \cdot 2H_2O$ (**III**) [9]. However, owing to only the formation of hydrogen bonds, the molecule acquires an almost linear shape [the Zn(1)Zn(3)Zn(2) angle is 168°, and the Zn(1)···Zn(3) and Zn(2)···Zn(3) distances are 5.39 and 5.03 Å, respectively).

Hydrogen bonds nos. 3 and 6 are localized in a relatively small-sized region in the form of a column composed of translationally related trinuclear molecules. The column is aligned parallel to the axis with the smallest unit cell parameter in the crystal ($c = 7.03$ Å). The majority of the hydrogen bonds (nos. 1, 4–6, 8, 10, 12, 14) are formed inside a strongly puckered layer and link chain fragments together (Fig. 2). In the layer, hydrogen bonds nos. 1 and 5 are formed only between the chains. Hydrogen bonds nos. 6, 10, and 14 form bridges through the intermediate O atoms and further
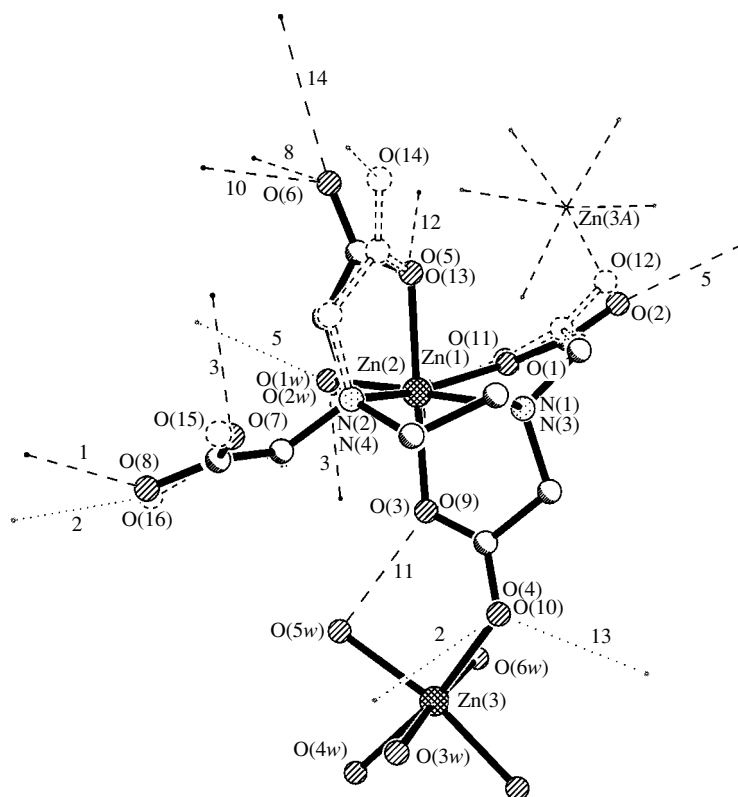
Fig. 3. Comparison (scale superposition) of the coordination environments of the Zn(1) (solid line) and Zn(2) (double dashed line) atoms. Different dashed and dotted lines indicate the hydrogen bonds formed between complexes.
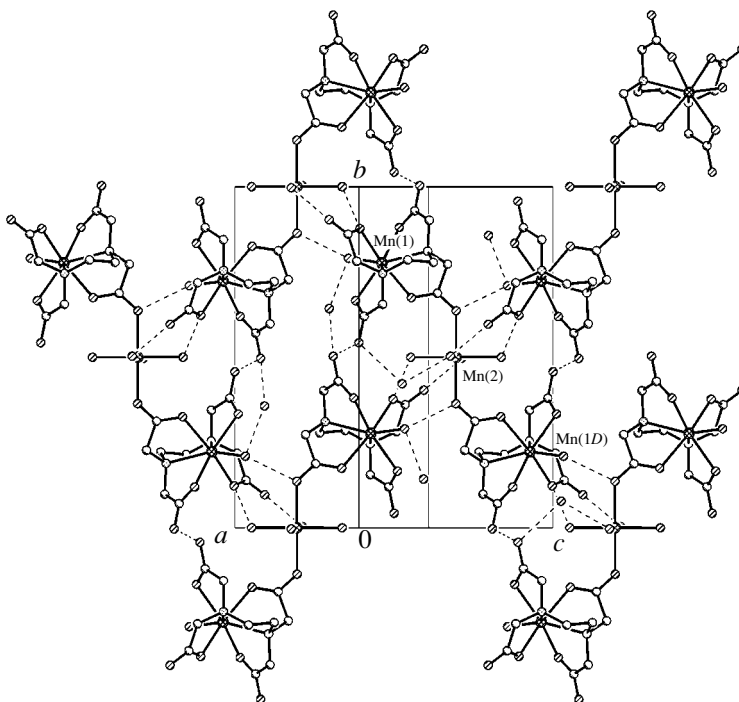

Fig. 4. Hydrogen bonds and packing of trinuclear molecules in a layer in structure **II**. Hydrogen bonds with the participation of the acid H atom are formed in the same layer.
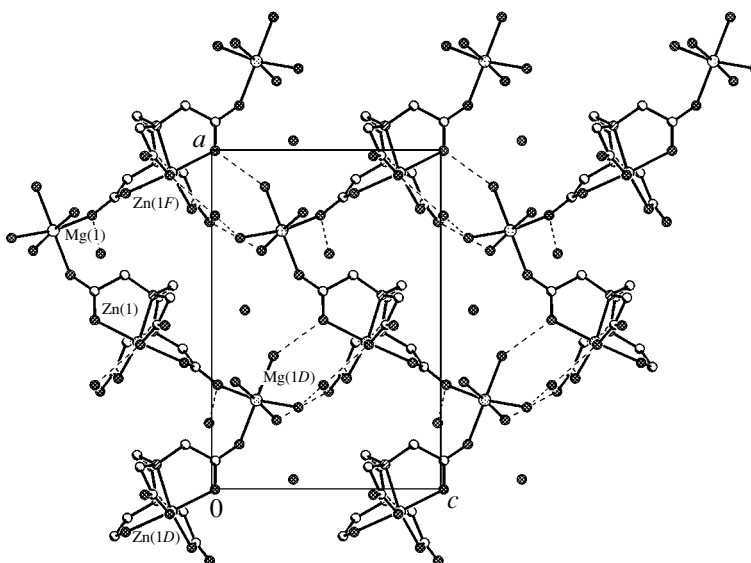
Fig. 5. Projection of the layer in structure **III** as an illustration of the role played by the hydrogen-bond system (dashed lines). Zigzag chains formed by covalently bonded Zn and Mn complexes are aligned parallel to the *a* axis.

strengthen the chains. Hydrogen bonds nos. 4, 8, and 12 play a special role. These hydrogen bonds are formed between the adjacent columns and ensure the closest intermolecular contact with a distance [Zn(1)⋯Zn(3), 5.38 Å] equal to the corresponding distance in the molecular complex itself. The formation of this contact and the change in the coordination functions of the acetate groups of the H$Edta^{3-}$ ligand substantially affect the geometric parameters of molecule **I**. This results in a difference between the structures of the Zn(1) and Zn(2) complexes (Fig. 3). The difference between the positions of equivalent atoms in the complexes can be relatively large. For example, the difference between the equivalent positions amounts to 1.01 Å for the O(6) and O(14) atoms and 0.46 Å for the O(2) and O(12) atoms with a root-mean-square deviation of 0.07 Å.

The hydrogen bonds with the participation of the O(6) atom most strongly distort the coordination sphere of the peripheral zinc atoms (Fig. 3). One of these hydrogen bonds is among the bonds providing the closest contact. Hydrogen bond no. 2 with the participation of the acid H atom and hydrogen bond no. 13 involving the same terminal O(10) atom are interlayer hydrogen bonds. The above contact that is found in compound **I** and is predominantly governed by hydrogen bonds nos. 4, 8, and 12 is also observed in related compounds **II** and **III**. The specific feature of these contacts is the same (almost parallel) direction of several (three) hydrogen bonds linking the complexes of the adjacent fragments. In compounds of type **II** (Fig. 4), which are represented by the isostructural series [Me(H$Edta$)(H$_2$O)]$_2$[Me(H$_2$O)$_4$] · 4H$_2$O (Me = Mn^{2+}, Fe^{2+}, Cd^{2+}) [2–5], similar contacts are multiply repeated by the inversion center and link individual tri-

nuclear molecules into layers. In structures **II**, this contact is the shortest: the Mn⋯Mn distance (5.46 Å) is shorter than that between the metal atoms in the trinuclear molecule (5.78 Å).

In crystals of isostructural series **III** MgMe($Edta$)(H$_2$O)$_6$ (Me = Co, Cu, Zn) [9, 10] with a metal : ligand ratio of 1 : 1, the main structural units are the chains formed by coordinationally bonded complexes. As was noted above, in structure **III**, chain fragments similar in composition to trinuclear complex **I** have a corner structure. However, the H$_2$O molecules of the coordination sphere of the central Mg(1) atom (Fig. 5) form hydrogen bonds with oxygen atoms of the $Edta$ ligand of the adjacent chain in a way similar to those formed by the aforementioned contact in structure **I**. The crystallization water molecules in structure **III** form bridges between the complexes in contact and additionally enhance the effect exerted by the above system of hydrogen bonds. A similar function in compound **I** is fulfilled by the O(1w) and O(2w) water molecules of the coordination spheres of the Zn(1) and Zn(2) atoms.

CONCLUSIONS

Thus, we can conclude that the contact formed in crystal **I** by the hydrogen bonds involving crystallization water molecules is energetically favorable and can affect both the structure of individual fragments and the crystal as a whole.

REFERENCES

1. M. A. Poraĭ-Koshits, Ya. M. Nesterova, T. N. Polynova, and V. T. de Garcia Banus, Koord. Khim. **1** (5), 682 (1975).

2. X. Solans, M. Font-Bardia, M. Aguilo, *et al.*, Acta Crystallogr., Sect. C: Cryst. Struct. Commun. **43** (4), 648 (1987).

3. T. Mizuta, J. Wang, and K. Miyoshi, Inorg. Chim. Acta **230** (1–2), 119 (1995).

4. S. Richards, B. Pedersen, J. V. Silverton, and J. L. Hoard, Inorg. Chem. **3** (1), 27 (1964).

5. I. N. Polyakova, A. L. Poznyak, V. S. Sergienko, and L. V. Stopolyanskaya, Kristallografiya **46** (1), 47 (2001) [Crystallogr. Rep. **46**, 40 (2001)].

6. G. M. Sheldrick, Acta Crystallogr., Sect. A: Found. Crystallogr. **46** (6), 467 (1990).

7. G. M. Sheldrick, *SHELXL93: Program for the Refinement of Crystal Structures* (Univ. of Göttingen, Germany, 1993).

8. M. A. Poraĭ-Koshits and T. N. Polynova, Koord. Khim. **10** (6), 725 (1984).

9. X. Solans, M. Font-Altaba, J. Oliva, and J. Herera, Acta Crystallogr., Sect. C: Cryst. Struct. Commun. **39**, 435 (1983).

10. A. I. Pozhidaev, T. N. Polynova, and M. A. Poraĭ-Koshits, Zh. Strukt. Khim. **14**, 570 (1973).

Translated by O. Borovik-Romanova

STRUCTURE
OF ORGANIC COMPOUNDS

X-ray Mapping in Heterocyclic Design:
XIV. Tricyclic Heterocycles Based
on 2-Oxo-1,2,5,6,7,8-Hexahydroquinoline-3-Carbonitrile

O. S. Mazina, V. B. Rybakov, V. V. Chernyshev,
E. V. Babaev, and L. A. Aslanov

Moscow State University, Vorob'evy gory, Moscow, 119992 Russia

e-mail: rybakov@biocryst.phys.msu.su

Received November 11, 2003

Abstract—The structures of four compounds are studied using single-crystal X-ray diffraction: 1-[2-(4-chlorophenyl)-2-oxoethyl]-2-oxo-1,2,5,6,7,8-hexahydroquinoline-3-carbonitrile [$a = 4.908(4)$ Å, $b = 11.644(10)$ Å, $c = 13.587(2)$ Å, $\beta = 94.31(5)°$, $Z = 2$, space group $P2_1$]; 2-[2-(4-chlorophenyl)-2-oxoethoxy]-5,6,7,8-tetrahydroquinoline-3-carbonitrile [$a = 7.6142(8)$ Å, $b = 14.778(2)$ Å, $c = 14.132(2)$ Å, $\beta = 100.38(1)°$, $Z = 4$, space group $P2_1/c$]; 4-(aminocarbonyl)-2-(chlorophenyl)-6,7,8,9-tetrahydro[1.3]oxazolo[3,2-*a*]quinolin-3-ium perchlorate [$a = 5.589(7)$ Å, $b = 24.724(15)$ Å, $c = 13.727(5)$ Å, $\beta = 97.66(9)°$, $Z = 4$, space group $P2_1/n$]; and (3-amino-5,6,7,8-tetrahydrofuro[2,3-*b*]quinolin-2-yl)-(4-chlorophenyl) methanone [$a = 7.150(2)$ Å, $b = 7.4288(10)$ Å, $c = 15.314(3)$ Å, $\alpha = 98.030(10)°$, $\beta = 99.21(2)°$, $\gamma = 105.34(2)°$, $Z = 2$, space group $P\bar{1}$]. The structures are solved by direct methods and refined by the full-matrix least-squares procedure in the anisotropic approximation to $R = 0.0728$, 0.0439, 0.1228, and 0.0541, respectively. The structure of 1-(4-chlorophenyl)-4-piperidin-1-yl-8,9-dihydro-7*H*-pyrrolo[3.2.1-*ij*]quinoline-5-carboxamide [$a = 23.9895(9)$ Å, $b = 5.1557(3)$ Å, $c = 17.0959(9)$ Å, $\beta = 106.43°$, $Z = 4$, space group P_1/c] is investigated by X-ray powder diffraction. This structure is solved using the grid search procedure and refined by the Rietveld method to $R_{wp} = 0.0773$, $R_{exp} = 0.0540$, $R_p = 0.0585$, $R_b = 0.1107$, and $\chi^2 = 1.78$. © 2004 MAIK *"Nauka/Interperiodica"*.

INTRODUCTION

Readily available derivatives of 6-methyl-cyanopyridones-2 are promising substances as precursors of complex condensed heterocyclic compounds. For example, it is known that the phenacylation of these pyridones results the formation of *N* and *O* alkylation products. It should be noted that, in alkaline media, *O* isomers easily enter into cyclization reactions with the formation of furo[2,3-*b*]pyridine derivatives, whereas *N* isomers are cyclized to form 5-indolizinones [1, 2] (see Scheme 1):
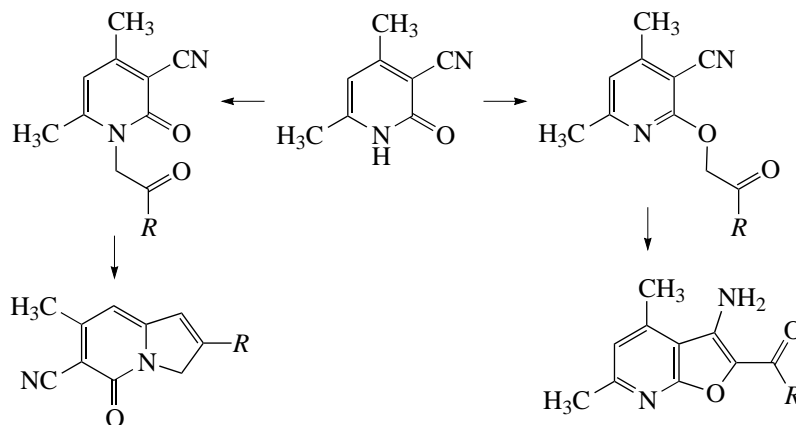
Scheme 1

In the present work, we demonstrated that the possible heterocyclization reactions of 6-methyl-cyanopyridones-2 are not exhausted by the above processes. The synthesis of the studied compounds was performed according to the following scheme:

Scheme 2
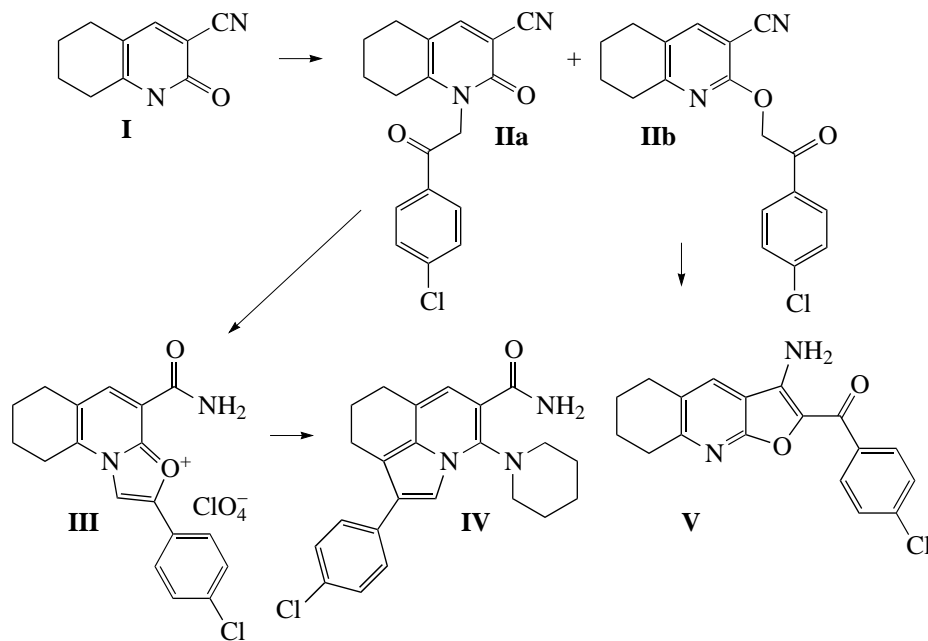
By using compound **I** as an example, we found one more direction of the heterocyclization of *N*-phenyl derivatives of the aforementioned pyridones, namely, the transformation of *N* isomer **IIa** into compound **III**, which, in turn, can be recycled into the poorly investigated compound **IV**.

Earlier, the phenacylation of compound **I** was not described. We revealed that this reaction results in the formation of *N* and *O* isomers (in the ratio 1 : 1); in this case, it is possible to separate the mixture of isomers. As could be expected, compound **IIb** is cyclized with the formation of compound **V**.

Table 1. Physicochemical characteristics of the compounds synthesized

Compound	Melting temperature T_m, °C	^{1}H NMR* (DMSO-d_6)
IIa	233	8.10 and 7.69 (d, 8.3 Hz, 2H, 14-CH + 15-CH and 17-CH + 18-CH)**; 8.03 (s, 1H, 4-CH); 5.66 (s, 2H, 11-CH$_2$); 2.57 (m, 4H, 6-CH$_2$ + 9-CH$_2$); 1.73 and 1.64 (m, 2H, 7-CH$_2$ and 8-CH$_2$)***
IIb	247	8.01 and 7.64 (d, 8.6 Hz, 2H, 14-CH + 15-CH and 17-CH + 18-CH)**; 7.98 (s, 1H, 4-CH); 5.97 (s, 2H, 11-CH$_2$); 2.66 and 2.56 (t, 5.8 Hz and 6.0 Hz, 2H, 6-CH$_2$ and 9-CH$_2$)***; 1.70 (m, 4H, 7-CH$_2$ + 8-CH$_2$)
III	283	9.52 (s, 1H, 11-CH); 8.59 (s, 1H, 4-CH), 8.32 and 8.24 (s, 1H, 31-NH$_2$); 8.12 and 7.8 (d, 8.6 Hz, 2H, 14-CH + 15-CH and 17-CH + 18-CH)**; 3.14 and 2.98 (t, 5.9 Hz and 5.6 Hz, 2H, 6-CH$_2$ and 9-CH$_2$)***; 2.02 and 1.86 (m, 2H, 7-CH$_2$ and 8-CH$_2$)***
IV	262	7.78 and 6.41 (s, 1H, 31-NH$_2$); 7.66 and 7.47 (d, 8.5 Hz, 2H, 17-CH + 18-CH and 14-CH + 15-CH)**; 7.53 (s, 1H, 4-CH); 6.41 (s, 1H, 11-CH); 3.17 and 3.05 (s, 2H, 19-CH$_2$ and 23-CH$_2$)***; 2.96 and 2.78 (t, 2H, 5.6 Hz, 8-CH$_2$ and 6-CH$_2$)***; 1.95 (m, 2H, 7-CH$_2$); 1.82 and 1.70 and 1.40 (m, 6H, Pip (CH$_2$–CH$_2$–CH$_2$))
V	278	8.16 (s, 1H, 4-CH); 8.11 and 7.63 (d, 8.3 Hz, 2H, 14-CH + 15-CH and 17-CH + 18-CH)**; 7.56 (s, 2H, 31-NH$_2$); 2.91 and 2.86 (t, 6.4 Hz and 6.1 Hz, 2H, 6-CH$_2$ and 9-CH$_2$)***; 1.82 (m, 4H, 7-CH$_2$ + 8-CH$_2$)

  * The assignment of the signals is given in accordance with the atomic numbering used in X-ray diffraction analysis (Figs. 2–6).
 ** The reverse assignment of CH$_2$ groups is possible.
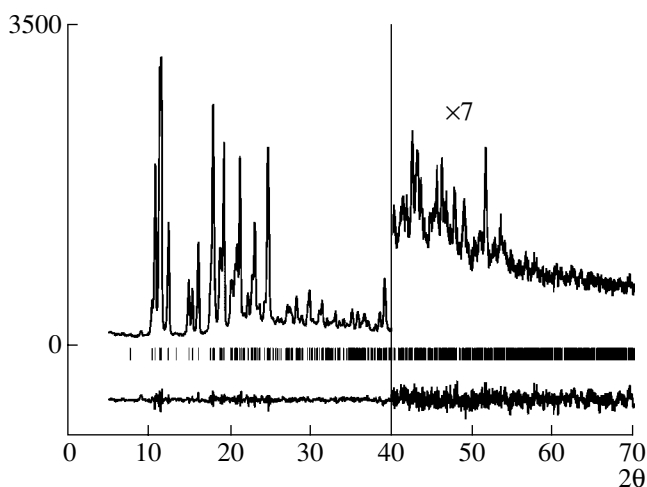*** The reverse assignment of CH groups is possible.

Fig. 1. Experimental and difference X-ray powder diffraction patterns (after the final Rietveld refinement) for structure **IV**.
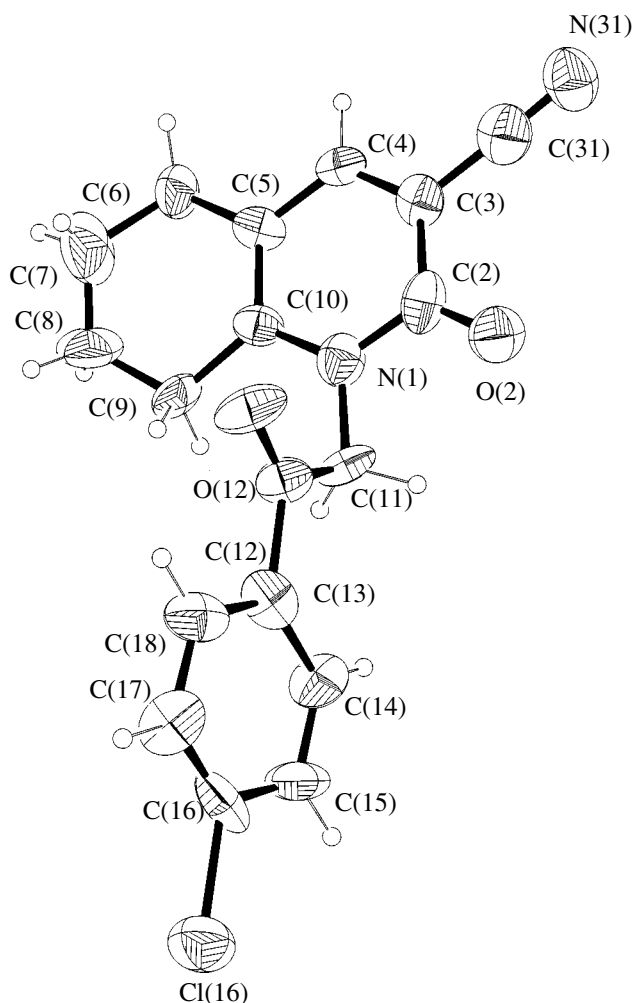
In this work, we did not analyze the possibility of cyclizing compound **IIa** into indolizine. It is known [3] that, under the action of acids, *N*-phenacylpyridones-2 are able to undergo cyclocondensation with the formation of bicyclic oxazolopyridinium salts. In [3], it was shown that oxazolopyridinium salts with a methyl group in the fifth position can be recyclized to form 5-substituted indolizines. In the case of compound **IIa**, a similar cyclization proceeds with the formation of tricyclic compound **III**. It is worth noting that the cyclization is accompanied by the hydrolysis of the nitrile group and the formation of the amide group in the system. Compound **III** also contains the methylene group in the position appropriate for recyclization. It turned out that, under the action of the secondary amine, the tricyclic system of oxazolopyridinium undergoes previously unknown recyclization into a poorly studied tricyclic system of compound **IV**. Note that the topological feature of the observed recyclization is the transformation of a partially hydrogenated *cata*-condensed tricyclic system (in which each fusion atom is shared only by two rings) into a *peri*-condensed system (involving the atom shared by three rings).

EXPERIMENTAL

Compounds **I–V** were synthesized according to Scheme 2.

Compound 2-oxo-1,2,5,6,7,8-hexahydroquinoline-3-carbonitrile (I) was prepared using the procedure described in [4] and was investigated in our previous work [5]. The physicochemical characteristics of the compounds synthesized are presented in Table 1.

1-[2-(4-Chlorophenyl)-2-oxoethyl]-2-1,2,5,6,7,8-hexahydroquinoline-3-carbonitrile (IIa) and 2-[2-(4-chlorophenyl)-2-oxoethoxy]-5,6,7,8-tetrahydroquinoline-3-carbonitrile (IIb). These compounds were synthesized according to a procedure similar to that proposed in [1]. Potassium hydroxide (0.0057 mol) and ethanol (5 ml) were placed in a round-bottomed flask. Compound **I** (0.0057 mol) was added portionwise with stirring to the prepared solution. The mixture was allowed to stand in an ultrasonic bath for 40 min, and then the alcohol was evaporated with a rotary evaporator. Dimethylformamide (10 ml) and phenacyl bromide (0.0057 mol) were added to the dry residue. The mixture was allowed to stand at an elevated temperature ($T \sim 50°C$) for 18 h with stirring. After completing the reaction (controlled by thin-layer chromatography indicating the absence of compound **I**), the reaction mixture was cooled and poured into water. The precipitate was filtered off and dried in air. The mixture of *N* and *O* isomers was separated using a column (sorbent, SiO₂; chloroform : hexane = 1 : 1). The yields of compounds **IIa** and **IIb** were equal to 43 and 47%, respectively.

4-(Aminocarbonyl)-2-(chlorophenyl)-6,7,8,9-tetrahydro[1.3]oxazolo[3,2-*a*]quinolin-3-ium perchlorate (III). Compound **III** was prepared from com-

Fig. 2. Molecular structure and atomic numbering for compound **IIa**.

Table 2. Crystal data, data collection, and refinement parameters for structures **IIa**, **IIb**, **III**, **IV**, and **V**

Empirical formula	$C_{18}H_{15}ClN_2O_2$ (IIa)	$C_{18}H_{15}ClN_2O_2$ (IIb)	$C_{18}H_{16}ClN_2O_2 \cdot ClO_4$ (III)	$C_{23}H_{24}ClN_3$ (IV)	$C_{18}H_{15}ClN_2O_2$ (V)
Molecular weight	326.79	326.79	427.24	393.92	326.79
Crystal system	Monoclinic	Monoclinic	Monoclinic	Monoclinic	Triclinic
Space group	$P2_1$	$P2_1/c$	$P2_1/n$	$P2_1/c$	$P\bar{1}$
a, Å	4.908(4)	7.6142(8)	5.589(7)	23.9895(9)	7.150(2)
b, Å	11.644(10)	14.778(2)	24.724(15)	5.1557(3)	7.4288(10)
c, Å	13.587(8)	14.132(2)	13.727(5)	17.0959(9)	15.314(3)
α, deg					98.030(10)
β, deg	94.31(5)	100.38(1)	97.66(9)	106.43(3)	99.21(2)
γ, deg					105.34(2)
V, Å^3	774.3(10)	1564.2(4)	1881(3)	2028.18(2)	760.0(3)
Z	2	4	4	4	2
ρ_{calcd}, g/cm^3	1.401	1.388	1.508	1.290	1.428
$\mu(CuK_\alpha)$, cm^{-1}	2.28	2.26	3.46	1.80	2.32
θ range, deg	3.26–54.98	4.37–69.97	3.58–49.97	1.92–35.00	2.98–69.92
Crystal size, mm	$0.3 \times 0.3 \times 0.3$	$0.3 \times 0.3 \times 0.3$	$0.3 \times 0.3 \times 0.3$	Powder	$0.3 \times 0.3 \times 0.3$
Number of reflections measured	1576	3083	2030		2900
Number of unique reflections	1433 ($R_{int} = 0.074$)	2958 ($R_{int} = 0.028$)	1936 ($R_{int} = 0.244$)		2791 ($R_{int} = 0.079$)
Number of reflections refined	209	209	254		217
R factor [$I \geq 2\sigma(I)$] R_1/wR_2	0.0728/0.1399	0.0439/0.1099	0.1228/0.2983		0.0541/0.1379
$\Delta\rho_{max}/\Delta\rho_{min}$, e/Å^3	0.233/–0.180	0.175/–0.256	0.776/–0.518		0.597/–0.531
R_{wp}				0.0773	
R_{exp}				0.0540	
R_p				0.0585	
R_b				0.1107	
χ^2				1.78	

pound **IIa** according to a procedure similar to that described in [3]. Compound **IIa** (1 g) was dissolved in 96% H_2SO_4 (2 ml) and left to stand for a night. 70% $HClO_4$ (5 ml) was added to water (50 ml), and the H_2SO_4 mixture was poured into the prepared solution. The precipitate was filtered off, washed on a filter with water, and dried. The yield of compound **III** was 98%.

1-(4-Chlorophenyl)-4-piperidin-1-yl-8,9-dihydro-7H-pyrrolo[3,2,1-ij]quinoline-5-carboxamide (IV). This compound was synthesized according to a procedure similar to that described in [3]. Compound **III** (0.5 g) and piperidine (5 ml) were boiled in acetonitrile (15 ml) to the formation of a yellowish green thick solution. The solution was poured into water, and the precipitate was filtered off and recrystallized from acetonitrile. The yield of compound **IV** was 87%.

Table 3. Selected bond lengths d (Å) in structure **IIa**

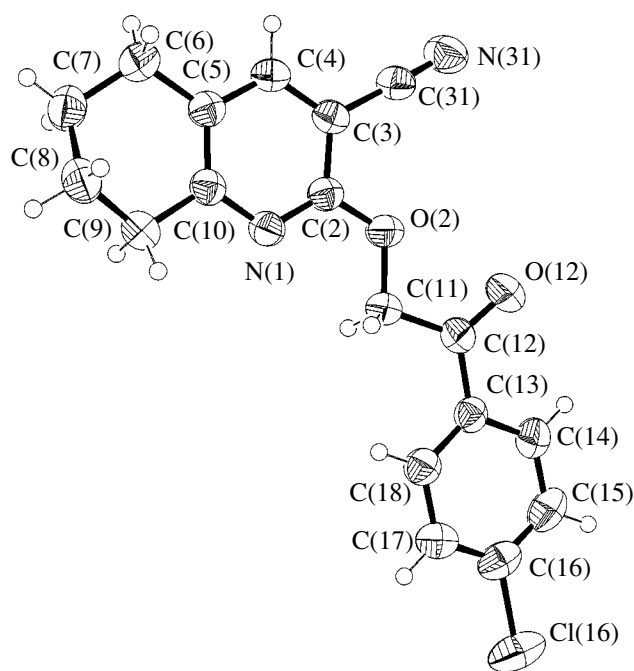| Bond	d	Bond	d
N(1)–C(2)	1.355(19)	C(6)–C(7)	1.50(2)
N(1)–C(10)	1.41(2)	C(7)–C(8)	1.36(2)
N(1)–C(11)	1.472(18)	C(8)–C(9)	1.48(2)
C(2)–O(2)	1.21(2)	C(9)–C(10)	1.479(18)
C(2)–C(3)	1.44(2)	C(11)–C(12)	1.499(18)
C(3)–C(4)	1.361(11)	C(12)–O(12)	1.168(17)
C(3)–C(31)	1.43(2)	C(12)–C(13)	1.55(2)
C(4)–C(5)	1.499(11)	Cl(16)–C(16)	1.781(17)
C(5)–C(10)	1.38(2)	C(31)–N(31)	1.13(2)
C(5)–C(6)	1.482(19)		

Fig. 3. Molecular structure and atomic numbering for compound **IIb**.

(3-Amino-5,6,7,8-tetrahydrofuro[2,3-*b*]quinolin-2-yl)-(4-chlorophenyl)-methanone (V). Compound **V** was prepared using a procedure similar to that proposed by Gewald [1]. Compound **IIb** was boiled in absolute methanol with a threefold excess of sodium methylate for 16 h. The precipitate was filtered off, washed on a filter with methanol, and dried. The yield of compound **V** was 68%.
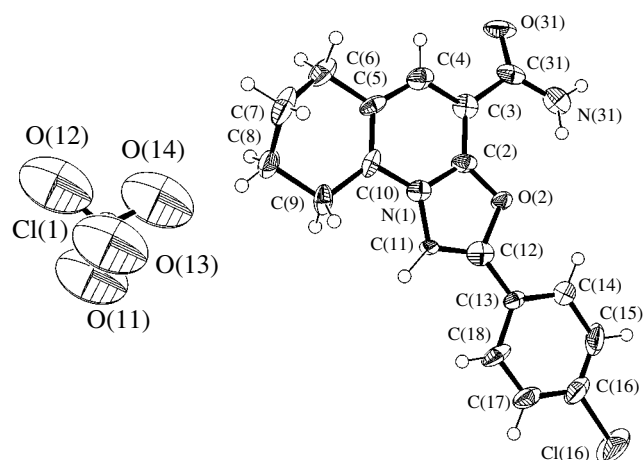

Fig. 4. Molecular structure and atomic numbering for compound **III**.

The experimental intensities of diffraction reflections for single crystals of compounds **IIa**, **IIb**, **III**, and **V** were measured on a CAD4 automated diffractometer [6] (CuK_α radiation, graphite monochromator, ω scan mode) at room temperature. The unit cell parameters were determined and refined using 25 reflections in the θ ranges 24°–26.5°, 30°–35°, 21°–25°, and 25°–29°, respectively. No correction for absorption was introduced because of the small linear absorption coefficients of the compounds studied and the small sizes of their crystals. The primary processing of the sets of diffraction data was performed with the WinGX program package [7]. All the subsequent calculations were carried out with the SHELX97 program package [8]. The

Table 4. Selected bond angles ω (deg) in structure **IIa**

Angle	ω	Angle	ω
C(2)–N(1)–C(10)	123.7(16)	C(8)–C(7)–C(6)	121(2)
C(2)–N(1)–C(11)	114.6(16)	C(7)–C(8)–C(9)	118.8(18)
C(10)–N(1)–C(11)	121.7(15)	C(10)–C(9)–C(8)	112.5(16)
O(2)–C(2)–N(1)	122(2)	C(5)–C(10)–N(1)	118.6(14)
O(2)–C(2)–C(3)	122(2)	C(5)–C(10)–C(9)	124.5(19)
N(1)–C(2)–C(3)	115.8(18)	N(1)–C(10)–C(9)	116.8(17)
C(4)–C(3)–C(31)	118.7(19)	N(1)–C(11)–C(12)	111.0(10)
C(4)–C(3)–C(2)	122.4(16)	O(12)–C(12)–C(11)	121.8(16)
C(31)–C(3)–C(2)	118.9(19)	O(12)–C(12)–C(13)	127.3(16)
C(3)–C(4)–C(5)	119.7(16)	C(11)–C(12)–C(13)	110.9(17)
C(10)–C(5)–C(4)	119.7(17)	C(17)–C(16)–Cl(16)	122.4(16)
C(10)–C(5)–C(6)	120.3(15)	C(15)–C(16)–Cl(16)	113.6(19)
C(4)–C(5)–C(6)	120.0(17)	N(31)–C(31)–C(3)	179(3)
C(5)–C(6)–C(7)	107.6(14)		

Table 5. Selected bond lengths d (Å) in structure **IIb**

Bond	d	Bond	d
N(1)–C(2)	1.312(2)	C(5)–C(6)	1.505(3)
N(1)–C(10)	1.353(2)	C(6)–C(7)	1.514(3)
C(2)–O(2)	1.350(2)	C(7)–C(8)	1.508(3)
C(2)–C(3)	1.409(2)	C(8)–C(9)	1.524(3)
O(2)–C(11)	1.426(2)	C(9)–C(10)	1.502(3)
C(3)–C(4)	1.375(3)	C(11)–C(12)	1.499(3)
C(3)–C(31)	1.436(3)	C(12)–O(12)	1.211(2)
C(31)–N(31)	1.136(3)	C(12)–C(13)	1.488(3)
C(4)–C(5)	1.390(3)	C(16)–Cl(16)	1.739(2)
C(5)–C(10)	1.394(2)		

crystal structures were determined by direct methods. The positional and thermal parameters for all the non-hydrogen atoms were refined in the anisotropic approximation. The hydrogen atoms, except for the hydrogen atoms involved in the formation of hydrogen bonds, were located from geometric considerations and refined as riding atoms together with the corresponding carbon atoms. The thermal parameters of these hydrogen atoms were calculated from those of the carbon atoms [U_{iso}(H) = 1.2U_{eq}(C) for the aromatic hydrogen atoms and U_{iso}(H) = 1.5U_{eq}(C) for the aliphatic hydrogen atoms]. The hydrogen atoms involved in the formation of hydrogen bonds were located from electron-density difference syntheses and independently refined in the isotropic approximation.

For compound **III**, the R factor is rather large due to the low quality of crystals.

The diffraction experiments for compound **IV** (available only in the form of a finely crystalline powder) were performed on a DRON-3 automated powder diffractometer (NPO Burevestnik) (CuK_α radiation; Ge monochromator; step width, 0.02° in 2θ) at room temperature. The unit cell parameters were determined with the ITO indexing program [9]. Preliminary information on the molecular structure of compound **IV** was obtained from the NMR spectroscopic data. The initial geometrical model was constructed using semiempirical and empirical methods with the MOPAC 6.0 [10] and PCMODEL [11] programs. The structure was solved by the grid search procedure [12] based on the preassigned molecular fragments. The Rietveld full-profile refinement of the structure was carried out according to the MRIA program [13]. The pseudo-Voigt function was used as a profile function, and the background was approximated by Chebyshev fifth-degree polynomials. The thermal parameters of the non-hydrogen atoms of the molecular skeleton were averaged in the course of refinement. The hydrogen atoms were placed at calculated positions. The experimental and difference X-ray powder diffraction patterns after the final refinement are shown in Fig. 1. The tick marks indicate the calculated positions of reflections.

The main parameters of the X-ray diffraction experiments and crystal data for compounds **IIa**, **IIb**, **III**, **IV**, and **V** are summarized in Table 2. The spatial arrangement of atoms in molecules and their numbering are depicted in Figs. 2–6 obtained with the ORTEP-3 graphic program package [14, 15]. The interatomic dis-

Table 6. Selected bond angles ω (deg) in structure **IIb**

Angle	ω	Angle	ω
C(2)–N(1)–C(10)	118.20(16)	C(5)–C(6)–C(7)	112.84(17)
N(1)–C(2)–O(2)	121.31(16)	C(8)–C(7)–C(6)	110.87(18)
N(1)–C(2)–C(3)	123.41(17)	C(7)–C(8)–C(9)	111.29(18)
O(2)–C(2)–C(3)	115.28(16)	C(10)–C(9)–C(8)	113.22(17)
C(2)–O(2)–C(11)	117.73(14)	N(1)–C(10)–C(5)	123.10(17)
C(4)–C(3)–C(2)	117.49(17)	N(1)–C(10)–C(9)	115.89(16)
C(4)–C(3)–C(31)	121.24(17)	C(5)–C(10)–C(9)	121.02(17)
C(2)–C(3)–C(31)	121.25(17)	O(2)–C(11)–C(12)	107.73(15)
N(31)–C(31)–C(3)	177.7(2)	O(12)–C(12)–C(13)	120.78(18)
C(3)–C(4)–C(5)	120.65(17)	O(12)–C(12)–C(11)	120.60(18)
C(4)–C(5)–C(10)	117.12(17)	C(13)–C(12)–C(11)	118.61(16)
C(4)–C(5)–C(6)	120.19(17)	C(15)–C(16)–Cl(16)	119.27(17)
C(10)–C(5)–C(6)	122.67(17)	C(17)–C(16)–Cl(16)	119.49(18)

Table 7. Selected bond lengths d (Å) in structure **III**

Bond	d	Bond	d	Bond	d	Bond	d
N(1)–C(11)	1.390(15)	C(3)–C(4)	1.381(18)	C(5)–C(6)	1.501(18)	C(12)–C(13)	1.459(18)
N(1)–C(10)	1.367(16)	C(3)–C(31)	1.540(19)	C(6)–C(7)	1.48(2)	C(16)–C(16)	1.710(15)
N(1)–C(2)	1.371(16)	C(31)–O(31)	1.198(15)	C(7)–C(8)	1.51(2)	Cl(1)–O(14)	1.3644(14)
C(2)–O(2)	1.361(15)	C(31)–N(31)	1.330(18)	C(8)–C(9)	1.534(18)	Cl(1)–O(11)	1.3648(12)
C(2)–C(3)	1.374(18)	C(4)–C(5)	1.392(18)	C(9)–C(10)	1.464(18)	Cl(1)–O(12)	1.3650(13)
O(2)–C(12)	1.388(15)	C(5)–C(10)	1.367(18)	C(11)–C(12)	1.343(18)	Cl(1)–O(13)	1.365(2)

tances and bond angles in the structures are presented in Tables 3–12.

The crystal data for the structures studied (CIF files) have been deposited with the Cambridge Structural Database (deposits CCDC nos. 24-9841–24-9845).

RESULTS AND DISCUSSION

In structure **IIa** (Fig. 2), the O(2), C(6), C(9), C(31), and N(31) atoms lie in the plane of the six-membered heterocycle, whereas the C(7) and C(8) atoms in the cyclohexene fragment deviate from its plane by 0.58 and 0.21 Å, respectively.

The *n*-chlorobenzoyl group of the molecule is nearly perpendicular to the plane of the heterocyclic fragment of the molecule: the corresponding dihedral angle between the planes is equal to 78.76(1)°.

The C(7)–C(8) distance (Table 3) is considerably shorter than the distances between the other atoms forming the six-membered aliphatic ring due to strong anisotropy of thermal vibrations of these atoms. However, by introducing the correction for anisotropy of thermal vibrations [16], this distance (1.61 Å) can be considered to correspond to the C–C single bond between sp^3-hybridized carbon atoms.

A comparison of the C(3)–C(4)–C(5)–C(10) fragment with a similar fragment in the 2-oxo-1,2,5,6,7,8-hexahydroquinoline-3-carbonitrile molecule [5] indicates a quasi-diene character of the fragments under consideration and a similar structure of the bicyclic fragments of the studied compounds.

In molecule **IIb** (Fig. 3), the C(6), C(9), O(2), C(31), and N(31) atoms lie in the plane of the pyridine ring, whereas the C(7) and C(8) atoms of the cyclohexene fragment deviate from the ring plane by –0.35 and 0.39 Å, respectively.

The dihedral angle between the planes of the heterocyclic fragment and the benzoyl group of the molecule is equal to 2.75(7)°; i.e., the phenacyloxy group virtually lies in the plane of the heterocyclic fragment.

In structure **III** (Fig. 4), the C(6) and C(9) atoms lie in the plane of the oxazolopyridine bicycle, and the C(7) and C(8) atoms deviate from the plane by –0.53 and 0.24 Å, respectively.

The C(31)–O(31)–N(31)H(31*A*)H(31*B*) amide group is rotated with respect to the plane of the bicycle by 18.83° and forms the intramolecular hydrogen bond with the O(2) atom. The hydrogen atoms of the amide group and the oxygen atoms of the perchlorate anion are involved in the formation of the intermolecular hydrogen bonds N(31)–H(31*A*)···O(12) and N(31)–H(31*B*)···O(13), which link molecules into chains. The parameters of the hydrogen bonds are listed in Table 13, and their spatial arrangement is shown in Fig. 7. The dihedral angle between the planes of the heterocyclic and phenyl rings is equal to 5.3(7)°.

The structure of the oxazolopyridinium cation can be represented by three resonance structures (see Scheme 3):
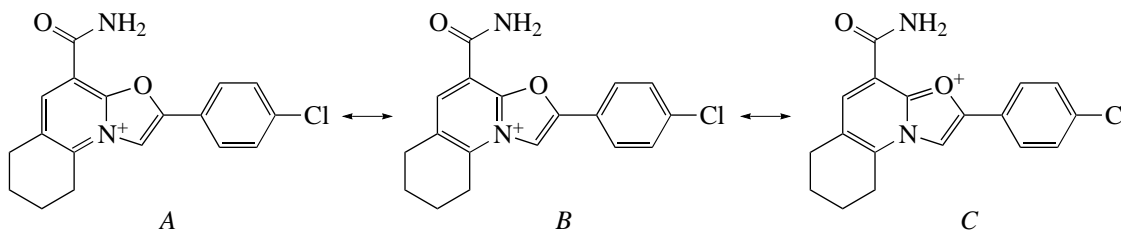
Scheme 3

The bond lengths in the C(3)–C(4)–C(5)–C(10) fragment (Table 7) indicate its quasi-diene structure.

Consequently, the resonance form *A* should make the least contribution and the structure of the molecule

Table 8. Selected bond angles ω (deg) in structure **III**

Angle	ω	Angle	ω
C(11)–N(1)–C(10)	129.9(11)	C(6)–C(7)–C(8)	111.2(13)
C(11)–N(1)–C(2)	106.7(10)	C(7)–C(8)–C(9)	110.7(12)
C(10)–N(1)–C(2)	123.3(11)	C(10)–C(9)–C(8)	112.2(11)
O(2)–C(2)–C(3)	129.4(12)	C(5)–C(10)–N(1)	116.4(12)
O(2)–C(2)–N(1)	109.3(10)	C(5)–C(10)–C(9)	126.4(11)
C(3)–C(2)–N(1)	121.3(12)	N(1)–C(10)–C(9)	117.1(12)
C(2)–O(2)–C(12)	106.8(10)	C(12)–C(11)–N(1)	108.3(11)
C(4)–C(3)–C(2)	115.3(12)	C(11)–C(12)–O(2)	108.9(11)
C(4)–C(3)–C(31)	119.5(12)	C(11)–C(12)–C(13)	133.8(13)
C(2)–C(3)–C(31)	125.0(12)	O(2)–C(12)–C(13)	117.3(12)
O(31)–C(31)–N(31)	126.0(13)	C(17)–C(16)–Cl(16)	119.0(14)
O(31)–C(31)–C(3)	117.7(13)	C(15)–C(16)–Cl(16)	120.7(14)
N(31)–C(31)–C(3)	116.1(12)	O(14)–Cl(1)–O(11)	109.51(10)
C(3)–C(4)–C(5)	123.2(12)	O(14)–Cl(1)–O(12)	109.49(11)
C(10)–C(5)–C(4)	120.2(11)	O(11)–Cl(1)–O(12)	109.46(9)
C(10)–C(5)–C(6)	118.6(13)	O(14)–Cl(1)–O(13)	109.48(10)
C(4)–C(5)–C(6)	121.1(12)	O(11)–Cl(1)–O(13)	109.46(11)
C(7)–C(6)–C(5)	113.2(12)	O(12)–Cl(1)–O(13)	109.44(9)

Table 9. Selected bond lengths d (Å) in structure **IV**

Bond	d	Bond	d	Bond	d	Bond	d
N(1)–C(11)	1.379(4)	C(31)–O(31)	1.226(4)	C(6)–C(7)	1.465(4)	C(16)–Cl(16)	1.736(4)
N(1)–C(10)	1.395(4)	C(31)–N(31)	1.376(5)	C(7)–C(8)	1.500(5)	C(19)–C(20)	1.469(4)
N(1)–C(2)	1.461(4)	N(31)–H(31A)	0.86	C(8)–C(9)	1.488(4)	C(19)–N(2)	1.523(4)
C(2)–C(3)	1.390(5)	N(31)–H(31B)	0.86	C(9)–C(10)	1.372(5)	C(20)–C(21)	1.480(4)
C(2)–N(2)	1.442(4)	C(4)–C(5)	1.390(8)	C(9)–C(12)	1.431(4)	C(21)–C(22)	1.538(3)
C(3)–C(4)	1.458(5)	C(5)–C(6)	1.456(6)	C(11)–C(12)	1.380(4)	C(22)–C(23)	1.516(3)
C(3)–C(31)	1.506(4)	C(5)–C(10)	1.478(8)	C(12)–C(13)	1.486(5)	C(23)–N(2)	1.482(4)

under investigation is more adequately described by a superposition of resonance forms *B* and *C* (see Scheme 4):
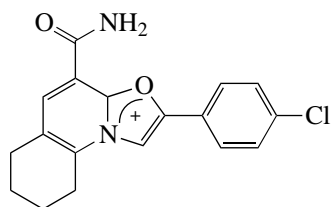
Scheme 4

One more structural feature of molecule **III** is that the N(1)–C(10) bond is shortened compared to the C–N single bond. This feature can be associated with the conjugation of a lone electron pair of the bridging nitrogen atom with the exocyclic amide group through the diene fragment.

In molecule **IV** (Fig. 5), the C(31), C(13), and N(2) atoms lie in the plane of the cycloannelated tricyclic fragment. The amide group of the molecule is rotated with respect to this plane through 57.3(1)°.

It can be seen from Table 9 that, in the indolizine fragment of the molecule, the formally single C–C

Table 10. Selected bond angles ω (deg) in structure **IV**

Angle	ω	Angle	ω
C(11)–N(1)–C(10)	105.6(2)	C(10)–C(9)–C(8)	122.1(3)
C(11)–N(1)–C(2)	134.1(2)	C(12)–C(9)–C(8)	131.4(3)
C(10)–N(1)–C(2)	120.2(3)	C(9)–C(10)–N(1)	110.6(3)
C(3)–C(2)–N(2)	133.3(3)	C(9)–C(10)–C(5)	126.1(4)
C(3)–C(2)–N(1)	116.7(3)	N(1)–C(10)–C(5)	123.3(4)
N(2)–C(2)–N(1)	109.5(3)	N(1)–C(11)–C(12)	110.7(3)
C(2)–C(3)–C(4)	122.6(3)	C(11)–C(12)–C(9)	106.3(3)
C(2)–C(3)–C(31)	125.8(3)	C(11)–C(12)–C(13)	125.4(3)
C(4)–C(3)–C(31)	111.5(3)	C(9)–C(12)–C(13)	127.8(2)
O(31)–C(31)–N(31)	120.6(3)	C(17)–C(16)–Cl(16)	120.3(12)
O(31)–C(31)–C(3)	120.7(3)	C(15)–C(16)–Cl(16)	120.2(3)
N(31)–C(31)–C(3)	118.0(3)	C(20)–C(19)–N(2)	112.7(3)
C(5)–C(4)–C(3)	122.0(5)	C(19)–C(20)–C(21)	108.6(3)
C(4)–C(5)–C(6)	131.1(6)	C(20)–C(21)–C(22)	110.7(2)
C(4)–C(5)–C(10)	115.1(5)	C(23)–C(22)–C(21)	112.5(2)
C(6)–C(5)–C(10)	113.9(5)	N(2)–C(23)–C(22)	113.4(2)
C(5)–C(6)–C(7)	121.6(4)	C(2)–N(2)–C(23)	132.1(2)
C(6)–C(7)–C(8)	122.1(3)	C(2)–N(2)–C(19)	110.3(2)
C(9)–C(8)–C(7)	113.5(3)	C(23)–N(2)–C(19)	114.5(2)
C(10)–C(9)–C(12)	106.5(3)		

Table 11. Selected bond lengths *d* (Å) in structure **V**

Bond	*d*	Bond	*d*	Bond	*d*	Bond	*d*
N(1)–C(2)	1.334(6)	C(4)–C(5)	1.392(7)	C(9)–C(10)	1.512(7)	C(12)–C(13)	1.496(6)
N(1)–C(10)	1.346(6)	C(5)–C(10)	1.399(6)	C(11)–C(31)	1.389(6)	C(16)–Cl(16)	1.729(5)
C(2)–O(2)	1.355(5)	C(5)–C(6)	1.507(6)	C(11)–C(12)	1.415(7)	C(31)–N(31)	1.345(7)
C(2)–C(3)	1.388(6)	C(6)–C(7)	1.469(9)	C(11)–O(2)	1.416(6)	N(31)–H(31*A*)	0.95(7)
C(3)–C(4)	1.389(6)	C(7)–C(8)	1.429(10)	C(12)–O(12)	1.255(6)	N(31)–H(31*B*)	0.79(6)
C(3)–C(31)	1.435(7)	C(8)–C(9)	1.507(7)				

bonds are substantially shortened and the formally double C–C bonds are significantly lengthened. However, it is possible to distinguish the bond chain [C(2)–C(3), C(4)–C(5), C(9)–C(10), C(11)–C(12) bonds] that corresponds to a tetraene structure typical of indolizine.

The piperidine fragment of the molecule adopts a chair conformation: the plane passes through the C(19),

Table 12. Selected bond angles ω (deg) in structure **V**

Angle	ω	Angle	ω
C(2)–N(1)–C(10)	114.4(4)	C(5)–C(10)–C(9)	120.8(4)
N(1)–C(2)–O(2)	121.3(4)	C(31)–C(11)–C(12)	126.7(4)
N(1)–C(2)–C(3)	126.7(4)	C(31)–C(11)–O(2)	109.9(4)
O(2)–C(2)–C(3)	112.0(4)	C(12)–C(11)–O(2)	123.2(4)
C(2)–C(3)–C(4)	117.4(5)	O(12)–C(12)–C(11)	117.4(4)
C(2)–C(3)–C(31)	106.0(4)	O(12)–C(12)–C(13)	118.6(4)
C(4)–C(3)–C(31)	136.5(5)	C(11)–C(12)–C(13)	124.0(5)
C(3)–C(4)–C(5)	118.4(4)	C(17)–C(16)–Cl(16)	118.9(4)
C(4)–C(5)–C(10)	118.6(4)	C(15)–C(16)–Cl(16)	120.0(4)
C(4)–C(5)–C(6)	119.9(4)	C(2)–O(2)–C(11)	105.6(3)
C(10)–C(5)–C(6)	121.4(4)	N(31)–C(31)–C(11)	126.2(5)
C(7)–C(6)–C(5)	114.0(4)	N(31)–C(31)–C(3)	127.5(4)
C(8)–C(7)–C(6)	117.7(7)	C(11)–C(31)–C(3)	106.3(4)
C(7)–C(8)–C(9)	115.5(6)	C(31)–N(31)–H(31A)	118(4)
C(8)–C(9)–C(10)	115.1(5)	C(31)–N(31)–H(31B)	123(5)
N(1)–C(10)–C(5)	124.4(5)	H(31A)–N(31)–H(31B)	119(7)
N(1)–C(10)–C(9)	114.7(4)		

Table 13. Parameters of interatomic contacts in the studied structures

D–H	d(D–H)	d(H···A)	ωDHA	d(D···A)	A
			III		
N(31)–H(31A)	0.86(1)	2.06(1)	164.6(8)	2.90(2)	O(12) [–x + 3/2, y + 1/2, –z + 3/2]
N(31)–H(31B)	0.86(1)	2.24(1)	130.9(7)	2.87(2)	O(2)
N(31)–H(31B)	0.86(1)	2.54(1)	120.9(7)	3.07(2)	O(13) [–x + 1/2, y + 1/2, –z + 3/2]
			IV		
N(31)–H(31A)	0.86	2.22	138	2.92	O(31) [–x + 1, –y + 1, –z]
N(31)–H(31B)	0.86	2.13	159	2.95	O(31) [x, y – 1, z]
			V		
N(31)–H(31A)	0.95(7)	2.10(7)	124(5)	2.750(7)	O(12)
N(31)–H(31B)	0.79(6)	2.47(7)	150(6)	3.176(7)	N(1) [x + 1, y, z]

Fig. 5. Molecular structure and atomic numbering for compound **IV**.

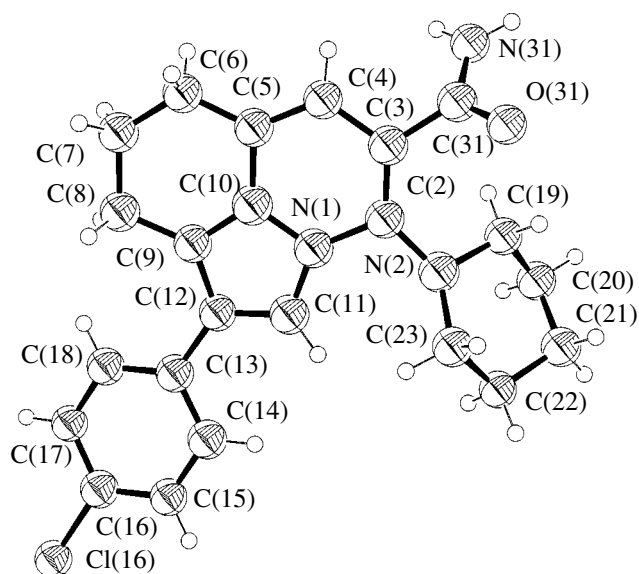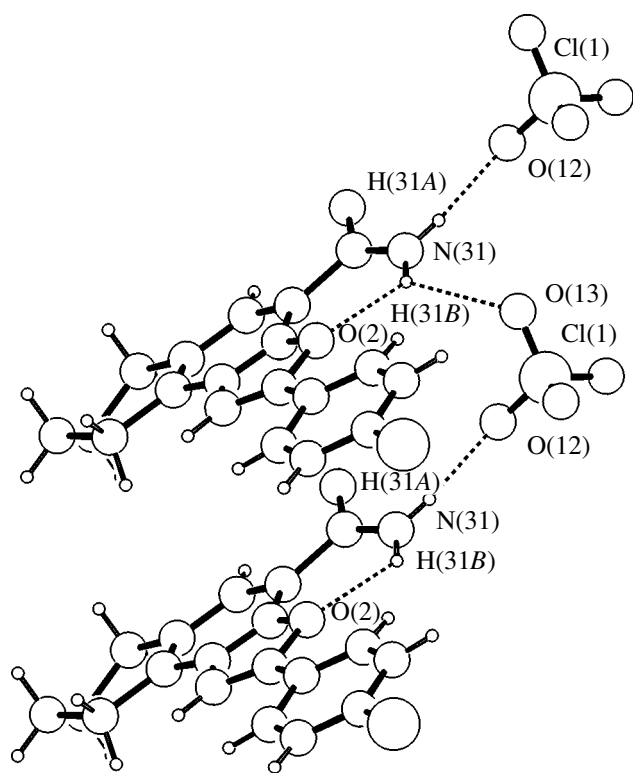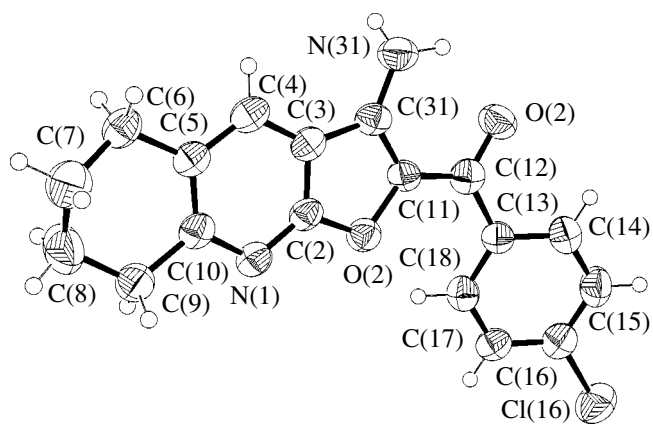**Fig. 6.** Molecular structure and atomic numbering for compound **V**.

Fig. 7. Spatial arrangement of hydrogen bonds in structure **III**.
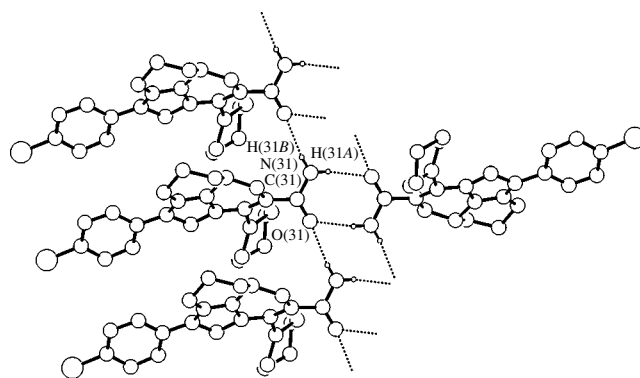

Fig. 8. Spatial arrangement of hydrogen bonds in structure **IV**.

The amide group of the molecule forms a system of hydrogen bonds in which the hydrogen atoms of the NH$_2$ group simultaneously interact with the oxygen atoms of the amide fragments of two different molecules. The parameters of the hydrogen bonds are presented in Table 13, and their spatial arrangement is given in Fig. 8.

In molecule **V**, the C(6) and C(9) atoms and the exocyclic amine group are located in the plane of the heterocyclic bicycle, whereas the C(7) and C(8) atoms deviate from this plane by –0.28 and 0.23 Å, respectively. As in molecule **IIa**, the C(7)–C(8) distance is shortened as a result of strong anisotropy of thermal vibrations of these atoms. However, taking into account the correction for anisotropy of thermal vibrations [16], this distance corresponds to the C–C single bond between the sp^3-hybridized carbon atoms.

The dihedral angle between the planes of the phenyl ring and the heterocyclic bicycle is equal to 20.0(2)°. This suggests a weak conjugation of the phenyl ring with the heterocyclic fragment.

The hydrogen atoms of the amino group and the nitrogen atom of the pyridine ring of the molecule form
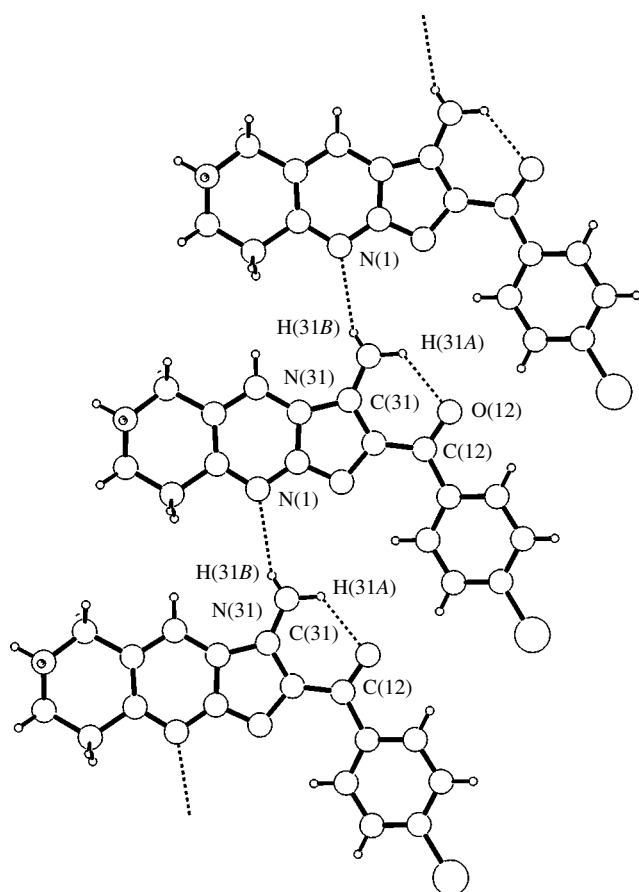
C(20), C(22), and C(23) atoms, and the C(21) and N(2) atoms deviate from the plane by 0.70 and –0.47 Å, respectively. The piperidine ring is rotated with respect to the plane of the heterocyclic fragment by 58.3(1)°.

The plane of the phenyl ring is rotated with respect to the plane of the heterocyclic fragment by 17.6(5)°.

Fig. 9. Spatial arrangement of hydrogen bonds in structure **V**.

intermolecular hydrogen bonds that link molecules into chains. The amino group also participates in the formation of the N(31)–H(31A)···O(12) intramolecular hydrogen bond and is responsible for the planar structure of the N(31)H$_2$–C(31)=C(11)–C(12)=O(12) fragment with the maximum deviation (by 0.03 Å) from the plane. The parameters of the hydrogen bonds are listed in Table 13, and their spatial arrangement is shown in Fig. 9.

REFERENCES

1. K. Gewald, J. Prakt. Chem. **318**, 313 (1976).
2. C.-F. Lin, Y.-F. Lin, Y.-C. Lo, *et al.*, Heterocycles **53**, 15 (2000).
3. E. V. Babaev, A. V. Efimov, D. A. Maiboroda, and K. Jug, Eur. J. Org. Chem., 193 (1998).
4. J. B. Paine, J. Heterocycl. Chem. **24**, 351 (1987).
5. D. V. Al'bov, O. S. Mazina, V. B. Rybakov, E. V. Babaev, V. V. Chernyshev, and L. A. Aslanov, Kristallografiya **49** (2), 208 (2004) [Crystallogr. Rep. **49**, 158 (2004)].
6. *Enraf–Nonius CAD4 Software: Version 5.0* (Enraf–Nonius, Delft, Netherlands, 1989).
7. L. J. Farrugia, *WinGX: X-ray Crystallographic Programs for Windows* (Univ. of Glasgow, UK, 2003).
8. G. M. Sheldrick, *SHELX97: Program for the Solution and Refinement of Crystal Structures* (Univ. of Göttingen, Germany, 1997).
9. J. W. Visser, J. Appl. Crystallogr. **2**, 80 (1969).
10. J. J. P. Stewart, *MOPAC 6.0: QCPE Program No. 455* (Department of Chemistry, Indiana Univ., Bloomington, USA, 1990).
11. *PCMODEL 7.0: Molecular Modelling Software for the Windows 95/NT. Sarena Software* (Bloomington, USA, 1999).
12. V. V. Chernyshev and H. Schenk, Z. Kristallogr. **213**, 1 (1998).
13. V. B. Zlokazov and V. V. Chernyshev, J. Appl. Crystallogr. **25**, 447 (1992).
14. M. N. Burnett and C. K. Johnson, ORTEP. Report ORNL 6895 (Oak Ridge National Laboratory, Tennessee, USA, 1996).
15. L. J. Farrugia, *ORTEP-3 for Windows* (Univ. of Glasgow, UK, 2003).
16. W. R. Busing and H. A. Levy, Acta Crystallogr. **17**, 142 (1964).

Translated by O. Borovik-Romanova